Prospects for Galactic dark matter searches with the Cherenkov Telescope Array (CTA)

Dissertation

zur Erlangung des akademischen Grades

doctor rerum naturalium

(Dr. rer. nat.)

im Fach Physik

eingereicht an der
Mathematisch-Naturwissenschaftlichen Fakultät
der Humboldt-Universität zu Berlin

von

Dipl. Phys. Caspar Moritz Hütten

Präsidentin der Humboldt-Universität zu Berlin:
Prof. Dr.-Ing. Dr. Sabine Kunst

Dekan der Mathematisch-Naturwissenschaftlichen Fakultät:
Prof. Dr. Elmar Kulke

Gutachter/innen:
1. Dr. Gernot Maier,
   Deutsches Elektronen-Synchrotron, Zeuthen
2. Prof. Dr. Elisa Bernardini,
   Humboldt-Universität zu Berlin
3. Prof. Dr. Gianfranco Bertone,
   Universität Amsterdam

Eingereicht am 6. Dezember 2016

Tag der mündlichen Prüfung: 21. April 2017

Für meine Eltern

Contents

Abstract

In the current understanding of structure formation in the Universe, the Milky Way is embedded in a clumpy halo of dark matter (DM). Regions of high DM density are expected to emit enhanced γ-radiation from the DM relic annihilation. This γ-radiation can possibly be detected by γ-ray observatories on Earth, like the forthcoming Cherenkov Telescope Array (CTA). This dissertation presents a semi-analytical density modeling of the subclustered Milky Way DM halo, and the γ-ray intensity at Earth from DM annihilation in Galactic subclumps is calculated for various substructure models. It is shown that the modeling approach is able to reproduce the γ-ray intensities obtained from extensive dynamical DM simulations, and that it is consistent with the DM properties derived from optical observations of dwarf spheroidal galaxies. A systematic confidence margin of plausible γ-ray intensities from Galactic DM annihilation is estimated, encompassing a variety of previous findings. The average distances, masses, and extended emission profiles of the γ-ray-brightest DM clumps are calculated. The DM substructure models are then used to draw reliable predictions for detecting Galactic DM density clumps with CTA, using the most recent benchmark calculations for the performance of the instrument. A Likelihood-based calculation with CTA analysis software is applied to find the instrumental sensitivity to detect the γ-ray-brightest DM clump in the projected CTA extragalactic survey. An alternative Likelihood-based analysis method is developed, to detect DM substructures as anisotropies in the angular power spectrum of the extragalactic survey data. The analyses predict that the CTA extragalactic survey will be able to probe annihilation cross sections of $\langle\sigma v\rangle \gtrsim 1\times 10^{-24}\,\mathrm{cm^3\,s^{-1}}$ at the 95% confidence level for a DM particle mass of $m_\chi \sim 500\,\mathrm{GeV}$ from DM annihilation in substructures. This sensitivity is compatible with long-term observations of single dwarf spheroidal galaxies with CTA. Independent of a particular source model, it is found that the CTA extragalactic survey will be able to detect anisotropies in the diffuse γ-ray background above 100 GeV at a relative amplitude of $C_\mathrm{P}^F \gtrsim 10^{-2}$.

Zusammenfassung

Im heutigen Standardmodell der kosmischen Strukturbildung wird angenommen, dass die Milchstraße in einen inhomogenen Halo Dunkler Materie DM eingebettet ist. Dabei emittieren Bereiche, welche eine erhöhte Dichte Dunkler Materie aufweisen, vermehrt γ-Strahlung, welche durch die Paarvernichtung von DM-Teilchen erzeugt wird. Diese γ-Strahlung könnte mit dem zukünftigen Cherenkov Telescope Array (CTA) nachgewiesen werden. Die vorliegende Arbeit beschreibt einen semianalytischen Ansatz zur Modellierung der Dichteverteilung von DM im Galaktischen Halo. Aus den verschiedenen Substrukturmodellen wird daraufhin die γ-Strahlungsintensität, welche die Erde erreicht, berechnet. Es wird gezeigt, dass der Modellierungsansatz in der Lage ist, die Ergebnisse komplexer dynamischer DM-Simulationen zu reproduzieren, und dass der Ansatz konsistent mit den Substruktureigenschaften der DM ist, welche aus optischen Beobachtungen von spheroidalen Zwerggalaxien abgeleitet wurden. Eine Spannbreite plausibler γ-Strahlungsintensitäten aufgrund der Paarvernichtung Galaktischer DM wird vorgeschlagen, welche die Vorhersagen verschiedener früherer Studien umfasst, und es werden die durchschnittlichen Massen, Abstände und ausgedehnten Strahlungsprofile der γ-strahlungsintensivsten DM-Verdichtungen berechnet. Schließlich werden die DM-Modelle für eine umfassende Berechnung der Nachweismöglichkeit Galaktischer Substrukturen mit CTA verwendet. Das Verhalten des CTA Detektorsystems wird dabei durch die aktuellste Berechnung der voraussichtlichen Leistungsfähigkeit des Instruments beschrieben. Die instrumentelle Sensitivität zum Nachweis der γ-strahlungsintensivsten DM-Substruktur wird für eine mit CTA geplanten großflächigen Himmelsdurchmusterung außerhalb der Galaktischen Ebene berechnet. Die Berechnung wird mit CTA Analyse-Software und einer Methode durchgeführt, welche auf einer Likelihood beruht. Eine alternative, ebenfalls Likelihood-basierte Analysemethode wird entwickelt, mit welcher DM-Substrukturen als räumliche Anisotropien im Multipolspektrum des Datensatzes einer Himmelsdurchmusterung nachgewiesen werden können. Die Analysen ergeben, dass eine Himmelsdurchmusterung mit CTA und eine anschließende Suche nach γ-Strahlung von DM-Substrukturen Wirkungsquerschnitte für eine Paarvernichtung in der Größenordnung von $\langle\sigma v\rangle \gtrsim 1 \times 10^{-24}\,\mathrm{cm^3\,s^{-1}}$ für eine DM-Teilchenmasse von $m_\chi \sim 500\,\mathrm{GeV}$ auf einem Vertrauensniveau von 95% ausschließen kann. Diese Sensitivität ist vergleichbar mit Langzeitbeobachtungen einzelner Zwerggalaxien mit CTA. Eine modellunabhängige Analyse ergibt, dass eine Himmelsdurchmusterung mit CTA Anisotropien im diffusen γ-Strahlungshintergrund oberhalb von 100 GeV für relative Schwankungen von $C_\mathrm{P}^F \gtrsim 10^{-2}$ nachweisen kann.

Acknowledgments

This dissertation was made possible by the PhD fellowship of the Research Training Group 1504, “Mass, Spectrum, Symmetry”, of the German Research Foundation (DFG) at the Humboldt-University Berlin and DESY Zeuthen. Besides the financial funding, attending the block courses of the research training group and workshops of the Humboldt Graduate School was an essential help to complete this dissertation.

Finishing the thesis would not have been possible without the personal support of many people. First of all, I would like to thank Gernot Maier for initiating and supervising the project. He always supported me to freely pursue my scientific interests and to present my work at summer schools and conferences. Being part of the VERITAS collaboration gave me the unique opportunity to work with the VERITAS telescopes at the Fred Lawrence Whipple Observatory in Arizona, providing indispensable insights into the experimental methods of γ-ray astronomy, and allowed me to discuss my research at many collaboration meetings and conference calls.

I am very grateful to Céline Combet and David Maurin (LPSC Grenoble), who accompanied the project over almost the whole course of the doctorate, and who helped me to significantly improve the quality of the work and the final manuscript. It would have been a much harder task to safely navigate between all the thesis’ cliffs and maelstroms without your guidance, the many extensive discussions, and your encouragement. Merci!

I would like to say a big “Thank you” to Anna O’Faoláin de Bhróithe for her careful proofreading of the manuscript, her critical comments, and helping to improve the grammar and language of the text. Of course, remaining linguistic errors are still mine.

Rolf Bühler, Orel Gueta, Iftach Sadeh, and Arne Schönwald provided many useful suggestions that increased the readability and quality of the dissertation. To Johanna Biank (MPIWG) I owe gratitude for enlightening remarks on the Greek quotations above the Chapters 1 and 4.

I wish to thank Nathan Kelley-Hoskins for sharing his outstanding programming skills, Meike de With for instructive discussions, Lucie Gérard for her valuable help with the CTA analysis software, the entire VERITAS group at DESY for the everyday advice, and all the PhD students at DESY for creating a pleasant work environment over the last three years.

Also, I would like to thank David Schinkel (Univ. Jena) for several useful suggestions of how to organize the literature, the document, and structuring the writing process of a dissertation.

It was Prof. Jürgen Renn from the Max-Planck-Institute for the History of Science Berlin (MPIWG), who initiated my interest in the topic of dark matter. The supplementary chapter in this thesis on the history of dark matter emerged from insightful discussions with him, Alexander Blum (MPIWG), Tricia Close-Koenig (Univ. Strasbourg), and Martin Lemke (Univ. Rostock).

Finally, I would like to thank my brother Felix, my parents, and all the friends who never doubted the successful completion of this dissertation.

1 | Introduction

> *Πάντα λίθον κίνει*
> *Turn every stone!*
>
> Epitomes of Zenobius (∼ 125 AD)[1]

Revealing the nature of dark matter (DM) constitutes one of the most challenging tasks for modern astrophysics and cosmology. At many astronomical scales, several observations consistently indicate that a large fraction of mass in our Universe is of unknown origin. From individual galaxies up to the Universe as a whole, there is about five times more mass present than the known matter budget can account for (Einasto, 2009). However, so far, DM has manifested its existence only through gravitational interaction. The possibility remains that there is no DM at all, and that rather we lack a fundamental understanding of gravitation at astronomical scales. Searching for non-gravitational evidence for DM is one way to resolve this question.

The most promising candidate to explain the numerous gravitational indications of DM is a long-lived weakly interacting massive particle (WIMP), not included in the Standard Model of particle physics. Such particles naturally result from theories like supersymmetric extensions of the Standard Model. These theories might solve various problems in particle physics like the hierarchy problem and fine-tuning (Martin, 2010). The fact that open questions in different fields of physics could be solved by a common concept, makes the scenario of new elementary particles to explain DM ("particle DM") overwhelmingly attractive. The search for DM thereby has become a challenge beyond the astrophysical case alone, at the borders between astrophysics, cosmology, and particle physics.

An important consequence of the WIMP scenario is that these particles are predicted to self-annihilate or decay into a variety of Standard Model particles (Bergström, 2009). Probing the secondary products emerging in these processes may provide an unambiguous – though indirect – hint for the existence of DM. In particular, final state photons in the same energy regime as the

---

[1] Cited after von Leutsch and Schneidewin (1839, p. 146).

mass of the primary particle are produced. As the WIMP mass is expected to be in the range of Gigaelectronvolt (GeV) to Teraelectronvolt (TeV), this facilitates an indirect detection of DM by γ-ray telescopes. Regions in the Universe with a high DM density would emit characteristic γ-radiation, which could be detected by γ-ray telescopes on Earth.

In this thesis, the sensitivity of the indirect detection of DM with the ground-based γ-ray Cherenkov Telescope Array (CTA, Acharya et al., 2013) is investigated. Several astrophysical targets suggest a high density of DM and have been considered for its indirect detection via γ-rays. Among them are the central region of our Galaxy, neighboring dwarf spheroidal galaxies, and galaxy clusters. This thesis focuses on another population, which constitutes a "high risk, high reward target" (Conrad et al., 2015) for an indirect DM search: Hierarchical structure formation in our Universe leaves a large number of DM clumps in the surroundings of today's Milky Way (Springel et al., 2008a; Diemand et al., 2008). These clumps are part of a large DM halo enclosing the Milky Way disk and are dubbed as "subhalos" of the Galaxy's DM host halo.[2] While the heaviest of these subhalos are supposed to harbor the satellite galaxies of the Milky Way, their majority may be lacking any baryonic counterpart. As such "dark" subhalos are not traced by luminous matter, the only evidence for their presence would be provided by γ-radiation from self-annihilation in their central cusps (and also possibly by gravitational lensing). Whereas the presence, distribution, and sizes of these subhalos are very uncertain, a γ-ray detection from entirely dark spots in the sky, with a characteristic spectral and constant temporal signature, would support an unambiguous interpretation in favor of DM.

Searches for Galactic DM subhalos in γ-rays were already proposed twenty years ago (Lake, 1990; Silk and Stebbins, 1993). For almost a decade now, the *Fermi*-Large Area Telescope (LAT) satellite (Atwood, 2009) has been used to search for localized DM emission from unknown objects in the sky (e.g., Zechlin and Horns, 2012; Bertoni et al., 2015; Schoonenberg et al., 2016). Whereas space-borne γ-ray detectors are sensitive to γ-rays up to several hundreds of GeV, ground-based instruments can be used to detect γ-rays with energies larger than several tens of TeV (Funk, 2015). Thus, ground-based instruments are able to probe the high-mass regime of the WIMP parameter space. Most ground-based γ-ray observatories exhibit a comparably small field of view, limited to a diameter of $\lesssim 5^\circ$ for current instruments. This impedes large-area γ-ray surveys from the ground, which are needed for a search for DM subhalos. However, this will change with the forthcoming CTA instrument. For the first time, the atmospheric Cherenkov technique for ground-based γ-ray observation will be used to perform a large-area survey in γ-rays. This thesis investigates how a large-area sky survey with CTA will be able to constrain the abundance and properties of DM in Galactic subhalos.

---

[2] Throughout this thesis, "Galaxy" and "Milky Way" synonymously refer to the system consisting of dark and baryonic matter, extending far beyond the Milky Way disk (see Chapters 2 and 4).

For this purpose, this thesis presents a careful assessment of the γ-ray fluxes expected from Galactic DM subhalos. Subsequently, two different methods for analyzing the data of a CTA large-area survey in a search for subhalos are discussed. The first method studies the γ-ray flux level from DM annihilation at which a dark subhalo can be resolved in the survey. This flux level can then be translated into the DM annihilation cross section, for which a signal should be detected, or, which would be excluded by a non-detection.

The second method is to consider γ-rays from the whole Galactic DM subhalo population, without seeking to resolve the individual objects. This is done by probing the diffuse γ-ray background (DGRB; Dermer, 2007), which contains all unresolved residual γ-ray emission at high Galactic latitudes, for spatial anisotropies. In particular, the DGRB may contain unresolved γ-ray emission from Galactic and extragalactic DM (Bringmann et al., 2014). The space-borne *Fermi*-LAT has recently found significant anisotropies in the DGRB on scales $\lesssim 2^\circ$ in the energy band between $0.5 - 500\,\mathrm{GeV}$ (Ackermann et al., 2012a; Fornasa et al., 2016), which have been discussed in the context of DM (e.g., Ando and Komatsu, 2013). Because the Galactic DM halo is assumed to be highly clumpy, γ-rays from Galactic DM annihilation might significantly contribute to an anisotropic DGRB (Fornasa et al., 2013).

Investigating CTA's performance to detect spatial anisotropies in the very-high-energy (VHE, $E \gtrsim 100\,\mathrm{GeV}$) γ-ray sky is of great interest, even beyond the case of DM. At the highest γ-ray energies, the overall γ-ray sky is expected to become more and more anisotropic (Ackermann et al., 2016). The CTA instrument will have a higher sensitivity in the VHE γ-ray band than the *Fermi*-LAT, as well as a superior angular resolution. Given that anisotropies have already been detected by the *Fermi*-LAT, an analogous search for small-scale anisotropies from high-mass DM annihilation and astrophysical sources with CTA is an obvious way forward. The ability of CTA to resolve small-scale anisotropies in the DGRB has been recently investigated by Ripken et al. (2014). This dissertation continues their work, based on a more up-to-date and realistic modeling of CTA's instrumental performance.

The dissertation is divided into four chapters. Chapter 2 introduces the concept of and evidence for DM. The WIMP paradigm for DM is motivated, and the various efforts that are undertaken for the non-gravitational detection of these particles are outlined. At the end of the chapter, the key concepts for an indirect detection of annihilating DM in γ-rays are presented.

Chapter 3 outlines how astrophysical γ-rays can be detected from the ground and introduces the CTA instrument. By describing the detection method and the instrumental layout, the key benefits and challenges of ground-based γ-ray astronomy become evident. The latest projections of the CTA instrumental performance, which are used for the studies in Chapter 5, are presented. At the end of Chapter 3, the space-borne *Fermi*-LAT instrument is shortly introduced.

Chapter 4 presents the modeling of the clumpy Galactic DM distribution, as the basis for all subsequent predictions of the γ-ray fluxes from DM and the sensitivity of CTA. A semi-analytical modeling approach with the `CLUMPY` code is chosen, complementary to relying on full dynamical DM simulations. This approach is able to reproduce the results from dynamical simulations, but is not limited to them; and a self-consistent modeling of different DM configurations is possible at low computational costs. Various models of the Galactic DM substructure are compared in hundreds of statistical realizations, and the uncertainty of key parameters is investigated. Reliable statements about the ensemble average γ-ray intensities (i.e., the spatially extended emission) from DM subhalos observed on Earth are derived, and the average masses and distances of the γ-ray-brightest DM clumps are given. The modeling is cross-checked with the DM properties of dwarf spheroidal galaxies. The results of this chapter have been obtained in collaboration with V. Bonnivard, D. Maurin, and C. Combet, where the primary contribution was made by the author of this thesis. An update of the `CLUMPY` code has been published in Bonnivard et al. (2015b), and the DM modeling has been already outlined in Hütten et al. (2016).

Chapter 5 develops the methods for detecting DM subhalos with the CTA instrument and presents the resulting sensitivity projections. This chapter contains three main results: In the first section, a model for the large-area CTA extragalactic survey is presented, based on the latest projections of the instrumental performance. These projections rely on extensive simulations, which have been performed by G. Maier and the Monte-Carlo working group of the CTA collaboration. It is shown how different pointing strategies influence the homogeneity of the survey exposure. In the second and third sections, the sensitivity of CTA to resolve individual Galactic DM subhalos or to detect Galactic DM subhalos as anisotropies in the DGRB is presented. The latter method is also discussed in a model-independent astrophysical context.

After the conclusions (Chapter 6), the thesis is followed by a supplementary essay on the history of the dark matter concept (Chapter 7) and by an appendix with additional figures and calculations. Several results presented in this dissertation have been derived in tight collaboration with other people and rely on efforts that have been conducted by many persons. However, this thesis is restricted to the author's own contribution to these works. It is quoted whenever figures and tables are used which have been already included in Bonnivard et al. (2015b) or Hütten et al. (2016), and whenever third-party results are used.

This ancient Greek adage, "Turn [or literally, 'move'] every stone!", quoted above the thesis' introduction, can be well ascribed to the search for DM: No clear evidence of the nature of DM has yet been found. As long as there is no unambiguous experimental indication of its properties, different detection prospects have to be pursued, tailored to a variety of promising physics candidates of DM. As different potential DM targets and detection methods are subject to inherent measurement uncertainties, complementary targets and methods need to be evaluated: figuratively, every stone has to be turned. This thesis serves this endeavor, by contributing a detailed study to the numerous efforts to solve the puzzle of DM.

2 | Dark matter

It cannot be seen, cannot be felt,
Cannot be heard, cannot be smelt.
It lies behind stars and under hills,
And empty holes it fills.

J.R.R. Tolkien (1937), The Hobbit.

The nature of dark matter (DM) is yet unknown. In this sense, the very existence of DM is not proven. However, there is a collection of astrophysical observations which are difficult to explain without postulating the existence of some DM. In Section 2.1, a synopsis of the evidence for DM is given. This is the general background which motivates all kind of searches for hypothetical DM, in particular the methods presented in this thesis. In Section 2.2, the specific DM candidates investigated in this thesis, namely, weakly interacting massive particles (WIMPs), are introduced. In Section 2.3, it is outlined how such WIMPs can be possibly detected, with the focus on the indirect detection with the methods of high-energy astrophysics.

2.1. Evidence for dark matter

2.1.1. Rotation curves in the Milky Way and remote spiral galaxies

As this thesis is about dark matter in the Milky Way (MW), the evidence for DM in the MW shall be discussed first. The visible MW consists of stars, dust and molecular clouds, forming a central bulge at galactocentric radii $R \lesssim 3\,\mathrm{kpc}$, and a thin disk up to $R \lesssim 30\,\mathrm{kpc}$. The surface density the MW disk can be surprisingly well described as decreasing exponentially from the center (Freeman, 1970):

$$\Sigma(R) = \frac{M_{\mathrm{disk}}}{2\pi\, R_{\mathrm{s}}^2}\, e^{-R/R_{\mathrm{s}}} = \Sigma_0\, e^{-R/R_{\mathrm{s}}}. \tag{2.1}$$

In Figure 2.1 (top left) it is shown that this description is in good agreement with the measured surface density of stars and gas in the range $5\,\mathrm{kpc} \lesssim R \lesssim 30\,\mathrm{kpc}$, adopting a scale radius $R_{\mathrm{s}} = 3\,\mathrm{kpc}$ and a local surface density $\Sigma(R_\odot = 8\,\mathrm{kpc}) = 6.8 \times 10^7\,\mathrm{M}_\odot/\mathrm{kpc}^2$ (Bovy and Rix, 2013).[1] Below, the mass of this disk enclosed within radius R, $M_{\mathrm{disk}}(R)$, is shown (Figure 2.1, middle left). From the gravitational potential Φ of the disk one can calculate the average speed $V(R)$ of stars in stable circular orbits in the disk,

$$V(R)^2 = R\, \frac{\partial \Phi}{\partial R'}\bigg|_{R'=R,\, Z=0}. \tag{2.2}$$

This prediction of the stars rotation curve, $V(R)$, is shown Figure 2.1 (bottom left, black solid line). On the same figure, a summary from various measurements of the actual stars velocities perpendicular to the galactocentric radial vector in the MW is overplotted, compiled by Iocco et al. (2015). It can clearly be seen that the prediction from the mass estimation significantly underestimates the measured velocities, even within the large measurement errors. Provided that the MW is in stationary equilibrium, this leads to two conclusions: (i) either the prediction of the rotation curves according to Equation 2.2 is wrong, or (ii), the estimation of the mass, Equation 2.1, acting on the stars is heavily underestimated. The first conclusion results in the renouncement of Newtonian and General relativistic gravity, and led to the postulation of alternative theories like the Modified Newtonian Dynamics (MOND) by Milgrom (1983). If one does not abandon the framework of classical gravitation, then Figure 2.1 (bottom left) shows the evidence for DM in the Milky Way.

In the right column of Figure 2.1, it is shown how the discrepancy is resolved if a spherical halo of DM is postulated, with its density parametrized by a Navarro-Frenk-White (NFW) profile (Navarro et al., 1996, see Equation B.2) and a total mass of $\rho_{\mathrm{DM}}(8\,\mathrm{kpc}) = 4\,\mathrm{GeV/cm}^3$. Figure 2.1

---

[1] Note that the dynamical mass measurement by Bovy and Rix (2013) is not independent from the DM content, which the authors account for.

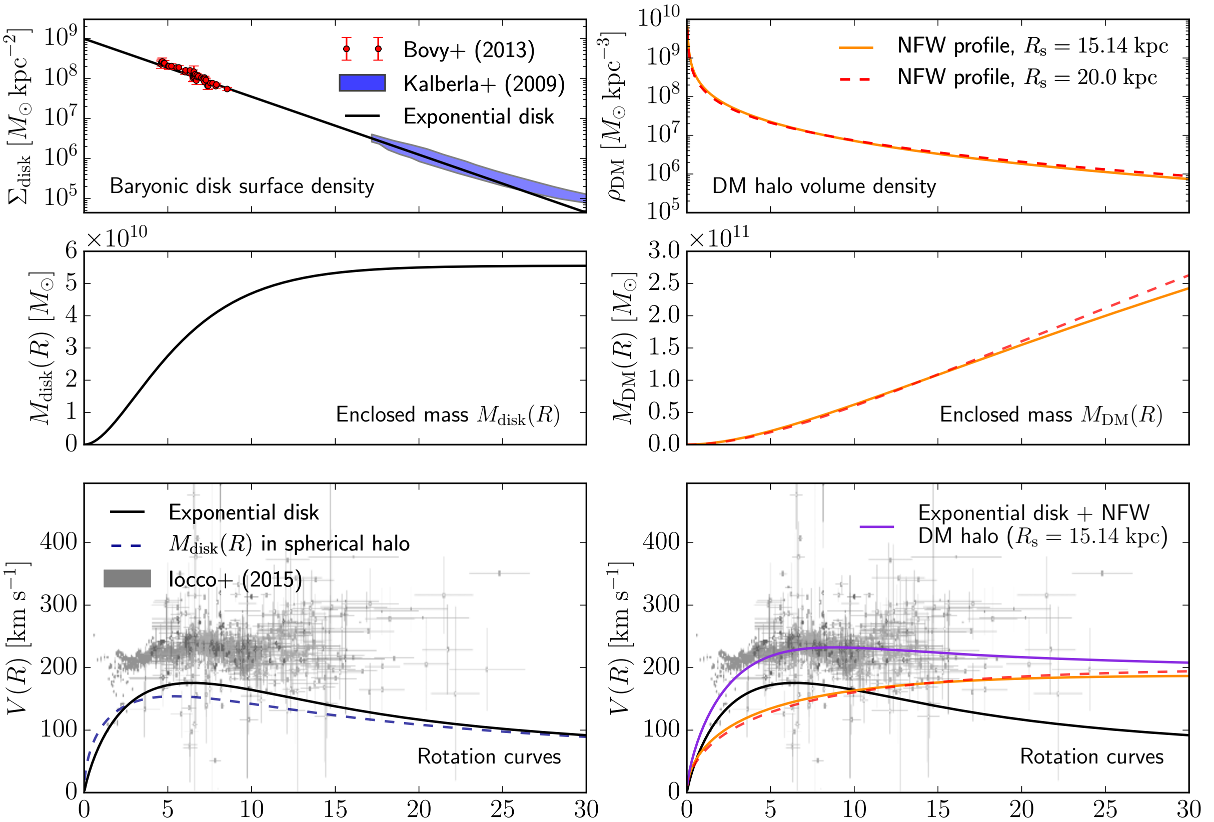

(a) R [kpc] (baryonic disk only)

(b) R [kpc] (baryonic disk + spherical DM halo)

Figure 2.1.: Evidence for DM in the central Milky Way. The left column shows a simple model of the Galaxy without DM, the right column when adding a spherical DM halo. *Top left:* Exponential surface density of the MW disk. The red points mark dynamical measurements of stars by Bovy and Rix (2013); the blue-shaded band denotes the abundance of neutral hydrogen in the outskirts of the MW (Kalberla and Kerp, 2009). *Middle left:* Mass of the disk within radius R. *Bottom left:* Rotation curve caused by the disk alone (black-solid line), and a spherical density distribution of $M_{\rm disk}(R)$ (blue-dashed line; i.e., the discrepancy is increased when taking into account the vertical extension of the disk). The data points show various measurements as reviewed by Iocco et al. (2015). *Top right:* Spherical Navarro-Frenk-White (NFW) DM density profile, with $\rho_{\rm DM}(8\,{\rm kpc}) = 4\,{\rm GeV/cm^3}$, and two different scale radii, R_s. $R_s = 20\,{\rm kpc}$ is often used in the literature, whereas $R_s = 15.14\,{\rm kpc}$ is used in the DM modeling of the MW in Chapter 4. It can be seen that this difference results in a insignificantly different mass distribution within the central 30 kpc. *Middle right:* Enclosed DM mass. The mass diverges for a NFW profile, indicating that this density model is not valid at very large distances $\gtrsim 200\,{\rm kpc}$. *Bottom right:* Rotation curve in the Galactic plane as sum of the baryonic disk and DM mass components. The discrepancy between the model and the data at small R is resolved when correctly modeling the central bulge.

(bottom right) shows that adding this DM budget to the baryonic disk mass would bring the predicted rotation curves in good agreement with the observations.[2]

---

[2] The discrepancy at $R \lesssim 5\,{\rm kpc}$ can be fully resolved by taking into account the central bulge of the MW,

The total baryonic mass of the exponential MW disk model is $M_{\mathrm{b}} \approx M_{\mathrm{disk}} = 5.6 \times 10^{10}\, M_{\odot}$, in agreement with Dehnen and Binney (1998); Rix and Bovy (2013); Courteau et al. (2014). Adopting a total mass of the DM halo of the MW, $M_{\mathrm{DM}} \approx 1 \times 10^{12}\, \mathrm{M}_{\odot}$ (Nesti and Salucci, 2013; McMillan, 2017), one finally obtains a baryon fraction of $\Omega_{\mathrm{b}}/\Omega_{\mathrm{m}} \approx 5\%$ in the MW.[3] Note however, that the total budget of baryonic mass M_{b} is poorly constrained,[4] and the total virial DM mass relies on largely theoretical considerations (see Chapter 4).

Historically, the discrepancy between predicted and measured rotation curves was at first discovered in remote galaxies, where the measurement of absolute star velocities is much less intricate than for our own Galaxy. Already Babcock (1939) noted a discrepancy for the Andromeda galaxy. Finally, the notion of DM was generally accepted through the findings by Bosma (1978) and Rubin et al. (1978, 1980), who studied the rotation curves of more than 20 galaxies, which all showed an unexpected flattening in their outskirts. Figure 2.2 shows the rotation curves for three galaxies, which all show a behavior similar to the MW.

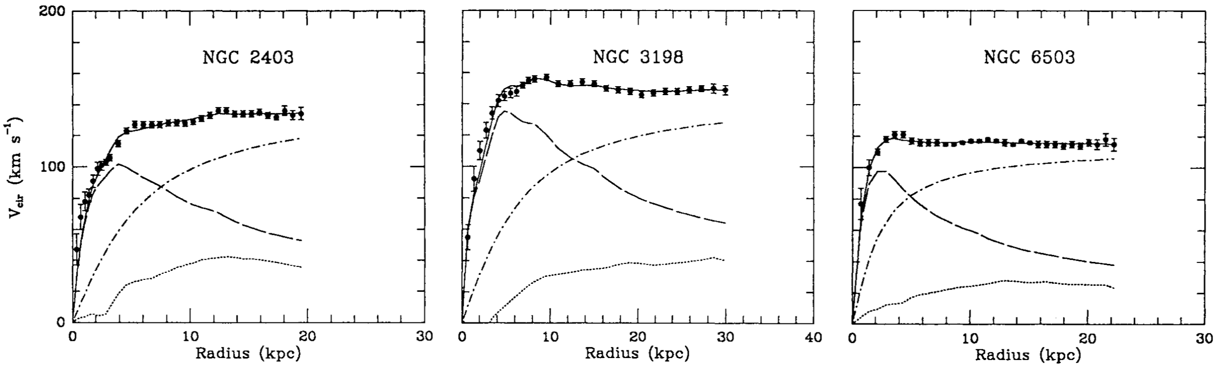

Figure 2.2.: Rotation curves for the three galaxies NGC 2403, NGC 3198, and NGC 6503. Figures taken from Begeman et al. (1991). The points denote the measurements, the dashed (dotted) lines the expected rotation curves from all visible matter (the gas mass alone), and the dot-dashed line the DM halo fit to bring the expectation in agreement with the data (square sum of all three components, solid line).

---

which has been neglected in this illustrative picture. For an exhaustive review of a complex MW modeling, see Chapter 4 of Courteau et al. (2014). The potential of the exponential disk, Equation 2.1, is given in Appendix A.1, and the potential of the NFW density profile is provided in Appendix B.1.

[3] Here and in the following, cosmic densities are expressed in terms of the Ω parameters, and the Hubble parameter, H, and the scale factor, a, are used. A short definition of these quantities is given in Appendix A.2.

[4] Also, the simple exponential model presented here underestimates the mass abundance in the very outskirts of the MW (as can be seen in Figure 2.1). The presence of ionized gas up to $r = 100\,\mathrm{kpc}$ could drive the total MW baryonic mass budget above $10^{11}\, M_{\odot}$ (Gupta et al., 2012). However, this fact does not alter the argument for the rotation curve measurements at $R \lesssim 30\,\mathrm{kpc}$.

2.1.2. Velocity dispersion in elliptical and spheroidal galaxies

The simple picture of circular orbits in a plane does not hold anymore for elliptical galaxies. Still, for those galaxies, the dynamical mass can be estimated by studying the random motion of the member stars. If the galaxy is in a stationary and collisionless equilibrium, the distribution function of the stars' average positions and momenta evolves according to the collisionless Boltzmann-equation. If the system can be considered spherically symmetric in phase-space, the Boltzmann-equation can be brought into the form of the spherical Jeans equation (Binney and Tremaine, 2008):

$$\frac{1}{\nu}\,\frac{\mathrm{d}\left(\nu\sigma_r^2\right)}{\mathrm{d}r} + \frac{2\sigma_r^2 - \sigma_\phi^2 - \sigma_\theta^2}{r} = -\frac{G\,M(r)}{r^2}\,. \tag{2.3}$$

Here, ν is the normalized number density of the member stars, which can be recovered from the surface brightness of the galaxy. The velocity dispersions $\sigma_r^2 = \langle v_r^2 \rangle$, $\sigma_\phi^2 = \langle v_\phi^2 \rangle$, and $\sigma_\theta^2 = \langle v_\theta^2 \rangle$ in radial and angular directions can be related to the line-of-sight velocity dispersion, $\sigma_{||}$, and the mass profile $M(r)$ can be estimated. However, the calculation of $M(r)$ from measured data is not trivial, and assumptions have to be made on the under-determined relation between $\sigma_{||}$ and $\sigma_{r,\phi,\theta}$. For details see, e.g., Bonnivard et al. (2014).

Results of such analyses show no clear evidence for DM in individual elliptical galaxies (Binney et al., 1990; Bertin et al., 1994; Méndez et al., 2001). However, this is commonly interpreted as a limitation of the applicability of a spherical Jeans analysis to such objects (Buote and Humphrey, 2012). Massive elliptical galaxies show bright X-ray emission, which results from a corona of hot gas surrounding them. From the gas temperature, the galaxy mass can be inferred independent of the dynamical measurement, which reveals a significantly higher mass budget for a variety of elliptical objects (Mathews and Brighenti, 2003; Ciotti and Pellegrini, 2004; Romanowsky et al., 2009, see also next subsection). Also, the effect of gravitational lensing can be observed for individual massive elliptical galaxies. However, observations of strong gravitational lensing alone provide rather uncertain mass estimations (Treu, 2010).

The Jeans analysis of spherical systems is still of practical use and of interest for this thesis. Dynamical measurements can be also applied to estimate the mass content of dwarf spheroidal galaxies (dSph) in the neighborhood of the MW. These dSph galaxies reveal a very low V-band mass-to-light ratio, $M/L_\mathrm{V} \gtrsim 100\,\mathrm{M}_\odot/\mathrm{L}_{\odot,\mathrm{V}}$, and even $M/L_\mathrm{V} \gtrsim 1000\,\mathrm{M}_\odot/\mathrm{L}_{\odot,\mathrm{V}}$ for some ultrafaint dSph objects (Simon and Geha, 2007; Simon et al., 2011). The common explanation for the high masses is that dSph galaxies are hosted by overdensities within the Galactic DM halo, and the movement of their member stars can be used to trace the DM content of these clumps (Walker et al., 2009; Charbonnier et al., 2011; Bonnivard et al., 2014, 2015a; Geringer-Sameth et al., 2015).

2.1.3. Galaxy clusters

Galaxy clusters, the largest gravitationally bound objects in the Universe, provide a diverse test ground for the evidence of DM. In the following, the inference of the DM content in clusters from (i) cluster dynamics (ii) intergalactic gas, and (iii) gravitational lensing is shortly summarized.

Dynamical measurements: Historically, the first evidence for DM was found by studying the dynamics within galaxy clusters. In the 1930s, F. Zwicky studied the velocity dispersion of objects in the Coma cluster and used the virial theorem to infer the total mass budget of the cluster. The scalar virial theorem for Newtonian mechanics, $2\overline{E}_{\text{kin}} - \overline{U} = 0$, states that the temporally average kinetic energy of a collisionless system of N point masses in equilibrium is equal to the half of the average virial $U = \sum\limits_{i=1}^{N} \vec{r}_i \vec{F}_i$, where $\vec{r}_i$ are the positions and $\vec{F}_i$ the forces on each particle. For the movement in a Newtonian gravitational potential, the virial is equal to the absolute value of the total potential energy of the system, $U = -E_{\text{pot}}$. The virial theorem is related to the Jeans equation 2.3 (see Binney and Tremaine, 2008), and provides a direct way to estimate the total mass $M = \sum_i M_i$ of a self-gravitating system.[5] By averaging

$$E_{\text{kin}} = \frac{1}{2} \sum_{i=1}^{N} M_i \, v_i^2 = \frac{M}{2} \langle v^2 \rangle \,, \tag{2.4}$$

one obtains the relation (where the time average is discarded for readability),

$$M = \frac{-E_{\text{pot}}}{\langle v^2 \rangle} \,. \tag{2.5}$$

It has been shown that for many astrophysical systems, the potential energy is tightly correlated to the half-mass radius R_{h}, and the relation $-E_{\text{pot}} \approx \frac{1}{2} \, G \, M^2 / R_{\text{h}}$ holds (Binney and Tremaine, 2008).[6] Similar to the Jeans analysis, for an approximately constant mass-to-light-ratio of all galaxies, R_{h} is identical to the half-light radius and can be inferred from the surface brightness of the cluster. For the average velocities in an isotropic system, $\langle v^2 \rangle = 3 \langle v_{||}^2 \rangle = 3 \sigma_{||}^2$ holds, with $v_{||}$ the line-of-sight velocity component and $\sigma_{||}$ the line-of-sight velocity dispersion. By measuring R_{h} and $\sigma_{||}$, Zwicky estimated a mass-to-light ratio in the Coma cluster of $M/L_{\text{V}} \gtrsim 400 \, \text{M}_{\odot}/\text{L}_{\odot,\text{V}}$ (Zwicky, 1933, 1937). However, later measurements revealed that the Coma cluster – as many other clusters – harbors a large amount of hot, X-ray emitting intergalactic gas, which outweighs the optically bright galaxies. As of today, about 85% of the total mass of the Coma cluster is attributed to DM, while only 2% of the mass is contained in galaxies and 13% in gas (Lokas

---

[5] However, the virial theorem can not be used to recover the mass profile $M(r)$.

[6] In particular, for a constant-density sphere, $E_{\text{pot}} = -3/5 \, G M^2 / R_{\text{sphere}}$, one obtains $R_{\text{h}} = 3/5 \times 2^{-1/3} \, R_{\text{sphere}} = 0.476 \, R_{\text{sphere}}$.

and Mamon, 2003). Similar results are obtained for a variety of clusters (Bahcall and Fan, 1998; Carlberg et al., 1999).

Also, the MW and the nearby Andromeda (M31) galaxy, together with all their dSph galaxies, form a virial system, the local group. Using the timing argument of Kahn and Waltjer (1959), the relative motion of the two galaxies suggests a total collective mass of $M_{\mathrm{gal}} + M_{\mathrm{M31}} = (4.93 \pm 1.63) \times 10^{12}\,\mathrm{M}_{\odot}$ (van der Marel et al., 2012), in agreement with the individual DM masses of both galaxies estimated from rotation curve measurements and satellite dynamics.

Intergalactic gas temperature: The presence of hot gas in clusters, which can be studied by its bright X-ray emission and the upscattering of Cosmic Microwave Background (CMB) photons via the Sunyaev-Zeldovich effect (Sunyaev and Zeldovich, 1970), constitutes an independent evidence for DM. In hydrostatic equilibrium, the pressure of an ideal gas with density ρ_{gas}, temperature T_{gas}, and particle mass μ is counterbalanced by the gravitational pressure of the system. Provided spherical symmetry, it holds that

$$-G\,\frac{M(r)\,\rho_{\mathrm{gas}}(r)}{r^2} = \frac{k_{\mathrm{B}}}{\mu}\,\frac{\mathrm{d}(\rho_{\mathrm{gas}}\,T_{\mathrm{gas}})}{\mathrm{d}r}\,, \tag{2.6}$$

from which the enclosed mass $M(r)$ can be inferred. Measurements of the gas density and temperature in various clusters yield $\Omega_{\mathrm{b}}/\Omega_{\mathrm{m}} \approx 16\%$ (D'Amico et al., 2011).

Strong and weak gravitational lensing by galaxies and galaxy clusters: The effect of gravitational lensing allows an almost direct mapping of astrophysical mass distributions, independent of dynamical tracers as stars or galaxies. Commonly one distinguishes between strong, weak, and micro-lensing according to the strength of the lensing effect. Around hundred strong lensing objects have been discovered so far (Mellier, 2010). The observations favor the existence of DM in these objects, with the DM-to-baryon fraction rising with mass (Koopmans et al., 2009; Auger et al., 2010). However, strong gravitational lensing can only probe the mass content within the most central region of the lensing object (Mellier, 2010). Eventually, there has been some dispute over whether or not results from strong lensing favor or disfavor the hypothesis of DM (Sanders, 2014).[7]

In contrast, weak gravitational lensing provides some of the most powerful evidence for the existence of DM. The cases of the clusters 1E0657-56 (Clowe et al., 2004, 2006, “Bullet cluster”) and MACS J0025.4-1222 (Bradač et al., 2008) are considered as main arguments against alternative theories of gravitation. Both clusters consist of two subclusters, which interpenetrated in the merging process. In both cases, weak gravitational lensing allows the dominant mass

---

[7] Note that strong and also weak lensing has been used to investigate the central density cusps of very massive galaxies and galaxy clusters at $z \lesssim 1$, and yields slightly steeper central densities than predicted by standard DM models (Mandelbaum et al., 2008; Treu et al., 2003; Dye et al., 2008; Grillo, 2012).

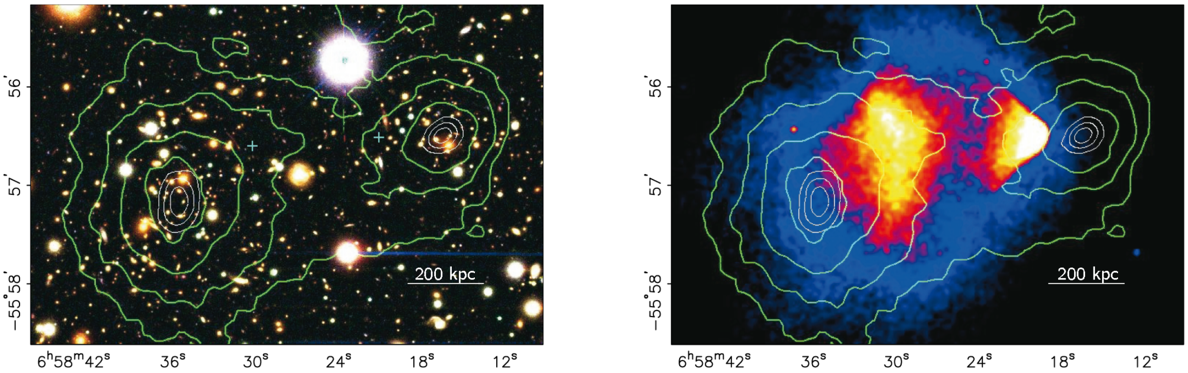

Figure 2.3.: The case of the "Bullet cluster" 1E0657-56. *Left:* Optical image taken with the Magellan telescope. *Right:* X-ray image from Chandra. In both images, the reconstructed gravitational convergence from weak lensing of background objects in overlaid in green. The white circles denote the 1, 2, 3σ errors on the peaks of the gravitational potential. Pictures taken from Clowe et al. (2006).

potential to be traced, which reveals a displacement from the gas distribution (Figure 2.3). The gas has heavily interacted, has been heated in the merging, and has lost momentum. In turn, the main masses of the subclusters seem to have experienced less interaction than the gas alone. This is supported by the distribution of the galaxies in the clusters, which trace the lensed potential, and are not held back by the massive intergalactic gas content. The displacement between the clusters' gravitational potential and the gas cannot be explained by theories like MOND, whereas it strongly supports the assumption of DM. It shows that the DM content of the subclusters must be collisionless, and must have a small self-interaction cross section. Weak lensing shows evidence for a high DM content also in other cluster systems, although combinations with complementary (X-ray, dynamical) measurements are made to obtain more stringent mass estimates (High et al., 2012; Mandelbaum, 2014; Okabe and Smith, 2016).

Finally, it shall be noted that gravitational microlensing could be used to search for dark DM subhalos in the MW, the objects whose indirect detection from DM self-annihilation is the subject of this thesis. Examining optical surveys for microlensing events already has been used to rule out that baryonic dark objects (MACHOs) significantly contribute to the MW's DM content (Tisserand et al., 2007). In turn, it has been shown that DM structures on sub-galactic scales could leave a measurable imprint in the lensing response (Metcalf and Madau, 2001; Moustakas and Metcalf, 2003; Cyr-Racine et al., 2016; Fedorova et al., 2016). Recently, the presence of a subhalo of mass $m < 10^9\,\mathrm{M}_\odot$ in the galaxy SDP.81 has been claimed by Hezaveh et al. (2016). Searching for microlensing events potentially constitutes a search for dark subhalos complementary to the methods presented in this thesis (Zackrisson and Riehm, 2010; Erickcek and Law, 2011, see also the prospects given in the summary of the thesis).

2.1.4. Cosmological dark matter

The evidence for DM previously described only gives a rough estimate of the fraction $\Omega_\mathrm{b}/\Omega_\mathrm{m}$ in the various systems. The results scatter for different methods and objects, and objects of different evolutionary stages are compared. In contrast, observation of the CMB and statistical properties of large-scale structures give a precise picture of the global DM content in the Universe.

Baryogenesis and CMB photon density: After the CMB was discovered (Penzias and Wilson, 1965), indications became stronger that it consists of perfectly thermalized photons at a temperature of $T = 2.73\,\mathrm{K}$ (finally proven y the Cosmic Background Explorer (COBE) satellite, Mather et al., 1990). The fraction η of the number densities of photons and nucleons in the Universe remains constant during its expansion, and is given by

$$\eta = \frac{n_\mathrm{b}}{n_\gamma} = \frac{\Omega_\mathrm{b}^0}{m_\mathrm{n}\, n_\gamma^0}\,\frac{3\,H_0^2}{8\pi\,G} = 2.74\times 10^{-8}\,\Omega_\mathrm{b}^0\,h^2\,\left(\frac{2.73\,\mathrm{K}}{T_0}\right)^3\,, \tag{2.7}$$

where m_n the nucleon mass, and the present-day CMB photon density is directly calculated from the photon number density at temperature T_0. The ratio η strongly determines the number of light elements (^{2}H, ^{3}He, ^{4}He, ^{7}Li) that have been synthesized in the early Universe ("big bang baryogenesis"). From observations of low metallicity stars and absorption spectra of distant objects, one robustly obtains $1.5\times 10^{-10} \lesssim \eta \lesssim 6\times 10^{-10}$.[8] Consequently, today's baryon content of the Universe must be

$$\Omega_\mathrm{b}^0\,h^2 \lesssim 0.022. \tag{2.8}$$

If there was no DM or dark energy, the Universe would be incredibly hyperbolic.[9] As observations of the CMB indicate that the Universe is flat, big bang baryogenesis suggests that there must be a vast amount of other form of energy density to account for the flatness.

Linear structure growth in an expanding universe: If one observes structures today in the Universe, these structures must have grown from some initial inhomogeneities in the early Universe. The amplitude and evolution of such early inhomogeneities is a key ingredient to understanding galaxy formation. Before the decoupling of the baryonic matter and radiation in the early Universe, matter and radiation formed a hot joint pressurized plasma. A pressurized medium can only collapse – and let structures grow – on scales larger than the Jeans length,

$$\lambda_J(t) = \sqrt{\frac{8\pi^2}{3}\,\frac{a_0}{a(t)}}\,\frac{c_\mathrm{s}(t)}{H(t)\,\sqrt{\Omega(t)}}\,, \tag{2.9}$$

---

[8] Conversely, the independent measurement of Ω_b^0 by Planck can be used to constrain η, and consequently the primordial element abundances (Ade et al., 2016).

[9] The current radiation density Ω_r^0 is negligible.

with $\Omega(t)$ the density, and c_{s} the sound speed of the medium. However, the Jeans length for the baryon-electron-photon plasma always was larger than the causal horizon, $\lambda_J(t) > D_{\mathrm{H}}(t) = a(t)\int_0^t \frac{1}{a(t')}\,\mathrm{d}t'$ (see Appendix A.2). Matter and radiation inhomogeneities therefore did not grow, but oscillated in thermal equilibrium. Not before the decoupling of the radiation at $z = 1100$, the Jeans length dropped such that the baryonic matter could collapse. Since then, relative structure in the Universe, $\delta(t, \vec{r}) := (\rho(t, \vec{r}) - \overline{\rho}(t))/\overline{\rho}(t)$, has grown according to $\delta \propto a = (1+z)^{-1}$.[10] Today, the Universe is heavily clustered in the non-linear regime, with $\delta \gtrsim 1$. Therefore, at the decoupling of matter and radiation, the plasma should have had an intrinsic fluctuation of $\delta(z_{\mathrm{dec}}) \gtrsim 1/z_{\mathrm{dec}} = 10^{-3}$, which should be be conserved as a temperature anisotropy in the CMB. However, it became evident in the 1980s that such an anisotropy level does not exist (Uson and Wilkinson, 1982). Not before 1992, the COBE satellite detected anisotropies in the CMB, but at a level of $\delta(z_{\mathrm{dec}}) = \Delta T/T = 1.1 \times 10^{-5}$, at the scale of COBE's angular resolution of $\sim 7^\circ$ (Smoot et al., 1992).

This contradiction between our understanding of the growth of structures and the CMB isotropy is resolved by the presence of DM. Any matter that does not couple to photons could already form structures at $z > 1000$. After the decoupling of the baryons and photons, the baryons are attracted by the potential sinks of the DM, and baryonic structures can form much faster than $\propto (1+z)^{-1}$ (Efstathiou and Bond, 1986). This is illustrated in Figure 2.4. It is evident that the DM budget, Ω_{DM}, must be significantly larger than the baryon content, Ω_{b}, to make the baryons adapt to the DM potential, and to trigger early galaxy formation. However, the ratio $\Omega_{\mathrm{DM}}/\Omega_{\mathrm{b}}$ cannot be inferred from the CMB fluctuation on a single angular scale alone.

Non-linear large-scale structure formation: Today, the matter perturbations of the early Universe have collapsed non-linearly, and matter has clustered to highly dense galaxies and galaxy clusters, separated by mostly empty intergalactic voids. These large-scale structures in the Universe have been traced by deep optical surveys like 2dF and SDSS, which were able to map the galaxy distribution almost completely up to $z \lesssim 0.2$. The study of the Ly-α absorption forest in the spectra of distant Active Galactic Nuclei (AGN) and of the Sunyaev-Zeldovich upscattering of CMB photons allows the distribution of baryonic matter in the Universe to be mapped even up to higher redshifts. This distribution of galaxies is supposed to follow the DM distribution in the Universe at the respective redshift.[11] In fact, the observation very well resembles the distribution one expects after a rigorous modeling of non-linear structure growth of DM (Springel et al., 2006).

---

[10] This is a consequence of linear perturbation theory in an expanding universe. See, e.g. the textbooks by Peebles (1980) or Padmanabhan (1993).

[11] The DM distribution can also be mapped directly by weak lensing of the CMB (cosmic shear), overcoming the so-called "galaxy bias".

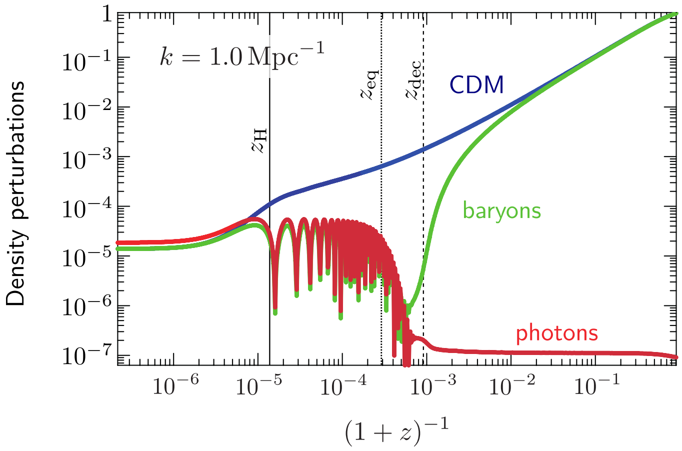

Figure 2.4.: Linear perturbation growth of cold DM, baryons, and photons from $z = 10^7$ until today, on the co-moving length scale $\lambda = 2\pi/k = 6.28\,\mathrm{Mpc}$. On the y−axis, the relative perturbations are given in terms of the matter power spectrum in k-space, $\delta_k(k, z) \propto \sqrt{\frac{P_\delta(k,z)}{\mathrm{Mpc}^3}}$ (see Appendix A.2 for details), normalized such that $\delta_k(k, 0) = 1$. Before horizon-entry of the scale λ at z_{H}, structures grow $\propto a^2$. After horizon entry, the DM fluctuations only grow $\propto \ln(a)$ during the radiation dominated era, $z_{\mathrm{H}} > z > z_{\mathrm{eq}}$, and grow faster, $\propto a$, in the matter-dominated era, $z < z_{\mathrm{eq}}$. Baryonic and radiation perturbations start to oscillate after horizon entry, and structures are suppressed. After decoupling, $z < z_{\mathrm{dec}}$, baryons fall into the DM potential, and the photon structure growth is halted. Figure adapted from Baumann (2013).

The observed large-scale structure favors a hierarchical bottom-up structure formation. Hierarchical bottom-up structure formation implies that structure growth occurs first on the smallest scales, and the small-scale protohalos then later merge, in the non-linear regime, to the DM halos of galaxies, clusters and filaments. Such a bottom-up structure formation requires ‘cold’ dark matter (CDM), with a small co-moving free-streaming scale at the present epoch, $t = t_0$:

$$\lambda_{\mathrm{FS}}(t_0) = a_0 \int_{t_d}^{t_0} \frac{v_{\mathrm{DM}}(t')}{a(t')}\,\mathrm{d}t'\,, \tag{2.10}$$

where t_d is the time of kinetic decoupling of the DM. For the DM in thermal equilibrium in the early Universe, this leads to a numeric value of (Padmanabhan, 1993; Schneider et al., 2013; Viel et al., 2013):[12]

$$\lambda_{\mathrm{FS}}(t_0) \sim \left(\Omega^0_{\mathrm{CDM}}\, h^2\right)^{1/3} \left(\frac{m_\chi}{\mathrm{keV}}\right)^{-4/3} \mathrm{Mpc}\,, \tag{2.11}$$

where the particle mass m_χ determines when the DM becomes non-relativistic. Cold DM implies heavy particles, $m_\chi \gtrsim$ GeV, that have been non-relativistic during the largest time of structure growth, and one obtains $\lambda_{\mathrm{FS}}(t_0) \lesssim 5 \times 10^{-3}\,\mathrm{pc}$. In contrast, DM particles that become non-relativistic very late, or are still relativistic, are called ‘hot’, and form structures ‘top-down’:

---

[12] More exact calculations account for the time of the kinetic DM decoupling, which is dependent of the mass m_χ.

Structures collapse first on large scales above the free-streaming scale, and on smaller scales $< \lambda_{\mathrm{FS}}$ later on, when the DM has sufficiently cooled down during the expansion. It has been shown that therefore, for hot DM, small-scale collapse occurs too late, and emerging present-day structures appear incompatible with observation (White et al., 1983). The exact process of the non-linear emergence of today's DM structures can only be modeled numerically. However, basic features of hierarchical bottom-up structure formation can be described analytically through the heuristic formalism by Press and Schechter (1974). Their model of top-hat spherical collapse predicts, at redshift z, a galaxy mass distribution (Dodelson, 2003; Mo et al., 2010):

$$\frac{\mathrm{d}n}{\mathrm{d}M}(z,\,k) = \sqrt{\frac{2}{\pi}}\left(\frac{m(k)+3}{3}\right)\frac{\rho_{\mathrm{M}}(z)}{M^2}\left(\frac{M}{M_{\mathrm{c}}(z,\,k)}\right)^{\frac{m(k)+3}{6}}\exp\left[-\frac{1}{2}\left(\frac{M}{M_{\mathrm{c}}(z,\,k)}\right)^{\frac{m(k)+3}{3}}\right], \quad (2.12)$$

where n is the galaxy number density per co-moving volume. The mass M_{c} denotes the largest mass of collapsed objects at a given redshift and length scale, and is proportional to $M_{\mathrm{c}}(z,\,k) \propto (1+z)^{-\frac{6}{m(k)+3}}$ in a matter-dominated universe. The index $m(k)$ is the slope of the matter power spectrum $P(k,\,z) \propto k^m$ around the length scale k. For a scale-invariant primordial spectrum, $n_{\mathrm{s}} = 1$, $P(k,\,z) \propto k^{-3}\ln(k)$ at the smallest scales, which enter the horizon first, and $m(k) > -3$ at larger scales ($m(k \to 0) \to 1$ at very large scales, see Appendix A.2). Thus, the Press-Schechter theory predicts for the smallest scales a distribution $\frac{\mathrm{d}n}{\mathrm{d}M}(z) \propto M^{-2}$. This reflects the bottom-up halo formation scenario, with a lot of small primordial low mass halos, which later merge into less abundant more massive halos. The cut-off at the low mass end is determined by the DM free-streaming scale, which depends on the particle mass and time of kinetic decoupling. Rigorous calculations show that today, the smallest collapsed DM objects in a supersymmetric DM scenario are expected to have masses of $\sim 10^{-6}\,\mathrm{M}_\odot$ (Hofmann et al., 2001; Berezinsky et al., 2003; Green et al., 2004; Profumo et al., 2006).

The original Press-Schechter theory was later extended by the excursion set formalism (Bond et al., 1991), halo merger trees (Sheth and Lemson, 1999) and to account for non-spherical collapse (Sheth et al., 2001). This extended Press-Schechter formalism is remarkably well in agreement with full numerical simulations of non-linear structure growth in a Λ-cold dark matter (ΛCDM) universe and with observations (e.g., Tinker et al., 2008). However, it treats all objects as isolated "field halos" and does not account for tidal mass losses of objects once they have merged into larger halos (Binney and Tremaine, 2008). Thus, the abundance of small-scale halos within host halos – those subhalos which are the subject of this thesis – can, strictly speaking, only insufficiently be described by an analytical EPS formalism. However, numerical simulations have shown that bound small-scale halos also approximately follow a mass distribution $\frac{\mathrm{d}n}{\mathrm{d}M}(z=0) \propto M^{-2}$, resembling the prediction given by Equation 2.12.

Cosmic microwave anisotropy: The satellite detectors WMAP and Planck, combined with balloon- and earth-bound observations, have extracted almost all available information from the CMB temperature anisotropy.[13] The angular power spectrum of the CMB temperature reveals the matter-radiation perturbations at the time of last scattering on all angular scales. From the position of the peaks in the spectrum and their relative power, one is able to extract precise information about the amount of baryonic and non-baryonic matter at the time of the last scattering. Combined with measurements of the accelerated expansion of the Universe and large-structure surveys, the recent results from Planck (Ade et al., 2016) give:[14] $\Omega^0_{\mathrm{CDM}} = 0.119/h^2$, $\Omega^0_{\mathrm{b}} = 0.022/h^2$, $\Omega^0_{\mathrm{r}} = 4.18 \times 10^{-5}/h^2$, $\Omega^0_{\mathrm{m}} = \Omega^0_{\mathrm{CDM}} + \Omega^0_{\mathrm{b}} = 0.141/h^2$, $h = 0.678$. Thus, on the global scale, the Universe contains $\Omega_{\mathrm{CDM}}/\Omega_{\mathrm{b}} = 5.4$ times more DM than baryonic matter.

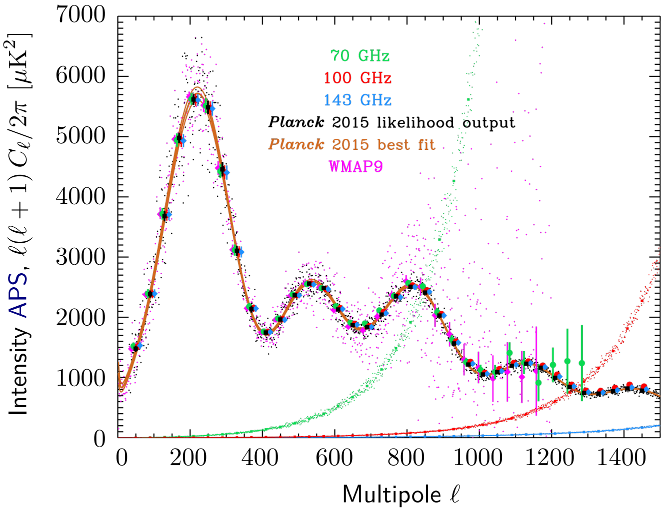

Figure 2.5.: Angular power spectrum $\mathcal{D}_\ell = \ell(\ell+1)/2\pi\, C_\ell$ of the CMB, as measured by Planck (Aghanim et al., 2016). The position of the first peak gives a degenerated indication of the curvature, Ω_{k}, and dark energy, Ω^0_Λ. The relative amplitude of the overtones to the first peak indicates the total matter content, $h^2\,\Omega^0_{\mathrm{m}}$. The relative height of the even to the odd peaks indicates the baryon to DM content.

Altogether, different astrophysical observations give an astonishingly coherent picture of DM. Although observational evidence often is affected by large uncertainties, DM is by far the best explanation for many – unrelated – phenomena. Therefore, not before a more successful concept emerges, there remains strong evidence for the existence of DM.

---

[13] The effect of diffusion damping washes out CMB temperature structures below $\sim 5\,$arcmin, which is already reached by Planck's beam size. Still, valuable information is yet to be extracted from the CMB polarization.

[14] There is some degeneracy to constrain Ω^0_Λ and Ω_0 from the CMB alone. Moreover, the constraints on the parameters improve when including polarization and lensing information into a global parameter fit. Note that $h^2\Omega^0_{\mathrm{m}}$ and $h^2\Omega_{\mathrm{b}}0$ are considered as 'standard parameters', whereas the others are derived from a set of seven standard parameters. $h^2\Omega^0_{\mathrm{r}}$ is directly derived from the CMB temperature.

2.2. Weakly interacting massive particles as dark matter

> *The great tragedy of Science – the slaying of a beautiful hypothesis by an ugly fact.*
>
> Thomas Huxley (1893, p. 229)

Observational evidence constrains the properties of possible DM candidates. Obviously, the DM must not carry electric charge: It neither emits nor absorbs light, and behaves in a collisionless manner. If DM consists of elementary particles, they must be stable, at least for the age of the Universe, and preferably heavy. If such a particle additionally interacts non-gravitationally, then this coupling must be very weak. In this case, it is generically termed weakly interacting massive particle (WIMP). The main appeal of WIMPs as DM candidates is that they alone are sufficient to account for the full DM budget of the Universe and that they constitute the most promising candidates for a non-gravitational detection. Thermal production of WIMP DM in the early Universe naturally fits into the standard model of cosmology, and is in agreement with the cold DM scenario necessary for the early structure formation. Finally, there exists the so-called "WIMP miracle": A DM particle with a mass and an interaction cross section on the natural scale of the weak interaction predicts a relic abundance of thermally produced DM that perfectly matches today's observed DM budget in the Universe. However, even though WIMPs constitute the most coherent and "beautiful" DM candidate, their existence remains a hypothesis. Alternative hypothetical particles also may account for cold DM, like sterile, right-handed neutrinos (Dodelson and Widrow, 1994; Abazajian et al., 2001), axion-like particles (Rosenberg and van Bibber, 2000), or stable states in theories with extra-dimensions ("Kaluza-Klein DM"; Kolb and Slansky, 1984).[15] If no signature of WIMPs is found on the long term, the WIMP hypothesis will be severely challenged (Bertone, 2010b). Within this context, this thesis serves the possible detection – or "slaying" – of WIMP dark matter.

WIMP pair annihilation and thermal production of the WIMP relic density: The WIMP scenario predicts a non-negligible annihilation rate of WIMPs into standard model particles in the present-day epoch of the Universe. This is the key concept for an indirect search for DM with the methods of high-energy astrophysics.

A relic density of WIMPs in the present day Universe can be well explained by the thermodynamics of the early Universe. It is assumed that until the time of the electroweak phase transition at temperatures of about 100 GeV (at about 10^{-12} s after the big bang), some WIMP

---

[15] An exhaustive review of potential DM candidates is given by Bertone (2010a).

DM particle χ is largely abundant, and in thermal equilibrium with the particle soup of the early Universe. During expansion of the Universe, the WIMP decouples from the thermal bath, and its particle number density at this point is “frozen out”. From this point on, the WIMP relic density only evolves with the Hubble flow. If today’s DM budget is the leftover from thermally frozen WIMPs in the early Universe, then the WIMP particle-antiparticle pair annihilation rate at the moment of freeze-out is given by the analytical approximation (see Appendix A.3 for a derivation):

$$\langle \sigma v \rangle_f = \sqrt{\frac{4\pi^3 G}{45}} \, \frac{T_0^3}{\rho_{\mathrm{crit}}^0} \, \frac{g_{*s}(T_0)}{\sqrt{g_*(T_f)}} \, \frac{m_\chi}{T_f} \, \frac{1}{\Omega_\chi^0} \, . \tag{2.13}$$

Here, $\langle \sigma v \rangle_f$ is the annihilation cross section at freeze-out temperature, T_f, averaged over the relative velocity v of the annihilating WIMPs. T_0 is today’s CMB temperature, ρ_{crit}^0 is today’s critical density (as function of the Hubble parameter, H_0), and $\Omega_\chi^0 \equiv \Omega_{\mathrm{CDM}}^0$ today’s WIMP relic density. The dimensionless g_* denotes the effective degrees of freedom of the relativistic particles (Equation A.21), and g_{*s} the *entropic* degrees of freedom as defined in Equation A.26. For only photons and three neutrino species left today as radiation, $g_{*s}(T_0) = 3.909$. The ratio of the WIMP mass to the freeze-out temperature, $x_f := m_\chi / T_f$, can be calculated, as a function of m_χ, by the implicit equation (see Appendix A.3 for a derivation):

$$g_*^{-1}\left(m_\chi / x_f\right) m_\chi \, x_f^{3/2} \, e^{-x_f} = \sqrt{8\pi^3} \, \frac{\rho_{\mathrm{crit}}^0}{g_{*s}(T_0)} \, \frac{\Omega_\chi^0}{g_\chi} . \tag{2.14}$$

Note that Equation 2.14 depends on g_χ, the degrees of freedom of the WIMP particle. In case of a fermionic Majorana particle, $\overline{\chi} = \chi$, $g_\chi = 2$, and in case of a Dirac-like WIMP, $\overline{\chi} \neq \chi$, $g_\chi = 4$. In the following, $g_\chi = 2$ is assumed. From Equation 2.14 one obtains the result $x_f \gg 1$ for heavy particles, $m_\chi = \mathcal{O}(\mathrm{GeV})$ on the weak scale, which expresses that the DM is non-relativistic at freeze-out. For lighter particles, this ratio decreases; and freeze-out occurs later and at higher velocities. Both effects suppress small-scale structure formation, as it has been discussed in Subsection 2.1.4.

Figure 2.6 presents the freeze-out annihilation cross section obtained from numerically solving Equation 2.13 and Equation 2.14.[16] The result is found at the level of $\langle \sigma v \rangle_f \sim 10^{-26}\,\mathrm{cm}^3\,\mathrm{s}^{-1}$ over a wide range of WIMP masses, where the mass-dependent variation is due to the relativistic degrees of freedom at time of freeze-out, $g_*\left(T_f\right)$ (see Figure A.2 in the appendix). Especially

---

[16] The software `Mathematica` has been used for this purpose, with the most recent values from Planck (Ade et al., 2016), and the temperature-dependent relativistic degrees of freedom at time of freeze-out, $g_*\left(T_f\right)$, from Laine and Schröder (2006), see Appendix A.3.

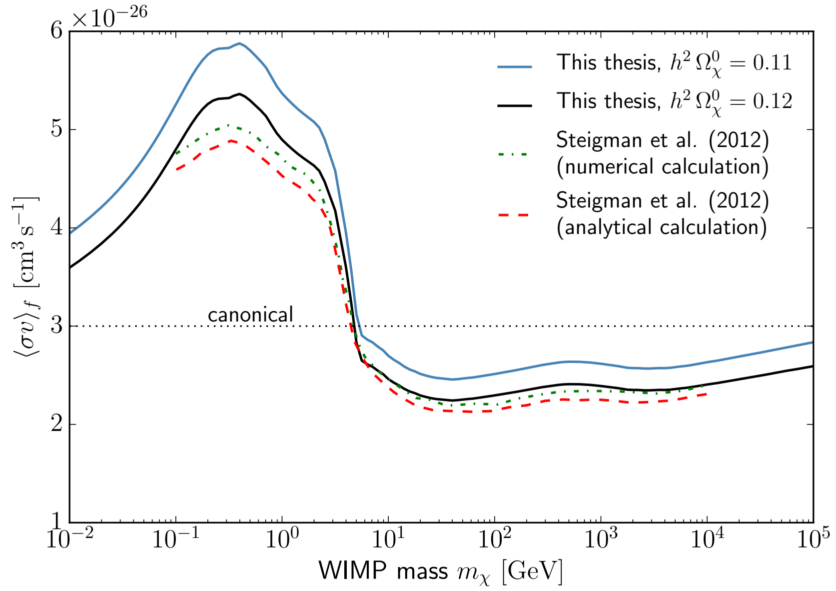

Figure 2.6.: Freeze-out annihilation cross section for thermally produced Majorana DM, as a function of the DM particle mass, m_χ, neglecting coannihilations. The approximate calculation of this thesis, for two values of the relic DM density $h^2\,\Omega^0_{\mathrm{CDM}}$ (assuming that the WIMP χ alone accounts for Ω^0_{CDM}) is compared to the calculations of Steigman et al. (2012), who used $h^2\,\Omega^0_{\mathrm{CDM}} = 0.11$. This depiction ignores the upper bound for possible WIMP masses, $m_\chi^{\mathrm{max}} \lesssim 3 \times 10^4$ GeV (Griest and Kamionkowski, 1990).

for WIMPs with masses $m_\chi \gtrsim 10\,\mathrm{GeV}$, the cross section is constant at

$$\langle \sigma v \rangle_f \approx 2.5 \times 10^{-26}\,\mathrm{cm^3\,s^{-1}}\,, \tag{2.15}$$

dubbed as the canonical cross section. At the highest masses, the required cross section again rises; however, Griest and Kamionkowski (1990) calculated an upper bound for possible WIMP masses $m_\chi^{\mathrm{max}} \lesssim 30\,\mathrm{TeV}$ (“unitary bound”), which could be even lower, $m_\chi^{\mathrm{max}} \lesssim 3\,\mathrm{TeV}$ (Bertone et al., 2005).[17] Also, Figure 2.6 shows that the estimated cross section inversely scales with the DM relic density in the Universe. A slightly higher estimate for Ω^0_{CDM}, as obtained by Planck (2015), suggests a respectively lower freeze-out cross section. In Figure 2.6, the calculation with Equation 2.13 is additionally compared to a more accurate analytical and fully numerical solution of the Boltzmann-equations by Steigman et al. (2012). It can be seen that the result obtained by a rather simple calculation from Equation 2.13 and Equation 2.14 overestimates the freeze-out cross section by no more than $\sim 20\%$.

---

[17] These calculations are based on a work from Jacob and Wick (1959), who find $\langle \sigma v \rangle < 4\pi/m_\chi^2 \approx 10^{-22}\,\mathrm{cm^3\,s^{-1}}\,(m_\chi/\mathrm{TeV})^{-2} \leftrightarrow m_\chi \lesssim 100\,\mathrm{TeV}$ for a thermal relic cross section.

The resulting cross section presented in Figure 2.6 can be altered by the presence of additional (unstable) particles with masses close to m_χ. Then, mutual interaction between the DM and these particles is present still around freeze-out (coannihilations; Griest and Seckel, 1991). If there is another particle $\widetilde{\chi}$ with $m_{\tilde{\chi}} \gtrsim m_\chi$, one can write (Vogl, 2014):

$$\langle \sigma v \rangle_{f,\,\mathrm{eff}} = \langle \sigma v \rangle_{f,\,\chi\chi} + \langle \sigma v \rangle_{f,\,\chi\tilde{\chi}}\, e^{-\frac{m_{\tilde{\chi}}-m_\chi}{T}} + \langle \sigma v \rangle_{f,\,\tilde{\chi}\tilde{\chi}}\, e^{-\frac{2(m_{\tilde{\chi}}-m_\chi)}{T}} \,, \tag{2.16}$$

Thus, for $m_{\tilde{\chi}} \approx m_\chi$ the DM annihilation cross section at freeze-out, $\langle \sigma v \rangle_{f,\,\chi\chi}$ might be significantly lower than the effective cross section, $\langle \sigma v \rangle_{f,\,\mathrm{eff}}$.[18] Including coannihilations is one of the reasons why the exact freeze-out cross section depends on a specific particle physics model, and dedicated parameter scans of particular Standard Model (SM) extensions have to be performed for a precise calculation of $\langle \sigma v \rangle_f$ (an example is shown later in Figure 2.10).

The order of magnitude of the canonical cross section, $\langle \sigma v \rangle_f \approx 10^{-26}\,\mathrm{cm}^3\,\mathrm{s}^{-1}$ is commonly quoted as the "WIMP miracle", as one obtains

$$\frac{\langle \sigma v \rangle_f}{c} \approx 1\,\mathrm{pb} \approx 0.1\,\frac{\alpha_W^2}{m_W^2} \,, \tag{2.17}$$

the leading order scattering cross section of a weak interaction (for particle momenta $p \ll m_W$). This congruence strongly supports the idea that DM might consist of a thermally produced particle, which self-annihilates through the weak interaction.

Present-epoch relic annihilation rate: The annihilation cross section at freeze-out only corresponds to the one of today if the cross section is velocity-independent. When ignoring possible resonance effects, the velocity-averaged cross section can be expanded in the expectation values $\langle v^{2n} \rangle$ (Jungman et al., 1996):

$$\langle \sigma v \rangle(v) = a + b\,\langle v^2 \rangle + \mathcal{O}(\langle v^4 \rangle) \,, \tag{2.18}$$

where v is the relative velocity between the WIMPs. The zero-order term is dubbed as s-wave annihilation, and terms up to the second order correspond to a p-wave component. In case of pure s-wave annihilation, $b = 0$, $\langle \sigma v \rangle_{\text{s-wave}}(T_0) = \langle \sigma v \rangle_f$. In case of the absence of a s-wave component, the present-day annihilation rate,

$$\langle \sigma v \rangle_{\text{p-wave}}(T_0) = \frac{T_0}{T_f}\,\langle \sigma v \rangle_f \approx 10^{-15}\,\langle \sigma v \rangle_f \,, \tag{2.19}$$

---

[18] In some cases, coannihilations may also slightly increase the annihilation rate (Edsjö and Gondolo, 1997).

is heavily suppressed. Consequently, only s-wave annihilation can be probed today in indirect detection experiments. When resonance effects are present, additional terms $\propto v^{-1}$ occur in Equation 2.18 and might dominate the annihilation in the low velocity limit. Such a resonance is provided by the non-relativistic Sommerfeld-enhancement (Hisano et al., 2005; Arkani-Hamed et al., 2009; Feng et al., 2010), and is taken into account in detailed cross section calculations. Finally, all predictions on the present-day annihilation cross section, channels and secondary products depend on a specific particle physics model of the WIMP.

2.2.1. Supersymmetric neutralinos as WIMP candidate

It is clear that the WIMP cannot be one of the known particles in the SM. The most prominent extension of the SM is the supersymmetric SM, or Supersymmetry (SUSY). The principal idea of SUSY is to lift the degeneracy between fermions and bosons, by introducing a new spacetime symmetry between fermions and bosons (Martin, 2010). The new symmetry is expressed by two new symmetry-generating Weyl-spinors, Q and $Q^\dagger$, with $Q|\text{Fermion/Boson}\rangle = |\text{Boson/Fermion}\rangle$ (Bertone et al., 2005). This symmetry must be broken, as the generated new particles, the "superpartners", cannot have the same masses as their known standard model partners and must be heavier than the currently accessible mass scales. The so-called Minimal Supersymmetric Standard Model (MSSM), or unconstrained MSSM (uMSSM), contains the most general Lagrangian with all symmetry breaking terms allowed by the symmetry to generate all SM model fields. Table 2.1 summarizes the newly introduced superpartners in the MSSM.

One key property of the MSSM is the ad-hoc conservation of a new multiplicative quantum number, the R-parity (Martin, 2010),

$$R = (-1)^{3(B-L)+2s} = (-1)^{3B+L+2s}\,, \tag{2.20}$$

with the baryon number B, the lepton number L, and the spin s. For all SM particles, $R = +1$ holds. The MSSM partners inherit the lepton and baryon numbers, but a spin differing by 1/2 from the SM particles (see Table 2.1), such that $R = -1$ for all MSSM superpartners. If R-parity is conserved, then there must be a lightest supersymmetric particle, which is stable and can only be destroyed by pair annihilation into SM particles (Bertone et al., 2005). Additionally, the lightest stable particle is expected to be neutral; A charged and stable supersymmetric particle would have been observed, and not accounted for the observed properties of DM. The lightest mass eigenstate then can be a sneutrino, $\widetilde{\nu}$, or a neutralino, χ^0. The scalar sneutrinos possess a large scattering cross section, for which direct detection experiments already have set limits that exclude sneutrinos accounting for the dominant DM budget (Falk et al., 1994; Bertone et al., 2005). This leaves the neutralinos as the only viable MSSM candidate for DM.

SM particles/fields, $R = +1$			MSSM partners, $R = -1$				
			gauge eigenstates		mass eigenstates		
symbol	name	spin	symbol	name	symbol	name	spin
q_L	quarks	1/2	$\widetilde{q}_L$, $\widetilde{q}_R$	squarks	$\widetilde{q}_1$, $\widetilde{q}_2$	squarks	0
l_L	charged leptons	1/2	$\widetilde{l}_L$, $\widetilde{l}_R$	sleptons	$\widetilde{l}_1$, $\widetilde{l}_2$	sleptons	0
ν_L	neutrinos	1/2	$\widetilde{\nu}$	sneutrinos			0
g	gluons	1	$\widetilde{g}$	gluinos			1/2
$W^{\pm}$	W bosons	1	$\widetilde{W}^{\pm}$	winos	$\chi^{\pm}_{1,2}$	charginos	1/2
$H^{\pm}$	Higgs boson	0	$\widetilde{H}^{\pm}$	higgsinos			
B	B boson	1	$\widetilde{B}$	bino	$\chi^{0}_{1,2,3,4}$	neutralinos	1/2
W_i	W_3-field	1	$\widetilde{W}_i$	winos			
H^0_1	Higgs boson	0	$\widetilde{H}^0_1$	higgsino			
H^0_2	Higgs boson	0	$\widetilde{H}^0_2$	higgsino			

Table 2.1.: SM particles and their supersymmetric partners in the MSSM, adopted from Edsjö (1997) and Bertone et al. (2005). Note that for the SM particles, only the gauge eigenstates are shown. The photon γ, and the Z^0 are obtained as linear combinations of the B and W_i; and the gauginos, combinations of the $\widetilde{B}$ and $\widetilde{W}_i$, can correspondingly be named photino, $\widetilde{\gamma}$, or zino, $\widetilde{Z}^0$. Also, the light, heavy, and pseudo-scalar Higgs bosons, h^0, H^0, and A^0 are mass eigenstates of the H^0_1 and H^0_2 (Martin, 2010).

The neutralino mass eigenstates result from the mixing of the four gauge interaction eigenstates, and the lightest neutralino, χ^0_1, can be written as

$$\chi^0_1 = N_{11}\,\widetilde{B} + N_{12}\,\widetilde{W}_i + N_{13}\,\widetilde{H_1}^{0} + +N_{14}\,\widetilde{H}^0_2\,, \tag{2.21}$$

where the coefficients result from the diagonalized neutralino mass matrix. A consequence of all R-parity conserving MSSM models is that the degrees of freedom of the superpartners have to sum up to the same degrees of freedom of the SM particles (Edsjö, 1997). Therefore, the neutral superpartners of the neutral SM gauge fields – the neutralinos – must have $2 \times 3 + 2 \times 1$ degrees of freedom. Each of the four spin 1/2 neutralinos then has two degrees of freedom left, and must be a Majorana particle (Jungman et al. (1996); see also Table 2.1).[19] Majorana neutralinos possess much smaller scattering cross sections (Bertone et al., 2005), and have not yet been ruled out by direct detection experiments. Similar to ruling out sneutrinos as DM candidates, direct detection and collider experiments also disfavor Dirac-like DM fermions (Massó et al., 2009; Fortin and Tait, 2012). These experiments have set strong constraints on electric or magnetic dipole moments for heavy ($m_\chi \gtrsim 10\,\mathrm{GeV}$) particles, which are only present for Dirac

---

[19] Note that this does not need to apply to theories where an unbroken *R-symmetry* is preserved, instead of *R-parity*; and neutralinos may be Dirac-like (Buckley et al., 2013).

fermions (Ho and Scherrer, 2013). Therefore, Majorana-like neutralinos constitute an excellent DM candidate, in no tension with experimental results.

Different neutralino mass eigenstates, according to Equation 2.21, show different annihilation properties. If N_{11} and N_{12} in Equation 2.21 dominate, the lightest neutralino is gaugino dominated; for a large fraction of N_{13} and N_{14} it is higgsino dominated. In the low velocity limit, pure gaugino neutralinos have a vanishing tree-level amplitude for annihilation into massive gauge bosons, whereas pure higgsino neutralinos effectively have not (Bertone et al., 2005). In fact, for many constrained MSSM models,[20] neutralinos turn out to have a large bino component, N_{11}, throughout the parameter space, and consequently dominantly annihilate into fermions (Giuliani, 2011). Additionally, in the low velocity limit, only t-channel leading order annihilation into massive gauge bosons via chargino or neutralino exchange is unsuppressed (Bertone et al., 2005). Therefore, in this thesis, annihilation into fermions is considered only.

Having said that, the conclusions of this thesis are not dependent on the the fermionic annihilation channel, as annihilation into massive gauge bosons produces comparable final state γ-ray spectra (see Figure 2.11 in the following subsection). In contrast, processes at the next-to-leading order may result into significant hardening of the final state γ-ray spectra, which might indeed alter the prospects on indirect DM detection with γ-rays. With the MSSM Lagrangian at hand, the annihilation amplitudes of the lightest neutralino into SM particles can be calculated, and several important features are discussed in the following, including three-body annihilations and direct annihilation into photons.

Annihilation into fermions,* $\chi\chi \to f\bar{f}$ *: At the tree level s-wave channel, neutralinos can annihilate into fermions via mediation of a pseudoscalar Higgs, A, or a Z-boson, or via exchange of vector-like sfermions (Jungman et al., 1996; Bertone et al., 2005).[21] The corresponding Feynman diagrams are shown in Figure 2.7. For all diagrams, the annihilation of Majorana particles into low mass fermions is suppressed for the velocity-independent s-wave channel. At low velocities, the Fermi statistics requires the Majorana WIMPs to have their spins anti-parallel, and so has the final state fermion-antifermion pair. To enable CP conserving equal helicity for a contrarily emitted fermion-antifermion pair, high mass final state fermions are required (Jungman and Kamionkowski, 1995; Giuliani, 2011). For a scalar weak mediator interaction with mediator η, the s-wave interaction Lagrangian reads $\mathcal{L}_{\text{int}} = -g\overline{\chi}\Psi_{\text{R}}\eta + \text{h.c.}$ ($\Psi = \tau,\ b,\ \ldots$),

---

[20] This refers, strictly speaking to minimal supergravity (mSUGRA) models; for a definition of mSUGRA see page 38.

[21] Annihilation via the scalar Higgs fields H^0, h^0 first occurs at the p-wave level.

and the cross section is (Bringmann et al., 2012):

$$\langle \sigma v \rangle^{\chi\bar{\chi}\to f\bar{f}}_{\text{s-wave}} \sim \frac{g^4 N_c}{32\pi m_\chi^2} \frac{m_f^2}{m_\chi^2} \frac{1}{(1+\mu)^2}\,, \tag{2.22}$$

where $\mu = m_\eta^2/m_\chi^2$ the square ratio of the scalar mediator and WIMP mass, and the color factor $N_c = 1$ for leptons and $N_c = 3$ for quarks. The same scaling $\propto m_f^2/m_\chi^2$ due to helicity conservation is present for vector-like mediators. For the pseudo-scalar Higgs exchange, the amplitude for annihilation into down-like quarks additionally scales proportional to $\tan\beta$, the ratio of the vacuum expectation values of the two Higgs bosons, H^0, h^0 (Bertone et al., 2005; Ellis and Olive, 2010). Thus, in summary, velocity-independent Majorana neutralino annihilation into fermions prefers heavy final states, if kinematically allowed, $\chi\chi \to t\bar{t}$, $b\bar{b}$, $\tau^+\tau^-$, $c\bar{c}$, $\mu^+\mu^-$, … For large $\tan\beta$, up-like quarks are additionally suppressed, such that the channels $\chi\chi \to b\bar{b}$, $\tau^+\tau^-$, $\mu^+\mu^-$, … remain.

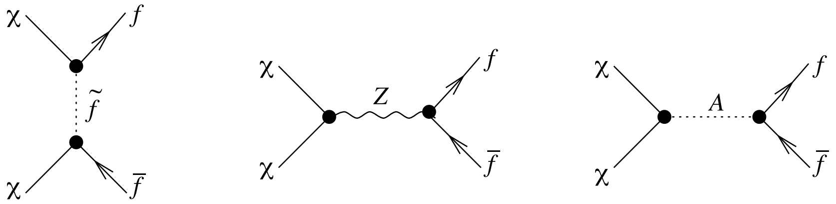

Figure 2.7.: Feynman diagrams for leading order neutralino-neutralino annihilation into fermions. *Left:* T-channel exchange of vector-like sfermion. *Center:* S-channel exchange of the Z vector boson. *Right:* S-channel exchange of pseudo-scalar Higgs boson, A^0. Figure taken from Bertone et al. (2005).

Three-body annihilation $\chi\chi \to f\bar{f}\gamma$ **:** It has been suggested to consider three body annihilations, dubbed as "virtual internal bremsstrahlung" process, contributing to the final state γ-ray spectrum (Bringmann et al., 2008; Bringmann and Calore, 2014). Due to the photon in the process, this process is suppressed by a factor α_{em}. However, at same time, the photon cancels the helicity conserving scaling $\propto m_f^2/m_\chi^2$ for s-wave annihilation, such that this process could obtain a relatively large contribution, depending on the WIMP mass. The s-wave cross section of this process for scalar-mediator interaction reads (Bringmann et al., 2012):

$$\langle \sigma v \rangle^{\chi\bar{\chi}\to f\bar{f}\gamma}_{\text{s-wave}} \sim \frac{\alpha_{\text{em}}\, g^4 N_c\, q_f^2}{64\pi^2 m_\chi^2}\, \mathcal{O}(\mu^{-4}). \tag{2.23}$$

Here, q_f denotes the electric charge of the final state fermions. The cross section scales with μ^{-4} instead of μ^{-2}, such that this process vanishes, compared to the 2-body interactions, for large mediator masses, $m_\eta \gg m_\chi$. The corresponding Feynman diagram is given in Figure 2.8. As later shown in Figure 2.11, a large branching fraction into this channel would, due to the prompt photon, significantly increase the number of very-high-energy (VHE) γ-rays. However, for the remainder of this thesis, the assumption is adopted that the two-body annihilation into heavy fermions dominates and that a spectral hardening due to three-body processes is negligible.

Figure 2.8: A schematic representation of the three body annihilation $\chi\chi \to f\bar{f}\gamma$, dubbed as virtual internal bremsstrahlung. Figure taken from Bringmann et al. (2012).

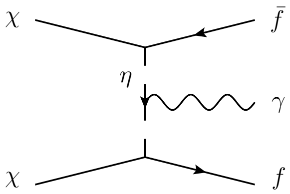

Direct annihilation $\chi\chi \to \gamma\gamma$ **:** The direct annihilation of DM neutralinos into γ-rays is of particular interest, as it produces a sharp spectral line at the WIMP mass. However, because of the photons only coupling to the electromagnetic field, this process first occurs at the one-loop level, and is suppressed by a factor $\alpha_{\text{em}}^2 \sim 2 \times 10^4$ compared to the tree-level 2-body interactions. The leading-order cross section is (Jungman and Kamionkowski, 1995; Bergström and Ullio, 1997; Giacchino et al., 2014):

$$\langle\sigma v\rangle^{\chi\bar{\chi}\to\gamma\gamma}_{\text{s-wave}} \sim \frac{\alpha_{\text{em}}^2\, g^4}{64\pi^2 m_\chi^2}\, \mathcal{O}\left(\frac{1}{(1+\mu)^2}\right).$$

In Figure 2.9, four out of the total 13 Feynman diagrams at the leading one-loop level for the $\chi\chi \to \gamma\gamma$ process are shown for illustration. However, due to the large suppression relative to the fermionic channels, direct annihilations $\chi\chi \to \gamma\gamma$ are not considered further in the following.

Several codes exist to calculate the exact branching ratios of the neutralino in different tree-level SM final state channels, as fermions, gauge bosons, and next-to-leading order processes. These include packages like `SoftSusy` (Allanach, 2002), `DarkSusy` (Gondolo et al., 2004) or `micrOmegas` (Bélanger et al., 2015) and also allow the calculation of the exact relic abundance of thermally produced DM for given MSSM parameters. However, the full broken MSSM Lagrangian contains 105 free parameters beyond the SM (Djouadi et al., 1999). To reduce this huge amount of parameters for reasonable predictions, several constrained MSSM models have been introduced. The so-called phenomenological MSSM (pMSSM) reduces the free parameter content by requiring no new sources of CP violation, no flavor changing neutral currents, and

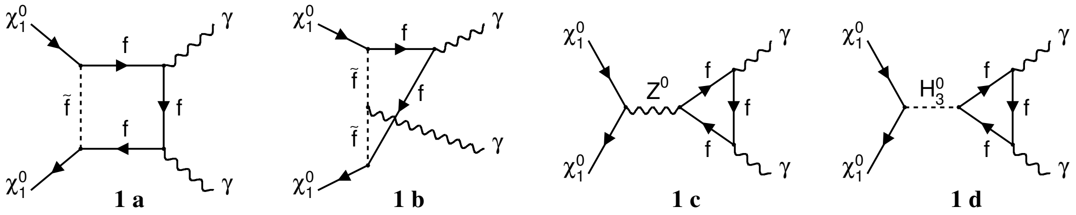

Figure 2.9.: Leading order Feynman diagrams at the one-loop level for the $\chi\chi \to \gamma\gamma$ annihilation. Four out of total 13 diagrams at the one-loop level are shown. Figure taken from Bergström and Ullio (1997).

the same masses of the first and second generation squarks. With this, the pMSSM parameter content is reduced to only 19 additional parameters (Djouadi et al., 1999). Finally, the even more constrained MSSM (CMSSM), also dubbed minimal supergravity (mSUGRA), reduces the additional MSSM parameter space to four scalar parameters and one sign. A parameter scan within the pMSSM is finally shown in Figure 2.10, in terms of the annihilation probability into the $b\bar{b}$ and $\tau^+\tau^-$ channels considered in this thesis. It can be seen in Figure 2.10 that for the $\chi\chi \to b\bar{b}$ channel (Figure 2.10, left), several pMSSM models show s-wave annihilation cross sections more than one order of magnitude above the canonical value, Equation 2.15. Especially, some models above $m_\chi \gtrsim 1\,\mathrm{TeV}$ show $\langle\sigma v\rangle \gtrsim 10^{-22}\,\mathrm{cm}^3\,\mathrm{s}^{-1}$ due to Sommerfeld enhancement. Thus, a chance remains to find indirect DM signals far above the canonical scale, and viable MSSM DM models can be excluded by non-detection of super-thermal γ-ray fluxes.

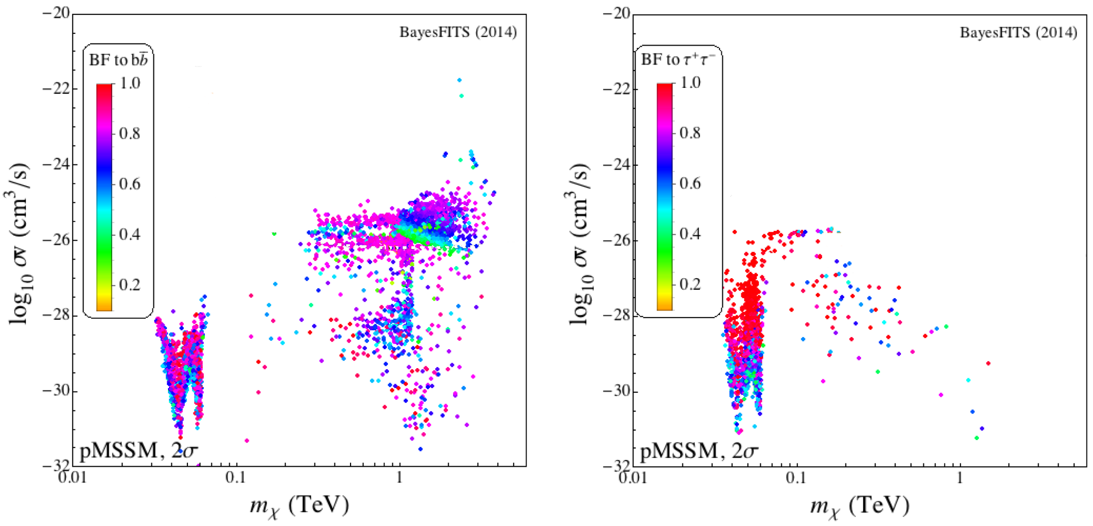

Figure 2.10.: Two slices through a pMSSM model scan for the s-wave (present-day) annihilation cross section, including coannihilations and Sommerfeld enhancement effects. “BF” denotes the branching fraction into the respective final states. Figure taken from Roszkowski et al. (2015).

2.2.2. Final prompt γ-ray spectra

The SM particles resulting from DM annihilation can be probed in indirect DM detection experiments. This thesis is about γ-radiation generated in DM annihilations. In general, these γ-rays result from tertiary reactions of the annihilation final states. For simplicity, the γ-radiation resulting from all subsequent processes is usually referred to as the final state radiation. The γ-rays may be produced at the place of annihilation ("prompt" emission). Alternatively, charged leptons produced in the DM annihilation may leave the region of annihilation and upscatter CMB photons or starlight (Profumo and Jeltema, 2009; Zavala et al., 2011, inverse Compton up-scattering). The same may occur for final-state hadrons, which interact with interstellar or intergalactic gas, producing high-energy photons as well (Fornasa et al., 2013). However, delayed γ-ray emission results in a mainly diffuse γ-ray signal, with the information about the directional origin of annihilation being lost. In this thesis, only prompt γ-ray signals from DM annihilation are investigated.

Hadronic final state: Heavy quarks quickly decay with $\mathcal{O}(10^{-12} - 10^{-8}\,\mathrm{s})$ into lower mass quarks, $t \to b \to c \to s \to u/d$, and a parton shower emerges. The hadronic shower ends with the production of pions. The charged pions then decay via muons into stable electrons, positrons and neutrinos, whereas γ-rays are produced in the π^0 decay. γ-rays can additionally be emitted in the shower via bremsstrahlung and Synchrotron radiation, through collisions or interaction with external magnetic fields.

Leptonic final state: In case of annihilation into heavy τ leptons, the τ may directly decay into hadrons,[22]

$$\begin{aligned} \tau^{\pm} &\to \pi^{\pm} + \pi^{0} + \overset{(-)}{\nu}_{\tau} && (25.5\%) \\ &\to \pi^{\pm} + 2\pi^{0} + \overset{(-)}{\nu}_{\tau} && (9.3\%) \\ &\to 2\pi^{\pm} + \pi^{0} + \pi^{\mp} + \overset{(-)}{\nu}_{\tau} && (2.7\%) \\ &\to \pi^{\pm} + 3\pi^{0} + \overset{(-)}{\nu}_{\tau} && (1.1\%), \end{aligned}$$

and in almost 40% of all τ decays neutral pions are produced. Because the neutral pions directly decay into γ-rays with a branching fraction $> 98\%$, the $\chi\chi \to \tau^{+}\tau^{-}$ annihilation results in a harder final state γ-ray spectrum compared to hadronic final states (see Figure 2.11).

An exact calculation of parton showers and hadronization is provided by Monte-Carlo event generators like `Pythia` (Sjöstrand et al., 2015) and `Herwig` (Bellm et al., 2016). Figure 2.11 presents the prompt final state γ-ray spectra calculated by Cirelli et al. (2011). Figure 2.11 (left) presents the γ-ray spectra for different SM annihilation products. Most annihilation channels

---

[22] `http://pdg.lbl.gov/2015/reviews/rpp2015-rev-tau-branching-fractions.pdf`

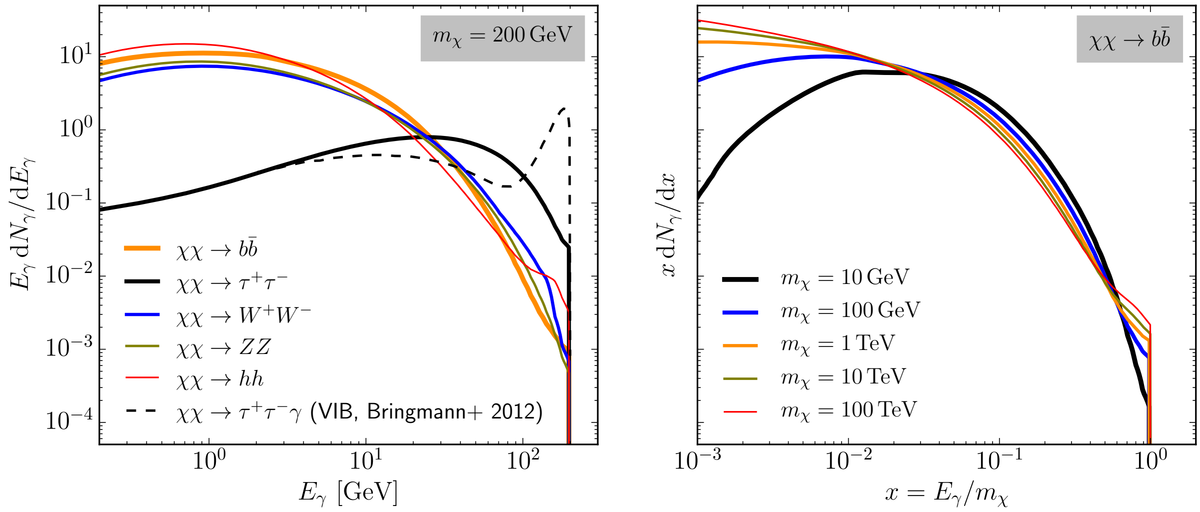

Figure 2.11.: *Left:* Spectrum of the final γ-ray yield per annihilation of a $m_\chi = 200\,\mathrm{GeV}$ neutralino for different annihilation channels. The 2-body final states are adopted from Cirelli et al. (2011), the 3-body virtual internal bremsstrahlung spectrum is taken from Bringmann et al. (2012). *Right:* Comparison of the shape of the final state γ-ray spectrum from the same annihilation channel, but different neutralino masses.

produce rather featureless and similar γ-ray spectra. Only the leptonic channel, $\chi\chi \to \tau^+\tau^-$, exhibits a harder spectral shape, due to the direct decays into neutral pions. Note that the total energy deposited in γ-rays per annihilation, $E_\gamma^{\mathrm{tot}} = \int E_\gamma\, \mathrm{d}N_\gamma/\mathrm{d}E_\gamma\, \mathrm{d}E_\gamma$, is not necessarily the same for different channels. In Table 2.2, the fraction of the WIMPs' rest energies which is transferred into γ-rays is shown for the different annihilation channels. This illustrates that DM annihilation not only produces prompt γ-rays, but also a large amount of other particles such as electrons, positrons, neutrinos and (anti-)hadrons. In Figure 2.11 (right), the final state γ-ray spectrum from the same annihilation channel, but different DM masses is shown. More massive WIMPs produce a larger parton shower, resulting in an increasing number of prompt γ-rays. However, the relative amount of energy deposited in γ-rays is the same for all spectra, $E_\gamma^{\mathrm{tot}}/2m_\chi(\chi\chi \to b\bar{b}) \approx 27\%$. For a 100 GeV WIMP, a total number of $\sim 10^7$ final state photons are emitted per annihilation, however, most of them at low energies (Cembranos et al., 2011).

channel	$\chi\chi \to b\bar{b}$	$\chi\chi \to \tau^+\tau^-$	$\chi\chi \to \tau^+\tau^-\gamma$	$\chi\chi \to W^+W^-$	$\chi\chi \to ZZ$	$\chi\chi \to hh$
$E_\gamma^{\mathrm{tot}}/2m_\chi$	27%	16%	42%	20%	20%	24%

Table 2.2.: Relative amount of total energy deposited in γ-rays after annihilation of non-relativistic neutralinos with $E_\chi \approx m_\chi$ for different annihilation channels.

2.3. Dark matter detection methods

Dark matter searches are divided into direct and indirect search strategies. An indirect search for DM focuses on observing the relic DM annihilation through the secondary SM annihilation products and is the subject of this thesis. Alternatively, direct searches attempt to detect DM particles themselves, when DM particles scatter with SM target particles. A third strategy consists of producing DM in particle colliders and of observing signatures of the DM in the collision products. Direct and collider searches for DM complement the indirect methods and are mentioned at the end of the section. So far, none of these different methods have shown clear evidence for particle DM.

2.3.1. Indirect detection of dark matter

Although DM has been frozen out, self-annihilation of DM still occurs today. In cosmic average, the annihilation probability per DM particle is smaller than one over its whole lifetime, such that the total cosmic DM budget is conserved.[23] However, in regions of highly clustered DM, annihilation may still take place at a considerable rate. The annihilation rate Γ in a volume V is

$$\frac{\Gamma}{V} = \langle \sigma v \rangle \, \frac{N_{\mathrm{pairs}}}{V^2} \,, \tag{2.24}$$

where N_{pairs} is the the number of possible mutual interactions, and $\langle \sigma v \rangle$ the present-day relic annihilation cross section. For Dirac particles, $N/2$ particles can interact with $N/2$ anti-particles, and $N_{\mathrm{pairs}}^{\chi \neq \overline{\chi}} = N^2/4$. For Majorana particles, $N_{\mathrm{pairs}}^{\chi = \overline{\chi}} = N(N+1)/2 \approx N^2/2$, double the amount of interactions is possible. Thus, with the mass density $\rho = m_\chi \, n$ and the particle density $n = N/V$,

$$\frac{\mathrm{d}\Gamma}{\mathrm{d}V} = \frac{\langle \sigma v \rangle}{\delta} \left(\frac{\rho}{m_\chi} \right)^2 \,, \tag{2.25}$$

where $\delta \equiv 2$ for Majorana DM, and $\delta \equiv 4$ for Dirac DM. Each annihilation produces a final state γ-ray spectrum $\mathrm{d}N_\gamma/\mathrm{d}E$, such that

$$\frac{\mathrm{d}N_\gamma}{\mathrm{d}V \, \mathrm{d}E \, \mathrm{d}t} = \frac{\mathrm{d}N_\gamma}{\mathrm{d}E} \, \frac{\mathrm{d}\Gamma}{\mathrm{d}V} = \frac{\langle \sigma v \rangle}{\delta \, m_\chi^2} \, \frac{\mathrm{d}N_\gamma}{\mathrm{d}E} \, \rho^2 \,. \tag{2.26}$$

---

[23] See Appendix A.3, especially Equation A.19 and Equation A.20 for a rigorous treatment of the freeze-out condition.

Finally, in Euclidean spacetime the flux at the observer scales inversely proportional to the square distance l of the annihilation,

$$\frac{\mathrm{d}N_\gamma}{\mathrm{d}V\,\mathrm{d}E\,\mathrm{d}t\,\mathrm{d}A} = \frac{\langle\sigma v\rangle}{\delta\, m_\chi^2}\,\frac{\mathrm{d}N_\gamma}{\mathrm{d}E}\,\frac{\rho^2}{4\pi l^2}\,. \tag{2.27}$$

Integrating the density in spherical coordinates centered at the observer, $l = 0$, yields the particle flux at the observer:

$$\frac{\mathrm{d}N_\gamma}{\mathrm{d}E\,\mathrm{d}t\,\mathrm{d}A} = \frac{\mathrm{d}\Phi}{\mathrm{d}E} = \frac{1}{4\pi}\,\frac{\langle\sigma v\rangle}{\delta\, m_\chi^2}\,\frac{\mathrm{d}N_\gamma}{\mathrm{d}E}\int\limits_l\int\limits_{\Delta\Omega}\rho^2\,\mathrm{d}l\,\mathrm{d}\Omega. \tag{2.28}$$

Eq. 2.28 is only valid when neglecting diffusion processes. Charged final state products are deflected by interstellar and intergalactic fields, and so their propagation to the observer is deformed. Consequently, Equation 2.28 only holds for fluxes from prompt γ-ray and neutrino final state radiation. Also, Equation 2.28 is only valid for the final state radiation emitted in the cosmic neighborhood at $z \approx 0$. For extragalactic DM annihilation, the γ-ray spectrum at the observer is redshifted and damped by energy-dependent extinction. However, γ-ray emission from nearby Galactic DM subhalos is considered in this thesis only, and the final state γ-ray flux can be successfully described by Equation 2.28.

The γ-ray flux in the form of Equation 2.28 often is splitted into a "particle physics" factor and "astrophysical J-factor",

$$\frac{\mathrm{d}\Phi}{\mathrm{d}E}(E,\,\vec{k},\,\Delta\Omega) = \frac{\mathrm{d}\Phi^{\mathrm{PP}}}{\mathrm{d}E}(E)\times J(\vec{k},\,\Delta\Omega)\,, \tag{2.29}$$

where $\vec{k} = (\psi, \vartheta)$ denotes the direction of observation. The J-factor integrated over a solid angle $\Delta\Omega$ then reads

$$J(\vec{k},\,\Delta\Omega) = \int\limits_0^{2\pi}\int\limits_0^{\theta_{\mathrm{int}}}\int\limits_{\mathrm{l.o.s}}\rho^2(\vec{k};\,l,\,\theta,\,\phi)\,\mathrm{d}l\,\sin\theta\,\mathrm{d}\theta\,\mathrm{d}\phi\,. \tag{2.30}$$

Here, θ_{int} denotes the radius of the solid angle region around the pointing direction $\vec{k}$, over which the J-factor is integrated.

A note on DM decay: It has been argued that the lightest MSSM neutralino is stable, as guaranteed by R-parity conservation. However, R-parity may be violated, or SUSY would not provide an adequate description for a beyond-SM theory. From a model-independent point of view, a hypothetical DM particle is only required to be stable for the age of the Universe,

$t_{\mathrm{cosmo}} = 4.4 \times 10^{17}\,\mathrm{s}$. Although there is not such a theoretical necessity for WIMP decay as for annihilation, secondary fluxes from WIMP decay may even outweigh annihilation fluxes. Buchmüller et al. (2007) calculate an expected neutralino lifetime $\tau_\chi \gtrsim 10^{27}\,\mathrm{s} \approx 10^{10}\,t_{\mathrm{cosmo}}$ for gravitino DM. With $\Gamma_{\mathrm{decay}} = \dot{N} = N/\tau_\chi$, such a long lifetime still results in competitive secondary fluxes,

$$\frac{\mathrm{d}\Phi^{\mathrm{decay}}}{\mathrm{d}E} = \frac{1}{4\pi}\frac{1}{\tau_\chi\, m_\chi}\frac{\mathrm{d}N_\gamma}{\mathrm{d}E}\int\limits_l\int\limits_{\Delta\Omega}\rho\,\mathrm{d}l\,\mathrm{d}\Omega\,, \tag{2.31}$$

where, in general, $\frac{\mathrm{d}N_\gamma^{\mathrm{decay}}}{\mathrm{d}E}(m_\chi, E) = \frac{\mathrm{d}N_\gamma^{\mathrm{annihil}}}{\mathrm{d}E}(m_\chi/2, E)$. However, DM decay in a given density distribution ρ scales with $\propto \rho$ instead $\propto \rho^2$ as for annihilation, which results in a much broader, spatially extended emission. Background-dominated instruments with a high angular resolution like the Cherenkov Telescope Array (CTA) are much more sensitive to point-like, highly concentrated signals, like those that arise from DM annihilations. Therefore, DM annihilation is the focus of this thesis, and the applicability of the indirect methods developed here to detect DM decay is shortly discussed in the conclusions of the thesis.

Targets for indirect searches for DM: Dark matter annihilation cannot be observed locally. At earth, a local DM density of $\mathcal{O}(1\,\mathrm{GeV\,cm^{-3}})$ is expected (see Chapter 4). For a canonical cross section and $m_\chi > 1\,\mathrm{GeV}$, this results in less than 10^{-26} annihilations per second and cubic centimeter (Equation 2.25).[24] Even for a detector with a cubic kilometer in size, this leads to less than about one annihilation every 1000 years. Therefore, indirect DM detection is only promising for astrophysical probes, where sufficiently close and dense DM budgets are present.

The γ-ray flux from astrophysical DM targets scales with the J-factor, Equation 2.30, as an interplay of the density and the distance to the target. Several astrophysical DM-rich objects provide J-factors for which current γ-ray and neutrino experiments are able to probe DM annihilation close to the canonical cross section. The Galactic center (GC) region features by far the largest J-factors, and has been early identified as a prominent target for indirect DM searches (Silk and Bloemen, 1987). Although γ-ray emission has been observed from the GC since EGRET (Mayer-Hasselwander et al., 1998), it is complicated to assign the origins of the radiation and to pinpoint a potential contribution from DM annihilation (Stecker, 1988). In contrast, dSph galaxies provide clean targets for indirect DM searches, with low background radiative processes (Lake, 1990). However, the J-factors of these objects are expected at least a factor ten lower than for the GC (Bonnivard et al., 2015a; Geringer-Sameth et al., 2015). Studying the fluxes from dark DM subhalos in the MW is finally the subject of this thesis.

---

[24] The same rates result from decay with $\tau_\chi \gtrsim 10^{27}\,\mathrm{s}$.

Considerable DM signals are also expected from extragalactic sources. Galaxy clusters constitute far-away, but large DM reservoirs. In total, several clusters may provide J-factors similar to those of local dSph (Nezri et al., 2012; Combet et al., 2012). For clusters, large uncertainties arise on the expected DM fluxes from the boost of the annihilation signal by substructures, and potential signals are again superposed by astrophysical γ-ray-emission. Galactic DM and the global relic DM content of the Universe may also leave an imprint of the diffuse γ-ray emission, which is further discussed in the context of this thesis in Subsection 5.3.1.[25]

Status of indirect DM experiments: The launch of the *Fermi* satellite in 2008, carrying the γ-ray LAT (see Section 3.3), has opened an epoch of competing searches for DM in γ-rays. During its past eight years, LAT observations have set stringent constraints on DM-induced γ-ray emission from various targets and populations: The latest results published by the LAT collaboration comprise searches for γ-ray lines (Ackermann et al., 2015a), a search for an excess in the γ-ray continuum spectrum of the diffuse Galactic and extragalactic emission (Ackermann et al., 2015d), emission from galaxy clusters (Ackermann et al., 2010a, 2015c), dSph galaxies (Ackermann et al., 2015e; Drlica-Wagner et al., 2015; Albert et al., 2017), and dark subhalos (Ackermann et al., 2012c, *Fermi*-LAT implications for the latter are further discussed in Chapter 5). *Fermi*-LAT's observation of small-scale anisotropies in the diffuse γ-ray background (Ackermann et al., 2012a) has also been used to set upper limits on the DM annihilation cross-section (Ando and Komatsu, 2013; Gómez-Vargas et al., 2014; Lange and Chu, 2014). An updated analysis for anisotropies and DM implications has been recently published by Fornasa et al. (2016). Towards the GC, the presence of a γ-ray excess which can be attributed to DM is continuously disputed (e.g., Hooper and Linden, 2011; Abazajian, 2011; Calore et al., 2015; Daylan et al., 2016; Bartels et al., 2016; Calore et al., 2016a). The most stringent limits on WIMP DM by the *Fermi*-LAT are obtained from the non-detection of γ-rays in a combined analysis of observed dSph galaxies, which exclude WIMPs with masses $m_\chi \lesssim 100\,\mathrm{GeV}$ at the thermal relic cross section (Albert et al., 2017). Further improvement of limits is expected from the full 10-years dataset of the complete *Fermi*-LAT mission (Charles et al., 2016).

From Earth-bound γ-ray experiments (see Section 3.1), comparable limits on the annihilation cross section are obtained, while probing higher DM masses. The H.E.S.S. experiment has observed the GC region for over 250 h, and, from the absence of evidence for DM in the data, excludes cross sections $\sigma \gtrsim 10^{-25}\,\mathrm{cm}^3\,\mathrm{s}^{-1}$ for $m_\chi \approx 1\,\mathrm{TeV}$ for continuous spectra (Abdallah et al., 2016b) and $\sigma \gtrsim 10^{-27}\,\mathrm{cm}^3\,\mathrm{s}^{-1}$ for γ-ray line emission (Abdallah et al., 2016a, based on 18 hours of data). Somewhat weaker, yet consistent limits are obtained by stacked observations of several dSph objects by H.E.S.S. (Abramowski et al., 2014) and VERITAS (Zitzer, 2015), or

---

[25] See Conrad et al. (2015) for a detailed review on the various targets for indirect DM searches and recent results.

by the deep observation of a single dSph by MAGIC (Aleksić et al., 2014; Rico et al., 2016). In the later Figure 5.7, several of these limits are compared to the results of this thesis.

Searches for astrophysical neutrinos from point-like DM annihilation sources also have been performed with the IceCube neutrino detector (Ahrens et al., 2004). For IceCube, limits on the DM neutrino flux from the Sun (Aartsen et al., 2013a, 2016a), nearby galaxies and galaxy clusters (Aartsen et al., 2013b), and the Galactic center region (Aartsen et al., 2016b) have been derived. These limits can be directly compared to the ones from γ-ray experiments, and are competitive at $m_\chi \gtrsim 10\,\mathrm{TeV}$, close to the unitary bound.

Space-based cosmic ray experiments investigate the composition of the diffuse cosmic ray flux, and search for a an excess of particles that can only originate from DM annihilations. This mainly comprises antimatter particles like positrons, antiprotons, and heavier anti-nuclei, which are seldom produced in classical physical processes (Silk, 1989; Kamionkowski and Turner, 1991; Donato et al., 2004). The PAMELA experiment reported an excess in the positron-electron ratio between 10 and 100 GeV (Adriani et al., 2009). This effect was independently confirmed by the *Fermi*-LAT experiment (Ackermann et al., 2012b) and AMS-02 (Accardo et al., 2014), whereas the recent results by AMS-02 experiment indicate that the positron fraction again decreases above 200 GeV. Recently, the AMS collaboration has made public preliminary results on the measurements of the anti-proton/proton fraction. First interpretations find “no unambiguous antiproton excess” (Giesen, 2015), and are in agreement with the antiproton/proton ratio measured by PAMELA (Cirelli and Giesen, 2013). This lack of evidence for DM can be translated into strong limits on the DM annihilation cross section, close to the thermal relic cross section for $m_\chi \lesssim 100\,\mathrm{GeV}$ and several channels (Ibarra et al., 2014; Jin et al., 2015; Giesen, 2015).

Indirect searches for DM also have found no signatures from DM decay, and by this, set limits onto the DM lifetime larger than than the expected lifetime, $\tau_\chi \gtrsim 10^{27}\,\mathrm{s}$, for a wide range of DM masses (Ibarra et al., 2014; Ando and Ishiwata, 2015).

2.3.2. Outlook: Direct detection and collider experiments

Direct DM detection: The earth is exposed to a WIMP particle flux of $\mathcal{O}(10^5\,\mathrm{cm}^{-2}\,\mathrm{s}^{-1})$, while it moves through the Galactic DM halo.[26] Weak scattering of these WIMPs on SM nuclei might result into event rates larger than one event per kg and year (Undagoitia and Rauch, 2016). Although still constituting a weak signal for a $\mathcal{O}(< 10^3\,\mathrm{kg})$ detector, this turns direct detection of (in)elastic WIMP-nucleon scattering into a viable search strategy. Also, WIMP inelastic scattering with the target atoms’ electron shell may occur for lighter, sub-GeV particles (Essig et al., 2012). The current direct detection experiments have set strong limits on

---

[26] Assuming a local DM density of $0.3\,\mathrm{GeV\,cm^{-3}}$, $m_\chi = 100\,\mathrm{GeV}$, and a relative velocity of $220\,\mathrm{km\,s^{-1}}$ of the earth relative to the Galaxy’s rest frame.

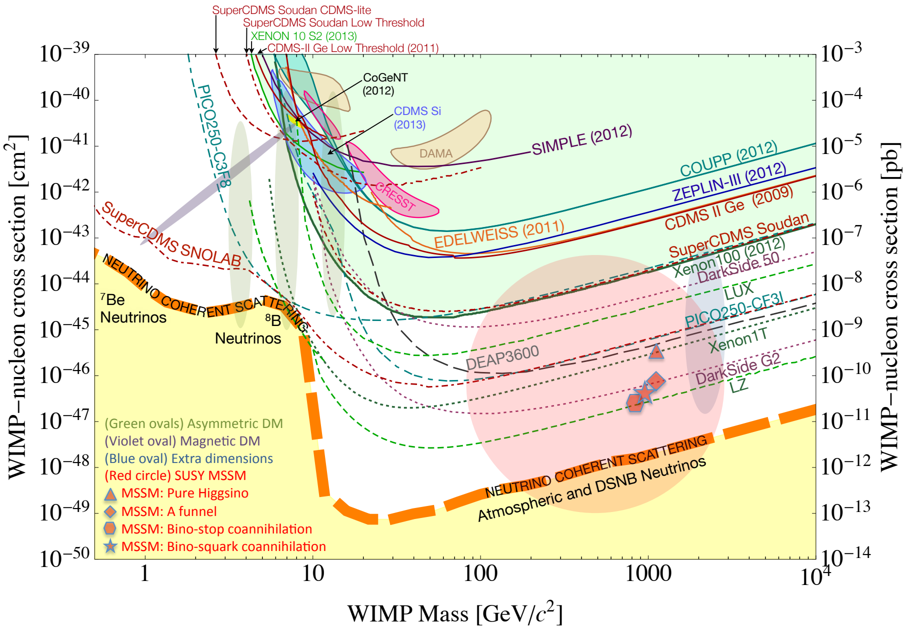

Figure 2.12.: Overview over present and future spin-independent WIMP-nucleus scattering searches. Limits on the cross sections are given as solid lines, future sensitivities as dashed curves. Putative hints for DM signals are shown as framed shaded areas. The unframed shaded areas indicate several model predictions by theory. The shaded yellow area at the bottom shows the irreducible background from neutrino scattering. Figure taken from Cushman et al. (2013).

the spin-dependent and spin-independent scattering cross sections. Figure 2.12 shows various limits on spin-independent WIMP-nucleus scattering for $m_\chi \gtrsim 1\,\mathrm{GeV}$ DM. Notably, DAMA and the successive LIBRA experiment reported an annual modulation of a signal on the $9\,\sigma$ level (Bernabei et al., 2013), which is in accordance with a Galactic DM particle flux, and also in the correct phase. Likewise, CoGeNT detected an annual modulation on the $2\,\sigma$ level (Aalseth et al., 2014). Weak signals which could hint to a DM detection have also been found by CRESST-II (Angloher et al., 2012) and CDMS II (Agnese et al., 2013). However, various other experiments could not confirm the signals of DAMA/CoGeNT/CRESST, and set limits orders of magnitude below (see Figure 2.12). Several alternative sources for the signals have been proposed, like a modulating muon flux (Blum, 2011) or instrumental systematics, but none of the alternative explanations completely accounts for the observed signals (Bernabei and Belli, 2010; Bernabei et al., 2014). Note that the incompatibility of the DAMA/LIBRA findings to other direct DM searches may be alleviated by the different sensitivities to spin-independent and spin-dependent DM-nucleus scattering of the experiments (Bertone et al., 2005; Sanders, 2014).

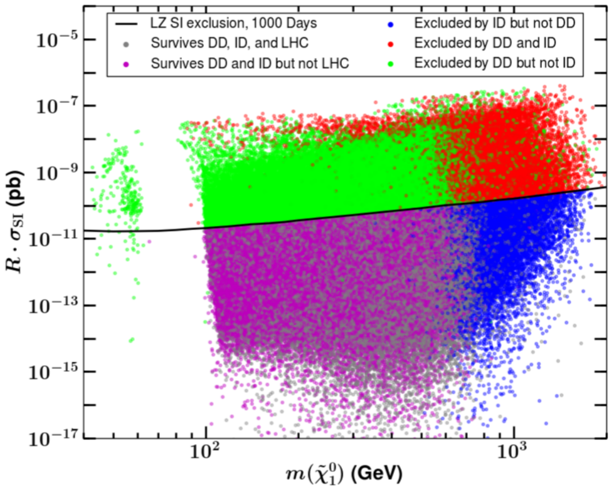

Figure 2.13.: Comparison of the sensitivity of different DM detection strategies, to spin-independent interaction in the pMSSM. $\tilde{\chi}_1^0$ denotes the lightest neutralino, and σ_{SI} the spin-independent interaction cross section. The vertical axis is scaled by a factor $R = \Omega^0_{\mathrm{CDM}} h^2|_{\mathrm{model}} / \Omega^0_{\mathrm{CDM}} h^2|_{\mathrm{Planck}}$. LZ denotes the LUX-ZEPLIN experiment (Akerib et al., 2004). The gray dots indicate the pMSSM models that have not yet been ruled out by the combination of the limits obtained from the different experiments. DD: direct detection. ID: indirect detection. Figure taken from Cahill-Rowley et al. (2015).

Collider searches: Experiments with particle accelerators like the Large Hadron Collider (LHC) set constraints on beyond-SM physics, and in particular on heavy DM candidates. However, interpretation of collider data is highly model dependent, and DM searches at the LHC effectively rule out specific SUSY models that could provide a neutralino DM candidate (Bertone et al., 2005). Cahill-Rowley et al. (2015) list a compilation of various SUSY searches at the LHC.

Combining limits: To compare the limits obtained for the DM interaction cross section from indirect, direct, and collider experiments, the framework of an effective field theory can be applied (Goodman et al., 2010; Fox et al., 2012; Bauer et al., 2015). Under the assumption that the energies involved in the processes are much lower than mediator masses, the mediator can be integrated out of the interaction amplitudes. Then, the cross section for annihilation, scattering, and WIMP production can be directly compared, provided that the same particles are present in the interactions as initial or final states in the different experiments, $\sigma(\chi q \to \chi q) \simeq \sigma(\chi\chi \to q\bar{q})$ (D'Amico et al., 2011). Consequently, for nuclear interactions dominating in direct and collider experiments, these experiments can only be compared to the indirect limits from annihilation into light quarks and gluons within the effective field theory approach. Figure 2.13 shows a compilation of pMSSM models that have been ruled out by the combined presence of limits from different indirect, direct, and collider experiments. The next generation of various DM experiments is able to conjointly probe further promising DM candidates (Bertone et al., 2016).

3 | Detecting astrophysical γ-rays

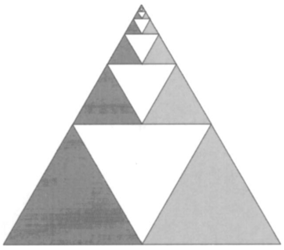

An abstract representation of an electromagnetic shower (see Equation 3.1).[1]

In the previous chapter, it has been argued that dark matter (DM) in our cosmos can be traced by its annihilation into high-energy γ-rays. However, the detection of extraterrestrial high-energy photons is an intricate endeavor: The Earth' atmosphere is opaque to radiation of energies $E_\gamma \gtrsim$ keV, such that no primary radiation reaches detectors at sea level. With the advent of the space age, detectors for high-energy radiation could be lifted above the atmosphere for the first time, and extraterrestrial γ-radiation ($\geq 50\,\mathrm{MeV}$) was already observed in 1961 by NASA's Explorer 11 mission, only four years after the Sputnik I launch. Around the same time, techniques were developed that finally made it possible to detect very-high-energy (VHE) photons, with $E_\gamma \gtrsim 100\,\mathrm{GeV}$, even at ground level. The Cherenkov Telescope Array (CTA),

---

[1] Picture taken from Mabry (1999).

whose DM detection prospects are the subject of this thesis, will mark the fourth generation of Earth-bound detectors to detect VHE photons. The following chapter summarizes the physical processes which allow the detection of extraterrestrial γ-rays at ground level (Section 3.1) and introduces the CTA instrument (Section 3.2). The space-borne *Fermi*-Large Area Telescope (LAT) is shortly presented in Section 3.3, as several comparisons between CTA and the *Fermi*-LAT are given throughout this thesis.

3.1. Foundations of ground-based γ-ray observation

3.1.1. Extensive air showers

Photon-electron cascades: Electromagnetic air showers

When a high-energy photon approaches Earth, it is usually absorbed in the lower stratosphere. It does so by dominantly converting into an electron-positron pair in the Coulomb field of a nucleus in the atmosphere (Grieder, 2010).[2] At photon energies above $\sim 1\,\mathrm{GeV}$, where screening of the nuclear charge Ze by the atomic electron cloud is effective, and for an average atmospheric composition (e.g., Grieder, 2010, p. 153), the average interaction length for this process approaches the constant value $\chi_{\mathrm{pair}} = 47\,\mathrm{g/cm^2}$. This atmospheric grammage (also called column density or overburden) translates to a height above sea level of around 25 km, at which a high-energy photon usually is pair-converted. After conversion of the primary γ-ray, the secondary high-energy electron and positron are elastically scattered off the nuclei of atmospheric molecules (by Rutherford/Coulomb-scattering), and subsequently emit high-energy bremsstrahlung photons. In this way, a photon-electron cascade, also dubbed as electromagnetic shower, is triggered: Bremsstrahlung photons convert into electrons and positrons, which in turn lose energy by emitting further bremsstrahlung photons. This picture of an electromagnetic shower is illustrated in Figure 3.1. Bremsstrahlung emission and pair creation are very similar quantum electrodynamic scattering processes, and so χ_{pair} is closely related to the radiation length for bremsstrahlung emission, χ_{r}, via $\chi_{\mathrm{pair}} = 9/7\,\chi_{\mathrm{r}}$ (Grieder, 2010). When both radiation lengths are considered approximately equal and all other interactions processes are neglected during the shower development, then the cascade develops exponentially and the number N of shower particles after k

---

[2] Note that at sufficiently high energies, also the pair creation of muons is energetically possible. However, the radiation length (or cross section) for pair creation scales proportional to e^4/m^2, such that the photon conversion into muons is suppressed by a factor $(m_e/m_\mu)^2 = 2.3\times10^{-4}$ compared to electrons (Grieder, 2010).

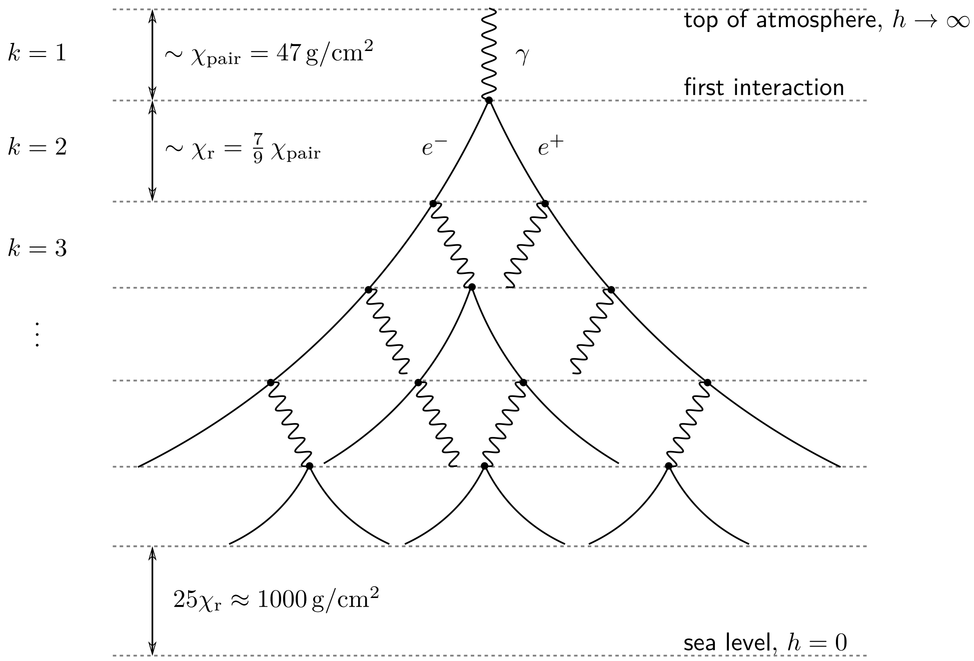

Figure 3.1.: Schematic sketch of the exponential growth of an γ-ray induced electromagnetic air shower, before reaching the shower maximum. The curved electron/positron tracks denote the opposite deflection in the Earth's magnetic field, the dots indicate that the splittings occur as interactions in the Coulomb field of nearby nuclei. The depiction neglects the different radiation lengths for pair creation and bremsstrahlung emission. Figure adapted from Guenette (2010).

2-foldings is $N(k) = 2^k$. The ratio of electrons[3] in the shower, N_e, to all shower particles is

$$\frac{N_e}{N}(k) = \sum_{i=i_0}^{k} (-2)^{i-k} \overset{k\to\infty}{=} 2\sum_{i=1}^{\infty} 4^{-i} = \frac{2}{3}\,, \tag{3.1}$$

where $i_0 = 1$ for a γ-ray induced cascade and $i_0 = 0$ for an electron induced cascade.[4] The shower growth is finally halted when, at lower energies, the electrons start to lose their energy dominantly via ionization rather than bremsstrahlung emission. The critical energy where both energy loss processes of the electrons become equal is about $E_{\mathrm{crit}} \approx 84\,\mathrm{MeV}$.[5] Assuming that the available energy E_0 of the primary γ-ray is always equally divided between the secondary particles in each splitting, the average energy of a particle in the shower is lowered to E_{crit} after $k_{\mathrm{max}} \approx \ln(E_0/E_{\mathrm{crit}})/\ln 2$ splittings. At this moment, the shower has traversed the atmospheric

---

[3] For the remainder of this section, if not otherwise stated, "electrons" is used to mean electrons and positrons.

[4] The limit of Equation 3.1 is attributed to be first found by Archimedes 250 − 200 BC (e.g., Swain and Dence, 1998) and is illustrated by the picture below the heading of this chapter.

[5] This energy is in the same order of magnitude where also pair creation by photons is passed by Compton scattering.

grammage of

$$X_{\mathrm{max}} \approx k_{\mathrm{max}}\,\chi_{\mathrm{r}} \approx \left(\ln \frac{E_0}{\mathrm{GeV}} + 2.5\right) \times 53.4\,\frac{\mathrm{g}}{\mathrm{cm}^2}\,. \tag{3.2}$$

This characteristic grammage X_{max} is called the shower maximum, where the maximum number of particles is reached. At X_{max}, the shower has grown to $N_{\mathrm{max}} \approx E_0/E_{\mathrm{crit}}$ particles, where approximately

$$N_e(X_{\mathrm{max}}) \approx \frac{2}{3}\,\frac{E_0}{E_{\mathrm{crit}}} \approx 8\,\frac{E_0}{\mathrm{GeV}} \tag{3.3}$$

electrons are created in the cascade. In the subsequent development of the shower, the number of electrons again decreases exponentially, as they are absorbed in the lower atmosphere. Equations 3.2 and 3.3 express the two basic properties of an electromagnetic shower. Firstly, with increasing energy of the primary γ-ray, the shower maximum penetrates only logarithmically into larger atmospheric grammages. As the atmospheric grammage itself scales logarithmically with the height above ground, $h_{\mathrm{max}} \sim \ln(X_0/X_{\mathrm{max}})$ where $X_0 = X(h = 0) \approx 1020\,\mathrm{g/cm}^2$ is the total grammage, only few electrons from electromagnetic showers reach ground level. Secondly, the number of particles at the shower maximum increases linearly with the energy of the primary γ-ray. The simple picture is confirmed by a more rigorous treatment, applying a proper probabilistic account for bremsstrahlung emission and photon conversion, and including ionization losses (Grieder, 2010). Figure 3.2 shows the result after the calculation under the so-called *approximation B* of classical cascade theory (Rossi and Greisen, 1941).

The development of particles within the shower as a function of the atmospheric grammage is often referred to as the longitudinal shower development. However, Imaging Atmospheric Cherenkov Telescopes (IACTs) are able to discriminate γ-ray induced showers from nuclei-induced showers mainly by their different lateral development. In the highly relativistic regime, the secondary electrons and bremsstrahlung photons are beamed into the forward direction of the primary particle, and the opening angle of electromagnetic showers is generally very small. The lateral spread of the shower is dominated by the electron-nucleus Coulomb scatterings and scales with the so-called Molière radius, $R_{\mathrm{mol}}(h) = E_{\mathrm{scatt}}/E_{\mathrm{crit}}\,\chi_{\mathrm{r}}/\rho(h)$, where $E_{\mathrm{scatt}} = 21\,\mathrm{MeV}$ and ρ the atmospheric density (Molière, 1942; Grieder, 2010). Around 90% of the shower particles are contained in a cylinder within R_{mol}, and it is $R_{\mathrm{mol}} \approx 200\,\mathrm{m}$ at $h \approx 8\,\mathrm{km}$, the height of the shower maximum for $E_\gamma \approx 1\,\mathrm{TeV}$ (Aharonian et al., 2008b). Additionally, depending on the relative directions between the shower axis and the geomagnetic field lines, the electrons and positrons are separated. For strong geomagnetic deflection, the electron-positron separation may outweigh the Coulomb scattering spread and may significantly worsen the identification of electromagnetic showers.

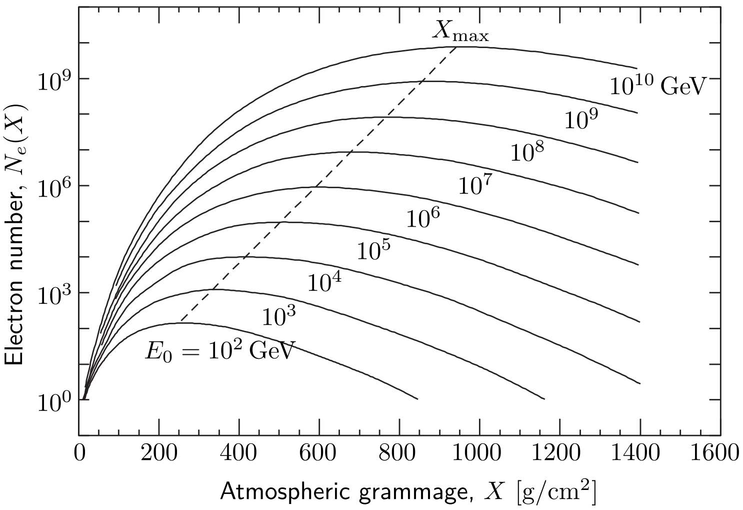

Figure 3.2.: Average development of the electron content, N_e, in an electromagnetic air shower as a function of the atmospheric grammage, X, in classical cascade theory (approximation B). The dashed line indicates the shower maximum, $X_{\max}$, for different primary γ-ray energies, E_0, between 100 GeV and 10^{19} eV. The curves show that $X_{\max}$ increases logarithmically with increasing E_0 (Equation 3.2), and that the electron number at shower maximum, $N_e(X_{\max})$, increases linearly with E_0 (Equation 3.3). However, $N_e(X_{\max})$ is significantly lower than predicted by Equation 3.3, due to ionization losses and a smooth transition from the growing to the declining phase of the shower. Note that sea level is located at around $X \approx 1000\,\mathrm{g/cm^2}$, such that for $E_0 \gtrsim 1$ TeV shower electrons reach the ground. Figure taken from Grieder (2010).

Hadronic air showers

Not only γ-rays, but also charged particles like electrons and atomic nuclei reach the Earth from outer space. These high-energy, charged extraterrestrial particles are termed *cosmic rays* and constitute the largest amount of background noise for Earth-bound detection of γ-rays. In particular, the showers initiated by cosmic-ray electrons are indistinguishable from γ-ray induced showers,[6] and consequently cosmic electrons constitute an irreducible background for Earth-bound γ-ray astronomy. In turn, showers initiated by atomic nuclei can be efficiently distinguished from those triggered by γ-rays or electrons. Figure 3.3 illustrates the development of a shower triggered by a high-energy proton. Hadronic particles interact highly inelastically with the atmospheric nuclei via the strong force. In such a high-energy hadron collision, the collision partners are completely destroyed, and a number of elementary particles is created out

---

[6] Apart from the fact, that the first interaction of an electron is bremsstrahlung, and the average grammage of the first interaction is a factor 7/9 smaller (higher in the atmosphere) than for a γ-ray. In fact, the Cherenkov light imprint significantly differs at very low primary energies ($E_0 \lesssim 20$ GeV) between γ-ray and electron showers (Sahakian et al., 2006). However, in the VHE regime at $E_0 \gtrsim 100$ GeV, the difference between γ-ray and electron showers is unresolvable for current instruments.

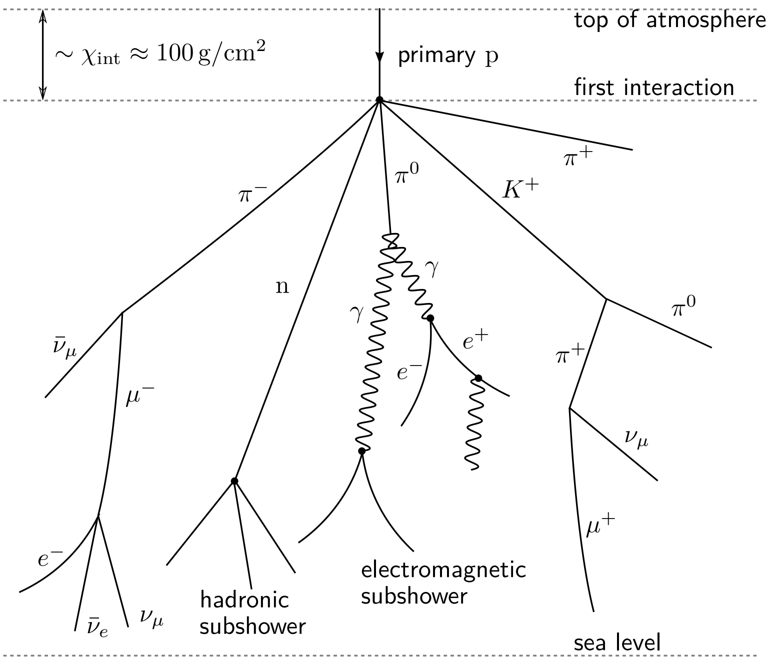

Figure 3.3.: Sketch of a hadronic particle air shower. Figure adapted from Perkins (2003).

of the available energy. Quarks then recombine to nucleons or mesons like pions and kaons.[7] The secondary hadrons again inelastically collide with atmospheric nuclei, creating lower energetic hadronic subshowers. Unstable hadrons in the shower also decay, and the probability for decaying rather than interacting increases with decreasing hadron energy. For a typical atmospheric density profile,[8] the critical energy, below which decay of secondary hadrons outweighs subshower initiation, is $E_{\mathrm{c}} \approx 140\,\mathrm{GeV}$ for pions and $E_{\mathrm{c}} \approx 1\,\mathrm{TeV}$ for the K^+. Towards the end of the shower development, hadrons thus decay, mostly via pions, into muonic leptons. Secondary π^0 mesons dominantly decay into γ-rays and create electromagnetic subshowers (Figure 3.3). As the muons are relatively long-lived, they may survive until sea level, such that hadronic showers usually leave a particle imprint on the ground. Excluding photons, about one third of the vertical secondary particle flux $> 1\,\mathrm{GeV}$ from hadronic showers at sea level are muons, with the other two thirds being neutrinos. Nucleons and electrons (mostly from muon decays) also reach sea level, but they constitute less than 1% of the particle flux on the ground. (Olive, 2014).

Figure 3.4 compares the morphologies of typical electromagnetic and hadronic showers. Com-

---

[7] In principle, all kind of mesons and heavy baryons are generated. However, pions and kaons are the particles with the shortest lifetime usually considered, $\tau \gtrsim 10^{-8}\,\mathrm{s}$ (except the electromagnetic π^0 decay with $\tau = 8 \times 10^{-17}\,\mathrm{s}$) and leptonic decay products from particles with shorter lifetime are usually called prompt leptons.

[8] Assuming the same exponential atmospheric profile as defined in Figure 9, which results in $\rho(h) = \rho_0\,\exp(-h/H)$ with $H = 8.0\,\mathrm{km}$. The critical energy then computes to $E_{\mathrm{c}} = m\,H/\tau$, where m is the mass of the secondary hadron and τ its lifetime (Perkins, 2003). For the K^0_{L} particle, $E_{\mathrm{c}} \approx 260\,\mathrm{GeV}$.

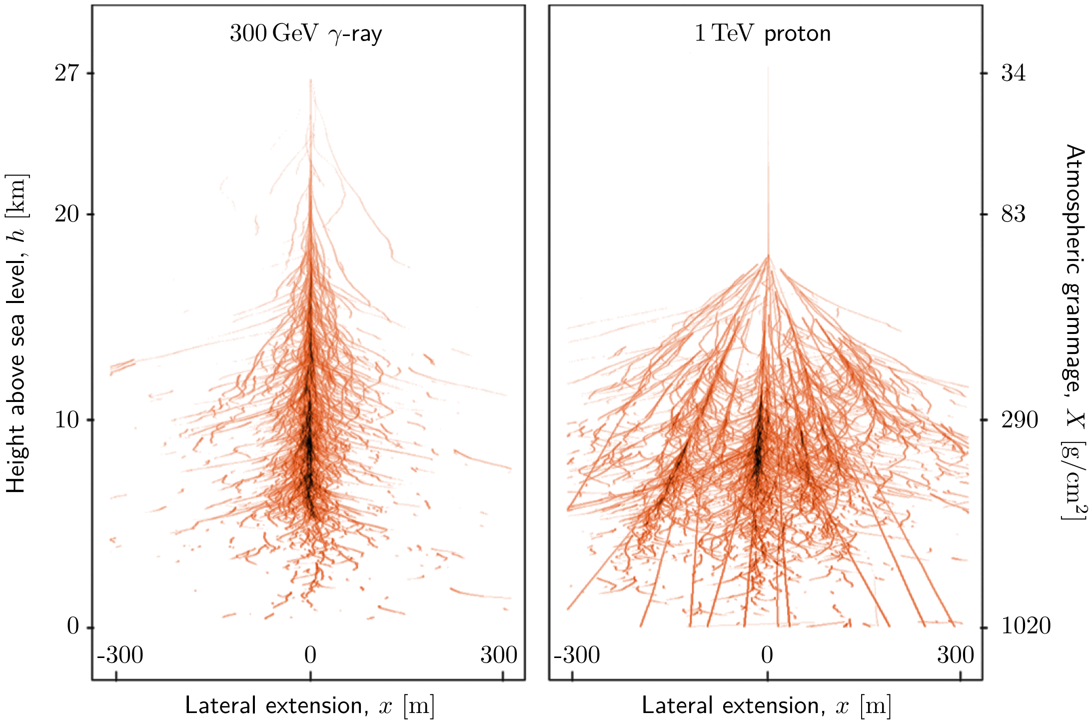

Figure 3.4.: Comparison between an electromagnetic air shower (triggered by a 300 GeV primary γ-ray) and a hadronic air shower (initiated by a 1 TeV proton). The figure shows the secondary particles projected onto a plane in (x, h) direction. Figure taken from Aharonian et al. (2008b).[9]

pared to electromagnetic showers, hadronic showers are much more complex in their spatial development and energy deposition in the atmosphere. In particular, the inelastic collisions and decays produce secondary particles with much larger transversal momentum, such that the showers are spread out over much larger areas. Additionally, because of the diverse branching channels, the shower development and energy deposition is much more irregular than for electromagnetic cascades. Lastly, the interaction length of protons – which constitute about 90% of the cosmic rays above 100 GeV – is $\chi_\mathrm{p} \approx 120\,\mathrm{g\,cm^{-2}}$ (Olive, 2014; Mocchiutti et al., 2003), three times larger than for electrons and γ-rays (χ_pair, $\chi_\mathrm{r} \approx 40\,\mathrm{g/cm^2}$). Therefore, the average heights of the first interaction and the shower maximum of hadronic showers are located at significantly lower heights above ground than for electromagnetic showers. All these differences between hadronic and electromagnetic showers can be used to identify the primary particle species.

The ratio of γ-rays to cosmic rays hitting the atmosphere strongly depends on the γ-ray source under consideration. Whereas the cosmic-ray background can be considered as perfectly

---

[9] For the translation from heights, h, to atmospheric grammages, X, a simple isothermal atmosphere with constant gravitational acceleration $g = 9.81\,\mathrm{m/s^2}$, temperature $T = 273\,\mathrm{K}$, a pressure of 100 kPa at sea level, and an average molar mass of air of 0.029 kg/mol has been assumed.

diffuse on small scales, γ-rays are not isotropized by magnetic fields and may originate from very localized spots in the sky. Averaged over large solid angles and at primary energies $\gtrsim 100\,\mathrm{GeV}$, approximately only about one electromagnetic shower out of 1000 is initiated by a γ-ray, and only about one shower out of 100 is electromagnetic and not hadronic (see also Figure 5.11 in Chapter 5). Therefore, for Earth-based γ-ray observation, it is crucial to efficiently distinguish electromagnetic from hadronic showers in order to reject the large hadronic background.

Detection methods of extended air showers

Observing cosmic rays and γ-rays at ground level via their particle showers can be understood as using the Earth's atmosphere as the actual detector medium, serving as *sampling calorimeter*. The instruments on the ground then serve for "reading out" the energy deposited in the atmosphere and reconstructing the origin of the primary event.

Two approaches exist to measure an extended air shower (EAS) at ground level: Either by directly detecting the particles in the shower, or by recording the Cherenkov light emitted by the shower particles.[10] The first approach is performed by EAS arrays, while the second one is pursued by atmospheric Cherenkov telescopes. Detecting the shower particles in EAS arrays requires the experiment to be located at high altitudes, as close as possible to the shower maximum. Only sufficiently energetic primary particles produce enough shower particles reaching the ground, such that, depending on the altitude, EAS arrays have a relatively large energy threshold, $E_0 \gtrsim 1\,\mathrm{TeV}$. Cherenkov telescopes allow a lower energy threshold, $E_0 \gtrsim 20\,\mathrm{GeV}$ and a better angular and energy resolution, but they are only able to operate during clear, dark nights and have a small field of view (FOV) of $\lesssim 0.01\,\mathrm{sr}$ (compared to $\lesssim 2\pi\,\mathrm{sr}$ for EAS arrays).

Due to their high energy threshold and poor angular resolution, EAS arrays are more suited for the study of the energy spectrum of the diffuse cosmic rays at high energies rather than for resolving γ-ray sources. The first EAS array experiments devoted to cosmic rays are dated back into the 1940s, and over a dozen experiments are operating today (for a review, see Kampert and Watson, 2012). The high-altitude MILAGRO detector at 2650 m above sea level (a.s.l.), constructed in the late 1990s in New Mexico, was the first EAS array to also successfully extract γ-ray showers from the cosmic-ray background at ground level. MILAGRO has recently been succeeded by the HAWC experiment located at 4100 m a.s.l. in northern Mexico.

The history of Cherenkov astronomy started in the 1950s with pioneering works by B. Galbraith and J. Jelly (for a historical review of the field, see Weekes, 2007; Hillas, 2013). However, it was only in 1989 that the Whipple telescope unambiguously detected the first astrophysical γ-rays at ground level, originating from the Crab Nebula (Weekes et al., 1989), by imaging the

---

[10] Additionally, showers can be traced by radio and fluorescence emission, which is not further discussed here.

Cherenkov light of the γ-ray showers. The success of the Whipple experiment proved the strength of the imaging technique for Cherenkov astronomy, and similar Imaging Atmospheric Cherenkov Telescopes (IACTs) were constructed in the southern hemisphere (CANGAROO in Australia) and Europe (CAT). The construction of the five HEGRA telescopes in the mid 1990s on the island of La Palma marked the second generation of IACTs, and the performance of a stereoscopic IACT array was explored for the first time. At the beginning of the new millennium, several third generation IACTs were constructed: the Very Energetic Radiation Imaging Telescope Array System (VERITAS) array in southern Arizona, the Major Atmospheric Gamma Imaging Cherenkov Telescopes (MAGIC) telescopes on La Palma, and the High Energy Stereoscopic System (H.E.S.S.) array in Namibia in the southern hemisphere. These three experiments are shown in Figure 3.5. Since then, new camera concepts and telescope designs have been explored, e.g., with the FACT telescope located aside the MAGIC array. The forthcoming CTA (with one array in the northern and one in the southern hemisphere) marks a joint effort to construct a fourth-generation instrument, combining the experience from all current IACT experiments.

Figure 3.5.: Currently operating third generation IACT arrays: The MAGIC telescopes on La Palma, Canarian Islands (*upper left*, mirror diameters 17 m), the four H.E.S.S. telescopes (mirror diameters 12 m) and the large H.E.S.S. II telescope (average mirror diameter 28 m) on the Khomas Highland in Namibia (*upper right*), and the VERITAS array near Tucson, Arizona, USA (*bottom*, mirror diameters 12 m). Image credits by the MAGIC/H.E.S.S. & VERITAS collaborations.

3.1.2. Imaging atmospheric Cherenkov technique

Cherenkov radiation in extended air showers

When charged particles move faster through a medium than the phase velocity of light, energy is deposited by coherent emission of so-called Cherenkov light by the surrounding medium (Jackson, 1998). Not long after the effect had been properly explained (Cherenkov, 1934), it was was proven by B. Galbraith and J. Jelly that Cherenkov photons are also emitted by the atmosphere when an extended air shower passes. In fact, around 0.1‰ of the non-anthropic night-sky optical background light, dominated by air glow, starlight and Galactic background, arises from Cherenkov radiation in the atmosphere, accompanying extended air showers (Grieder, 2010).

The coherence condition, or Cherenkov relation, for the emission of Cherenkov photons can be written as (Jackson, 1998):

$$\cos\theta = \frac{1}{\beta n} = \frac{c_{\text{med}}}{v}\,. \tag{3.4}$$

Here, n is the refractive index of the medium traversed by a charged particle, $\beta = v/c$ the particle's velocity, and $c_{\text{med}} = c_0/n$ the phase velocity of light in the medium. Obviously, Equation 3.4 only has real solutions for $c_{\text{med}} \leq v$, and the Cherenkov light is emitted under the angle θ with respect to $\vec{v}$. The minimum kinetic energy of a charged particle in the atmosphere at height h, for which Cherenkov light is emitted at $\cos\theta = 1$, is

$$E_{\text{min}}(h) = mc^2\,\frac{n(h)}{\sqrt{n(h)^2-1}} = mc^2\,\gamma_{\text{min}}(h)\,, \tag{3.5}$$

giving an emission threshold of $E_{\text{min}} \approx 34\,\text{MeV}$ for electrons at $h = 8\,\text{km}$ above sea level. However, the refractive index of air n strongly varies throughout the Earth's atmosphere and, for an isothermal atmosphere, increases exponentially with decreasing height above ground (Bernlöhr, 2000; Grieder, 2010). As a consequence, the emission threshold energy decreases, while the Cherenkov angle, θ, increases with decreasing height above the ground. Therefore, continuously emitted Cherenkov light from forward beamed electrons is concentrated on the ground within a ring-like region, with the shape and intensity dominated by the emission at the shower maximum. For an electromagnetic cascade initiated by a 1 TeV γ-ray, the shower maximum is at approximately $h_{\text{max}} \approx 8\,\text{km}$. The Cherenkov opening angle is $\theta(h_{\text{max}}) \approx 1^\circ$, such that the light pool at ground level has an approximate diameter of $200 - 300\,\text{m}$. Scattering and velocity dispersion of the shower electrons at each moment in the shower development cause the ring-like image to be blurred, such that a typical Cherenkov light pool is obtained (see Figures 3.6 and 3.7). As the resulting light pool on ground is approximately uniformly illuminated, any optical imaging system located in the pool is able to record a projected image of the shower develop-

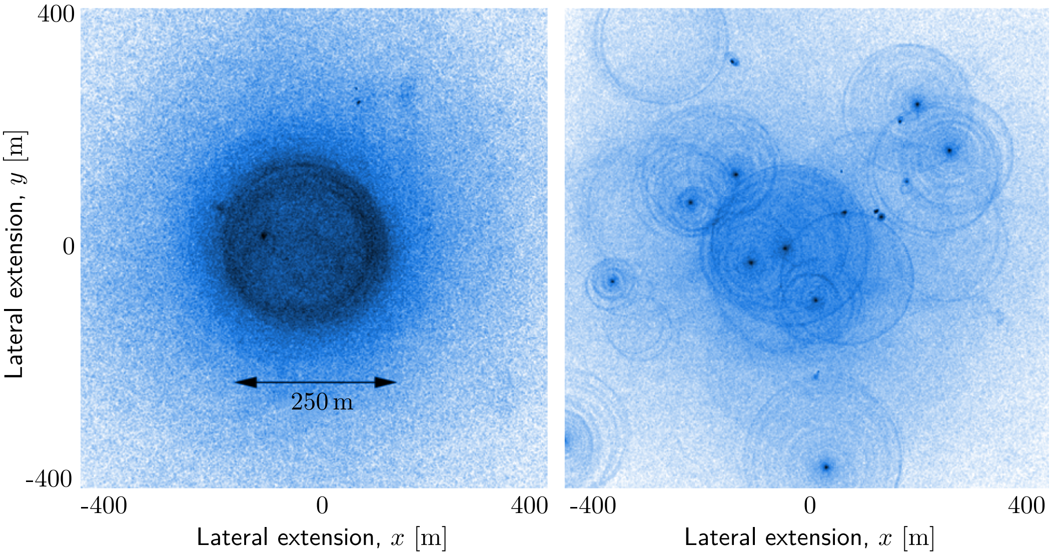

Figure 3.6.: Comparison between the time-integrated Cherenkov light pool at ground level of an electromagnetic air shower (*left*; triggered by a 300 GeV primary γ-ray, like in Figure 3.4) and a hadronic air shower (*right*; initiated by a 1 TeV proton, like in Figure 3.4). Both showers approximately produce the same amount of Cherenkov light (see text). The figures are obtained by Monte-Carlo (MC) simulations of the showers and the showers' Cherenkov light emission. On the right figure, the intense dots originate from muons reaching the ground and most of the rings originate from the various electromagnetic subshowers. Figure taken from Aharonian et al. (2008b).

ment (see Figure 3.8). Depending on the lateral displacement of the shower axis with respect to the telescope location, the shower image gets elongated to an elliptical shape (Figure 3.8). The width of this ellipse preserves the lateral development of the shower, while the length depends on the longitudinal development and the shower displacement from the optical system.

The number N of Cherenkov photons emitted per unit length x and wavelength λ is described by the Frank-Tamm formula (Tamm and Frank, 1937; Jackson, 1998),

$$\frac{\mathrm{d}N}{\mathrm{d}x} = 2\pi\alpha Z^2 \int\limits_{\lambda(n>1/\beta)} \left(1 - \frac{1}{\beta^2 n(\lambda)^2}\right) \frac{\mathrm{d}\lambda}{\lambda^2}\,, \tag{3.6}$$

where α is the fine-structure constant and Z the electromagnetic charge number of the moving particle. Due to the λ^{-2} scaling, the spectrum is peaked at small wavelengths and therefore appears bluish in the optical band. Detection of Cherenkov light is most efficient in the near UV band, where the Cherenkov light intensity is highest, and the night sky background intensity decreases. At shorter wavelengths, the Cherenkov light is absorbed in the air, making a detection impossible. For a typical 1 TeV electromagnetic air shower and a telescope located

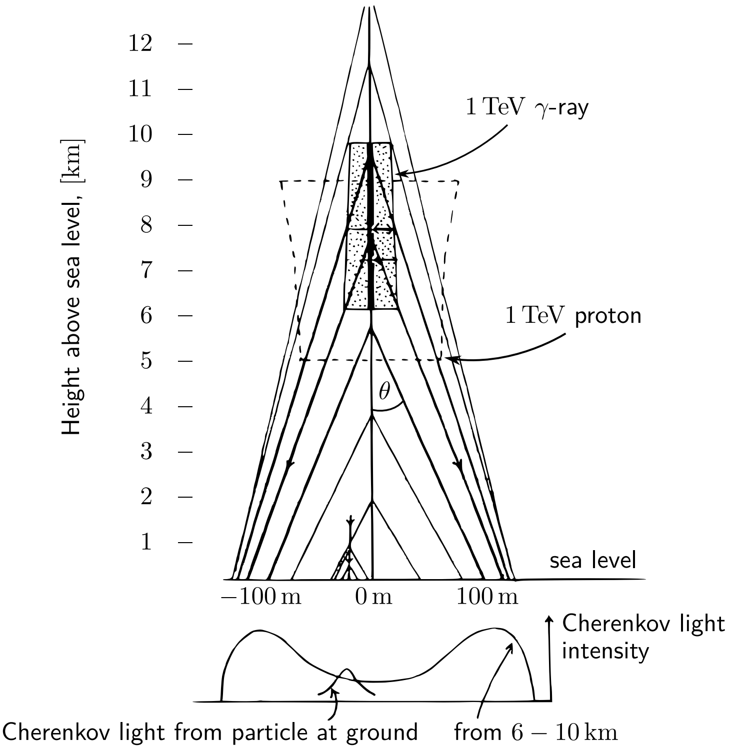

Figure 3.7.: Formation of a typical Cherenkov light pool at ground level originating from a vertically developing electromagnetic air shower. The angle θ denotes the Cherenkov light cone opening angle, which is varying with height and electron energy. The solid box is the region around the shower maximum, where the median 25% of all Cherenkov light is emitted (50% emitted above and below, and 25% laterally). The dashed box shows the corresponding region for a hadronic air shower. Figure taken from Hillas (1996).

at $h = 2\,\mathrm{km}$ above sea level, approximately 100 Cherenkov photons per square meter with a wavelength between 300 nm and 600 nm reach the ground within the shower pool (Hillas, 1996). For a telescope mirror surface of $100\,\mathrm{m}^2$, this results in merely 10^4 photons hitting the camera. Consequently, a suitable IACT camera needs (i) to be sensitive to signals consisting of $\lesssim 10^4$ photons in the near UV band, (ii) to have a suitable spatial resolution of the shower image within a field of view of several degrees, and (iii) to be capable of nanosecond time resolution to catch the short flashes of Cherenkov light. These requirements are fulfilled by a camera consisting of a large number ($\sim 10^3$) of individual Photomultiplier tubes (PMTs). One out of the four cameras of the VERITAS experiment is shown for example in Figure 3.9. Fewer Cherenkov photons are emitted by lower energetic showers, and the detection of γ-rays with IACTs is typically possible – depending on the telescope mirror size – down to a primary particle energy threshold of $E_0 \gtrsim 20\,\mathrm{GeV}$.

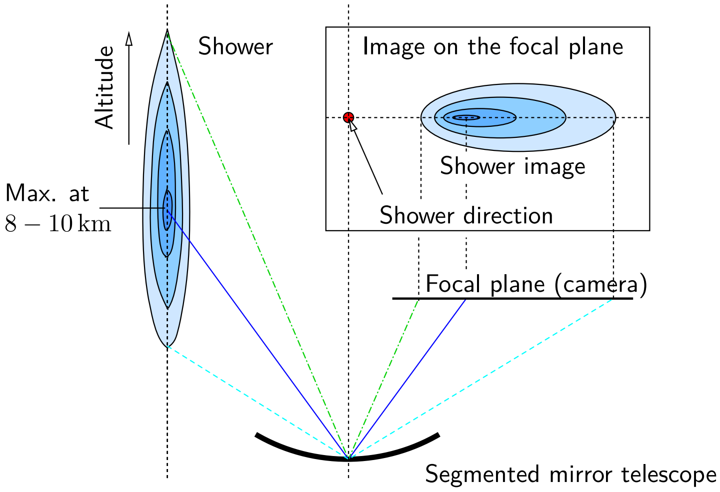

Figure 3.8.: Illustration of the Cherenkov light image of an electromagnetic air shower recorded by an IACT. The shower axis is parallel to the telescope pointing direction, however, laterally displaced. On the left, the ellipse contours denote the the shower electron density; on the right, the contours denote the Cherenkov light image in the camera plane. Figure taken from Völk and Bernlöhr (2009).

Shower reconstruction and classification of Cherenkov light images

Recording time-resolved Cherenkov light images of the air shower is the key component for detecting astrophysical γ-rays from Earth. Firstly, the angular direction in the sky of the primary particle can be pinpointed with an accuracy of better than $\sim 0.1°$. Secondly, the impact location of the shower axis on the ground can be estimated. Together with the measured Cherenkov light intensity of the image, the energy of the primary particle can be estimated. Thirdly, the image shape reflects the different lateral development of electromagnetic and hadronic air showers, which can be used for an efficient rejection of the cosmic-ray background.

Presuming knowledge on the lateral and longitudinal extension of an electromagnetic air shower at any primary energy, the ratio of the length and width of a single shower image can be used to determine the impact distance of the shower axis with respect to the telescope. Consequently, a single shower image can be used to reconstruct both arrival direction and impact position on the ground of the shower axis (for details, see Fegan, 1996; Grieder, 2010). However, a much better shower reconstruction can be achieved by a stereoscopic imaging with two or even more telescopes.[11] This is illustrated in Figure 3.10. Superposing the shower images from different telescopes recording the same shower in a joint coordinate system directly reveals the angular direction of the primary particle (Figure 3.10, left). From intersecting the major

---

[11] This can be compared to the analogy that observing with a monoscopic eye or telescope requires some additional knowledge about the observed object (physical diameter, absolute luminosity) to determine its distance.

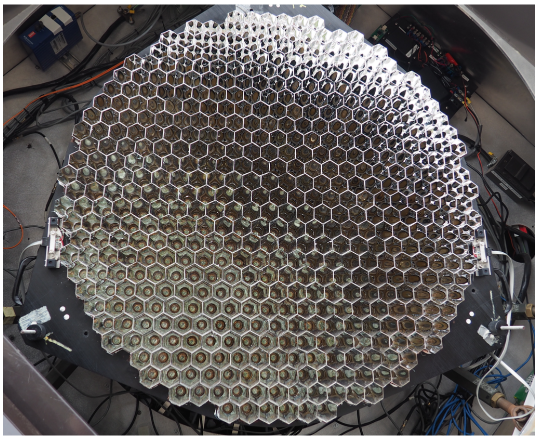

Figure 3.9.: Design of a typical IACT camera, using the example of the VERITAS experiment. The cameras of the four VERITAS telescopes each consist of 499 PMTs, and cover a FOV radius of 1.75°. Each pixel covers an area of 0.15° in diameter, somewhat larger than the optical resolution of the mirror system (Holder et al., 2006). The picture also shows the hexagonal light cones mounted on top of the PMTs, ensuring that all photons hitting the camera are reflected into one of the PMTs. The diameter of the camera is $\sim 1\,\mathrm{m}$. Picture taken by the author.

axes in the ground coordinate system, the impact point of the shower axis at ground level is obtained (Figure 3.10, right). Because of the imperfect reconstruction of the major image axes, the intersection point is calculated as the average of the multiple bi-axis intersections, where the average is weighted by $\sin\alpha$, the angle between two major axes. To obtain a maximum parallax between the shower images, while still having several telescopes located in the Cherenkov light pool, the typical distance of telescopes in an IACT array optimized to the detection of $\lesssim 5\,\mathrm{TeV}$ γ-rays is about $100\,\mathrm{m}$.

Besides the directional reconstruction, the shower image shapes provide the main discriminator between electromagnetic and hadronic events. As illustrated in Figure 3.6, the Cherenkov light pool from hadronic air showers is much more inhomogeneous and so are the shower images recorded in IACT cameras. Together with the shower axis parameters from the stereoscopic reconstruction, the shape, length, and width of the shower images can be efficiently used to reject hadron initiated air showers.

Cherenkov light from individual muons close to the ground is also sometimes recorded. For large impact parameters, these muons may mimic the image shape of a faint γ-ray shower (Völk and Bernlöhr, 2009). Observation with several telescopes can however suppress the background from individual muons. For several sufficiently displaced telescopes, muons show up only in a single telescope. A joint trigger condition for signal events to be recorded by at least two telescopes then can efficiently reject the muon events.

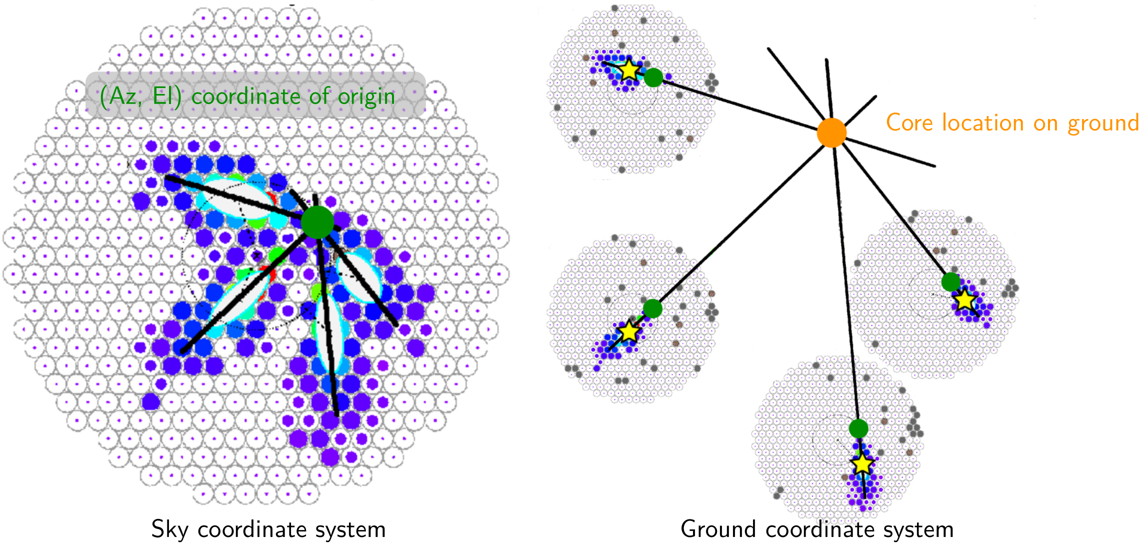

Figure 3.10.: Stereoscopic reconstruction of the air shower origin in the sky (*left*) and the impact point of the shower axis on the ground (*right*). The shower direction (green point on the left) is obtained as intersection of the major semiaxes of the shower ellipses of all images in the same camera coordinate system. On the right, the shower axis intersection point at ground is obtained as intersection of the lines connecting the center of gravity (yellow star) of each shower image, and the shower direction (green point) in the camera images located in the ground coordinate system of the telescopes. The figure illustrates a real, most likely electromagnetic event recorded by the VERITAS array. Figure courtesy of S. Vincent.

A final source of background comes from hadronic air showers that appear like electromagnetic showers. Electromagnetic subshowers, which dominate the Cherenkov light intensity of a hadronic shower, mainly arise from π^0 decays and to a negligible fraction also from electrons after muon decays. In each hadronic interaction, approximately 1/3 of the available energy is transferred into neutral pions, which immediately decay ($\tau = 8 \times 10^{-17}\,\mathrm{s}$) and trigger electromagnetic subshowers. For repeated hadronic subcascades triggered by the long-lived charged pions, as much as 90% of the primary energy can be deposited in electromagnetic subshowers for VHE primary particles, and less for primary energies approaching $E_\mathrm{c} \approx 140\,\mathrm{GeV}$ (Engel et al., 2011). Hadronic events mimicking γ-ray events mainly arise from showers where only few electromagnetic subshowers are created or only a single subshower reaches the detector array (Maier and Knapp, 2007). As a result, the primary energy reconstructed from the Cherenkov light in a γ-ray-mimicking hadron shower at $E \sim 1\,\mathrm{TeV}$ is on average about a factor two to three smaller than the actual energy of the primary hadron. This is of importance for the residual background of Earth-bound γ-ray telescopes, as the residual background from misclassified hadronic showers follows the hadronic cosmic-ray energy spectrum, but shifted by a factor ~ 3 towards lower energies.

Night sky background rejection

An IACT with an effective collection area of $\sim 10^5\,\mathrm{m}^2$ records, for an energy threshold of $E_0 \gtrsim 100\,\mathrm{GeV}$ around 10^3 showers per second. Still, the time resolution of the instrument must by far exceed a milli-second to extract the dim Cherenkov light from the night sky background level. As introduced on page 58, the optical night sky background light comprises air glow, the starlight, unresolved optical emission in the Galaxy, and zodiacal light (Grieder, 2010).

The time dispersion of Cherenkov photons due to different emission heights and phase velocities in the air is small, and at a given distance from the shower core, the Cherenkov light flash of a typical electromagnetic air shower lasts $\lesssim 10\,\mathrm{ns}$.[12] During this short time interval, the Cherenkov light of an average air shower may outweigh the average night sky background by a factor ~ 10 and can be clearly detected above the night sky background noise. To achieve such a fast time response, IACT cameras have to be equipped with ultra-fast PMTs. Additionally, a highly efficient electronic read-out system is needed, which is able to store the recording – and, because of the vast amount of information, to trigger and store only information from actual showers.

A stereoscopic array of several IACTs offers the advantage of an efficient night sky background rejection by requiring a trigger condition between several telescopes. Fake shower images due to night sky background fluctuations in individual telescopes are ignored by only reading out events which occur in several telescopes within $\sim 10\,\mathrm{ns}$.

Current IACTs reach a time resolution down to $\lesssim 2\,\mathrm{ns}$. Such precise timing facilitates tracing the time development of the Cherenkov light front in the shower image. The arrival time differences of Cherenkov photons emitted at different heights in the shower development is fairly complex, depending on the distance and orientation of the shower and the varying refractive index, $n(h)$, of the air. However, with the help of dedicated Monte-Carlo (MC) simulations, the information about the time gradient of the shower images provides another independent measurement for the shower reconstruction.

---

[12] For hadronic air showers, the Cherenkov light time dispersion is somewhat larger than for electromagnetic showers.

3.2. The Cherenkov Telescope Array

The Cherenkov Telescope Array (CTA) will be the next generation ground-based IACT γ-ray observatory. It will feature unprecedented energy resolution and angular separation for γ-rays in the range between $20\,\mathrm{GeV} \lesssim E_\gamma \lesssim 300\,\mathrm{TeV}$. It will also have an effective collection area of about an order of magnitude larger size than current IACTs over the whole energy range (Acharya et al., 2013). The goal is to improve the γ-ray flux sensitivity by a factor 10 to significantly increase the energy range to lower and higher energies compared to current instruments and to increase the duty cycle by automating as much of the operation as possible (Doro, 2011).

CTA will consist of two arrays, one in the northern and one in the southern hemisphere. The northern array will be constructed at the MAGIC site on La Palma (28°46′ N, 17°53′ W, 2180 m a.s.l.) and the southern array at the ESO site at Cerro Paranal in the Atacama desert, Chile (24°38′ S, 70°24′ W, 2150 m a.s.l.). This thesis focuses primarily on the southern site.

As outlined in the previous section, the performance of IACTs is determined by the light collection capability of the optical system, a combination of the mirror area and the photon collection area (determined by the FOV size and telescope spacing), and the photon detection and imaging efficiency of the camera (determined by the pixel size and PMT efficiency, Actis et al., 2011; Acharya et al., 2013). To fulfill the sensitivity requirements over three orders of magnitude in γ-ray energies, CTA will consist of different telescope types operating together. In doing so, the three different energy ranges are scanned by a particular telescope type. An illustration of the different telescope types and designs is shown in Figure 3.11.

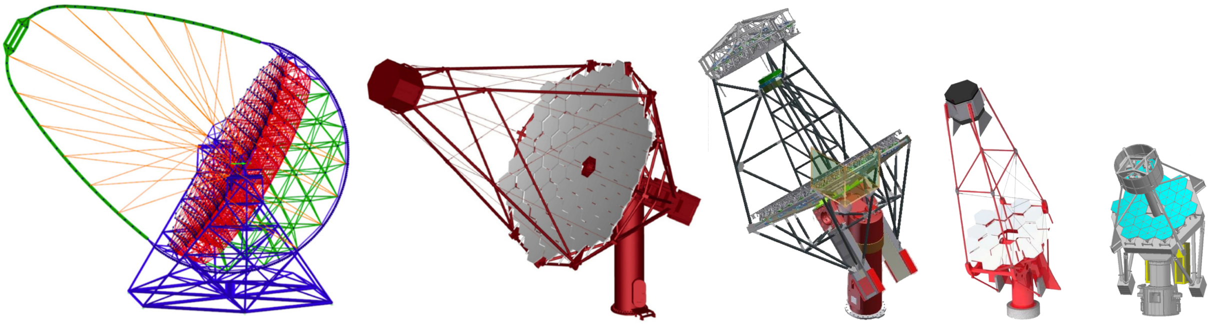

Figure 3.11.: Possible design layouts for the different CTA telescope types (not to proper scale). From left to right: Parabolic large size telescopes (LST) design (mirror diameter 23 m), figure from Acharya et al. (2013); Davies-Cotton medium size telescopes (MST) design (mirror diameter 12 m), figure from Acharya et al. (2013); dual mirror MST design (primary mirror diameter 9.5 m), figure from Byrum et al. (2015); Davies-Cotton small size telescopes (SST) design (mirror diameter 4 m), figure from Acharya et al. (2013); dual mirror ASTRI SST design (primary mirror diameter 4 m), figure from Pareschi et al. (2013).

The low energy regime $< 100\,\mathrm{GeV}$ – ***LST:*** At the lowest energies accessible for IACTs, the rates from VHE γ-ray showers and background events are relatively high. In this regime, the sensitivity is limited by the systematic uncertainty about the background rate rather than the photon statistics and the size of the effective collection area. However, the Cherenkov light pools generated by low-energy air showers are dim, yielding less than ~ 10 Cherenkov photons per square meter at the shower core at ground level (Bernlöhr, 2000). A large mirror surface is thus necessary to collect enough photons to discriminate the Cherenkov light pulses from the night sky background and to reconstruct the particle energies and directions from the shower images. As a balance between costs and complexity of instrumentation, a small number of closely ($\gtrsim 100\,\mathrm{m}$) spaced large size telescopes (LSTs), with a mirror dish diameter of $D = 23\,\mathrm{m}$ each, will be used. To successfully reconstruct the shower events, the time dispersion and optical aberration of the Cherenkov photons has to be balanced: A parabolic mirror shape conserves the light travel time in focusing, and is chosen for the LST optical system. In turn, parabolic mirrors produce stronger comatic aberration of off-axis wavefronts than, e.g., the spherical Davies-Cotton design (see next paragraph). A sufficient optical point spread function (PSF) of the LSTs can be achieved with a focal length of $f = 28\,\mathrm{m}$ (i.e., $f/D = 1.2$) within a FOV radius of $2° - 2.5°$. The pixel size[13] of the camera, corresponding to the targeted PSF of the telescope optics, will be $\lesssim 0.1°$ (Ambrosi et al., 2013; Vercellone, 2014).

The central energy regime – ***MST:*** The energy regime between 100 GeV and 10 TeV is most easily accessible for Earth-bound γ-ray observatories: The Cherenkov light pools are bright and extended enough to be stereoscopically imaged by telescopes with $\sim 10\,\mathrm{m}$ dish size, mounted $\sim 100\,\mathrm{m}$ meters apart, allowing a good reconstruction of the VHE shower direction and energy. At the same time, event rates are high enough to measure fluxes within one pool size of around $10^4\,\mathrm{m}^2$. For CTA, an area of $\sim 1\,\mathrm{km}^2$ (much larger than one shower light pool) will be equipped with 25 (15) medium size telescopes (MSTs) at the southern (northern) CTA site with a mirror diameter of 12 m. This allows a uniform sampling of the showers' light at distances of $\sim 70 - 150\,\mathrm{m}$ from the shower axes over the instrumented area, providing an optimal stereoscopic reconstruction of the shower direction (Acharya et al., 2013). Most importantly, the overall event rate will be higher than for the smaller current arrays, increasing the sensitivity to fainter sources in this energy regime.

As already two generations of IACT arrays have been operating in this energy regime, experience with the shower physics, telescope design, and shower reconstruction has already been gathered. Due to the smaller dimensions of the MST optical system, an equal-light path conserving focusing is less important than for the LST. Instead of a parabolic design, the Davies-Cotton

---

[13] The "pixel size" refers to the edge length for square pixels, the flat-to-flat diameter for hexagonal pixels, and to the diameter for circular pixels.

design (Davies and Cotton, 1957) is chosen for the MST, which produces sharper off-axis images at comparable f/D ratios. For the Davies-Cotton MST mirror, around 84 hexagonal mirror facets (with flat-to-flat diameter of 1.2 m) with spherical curvature and focal length $f_{\text{facets}} = 16\,\text{m}$ will be mounted on a dish support structure with spherical curvature of $f \approx f_{\text{facets}}/2$ and diameter $D = 12\,\text{m}$.[14] An illustration of the Davies-Cotton mirror design is given in Figure 3.12. The above parameters provide a ratio $f/D = 1.6$, and a FOV radius of about $3.5° - 4°$, where the optical PSF is smaller than the target pixel size of 0.14°. A prototype MST with these specifications is currently tested in Berlin-Adlershof (Behera et al., 2012; Baehr, 2012).

Besides the well-know Davies-Cotton design, a new dual-mirror concept is tested for CTA. The dual-mirror optics, based on a telescope design proposed by K. Schwarzschild and A. Couder (for references, see Vassiliev et al., 2007), is expected to provide an accurate, time conserving focusing under large off-axis angles ($\lesssim 10°$) with a small ratio $f/D < 1$ (Vassiliev et al., 2007; Rousselle et al., 2013). This facilitates building a compact telescope with a small-sized camera, which can be equipped with low-cost and innovative PMTs. Dual mirror telescopes are envisaged both for the MSTs, as well for the small size telescopes (SST, see next paragraph, Vercellone, 2014). An illustration of the Schwarzschild-Couder dual mirror optics is provided in Figure 3.13.

The high energy regime – SST: At the highest energies, $E_\gamma \gtrsim 10\,\text{TeV}$, γ-ray event rates are low. For example, less than 20 γ-rays per square kilometer and hour are reaching Earth from the Crab Nebula above energies of 10 TeV (Abdo et al., 2011). However, the showers are very bright, with more than $\sim 10^4$ photons per square meter, and extended. Therefore, their Cherenkov light can be recorded and imaged by sparsely (with distances $d \approx 250\,\text{m}$) deployed telescopes with small mirror surfaces. Still, around 70 of such small size telescopes (SSTs) are needed to cover an envisaged area of $1\,\text{km}^2$, such that reducing costs and technical complexity is crucial for the production of these telescopes. As for the MSTs, SSTs are currently tested both in a Davies-Cotton and in a dual mirror design. As a large FOV radius of about $\gtrsim 4.5°$ is crucial to image showers for the sparsely spaced telescopes, the dual mirror design is of particular interest for the SST (Pareschi et al., 2013; Vercellone, 2014). SSTs are planned only for the southern site.

Instrumental characteristics of CTA

The prospective performance of CTA has been extensively studied, depending on the geographical location of site candidates, available telescopes, and different array layouts. To calculate the instrumental characteristics, a large chain of simulations and analysis steps is applied. In

---

[14] In fact, a modified Davies-Cotton design is planned for the MST, where the focal length of the dish support structure is $f = 19\,\text{m}$, actually being *larger* than the focal length of the mirror facets. This design is chosen to minimize the photon time dispersion in the Davies-Cotton layout (Behera et al., 2012).

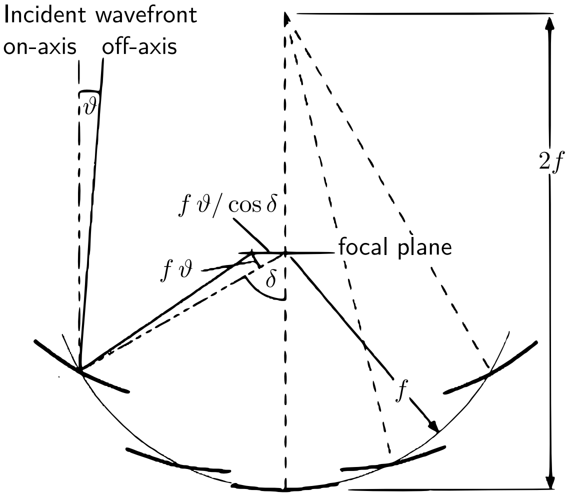

Figure 3.12.: Davies-Cotton mirror design. The focal plane is located at the distance f from the optical support structure, denoted by the thin solid circle segment. The focal length of the individual mirror facets is $2f$. Figure taken from Actis et al. (2011).

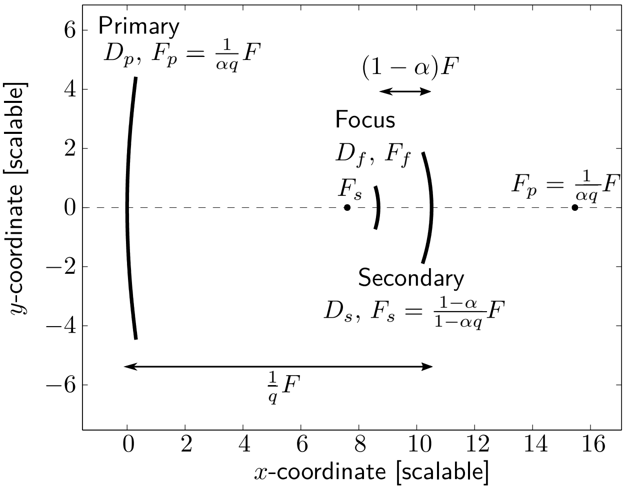

Figure 3.13.: Dual mirror design with a primary and secondary mirror, and the focal plane (camera) located in between. The diameters D and focal lengths F are defined as in the figure. The optical system parameters α and q determine the best suited aspherical curvature of the mirrors. Figure taken from Vassiliev et al. (2007).

this thesis, high-level results from these simulations are used. Therefore, only a short synopsis of the simulation chain is given (for more details, see Bernlöhr et al., 2013):

To calculate the instrumental response of an IACT array, particle showers originating from primary cosmic and γ-rays with determined energy spectrum are simulated, together with their Cherenkov light yield in the atmosphere. For CTA, this is done with the CORSIKA air shower generator (Heck et al., 1998). Consequently, the light recorded by a defined telescope array with specified detailed telescope properties (mirrors, cameras) is computed with the `sim_telarray` package (Bernlöhr, 2008). The simulated shower signatures are then processed through an offline analysis software, which performs the reconstruction of the shower parameters and the separation of cosmic and γ-rays. By comparing the results after the analysis chain with the input parameters of the simulated showers, the instrumental characteristics, dubbed as instrument response functions (IRFs), comprising the *effective collection area* of γ-rays, the *residual background rate*, the *angular resolution* and *energy resolution* can be calculated. Note that the calculated IRFs depend on user-defined analysis parameters, which might be optimized for different purposes (e.g, the observation time, the expected source morphology, and the expected γ-ray energy spectrum of a source) and therefore are not unique. However, the only free parameter of the IRFs used in this thesis is the approximate livetime of the observation.

The analysis chain usually starts with extracting the PMT signal pulse information from each camera pixel ("trace integration") and an automated cleaning of the recorded shower event images. In a second step, the geometric information of each shower image is usually reduced to six independent Hillas-parameters (Hillas, 1985; Fegan, 1996), describing the RMS length of the major and minor semiaxis of the ellipse-like image, the position of the center of gravity of the image (x, y coordinates in the camera), and the position of the intersection of the semiaxes.[15] Additionally, several other parameters are extracted, as, for instance, the total charge collected in the cleaned shower image and the time gradient of the pixel pulses in the image. From these parameters, the stereoscopic reconstruction of the arrival direction and primary energy is performed, as described in the previous subsection.[16] The last analysis step then consists of an algorithm to separate probable γ-ray events from cosmic-ray events. For the CTA analysis used here, a boosted decision tree (BDT) algorithm is applied (Bernlöhr et al., 2013), using the six discriminator variables, *reduced length* and *reduced width* of the shower image (Aharonian et al., 2006), the second largest image amplitude per event, the reconstructed emission height, and the χ^2 values of the energy and emission height estimation.[17] The BDT cut values then are optimized to achieve the maximum sensitivity to a point source for a fixed observation time. To be independent of a particular source spectrum, the optimization and cut choice is independently done for 21 energy bins between 10 GeV and 100 TeV (5 bins per energy decade).[18] In order to claim a detection, all of the following three conditions must be fulfilled in each energy bin following the analysis:

- A significance of 5σ, according to Equation 17 from Li and Ma (1983), over background fluctuations is required. Therefore, the energy-dependent source region ("on-region") is chosen to be the 68% containment region of the angular resolution in the corresponding energy bin. A background region ("off-region") with the same distance ϑ from the camera center and five times larger than the on-region is chosen.
- At least 10 events have to recorded on the on-region.
- The signal excess in the on-region and energy bin must be at least 5% of the background rate determined from the off-region.

The IACT instrument response depends on the atmospheric conditions, the angle between the incident γ-ray shower and the pointing direction (off-axis angle ϑ, see Figure 3.12 for a graphic definition of ϑ), the sky elevation of the pointing direction, and also the azimuthal

---

[15] The original set of parameters by Hillas (1985) is defined differently, but can be calculated from the quoted parameters (and vice versa). For reconstruction approaches without Hillas parametrization, see Vincent (2015).

[16] For the energy reconstruction, all events are assumed to be γ-rays, although still containing mostly cosmic rays.

[17] No directional cuts are applied for the IRFs used for simulations in this thesis.

[18] However, a γ-ray power-law spectrum with index $\Gamma = -2.57$ is assumed in each energy bin.

pointing direction (the latter due to the Earth' magnetic vector field separating electrons and positrons in the shower). To reduce computational costs and complexity of the CTA performance estimation, several simplifying assumptions are made:

- An average standard atmospheric profile is used for each of the CTA sites, based on the Global Data Assimilation System (GDAS) interpolations and satellite data.
- For γ-ray showers arriving under off-axis angles $\vartheta > 0°$, the instrumental response is evaluated for six rings around the pointing directions with the inner and outer radii being [0°, 1°] (central on-axis region), [1°, 2°], [2°, 3°], [3°, 4°], [4°, 5°], and [5°, 6°]. A finer binning is hindered by the number of simulated showers required to obtain enough statistics in each bin. Because a finer characterization of the off-axis performance is needed for the purpose of this thesis, some additional fitting to the simulation results is applied (see Equation 3.7 below).
- All observations are assumed to be taken at an elevation of $\mathrm{EL} = 70°$ above the horizon (zenith angle of 20°). For lower elevations, $\mathrm{EL} \gtrsim 40°$, the performance is expected to be comparable to the high-elevation performance at high energies. However, due to the increased threshold energy at lower elevations, the performance worsens at the lowest energies, $E \lesssim 300\,\mathrm{GeV}$. It is foreseen that most of the data relevant to this thesis (namely the extragalactic survey data) will be taken at elevations $55° \lesssim \mathrm{EL} \leq 90°$, and $\mathrm{EL} = 70°$ is considered as a fair description of the average elevation.
- For the azimuthal pointing direction, an average performance of the southern CTA between the two extreme cases, pointing towards South (perpendicular to the magnetic field, causing large deflections and shower image blurring) and pointing towards North (parallel to the magnetic field, with a marginal electron-positron separation) is chosen. The average pointing direction is indicated by the subscript "`_avg`" in the quoted IRF descriptions.

After a long phase of exploring various site candidates and array layouts, the CTA collaboration has decided on two final array layouts to be erected at the Paranal and La Palma sites. For the southern Paranal site, which is the focus of this thesis, the final distribution of telescopes is the 3HB9-NG layout, comprising 4 LSTs, 25 MSTs, and 70 SSTs (see Table 3.1). To explore the CTA performance during the construction phase, an example of an unfinished array under construction is defined for the 3HB9-NG layout. The chosen "construction array" for the Paranal site provides the best performance of an unfinished final array for a number of 15 MSTs and 50 SSTs. During the exploration phase of possible array and site realizations, different sets of IRFs have been produced, termed as Production 1 (~ 2013), Production 2 (~ 2014; `Prod2`), and recently, Production 3 (2016; `Prod3`). Most IRF data from the `Prod2` simulations are publicly

---

[19] The MAGIC I camera consists of PMTs of two different pixel sizes.

Instrument	Pixels per camera	Mirror design	FOV	N_{tel}	Threshold [GeV]	Total mirror area [m^2]	Sensitivity % Crab
H.E.S.S.	960	DC	5°	4	~ 100	428	1.0
H.E.S.S. II	2048	PB	3.2°	1	~ 30	614	
MAGIC I/II	576[19]/1039	PB	3.5°	2	~ 30	468	1.3
VERITAS	499	DC	3.5°	4	~ 85	424	1.0
CTA LST	~ 2500	PA	4.5°	$\leq 4^{\mathrm{a,\,b}}$	~ 20	$\leq 1660^{\mathrm{a,\,b}}$	0.18^{a} 0.3^{b}
MST	~ 1800	DC/SC	$7-8°$	$\leq 25^{\mathrm{a}}/15^{\mathrm{b}}$	~ 100	$\leq 2830^{\mathrm{a}}/1700^{\mathrm{b}}$	
SST	~ 1300	DC/SC	$\sim 9°$	$\leq 70^{\mathrm{a}}/0^{\mathrm{b}}$	~ 200	$\leq 880^{\mathrm{a}}/0^{\mathrm{b}}$	

Table 3.1.: Performance of the CTA instrument in comparison with current IACTs. Table adapted from Hinton (2009); Actis et al. (2011). CTA specifications taken from Acharya et al. (2013); Vercellone (2014). $^{\mathrm{a}}$southern site/$^{\mathrm{b}}$northern site. PB: Parabolic, DC: Davies-Cotton, SC: Dual mirror ("Schwarzschild-Couder"). The sensitivities correspond to the differential sensitivity at 1 TeV for an observation over 50 h, with the latest values provided by the experiments.

available[20] and have been used for the study in Hütten et al. (2016), which is part of this thesis. In this thesis, in addition, results are shown for the newest `Prod3` calculations. For the `Prod2 South` calculations used in Hütten et al. (2016), adapted to a generic site location in the southern hemisphere, a slightly larger number of available telescopes had been assumed (4 LSTs, 24 MSTs, and 72 SSTs). However, no large differences are obtained compared to the `Prod3 Paranal` results (see Figure 5.8 on page 128 for a comparison). For this thesis, all calculations are based on the 3HB89-NG telescope configuration, which largely matches the final layout. In Figure 3.14, the 3HB89-NG telescope collocation for the Paranal site and its construction array subset, 3HB89-TS-CA-NG, are shown.

Given the final array layout, a definition of the sensitivity, and a specified analysis procedure, the resulting foreseen CTA instrumental characteristics are presented below:

Effective collection area: Figure 3.15 (off-axis dependence) and Figure 3.16 (energy dependence) show the effective γ-ray collection areas, optimized for an observation time of 30 min and the southern CTA array. As mentioned before, the collection areas for γ-rays hitting the camera plane under different angles ϑ are computed for six coarse bins between $\vartheta = 0°$ and $\vartheta = 6°$. For the realistic simulation of off-axis events as required for this thesis, the effective areas and background rates have been additionally fitted by a generalized Gauss function:

$$f(\vartheta) = A\,\exp\left[-\frac{1}{2}\left(\left(\frac{\vartheta}{B}\right)^6 + \left(\frac{\vartheta}{C}\right)^4 + \left(\frac{\vartheta}{D}\right)^2\right)\right], \tag{3.7}$$

---

[20] `http://portal.cta-observatory.org/Pages/CTA-Performance.aspx`

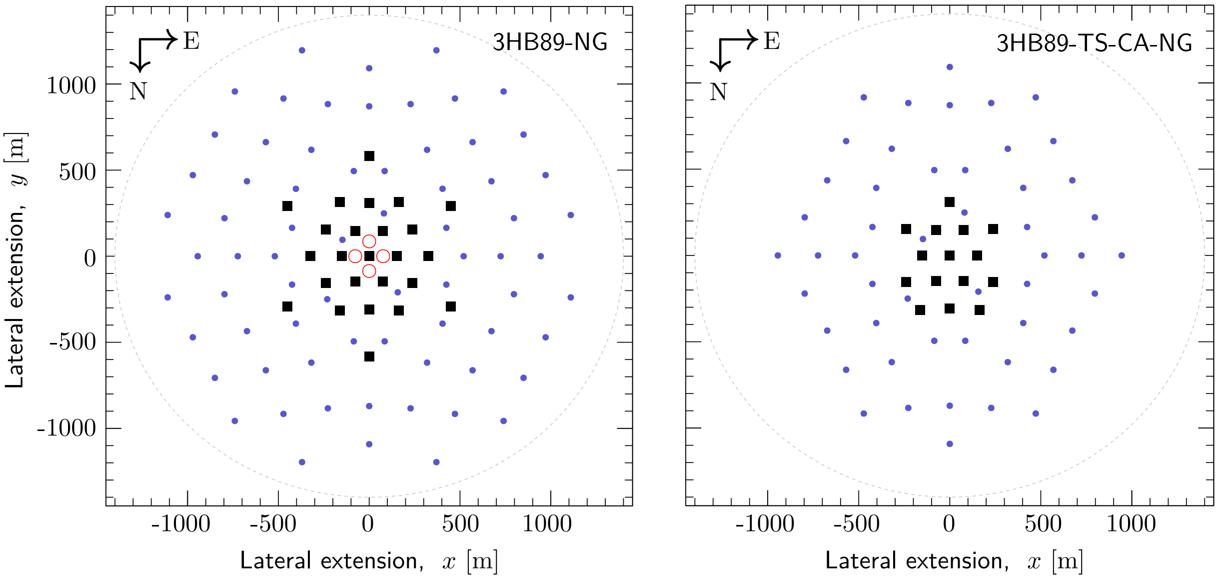

(a) Full `Prod3 HB89` array layout for the Paranal site (4 LSTs, 25 MSTs, 70 SSTs).

(b) Construction array layout `Prod3 HB89 CA-NG` (15 MSTs, 50 SSTs).

Figure 3.14.: CTA array layout used in this this thesis, largely matching the final configuration to be constructed at the southern site at Cerro Paranal in Chile. The construction array on the right is a subset of telescopes in the full array on the left. Red circles denote LSTs, black squares MSTs, and blue dots SSTs. Figures courtesy of G. Maier.

with the four free fit parameters A, B, C, and D. Equation 3.7 implies a radially symmetric performance around the pointing direction. It ensures that the effective area is regular at $\vartheta = 0°$ ($\mathrm{d}f/\mathrm{d}\vartheta(\vartheta = 0°) = 0$), and smoothly approaches zero, $f(\vartheta \to \infty) \to 0$. Incorporating only even powers of the polynomial in the exponent results in a monotonously decreasing function. The coefficients A and B drive the flatness of f around $\vartheta = 0°$ compared to a Gaussian function, i.e. the width of the central plateau. With only three free parameters to describe the off-axis shape, Equation 3.7 fits the MC results well, under meaningful physical constraints.

In Figure 3.15, this fitting procedure is illustrated: Here, the dots correspond to the results of the MC simulation chain, whereas the lines denote the fit according to Equation 3.7 at several energies. The quoted energies denote the the logarithmic centers of the underlying energy bins (with five bins per energy decade). The shaded areas additionally indicate the width of the FOV, ϑ_{fov}, and the acceptance $\widetilde{A}$, both obtained from the fit and defined by (Baldini, 2014):

$$\widetilde{A}(E) := \int_{S^2} A_{\mathrm{eff}}(E,\, \vartheta)\,\mathrm{d}\Omega \;=\; A_{\mathrm{eff}}(E,\, \vartheta = 0°) \times 2\pi\ (1 - \cos\vartheta_{\mathrm{fov}})\ . \tag{3.8}$$

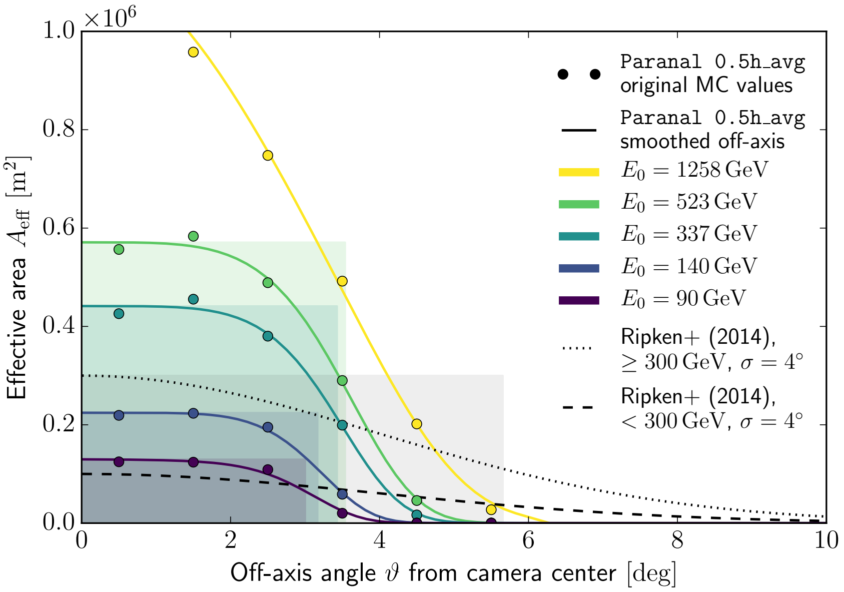

Figure 3.15.: Effective areas of the southern CTA as a function of ϑ, the angle between the pointing direction and the incident γ-ray with primary energy E_0. The areas are given for the `Prod3 0.5h_avg` cuts. The off-axis scaling is shown for different $E_0 \lesssim 1$ TeV. The shaded bands indicate the FOV sizes, in terms of cylinders with radius $\vartheta_{\rm fov}$ and the same acceptance as the actual FOV shapes (see Equation 3.8). Additionally, the effective area model from Ripken et al. (2014) is shown in this figure.

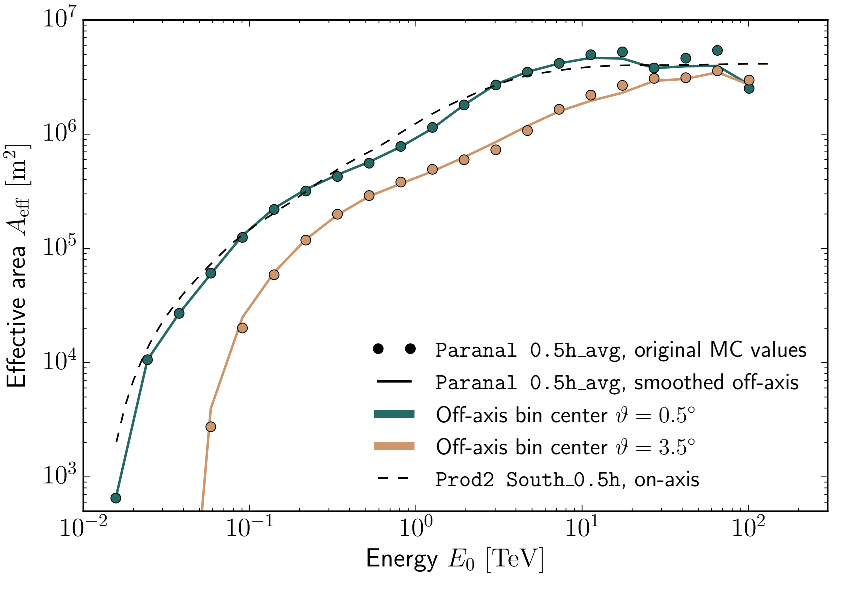

Figure 3.16.: Energy dependence of the effective collection areas. The instrumental response improves with increasing γ-ray energies and approaches a plateau at $E_0 \gtrsim 10$ TeV. The on-axis effective area from the `Prod2` simulations (dashed line), as used in Hütten et al. (2016), is shown for comparison.

In Table 3.2, the values for the on-axis effective areas, $\widetilde{A}$, and ϑ_fov are given for several energy bins. The acceptance $\widetilde{A}$ is instructive to assess the off-axis performance of the instrument: In Figure 3.16, also the simplified model of the CTA effective area by Ripken et al. (2014) is given. One main result of this thesis is a refined calculation of the sensitivity analysis by Ripken et al. (2014) with a realistic assessment of the CTA performance (presented in Chapter 5). The values of $\widetilde{A}$ in Table 3.2 suggest a somewhat better performance assumed by Ripken et al. (2014) than inferred by the `Prod3` simulations. However, the actual size of the effective areas depend on the applied cuts and are only meaningful together with full set of IRFs. For a rough comparison of the CTA survey potential compared to the *Fermi*-LAT, Table 3.2 also shows the exposure factor, $\mathcal{E}_f(E) = \widetilde{A}(E) \times T_\text{obs}$, for an observation time of $T_\text{obs} = 500\,\text{h}$.

Energy	ϑ_fov (eff. area)	ϑ_fov (bck. rate)	$A_\text{eff}(\vartheta = 0°)$ [m^2]	$\widetilde{A}$ [m^2 sr]	$\mathcal{E}_f$ [m^2 sr yr]
58 GeV	2.4°	2.0°	6.1×10^4	330	19
91 GeV	3.0°	2.9°	1.3×10^5	1.1×10^3	63
140 GeV	3.2°	3.3°	2.2×10^5	2.2×10^3	130
338 GeV	3.4°	3.7°	4.4×10^5	5.0×10^3	290
524 GeV	3.5°	3.8°	5.7×10^5	6.8×10^3	390
1.26 TeV	3.4°	4.2°	1.1×10^6	1.3×10^4	740
11.3 TeV	3.6°	–	4.7×10^6	5.8×10^4	3.3×10^3
27.1 TeV	4.8°	–	3.8×10^6	8.3×10^4	4.7×10^3
$<$ 300 GeV	5.66°	5.66°	1×10^5	3.1×10^3	170
$\geq$ 300 GeV	5.66°	5.66°	3×10^5	9.2×10^3	520

Table 3.2.: Width of the FOV, on-axis effective area, acceptance, and exposure factor for $T_\text{obs} = 500\,\text{h}$ at different energies for the CTA Paranal `Prod3 0.5h_avg` cuts. The FOV size, ϑ_fov, is given both calculated from the effective areas and the background rates. Too few MC background events have been computed above 10 TeV to provide a meaningful FOV size for the background. The last two separated rows present the the Gaussian model by Ripken et al. (2014), with $\vartheta_\text{fov} = \sqrt{2}\,\sigma_\text{fov}$, and $\sigma_\text{fov} = 4°$. The quoted energies denote the logarithmic centers of the corresponding energy bins.

Residual background rate: As outlined in the previous section, CTA suffers from a large irreducible background from cosmic rays. The γ-ray-hadron/electron separation algorithms perform differently at different energies, and surviving hadronic cosmic-ray events are shifted non-linearly in energy. Therefore, the background rate is not a simple fraction of the cosmic-ray flux, multiplied with the γ-ray effective areas, but is rather given as the final rate of events surviving a specified set of analysis cuts. The associated reconstructed energy of a background event, E_R, matches the Cherenkov light imprint of a γ-ray with the corresponding primary energy E_0.

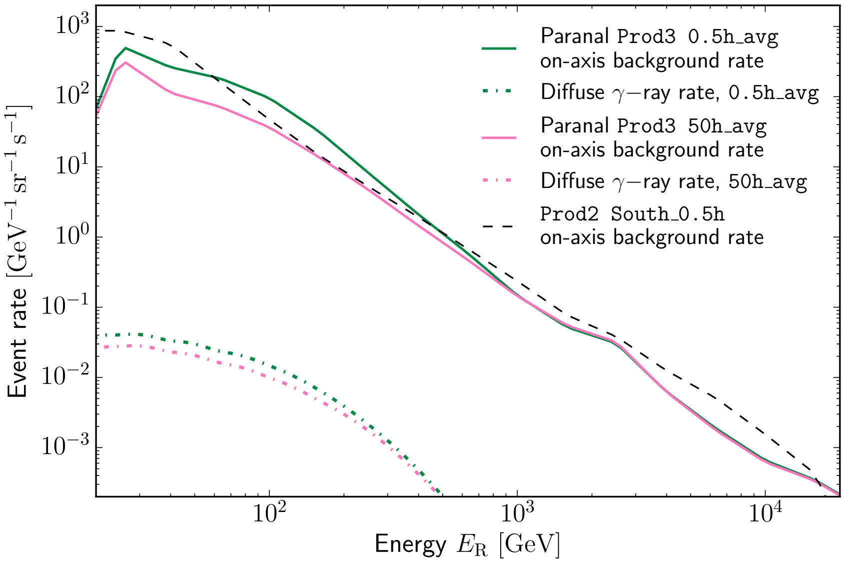

Figure 3.17.: Extragalactic diffuse γ-ray and background rates after γ-hadron separation cuts for the CTA on-axis performance, illustrated for two different observation time optimizations. The dot-dashed lines show the effective areas, multiplied with the extragalactic γ-ray flux from Ackermann et al. (2015b, see text for details). The rates are given over the reconstructed γ-ray-like energies, E_R. The background rates (solid lines) are given on-axis, optimized for 30 minutes and 50 h of observation. The background rate from the `Prod2` simulation (dashed line), as used in Hütten et al. (2016), is shown for comparison.

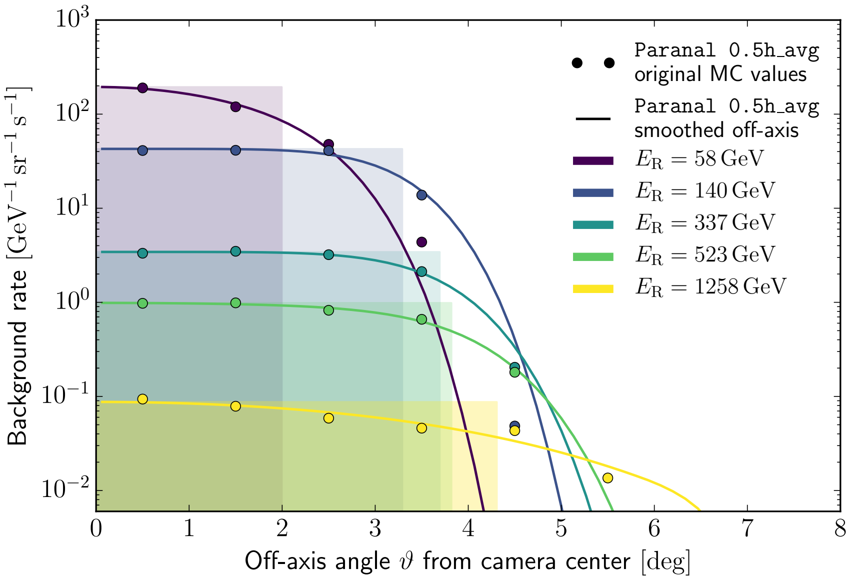

Figure 3.18.: Background rates for the CTA off-axis performance at different reconstructed γ-ray energies below $\sim 1\,\mathrm{TeV}$. As in Figure 3.15, the shaded areas indicate the FOV size according to Equation 3.8.

In Figure 3.17, the differential residual background rate for the southern site at Paranal is shown for the two different cuts `Prod3 0.5h_avg` and the `Prod3 50h_avg` (optimized for an observation time of 30 min and 50 h, respectively). The dot-dashed lines additionally show the event rate of the extragalactic diffuse γ-ray background (DGRB), obtained by integrating the γ-ray intensity over the CTA on-axis effective area, A_{eff},[21]

$$\frac{\mathrm{d}N_{\mathrm{events}}}{\mathrm{d}E\,\mathrm{d}\Omega\,\mathrm{d}t} = \int_{A_{\mathrm{eff}}(E)} \frac{\mathrm{d}I}{\mathrm{d}E\,\mathrm{d}\Omega}\,\mathrm{d}A\,, \tag{3.9}$$

where $\frac{\mathrm{d}I}{\mathrm{d}E\,\mathrm{d}\Omega}$ is the DGRB intensity given by (Ackermann et al., 2015b, model B). This intensity corresponds to the diffuse foreground-cleaned γ-ray intensity above $|b| > 20°$, measured by the *Fermi*-LAT up to 820 GeV and is further explained and discussed in Chapter 5. In this context, Figure 3.17 and Table 3.3 show that events from diffuse γ-radiation are outweighed, on average, by almost four orders of magnitude by the residual background rate.

Comparing the two different analysis cuts in Figure 3.17 shows that harder cuts can be applied for longer observation times. Harder cuts imply losing more γ-rays, resulting in lower effective areas, but they also significantly suppress more background events. At high energies, where little cosmic-ray background is present, the different cuts become comparable.

In Figure 3.18, analogous to the effective areas in Figure 3.15, the off-axis intensity of the background rate is shown at different energies. The MC results from the `Prod3` simulations have been fitted by the same formula 3.7. These fit descriptions, for both the off-axis effective areas and the off-axis background rates, are used in Chapter 5 for the study of the CTA sensitivity to γ-ray anisotropies in the residual background.

Energy threshold	Diffuse γ-ray rate		Background rate		γ-rays/background ratio	
	on-axis [Hz deg^{-2}]	total FOV [Hz]	on-axis [Hz deg^{-2}]	total FOV [Hz]	on-axis	total FOV
30 GeV	8.9×10^{-4}	2.2×10^{-2}	5.8	124.9	1.5×10^{-4}	1.8×10^{-4}
100 GeV	3.6×10^{-4}	1.2×10^{-2}	1.8	66.1	2.0×10^{-4}	1.8×10^{-4}
300 GeV	0.4×10^{-4}	1.6×10^{-3}	0.25	11.8	1.7×10^{-4}	1.4×10^{-4}
500 GeV	8.0×10^{-6}	3.2×10^{-4}	0.10	5.4	0.8×10^{-4}	0.6×10^{-4}

Table 3.3.: Diffuse (DGRB) γ-ray and background rates after γ-hadron separation cuts `Prod3 0.5h_avg` for the southern CTA on-axis performance, integrated over the energy above different energy thresholds (up to $E_{\mathrm{max}} = 100$ TeV). The diffuse γ-ray rate corresponds to the DGRB according to Equation 5.13, which is further discussed in Subsection 5.3.1. Events in the "total FOV" comprise all events within the angular direction $\vartheta_{\mathrm{cut}} = 6°$ from the camera pointing position.

---

[21] No finite energy resolution is considered here, i.e. $E_{\mathrm{R}} \equiv E_0$.

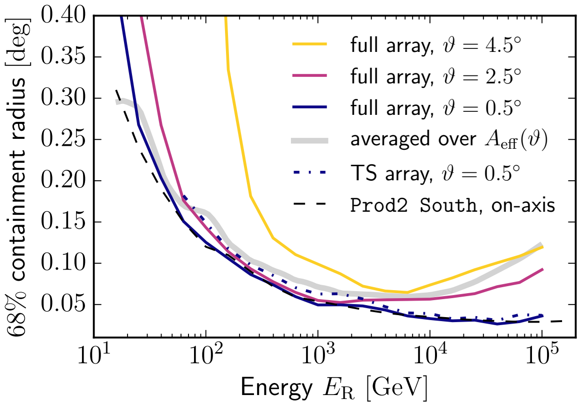

Figure 3.19.: Angular resolution of the southern CTA at Paranal, and `Prod3` simulations. The solid lines denote the performance of the full array and the dot-dashed line the on-axis performance of the array under construction (ϑ: off-axis angle).

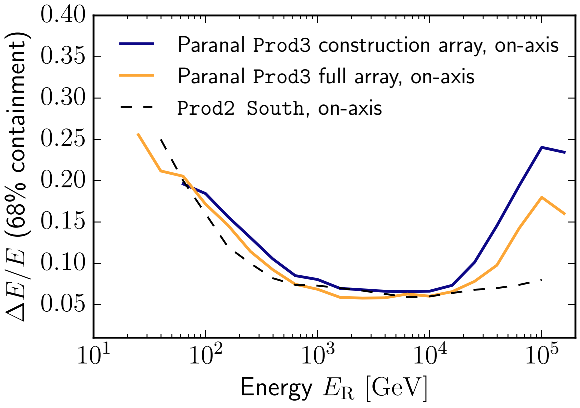

Figure 3.20.: Energy resolution of the southern CTA, for on-axis incident events. Because of fewer telescopes, the construction array performs slightly worse. As in Figure 3.19, the `Prod2` values are given for comparison (dashed line).

Angular resolution: Figure 3.19 presents the CTA (South) angular resolution as a function of the reconstructed γ-ray energy of a shower. The angular resolution is given as a model-independent radius of a circular region containing 68% of the events from an original point-like source. These resolutions are highly similar for the different observation time optimizations. The angular resolution depends on the luminosity, extension and number of available stereoscopic shower images, and the imaging quality of the camera. Therefore, the resolution improves with the primary γ-ray energy. It degrades with off-axis angles ϑ from the camera center, as shower images tend to be cut at the edge of the camera FOV. This in particular affects low-energy events, $E_R \lesssim 100\,\text{GeV}$ recorded by the LSTs with a small FOV of diameter $< 5°$. The angular resolution can be parametrized as a probability distribution $p(\vec{k}_R|E, \vec{k}) = \mathrm{d}P/\mathrm{d}\theta(\theta, E)$, where the latter form $\mathrm{d}P/\mathrm{d}\theta$ implies spherical symmetry of the distribution. Here, $\vec{k}$ is the true direction in the sky of the incident γ-ray, and $p = \mathrm{d}P/\mathrm{d}\theta$ the differential probability to observe the γ-ray from a direction $\vec{k}_R$, displaced by an angle θ from the true direction $\vec{k}$. The probability distribution for the angular resolution is also denoted point spread function (PSF). For this thesis, a Gaussian probability for the angular resolution is adopted. Its usage is further discussed throughout the thesis. In particular, the PSF averaged of the effective area (as shown in Figure 3.19) is properly defined in Chapter 5 in the context of survey observations with CTA.[22]

---

[22] A description used for angular resolutions in γ-ray astronomy with wider tails is given by a so-called King-function, $p(\theta) \sim (1+\theta^2/\theta_0^2)^{-\gamma}$ (Knödlseder et al., 2016). This two-parameter description gives a more accurate model of the angular resolution, by a fit to two containment radii (usually, the 80% containment radius is additionally considered). In this sense, adopting a Gaussian for this thesis results into a somewhat optimistic performance description of the CTA.

Energy resolution: The energy E_0 of a primary γ-ray-like particle is inferred from the total Cherenkov light intensity recorded by the array, using the information about the impact location on ground of the shower. Because of the finite measurement accuracy, shower-to-shower variations of the Cherenkov light, and variation of the atmospheric conditions, the energy estimation is limited. Additionally, a systematic bias may occur due to a inaccurate absolute calibration of the response of the camera PMTs and misestimating the atmospheric composition. When systematic deviations can be neglected, then the reconstructed γ-ray energy, E_R, symmetrically scatters around the true γ-ray-like energy, and the mean $\langle E_\mathrm{R}\rangle$ coincides with the true energy, $\langle E_\mathrm{R}\rangle = E_0$, while it is $\Delta E := \sqrt{\langle E_\mathrm{R}^2\rangle - \langle E_\mathrm{R}\rangle^2}$.

Figure 3.20 shows the energy resolution $\Delta E/E$, or *energy dispersion*, of the southern CTA, for on-axis incident γ-ray-like events. As for the PSF, the performance is identical for the different benchmark analysis cuts. Due to having fewer telescopes, the construction array performs slightly worse than the full 3HB9 array.

The impact of a finite energy resolution is most important for searches for spectral features like spectral lines, wiggles, and cut-offs. In this thesis, however, the effect of energy dispersion is neglected and a perfect energy resolution is assumed. This assumption highly simplifies the extensive simulations of $\gtrsim 10^8$ events performed in this thesis, and the unbinned Likelihood fit applied on these events. Neglecting the energy dispersion is justified as only featureless DM induced γ-ray spectra are investigated (as shown in Figure 2.11). The cut-off of the spectra at the DM mass, however, would be less prominent for a finite energy resolution, and neglecting the energy dispersion results in somewhat optimistic results. On the other hand, most emission from these DM γ-ray spectra results from an energy range at least one order of magnitude below the cut-off. As only few events arise around the cut-off at the sensitivity limit, it can be argued that neglecting the energy dispersion dominantly affects only high energies (and consequently, DM masses), where the background is low.

Events from smooth energy spectra are still affected by the energy dispersion. For steep spectra, a convolution with a finite energy resolution causes a shift of the convolved spectrum towards higher energies. For a power-law spectrum, $\mathrm{d}N/\mathrm{d}E_0 \sim E_0^{-\Gamma}$, Baldini (2014) finds that binning in logarithmic intervals and constant $\Delta E/E$ introduces an bias of E_R of approximately

$$\frac{\langle E_\mathrm{R}\rangle}{E_0} = \left(\frac{\mathrm{d}N_\mathrm{R}}{\mathrm{d}N_0}\right)^{\Gamma} \qquad \text{with} \qquad \frac{\mathrm{d}N_\mathrm{R}}{\mathrm{d}N_0} \approx 1 + \frac{(\Gamma-1)(\Gamma-2)}{2}\left(\frac{\Delta E}{E}\right)^2 . \tag{3.10}$$

In the Figures 3.17 to 3.20, quantities are given as a function of E_R, indicating possible biases compared to the true γ-ray-like energies, E_0. This effect is by definition accounted for in a Likelihood-based analysis, where the Likelihood is calculated for a specific tested spectral shape (or for deciding between different spectral shapes).

Flux sensitivity: For a particular set of IRFs, the flux sensitivity can be calculated. Figure 3.21 shows the CTA differential sensitivity to detect point-like sources within 50 h of observation. The definition of an unambiguous detection corresponds to the list of requirements specified on page 69. For comparison, the sensitivity of the *Fermi*-LAT is also shown. For the latter instrument, the sensitivity corresponds to the detection of a point source located at the Galactic North pole, with test statistic TS = 25 (see page 124 for a definition of TS) and more than 10 events from the source location, after 10 yr of all-sky monitoring, following a `Pass8` analysis.[23] It can be seen that the *Fermi*-LAT competes with the projected CTA performance at the lowest energies for long-time exposures, which are needed for indirect DM searches.[24]

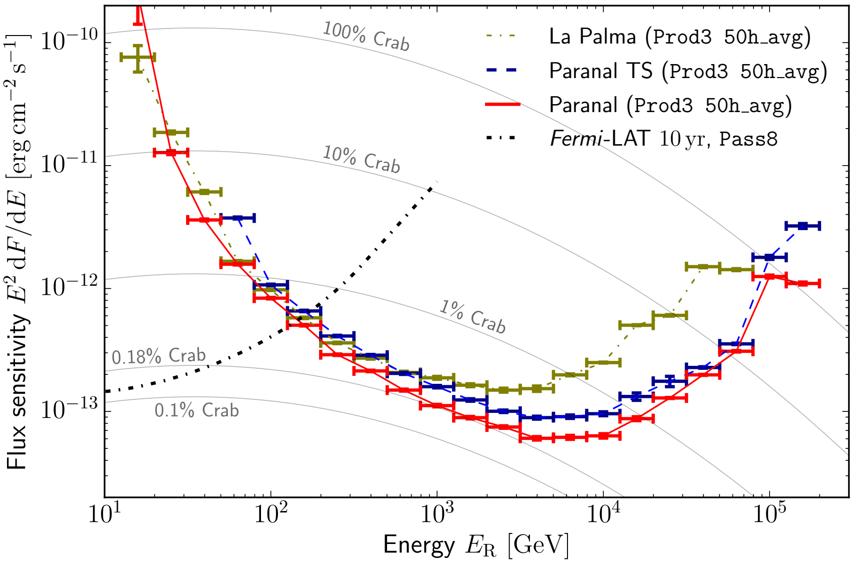

Figure 3.21.: Differential flux sensitivity of various CTA configurations for 50 h of on-axis point-source observation and the sensitivity requirements described in the text. Shown are sensitivities of the northern (La Palma, olive dot-dashed line) and southern (Paranal, red-solid line) arrays, together with the southern construction array (Paranal TS, blue-dashed line). For comparison, the spectrum (and fractions thereof) of the Crab Nebula (Meagher, 2015) is overplotted, as is the sensitivity of the LAT (given for a TS = 25 detection of a point source located at the Galactic North pole after 10 yr of operation, see also the main text).

---

[23] *Fermi*-LAT performance values taken from `http://www.slac.stanford.edu/exp/glast/groups/canda/lat_Performance.htm`

[24] For a detailed comparison between CTA and the *Fermi*-LAT for observations in various cases of source physics, see Funk and Hinton (2013).

3.3. Space-borne telescopes: The *Fermi* Large Area Telescope

The *Fermi*-LAT spacecraft (formerly named Gamma-ray Large Area Space Telescope, GLAST) is an artificial satellite, launched to low-Earth orbit in June 2008. It carries the LAT and Gamma-Ray Burst Monitor (GBM) instruments. The spacecraft has been launched into an almost circular orbit at $\sim$ 530 km a.s.l., with a total launch mass of 4303 kg, of which are 2900 kg scientific payload.[25] Its mission duration was foreseen to last at minimum for five years, and has been extended to 10 years until at least 2018.

The LAT (Atwood, 2009) is the main instrument on board the *Fermi* satellite, a photo-conversion detector sensitive to γ-ray radiation – and also cosmic rays – between $\sim$ 20 MeV and several hundreds of GeV. Up to 2016, the LAT detector is the most sensitive and single currently operating space-borne high energy γ-ray observatory. The LAT comprises three main parts: A photo-converter, a particle tracker, and a calorimeter. A fourth integral component of the instrument is the thin plastic scintillator (see Figure 3.22) covering the detector to provide an anti-coincidence shield, turning the LAT into a detector tailored for γ-ray detection.

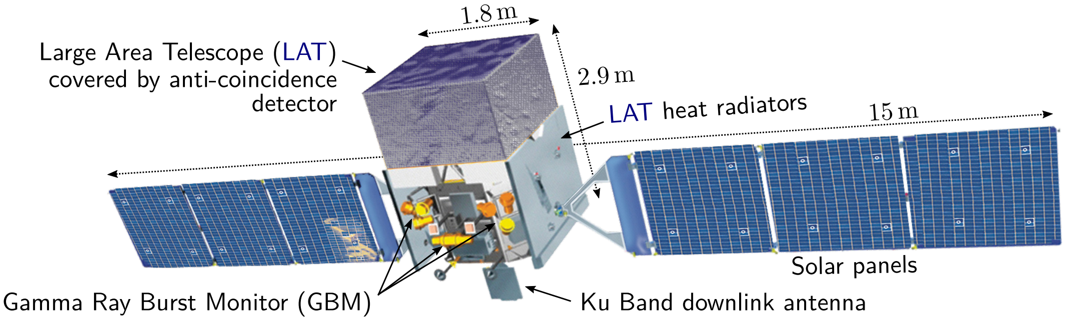

Figure 3.22.: Depiction of the *Fermi* spacecraft, carrying the LAT and GBM instruments. Besides the main instruments, also the K-under microwave band antenna used for downlink communication and the radiators for dissipating the heat from the LAT electronics are indicated. Image credit: NASA/Sonoma State University/Aurore Simonnet.

The plastic anti-coincidence detector allows the rare γ-rays to be unambiguously discriminated from the cosmic-ray background: While γ-rays pass it without interaction, charged particles cause a flash of scintillation light, indicating the presence of a background event. Within the detector, the photo-converter, consisting of 16 layers of tungsten ($Z = 74$) foils, triggers pair production of an incident γ-ray. The photo-converter is interleaved with 18 silicon planes,

---

[25] `http://www.nasa.gov/pdf/221503main_GLAST-041508.pdf`

tracking the paths of the produced electron-positron pair. The tracking provides additional information about the γ-ray (by the splitting multiplicity) and allows the arrival direction of the γ-ray to be reconstructed. The tracking accuracy improves with the γ-ray energy and results in a 68% containment angle of 0.8° at 1 GeV and approaches $\lesssim 0.1°$ above 100 GeV for `P8R2_SOURCE_V6` cuts.[26] The electron-positron pair is then absorbed in a calorimeter below the tracker, comprising 96 CsI(Tl) crystals, where the pair deposits its energy in electromagnetic showers. The scintillation light read out from the crystal towers then serves for the energy estimation of the primary γ-ray. The total dimensions of the tracker/converter and calorimeter are 145 cm × 145 cm in width and 81 cm in height, providing an acceptance-corrected average FOV of 2.4 sr ($\vartheta_{\mathrm{fov}} = 52°$, comparable to the FOV of the human eye) around the pointing direction of the satellite. For events hitting the detector on-axis and `P8R2_SOURCE_V6` cuts, the resulting effective area and acceptance for $2\,\mathrm{GeV} \lesssim E_\gamma \lesssim 200\,\mathrm{GeV}$ are $\sim 0.9\,\mathrm{m}^2$ and $\sim 2.4\,\mathrm{m}^2\,\mathrm{sr}$, respectively.[27] For a ten year operation cycle, this results in an exposure factor of $24\,\mathrm{m}^2\,\mathrm{sr}\,\mathrm{yr}$, somewhat lower than what is obtained for the allocated time for the CTA extragalactic survey (see Table 3.2 and Chapter 5).[28] In particular at energies $\gtrsim 100$ GeV, the large FOV of the LAT and its almost 24 h duty cycle cannot outweigh its relatively small effective area, and it is hardly able to collect the very rare VHE photons traversing the Galaxy.

The *Fermi* satellite continuously reorientates itself, pointing the LAT away from the Earth and the γ-ray-bright atmospheric limb. Moreover, it observes in "rocking mode", alternating the pointing position by 35° relative to zenith in each orbit. Together with its large FOV, this allows the LAT to uniformly scan the whole sky once in every two orbits. Most of *Fermi*-LAT's observation time ($\gtrsim 80\%$) is allocated to this survey mode, while the remainder is dedicated to pointed observations and follow-up observations of transient sources.

The main trigger instrument for LAT follow-up observations is the GBM (Meegan et al., 2009) located on the same spacecraft. The GBM consists of 12 Sodium Iodide (NaI), and two Bismuth Germanate (BGO) scintillation detectors, mounted below the LAT (see Figure 3.22).[29] In a lower energy range than the LAT, $8\,\mathrm{keV} \lesssim E_\gamma \lesssim 40\,\mathrm{MeV}$, it continuously monitors the entire sky (including the Earth's atmosphere) for short bursts of γ-ray emission. However, this instrument does not play any role for the time-independent emission from DM.

---

[26] `http://www.slac.stanford.edu/exp/glast/groups/canda/lat_Performance.htm`

[27] See Figure 26.

[28] Note that this comparison of the effective areas alone misses the fundamentally different background characteristics of the instruments.

[29] `http://gammaray.msfc.nasa.gov/gbm/instrument/`

4 | Modeling the statistical abundance of Galactic dark matter subhalos

> *Χρὴ τὸ λέγειν τε νοεῖν τ′ ἐὸν ἔμμεναι [. . .]*
> *What can be spoken and thought of must exist.*
>
> Parmenides ($\sim 520 - 460$ BC), Fragments B6:1.[1]

In Chapter 2 it has been outlined that the cold dark matter (DM) scenario of cosmic structure formation predicts a hierarchical bottom-up clustering of the DM. Structure growth in a Press-Schechter framework (Equation 2.12) suggests the presence of a large amount of small-scale DM overdensities in today's Universe. Extensive numerical studies have confirmed that small-scale overdensities also might have survived within larger structures of the size of Milky-Way-like DM halos (Springel et al., 2005; Diemand et al., 2007; Springel et al., 2008a; Diemand

---

[1] Greek quotation after Graham (2010), English translation after Owen (1960). Variations on Owen's interpretation are given by G.W.F. Hegel (1820, Vorrede, „Was vernünftig ist, das ist wirklich; und was wirklich ist, das ist vernünftig.“ – “What is reasonable is real, and what is real is reasonable”), and L. Wittgenstein (1922, Proposition 3.02, „Was denkbar ist, ist auch möglich – “What is thinkable is also possible”). However, different translations and interpretations exist for the fragment, as discussed by M. Heidegger (Oberst, 2009, p. 143), Boodin (1943), and Hansen (2011).

et al., 2008). A large amount of clustered DM on subgalactic scales has two consequences for potential signals from its relic annihilation. Firstly, as the annihilation probability rises with the square density, subclustering results into a boost of the overall emission from remote galaxies and the diffuse emission within the Milky Way (Bergström et al., 1998; Berezinsky et al., 2003). Secondly, a square-density radiation profile from high-density regions results into sharply localized annihilation signals, which could be individually detectable in γ-rays and neutrinos (Calcáneo-Roldán and Moore, 2000; Tasitsiomi and Olinto, 2002; Berezinsky et al., 2003). Such signals are searched for from the directions of neighboring dwarf spheroidal galaxies (dSph), which are assumed to be hosted by subgalactic DM overdensities. However, signals might also arise from locations that are not traced by luminous matter, so-called "dark subhalos", which are the subject of this thesis. In this chapter, a semi-analytical modeling of the Milky Way (MW) subhalo population is presented. The modeling of various configurations of the Galactic DM halo and its subhalos is presented in Section 4.1. In Section 4.2, the computation of the J-factors from DM annihilation in a subclustered Galaxy is outlined. The resulting J-factors are presented in Section 4.3. The γ-ray fluxes associated to these J-factors are the basis for Chapter 5, which presents the detection prospects of dark clumps with the Cherenkov Telescope Array (CTA).

4.1. Semi-analytical modeling of the Galactic dark matter halo

The up-to-date picture of a subclustered DM Galaxy halo is based on simulating the gravitational interaction of cold DM evolving in an expanding ΛCDM[2] Universe (for a review, see Kuhlen et al., 2012). Such N-body simulations of the formation of Galaxy-like DM halos are calibrated by empirical knowledge, e.g., the properties of the Cosmic Microwave Background (CMB), the observed large-scale structure, and the MW rotation curve. Although the DM distributions derived from these simulations agree with various observations, many uncertainties remain about the DM clustering on subgalactic scales.

To derive reliable projections about the γ-ray emission from the subclustered DM and to quantify a systematic modeling uncertainty, a semi-analytical approach is adopted in this thesis. The current-day Galactic DM density distribution is boiled down to a handful of key properties, parameters and analytical functions, which are then used to compute the γ-ray intensities from DM annihilation. This approach allows a simple comparison of various dynamic DM simulations such as the Aquarius (Springel et al., 2008a), Phoenix (Gao et al., 2012) or Via Lactea II (VL II; Diemand et al., 2008) simulations, and more recent attempts to include the mutual

---

[2] ΛCDM Universe: A solution of the Einstein equations, obeying the cosmic principles and having been driven by radiation, cold DM, and a cosmological constant $\Lambda \neq 0$.

hydrodynamical interaction of DM and baryonic matter (Mollitor et al., 2014; Sawala et al., 2016; Wetzel et al., 2016). Additionally, parameters can be varied to study their impact on the γ-ray flux, to identify the crucial quantities for the prospects of indirect detection of DM substructures in γ-rays.

For the remainder of the thesis, the following variable convention is applied when referring to DM properties: The mean of a quantity Q is assigned with a bar, $\overline{Q}$, and the median with a tilde, $\widetilde{Q}$. Properties of the Galactic host halo at the global level are indicated with a capital letter (e.g., the halo mass M, positions R within the halo, and distances D within the Galaxy to the observer); densities are denoted with the letter ρ. Properties of individual subhalos are in contrast labeled with a lowercase letter (e.g., subhalo mass m and distance r from the subhalo center) and densities of subhalos with the letter ϱ. It is frequently referred to the brightest subhalo, and variables assigned to the brightest object are indicated with a star, $Q^\star$.

4.1.1. A model for the overall Galactic dark matter density

As outlined in Subsection 2.1.1, the MW rotation curve can be well reproduced by assuming a spherically symmetric gravitational DM potential as proposed by Navarro et al. (1996, "NFW profile"). In the following, a very similar description (compared to the NFW profile) is used, describing the mean density $\overline{\rho}_\mathrm{host}$ of the Galactic DM host halo by

$$\overline{\rho}_\mathrm{host}(R) = \overline{\rho}_\mathrm{s,\,host} \exp\left(-\frac{2}{\alpha_E}\left[\left(\frac{R}{R_\mathrm{s}}\right)^{\alpha_E} - 1\right]\right) , \tag{4.1}$$

with $\alpha_\mathrm{E} = 0.17$ and the scale radius $R_\mathrm{s} = 15.14\,\mathrm{kpc}$, following the more recent results by Navarro et al. (2010) for the Aquarius A1 halo.[3] The density profile (4.1) is commonly dubbed as "Einasto profile" after having been first proposed by Einasto (1965) and Sersic (1968), however, not in a DM context. A more illustrative representation of Equation 4.1 and a comparison to the NFW model is given in Appendix B.1. Following the findings for the DM density in the Solar Galactic neighborhood by Nesti and Salucci (2012) and Read (2014),[4] the normalization $\overline{\rho}_\mathrm{s,\,host}$ is chosen to provide $\rho_\odot := \overline{\rho}_\mathrm{host}(R_\odot = 8\,\mathrm{kpc}) = 0.4\,\mathrm{GeV\,cm^{-3}}$.[5]

Actually, $R_\odot$ and $\rho_\odot$ are rather difficult to determine precisely (Hessman, 2015). Moreover, it is continuously disputed whether the very central region of the Galactic DM halo is as cuspy

---

[3] Note that the value $R_\mathrm{s} = 15.14\,\mathrm{kpc}$ is based on the outdated Hubble parameter $h = 0.73$ from WMAP and has been retained following the study by Fornasa et al. (2013). Adopting an up-to-date value $h = 0.68$ (Ade et al., 2016) negligibly alters the derived subhalo properties.

[4] Higher estimates are found by Garbari et al. (2012) or Famaey (2015).

[5] These values give a model for the Galactic DM halo with the radii $R_{200} = 214\,\mathrm{kpc}$ and $R_{50} = 363\,\mathrm{kpc}$, within which the mean density is 200 (50) times the critical density (based on Ade et al., 2016). The halo yields $V_\mathrm{max} = 187\,\mathrm{km\,s^{-1}}$ at 33.4 kpc for circular orbits, similar to the NFW potential studied in Figure 2.1.

as predicted by Equation 4.1, or better described by a flatter Burkert profile (see, e.g., Gentile et al., 2004, and Figure B.1). This study being focused on the substructure detection, the existing uncertainties about the location in the Galactic halo, $R_\odot = (8.0 \pm 0.5)\,\mathrm{kpc}$ (Malkin, 2013), and the central DM density can be considered as subordinate. However, we come back later to the problem of core profile shapes for modeling the inner densities, $\overline{\varrho}_{\mathrm{sub}}$, of the subhalos.

For all subsequent calculations, an outer radius of the Galactic DM, up to which the halo and subhalos are modeled, is defined as $R_{\mathrm{gal}} = 260\,\mathrm{kpc}$. This choice is motivated by yielding a total MW mass of $M_{\mathrm{gal}} = 1.1 \times 10^{12}\,\mathrm{M}_\odot$, as suggested by Nesti and Salucci (2013).

4.1.2. Modeling the Galactic dark matter density of substructures

The Galactic DM distribution can be decomposed into a smooth component of particles, which freely move in the global gravitational potential of the Galaxy, and a subclustered DM component. The dynamics of subclustered DM is dominated by the gravitational potential of a substructure, defined by hosting some mass m bound in the substructure. The smooth DM density, ρ_{smooth}, is defined as

$$\rho_{\mathrm{smooth}} := \overline{\rho}_{\mathrm{host}} - \overline{\rho}_{\mathrm{subs}}\,, \tag{4.2}$$

where $\overline{\rho}_{\mathrm{subs}}$ denotes the density distribution of subclustered DM, averaged over sufficiently large volumes. This decomposition and averaging of ρ_{subs} implicitly assumes that subclustering occurs on mass and distance scales much smaller than those of the overall Galactic halo. As presented below, the heaviest subclusters are assumed to have masses $m \leq 0.01\,\mathrm{M}_{\mathrm{gal}}$ in this thesis.

Substructure definition: It is assumed that $\overline{\rho}_{\mathrm{subs}}$ can be described as (Charbonnier et al., 2012):

$$\overline{\rho}_{\mathrm{subs}}(R) := \int_{m_{\mathrm{min}}}^{m_{\mathrm{max}}} m\,\frac{\mathrm{d}^2 N}{\mathrm{d}V\,\mathrm{d}m}(R,\, m)\,\mathrm{d}m\,, \tag{4.3}$$

with

$$\frac{\mathrm{d}^2 N}{\mathrm{d}m\,\mathrm{d}V}(m,\, R) := N_{\mathrm{tot}} \times \frac{\mathrm{d}P}{\mathrm{d}m}(m) \times \frac{\mathrm{d}P}{\mathrm{d}V}(R)\,, \tag{4.4}$$

where m_{min} and m_{max} are the masses of the lightest and heaviest subhalo, and N_{tot} the total number of subhalos in the Galaxy. The probabilities $\mathrm{d}P/\mathrm{d}m$ and $\mathrm{d}P/\mathrm{d}V$ describe the chance to find a subhalo in the mass interval $\mathrm{d}m$ and volume $\mathrm{d}V$. As proper probability densities, they are normalized to 1 between $[m_{\mathrm{min}},\, m_{\mathrm{max}}]$ and within the radius R_{gal}, respectively. A separation of the variables according to Equation 4.4 implies that the chance to find a subhalo with mass m is independent of its position R in the host. This allows us to treat $\mathrm{d}P/\mathrm{d}m$ and $\mathrm{d}P/\mathrm{d}V$ separately, and the total mass of the Galaxy bound in subhalos, $M_{\mathrm{subs}} := 4\pi \int_0^{R_{\mathrm{gal}}} \overline{\rho}_{\mathrm{subs}}\, R^2\,\mathrm{d}R$, is obtained by

$$M_{\rm subs} = N_{\rm tot} \times \int_{m_{\rm min}}^{m_{\rm max}} m\, \frac{\mathrm{d}P}{\mathrm{d}m}(m)\, \mathrm{d}m \qquad \text{so that} \qquad \overline{\rho}_{\rm subs}(R) = M_{\rm subs} \times \frac{\mathrm{d}P}{\mathrm{d}V}(R)\,. \tag{4.5}$$

The validity of the separation (4.4) has been confirmed by, e.g., Gan et al. (2010) based on Boylan-Kolchin et al. (2008) and recently by Han et al. (2016) based on the Aquarius (Springel et al., 2008a) and Phoenix (Gao et al., 2012) simulations.

For a proper definition of subhalo masses m (as presented on the next page), N-body simulations throughout find the $\mathrm{d}P/\mathrm{d}m$ mass spectrum to follow a power-law distribution (e.g., Gao et al., 2004),

$$\frac{\mathrm{d}P}{\mathrm{d}m} \propto m^{-\alpha_{\rm m}}\,, \tag{4.6}$$

with the power-law slope $\alpha_{\rm m} \approx 2$ close to the value obtained by Press and Schechter (1974, Equation 2.12) for small-scale field halos. Like in Equation 2.12, an exponential cut-off of the mass spectrum is expected at the high-mass end (Angulo et al., 2009; Giocoli et al., 2010). For this thesis, a simple power-law mass spectrum according to Equation 4.6 is used, with a sharp cut at $m_{\rm max} = 0.01\, M_{\rm gal} = 1.1 \times 10^{10}\, \mathrm{M}_\odot$. This choice for $m_{\rm max}$ corresponds to the exponential suppression scale found by Angulo et al. (2009).[6] At the low mass end, the DM free-streaming scale is assumed to erase structure formation below $m_{\rm min} = 10^{-6}\, \mathrm{M}_\odot$ (Green et al., 2004). It is found in Chapter 5 that such low-mass halos are very unlikely to form resolvable objects for current instruments: Further lowering $m_{\rm min}$ causes an increase of the diffuse DM intensity, but is negligible for a search of individual objects.

Structural parameters of subhalos: The inner density of an individual subhalo, $\overline{\varrho}_{\rm sub}$ with $m = 4\pi \int_0^{r_{\rm sub}} \overline{\varrho}_{\rm sub}\, r^2\, \mathrm{d}r$, depends on both the subhalo mass m and its location R in the host halo. Independently of a specific density model, the subhalo mass distribution can be characterized by the concentration parameter (Diemer and Kravtsov, 2015),

$$c = c(m,\, R) := r_{\rm sub}/\, r_{-2}\,, \tag{4.7}$$

where $r_{\rm sub}$ is the radius of a subhalo (properly defined in the next paragraph) and r_{-2} the radius at which the logarithmic density slope becomes shallower than -2, $\mathrm{d}\log \overline{\varrho}_{\rm sub}/\mathrm{d}\log r|_{r_{-2}} = -2$. Only spherical subhalos are considered in this thesis. For the usual Einasto or NFW descriptions, $r_{-2} = r_{\rm s}$ (see Appendix B.1). In general, small structures are more concentrated than larger ones in a hierarchical bottom-up structure formation ($c \sim 10 - 50$ for micro-halos compared to $c \sim 5$ for galaxy clusters). Small structures emerge earlier at a higher mean cosmic density

---

[6] Note that $m \simeq 10^{10}\, \mathrm{M}_\odot$ also reflects the estimated DM mass of the Large Magellanic cloud (Besla, 2015).

$\rho_{\mathrm{crit}}(z)$, and the formed halo preserves ρ_{crit} from the time of collapse (Navarro et al., 1996). However, when older small structures merge into a younger larger one, they are affected by tidal forces when they closely pass by the center of gravity of the host halo. As a consequence, they lose the outskirts of their bound DM particles, which are more easily stripped away by the host halo than those gravitationally strongly bound at the subhalo centers (Bullock et al., 2001; Diemand et al., 2007). The disrupted DM finally forms the smooth halo component, ρ_{smooth}. For a DM host halo, an average "evolved" subhalo population can be described to have evolved from an "unevolved field halo" population prior to infall into the host (Bartels and Ando, 2015). In this context, it is also important to note that on average, subhalos which are today located closer to the center of the Galactic DM host halo have been accreted earlier. This is because (i) the host halo was smaller at earlier times (Taylor and Babul, 2005) and (ii) time is needed to lose angular momentum due to dynamical friction (Chandrasekhar, 1943a,b,c) for decreasing a subhalo's orbital radius. Consequently, the older subhalos found in the inner regions of the host halo have been less massive already at accretion or have been subject to stronger tidal mass loss over time. Surprisingly, an evolved mass distribution $\mathrm{d}P/\mathrm{d}m$ is obtained at $z = 0$ which is largely independent of the position R, i.e. the accretion history equally affects all mass decades. However, subhalos close to the halo center have, on average, their mass concentrated in smaller volumes (Zhao, 2004; Gan et al., 2010).

Definition of subhalo masses and sizes: Several definitions exist in the literature to account for the mass to either belong to the smooth halo or a subclustered mass m and to define the boundary of the substructure, r_{sub}: One is to define r_{sub} by where the density of a fitted subhalo profile equals the density of the smooth background profile, ρ_{smooth}, or a fraction thereof. This approach is, e.g., pursued by Springel et al. (2008a) and Mollitor et al. (2014). Alternatively, Binney and Tremaine (2008) define a tidal radius r_{tid}, within which the mass withstands the tidal stripping by an external potential to be

$$r_{\mathrm{tid}} = \left[\frac{m(r_{\mathrm{tid}})}{[2 - \mathrm{d}\ln M_{\mathrm{gal}}/\mathrm{d}\ln R] \times M_{\mathrm{gal}}(R)}\right]^{\frac{1}{3}} \times R\,, \tag{4.8}$$

where $m_{\mathrm{tid}} := m(r_{\mathrm{tid}})$ is the subhalo tidal mass within $r_{\mathrm{sub}} \equiv r_{\mathrm{tid}}$, and R is the position in the Galactic halo. In fact, it has been found that the two above definitions of subhalo masses are strongly correlated (see, e.g., Springel et al., 2008a).

For the semi-analytical modeling in this thesis, a population of subhalos $\frac{\mathrm{d}^2N}{\mathrm{d}V\,\mathrm{d}m}$ is defined for given virial masses $m \equiv m_{\mathrm{vir}}$. The virial mass corresponds to the mass of a bound region after collapse in a spherical top-hat structure formation, in which submasses have disentangled from the Hubble flow and form a self-gravitating system. For a given cosmology, this region can be assigned to a well-defined size (the radius of a "sub-universe" driven by the contained mass m_{vir}) after having relaxed into steady equilibrium.[7] The connection between the mass and radius of a spherical bound cosmic object can be expressed via a characteristic overdensity factor Δ in the approximation of a flat spacetime,

$$m_{\Delta} = \frac{4\pi}{3} r_{\Delta}^3 \times \Delta(z) \times \rho_{\mathrm{crit}}(z)\,, \tag{4.9}$$

where the mean density within r_{Δ} is Δ times ρ_{crit}, the critical density of the Universe (Equation A.5). After virialization of a system with mass m_{vir}, its Euclidean radius radius r_{vir} is obtained in a Einstein-deSitter spacetime ($\Omega_{\mathrm{K}} \equiv 0$, $\Omega_{\mathrm{m}} \equiv 1$), via $\Delta \equiv \Delta_{\mathrm{vir}} \approx 18\pi^2 \approx 178$ in Equation 4.9 (Peebles, 1980; Lee, 2010). For the ΛCDM case with dark energy additionally present, $\Omega_{\Lambda} \geq 0$, Bryan and Norman (1998) empirically find

$$\Delta_{\mathrm{vir}}(z) \simeq \frac{18\pi^2 + 82x - 39x^2}{\Omega_{\mathrm{m}}(z)}\,, \tag{4.10}$$

with $x := \Omega_{\mathrm{m}}(z) - 1$. For $z = 0$ and $\Omega_{\mathrm{m}}^0 = 0.308$ according to Ade et al. (2016), $\Delta_{\mathrm{vir}} \simeq 332$, and r_{vir} explicitly becomes

$$r_{\mathrm{vir}}(m_{\mathrm{vir}};\, z = 0) = 1.78 \times 10^{-2} \sqrt[3]{\frac{m_{\mathrm{vir}}}{\mathrm{M}_{\odot}}}\ \mathrm{kpc}\,, \tag{4.11}$$

where $h = 0.68 \Leftrightarrow \rho_{\mathrm{crit}}(z = 0) = 128\,\mathrm{M}_{\odot}\,\mathrm{kpc}^{-3}$ has been used.

Virial versus tidal masses: The relation (4.11) is now retained for describing the evolved subhalos after merging into a host halo, $r_{\mathrm{sub}} \equiv r_{\mathrm{vir}}$, thus neglecting tidal stripping effects. However, after modeling the Galactic density substructure with a power-law $\mathrm{d}P/\mathrm{d}m_{\mathrm{vir}}$ and suitable choices of the concentration $c_{\mathrm{vir}}(m_{\mathrm{vir}}, R)$, $\overline{\varrho}_{\mathrm{sub}}$, and $\mathrm{d}P/\mathrm{d}V$, a cross-check reveals that a reasonable physical mass spectrum is obtained. Figure 4.1 compares the input subhalo mass spectrum $\mathrm{d}N/\mathrm{d}m_{\mathrm{vir}}$ against the physical masses $\mathrm{d}N/\mathrm{d}m_{\mathrm{tid}}$ accounted to the simulated subhalos by Equation 4.8 for two specific Galaxy models (introduced in the next subsection). The figure shows that the physical masses of the evolved halos are by trend slightly lower than the unevolved masses m_{vir}. The lower panels show that for both models the mass loss according to Equation 4.8 only shifts down the normalization of the $\mathrm{d}N/\mathrm{d}m$, but leaves the slope ($\alpha_{\mathrm{m}} = 1.9$ in this case) largely unaffected. Therefore, it is concluded that $\mathrm{d}N/\mathrm{d}m_{\mathrm{tid}} \approx \mathrm{d}N/\mathrm{d}m_{\mathrm{vir}}$ is a sufficiently accurate description of the subhalo population in the applied modeling approach. However, r_{vir} has a limited physical meaning for evolved subhalos in a host halo.

---

[7] After relaxation, the virial relation $\overline{E}_{\mathrm{kin}} - \overline{U} = 0$ (page 22) holds, which explains the naming "virial" for the relaxed system.

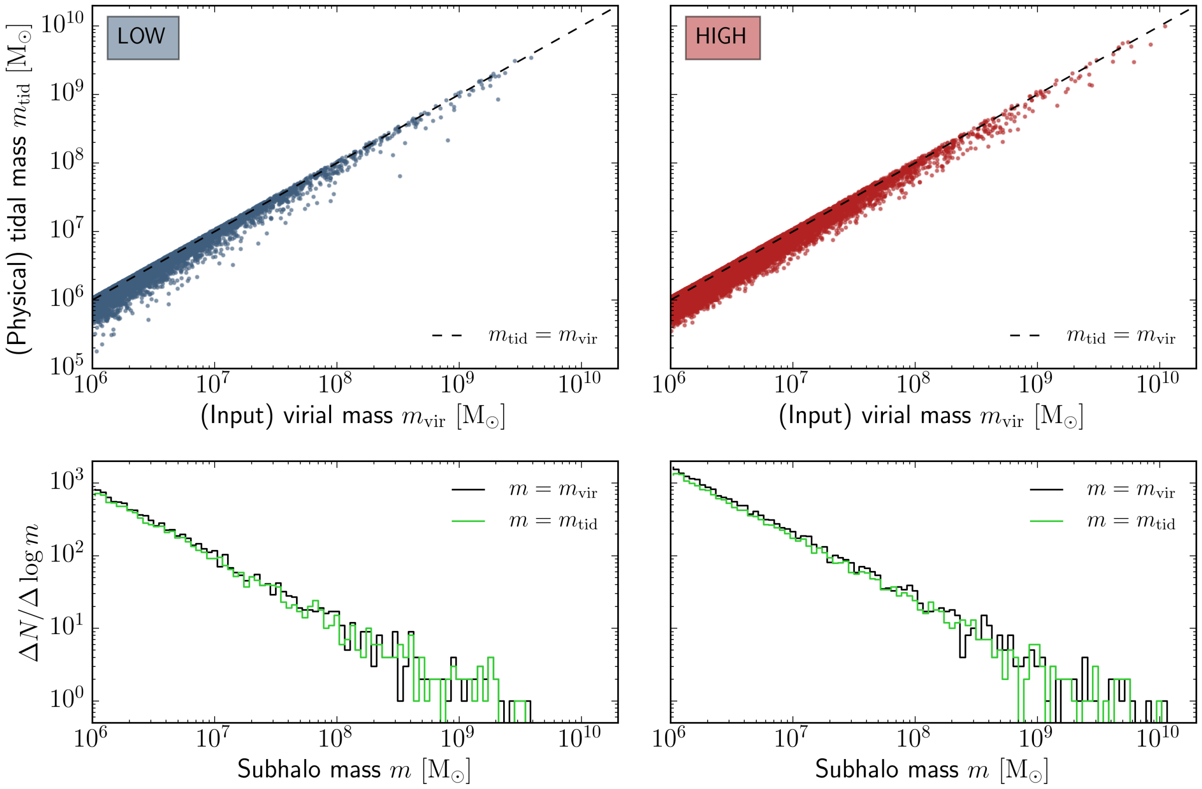

Figure 4.1.: Input field halo virial masses, $m_{\rm vir}$, versus physical subhalo tidal masses, $m_{\rm tid}$, according to Equation 4.8, in the semi-analytical DM modeling of a Galactic DM halo as described in this section. The models LOW and HIGH are specified in Table 4.1. All subhalos with $m_{\rm vir} \geq 10^6\,{\rm M}_\odot$ are shown.

4.1.3. Sets of substructure models

Given the previous definitions, specific choices for $\overline{\varrho}_{\rm sub}$, $N_{\rm tot}$, $\mathrm{d}P/\mathrm{d}m_{\rm vir}$, $\mathrm{d}P/\mathrm{d}V$, and $c_\Delta(m_\Delta,\, R)$ are presented in the following, with seven investigated configurations. An overview of the varied parameters and a motivation of the model numbering is given in Table 4.1 on page 96.

1. Inner density profile of the subhalos, $\overline{\varrho}_{\rm sub}$: The inner subhalo density, $\overline{\varrho}_{\rm sub}$, describes how the mass is on average distributed within the substructure. The same density profile as for the host halo is selected (model LOW), namely an Einasto profile,

$$\overline{\varrho}_{\rm sub}(r) = \overline{\varrho}_{\rm s,\,sub} \exp\left(-\frac{2}{\alpha_E}\left[\left(\frac{r}{r_{\rm s}}\right)^{\alpha_E} - 1\right]\right)\,, \tag{4.12}$$

with the same value $\alpha_{\rm E} = 0.17$. A self-similar subclustering is observed in many numerical simulations (e.g., Navarro et al., 1996; Springel et al., 2008a; Diemand et al., 2008), with both the Aquarius (Springel et al., 2008a) and VL II (Diemand et al., 2008) simulations preferring an Einasto profile (4.12). An alternative description of the subhalo inner density is the NFW profile, which exhibits a steeper slope at $r \to 0$,

$$\overline{\varrho}_{\rm sub}(r) = \overline{\varrho}_{\rm s,\,sub} \times 4 \left(\frac{r}{r_{\rm s}}\right)^{-1} \left(1 + \frac{r}{r_{\rm s}}\right)^{-2}, \tag{4.13}$$

as investigated in model VAR0. Given the mass $m_{\rm vir}$, $r_{\rm vir}(m_{\rm vir})$, and concentration $c_\Delta(m_\Delta,\, R)$ for a given subhalo, its density profile $\overline{\varrho}_{\rm s,\,sub}$ is fully determined. Its is reminded that only spherical subhalos are considered.

As discussed for the host halo, baryonic feedback onto the density cusps might significantly flatten the central subhalo regions and subsequently decrease the annihilation rate. In fact, flatter profiles have been suggested for dSph objects (Burkert, 1995). Treating the whole subhalo population as “dark” subhalos, a possible core-flattening is ignored in the presented subhalo modeling. However, the effect of baryonic feedback shall be considered by a decreased number $N_{\rm tot}$ of subhalos in the model LOW (see point 6). On the other hand, it has been recently found that very low-mass subhalos, which are unaffected by interactions with baryonic matter, might show profiles even cuspier than the NFW description (Ishiyama et al., 2010; Anderhalden and Diemand, 2013; Ishiyama, 2014). Although this would cause a 12% to 67% increase of the diffuse DM intensity in the MW from these low-mass clumps (Ishiyama, 2014), it is found that such enhanced emission from small-scale halos does not increase the number of individually detectable subhalos (see Hütten et al., 2016).

2. Sub-substructures within a subhalo: Bottom-up structure formation predicts hierarchical clustering down to the level of the free-streaming scale for masses $\lesssim 10^{-6}\,\mathrm{M}_\odot$. Because γ-radiation from DM annihilation scales with the square density, subclustering within a subhalo is expected to further boost its emission. Model VAR5 investigates this effect by adopting one additional sub-subhalo level with respect to the reference model LOW. Self-similarity is again assumed and the sub-subhalo population is modeled in the same way as the subhalo population LOW defined in this listing (which results in a sub-subhalo mass fraction $f_{\rm subsub} = 0.19$, the choice of E-AQ for $\mathrm{d}P/\mathrm{d}V$, and the SP parametrization for c_Δ). Bonnivard et al. (2015b) have shown that the annihilation flux level converges for an arbitrary number of substructure levels down to the free-streaming scale, such that one sub-subhalo level is considered to sufficiently quantify the effect of further subclustering. In any case, these sub-subhalos are not resolvable within $\varrho_{\rm sub}$, analogous to the arguing in the previous subsection for small-mass subhalos. Figure B.5 on page 211 illustrates the effect of sub-subhalos on the subhalo γ-ray intensity.

3. Mass-concentration parametrization $c_\Delta(m_\Delta,\, R)$***:*** A mass-concentration model is needed to fully determine the subhalo density distribution via $r_{\rm s} = c_\Delta(m_\Delta,\, R) \times r_\Delta$ for given m_Δ,

$r_\Delta(m_\Delta)$, and density profile. The subscript Δ indicates the ambiguity of different definitions of halo masses.[8] Several analytical approximations have been proposed to quantify the characteristic halo concentrations for different masses and redshifts z outlined in the previous subsection. Sánchez-Conde and Prada (2014) re-evaluate the findings about the concentrations at mass scales over 20 orders of magnitude and propose a universal parametrization of the halo-concentration at $z = 0$ based on Prada et al. (2012),

$$c_{200}(m_{200}, z = 0) = \sum_{i=0}^{5} c_i \times \left[\ln\left(\frac{m_{200}}{h^{-1}\mathrm{M}_\odot}\right)\right]^i , \tag{4.14}$$

with $c_i = (37.5153,\, -1.5093,\, 1.636\times10^{-2},\, 3.66\times10^{-4},\, -2.89237\times10^{-5},\, 5.32\times10^{-7})$. They note that the increase of the halo concentration towards lower masses significantly flattens compared to a simple power-law scaling adopted in earlier works. However, the universal scaling according to Equation 4.14 is explicitly derived from field halos in cosmological N-body simulations. It therefore does not account for an increase of the subhalo concentration towards the host halo center for bound objects. Nevertheless, Sánchez-Conde and Prada (2014) argue that their model can be well used for a modeling of Galactic density substructure, and Equation 4.14 (dubbed as "SP") is adopted for the benchmark model LOW. The $c_{200}(m_{200})$ relationship of Equation 4.14 is displayed in Figure 4.2 as black-dashed curve.

Higher subhalo concentrations towards the host halo center – where also the Galactic disk and observers on Earth are located – would cause cuspier annihilation profiles in this region. Therefore, distance-dependent concentration scalings are investigated in model VAR6. Deviating from the general dichotomous comparison, two distance-dependent scalings are considered in models VAR6a and VAR6b. The model from Pieri et al. (2011, P-VLII) is investigated in the model VAR6a,

$$c_{200}(m_{200},\, R,\, z = 0) = \left(\frac{R}{R_\mathrm{vir}}\right)^{-\alpha_\mathrm{R}} \times \left(C_1 \left[\frac{m_{200}}{\mathrm{M}_\odot}\right]^{-\alpha_1} + C_2 \left[\frac{m_{200}}{\mathrm{M}_\odot}\right]^{-\alpha_2}\right) , \tag{4.15}$$

calibrated to the VL II subhalos by $(\alpha_\mathrm{R}, C_1, C_2, \alpha_1, \alpha_2) = (0.286, 119.75, -85.16, 0.012, 0.0026)$. In the following, $R_\mathrm{vir} \equiv R_\mathrm{gal} = 260\,\mathrm{kpc}$ is adopted for Equation 4.15. The orange curves in Figure 4.2 display the concentration-relation from Equation 4.15 at $R = R_\odot = 8\,\mathrm{kpc}$ (dot-dashed line) and $R = R_\mathrm{gal} = 260\,\mathrm{kpc}$ (solid line). It can be seen that the distance-dependent description by Pieri et al. (2011) predicts significantly higher halo concentrations in the Solar

---

[8] The definitions of halo masses and sizes after self-gravitating collapse of field halos are continuously disputed in the literature (White, 2001). For instance, Navarro et al. (1996) approximate $\Delta \approx 200$, independent of a specific cosmology (for an overview of Δ choices, see Coe, 2010). The `CLUMPY` code uses the result from Giocoli et al. (2010) to translate between the r_vir for Δ_vir according to Equation 4.10 and $r_{200} := r_{\Delta=200}$.

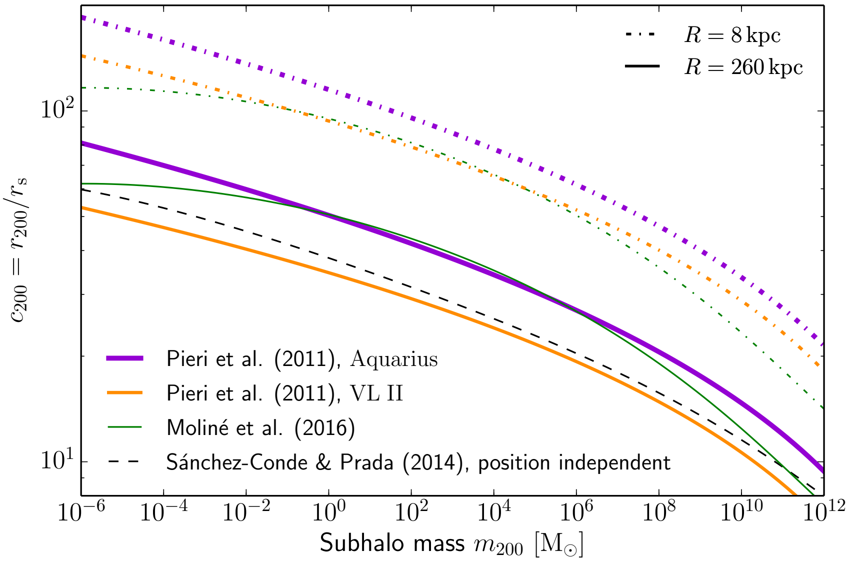

Figure 4.2.: Models for the concentration c_{200} of Galactic subhalos at redshift $z = 0$. Beside the distance-independent parametrization SP (Sánchez-Conde and Prada, 2014), shown are the values at the galactocentric distances $R = 8\,\mathrm{kpc}$ (dot-dashed lines) and $R = 260\,\mathrm{kpc}$ (solid lines) from Pieri et al. (2011) (violet and orange) and Moliné et al. (2017) (green). Figure taken from Hütten et al. (2016).

neighborhood than suggested by Sánchez-Conde and Prada (2014). Pieri et al. (2011) observe even higher subhalo concentrations in the Aquarius simulations (Springel et al., 2008a). These concentrations are also shown as violet curves in Figure 4.2 and are shortly commented on in the remainder of this chapter.

Recently, Moliné et al. (2017) have published an update on the findings from Sánchez-Conde and Prada (2014) which takes into account interactions of bound subhalos with their host halo. Their distance-dependent concentration-parametrization reads

$$c_{200}(m_{200},\, R,\, z=0) = c_0 \left[1 + \sum_{i=0}^{3} \times \left[a_i\, \ln\left(\frac{m_{200}}{10^8\, h^{-1}\mathrm{M}_\odot}\right)\right]^i\right] \times \left[1 + b\ln\left(\frac{R}{R_{200}}\right)\right], \quad (4.16)$$

with $c_0 = 19.9$, $a_i = (-0.195,\, 0.089,\, 0.089)$ and $b = -0.54$. This prescription in investigated as model VAR6b in Table 4.1, and shown as green curves in Figure 4.2. Although model "Moliné" predicts larger concentrations in the outskirts of the Galactic host halo (solid lines), its prediction is fairly comparable with the description P-VLII in the Solar neighborhood (green and orange dot-dashed curves).

4. ***Width of the mass-concentration distribution, σ_c:*** Simulations have clearly shown a halo-to-halo scatter of the subhalo mass concentration (see, e.g., Bullock et al., 2001). Therefore, a random component of the concentration is included in the subhalo modeling. The subhalo concentrations are assumed to be log-normal distributed around the mean $\bar{c}_\Delta(m_\Delta,\, R)$ from the previous paragraph,

$$\frac{\mathrm{d}P}{\mathrm{d}c}(m,\, R,\, c) = \frac{\exp\left[-\left(\frac{\ln c - \ln \bar{c}(m,\, R)}{\sqrt{2}\sigma_c}\right)^2\right]}{\sqrt{2\pi}\; c\; \sigma_c}\,, \tag{4.17}$$

with a constant σ_c. The value $\sigma_c = 0.14$ is selected as reference value (model LOW) as suggested by Wechsler et al. (2002); Prada et al. (2012). The impact of a larger $\sigma_c = 0.24$ (Bullock et al., 2001) is studied by a comparison to model VAR2. Incorporating a concentration scatter can be formally written as a generalization of Equation 4.4 (Bonnivard et al., 2015b),

$$\frac{\mathrm{d}^3N}{\mathrm{d}m\,\mathrm{d}V\,\mathrm{d}c}(m,\, R,\, c) = N_{\mathrm{tot}} \times \frac{\mathrm{d}P}{\mathrm{d}m}(m) \times \frac{\mathrm{d}P}{\mathrm{d}V}(R) \times \frac{\mathrm{d}P}{\mathrm{d}c}(m,\, R,\, c)\,. \tag{4.18}$$

5. Power-law slope α_{m} of the subhalo mass distribution $\mathrm{d}P/\mathrm{d}m_{\mathrm{vir}}$: For the reference model LOW, the value $\alpha_{\mathrm{m}} = 1.9$ is chosen to describe the subhalo mass function $\mathrm{d}P/\mathrm{d}m_{\mathrm{vir}} \propto m_{\mathrm{vir}}^{-\alpha_{\mathrm{m}}}$, calibrated to the findings for the Aquarius (Springel et al., 2008a) and VL II subhalos (Madau et al., 2008). Because the number of low-mass subhalos, and subsequently, the amount of the host halo mass bound into substructures M_{subs}, is very sensitive to a change of α_{m}, a slightly increased value of $\alpha_{\mathrm{m}} = 2.0$ is investigated in the model VAR1.

6. Number of subhalos N_{calib} between 10^8 and $10^{10}\,\mathrm{M}_\odot$: By choosing the number N_{calib} of subhalos with masses $10^8\,\mathrm{M}_\odot \leq m_{\mathrm{vir}} \leq 10^{10}\,\mathrm{M}_\odot$, together with $\mathrm{d}P/\mathrm{d}m_{\mathrm{vir}} \propto m_{\mathrm{vir}}^{-\alpha_{\mathrm{m}}}$, m_{min} and m_{max}, the total number N_{tot} of subhalos is determined. The so-defined number N_{calib} reflects the number of high-mass subhalos, out of which a large fraction is expected to be detectable in the optical band as satellite galaxies and also for which high-resolution N-body simulations give most reliable predictions. In fact, ΛCDM-only simulations (without a baryonic Ω_{b}) predict a significantly larger amount of these high-mass objects than the number of currently known satellite galaxies ($N_{\mathrm{calib}} \gtrsim 200$ versus $\gtrsim 20$ known satellites). The apparent conflict is known as the "missing satellites" problem (Bullock, 2013), an inversion of the "too-big-to-fail" argument (Boylan-Kolchin et al., 2011). Recent attempts to include the gravitational feedback of baryons into the simulation of Galaxy halo formation seem to solve this conflict (Mollitor et al., 2014; Sawala et al., 2016). Hydrodynamical feedback of baryons in the dense subhalo centers could flatten the central cusps and cause less massive halos to evolve (Brooks et al., 2013; Del Popolo et al., 2014; Maxwell et al., 2015). However, modeling a Galaxy evolution with mutual DM-baryon interaction is fairly complex and not yet fully understood. Alternatively, if DM was "warm", the number of high-mass subhalos would be also significantly reduced (Lovell et al., 2012). Altogether, $N_{\rm calib} = 150$ is chosen for the conservative model LOW, motivated by the hydrodynamical APOSTLE simulations (Sawala et al., 2016). A double amount of subhalos, $N_{\rm calib} = 300$ is selected for the models VAR4 based on ΛCDM-only simulations (Springel et al., 2008a). With Equation 4.5, also the total subclustered Galaxy mass, $M_{\rm subs}$, and $f_{\rm subs} := M_{\rm subs}/M_{\rm gal}$ can be calculated. The resulting numbers $N_{\rm tot}$ of total subhalos in the Galaxy and $f_{\rm subs}$ are listed in Table 4.1 for each model.

7. Spatial distribution of the subhalos $\overline{\rho}_{\rm subs} = M_{\rm subs} \times {\rm d}P/{\rm d}V$: Accretion history causes less subhalos of all mass decades to be found close to the Galaxy center. Because the average subhalo γ-ray brightness at Earth is very sensitive to the subhalo distribution ${\rm d}P/{\rm d}V$, two models for ${\rm d}P/{\rm d}V$ are considered for closer comparison: Springel et al. (2008a) fit the subhalo abundance $\overline{\rho}_{\rm subs}$ in the Milky-Way-like Aquarius A1 halo with an Einasto profile, $\alpha_E = 0.678$, and $R_{\rm s} = 199\,{\rm kpc}$ (model "E-AQ"). Subhalos are slightly more abundant near the Galactic core in the VL II simulations (Diemand et al., 2008), modeled by the number distribution $N(< R)$ given by Gao et al. (2004):

$$\frac{N(< x)}{N_{200}} = \frac{(1 + a\, c_{200})\, x^{\beta}}{1 + a\, c_{200}\, x^{\alpha}}, \; x := \frac{R}{R_{200}}\,, \tag{4.19}$$

with $a\, c_{200} \equiv 11$, $\alpha = 2$, $\beta = 3$ and $R_{200} = 213.5\,{\rm kpc}$ (Madau et al., 2008, model M-VLII). A differential reformulation of Equation 4.19 as $\overline{\rho}_{\rm subs}$ is given in Appendix B.5. While the E-AQ model is adopted for the benchmark model LOW, the M-VLII description is chosen for the model VAR3. Figure 4.3 displays these ${\rm d}P/{\rm d}V$ descriptions for the reference model LOW in terms of the local substructure fraction, $f_{\rm local} := \overline{\rho}_{\rm subs}(R)/\overline{\rho}_{\rm host}(R)$ (left), and in terms of $N(< R) = 4\pi \int_0^R {\rm d}P/{\rm d}V\, R'^2\, {\rm d}R'$ (right). N_{200} denotes the number of subhalos within R_{200}. The values for $f_{\rm local}(R_\odot)$ in the Solar neighborhood are also given in Table 4.1 for all models. In addition to the models E-AQ (black-dashed curve) and M-VLII (orange curve), further ${\rm d}P/{\rm d}V$ descriptions are shown in Figure 4.3. The joint fit to all Aquarius halos by a curved power-law (Springel et al., 2008a, cyan line) and the Einasto profile fitted to the Phoenix galaxy cluster simulations (Gao et al., 2012, green line) yield a subhalo abundance very similar to the E-AQ and M-VLII cases. In contrast, assuming the subhalo density to trace the overall Galactic density distribution ($\overline{\rho}_{\rm subs} \propto \overline{\rho}_{\rm host}$) heavily overestimates the number of subhalos close to the Sun (dot-dashed black line). Also, a generic "anti-biased" subhalo population has been proposed in the literature (Kuhlen et al., 2007; Siegal-Gaskins, 2008, dotted line), where $\overline{\rho}_{\rm subs} \propto R \times \overline{\rho}_{\rm host}$. However, this model still overrates the number of subhalos close to $R_\odot$ by more than a factor two compared to the results from N-body simulations. Han et al. (2016) show that a $\overline{\rho}_{\rm subs} \propto R^{1.3} \times \overline{\rho}_{\rm host}$ scaling is needed to correctly describe the Aquarius and Phoenix subhalo distributions.

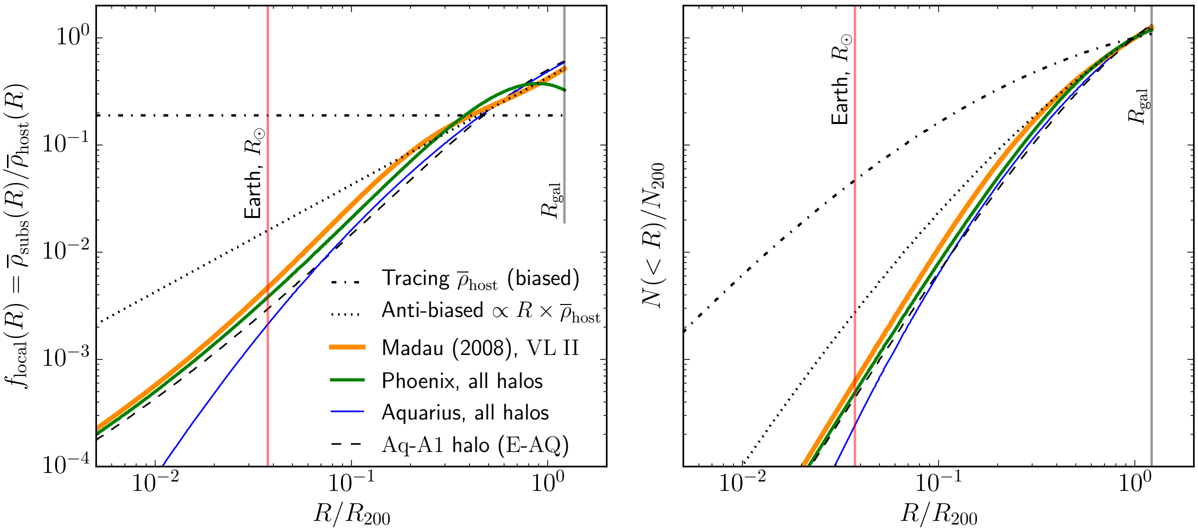

Figure 4.3.: Models for the subhalo spatial distribution $\mathrm{d}P/\mathrm{d}V$ up to $R_{\rm gal}/R_{200} = 1.22$ and other subhalo parameters based on the model LOW. The Earth is located at $R_\odot/R_{200} = 0.037$. The left panel corresponds to a differential description and the right panel to an integrated description.

	Model	VAR0	VAR1	LOW	VAR2	VAR3	VAR4	VAR5	VAR6a	VAR6b	HIGH
Varied parameters	inner profile	NFW	E	E	E	E	E	E	E	E	E
	$\alpha_{\rm m}$	1.9	2.0	1.9	1.9	1.9	1.9	1.9	1.9	1.9	1.9
	σ_c	0.14	0.14	0.14	0.24	0.14	0.14	0.14	0.14	0.14	0.14
	$\overline{\varrho}_{\rm sub}$	E-AQ	E-AQ	E-AQ	E-AQ	M-VLII	E-AQ	E-AQ	E-AQ	E-AQ	M-VLII
	$N_{\rm calib}$	150	150	150	150	150	300	150	150	150	300
	sub-subhalos?	no	no	no	no	no	no	yes	no	no	no
	$c(m)$	SP	SP	SP	SP	SP	SP	SP	Moliné	P-VLII	P-VLII
Derived parameters	$N_{\rm tot}$ $(\times 10^{14})$	6.1	150	6.1	6.1	6.1	12	6.1	6.1	6.1	12
	$f_{\rm subs}$ [%]	19	49	19	19	19	38	19	19	19	38
	$f_{\rm subs}(R_\odot)$ [%]	0.30	0.77	0.30	0.30	0.47	0.59	0.30	0.30	0.30	0.93
	$\widetilde{D}^\star_{\rm obs}$ [kpc]	22^{+32}_{-16}	13^{+27}_{-10}	19^{+27}_{-14}	21^{+33}_{-15}	20^{+22}_{-15}	17^{+26}_{-13}	21^{+30}_{-14}	8^{+18}_{-6}	9^{+14}_{-6}	8^{+11}_{-6}
	$\log_{10}(\widetilde{m}^\star_{\rm vir}/\mathrm{M}_\odot)$	$9.0^{+0.8}_{-1.4}$	$8.5^{+0.9}_{-1.5}$	$8.8^{+0.8}_{-1.4}$	$8.9^{+0.8}_{-1.4}$	$9.0^{+0.7}_{-1.3}$	$8.9^{+0.9}_{-1.4}$	$9.0^{+0.7}_{-1.4}$	$7.9^{+1.4}_{-1.6}$	$7.9^{+1.4}_{-1.5}$	$8.2^{+1.2}_{-1.5}$
	$\log_{10}\left(\frac{\widetilde{J}^\star(\theta_{\rm vir})}{\mathrm{GeV}^2\,\mathrm{cm}^{-5}}\right)$	$19.9^{+0.4}_{-0.3}$	$20.0^{+0.4}_{-0.3}$	$20.0^{+0.5}_{-0.3}$	$20.0^{+0.4}_{-0.3}$	$20.1^{+0.4}_{-0.3}$	$20.2^{+0.4}_{-0.3}$	$20.3^{+0.5}_{-0.3}$	$20.3^{+0.5}_{-0.4}$	$20.4^{+0.5}_{-0.3}$	$20.8^{+0.5}_{-0.4}$

Table 4.1.: Investigated Galactic subhalo models and parameter variations. The first seven lines correspond (from top to bottom) to: the subhalo density profile, the slope of the subhalo mass spectrum, the width of the concentration distribution, the subhalo spatial distribution, the number of objects between 10^8 and 10^{10} $\mathrm{M}_\odot$, the flag for sub-subhalos, and the mass-concentration relation. The columns are ordered by increasing flux of the brightest object. 'NFW' stands for a NFW density profile and 'E' for an Einasto profile with $\alpha_{\rm E} = 0.17$. 'E-AQ' is the Einasto profile fitted to the subhalo distribution of the Aq–A1 halo (Springel et al., 2008a), while 'M-VLII' corresponds to the VL II parametrization by Madau et al. (2008). Concentration relations are modeled after Sánchez-Conde and Prada (2014, 'SP'), Pieri et al. (2011, 'P-VLII') and Moliné et al. (2017). Derived parameters in the six bottom rows are: $N_{\rm tot}$ the total number of subhalos in the MW; $f_{\rm subs}$ the global mass fraction contained in subhalos; $f_{\rm subs}(R_\odot)$ the mass fraction contained in subhalos at the solar distance from the Galactic center (GC); $\widetilde{D}^\star_{\rm obs}$, $\widetilde{m}^\star_{\rm vir}$, and $\widetilde{J}^\star$ are the median distance from the observer, mass, and J-factor of the brightest subhalo from the 500 realizations of each model performed in Section 4.3. Table published in Hütten et al. (2016).

4.2. Modeling implementation in the CLUMPY code

The above described semi-analytical DM density modeling is implemented in the CLUMPY code,[9] which is used to compute the DM γ-ray fluxes in this thesis. CLUMPY has been developed by Charbonnier et al. (2012) to efficiently calculate γ-ray intensities and fluxes from DM annihilation or decay for semi-analytical galaxy cluster, galaxy, and dSph models.

The code, written in C/C++, provides an optimized line-of-sight integration of the J-factor according to Equation 2.30 (2.31) for annihilation (decay) from a subclustered DM density distribution ρ. Moreover, it efficiently computes two-dimensional J-factor skymaps by separating an inhomogeneous DM halo into regions whose J-factor contribution is spatially resolved in the computation and into regions which can be handled as unresolved average.[10] This allows a fast calculation of fluxes and intensities from complex DM structures, including several orders of hierarchical subclustering, at a high angular resolution. The main features of the code have been published in 2012. For the purpose of this thesis, several features have been added to the code by the author:

- All-sky J-factor maps for observers located within a Galactic halo can be calculated. Therefore, the code has being interfaced with the HEALPix library (Górski et al., 2005) and been rewritten to work in the HEALPix pixelization scheme. The HEALPix pixelization subdivides a sphere in $N_{\mathrm{pix}} = 12\, N_{\mathrm{side}}^2$ equal-area, iso-latitude pixels for any integer parameter N_{side}.
- Several DM subhalo parametrizations have been added (e.g., Equations 4.15 and 4.19).
- Via the interfaced HEALPix library, a Gaussian smoothing of DM J-factor skymaps can be applied, and the angular power spectrum (APS) of J-factor/γ-ray intensity maps can be calculated directly from within the code.
- The convergence of CLUMPY's resolution criterion $RE_{J_{\mathrm{clumps}}}$ (see next paragraphs) has been rigorously checked and slightly improved.
- Multiple bugs have been fixed, and the speed of the J-factor skymap calculation has been improved.

These features have been included in a second published release of the code (Bonnivard et al., 2015b), along with additional features added by the other authors. In particular, these include the consideration of sub-substructures, the tabulated γ-ray final state radiation spectra from Cirelli et al. (2011), and the random scatter of concentrations c_Δ. In the following, CLUMPY's

---

[9] `http://lpsc.in2p3.fr/clumpy/`

[10] It is remarked to not confuse the phrasing "resolved subhalos" in this section with the notion of resolved subhalos in the instrumental context of the next chapter. The computationally resolved number of subhalos in this thesis is always by far larger than the subhalos resolved by the CTA in the simulations of Chapter 5.

approach of the J-factor calculation, presented in detail by Charbonnier et al. (2012) and Bonnivard et al. (2015b), shall be quickly summarized:

The smooth DM component ρ_{smooth} is calculated via $\rho_{\mathrm{smooth}} = \overline{\rho}_{\mathrm{host}} - \overline{\rho}_{\mathrm{subs}}$ (Equation 4.2), where $\overline{\rho}_{\mathrm{host}}$ and $\overline{\rho}_{\mathrm{subs}} = M_{\mathrm{subs}} \times \mathrm{d}P/\mathrm{d}V(r)$ are given as input as described in the previous section. The line-of-sight integral in the annihilation flux, Equation 2.30, then is formally written

$$\frac{\mathrm{d}J}{\mathrm{d}\Omega} = \int_{l_{\mathrm{min}}=0}^{l_{\mathrm{max}}} \left(\rho_{\mathrm{smooth}} + \sum_i \rho_{\mathrm{cl}}^i\right)^2 \mathrm{d}l\,, \tag{4.20}$$

with the expanded elements of the sum

$$\frac{\mathrm{d}J_{\mathrm{smooth}}}{\mathrm{d}\Omega} := \int_0^{l_{\mathrm{max}}} \rho_{\mathrm{smooth}}^2\, \mathrm{d}l\,, \tag{4.21}$$

$$\frac{\mathrm{d}J_{\mathrm{cross-prod}}}{\mathrm{d}\Omega} := 2\int_0^{l_{\mathrm{max}}} \rho_{\mathrm{smooth}} \sum_i \rho_{\mathrm{cl}}^i\, \mathrm{d}l\,, \tag{4.22}$$

$$\frac{\mathrm{d}J_{\mathrm{subs}}}{\mathrm{d}\Omega} := \int_0^{l_{\mathrm{max}}} \left(\sum_i \rho_{\mathrm{cl}}^i\right)^2 \mathrm{d}l\,. \tag{4.23}$$

Calculating ρ_{smooth} with Equation 4.2, the term (4.21) is directly numerically integrated towards the desired directions $\vec{k}$. Charbonnier et al. (2012) have shown that the cross-product term (4.22) can be neglected for individual, resolved clumps, and Equation 4.22 can be calculated as

$$\frac{\mathrm{d}J_{\mathrm{cross-prod}}}{\mathrm{d}\Omega} \approx 2\int_0^{l_{\mathrm{max}}} \rho_{\mathrm{smooth}}\, \overline{\rho}_{\mathrm{subs}}\, \mathrm{d}l\,, \tag{4.24}$$

with the known input quantities ρ_{smooth} and $\overline{\rho}_{\mathrm{subs}}$. The subhalo term (4.23) is further divided into

$$\frac{\mathrm{d}J_{\mathrm{subs}}}{\mathrm{d}\Omega} = J_{\mathrm{drawn}} + \langle J_{\mathrm{subs}}\rangle = \int_0^{l_{\mathrm{crit}}} \left(\sum_i \rho_{\mathrm{cl}}^i\right)^2 \mathrm{d}l + \int_{l_{\mathrm{crit}}}^{l_{\mathrm{max}}} \left(\sum_i \rho_{\mathrm{cl}}^i\right)^2 \mathrm{d}l\,. \tag{4.25}$$

Above a critical distance l_{crit}, the J-factor contribution of the subhalos is given as a continuous, spatial average (see Charbonnier et al., 2012) and is numerically calculated as:[11]

$$\langle J_{\mathrm{subs}}\rangle := \int_{l_{\mathrm{crit}}}^{l_{\mathrm{max}}} \left(\sum_i \rho_{\mathrm{cl}}^i\right)^2 \mathrm{d}l \approx \int_{l_{\mathrm{crit}}}^{l_{\mathrm{max}}} \int_{m_{\mathrm{min}}}^{m_{\mathrm{max}}} \int_{c_{\mathrm{min}}=0}^{c_{\mathrm{max}}=\infty} \mathcal{L}(m,\, c)\, \frac{\mathrm{d}^3 N}{\mathrm{d}m\, \mathrm{d}V\, \mathrm{d}c}\, \mathrm{d}c\, \mathrm{d}m\, \mathrm{d}l\,, \tag{4.26}$$

---

[11] For a distance-dependent $\overline{c}_\Delta(m_\Delta,\, R)$, an average $\langle \overline{c}_\Delta(m_\Delta)\rangle := 4\pi \int_0^{R_{\mathrm{gal}}} \overline{c}_\Delta(m_\Delta,\, R)\, \mathrm{d}P/\mathrm{d}V\, R^2\, \mathrm{d}R$ is used to enable the $\langle J_{\mathrm{subs}}\rangle$ calculation according to Equation 4.26.

with the intrinsic clump luminosity given by

$$\mathcal{L}(m,\,c) := 4\pi \int_0^{r_{\rm vir}} \rho_{\rm cl}^2(r;\,m,\,c)\,r^2\,{\rm d}r\,. \tag{4.27}$$

The remaining resolved subhalos between the observer and the distance $D_{\rm obs} \leq l_{\rm crit}$ are calculated as

$$J_{\rm drawn} := \int_0^{l_{\rm crit}} \left(\sum_i \rho_{\rm cl}^i\right)^2 {\rm d}l \quad \approx \quad \sum_i \int_0^{l_{\rm crit}} \rho_{\rm cl,\,i}^2\,{\rm d}l\ , \tag{4.28}$$

where the cross-product terms between different subhalos are neglected. These halos are finally randomly drawn from the $\frac{{\rm d}^3N}{{\rm d}m\,{\rm d}V\,{\rm d}c}$ distribution, and the line-of-sight integral (4.28) is explicitly calculated for each clump centered at a distance $D_{\rm obs}$ from the observer.

The crucial value $l_{\rm crit}$, below which subhalos are resolved, is computed as a function of the angular skymap resolution expressed by $\theta_{\rm int}$, the clump masses $m_{\rm vir}$,[12] and the user-defined precision (maximum relative error) $RE_{J_{\rm clumps}}$ of the resolved objects. The parameter $RE_{J_{\rm clumps}}$ roughly expresses the minimal resolved intensity relative to the diffuse smooth DM emissions from $J_{\rm smooth} + \langle J_{\rm subs}\rangle + J_{\rm cross-prod}$: The higher the precision $RE_{J_{\rm clumps}}$, the larger $l_{\rm crit}$, and a larger fraction of the Galaxy's subhalos is individually computed. For a given smooth DM intensity level, $RE_{J_{\rm clumps}}$ also indirectly scales the minimum flux (J-factor) of subhalos to be resolved. A more precise definition of $RE_{J_{\rm clumps}}$ is given by Charbonnier et al. (2012). Suffice to say that limiting the computation of individually resolved clumps up to maximum distance $l_{\rm crit}$ drastically reduces the number of substructures, for which a dedicated line-of-sight integration has to be performed: The discussion of section C.6 shows a good convergence of `CLUMPY`'s precision requirement when resolving $\lesssim 10^4$ individual subhalos out of altogether $N_{\rm tot} \sim 10^{15}$ clumps in the Galaxy. In doing so, the algorithm is able to pre-select objects from *all mass decades*, spanning over the range from $\sim 10^{-6}\,{\rm M}_\odot$ to $\sim 10^{10}\,{\rm M}_\odot$, which need to be computed at a given demanded precision.

4.3. γ-rays from the Galactic subhalo models

This section presents the resulting J-factor component of the γ-ray fluxes from annihilation in the DM models introduced in Section 4.1 and computed as described in Section 4.2. In Subsection 4.3.1, the impact of the seven model variations (which have been listed in Subsection 4.1.3) on the γ-ray flux at Earth are discussed. In Subsection 4.3.2, the model predictions are compared to what is empirically known from optical observations of the Galactic satellite galaxies.

---

[12] A coarse mass-dependence with one logarithmic bin Δm_i per mass-decade is chosen in the code.

4.3.1. Impact of substructure properties

For each of the models presented in Table 4.1 on page 96, 500 full-sky J-factor maps are computed based on the models' Galactic density (sub-)structure.[13] From this statistical sample, mean and median properties on the full sky of the subhalo models are derived. The naming of the varied models VARi, $i \in [0, 6]$ has been ordered after increasing overall J-factor, $\widetilde{J}^\star(\theta_{\rm vir})$, from the median brightest subhalo in the full sky. The overall J-factor corresponds to the emission within $\theta_{\rm vir} = \arctan(r_{\rm vir}/D_{\rm obs})$ and $D_{\rm obs}$ the distance from the observer. The three bottom rows in Table 4.1 list these J-factors, together with the median mass $\widetilde{m}^\star_{\rm vir}$ of the brightest subhalo in each model and its median distance, $\widetilde{D}^\star_{\rm obs}$. All values are given with their 68% scatter around the median.

The ordering after increasing median brightness of the brightest subhalo already gives a coarse estimate about the influence of a modeling variation compared to the reference model LOW. For a more detailed consideration not only limited on the brightest object, the cumulative source count distribution $\overline{N}_X(>J)$ is built for each model X = LOW, HIGH, VARi, $i \in [0, 6]$. The distribution $\overline{N}_X(>J)$ displays the mean number of all halos with a J-factor larger than a certain threshold J-factor, J, averaged over the 500 sky-map simulations. The upper panel of Figure 4.4 shows this distribution for the reference model LOW (pale blue) and the model HIGH (red). It follows that for both models, the $\overline{N}_X(>J)$ can be well described by a power-law (indicated by the thin solid-red line), $\overline{N}_X(>J) \propto J^{1-\alpha}$, with $\alpha \sim 2$, except for the high-J end. For a power-law approximation of $\overline{N}_X(>J)$, Appendices B.6 and B.7 provide useful insights into the connection between $\overline{N}(>J)$ and $\widetilde{J}^\star$ which are several times used throughout this thesis.

The remaining models are displayed in the lower panel of Figure 4.4 relative to the source count distribution of the model LOW, as the ratio $\overline{N}_X(>J)/\overline{N}_{\rm LOW}(>J)$. They shall be discussed in the same order as having been introduced in Subsection 4.1.3:

- Modeling the subhalo densities $\overline{\varrho}_{\rm sub}$ with a NFW profile instead of an Einasto profile for the same structural parameters $m_{\rm vir}$, $r_{\rm vir}$, c_Δ (VAR0, blue) shifts down the flux from all subhalos by about 30%. This result becomes understandable from Figure B.1 in Appendix B.1.
- Considering the presence of further sub-subclusters in the subhalos (VAR5, light green) significantly boosts the overall emission of the brightest subhalo in median by more than a factor two, but has less impact on the fainter halos. This behavior is in agreement with the results of Bonnivard et al. (2015b, see their Figure 1).

---

[13] After the optimization of the code and for the required precision ($\sim 10^4$ resolved subhalos), an average skymap computation required about 10 CPU hours. The computing grid at DESY Zeuthen has been used to calculate in parallel the thousands of model runs presented throughout this thesis.

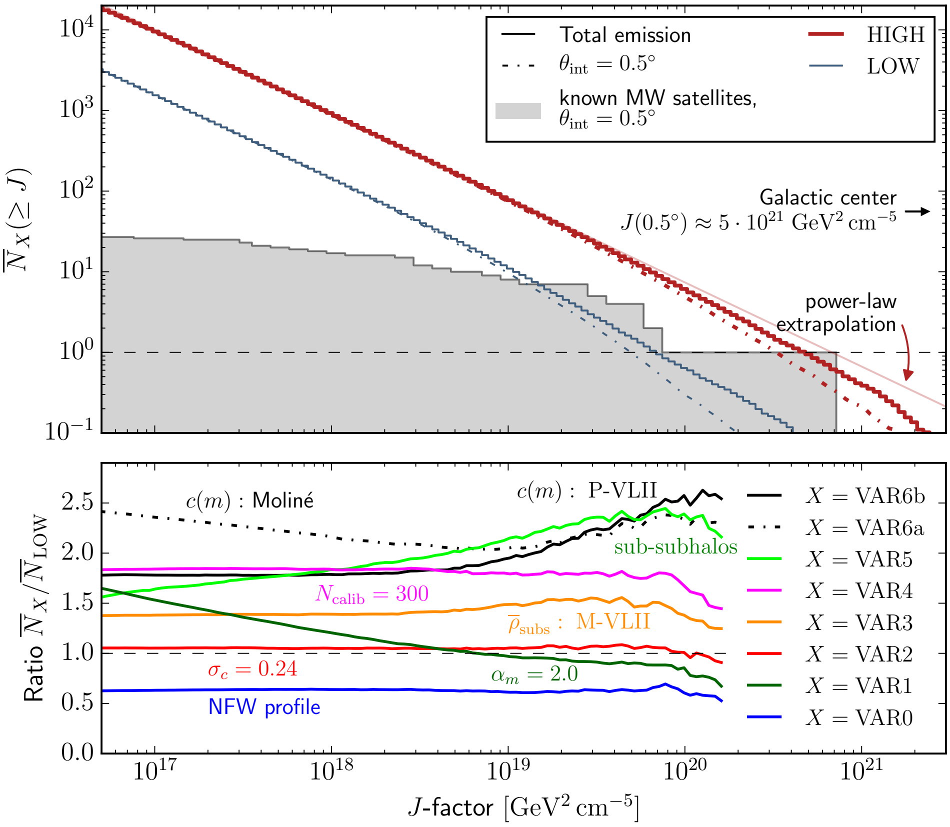

Figure 4.4.: *Top:* Cumulative source count distribution of Galactic subhalos (full sky, averaged over 500 simulations) for the models LOW and HIGH. The solid lines show the distribution of the total J-factors, $J(\theta_{\rm vir})$, the dot-dashed lines the distribution when only taking into account the emission from the central 0.5° of the subhalos, $J(0.5°)$. The gray-shaded histogram shows the cumulative distribution of all known satellite galaxies, including the Large and Small Magellanic clouds, with the values listed in Hütten et al. (2016). *Bottom:* ratio of all VARi models to LOW. Figure published in Hütten et al. (2016).

- The choice of the concentration relation c_Δ (VAR6) turns out to most significantly affect the overall brightness of the brightest subhalos. The two distance-dependent descriptions for c_Δ, P-VLII (VAR6a, solid-black line) and Moliné (VAR6b, dashed-black line) give a comparable value for the median brightest J-factor, significantly larger than for the distance-independent c_Δ (SP) description for the model LOW.
- A larger c_Δ scatter of the subhalo concentrations (VAR2, red) only marginally increases the median fluxes from all objects.
- Increasing the mass spectrum power-law slope $\alpha_{\rm m}$ for a constant calibration at the high-mass end from 1.9 to 2 (VAR1, green) increases the subhalos number $N_{\rm tot}$ by a factor 25.

However, these additional halos are found in the low-mass decades, which do not produce high J-factors. As a result, the slope of the $\overline{N}_X(>J)$ distribution is steepened, while slightly lower J-factors as for the model LOW are retained at the high-J end.

- Doubling the normalization of the subhalo mass spectrum (by doubling the number of high-mass halos, $N_{\rm calib}$, VAR4, magenta), constantly increases the number of halos above a given brightness by a factor ~ 1.8.
- A subhalo spatial distribution according to M-VLII, which shifts more subhalos towards the host halo center (VAR3, orange), results in an $\sim 40\%$ increase of the J-factors over all J-decades.

In summary, the presence of sub-subhalos, a distance-dependent description $c_\Delta(m_\Delta,\, R)$ of the subhalo concentration, the number $N_{\rm calib}$ of heavy subclumps in the Galaxy, and their distribution $\mathrm{d}P/\mathrm{d}V$ most significantly affect the detection prospects of the brightest halos.

The impact of the $c_\Delta(m_\Delta,\, R)$ and $\mathrm{d}P/\mathrm{d}V$ models on the subhalo brightness can be well understood by the fact that the brightest halos are found for all models rather close to Earth, $\widetilde{D}^\star_{\rm obs} \lesssim 20\,\mathrm{kpc}$ (see Table 4.1). Thereby, they are also located at comparably small galactocentric coordinates. Models that predict higher subhalo concentrations and an overall higher probability to find subhalos in this region will also drive the expected median subhalo brightness. Also note that the P-VLII and Moliné concentration models predict comparable subhalo concentrations at small R over a large mass range (Figure 4.2), explaining their agreement at the high-J end in Figure 4.4. For the even higher concentrations found by the P-Aq model (violet curves in Figure 4.2) compared to the P-VLII description, an further increase of $\sim 60\%$ for the flux from the brightest subhalos is found. The P-Aq model is not further discussed in the following, but it should be kept in mind that subhalo concentrations higher as predicted by the P-VLII model also would improve the sensitivities presented in Chapter 5. Therefore, reliable predictions on the subhalo concentrations are crucial for their indirect detection prospects in γ-rays.

Also the presence of sub-subhalos significantly increases the flux from the brightest subhalos. However, this additional boost arises from the outskirts of the extended halos. In full analogy to the substructure formation at the level of the Galactic halo system, also sub-subhalos are found with higher probability at larger distances from their host halo center (Springel et al., 2008b). Figure 4.5 displays how a radial $\overline{\varrho}_{\rm sub}$ distribution including sub-substructures translates into the annihilation γ-ray brightness. For a typical bright subhalo in the LOW/VAR5 models (see Table B.1 for more details about the specific halo example), the left panel compares the line-of-sight integrals $\mathrm{d}J/\mathrm{d}\Omega$ at a given angular distance from the subhalo center. The right panel shows the integrated J-factors around the subhalo center. Sub-subhalos cause a flux increase for the model VAR5 (green curve) over the model LOW (black curve) only at $\theta_{\rm int} \gtrsim 0.1^\circ$ for that

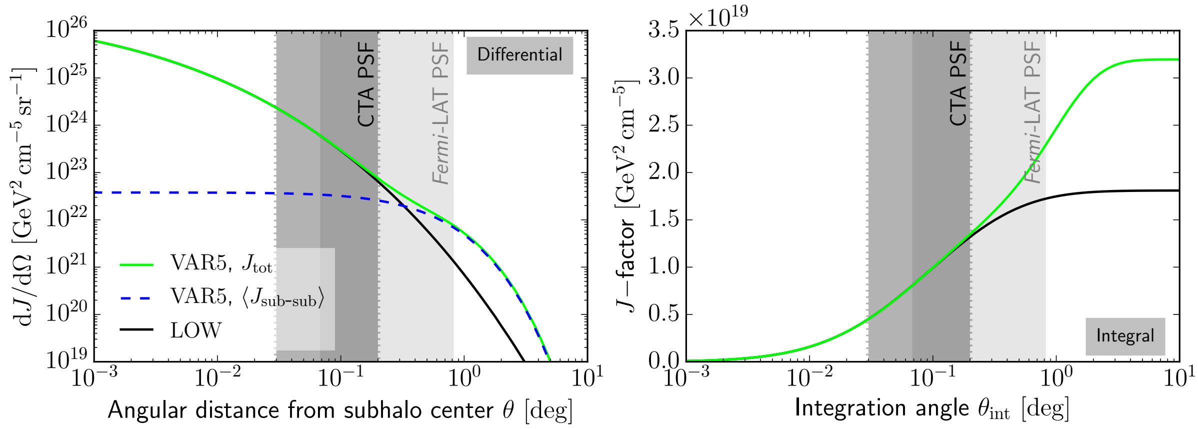

Figure 4.5.: The impact of sub-subhalos as a function of the distance from the subhalo center (left, differential) and as a function of the integration area (right, integral). For a typical bright detectable DM halo (see Table B.1), the signal with sub-subhalos (green-solid line) is compared to the signal without them (black-solid line). The angular resolutions (68% containment) for CTA at $E_\gamma \geq 30$ GeV and *Fermi*-LAT at $E_\gamma \geq 1$ GeV are overlaid (gray-shaded areas). Left panel published in Hütten et al. (2016).

specific halo. The gray-shaded bands denote the range of angular resolutions of the *Fermi*-Large Area Telescope (LAT) and CTA instruments. Both instruments are in principle able to resolve the spatial extension of the subhalo. However, for a background-dominated instrument like CTA, the sensitivity at the detection threshold is not much improved by an intensity increase at scales larger than the angular resolution. A more stringent arguing for this statement is given in Appendix C.3. Therefore, although sub-substructures produce broader objects with an increased overall flux, they are not considered for the CTA performance calculation in Chapter 5.[14]

Additionally to the presented models, also a scattering of the Einasto slope-transition α_{E} has been investigated. Springel et al. (2008a) find the Aq-A subhalos to be best described by Einasto profiles with varying slopes $0.16 \leq \alpha_{\mathrm{E}} \leq 0.20$. However, the impact on the J-factors of the brightest objects from this uncertainty is subordinate: For $\alpha_E = 0.16$, the J-factors increase by $\lesssim 20\%$ compared to $\alpha_E = 0.17$, and decrease by $\lesssim 60\%$ when choosing $\alpha_E = 0.20$.

For the remainder of this thesis, the model HIGH is built with the P-VLII $c_\Delta(m_\Delta, R)$ description, $N_{\mathrm{calib}} = 300$, and the M-VLII $\mathrm{d}P/\mathrm{d}V$ scaling to be changed compared to the model LOW (see Table 4.1). While model LOW is chosen as a conservative benchmark model, model HIGH represents an optimistic case, inspired by ΛCDM simulations without baryonic feedback. By accounting several descriptions from the VL II simulation to the model HIGH, it also reflects

---

[14] However, a spatial dependence of the sub-subhalo concentration c_Δ, i.e. applying the P-VLII or Moliné descriptions to the sub-sub level, has not been studied, which possibly could cause a flux increase within the CTA angular resolution. On the other hand, Moliné et al. (2017) note that the sub-substructures could be completely stripped away from their subhalo hosts in tidal interactions with the Galactic host halo.

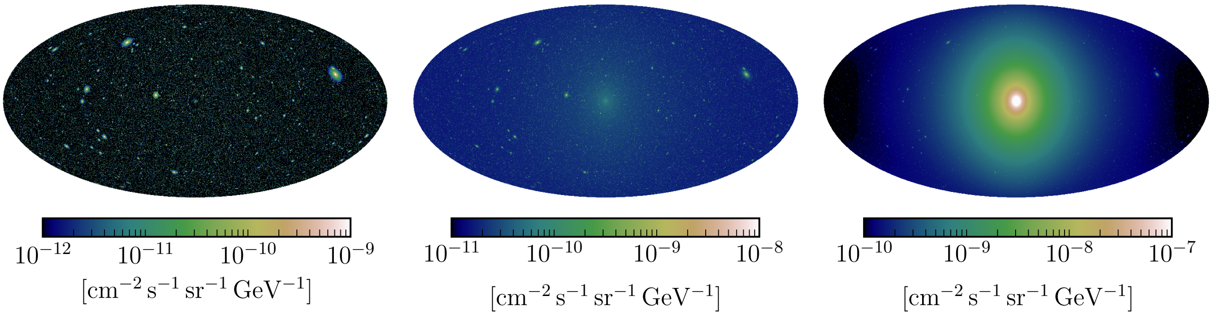

(a) Model LOW

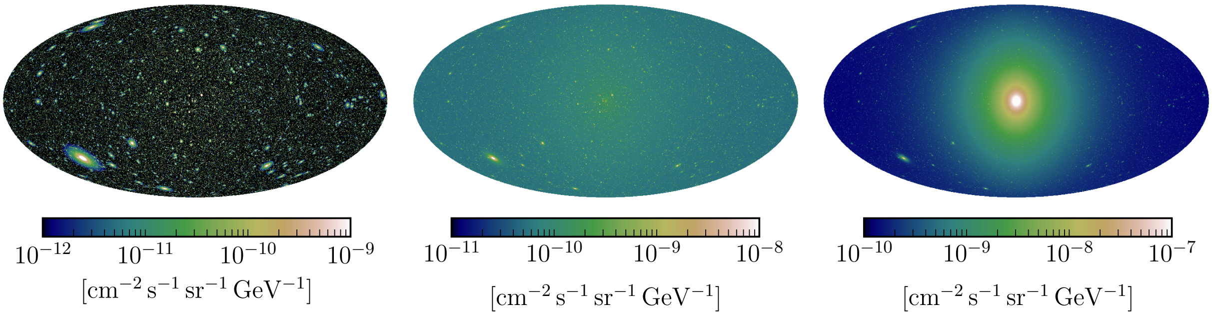

(b) Model HIGH

Figure 4.6.: One statistical realization of the Galactic differential intensity at 4 GeV, for the models LOW and HIGH. In the left column, only the flux from the resolved substructures is shown ($J_{\rm drawn}$). In the middle column, the flux from all substructures, resolved and unresolved, is shown ($J_{\rm drawn} + \langle J_{\rm subs}\rangle + J_{\rm cross-prod}$). In the right column, the total Galactic emission is shown ($J_{\rm smooth}$ additionally included). Note the different color scales between the columns. The particle physics term is computed from a thermal relic cross-section, $m_\chi = 200$ GeV, and $\chi\chi \to b\bar{b}$. The maps are drawn with a HEALPix resolution $N_{\rm side} = 512$. Figures published in Hütten et al. (2016).

the predictions directly derived from the VL II results. This is confirmed by a model comparison with N-body simulations postponed to Appendix B.2 and comparisons to the γ-ray detection prospects from works based on the VL II subhalo catalog in Chapter 5. Fur illustrative purpose, Figure 4.6 presents the differential γ-ray intensity skymaps at 4 GeV from the models LOW and HIGH. Showing the maps in units of intensity, a $m_\chi = 200$ GeV DM particle is assumed, purely annihilating into bottom quarks at a cross section of $\langle\sigma v\rangle = 3 \times 10^{-26}\,\mathrm{cm\,s^{-1}}$. Figure 4.6 also shows that the smooth Galactic DM component heavily dominates the Galactic DM emission and subhalos are only detectable at sufficiently large angular distances from the Galactic center.

4.3.2. Comparison of the DM subhalo models to known Milky Way satellites

The only up-to-date empirical evidence for a subclustered DM Galaxy halo are the satellite galaxies orbiting around the Milky Way (MW). In the same way as the Milky Way disk is assumed to have formed in the gravitational sink of the Galaxy's DM host halo, the MW's satellite galaxies would have formed in the cores of the most massive DM subhalos.[15] More than twenty of these dSph galaxies have been discovered so far, and more are expected to be found by ongoing optical surveys like the Dark Energy Survey.[16] These dSph objects, indicating the locations of high DM density, have been observed to derive one of the most stringent limits on the DM properties by indirect DM searches (Ackermann et al., 2015e, see also the discussion on page 45). From an analysis of the kinematics of their member stars, the density distribution of DM in dSph galaxies, their total DM mass, and the corresponding J-factors from the expected DM annihilation can be inferred (see, e.g., Charbonnier et al., 2011; Bonnivard et al., 2015a). In the context of this chapter, the empirically derived properties of these potential DM subhalos shall be compared to the previously modeled subhalo populations. This comparison is based on the values compiled in Table 4 of Hütten et al. (2016), which lists the properties of all spectroscopically confirmed MW satellite galaxies. These values are compiled from previously published analyses, including the properties of the irregular Large and Small Magellanic cloud objects. Additionally to the established classical and ultrafaint dSph galaxies, several recently discovered objects have been analyzed in Hütten et al. (2016) for their DM properties. The new objects include the Draco II, Triangulum II, Horologium I, and Pisces II dSph galaxies. As discussed in Subsection 4.1.2, the virial mass m_{vir} of the satellite galaxies is assumed to coincide with their physical tidal mass m_{tid}. Given the large measurement uncertainties for the observed dSph objects, the difference of the definitions of m_{vir} and m_{tid} is negligible.

The gray-shaded histogram in the upper panel of Figure 4.4 (on the previous page 101) displays the cumulative J-factor source count distribution built from the known MW satellites. These J-factors refer to an integration angle of $\theta_{\mathrm{int}} = 0.5^\circ$ and therefore have to be compared with the dot-dashed curves from the subhalo modeling. The satellite source count distribution is built on the median inferred J-factor values from the various objects, and the large uncertainties for the ultra-faint dSph galaxies are not included in this depiction. At the high-J end, the models LOW and HIGH encompass the distribution built on the known satellites, indicating that the model LOW might represent a somewhat too conservative model. The highest value in the gray-shaded distribution, which even overshoots the model HIGH, originates from the Triangulum II galaxy, which is subject to an uncertainty larger than one order of magnitude. A competing analysis

---

[15] Note that DM dominated satellite galaxies can be well distinguished from non DM dominated globular clusters. For details see Bullock et al. (2010).

[16] `http://www.darkenergysurvey.org`, Abbott (2005).

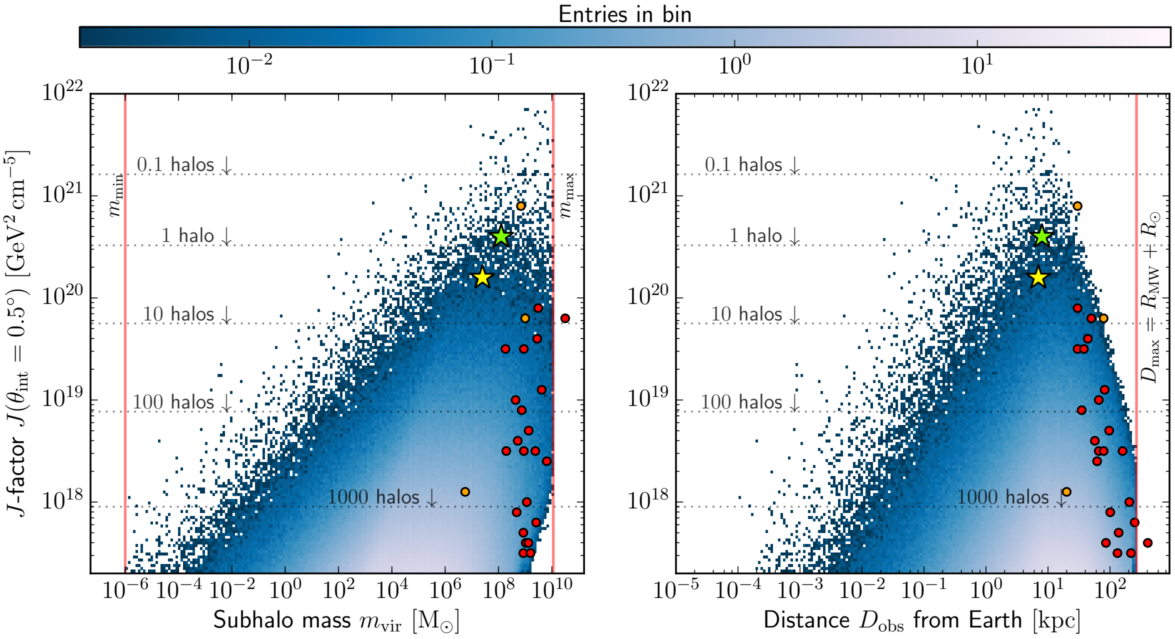

Figure 4.7.: Relation between the brightness of the subhalos $J(0.5^\circ)$ and their mass (left) or distance to the observer (right). The blue histograms are shown for the subhalo model HIGH and averaged over 500 simulations. The projection along the vertical axis gives the source count distribution $\langle \mathrm{d}N/\mathrm{d}J \rangle$. The dotted lines denote the integrated bins above the respective line, $\overline{N}_{\mathrm{HIGH}}(\geq J)$, identical to what is presented in Figure 4.4. The known MW satellites are overlaid as red dots (orange dots for the dSph discovered most recently). The yellow star marks the median brightest subhalo expected for a dark subhalo search with CTA and the green star for *Fermi*-LAT (see Subsections 5.2.1 and 5.2.4). In this figure, all J-values are calculated at $\theta_{\mathrm{int}} = 0.5^\circ$. Figure published in Hütten et al. (2016).

of this object by Hayashi et al. (2016) yields a median $J(0.5^\circ) = 1.6 \times 10^{20}$ GeV^2 cm^{-5}, in fair agreement with the model HIGH, while still within 1σ agreement with the value reported for Triangulum II in Hütten et al. (2016). At lower J-decades, less satellites have been found than should be present featuring a corresponding J-factor. This is in agreement with the assumption that most of these lower J halos are also the ones holding lower DM masses, and therefore being dark subhalos. On the other hand, it is expected that ongoing surveys will discover more dSph objects in the lower J range and few additional extraordinary DM-rich and close objects might be added. Under this assumption, Figure 4.4 suggests that the models LOW and HIGH reasonably encompass the uncertainty about the actual Milky Way subhalo population.

Further insight into the Galactic subhalo distribution is given by the two-dimensional histograms of Figure 4.7 in the $J - m_{\mathrm{vir}}$ (left) and $J - D_{\mathrm{obs}}$ planes (right) for the subhalo model HIGH (a depiction of model LOW is postponed to Figure B.3). Integrated in vertical projection, the one-dimensional histogram of Figure 4.4 is reproduced, indicated by the horizontal dotted lines. The red and orange (for the recently discovered dSph's) dots indicate the properties of the known MW satellites. This illustrates that the MW satellites in fact constitute a heavy and rather distant subset of the subhalo population. However, comparably large J-factors as for the dSph galaxies are also expected for lighter ($m_{\mathrm{vir}} \gtrsim 10^5\,\mathrm{M}_\odot$) and closer ($D_{\mathrm{obs}} \gtrsim 1\,\mathrm{kpc}$) objects, which could be provided by dark subhalos. In fact, the shaded blue model distributions prefer to find the largest J-factors on slightly lower mass and distance scales than obtained for the known dSph galaxies. The yellow and green stars show the median properties of the brightest subhalo expected in a survey with the CTA and *Fermi*-LAT instruments, derived in the following Chapter 5. These values depend on the covered survey area, and a larger median J-factor is obtained for *Fermi*-LAT (green star) because of the larger survey field adopted for the LAT.

5 | Detecting Galactic dark matter subhalos with CTA

> *They could see she was a real Princess and no question about it, now that she had felt one pea all the way through twenty mattresses and twenty more feather beds. Nobody but a Princess could be so delicate.*
>
> Hans Christian Andersen, The Princess on the Pea[1]

---

[1] English translation by Jean Hersholt (1886-1956) from `http://www.andersen.sdu.dk/vaerk/hersholt/`

The following chapter presents the projections for the Cherenkov Telescope Array (CTA) to observe Galactic dark matter (DM) subhalos. In Subsection 5.1.1, the best observation strategy for a subhalo discovery search with CTA is discussed. In Section 5.2, the discovery sensitivity to the brightest expected DM subhalo is investigated. This presentation follows the results published in Hütten et al. (2016). In Section 5.3, a complementary approach is investigated, to detect Galactic DM in the angular power spectrum (APS) of the residual diffuse γ-ray background (DGRB). The latter method is also discussed in a generic context of CTA's ability to detect fluctuations from unresolved very-high-energy (VHE) sources.

5.1. Survey or deep-field observation? Choosing the CTA observing strategy

5.1.1. Survey vs. deep-field search for subhalos

If unknown objects in the sky are searched with small field-of-view telescopes like CTA, two different strategies are suitable for a fixed observing time: Either a large fraction of the sky is scanned with a shallow exposure, or the total available time is invested to observe a small field in the sky, for the gain of a much better sensitivity to detect dim sources. Under the assumption that sources are found on average with equal probability anywhere in the sky, the answer to which strategy is preferable depends on the expected flux distribution of the sources to discover, and the background characteristics of the measurement (Dubus et al., 2013). For a power-law flux source count distribution with index $\alpha \sim 2$ (see Equation B.19 for a definition of α), as found in Chapter 4 for Galactic DM subhalos, it is obtained for background dominated measurements:

$$\frac{\overline{N}_{\mathrm{detectable}}(A_1,\, T)}{\overline{N}_{\mathrm{detectable}}(A_2,\, T)} \approx \sqrt{\frac{A_1}{A_2}}\,. \tag{5.1}$$

For a fixed total observation time T, the mean number of detectable subhalos, $\overline{N}$, increases with the square root of the observing field size, A, so that a large-field shallow survey is preferred to detect the brightest DM subhalo.[2] A derivation of Equation 5.1 is given in Appendix C.1.

---

[2] Note that it shown in the following Subsection 5.1.2 that the assumption of an isotropic source distribution is slightly violated for the subhalo model HIGH, for which Figure 5.3 shows that bright sources are found with higher probability towards the Galactic center (GC). However, a more rigorous assessment also must take into account that observations near the Galactic plane are subject to further complicating effects, like an increased diffuse γ-ray flux from hadronic cosmic ray interactions with the interstellar medium and a large abundance of Galactic γ-ray sources. These two mutually countervailing complications are neglected in the following.

A similar question arises for the sensitivity to the full subhalo population or any other unresolved γ-ray source class as anisotropies in the DGRB, the analysis method presented in Section 5.3. In a previous study, Ripken et al. (2014) found that observing anisotropies from a deep-field observation yields a somewhat better sensitivity than for distributing the same number of events on a larger fraction of the sky. However, the best strategy for an anisotropy search also depends on the flux distribution which generates the anisotropies. The power-spectral methods for detecting γ-ray anisotropies are introduced in detail in Subsection 5.3.2. To argue in favor of a survey for an anisotropy analysis, the following reasoning shall be anticipated: Combining Equation C.4 and the APS behavior discussed in Appendix C.5 (Equation C.17), one obtains for the median Poisson power of a power-law source count distribution with index $\alpha \approx 2$,

$$\frac{\widetilde{C}^I_{\mathrm{P}}(A_1)}{\widetilde{C}^I_{\mathrm{P}}(A_2)} \approx \left(\frac{A_1}{A_2}\right)^2 . \tag{5.2}$$

For $A_2 = 4\pi\,\mathrm{sr}$, $A_1/A_2 = f_{\mathrm{sky}}$ is the fraction of the sky. One factor f_{sky} in Equation 5.2 can be attributed to the APS suppression due to the limited sky coverage, as discussed in the later Subsection 5.3.2. Applying this correction, one obtains

$$\frac{\widetilde{C}^I_{\ell,\,\text{full-sky}}(A_1 < 4\pi\,\mathrm{sr})}{\widetilde{C}^I_{\ell,\,\text{full-sky}}(A_2 = 4\pi\,\mathrm{sr})} = f_{\mathrm{sky}} . \tag{5.3}$$

Thus, the full-sky equivalent power from power-law distributed point sources with index $\alpha \approx 2$, sampled on $f_{\mathrm{sky}} \times 4\pi\,\mathrm{sr}$, is still a factor f_{sky} smaller than the power sampled on the full sky. This can be understood as the APS from a power-law source count distribution spectrum with $\alpha \approx 2$ is dominated by the brightest halos (see Appendices C.5 and C.6), which are likely to be masked when observing only a portion of the sky. The analytical result from Equation 5.3 is obtained from several simplifying assumptions. In particular, point-like objects are presumed, which does not strictly hold for the γ-ray emission from DM. Therefore, the scaling found in Equation 5.3 is validated by a dedicated Monte-Carlo (MC) study, simulating DM subhalos of the model HIGH on $f_{\mathrm{sky}} = 0.25$ (within the region defined in Figure 5.2) and sampling their power spectra. The result is shown in Figure 5.1 and compared to the subhalo abundance on the full sky. At $10 \lesssim \ell \lesssim 200$, the ratio between the full-sky corrected part-sky spectrum (solid line) and the full-sky spectrum (dot-dashed line) is $\widetilde{C}^I_{\ell,\,\text{full-sky}}(A_1 = \pi\,\mathrm{sr})/\widetilde{C}^I_{\ell,\,\text{full-sky}}(A_2 = 4\pi\,\mathrm{sr}) \approx 0.33$, somewhat larger than the expected factor $f_{\mathrm{sky}} = 0.25$ from Equation 5.3, but still in fair agreement.

The improving factor of an anisotropy analysis on a large sky fraction with respect to the intensity sensitivity, $I_{\text{part-sky}}/I_{\text{full-sky}} \lesssim \sqrt{1/f_{\mathrm{sky}}}$ (see Subsection 5.3.2), then must be compared to the gain in deep-field APS sensitivity. A study postponed to Appendix C.10 argues that

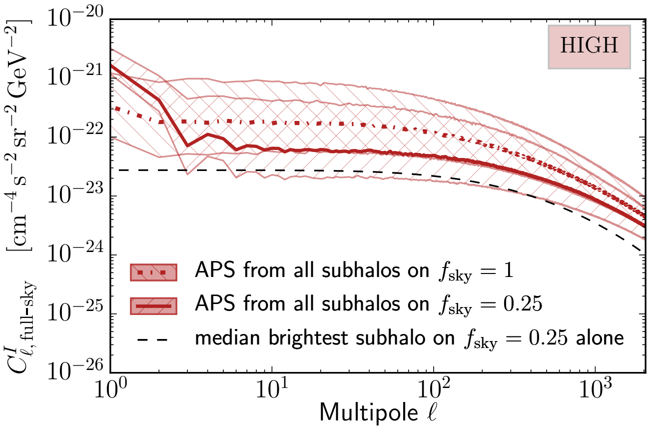

Figure 5.1.: Comparison of the median subhalo APS (without the smooth Galactic DM halo contribution) and its 68% confidence level (C.L.) scatter, when sampling the spectrum on the full sphere (dot-dashed line), and on a quarter of the sphere (solid line). Also, the APS arising from the brightest halo on the quarter-sky alone is shown (black-dashed line, see Table 5.1 for its properties). All spectra are shown in full-sky equivalent power, for which the part-sky spectra have been rescaled by a factor $1/f_{\text{sky}}$. The particle physics is chosen to be the same as in Figure 5.15. The rising power of the subhalos' APS (solid line) at low multipoles is a masking artifact. See Subsections 5.3.2 and 5.3.3 for more details.

a power spectral search for anisotropies on small sky fractions is heavily impeded by numeric artifacts. Artifacts can in principle be subtracted or excluded in the analysis, however, for the price of a worse sensitivity – which is expected to be overwhelming for very small fields.

With regard to the following studies, it is concluded that for both cases, (i) resolving the brightest subhalo and (ii) detecting γ-ray anisotropies from DM subhalos, a large sky area is preferable. Therefore, is focused on how data from the CTA extragalactic survey can be used to constrain the population of DM subhalos.

It is finally noteworthy that for part-sky observations, the scattering of the angular power C_ℓ slightly increases. From Figure 5.1, one obtains at $\ell \gtrsim 10$

$$\frac{\left(\sigma_{C_\ell}/\widetilde{C}^{I}_{\ell,\,\text{full-sky}}\right)_{A_1=\pi\,\text{sr}}}{\left(\sigma_{C_\ell}/\widetilde{C}^{I}_{\ell,\,\text{full-sky}}\right)_{A_2=4\pi\,\text{sr}}} \approx 1.5\,,$$

with the difference decreasing towards higher multipoles. Figure 5.1 also shows the APS from only the median brightest subhalo on $f_{\text{sky}} = 0.25$ (see Table 5.1, brightest halo within $\theta_{\text{int}} = 0.05°$). The brightest halo alone accounts for more than 50% of the APS from the whole population, in agreement with the discussion in Appendix C.6. We will come back later to compare this power of the brightest halo alone with the APS from the whole subhalo population.

5.1.2. A model for the CTA extragalactic survey

Two surveys are planned to be performed with CTA: A survey along the Galactic plane and an extragalactic survey outside the Galactic plane. In terms of total observed area and amount of data, the extragalactic survey will outweigh the Galactic one, with an approximately uniform exposure over 25% of the sky and an allocated observation time of around 400 to 600 hours (Dubus et al., 2013). A benchmark observation time of $T = 500\,\mathrm{h}$ is fixed for this thesis. The goal of the CTA extragalactic survey is a search for unknown VHE γ-ray emitters at high Galactic latitudes, either because they have not been selected before for multi-wavelength follow-up observations, or they do not show electromagnetic emission in any other waveband (so called "dark particle accelerators"). Moreover, a uniform survey allows an unbiased population study of high-latitude VHE γ-ray sources. A similar motivation also holds for the search for Galactic DM substructures: γ-ray signals from DM annihilation in dark subhalos, whose position is not indicated by the formation of dSph galaxies, can only be found by a survey. A DM-like energy spectrum from a dark VHE γ-ray source would provide a compelling evidence for the existence of weakly interacting DM.

In this thesis, it is assumed, for simplicity, that most of the extragalactic survey will be performed by the southern CTA, in a region centered at the Galactic south pole ($b < -30°$).[3] The red encircled area in Figure 5.2 illustrates this choice of the survey field, covering the targeted quarter of the full sky. The background colormap in Figure 5.2 shows the total Galactic DM intensity, which is dominated by the Galactic halo and increasing towards the Galactic center (GC). However, for Earth-bound γ-ray telescopes, the residual background outweighs any average astrophysical γ-ray intensity by at least a factor of 1000 (recall Figure 3.17 and Table 3.3, and also see Subsection 5.3.4), and diffuse γ-ray backgrounds are subordinate in a search for point-like γ-ray sources. Figure 5.3 shows that for the subhalo model LOW, no preference exists to find the brightest subhalo in a particular direction within the survey field. This is different for the subhalo model HIGH: For this model, the probability to find the brightest subhalo is clearly biased towards the direction of the GC. Still, the choice of the CTA survey area from Figure 5.2 is considered to be a realistic representation for a DM subhalo search with CTA.

The performance of a survey with Imaging Atmospheric Cherenkov Telescopes (IACTs) depends on the energy-dependent field of view (FOV) of the instrument and the spacing between the pointings by which the sky is rastered. For IACT observations, discrete exposures on fixed positions in the sky are usually performed. Observing the sky in a continuous drifting mode implies a drastically different mode of observation, data storage, and analysis, and will likely

---

[3] Depending on the final choice of the survey field and beginning of operation of the two CTA sites, a significant contribution to the survey data might also be provided by the northern array.

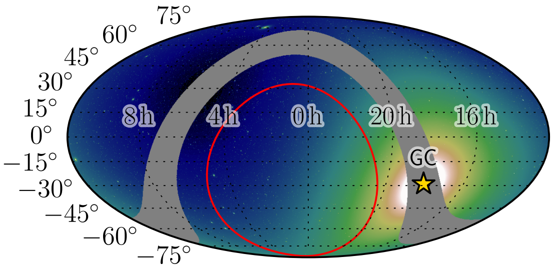

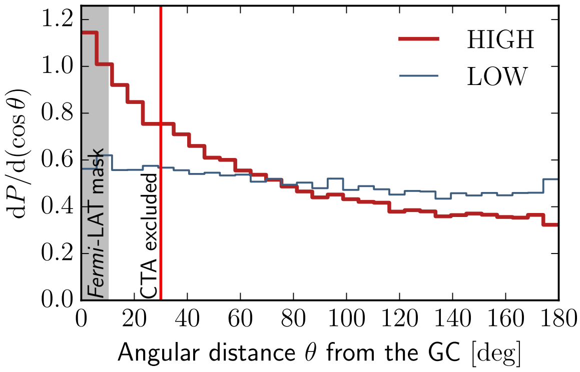

Figure 5.2.: Skymap (equatorial coordinates) showing the assumed CTA survey field in this thesis (within the red line) and the later discussed *Fermi*-LAT setup (gray masking band around the Galactic plane). The colormap in the back is the same as in Figure 4.6 (model LOW, total emission).

Figure 5.3.: Probability to find the brightest subhalo at the angular distance θ from the Galactic center (GC). The vertical lines indicate the sky cuts of each instrument (shown in Figure 5.2). Figures 5.2 and 5.3 have been published in Hütten et al. (2016).

not be an option for CTA. Dubus et al. (2013) investigated several tiling strategies to achieve a homogeneous exposure from a discrete sampling of the sky, relying on a plane Euclidean geometry. For a sky fraction as large as 25%, however, an Euclidean tiling procedure is not anymore appropriate. Therefore, a grid pattern relying on the HEALPix pixelization scheme is introduced in this thesis. The HEALPix tessellation (Górski et al., 2005) subdivides the sphere into equal-area, equal-latitude pixels, and by this, facilitates equally spaced pointing positions on a curved surface. Two different grid spacings are investigated: A HEALPix grid with $N_{\rm side} = 32$ results in an average distance between the pixel centers of $\Delta_{\rm fov} = 1.83° \approx 2°$.[4] Secondly, a HEALPix grid with $N_{\rm side} = 64$ is considered, yielding $\Delta_{\rm fov} = 0.91° \approx 1°$. In Figure 5.4, this approach for the survey tiling is illustrated for the $\Delta_{\rm fov} = 2°$ case: Each survey observation is pointed towards the center of a HEALPix pixel in Galactic coordinates. The HEALPix grid is indicated by white quadrangles and the CTA pointings by blue circles with 3° radius. It can be seen that the pointings widely overlap, guaranteeing a homogeneous overall exposure.

The homogeneity of the exposure is further investigated in Figure 5.5: For the $\Delta_{\rm fov} = 2°$ case and a total time of $T = 500\,\rm h$, the extragalactic survey area has been divided into $N_{\rm fov} = 2880$ single pointings, with an observation time of $t_{\rm obs} = 10.4\,\rm min$ towards each pointing. Relying on the modeling of the off-axis effective areas and background rates as described in Section 3.2, Figure 5.5 shows that this results in an average on-axis equivalent exposure of $t_{\rm obs} \approx 116\,\rm min$ on each spot in the sky. As the effective area and background acceptances are highly energy dependent (recall Figures 3.15 and 3.18), the effective exposure also strongly depends on the

---

[4] $\Delta_{\rm fov}$ is defined as the square root of the pixel area with size $\Delta^2_{\rm fov}$.

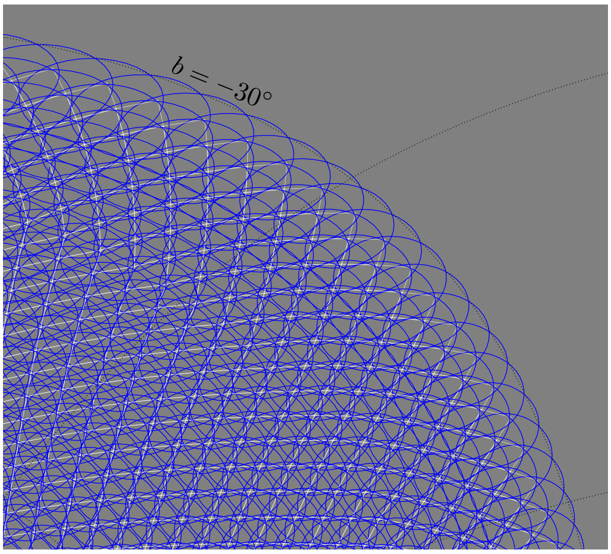

Figure 5.4.: Survey pointing strategy with grid spacing $\Delta_{\text{fov}} = 2°$. The radius of the blue circles is 3°, and denotes the CTA field of view size at around 100 GeV. The white diamond-shaped quadrangles indicate a HEALPix grid with $N_{\text{side}} = 32$, in which the pointing positions are centered. The whole image shows an area of approximately $30° \times 30°$.

chosen energy interval. For both the integrated background rate above $E \geq 100\,\text{GeV}$ and the differential effective area and background rate at $E = 500\,\text{GeV}$, an average exposure of $t \approx 120\,\text{min}$ is obtained, such that this observing time is considered as a fairly good description for a simplified survey assessment. The left and the right exposure maps in Figure 5.5 compare how the homogeneity of the exposure changes for different grid spacings. For $\Delta_{\text{fov}} = 2°$, a relative difference of $\Delta t/t \lesssim 3\%$ is obtained, whereas for a spacing of $\Delta_{\text{fov}} = 1°$, $\Delta t/t \lesssim 0.8\%$ can be achieved provided the Paranal `Prod3 0.5_avg` off-axis scaling. To achieve a $\Delta_{\text{fov}} = 1°$ spacing, $N_{\text{fov}} = 11{,}648$ single observations with $t_{\text{obs}} = 2.6\,\text{min}$ each have to be performed. Note that shorter observation times involve larger “exposure dead times”, where no data is taken in the time the telescopes move to their new pointing position. Assuming a delay as short as 10 s between each survey observation, a total time of 8 h during the whole survey is lost for $\Delta_{\text{fov}} = 2°$, and 32 h for the finer $\Delta_{\text{fov}} = 1°$. Accounting for the exposure variation and decrease at the edge of the survey field, the effective sky fraction covered by this survey setup is $f_{\text{sky}} \approx 23.4\%$ for $\Delta_{\text{fov}} = 1°$ and $f_{\text{sky}} \approx 22.7\%$ for $\Delta_{\text{fov}} = 2°$, rather independent of the considered energy interval. The obtained homogeneities are comparable to what has been found by Dubus et al. (2013).

For calculating a benchmark sensitivity of the survey setup chosen in this thesis, the sensitivity to a Crab-like point source for 2 h of on-axis observation is calculated using the `cssens` tool of the `ctools` software (Knödlseder et al., 2016). On the significance level of TS = 25 (see below

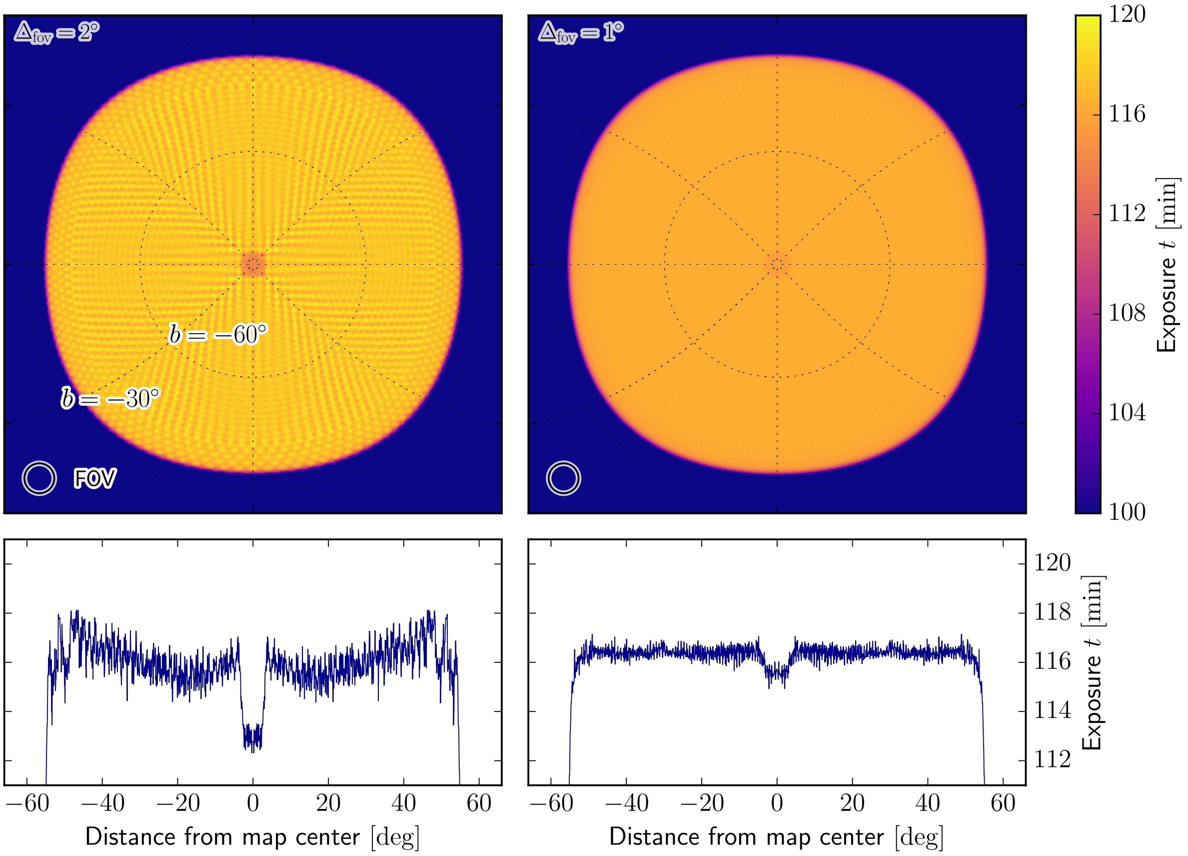

Figure 5.5.: Exposure map for the CTA extragalactic survey model adopted in this thesis. A total observation time of $T = 500\,\mathrm{h}$ sampling $f_{\rm sky} \approx 0.25$ around the Galactic south pole is assumed. The figure shows the on-axis equivalent exposure on each location in the sky, for the off-axis scaling of the Paranal `Prod3 0.5h_avg` background rate above 100 GeV (see Figure 3.15). The white circles mark the FOV with 3.5° radius at around 500 GeV. On the left, the survey is split into 2880 single pointings and an average spacing between the pointings of $\Delta_{\rm fov} = 2°$. On the right, the case of 11,648 pointings and $\Delta_{\rm fov} = 1°$ is shown. The hole in the center is due to the particular HEALPix scheme with its poles coinciding with the Galactic poles, and can be easily corrected for by an additional observation.

for the definition of TS) and without correcting for the trials in a blind search, a sensitivity to $2.5 \times 10^{-12}\,\mathrm{cm^{-2}\,s^{-1}}$ above 100 GeV (0.5% the flux of the Crab Nebula) is obtained. This is four times better than what had been estimated by Dubus et al. (2013), who projected that the CTA extragalactic survey may reach a sensitivity to fluxes of about $1 \times 10^{-11}\,\mathrm{cm^{-2}\,s^{-1}}$ above 100 GeV (2% the flux of the Crab Nebula) within $T = 370\,\mathrm{h}$. In the following, besides the benchmark observation time $t_{\rm obs} = 2\,\mathrm{h}$, also $t_{\rm obs} = 1\,\mathrm{h}$ is considered, as a somewhat more conservative choice, yielding a sensitivity to 0.7% the flux of the Crab Nebula.

5.2. The classical approach: Discovering the brightest subhalo

This section presents the sensitivity to the brightest dark clump to be detected in a CTA extragalactic survey. To reduce the computational costs of the analysis, a simplified approach is chosen: At first, the characteristics of the brightest clump in a CTA survey are assessed in Subsection 5.2.1, and the subsequent analysis is constrained to a trials-corrected sensitivity calculation of this object. In Subsection 5.2.2, the likelihood method and statistic used to draw the confidence level (C.L.) is presented. Finally, in Subsection 5.2.3, the sensitivity to the brightest DM subhalo is calculated using the benchmark average on-axis exposure of $t = 2\,\mathrm{h}$ ($1\,\mathrm{h}$) found in the previous section for the survey. In Subsection 5.2.4, a short comparison of the presented approach to dark halo searches with the *Fermi*-Large Area Telescope (LAT) is given.

5.2.1. Characterization of the γ-ray-brightest DM subhalo

A survey search for Galactic DM clumps presumes that their location and individual properties are not known in advance. Therefore, the expected γ-ray flux from the brightest subhalo can only be given as a statistical average. To assess the abundance of bright subhalos, the approach of Section 4.3 is repeated, but now specified for the setup of a CTA survey on 25% of the sky. Besides adopting the survey area, the effect of the instrumental angular resolution on the characteristics of the brightest detectable object is investigated.

For the survey area as defined in Figure 5.2 (with $f_{\mathrm{sky}} = 0.25$), the resulting subhalo flux source count distributions are displayed in Figure 5.6 for the models LOW and HIGH. The distributions are given for the different integration angles $\theta_{\mathrm{int}} = 0.05^\circ$ (angular resolution of CTA at $\gtrsim 1\,\mathrm{TeV}$), $\theta_{\mathrm{int}} = 0.1^\circ$ (angular resolution of CTA at $\lesssim 1\,\mathrm{TeV}$), and the full emission, $\theta_{\mathrm{int}} = \theta_{\mathrm{vir}}$. From the attenuation of the distributions at the high-J end when reducing θ_{int} follows that the brightest objects are also the most extended ones. In contrast to the full-sky analogue from Figure 4.4, the 68% credible interval (C.I.) bands of the source count distributions are shown in Figure 5.6 as shaded bands. These bands show how the numbers vary due to the random positions of the subhalos in the Galactic halo relative to the observer on Earth. Comparing the distributions of the models LOW and HIGH in Figure 5.6 with Figure 4.4 reveals that for the latter, the source count distributions shift to a factor ~ 4 smaller values on the horizontal J-factor (flux) axis. This is exactly what is predicted by Equation C.2 in the appendix, resulting from the fact that most of the brightest objects are now located in the unobserved part of the sky. Figure 5.6 additionally shows the subhalo distribution assumed by Brun et al. (2011), based on the Via Lactea II (VL II) subhalo catalog. They adopted the same fraction $f_{\mathrm{sky}} = 25\%$, however for a field centered at the position of the GC and excluding the Galactic plane. Their source

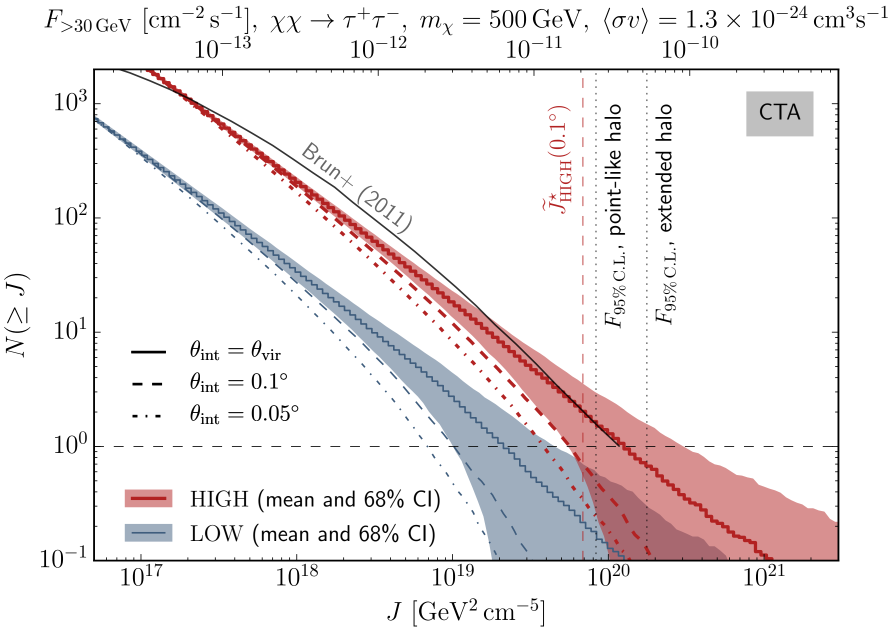

Figure 5.6.: Cumulative source count distribution of DM subhalos for the CTA setup. The upper $x-$axis shows the flux level for the DM particle model to which the CTA analysis of this section is most sensitive (adopting the subhalo model HIGH; see Figure 5.7). The annihilation cross-section is chosen so that CTA would observe one subhalo above the flux sensitivity threshold corresponding to the chosen DM annihilation spectrum. Increasing (decreasing) the annihilation cross-section would result in a shift of the upper $x-$axis and the vertical dashed lines to the left (right). Also, the result of Brun et al. (2011) is displayed, who used $\theta_{\mathrm{int}} \approx \theta_{\mathrm{vir}}$. Figure published in Hütten et al. (2016).

count flux distribution is based on the total extended emission of the subhalos, $\theta_{\mathrm{int}} = \theta_{\mathrm{vir}}$.[5] Comparing their distribution (black line in Figure 5.6) with the full subhalo emission of model HIGH (red-solid curve) reveals a good agreement between these models.[6] Brun et al. (2011) then calculate the sensitivity by concentrating the whole subhalo flux, $J(\theta_{\mathrm{vir}})$, into a point source. However, this assumption heavily overestimates the flux detectable with CTA, as a substantial part of the subhalos' emission in their outskirts is lost in the residual background noise. This is confirmed by the rigorous sensitivity calculation in the following subsections, which accounts for the interplay between the energy dependent angular resolution of CTA and the extension of the average brightest object. The vertical lines in Figure 5.6 anticipate this result for a specific DM particle model (upper x-axis): The right black-dotted line, indicating the flux sensitivity to the average brightest halo, is located at the position of the median brightest overall J-factor (scale on the lower x-axis).[7] A point-like object with the same energy spectrum would be detected at a

---

[5] They discard very extended objects with 90% of their total emission arising from an area larger than $\theta_{\mathrm{int}} = 1.5°$.

[6] Also, Brun et al. (2011) find a comparable 68% C.I. scattering of $N(\geq J)$, which is not included in Figure 5.6.

[7] Note that the J-factors of the median brightest subhalo are located at about $\widetilde{J}^\star \approx 1.4\, J_{\mathrm{lim}}$, where the source

Median properties of brightest subhalo within	*Fermi*-LAT scenario ($f_{\rm sky} = 82.6\%$)			CTA scenario ($f_{\rm sky} = 25\%$)		
	$\theta_{\rm int} = 0.1°$	$\theta_{\rm int} = 0.8°$	$\theta_{\rm int} = \theta_{\rm vir}$	$\theta_{\rm int} = 0.05°$	$\theta_{\rm int} = 0.1°$	$\theta_{\rm int} = \theta_{\rm vir}$
$\widetilde{D}^\star_{\rm obs}$ [kpc]	7^{+10}_{-5}	8^{+11}_{-6}	8^{+12}_{-6}	7^{+10}_{-5}	8^{+12}_{-6}	10^{+16}_{-8}
$\widetilde{R}^\star$ [kpc]	9^{+9}_{-3}	10^{+10}_{-3}	10^{+11}_{-3}	10^{+9}_{-2}	10^{+10}_{-3}	12^{+15}_{-4}
$\log_{10}(\widetilde{m}^\star_{\rm vir}/{\rm M}_\odot)$	$7.7^{+1.3}_{-1.5}$	$8.1^{+1.2}_{-1.6}$	$8.1^{+1.3}_{-1.5}$	$7.4^{+1.4}_{-1.4}$	$7.6^{+1.4}_{-1.5}$	$8.0^{+1.3}_{-1.6}$
$\widetilde{r}^\star_{\rm vir}$ [kpc]	$6.7^{+12}_{-4.6}$	$8.8^{+14}_{-6.1}$	$9.2^{+15}_{-6.3}$	$5.4^{+9.5}_{-3.5}$	$5.9^{+11}_{-4.0}$	$8.1^{+14}_{-5.8}$
$\widetilde{r}^\star_{\rm s}$ [kpc]	$0.13^{+0.42}_{-0.10}$	$0.19^{+0.55}_{-0.15}$	$0.21^{+0.62}_{-0.17}$	$0.12^{+0.36}_{-0.08}$	$0.14^{+0.43}_{-0.10}$	$0.22^{+0.69}_{-0.17}$
$\widetilde{c}^\star_{\rm vir}$	50^{+23}_{-16}	44^{+22}_{-15}	43^{+22}_{-15}	45^{+16}_{-14}	43^{+17}_{-14}	37^{+17}_{-13}
$\widetilde{\theta}^\star_{\rm vir}$ [deg]	45^{+16}_{-12}	48^{+15}_{-12}	49^{+14}_{-12}	37^{+16}_{-11}	38^{+15}_{-11}	39^{+15}_{-10}
$\widetilde{\theta}^\star_{\rm s}$ [deg]	$1.2^{+1.4}_{-0.6}$	$1.5^{+1.6}_{-0.8}$	$1.6^{+1.6}_{-0.8}$	$1.0^{+1.1}_{-0.5}$	$1.1^{+1.1}_{-0.5}$	$1.3^{+1.1}_{-0.6}$
$\widetilde{\theta}^\star_{\rm h}$ [deg]	$0.16^{+0.20}_{-0.08}$	$0.20^{+0.20}_{-0.10}$	$0.22^{+0.22}_{-0.11}$	$0.13^{+0.16}_{-0.05}$	$0.14^{+0.14}_{-0.07}$	$0.18^{+0.14}_{-0.08}$
$\log_{10}\left(\widetilde{J}^\star/{\rm GeV^2\,cm^{-5}}\right)$	$20.3^{+0.4}_{-0.3}$	$20.7^{+0.4}_{-0.3}$	$20.8^{+0.5}_{-0.4}$	$19.7^{+0.3}_{-0.3}$	$19.9^{+0.4}_{-0.3}$	$20.3^{+0.5}_{-0.4}$

Table 5.1.: Median properties of the brightest subhalo for the survey setups tailored to the *Fermi*-LAT (Subsection 5.2.4) and CTA instruments (this subsection), and for the subhalo model HIGH. The uncertainties denote the 68% C.I. around the median. For both instruments, the results are given for different angular resolutions. $D_{\rm obs}$ is the distance from the observer, R the distance from the GC, $m_{\rm vir}$ the subhalo mass; $r_{\rm vir}$ and $r_{\rm s}$ denote its virial and scale radius, $c_{\rm vir} = r_{\rm vir}/r_{\rm s}$, and $\theta_{\rm vir,\,s} = \arctan(r_{\rm vir,\,s}/D_{\rm obs})$. $\theta_{\rm h}$ is the radius enclosing half of the total emission, $J(\theta_{\rm h}) = 0.5\,J(\theta_{\rm vir})$. For reliable medians and C.I.s, the values are obtained from 10^4 simulations. The J-factors of the brightest object for the *Fermi*-LAT and CTA are also displayed in Figure 4.7. Table published in Hütten et al. (2016).

somewhat lower overall flux level (left black-dotted line). This line fairly matches the flux from the median brightest halo, when only the emission from the innermost $\theta_{\rm int} = 0.1°$ is considered (red-dashed line).

After having read off the J-factors of the average brightest halo in Figure 5.6, it is of further interest to pinpoint its average physical properties, i.e., its mass, angular extension, and distance from Earth. In particular, the average mass indicates whether this object is expected to be a dark subhalo, only detectable by a γ-ray survey, or constitutes a dSph object, which will be most likely detected by dedicated optical observations. To robustly determine the properties and the variance of the brightest object, 10^4 `CLUMPY` runs were performed in the CTA survey field. Table 5.1 (right) lists its median properties at the same integration angles as in Figure 5.6 for the model HIGH.[8] It is found that the average properties of the brightest subhalo depend on the

---

count distributions intersect $\overline{N}(\geq J) = 1$ (see discussion in Appendix B.7).

[8] The corresponding values for model LOW are postponed to Table C.1 in Appendix C.2.

integration angle: The subhalo with the largest total J-factor, $J(\theta_{\mathrm{vir}})$, may not be the brightest object in terms of the J-factor within some $\theta_{\mathrm{int}} < \theta_{\mathrm{vir}}$. Because θ_{int} serves as a proxy for the angular resolution of the instrument, it follows that different angular resolutions probe slightly different populations. Comparing the proxy values for CTA with the *Fermi*-LAT instrument in Table 5.1 suggests that the higher angular resolution of CTA selects a population of slightly lighter objects.

All subhalo source count distributions presented so far include the most massive DM subhalos, which could have triggered star formation and constitute the dSph galaxies of the Milky Way (MW). As motivated in the previous paragraph, including dSph objects into the estimation of the CTA survey sensitivity to dark clumps might bias the number of plausible optically dark subhalo candidates. This issue is studied by computing again the subhalo abundance, now discarding clumps heavier than $10^6\,\mathrm{M}_\odot$ or $10^7\,\mathrm{M}_\odot$ (According to table 4 in Hütten et al. (2016), all known dSph galaxies so far exhibit a median virial mass larger than $10^6\,\mathrm{M}_\odot$, while most dSph are likely to have masses even larger than $10^7\,\mathrm{M}_\odot$). It is found that when excluding all objects above $10^7\,\mathrm{M}_\odot$, the median J-factor within $\theta_{\mathrm{int}} = 0.05°$ of the brightest subhalo remains unaffected at the value $\log_{10}(\widetilde{J}^\star(0.05°)/\mathrm{GeV}^2\,\mathrm{cm}^{-5}) = 19.7^{+0.3}_{-0.2}$. In contrast, the full J-factor of the median brightest DM subhalo decreases by a factor ~ 2 compared to Table 5.1, giving a value of $\log_{10}(\widetilde{J}^\star(\theta_{\mathrm{vir}})/\mathrm{GeV}^2\,\mathrm{cm}^{-5}) = 20.0^{+0.4}_{-0.3}$. This results from now lighter, but more concentrated halos being selected as brightest objects by the mass cut. When rejecting all objects above $10^6\,\mathrm{M}_\odot$, however, $\log_{10}(\widetilde{J}^\star(0.05°)/\mathrm{GeV}^2\,\mathrm{cm}^{-5}) = 19.5^{+0.3}_{-0.2}$ and $\log_{10}(\widetilde{J}^\star(\theta_{\mathrm{vir}})/\mathrm{GeV}^2\,\mathrm{cm}^{-5}) = 19.8^{+0.4}_{-0.3}$ is obtained, and the median brightest dark subhalo has a factor 2 smaller J-factor even within the central $\theta_{\mathrm{int}} = 0.05°$. The conclusions for a survey search of dark halos are therefore only negligibly affected when excluding the heaviest objects from the statistical sample. In the following, the full source count distributions are retained without a mass cut and the values in Table 5.1 (right) are adopted to characterize the properties of the median brightest subhalo J-factor-profile in a CTA extragalactic survey.

From the 68% C.L. of the J-factors quoted in Table 5.1, it is visible that the J-factor variance of the brightest object is skewed towards high-J values, even stronger than a log-normal distribution. An expected analytical shape of the J-factor sample variance is derived in Appendix B.7, which agrees well with the MC samples on which the values in Table 5.1 are based.

5.2.2. Likelihood-based analysis method

The CTA sensitivity to the brightest subhalo in the survey field is calculated for a template of the median brightest object as described in Table 5.1. Concerning the ambiguity of the brightest object with respect to the integration angle, the J-factor profile of the object with the largest J-

factor within $\theta_{\mathrm{int}} = 0.05^\circ$ is chosen. A rigorous treatment would imply a coupling of the spatial halo shape with the DM annihilation γ-ray spectrum and the energy-dependent instrumental resolution. However, the difference compared to a fixed spatial template is expected to be marginal. For example, the J-factor profile brightest within $\theta_{\mathrm{int}} = 0.05^\circ$ on $f_{\mathrm{sky}} = 25\%$ has a J-factor of $\log_{10}\left(\widetilde{J}^\star(\theta_{\mathrm{int}} = 0.1^\circ)/\mathrm{GeV}^2\,\mathrm{cm}^{-5}\right) = 19.9^{+0.4}_{-0.3}$ and it is $\log_{10}\left(\widetilde{J}^\star(\theta_{\mathrm{int}} = \theta_{\mathrm{vir}})/\mathrm{GeV}^2\,\mathrm{cm}^{-5}\right) = 20.2^{+0.5}_{-0.4}$, only slightly different than for the halos brightest within $\theta_{\mathrm{int}} = 0.1^\circ$ and $\theta_{\mathrm{int}} = \theta_{\mathrm{vir}}$.

For the sensitivity calculation, two different analysis methods can be applied: For instance, a classical point-source analysis can be done, where a signal region tailored to the angular resolution of the instrument is defined, and the sensitivity is calculated according to Equation 17 of Li and Ma (1983). In Appendix C.3, it is shown that the J-factor profile of the subhalos is sufficiently steep such that their flux falling within the angular resolution of the instrument can be reasonably approximated as point-like for background-dominated γ-ray observatories. In this case, only the subhalo flux from within the defined signal region is measured. Alternatively, a likelihood-based method can be used, where a likelihood is calculated for a model of the full spatial extent of the halo and the expected energy spectrum. By not relying on the point-source approximation, it is expected that the latter method yields more robust results, and an unbinned likelihood analysis is pursued in the following.

Likelihood function: For the calculation of the CTA flux sensitivity to the brightest dark subhalo, the open-source CTA analysis software `ctools`[9], resting upon the `gammalib` library[10] is used (Knödlseder et al., 2016). Events are simulated with the `cssens` tool for the chosen CTA instrumental setup, and the `ctlike` optimizer is used to calculate the maximum log-likelihood ratio. For a hypothesis $\mathcal{M}$ to test in a (mock) dataset, the likelihood ratio λ is given by

$$\lambda = \frac{\max \mathscr{L}(\mathcal{M}_{\mathrm{bkg}}(\boldsymbol{\Theta}_{\mathrm{bkg}}) \,|\, \boldsymbol{X})}{\max \mathscr{L}(\mathcal{M}_{\mathrm{sig}}(\boldsymbol{\Theta}_{\mathrm{sig}}) + \mathcal{M}_{\mathrm{bkg}}(\boldsymbol{\Theta}_{\mathrm{bkg}}) \,|\, \boldsymbol{X})} = \frac{\mathscr{L}(\mathcal{M}_{\mathrm{bkg}}(\widehat{\widehat{\boldsymbol{\Theta}}}_{\mathrm{bkg}}) \,|\, \boldsymbol{X})}{\mathscr{L}(\mathcal{M}_{\mathrm{sig}}(\widehat{\boldsymbol{\Theta}}_{\mathrm{sig}}) + \mathcal{M}_{\mathrm{bkg}}(\widehat{\boldsymbol{\Theta}}_{\mathrm{bkg}}) \,|\, \boldsymbol{X})}. \tag{5.4}$$

where $\boldsymbol{X} = (N_{\mathrm{obs}},\, E_{\mathrm{R},\,1\ldots N_{\mathrm{obs}}}, \vec{k}_{\mathrm{R},\,1\ldots N_{\mathrm{obs}}})$ represents the mock data,[11] the vector $\boldsymbol{\Theta}$ the adjustable parameters in the models under which the likelihood is maximized, and $\widehat{\boldsymbol{\Theta}}$ the corresponding estimators at the maximum likelihood. For a specific model $\mathcal{M}$ provided to `ctlike`, the maximum likelihood of the background hypothesis is obtained for the parameters $\widehat{\widehat{\boldsymbol{\Theta}}}_{\mathrm{bkg}}$ under the constraint $\mathcal{M}_{\mathrm{sig}} = 0$. The full unbinned likelihood function in Equation 5.4 is given by

$$\mathscr{L}(\mathcal{M} \,|\, N_{\mathrm{obs}},\, E_{\mathrm{R},\,1\ldots N_{\mathrm{obs}}}, \vec{k}_{\mathrm{R},\,1\ldots N_{\mathrm{obs}}}) = p(N_{\mathrm{obs}} \,|\, N_{\mathrm{pred}}(\mathcal{M})) \times \prod_{1}^{N_{\mathrm{obs}}} p(E_{\mathrm{R,\,i}},\, \vec{k}_{\mathrm{R,\,i}} \,|\, \mathcal{M}). \tag{5.5}$$

---

[9] `http://cta.irap.omp.eu/ctools/`, version 1.1.0 has been customized for the analyses in this thesis.

[10] `http://cta.irap.omp.eu/gammalib/`, with version 1.1.0 used for this thesis.

[11] N, E, and $\vec{k}$ denote the number of photons, their energy, and the angular direction of their origin.

In Equation 5.5, N_{obs} denotes the total number of (simulated mock) events, and $E_{\mathrm{R,\,i}}$ and $\vec{k}_{\mathrm{R,\,i}}$ are the reconstructed energy and angular direction of each event. For a Poisson distributed number of total events,

$$p(N_{\mathrm{obs}}\,|\,N_{\mathrm{pred}}) = \frac{{N_{\mathrm{pred}}}^{N_{\mathrm{obs}}}\, e^{-N_{\mathrm{pred}}}}{N_{\mathrm{obs}}!}. \tag{5.6}$$

The total number of predicted events, N_{pred}, within the considered range of 30 GeV and 200 TeV then is given by

$$N_{\mathrm{pred}}(\mathcal{M}) = t_{\mathrm{obs}} \int\limits_{E_{\mathrm{min}}=30\ \mathrm{GeV}}^{E_{\mathrm{max}}=200\ \mathrm{TeV}} \int\limits_{\Delta\Omega_{\mathrm{obs}}} p(E_{\mathrm{R}},\,\vec{k}_{\mathrm{R}}\,|\,\mathcal{M})\;\mathrm{d}E_{\mathrm{R}}\,\mathrm{d}\Omega_{\mathrm{obs}}, \tag{5.7}$$

where t_{obs} denotes the duration of the observation.[12] An instrumental dead time of 5% where no data is recorded during read-out is applied, and the actual event simulation and analysis corresponds to a livetime of $t_{\mathrm{live}} = 0.95\,t_{\mathrm{obs}}$. The probability $p(E_{\mathrm{R}},\,\vec{k}_{\mathrm{R}}\,|\,\mathcal{M})$ to observe an event with energy E_{R} and from the direction $\vec{k}_{\mathrm{R}}$ is determined by the differential intensity $\mathrm{d}\Phi_{\mathcal{M}}/(\mathrm{d}E\,\mathrm{d}\Omega)$ predicted by the model $\mathcal{M}$, after integrating over the on-axis effective area, $A_{\mathrm{eff}}(E) = A_{\mathrm{eff}}(E,\,\vartheta = 0°)$, and convolving with the energy and angular instrument response,

$$p(E_{\mathrm{R}},\,\vec{k}_{\mathrm{R}}\,|\,\mathcal{M}) = \int\limits_{E,\,\Omega,\,A_{\mathrm{eff}}(E)} p(E_{\mathrm{R}}\,|\,E,\,\vec{k}) \times p(\vec{k}_{\mathrm{R}}\,|\,E,\,\vec{k}) \times \frac{\mathrm{d}\Phi_{\mathcal{M}}}{\mathrm{d}E\,\mathrm{d}\Omega}(E,\,\vec{k})\;\;\mathrm{d}A\,\mathrm{d}E\,\mathrm{d}\Omega, \tag{5.8}$$

with E and $\vec{k}$ the true energy and direction of the event.[13] For computation reasons, the energy dispersion of the events is ignored and it is set $p(E_{\mathrm{R}}\,|\,E,\,\vec{k}) \equiv \delta(E - E_{\mathrm{R}})$. The angular resolution, $p(\vec{k}_{\mathrm{R}}\,|\,E,\,\vec{k})$, is modeled by a two-dimensional Gaussian with energy dependent width $\sigma(E)$.

For the signal model $\mathcal{M}_{\mathrm{sig}}$, $\mathrm{d}\Phi_{\mathcal{M}_{\mathrm{sig}}}/(\mathrm{d}E\,\mathrm{d}\Omega)$ is the γ-ray intensity from DM annihilation given by Equation 2.29. For the background model $\mathcal{M}_{\mathrm{bkg}}$, the intensity $\mathrm{d}\Phi_{\mathcal{M}_{\mathrm{bkg}}}/(\mathrm{d}E\,\mathrm{d}\Omega)$ is given by the residual cosmic ray background after cuts, for which the background rate model shown in Figure 3.17 is used, so that

$$p(E_{\mathrm{R}},\,\vec{k}_{\mathrm{R}}\,|\,\mathcal{M}_{\mathrm{bkg}}) = \frac{\mathrm{d}N_{\mathrm{bkg}}}{\mathrm{d}E_{\mathrm{R}}\,\mathrm{d}\Omega_{\mathrm{obs}}\,\mathrm{d}t} = f(E_{\mathrm{R}},\,\vec{k}_{\mathrm{R}}). \tag{5.9}$$

For the likelihood optimization, the normalization of the background rate is allowed to vary. The

---

[12] The likelihood calculation is performed independently of the event arrival times, as both the DM annihilation flux and cosmic ray background are constant in time.

[13] In general, the effective area additionally depends on the time-dependent zenith and azimuthal coordinates of the observation, i.e. $A_{\mathrm{eff}} = A_{\mathrm{eff}}(E,\,\vec{k},\,t)$. However, all calculations are done with the constant CTA benchmark instrumental characteristics introduced in Chapter 3.

signal model $\mathcal{M}_{\text{sig}}$ for Galactic DM annihilation is, according to Equation 2.29, separable into a spatial part, given by the fixed template J-factor map of the brightest halo, and a spectral part being a function of the particle mass m_χ and the annihilation cross-section $\langle \sigma v \rangle$. For scanning the weakly interacting massive particle (WIMP) parameter space, the γ-ray spectra of 24 DM particle masses in the range $50\,\text{GeV} \leq m_\chi \leq 100\,\text{TeV}$ for each of the two annihilation channels, $\chi\chi \to b\bar{b}$ and $\chi\chi \to \tau^+\tau^-$ are considered. For each m_χ and annihilation channel, the γ-ray spectrum $\mathrm{d}N_\gamma^f/\mathrm{d}E$ is computed from the tables provided by Cirelli et al. (2011). For each spectral model, the flux level is the only free parameter, such that $\mathbf{\Theta}_{\text{sig}} = \langle \sigma v \rangle$.

Pre- and post-trial sensitivity: The results of the sensitivity analysis are given at the 95% C.L., after a trials correction is applied to account for the unknown position of the brightest halo, which can be located anywhere in the survey field (Biller, 1996; Gross and Vitells, 2010). The correction is calculated via a simplified approach. The number of independent trials to search for a point source is assumed to be identical to the division of the survey area by the angular resolution of the instrument. For the resolution, a constant value $\theta_{68\%} = 0.05°$ is taken, matching the 68% containment radius of the CTA at $E \gtrsim 1\,\text{TeV}$. This resolution corresponds to a beam area of $\Omega_B = 2.4 \times 10^{-6}\,\text{sr}$, and approximately $N_{\text{trials}} = \pi/(2.4 \times 10^{-6}) = 1.3 \times 10^6$ independent trials are obtained on $f_{\text{sky}} = 0.25\%$. The confidence level $1 - p_{\text{post}}$ compatible with a background fluctuation in the survey is translated to a pre-trial confidence level, $1 - p_{\text{pre}}$, via (Biller, 1996)

$$p_{\text{pre}} = 1 - (1 - p_{\text{post}})^{1/N_{\text{trials}}}. \tag{5.10}$$

For a $1 - p_{\text{post}} = 95\%$ confidence level, it is obtained $p_{\text{pre}} = 3.9 \times 10^{-8}$. This p-value can be expressed as a Gaussian one-sided confidence level of 5.4 standard deviations. The described approach neglects the different number of trials at different CTA resolutions. Additionally, approximating the number of trials by the size of the angular resolution results in a rather optimistic result concerning the number of potential false detections. Scanning the the survey area on a finer grid or the angular coordinates being free variables in a Likelihood fit might yield a better sensitivity to faint signals, but also increases the chance of statistical type I errors. This issue is particularly relevant when comparing the DM sensitivities of different methods in Section 5.3. For the time-being, Equation 5.10 for a constant number of $N_{\text{trials}} \sim 10^6$ is considered sufficiently accurate and gives a reliable estimate for the magnitude of the required correction for a quarter-sky survey with CTA.

Distribution of the test statistic (TS): The logarithm of the likelihood ratio (5.4),

$$\mathrm{TS} = -2\log\lambda\,, \tag{5.11}$$

is used as the test statistic to reject the signal hypothesis $\mathcal{M}_{\mathrm{bkg}} + \mathcal{M}_{\mathrm{sig}}$ at the confidence level $1 - p_{\mathrm{pre}}$. With the flux level scaling with the cross section $\langle\sigma v\rangle$ being the only free parameter in the signal model, the hypothesis $\mathcal{M}_{\mathrm{bkg}} + \mathcal{M}_{\mathrm{sig}}$ has one more degree of freedom than the hypothesis of only background events. In the limit of a large event number and restricting $\langle\sigma v\rangle \geq 0$, the expected background events test statistic is (Cowan et al., 2011; Conrad, 2015)

$$p(\mathrm{TS}) = \frac{1}{2}\,\delta(\mathrm{TS}) + \frac{1}{2}\,\chi^2_{k=1}(\mathrm{TS})\,, \tag{5.12}$$

known as Wilks' theorem (Wilks, 1938; Wald, 1943). The distribution (5.12) has been tested for the above analysis with 10^5 simulations of background-only event sets. It has been found that the distribution depends on the spectral shape of the assumed signal model, $\mathcal{M}_{\mathrm{sig}}$. Therefore, the test statistic for the sensitivity analysis is directly based on the result from these MC simulations, rather than Equation 5.12. Table 5.2 compares the TS values from the simulations (left and middle columns) with the expectation from Equation 5.12 (right columns, constant values independent of the DM spectrum). In order to obtain reliable TS values from the simulations, the $N_{\mathrm{sim}} = 10^5$ samples, distributed over 24 spectra, are merged into five groups, and the $\mathrm{TS}(p_{\mathrm{pre}} = 0.05)$ is calculated separately for each group. To obtain $\mathrm{TS}(p_{\mathrm{pre}} = 3.9 \times 10^{-8})$, an exponential tail is fitted to the distributions, and the TS value is computed from this extrapolation. Figure C.7 in Appendix C.8 confirms that the obtained TS values approximately correspond to the expected $\chi^2_{k=1}$ distribution according to Equation 5.12 (black line), but deviate for very low and high DM masses. The values listed in Table 5.2 are retained for all analyses in this section, which rely on different instrument responses.[14]

Instrument models and cross-checks: The CTA sensitivity to Galactic DM subhalos is finally computed for different benchmark performances of the CTA extragalactic survey. The performance of the following on-axis instrumental models and cuts is compared:

- Southern site `Prod2 0.5h` (optimized for 30 min. observations)
- Paranal site, `Prod3 0.5h_avg` (optimized for 30 min. observations)
- Paranal site, `Prod3 5h_avg` (optimized for 5 h observations)

---

[14] The MC values listed in Table 5.2 have been obtained using the `Prod2 South_0.5h` IRFs. Running $N_{\mathrm{sim}} = 10^5$ times the `cssens` tool has been computationally too expensive to repeat the TS calculation for all considered instrumental cuts. Each `cssens` calculation consists of $\sim$ 20 iterations, each time simulating $\sim 5 \times 10^5$ background events, and subsequently running the likelihood fit. Nevertheless, a crude check has been done, indicating that different IRFs give distributions less scattered than for different spectral models.

	$p_{\rm pre} = 0.05$ $(1.6\,\sigma)$			$p_{\rm pre} = 3.9 \times 10^{-8}$ $(5.4\,\sigma)$		
m_χ range [GeV]	$\chi\chi \to b\bar{b}$	$\chi\chi \to \tau^+\tau^-$	$0.5\,\chi^2_{k=1}$	$\chi\chi \to b\bar{b}$	$\chi\chi \to \tau^+\tau^-$	$0.5\,\chi^2_{k=1}$
$50 - 100$	1.5	1.5	2.71	24	28	29.1
$150 - 500$	2.5	2.9	2.71	31	32	29.1
$600 - 1000$	3.4	2.5	2.71	35	30	29.1
$1500 - 7500$	3.0	1.9	2.71	34	28	29.1
$10^4 - 10^5$	2.0	1.1	2.71	29	26	29.1

Table 5.2.: Test statistic values used for the CTA sensitivity analysis in this section. The values given in the left and middle columns ($\chi\chi \to XX$) are obtained from MC calculations, the right columns are expected from the distribution (5.12). The pre-trial p-value from the left block results in a post-trial p-value of 0.05 after accounting for $N_{\rm trials} = 1.3 \times 10^6$ trials. Table published in Hütten et al. (2016).

- Paranal site under construction, `Prod3 5h_avg` (optimized for 5 h observations)
- La Palma site, `Prod3 0.5h_avg` (optimized for 30 min. observations)

All these instrument responses have been optimized for the observation of point-like halos, whereas the benchmark DM subhalo studied in this analysis is extended. Additionally, the instrument response functions (IRF) have been calculated for an analysis according to Li and Ma (1983), obeying the requirements described in Section 3.2. This setup is not exactly reproduced in this analysis, where a likelihood analysis is done and a different significance level is required (95% C.L.). Still, point-source IRFs can be safely used for analyzing the highly concentrated DM template halo. Table 5.1 shows that the brightest subhalos possess a half-emission radius of $\theta_{\rm h} = 0.13°$, only slightly above the CTA angular resolution. The inconsistency between the IRF generation and the applied analysis is ignored given the fact that the whole CTA instrumental models rely on the projection of a particular observational condition.

To strengthen the reliability of the analysis setup, the method has been cross-checked against other CTA projections for indirect DM detection in the literature. The sensitivity to the Sculptor dSph galaxy has been calculated with the `Prod2 South` IRFs, and a result consistent with Carr et al. (2015) is obtained. This guarantees that the following results can be compared to the CTA prospects towards other indirect DM targets.

5.2.3. Results: CTA sensitivity to resolve the γ-ray-brightest DM subhalo

Figure 5.7 presents the projected sensitivity of CTA to the WIMP DM annihilation cross-section by searching for Galactic dark subhalos in the planned extragalactic survey. It shows the results based on the on-axis `Prod2 South_0.5` IRFs, and $t_{\rm obs} = 1$ h (a survey sensitivity of 7 mCrab):

- In the left panel, the sensitivity of CTA is given to detect γ-rays from DM annihilation in the γ-ray-brightest DM subhalo for an annihilation cross section $\langle\sigma v\rangle$. The sensitivity

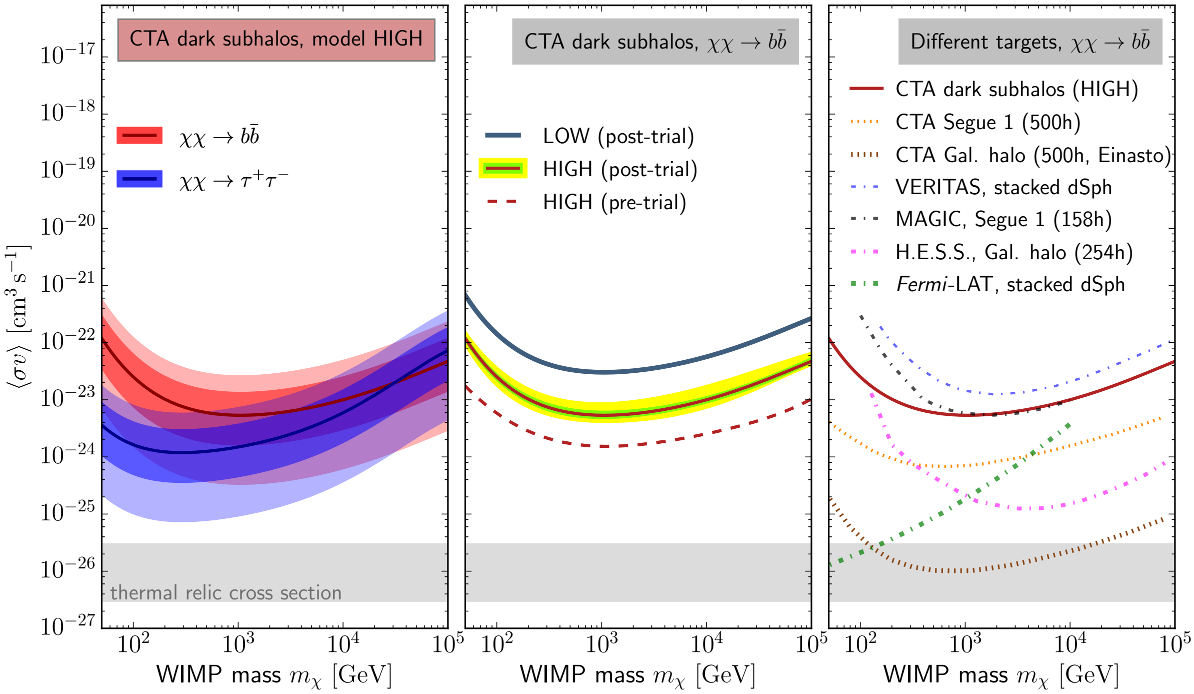

Figure 5.7.: Sensitivity of the CTA extragalactic survey to find the brightest Galactic subhalo in the survey field (I): Baseline calculation for `Prod2 South_0.5h` and $t_{\mathrm{obs}} = 1\,\mathrm{h}$ (7 mCrab survey sensitivity). All sensitivities are given at the 95% C.L.. *Left:* median (solid lines) and 68% (95%) C.I. J-factor (model HIGH) uncertainty around the median (colored areas) for annihilation into $b\bar{b}$ and $\tau^+\tau^-$. *Center:* comparison of LOW, HIGH (pre- & post-trial), also showing the 68% (95%) C.I. band from the background fluctuation. *Right:* Comparison of this analysis to the CTA sensitivity for other targets (Segue I & the GC from Carr et al., 2015) and to the limits from running experiments (Very Energetic Radiation Imaging Telescope Array System (VERITAS): Staszak (2015), Major Atmospheric Gamma Imaging Cherenkov Telescopes (MAGIC): Aleksić et al. (2014), High Energy Stereoscopic System (H.E.S.S.): Lefranc and Moulin (2015), *Fermi*-LAT: Ackermann et al. (2015e)). Figure adapted from Hütten et al. (2016).

is shown for annihilations taking place into pure $\chi\chi \to b\bar{b}$ and $\chi\chi \to \tau^+\tau^-$ channels. These two channels represent the cases of a rather soft and hard annihilation spectrum respectively, and mixing channels would result into a sensitivity in between these benchmark spectra. The solid lines indicate the sensitivity to the J-factor shape of the median brightest template halo, while the shaded bands give the 68% (95%) statistical uncertainty caused by the J-factor variance of the brightest object. The J-factor variance quoted in Table 5.1 propagates into the same variation in flux and sensitivity to $\langle\sigma v\rangle$, and it can be seen that this scatter is as large as one order of magnitude within the 68% C.I., and two orders of magnitude within the 95% C.I.. Because of this large uncertainty, and because the sample variance is skewed to low $\langle\sigma v\rangle$ even on a logarithmic scale, relatively small annihilation cross-sections are reached within the 95% C.I..

- In the central panel, the uncertainty of the DM density modeling of the Milky Way is shown. The two models LOW and HIGH have been selected as a conservative and optimistic case of DM subclustering in the MW respectively. The J-factors from the median brightest object in these models differ by one order of magnitude (recall Figure 5.6), which results in an equivalent difference in sensitivity. To show the impact of the trials correction for a survey search, the red-dashed line shows the sensitivity at the $1 - p_{\mathrm{post}} \equiv 1 - p_{\mathrm{pre}}$ confidence level (recall page 123). For the model HIGH, additionally the 68% (95%) C.I. bands resulting from the fluctuation of the residual cosmic ray background are shown. Comparing this fluctuation with the left panel, it can be seen that the J-factor variance by far dominates the overall uncertainty of the sensitivity.
- In the right panel, the sensitivity of a CTA search for dark halos is put into context. It is obvious that the presented projection for such an analysis of the CTA extragalactic survey is less sensitive to detect or constrain the properties of DM than different analyses with the same instrument. Observations of the Galactic halo with CTA represents the most promising findings for DM searches (brown-dashed line), and pointed observations towards known MW satellite galaxies may as well outweigh a blind search for dark subhalos (orange-dashed line). However, these competing strategies rely as well on certain assumptions on observing time and models of the DM distribution, and therefore also suffer from systematic errors which are not shown here. Especially, the DM content of the Segue I dSph, for which limits/sensitivities on $\langle\sigma v\rangle$ are derived in the figure, is very debated in the literature (Bonnivard et al., 2016; Domínguez et al., 2016). Lastly, limits already obtained from indirect searches for DM annihilation are shown for comparison (dot-dashed lines). This suggests that measurements by the *Fermi*-LAT and H.E.S.S. experiments already have by far excluded the parameter space reachable for a dark halo search with CTA.

Figure 5.8 compares the performance of the different CTA sites. For the southern CTA site, little changed between the generic `Prod2` simulations and the final Paranal site layout, according to the `Prod3` performance calculation. The sensitivity of the northern array is worse at higher energies and DM masses due to the missing small size telescopes (SSTs) at the La Palma site. As a sanity cross-check of the likelihood analysis, the DM sensitivities – "integrated" over the DM annihilation spectra – in Figure 5.8 (left) are compared to the differential flux sensitivities, which characterize the set of optimized IRFs (Figure 5.8, right). These differential sensitivities rely on the method from Li and Ma (1983), based on which the IRFs are optimized. From this coarse comparison it is concluded that IRFs optimized for an analysis after Li and Ma (1983) give reliable results also in combination with a likelihood analysis. In Figure 5.8, the template

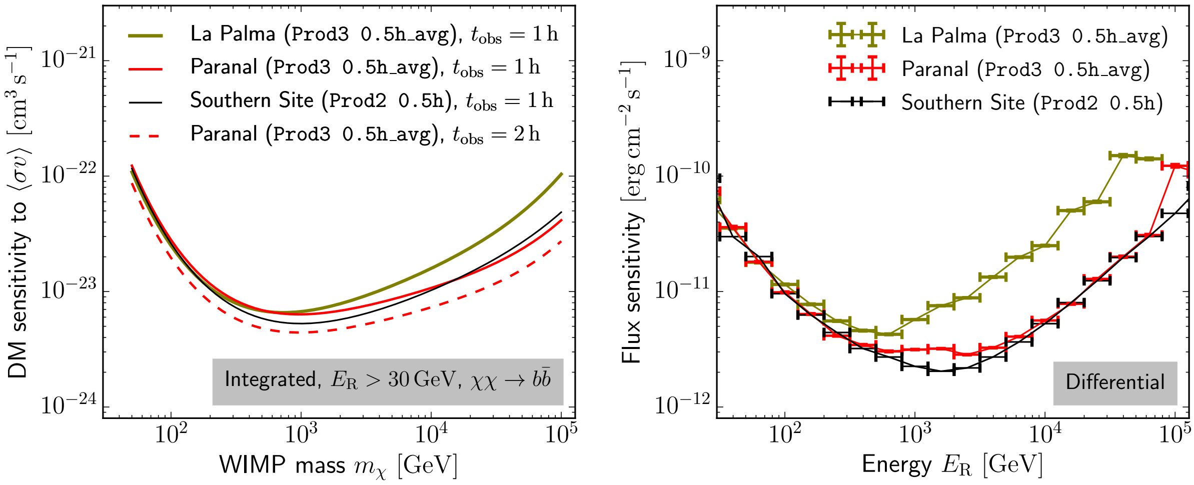

Figure 5.8.: Sensitivity of the CTA extragalactic survey to find the brightest Galactic subhalo in the survey field (II): Comparison of different CTA sites, and to a survey sensitivity of 5 mCrab. *Left:* Sensitivities at the 95% C.L. for the $\chi\chi \to b\bar{b}$ annihilation channel. The black curve describes the `Prod2 South_0.5h` performance, and corresponds to the baseline sensitivity shown in Figure 5.7. This is compared to the more accurate `Prod3` simulations for the final layouts at the Paranal (red) and La Palma (dark yellow) sites. The red-dashed line shows the sensitivity for the Paranal site and a survey sensitivity of 5 mCrab ($t_{\rm obs} = 2\,\rm h$). This corresponds to the sensitivity compared to the APS calculation in Section 5.3. *Right:* Differential flux sensitivities for the IRFs used for the sensitivity calculations.

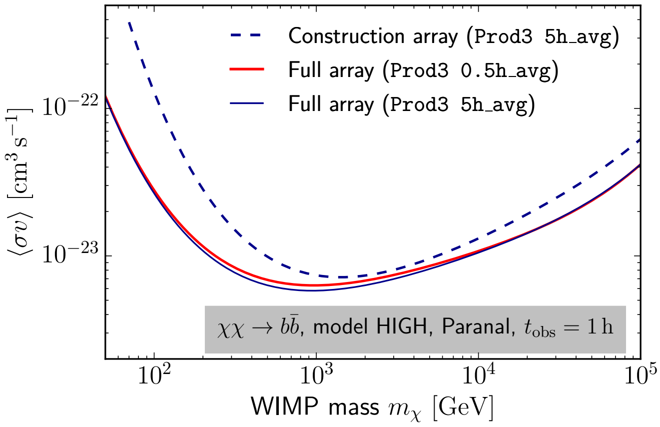

Figure 5.9.: Sensitivity of the CTA extragalactic survey to find the brightest Galactic subhalo in the survey field (III): Comparison of different IRF optimizations, and to an array under construction for the Paranal site. All sensitivities are given at the 95% C.L., for the $\chi\chi \to b\bar{b}$ annihilation channel, and a survey sensitivity of 7 mCrab. The blue-solid curve shows the difference in sensitivity when using the `5h_avg` cuts instead of the cuts optimized for 30 min of observation. The blue-dashed line presents the sensitivity for an incomplete array under construction (see Figure 3.14).

halo observation over $t = 2\,\mathrm{h}$ is also studied, which corresponds to a sensitivity to 0.5% of the flux of a Crab-like spectrum and which is suggested by the survey performance study in Subsection 5.1.2. This sensitivity will be chosen as benchmark sensitivity to be compared to the search for DM annihilation in the diffuse γ-ray background presented in the following section.

Figure 5.9 finally compares the performance of different cuts and to an incomplete southern "construction array" (see Figure 3.14 in Chapter 3). Only a marginal difference in sensitivity is obtained for the different optimization cuts `Prod3 0.5h_avg` and `Prod3 5h_avg` (both applied to the same observation over $t_{\mathrm{obs}} = 1\,\mathrm{h}$). This result further supports that the presented conclusions about the CTA subhalo sensitivities are rather insensitive to the optimization cuts. For the example of an incomplete array under construction, a somewhat worse performance is obtained. In particular at the lowest energies, a significant performance loss is caused by the missing large size telescopes (LSTs) in this example of an incomplete array.

At the end of this section, the above findings shall be compared to the results of Brun et al. (2011), who were the first to assess the CTA sensitivity to Galactic dark subhalos. Opposite to this analysis, they found a significantly more optimistic sensitivity towards dark halos, claiming that CTA might be able to probe DM annihilation below the thermal relic cross section from these objects. As discussed in Subsection 5.2.1, they based their analysis on a similar J-factor distribution of Galactic DM subhalos as obtained for the model HIGH of this analysis. Therefore, differences must be found in the analysis itself and in the assumptions about the performance of the CTA instrument. Firstly, this thesis presents sensitivities at the 95% C.L., whereas Brun et al. (2011) quote their sensitivity on the 90% C.L.. Choosing the 90% C.L., the pre-trial sensitivity of this analysis (red-dashed line in Figure 5.7) is lowered by a factor two, while the post-trial sensitivity is not affected; Brun et al. (2011) did not consider a post-trial correction. As shown in Figure 5.7, accounting for the trials penalty results in a factor 5 worsening of the sensitivity (factor ~ 10 when correcting for a 90% pre-trial C.L.). Secondly, Brun et al. (2011) used a simplified projection of the CTA performance. They extrapolated the H.E.S.S. instrumental response to a factor 10 larger effective area and a factor 2 better background rejection. However, this neglects that the CTA improvement compared to current instruments is energy-dependent. According to the `Prod2/Prod3` simulations, the largest improvement in differential sensitivity is reached at energies above $\sim 1\,\mathrm{TeV}$. Therefore, for annihilation spectra peaking at sub-TeV energies, a factor 10 extrapolation of the H.E.S.S. performance overestimates the projected CTA performance. Thirdly, it was mentioned in Subsection 5.2.1 that Brun et al. (2011) based their analysis on point-like subhalos, with their total emission, $J(\theta_{\mathrm{vir}})$, enclosed within the instrumental resolution. As shown in Figure 5.6, this overestimates the flux of the brightest subhalo by another factor ~ 2. Finding a factor ~ 100 worse sensitivity towards Galactic subhalos in this analysis provides a significant update of the projected CTA DM performances.

5.2.4. Comparison to dark halo searches with the *Fermi*-LAT

The *Fermi*-LAT is the natural all-sky γ-ray survey instrument, and the prospects for detecting subhalos with the *Fermi*-LAT have been investigated in many studies, e.g., by Stoehr et al. (2003); Kuhlen et al. (2008, 2009); Springel et al. (2008b); Pieri et al. (2008, 2011); Zechlin and Horns (2012); Zechlin et al. (2012) and Berlin and Hooper (2014). In this subsection, the subhalo modeling approach from Chapter 4 is compared to the recently published results of Bertoni et al. (2015) and Schoonenberg et al. (2016), who both based their DM modeling on the VL II subhalo catalog. By this analogous treatment of the *Fermi*-LAT, some differences between a search for subhalos and exploring the CTA extragalactic survey are highlighted.

Analogously to Subsection 5.2.1 for the CTA case, the subhalo source count distribution is built for a setup tailored to the *Fermi*-LAT experiment. As done in Schoonenberg et al. (2016), only the subhalo population outside the Galactic plane at $|b| > 10°$ is considered. The Galactic plane mask is shown in Figure 5.2 as a gray shaded band. For characterizing the *Fermi*-LAT angular resolution, the J-factor integration angle is limited to $\theta_{\rm int} = 0.8°$ (corresponding to *Fermi*-LAT's 68% containment radius at 1 GeV), also adopting the choice made by Schoonenberg et al. (2016).

Figure 5.10 shows the cumulative source count distributions for this setup in the same manner as has been done for CTA in Figure 5.6, comparing the subhalo models LOW (pale blue) and HIGH (red). The lower x-axis again expresses the subhalo brightness in terms of the particle-physics independent J-factor, while the upper x-axis gives the integrated energy flux distribution above 1 GeV for a specific DM particle model ($m_\chi = 100\,\mathrm{GeV}$, thermal annihilation cross-section, and pure annihilation into bottom quarks). The findings of Schoonenberg et al. (2016, black-solid line)[15] and Bertoni et al. (2015, black-dotted line) are shown together with these distributions. While the results from Schoonenberg et al. (2016) can be compared without restrictions to LOW and HIGH, Bertoni et al. (2015) consider only subhalos at $|b| > 20°$, meaning that moving to a $|b| > 10°$ field, their dotted line should be even higher than that shown in Figure 5.10.[16] For low J values, the Schoonenberg et al. (2016) result is encompassed by the HIGH and LOW assumptions. For the largest J-factors, the HIGH model is consistent with Schoonenberg et al. (2016) within uncertainties.[17] In contrast, the distribution from Bertoni et al. (2015) is in slight tension with both the subhalo modeling of this thesis and Schoonenberg et al. (2016).

---

[15] For this purpose, their distributions of point-like and extended halos have been added, which they treat differently by using a simplified calculation of the J-factors. Such an artificial distinction is not made by performing the full line-of-sight integration of all objects in `CLUMPY`.

[16] Additionally, Bertoni et al. (2015) did not specify a restricted integration angle, and the comparison is only valid provided that their calculation of the DM spectra is consistent with Cirelli et al. (2011).

[17] Like Brun et al. (2011) for the CTA case, the 68% C.I. sample variance of $N(\geq J)$ found by Schoonenberg et al. (2016) based on the Via Lactea II subhalo catalog (Diemand et al., 2008) is comparable to the one found with `CLUMPY`, and is not shown in Figure 5.10.

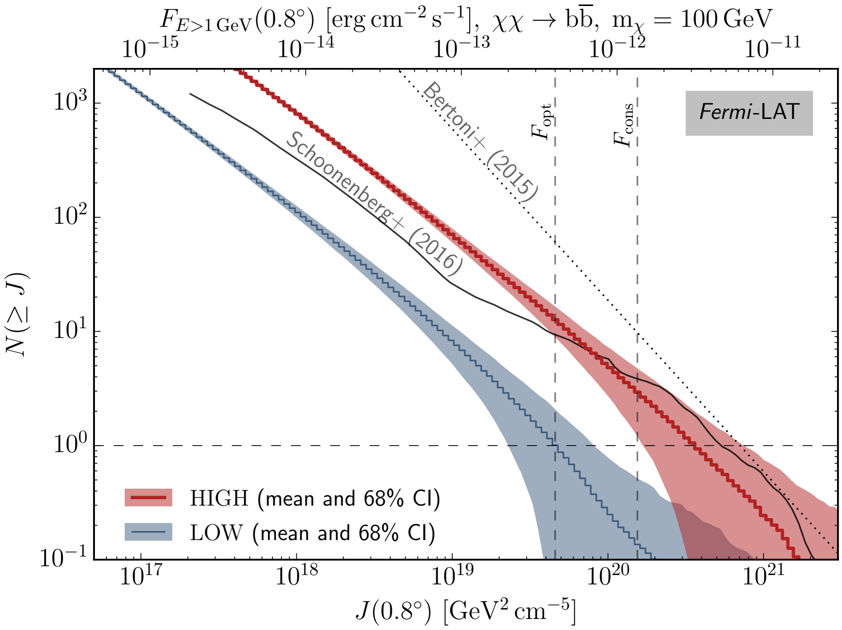

Figure 5.10.: Cumulative source count distribution of DM subhalos for the *Fermi*-LAT setup. The colored bands denote the 1σ standard deviation around the mean $\overline{N}$ from the 500 simulations. The lower x−axis gives J-factors and the upper x−axis the corresponding flux for a given particle physics model, using $\langle\sigma v\rangle = 3 \times 10^{-26}\,\mathrm{cm}^3\,\mathrm{s}^{-1}$. The Bertoni et al. (2015) (dotted line) and Schoonenberg et al. (2016) results (solid line) are also displayed. The vertical dashed lines show the conservative and optimistic detection thresholds chosen by Schoonenberg et al. (2016). Taking into account an up-to-date LAT sensitivity (see text), these thresholds would move by an approximate factor 2 to the left. Figure published in Hütten et al. (2016).

Schoonenberg et al. (2016) use the *Fermi*-LAT detection threshold in the 3FGL for sources with a similar, relatively hard spectral shape as expected from DM annihilations to estimate the number of detectable subhalos for a specific DM particle physics model. For a pure $\chi\chi \to b\bar{b}$ annihilation γ-ray spectrum, they assume a conservative detection threshold $F_{\mathrm{cons,\,b\bar{b}}} = 1.35 \times 10^{-12}\,\mathrm{erg\,cm^{-2}\,s^{-1}}$, and an optimistic detection threshold $F_{\mathrm{opt,\,b\bar{b}}} = 4.0 \times 10^{-13}\,\mathrm{erg\,cm^{-2}\,s^{-1}}$ (both fluxes integrated above 1 GeV). Taking these flux thresholds, the number of potentially detectable or possibly already detected subhalos can be given. For the specific particle physics model chosen in Figure 5.10 and the optimistic threshold $F_{\mathrm{opt,\,b\bar{b}}}$, model HIGH predicts 13 ± 4 detectable subhalos to be present in the 3FGL, while still 1 ± 1 are predicted by the conservative model LOW; for $F_{\mathrm{cons,\,b\bar{b}}}$, model HIGH (LOW) still yields 3 ± 2 (0.1 ± 0.4) halos. These numbers are based on the 3FGL catalog relying on four years of *Fermi*-LAT observations as from 2012. However, the LAT yields a significantly better sensitivity after eight years of data taking and applying an improved analysis chain (Atwood et al., 2013). In the regime between 1 GeV and 10 GeV, where the sensitivity is limited by the background level, the double exposure time results in a factor $\sqrt{2}$ improvement in sensitivity, and the redesigned `Pass8` reconstruction additionally improves the sensitivity by about 30% compared to the `Pass7` analysis underlying the 3FGL catalog.[18] Combining these improvements, the flux thresholds above 1 GeV after eight years of observation with `Pass8` reconstruction can be approximated as $F_{8\text{years}} \approx 0.5\, F_{3\text{FGL}}$. With this, the number of detectable clumps increases by a factor $\sim 0.5^{1-\alpha} \sim 2$, where $1 - \alpha \approx -1$ is the slope of the source count distribution displayed in Figure 5.10. Therefore, several DM subhalos should already have been detected by the *Fermi*-LAT for DM models with $\langle\sigma v\rangle \approx 3 \times 10^{-26}\,\mathrm{cm^3\,s^{-1}}$ and particle masses $m_\chi \lesssim 100\,\mathrm{GeV}$, even assuming a conservative subhalo model LOW and a conservative detection threshold. In turn, an exclusion of the DM hypothesis for most of the unidentified 3FGL objects excludes these DM models, $\langle\sigma v\rangle < 3 \times 10^{-26}\,\mathrm{cm^3\,s^{-1}}$ and $m_\chi < 100\,\mathrm{GeV}$, consistent with *Fermi*-LAT's finding from stacked dSph galaxy observations (Ackermann et al., 2015e). These latter quoted limits are even more stringent after a total time of eight years of *Fermi*-LAT observation.

Note that the angular resolution of the *Fermi*-LAT improves at higher energies, and reaches a 68% containment radius of 0.2° at $\sim 10\,\mathrm{GeV}$, and 0.1° above $\sim 100\,\mathrm{GeV}$ (Atwood, 2009; Atwood et al., 2013). Therefore, the choice of $\theta_{\text{int}} = 0.8°$ in this paragraph is only a crude proxy for the description of the LAT performance, chosen for comparison with Schoonenberg et al. (2016).

The median properties of the brightest object within the masked *Fermi*-LAT sky and for the model HIGH are presented in Table 5.1 (left), compared to the results found for the CTA-like extragalactic survey. Again, the properties of the brightest objects are given for different integration angles, θ_{int}. In contrast to CTA, virtually the same objects are selected within the range of resolutions of the *Fermi*-LAT: The LAT might find the median γ-ray-brightest subhalo at a distance of 8^{+11}_{-6} kpc, with a mass between $\sim 10^7\,\mathrm{M_\odot} - 10^9\,\mathrm{M_\odot}$. The factor ~ 3 larger field of view of the *Fermi*-LAT compared to the CTA extragalactic survey setup ($f_{\text{sky}} = 83\%$ vs. $f_{\text{sky}} = 25\%$) yields a similar increase of the median brightest subhalo to be detected, such that the larger survey field alone increases the detection prospects for the *Fermi*-LAT.[19]

However, after having detected a potential DM subhalo candidate, alternative interpretations of the signal, like, e.g., VHE blazars and milli-second pulsars, have to be excluded. Many studies have been addressing the issue of separating the characteristics from DM and astrophysical sources (e.g. Belikov et al., 2012; Zechlin and Horns, 2012; Mirabal et al., 2012, 2016). To sort out alternative explanations of a signal, CTA will be a particularly adapted instrument for follow-up observations to investigate the temporal, spectral and spatial morphology of DM subhalo candidates.

---

[18] `http://www.slac.stanford.edu/exp/glast/groups/canda/lat_Performance.htm`

[19] The median brightest subhalos for the *Fermi*-LAT and CTA are also visually compared by the asterisks in Figure 4.7.

5.3. Detecting fluctuations in the diffuse γ-ray background

The DM detection prospects presented in the previous section targeted at the single brightest Galactic subhalo. However, when searching for a whole population of sources, it might be advantageous to also include its fainter members in an analysis: Although the brightest object alone might not be detectable at a given C.L. in a given dataset, the presence of additional fainter sources might cause the whole population to be detectable in the same data. When the locations of potential sources are known, this is usually accounted for by "stacking" the events from possible source locations. A similar search for potentially existing unresolved sources is also possible when the location and number of sources are not known: In this case, the angular power spectrum (APS) of the data can be analyzed. Such an approach to γ-ray data has been successfully applied for the *Fermi*-LAT experiment (Ackermann et al., 2012a; Fornasa et al., 2016), and also previously suggested for CTA (Ripken et al., 2014). Figure 5.1 indicated a factor two larger angular power of the whole subhalo population than of the brightest halo alone. Provided that the sensitivity to the APS is compatible with the analysis presented in the previous section, a flux sensitivity improvement by a factor $\sim \sqrt{\widetilde{C}_{\text{all halos}} / \widetilde{C}_{\text{brightest halo}}} \approx \sqrt{2}$ would be obtained (see Subsection 5.3.2). Following the work of Ripken et al. (2014), this section tackles the question of whether an APS analysis provides a promising approach for CTA.

It is stressed that after a detection of a signal in the APS, its physical origin still has to be determined. Like in the case of a single object, this can be achieved by probing the energy dependence of the APS and its shape, which encodes the spatial morphology of the sources. However, the possibility of a follow-up observation is not available in this context, and the origin of the radiation has to be determined not only for a single object, but for possibly several contributing populations. This turns a physical interpretation of an APS signal into an even harder task than for the detection of a single source. The following study only addresses the question of whether CTA will be able to probe unresolved sources in the VHE regime of the diffuse γ-ray background (DGRB). This is done for the DM subhalo population with a particular energy spectrum, flux distribution, and consisting of spatially extended objects. However, the results are also given in a general context, to be interpreted in terms of CTA's general performance to detect arbitrary (in particular, much simpler point-like) populations in the DGRB.

In Subsection 5.3.1, the DGRB and possible contributing sources are introduced. Subsection 5.3.2 reviews the concept of angular power spectra and methods for their analysis. Subsection 5.3.3 discusses the APS of Galactic DM subhalos. After describing the simulation setup and analysis (Subsections 5.3.4 and 5.3.5) of a subhalo search in the CTA extragalactic survey APS, Subsection 5.3.6 presents the results of this study. Subsections 5.3.7 and 5.3.8 discuss the results in the light of existing measurements and possible systematic problems in a data analysis.

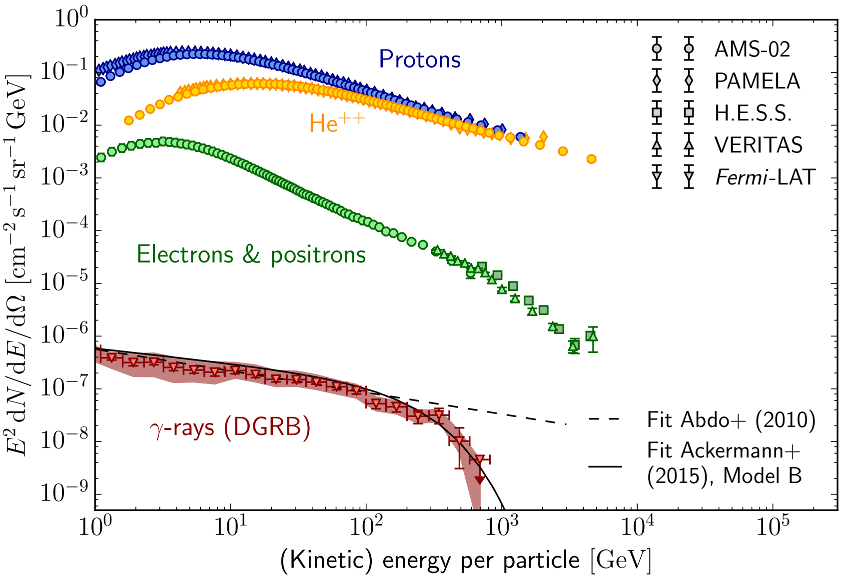

Figure 5.11.: The DGRB at $|b| > 20°$, as measured by the *Fermi*-LAT with 50 months of data (Ackermann et al., 2015b), and its comparison to the cosmic-ray intensities. For the He^{++} intensity, the kinetic energy is given per nucleus. The AMS-02 data are taken from Aguilar et al. (2015a, proton intensity), Aguilar et al. (2015b, helium intensity), and Aguilar et al. (2014, electron intensity); the PAMELA results from Adriani et al. (2011), and the H.E.S.S. and VERITAS electron spectra from Aharonian et al. (2008a), and Staszak (2015), respectively. For the DGRB spectrum, the systematic uncertainty band due to the Galactic foreground modeling is shown, and the fitted parametrizations according to Equation 5.14 (Abdo et al., 2010, dashed line) and Equation 5.13 (Ackermann et al., 2015b, model B, solid line).

5.3.1. The diffuse γ-ray background: Definition and contributors

Galactic and extragalactic sources of various kinds contribute to the total γ-ray sky. Whereas the γ-ray emission from within the MW mostly arises from regions around the Galactic plane, almost all extragalactic contributors are, because of their vast distance, virtually point-like and distributed isotropically on the sky. The DGRB[20] is defined to comprise all γ-rays outside the Galactic plane that cannot be assigned neither to a diffuse Galactic component, nor to any resolved γ-ray source in the sky (Dermer, 2007). It therefore consists of primarily unresolved extragalactic point sources. However, also unresolved sources of Galactic origin at high latitudes, and unaccounted large-scale Galactic diffuse emission might, by definition, contribute to the DGRB. DM annihilation in the Milky Way DM halo might contribute to both latter cases: Annihilation of smooth DM particles in the Galactic halo would form a large-scale diffuse component, further boosted by annihilation in unresolved subclumps.

Because the DGRB emission is weak, it is highly susceptible to contamination of background

---

[20] The DGRB is sometimes also denoted as isotropic γ-ray background (IGRB).

noise. As outlined in Chapter 3, Earth-bound γ-ray observatories suffer from a large level of cosmic-ray background. This makes a ground-based measurement of the absolute DGRB intensity and its energy spectrum virtually unfeasible. In contrast, space-borne γ-ray observatories have measured an isotropic component in the γ-ray sky since the early days of γ-ray satellites (Kraushaar et al., 1972). The most precise measurement of the DGRB, extending up to γ-ray energies of almost 1 TeV, has been recently reported by Ackermann et al. (2015b), from 50 months of observation by the *Fermi*-LAT space telescope: The differential energy spectrum of this measurement is displayed in Figure 5.11 (red triangles).

The measurement comprises γ-ray events at $|b| > 20°$ between 100 MeV and 820 GeV, after the resolved sources, Galactic diffuse emission, and contamination from cosmic-ray events have been subtracted. The subtraction requires dedicated models of these components. The red band in Figure 5.11 shows the systematic uncertainty of the DGRB level. The largest part of this uncertainty is introduced by the modeling of the Galactic diffuse emission, which extends to high Galactic latitudes. Ackermann et al. (2015b) consider different Galactic emission models, and the solid line in Figure 5.11 represents an analytical description of the DGRB for the lowest assumption on the Galactic foreground (which results in the highest possible DGRB level). This 'model B' yields a description of the DGRB intensity energy spectrum by a power-law with exponential cut-off according to

$$\begin{aligned}\left(\frac{\mathrm{d}I}{\mathrm{d}E}\right)_{\mathrm{DGRB}} &= (1.12 \pm 0.08) \times 10^{-7} \times \\ &\left(\frac{E}{100\,\mathrm{MeV}}\right)^{-2.28\pm0.02} \times \exp\left(-\frac{E}{(206 \pm 31)\,\mathrm{GeV}}\right)\ \mathrm{cm}^{-2}\,\mathrm{s}^{-1}\,\mathrm{sr}^{-1}\,\mathrm{MeV}^{-1}\,. \quad (5.13)\end{aligned}$$

The measurement by Ackermann et al. (2015b) is the first observation of a cut-off in the DGRB energy-spectrum above $\gtrsim 200$ GeV and hints at an extragalactic origin of the bulk fraction of the radiation. At VHE energies, above $\gtrsim 100$ GeV, the pair-creation cross section rises for interactions with $\lesssim 1$ eV photons (Franceschini et al., 2008), which numerously fill the Universe as extragalactic background light (Khaire and Srianand, 2015). This causes the mean free path of a $\gtrsim 1$ TeV γ-ray to be less than ~ 400 Mpc,[21] and VHE radiation from farther sources is pair-converted before arriving at Earth. The dashed line in Figure 5.11 indicates the pure power-law fit to the previous measurement of the DGRB from 10 months of *Fermi*-LAT data by Abdo et al. (2010) up to 100 GeV below the cut-off,

$$\left(\frac{\mathrm{d}I}{\mathrm{d}E}\right)_{\mathrm{DGRB}} = (1.45 \pm 0.25) \times 10^{-7} \times \left(\frac{E}{100\,\mathrm{MeV}}\right)^{-2.41\pm0.05}\ \mathrm{cm}^{-2}\,\mathrm{s}^{-1}\,\mathrm{sr}^{-1}\,\mathrm{MeV}^{-1}\,. \quad (5.14)$$

---

[21] Strictly speaking, the γ-ray horizon of 1 TeV γ-ray is $z \approx 0.1$ (Franceschini et al., 2008; Domínguez et al., 2013), corresponding to a proper distance (Equation A.9) of 431 Mpc.

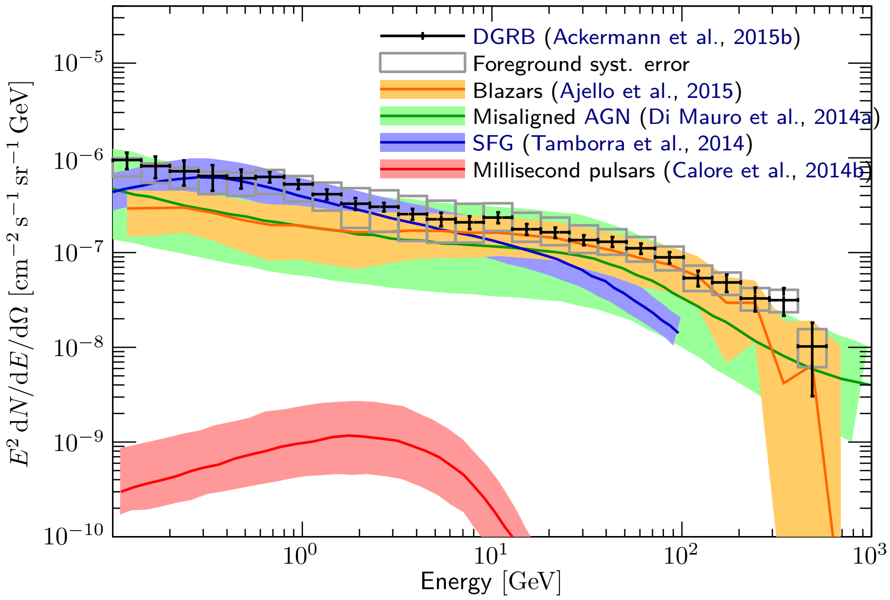

Figure 5.12.: Compilation of different possible contributors to the DGRB, with their systematic uncertainty bands. See text for further details. Figure taken from Fornasa and Sánchez-Conde (2015).

Below its cut-off, the DGRB shows a spectrum much harder than that of the cosmic-ray electrons, whose intensity decreases with a spectral index of $\Gamma_e \sim -3.3$ below 1 TeV (Aguilar et al., 2014), and even steeper at higher energies, $E \gtrsim 1$ TeV, with $\Gamma_e \sim -3.9$ (Aharonian et al., 2008a) or $\Gamma_e \sim -4.1$ (Staszak, 2015), respectively. As shown in Figure 5.11, an extrapolation of the unsuppressed DGRB spectrum would result in a significantly increased γ-ray-to-electron ratio in the VHE regime. Since cosmic nuclei are well rejected at these energies, this would improve the signal-to-noise ratio for diffuse γ-rays in the TeV-regime for Earth-bound γ-ray telescopes. However, according to Ackermann et al. (2015b), the DGRB is suppressed at even lower energies than for the electron spectrum.

In Figure 5.12 and Table 5.3, the most well-understood source populations possibly contributing to the DGRB above 100 MeV are shown, as compiled by Fornasa and Sánchez-Conde (2015). From this, it can be seen that most of the DGRB can be accounted for by three candidates: Unresolved distant blazars (Active Galactic Nuclei (AGN) whose jet is aligned with the observers' line of sight), star-forming galaxies, and misaligned AGN. Above 10 GeV, hard-spectra blazars alone can possibly explain the entire DGRB emission, as indicated in Figure 5.12. A further discussion of possible contributors is given in the review by Fornasa and Sánchez-Conde (2015) and by Di Mauro (2016b).

Still, given the coarse estimations summarized in Table 5.3, the possibility remains that a significant fraction of the DGRB arises from Galactic and extragalactic DM annihilation. The

Contribution	Percentage of DGRB
Blazars	$\sim 20\%$
Misaligned AGN	$\sim 25\%$
Star-forming galaxies (SFG)	$\lesssim 20\%$
Millisecond pulsars	$< 1\%$
Galaxy clusters	$< 1\%$
Small Solar system bodies	$\sim 1\%$ to $\sim 100\%$
Gamma-Ray bursts	$\lesssim 0.1\%$

Table 5.3.: Contribution of different source classes to the DGRB above 100 MeV, compiled by Fornasa and Sánchez-Conde (2015) on the basis of an extensive literature review. Note that for most quoted percentages, the reference DGRB is the measurement from Abdo et al. (2010), such that referring the intensities to the DGRB from Ackermann et al. (2015b) would give higher percentages.

dataset of the *Fermi*-LAT has been analyzed two times for unresolved sources in the APS of the DGRB: Based on 22 months of data in the energy range between $1\,\mathrm{GeV} \leq E \leq 50\,\mathrm{GeV}$ (Ackermann et al., 2012a), and based on 81 months of data in the range $0.5\,\mathrm{GeV} \leq E \leq 500\,\mathrm{GeV}$ (Fornasa et al., 2016). For both datasets, a significant excess of anisotropy above the noise background has been found, and the maximum contribution of DM to the unresolved source populations has been derived (Ando and Komatsu, 2013; Gómez-Vargas et al., 2014).

Additionally, the DGRB is not an observer-independent quantity, but is dependent on the instrumental sensitivity: Resolving sources and extended structures with better angular resolution and a larger observing time will reduce the level of the DGRB. Thereby, the remaining DGRB places a limit on the flux of unresolved populations, including DM. Better limits on the DGRB imply better limits on these fluxes too, and strong limits on DM models of Galactic and extragalactic DM have been derived from this argument for the latest DGRB measurement by the *Fermi*-LAT (Ackermann et al., 2015d; Di Mauro and Donato, 2015; Di Mauro, 2016a).

From the ground, the absolute DGRB level cannot be probed with current or next generation instruments. However, assuming that the residual background is intrinsically isotropic, any observed small-scale anisotropy in the data can be attributed to the γ-ray sky. By this, information about the faint DGRB may be also obtained from the ground, and the prospects for searching γ-ray anisotropies in the VHE part of the DGRB with CTA are presented in the following.

5.3.2. Power-spectral methods

Anisotropies in the DGRB can be detected and quantified by the decomposition of the spatial distribution of γ-ray events into their angular power spectrum (APS). The following subsection summarizes the methods needed for an APS analysis of γ-ray events.

Definition & estimator of the angular power spectrum: Any square-integrable function $I(\vartheta, \varphi) = I(\vec{k})$ on the sphere can be written as a linear combination of spherical harmonics $Y_{\ell m}(\vec{k})$,

$$I(\vec{k}) = \sum_{\ell=0}^{\infty} \sum_{m=-\ell}^{m=+\ell} a_{\ell m} \, Y_{\ell m}(\vec{k}). \tag{5.15}$$

The auto-correlation APS, or simply APS in the following, is defined as the covariance of the uncorrelated coefficients $a_{\ell m}$,

$$\langle a_{\ell m} a^{*}_{\ell' m'} \rangle = C_\ell \, \delta_{\ell\ell'} \, \delta_{mm'} \quad \Rightarrow \quad C_\ell = \langle |a_{\ell m}|^2 \rangle \, . \tag{5.16}$$

For a statistically isotropic field with $\langle a_{\ell m} \rangle = 0$, the ensemble average of the $a_{\ell m}$,

$$\widehat{C}_\ell = \frac{1}{2\ell + 1} \sum_m |a_{\ell m}|^2 \, , \tag{5.17}$$

provides an unbiased estimator for C_ℓ. Its accuracy is unalterably limited by the available modes m, which increase for large ℓ.

Numeric multipole expansion: Inverting Equation 5.15, for a given map $I(\vec{k})$, the coefficients $a_{\ell m}$ of the complete basis $Y_{\ell m}$ are calculated by the integral

$$a_{\ell m} = \int_\Omega I(\vec{k}) \, Y^{*}_{\ell m}(\vec{k}) \, \mathrm{d}\Omega \overset{\text{discrete equal-area grid}}{\approx} \frac{4\pi}{N_{\text{pix}}} \sum_{i=1}^{N_{\text{pix}}} I(\vec{k}_i) \, Y^{*}_{\ell m}(\vec{k}_i) \, . \tag{5.18}$$

When dealing with data, $I(\vec{k})$ consists of a discrete pixelized map, containing the sampling grid, or, in case of event data, the binned events. For a map containing N_{pix} pixels, $I = I(\vec{k}_i)$, with $\vec{k}_i = \vec{k}_1, \vec{k}_2, \ldots, \vec{k}_{N_{\text{pix}}}$. The number of coefficients $a_{\ell m}$ for an expansion up to ℓ_{max} is

$$N_{a_{\ell m}} = \sum_{\ell=0}^{\ell_{\text{max}}} (2\ell + 1) = (\ell_{\text{max}} + 1)^2 \, . \tag{5.19}$$

The information of a map pixelized in the spatial domain is limited by N_{pix} and

$$I(\vec{k}_i) = \sum_{\ell=0}^{\ell_{\text{max}}} \sum_{m=-\ell}^{m=+\ell} a_{\ell m} \, Y_{\ell m}(\vec{k}_i) \tag{5.20}$$

can be written as a finite sum of spherical harmonics. For an equal-area grid in angular space, $N_{a_{\ell m}} \approx N_{\text{pix}}$ holds, and $\ell_{\text{max}} \approx \sqrt{N_{\text{pix}}}$.

In this thesis, the $a_{\ell m}$ coefficients according to Equation 5.18 of pixelized maps are calculated with the `anafast` routine provided by the HEALPix package (Górski et al., 2005). `anafast` relies on the `libsharp` library (Reinecke and Seljebotn, 2013) for an efficient computation of the $a_{\ell m}$. The HEALPix tessellation (introduced in Sections 5.1 and 4.2) is used as the event binning scheme. The iso-latitude HEALPix tessellation allows the usage of a limited number of precomputed Legendre polynomials, resulting in a faster spherical harmonic transformation than for non iso-latitude tessellations. For a pixelization in the HEALPix scheme, $N_{\mathrm{pix}} = 12 N_{\mathrm{side}}^2$, with N_{side} the HEALPix resolution parameter. A numeric decomposition of a HEALPix map therefore is reasonable up to $\ell_{\max} \lesssim \sqrt{N_{\mathrm{pix}}} = \sqrt{12}\, N_{\mathrm{side}}$.[22] At larger multipoles, the spectrum is suppressed by the pixel window function (see Figure 5.19). All power spectra in this thesis are evaluated up to $\ell_{\max} = 0.5\, N_{\mathrm{side}}$, ignoring the pixel window suppression.

Angular power spectrum of unclustered point sources: For unclustered point-like sources, the angular power is constant over all multipoles and can be expressed by a single scalar quantity, the Poisson power C_{P}. Ando (2009) has shown that for a number density n of point sources, distributed isotropically (but not necessarily homogeneously) in space, the constant angular power can be calculated by:

$$C_\ell \approx \frac{1}{16\pi^2} \int\limits_{L_{\min}}^{L_{\max}} \int\limits_{0}^{l_{\max}} \frac{L^2}{l^2} \frac{\mathrm{d}\overline{n}(l,\, L)}{dL}\, \mathrm{d}l\, \mathrm{d}L =: C_{\mathrm{P}}, \tag{5.21}$$

where $\overline{n}(l,\, L)$ is the number density averaged over the solid angle Ω. The coordinates $(l,\, \Omega)$ indicate spherical coordinates with the observer at $l = 0$, and L denotes the luminosity of the objects in arbitrary units.[23] Expressing luminosities and distances by the flux $F = L/(4\pi\, l^2)$, Equation 5.21 can be written as

$$C_{\mathrm{P}} = \frac{1}{4\pi} \int_{F_{\min}}^{F_{\max}} F^2 \frac{\mathrm{d}N}{\mathrm{d}F}\, \mathrm{d}F\, . \tag{5.22}$$

Here, $\mathrm{d}N/\mathrm{d}F$ is the source count distribution of fluxes F at the observer.

Fluctuation power spectrum: It is often useful to express the angular power in dimensionless units, i.e., to state a relative power with respect to the mean intensity. Because the multipole moments, $C_\ell^I = \langle |a_{\ell m}|^2 \rangle$, are proportional to the square intensity I, the dimensionless fluctuation power is defined as

$$C_\ell^F := \frac{C_\ell^I}{\langle I \rangle^2}. \tag{5.23}$$

---

[22] Note that the discrete transformations (5.18) and (5.20) are not strictly commutative on the sphere, and subsequent forward and backward transformations with a finite $\ell_{\max}$ still result in a loss of information.

[23] For point-like DM subhalos, $L = \frac{\langle \sigma v \rangle}{2\, m_\chi^2} \frac{\mathrm{d}N_{\mathrm{sub}}}{\mathrm{d}E}\, \mathcal{L}$, with $\mathcal{L}$ as defined in Equation 4.27.

By this, different components to a power spectrum can be compared, independently of their intrinsic dimensionful intensities. Note that the quantity of a fluctuation power is only applicable to strictly positive intensities. To avoid confusion between the dimensionful intensity APS and dimensionless fluctuation APS, in the following, the former is consequently marked with a superscript 'I', and the latter with a 'F'. The fluctuation APS from different components sums up according to

$$C_\ell^F = \frac{\langle I_1\rangle^2 \, C_{\ell,1}^F + \langle I_2\rangle^2 \, C_{\ell,2}^F + \ldots}{\langle I_1 + I_2 + \ldots\rangle^2} \tag{5.24}$$

Event fluxes: When the full sphere is divided into N_{pix} equal-area bins, then a mean intensity can be defined in event units,

$$\langle I_{\mathrm{ev}}\rangle := \frac{N_{\mathrm{ev}}}{N_{\mathrm{pix}}} \,. \tag{5.25}$$

In these units, each event corresponds to a flux

$$F_{\mathrm{ev}} := \frac{4\pi}{N_{\mathrm{pix}}} . \tag{5.26}$$

Note that Equation 5.26 can be multiplied with a constant in flux units to recover a physical flux.

Shot-noise APS: Discrete events, even when isotropically distributed on the sphere, cause a noise power. For each event, a source count distribution can be formally build,

$$\frac{\mathrm{d}N_{1\,\mathrm{ev.}}}{\mathrm{d}F}(F) := \frac{1}{F_{\mathrm{ev}}}\,\delta\left(\frac{F}{F_{\mathrm{ev}}} - 1\right) , \tag{5.27}$$

with δ the Dirac Delta-function. For any event distribution incorporating a random component of the events' position, N_{pix} can be chosen large enough that each pixel on the sphere contains at most a single event. Then, a shot-noise source count distribution can be defined for the N_{ev} events on the sphere, each with flux F_{ev} (the subscript N denotes 'Noise'),

$$\frac{\mathrm{d}N_{\mathrm{N}}}{\mathrm{d}F}(F) \equiv \sum^{N_{\mathrm{ev}}} \frac{\mathrm{d}N_{1\,\mathrm{ev.}}}{\mathrm{d}F}(F) = \frac{N_{\mathrm{ev}}}{F_{\mathrm{ev}}}\,\delta\left(\frac{F}{F_{\mathrm{ev}}} - 1\right) . \tag{5.28}$$

With Equation 5.22, the intensity APS of $\mathrm{d}N_{\mathrm{N}}/\mathrm{d}F$ can be calculated, which constitutes an estimator of the noise power, C_{N}, of discrete event counts:

$$\widehat{C}_{\mathrm{N}}^I = \frac{1}{4\pi}\int F^2\,\frac{\mathrm{d}N_{\mathrm{N}}}{\mathrm{d}F}\,\mathrm{d}F = \frac{N_{\mathrm{ev}}\,F_{\mathrm{ev}}^2}{4\pi} = 4\pi\,\frac{N_{\mathrm{ev}}}{{N_{\mathrm{pix}}}^2} \,. \tag{5.29}$$

For event intensities as defined in Equation 5.25, one obtains the corresponding shot-noise fluctuation APS

$$\widehat{C}_{\mathrm{N}}^{F} = \frac{\widehat{C}_{N}^{I}}{\langle I_{\mathrm{ev}}\rangle^{2}} = \frac{4\pi}{N_{\mathrm{ev}}}\,, \tag{5.30}$$

being independent of the pixelization, N_{pix}. Generally, events can be distinguished in signal events, N_{sig}, and background events, N_{b}, such that $N_{\mathrm{ev}} = N_{\mathrm{sig}} + N_{\mathrm{b}}$. As the intensity APS is additive for uncorrelated spectra, one can simply divide the terms,

$$\widehat{C}_{\mathrm{N}}^{I} = \widehat{C}_{\mathrm{N,\,sig}}^{I} + \widehat{C}_{\mathrm{N,\,b}}^{I} = 4\pi\,\frac{N_{\mathrm{sig}} + N_{\mathrm{b}}}{{N_{\mathrm{pix}}}^{2}}. \tag{5.31}$$

Point-source APS: Equation 5.29 strictly holds only for single events in each pixel. If all N_{ev} events fall into a single pixel, then this corresponds to the flux $F_{\mathrm{point}} = 4\pi\,N_{\mathrm{ev}}/N_{\mathrm{pix}}$, and the fluctuation APS calculates to

$$\widehat{C}_{1\,\mathrm{point}}^{F} = 4\pi. \tag{5.32}$$

Note that for uncorrelated contributions to the APS, each contribution can be calculated independently (e.g., via Equation 5.22), and the different components can be linearly added. Therefore, for uncorrelated events, Equation 5.29 also holds when multiple events events fall into a single pixel.

Beam window function: Folding a function $I(\vec{k})$ on the sphere with an instrumental beam $p(\vec{k}_{\mathrm{R}}|\,\vec{k})$ corresponds to a multiplication of the spherical harmonic transformations of I and $p(\vec{k}_{\mathrm{R}}|\,\vec{k})$ in $(\ell,\,m)$ space. For a spherically symmetric beam $p(\vec{k}_{\mathrm{R}}|\,\vec{k}) = \mathrm{d}P/\mathrm{d}\theta$ (Knox, 1995),

$$C_{\ell,\,\mathrm{folded}}^{I} = (W_{\ell}^{\mathrm{beam}})^{2}\,C_{\ell}\,. \tag{5.33}$$

The window function W_{ℓ} in ℓ-space is calculated from $\mathrm{d}P/\mathrm{d}\theta$ in angular space by

$$W_{\ell}^{\mathrm{beam}}(E) = \frac{2\pi}{\Omega_{B}}\int_{-1}^{1} \mathcal{P}_{\ell}(\cos(\theta)) \times \frac{\mathrm{d}P}{\mathrm{d}\theta}(\theta,\,E)\;\mathrm{d}(\cos\theta)\,\mathrm{d}E\,, \tag{5.34}$$

where $\mathcal{P}_{\ell}$ is the Legendre polynomial of the ℓ-th order. $\Omega_{B} = \int \mathrm{d}P/\mathrm{d}\theta\mathrm{d}\Omega$ for the full beam size. For a Gaussian beam,

$$\frac{\mathrm{d}P}{\mathrm{d}\theta}(\theta,\,E) = \exp\left(-\frac{\theta^{2}}{2\,\sigma_{\mathrm{psf}}^{2}(E)}\right), \quad \Omega_{B} = 2\pi\sigma_{\mathrm{psf}}(E)^{2}\,. \tag{5.35}$$

The window function in ℓ-space is also Gaussian,

$$W_\ell^{\mathrm{beam}}(E) = \exp\left(-\frac{\ell(\ell+1)}{2}\,\sigma_{\mathrm{psf}}^2(E)\right), \tag{5.36}$$

where σ_{psf} is measured in radians (Knox, 1995; Page et al., 2003).

Limited sky coverage & windowing: A masking (multiplication) of a function with a window in angular space results in a convolution in ℓ-space. Consequently, the orthonormality of the $Y_{\ell m}$ is destroyed (Peebles, 1980; Komatsu et al., 2002), and the C_ℓ become correlated, i.e. Equation 5.16 no longer holds. Formally, the resulting masked APS, or pseudo APS, can be estimated via

$$\widehat{C}^I_{\ell,\,\text{part-sky}} = \frac{1}{2\ell+1}\sum_{\ell'}\sum_{mm'} M_{\ell\ell' mm'}\, C^I_{\ell',\,\text{full-sky}}\,, \tag{5.37}$$

where the convolution kernel $M_{\ell\ell'}$,

$$M_{\ell\ell' mm'} = \int_\Omega W(\vec{k})\, Y^*_{\ell m}(\vec{k})\, Y_{\ell m}(\vec{k})\,\mathrm{d}\Omega\,, \tag{5.38}$$

is a function of the window function $W(\vec{k})$ in angular space (Wandelt et al., 2001; Komatsu et al., 2002; Poutanen et al., 2004). Inverting Equation 5.37, the estimator $\widehat{C}^I_{\ell,\,\text{full-sky}}$ can be calculated from a given $C^I_{\ell,\,\text{part-sky}}$ and known $W(\vec{k})$. Several approaches exist to efficiently calculate $(M_{\ell\ell' mm'})^{-1}$ and to reconstruct $\langle C^I_{\ell,\,\text{full-sky}}\rangle$, like polSpice (Szapudi et al., 2001) or the Master algorithm (Hivon et al., 2002). However, applying the unfolding to numeric data heavily amplifies noise (Ackermann et al., 2012a), and depends on the exact knowledge of the window function, $W(\vec{k})$. The `deconvolve_mask` code implementation[24] of the MASTER approach has been tested on simplified toy-models of Cherenkov telescope data, and was only able to reconstruct the full-sky APS for a coarse binning of the multipoles ($\Delta\ell > 100$), resulting in a heavy loss of information. However, for suitable localized $M_{\ell\ell'}$ at $\ell \lesssim \ell_{\mathrm{window}}$, corresponding to a large angular extension of the $W(\vec{k})$, the unfolding can be circumvented by a simple approximation. At sufficiently high multipoles, the multipole correlation due to the mask vanishes, and the original spectrum – assuming isotropy on scales larger than the window – is only linearly suppressed by a factor f_{sky} (Komatsu et al., 2002):

$$\widehat{C}^I_{\ell,\,\text{full-sky}} \approx \frac{C^I_{\ell,\,\text{part-sky}}}{f_{\mathrm{sky}}} \qquad \text{for } \ell \gg \ell_{\mathrm{window}}, \tag{5.39}$$

---

[24] `http://wwwmpa.mpa-garching.mpg.de/~komatsu/CRL/cmb/binned_cl_master/`, written by E. Komatsu and R. Flauger.

where f_{sky} is the unmasked part of the sky. In particular, for a Gaussian window with $\sigma_{\mathrm{window}} \ll 1$, the linear regime is fastly reached at $\ell_{\mathrm{window}} \approx \pi/\sigma_{\mathrm{window}}$. In the following context, Equation 5.39 applies for a Gaussian window with $f_{\mathrm{sky}} \approx 2\pi\sigma^2_{\mathrm{window}}/4\pi = \sigma^2_{\mathrm{window}}/2$.[25] However, the correlation between neighboring multipoles cannot be neglected even in the linear case (5.39), manifesting itself by a bias of the variance of the APS. This is further discussed below.

Regarding the fluctuation APS, a mean intensity (with respect to the full sky) for part-sky coverage can be defined as $\langle I_{\text{part-sky}}\rangle = f_{\mathrm{sky}}\,\langle I_{\text{full-sky}}\rangle$. With this, the fluctuation APS reads

$$\widehat{C}^F_{\ell,\,\text{full-sky}} := \frac{\widehat{C}^I_{\ell,\,\text{full-sky}}}{\langle I_{\text{full-sky}}\rangle^2} = f_{\mathrm{sky}}\, C^F_{\ell,\,\text{part-sky}}\,. \tag{5.40}$$

Like in Euclidean Fourier transformation, sharp window edges in angular space result in global artifacts in ℓ-space, and it is $\ell_{\mathrm{window}} \to \infty$, a problem commonly know as spectral leakage. The consequences of this effect on IACT data is discussed in Appendix C.10.

The total measured APS – an example: Taking the last definitions together, one can describe the generic shape of a measured event counts APS. An intrinsic signal full-sky APS, $C^I_{\ell,\,\text{sig, full-sky}}$, is altered by the beam function W^{beam}_ℓ and attenuated by a factor f_{sky} when measured on a limited sky patch. The residual background is assumed to be isotropic with no intrinsic power ($C^I_{\ell,\,\text{bck}} = 0$). However, the noise from N_{ev} disjoint, binned signal- and background events additionally adds a noise power, C^I_{N}, to the measurement. With this, the total measured APS reads:

$$C^I_{\ell,\,\text{tot}} = f_{\mathrm{sky}}\,(W^{\text{beam}}_\ell)^2\, C^I_{\ell,\,\text{sig, full-sky}} + C^I_{\mathrm{N}} \quad (\ell \gg \ell_{\mathrm{window}}). \tag{5.41}$$

If the APS is sampled on $f_{\mathrm{sky}} < 1$, then the sky mask window can be thought of as a very broad beam, and the spectrum, independent of the exact window shape, approaches C_{point} at very low ℓ. In total, all APS of binned events on a partial skymap show the asymptotic behavior:

$$C^F_{\ell,\,\text{tot}} \to \begin{cases} \widehat{C}^F_{1\,\text{point}} = 4\pi & \text{for } \ell \to 0 \text{ and } f_{\mathrm{sky}} < 1, \\ \widehat{C}^F_{\mathrm{N}} = \frac{4\pi}{N_{\mathrm{ev}}} & \text{for } 1/\sigma_{\mathrm{psf}} \ll \ell \lesssim 2\,N_{\mathrm{side}}. \end{cases} \tag{5.42}$$

The resulting spectrum, Equation 5.41, is illustrated in Figure 5.13 for a simple toy simulation of event data, inspired by the algorithm presented in Ripken et al. (2014). For this illustrating example, $N_{\mathrm{ev}} = 10^7$ events were simulated, assigned to N_{point} point sources with 20 events per source, and assuming a Gaussian beam with $\sigma_{\mathrm{psf}} = 0.1°$. The sky was masked by a Gaussian window with $\sigma_{\mathrm{window}} = 5°$. The events were distributed as follows: Firstly, a random position

---

[25] A more detailed discussion of the behavior of Equation 5.39 for a Gaussian window is given in section C.4.

on the sky was drawn. For the resulting position, the distance ϑ to the window center, and the corresponding Gaussian window attenuation, $d = \exp(-0.5\,(\vartheta/\sigma_{\mathrm{window}})^2)$, was evaluated. Secondly, the value d was compared to a uniform random number $r \in [0, 1]$. For $d > r$, the position was assigned to a source, and 20 events were drawn around this position, randomly smeared out by the Gaussian beam. The algorithm was repeated until all 10^7 events were distributed. Finally, the events were binned on a map in the HEALPix pixelization scheme with $N_{\mathrm{side}} = 4096$, and the APS was calculated. The simulation was repeated six times, generating six independent samples.

The above algorithm corresponds to the distribution of $N_{\mathrm{point}} = N_{\mathrm{ev}}/20 = 5{\times}10^5$ point sources on $f_{\mathrm{sky}} = 3.8{\times}10^{-3}$. In Figure 5.13, the Gaussian window dominates the spectrum on the lowest $\ell_{\mathrm{window}} \approx 40$ multipoles. According to Equation 5.22, $5{\times}10^5$ equal point sources cause a constant fluctuation APS of $C^F_{\mathrm{sig,\,part\text{-}sky}} = 4\pi/N_{\mathrm{point}} = 2.5 \times 10^{-5}$. If the full sphere were populated with these sources, one would obtain 1.3×10^8 sources and $C^F_{\mathrm{sig,\,full\text{-}sky}} = 4\pi/N_{\mathrm{point}} = 9.6 \times 10^{-8}$. The constant power then is suppressed at angular scales around $\sigma_{\mathrm{psf}} = 0.1°$, down to the noise power of the 10^7 drawn events. The different spectra scatter around the expected curve, but a correlation from the windowing is clearly visible in Figure 5.13.

Error on the APS: Random locations of sources or noise events on the sphere cause a Gaussian variance of each multipole in the APS (Knox, 1995):

$$\widehat{\sigma}^2_{C_\ell} = \frac{2}{2\ell + 1}\, C_\ell^2. \tag{5.43}$$

If the APS is sampled only on a fraction of the sky, the error increases according to

$$\widehat{\sigma}^2_{C_\ell} \approx \frac{2}{(2\ell + 1)\, f_{\mathrm{sky}}}\, C_\ell^2 \tag{5.44}$$

for uncorrelated multipoles. However, for correlated multipoles the variance increases slower than $\sim 1/f_{\mathrm{sky}}$ (Campbell, 2015). Therefore, a set of 1000 simple Monte-Carlo simulations has been performed, for each run randomly drawing $N_{\mathrm{ev}} = 10^8$ events on the sphere. When uniformly distributing N_{ev} on $f_{\mathrm{sky}} = 0.25$, a standard deviation only increasing 10% compared to the full sky was observed, $\sigma_{C_\ell,\,\mathrm{part\text{-}sky}} \approx 1.1\, \sigma_{C_\ell,\,\mathrm{full\text{-}sky}}$, instead of a factor 2 according to Equation 5.44. For $f_{\mathrm{sky}} = 1.9{\times}10^{-4}$ (Gaussian FOV with $\sigma_{\mathrm{fov}} = 3.5°$), $\sigma_{C_\ell,\,\mathrm{part\text{-}sky}} \approx 4.6\, \sigma_{C_\ell,\,\mathrm{full\text{-}sky}}$ was observed in the MC simulations, instead of an expected factor $1/\sqrt{f_{\mathrm{sky}}} = 23.2$. Further information can be found in **??** in Appendix C.8. If $C^I_{\ell,\,\mathrm{sig,\,part\text{-}sky}}$ is computed as

$$C^I_{\ell,\,\mathrm{sig,\,part\text{-}sky}} = \left(C^I_{\ell,\,\mathrm{tot}} - \widehat{C}^I_{\mathrm{N}}\right) \times (W_\ell^{\mathrm{beam}})^{-2}\,, \tag{5.45}$$

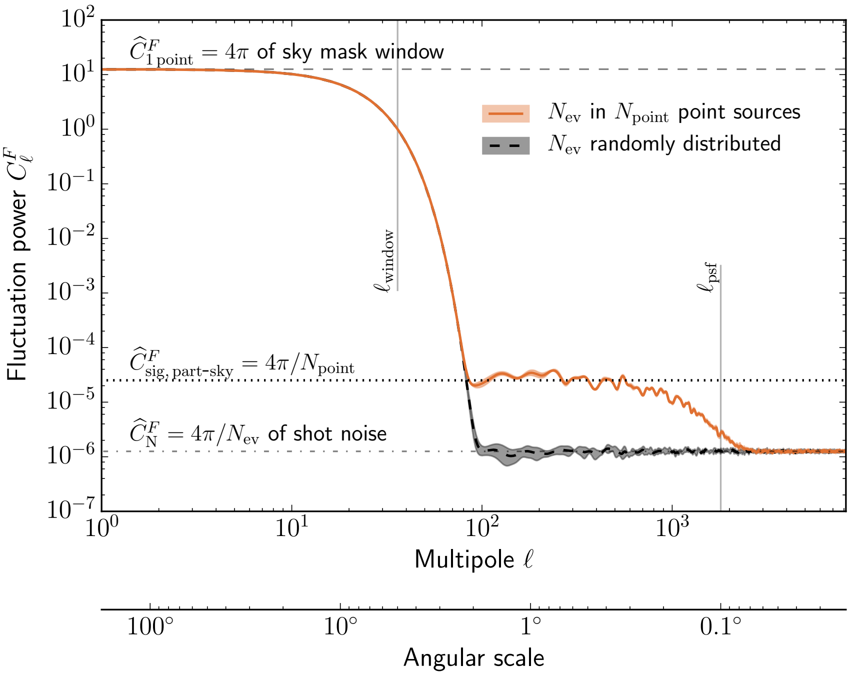

Figure 5.13.: Example of an angular power spectrum from event data with $N_\mathrm{ev} = 10^7$, $N_\mathrm{point} = 10^5$ point sources with equal flux each, a Gaussian window with $\sigma_\mathrm{fov} = 5.0°$, $N_\mathrm{pix} = 12 \times 4096^2 = 2.01 \times 10^8$, and a Gaussian beam of $\sigma_\mathrm{psf} = 0.1°$.

then the noise estimator $\widehat{C}^I_\mathrm{N}$ is exactly known and the error on the reconstructed signal intensity APS can be estimated as (Knox, 1995):

$$\widehat{\sigma}_{C^I_{\ell,\,\mathrm{sig}}} = \frac{\sigma_{C^I_{\ell,\,\mathrm{tot}}}}{(W^\mathrm{beam}_\ell)^2} = \sqrt{\frac{2}{(2\ell+1)\,f_\mathrm{sky}}}\left(f_\mathrm{sky}\,C^I_{\ell,\,\mathrm{sig,\,full\text{-}sky}} + \frac{\widehat{C}^I_\mathrm{N}}{(W^\mathrm{beam}_\ell)^2}\right). \tag{5.46}$$

5.3.3. Subhalo angular power spectrum

Before investigating the imprint of Galactic DM subhalos in the CTA extragalactic survey APS $C^I_{\ell,\,\mathrm{tot}}$, the expected intrinsic source APS $C^I_{\ell,\,\mathrm{sig,\,full\text{-}sky}}$ from the subhalos is studied first. For this purpose, the subhalo APS is computed for 500 skymaps of the Galactic DM emission using the `CLUMPY` code with a spatial resolution $N_\mathrm{side} = 4096$. For the contribution to the APS from the substructures, it must be ensured that a sufficient convergence of the APS is reached for a limited number of resolved subhalos. Appendix C.6 shows that an accuracy better than 5% at all multipoles is reached when resolving the $\sim 10^4$ brightest subhalos.

The overall angular power from Galactic DM on the full sky is made out of of several contri-

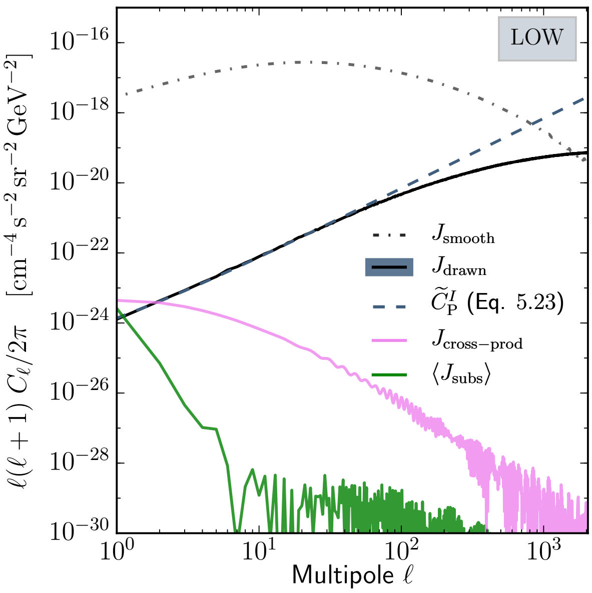

Figure 5.14.: Different components of the γ-ray intensity APS from Galactic DM in the full sky. The pale-blue band denotes the contribution from resolved subhalos and its cosmic variance. See text for further explanations. A similar figure has been published in Bonnivard et al. (2015b).

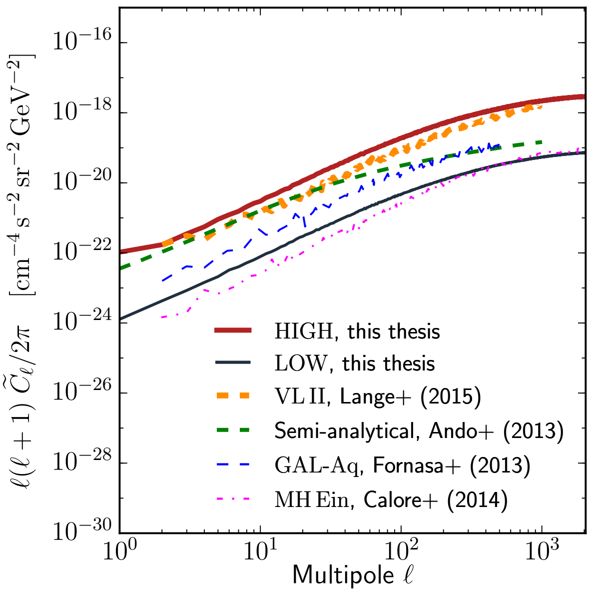

Figure 5.15.: Comparison of the median intensity APS of resolved subhalos in models LOW and HIGH, in the full sky, to other works. Slightly modified figure published in Hütten et al. (2016).

butions, the APS of which are shown in Figure 5.14. Here, the intensity spectra are given as differential intensity power at $E = 4\,\mathrm{GeV}$ for $m_\chi = 200\,\mathrm{GeV}$, $\chi\chi \to b\bar{b}$ annihilation channel, and a thermal relic cross-section $\langle\sigma v\rangle = 3\times 10^{-26}\,\mathrm{cm}^3\mathrm{s}^{-1}$ to ease comparison with other works in Figure 5.15. Like the intensities, the total intensity APS is obtained as the sum of its different components.[26]

According to Figure 5.14, the subhalo spectrum is largely dominated by the smooth Galactic DM component (dot-dashed line). However, this dominance is caused by the DM density spike towards the Galactic center. As shown in the next subsection, this component is largely suppressed when masking regions close to the GC. The contribution to the APS from unresolved substructures (green curve) is negligible for the chosen accuracy level and, by definition, does not contribute to fluctuations at small scales (the figure only shows numeric noise). The cross-product term adds a small power to the lowest multipoles, but is also negligible at $\ell \gtrsim 4$. Note that the vertical axis of Figure 5.14 is multiplied by $\ell(\ell+1)/2\pi$, additional to a logarithmic scale which spans over 15 orders of magnitude.

---

[26] This only holds on the full sky without a correlation of the APS components from masking artifacts.

The pale-blue shaded band finally presents the APS of the subhalo model LOW.[27] This band indicates the 68% C.I. at each multipole around the median (black-solid line) from the 500 halo simulations. From this, the angular power from the subhalos is subject to a rather large scattering over one order of magnitude in C_ℓ. As already anticipated in Figure 5.1, on average, the brightest subhalo alone accounts for almost half of the overall subhalo power, and its flux scattering dominates the subhalo APS variance. Also, the shaded band indicates that the variance has a long tail towards high powers, skewed even with respect to a log-normal distribution. A detailed discussion about the contribution of the brightest halos to the subhalo APS variance and its shape is postponed to Appendix C.5.

The black-solid median curve shows that the subhalo APS is constant over a wide range of multipoles – as expected from unclustered point-sources – and is attenuated at $\ell \gtrsim 100$. The attenuation indicates the angular extension of the brightest subhalos dominating the spectrum (Ando, 2009). Additionally, Figure 5.14 shows the subhalo APS calculated from the source count distribution $\mathrm{d}N/\mathrm{d}J$ – with J being the overall J-factor, $J(\theta_{\mathrm{vir}})$ – of each map with Equation 5.22 (dashed line).[28] This confirms that the two characterizations of the subhalos by (i) their source count distribution, as shown in Figure 4.4, and (ii) by the APS correspond to each other. At high ℓ, the point-like description from Equation 5.22 fails to account for the subhalo extension and therefore does not reproduce the APS attenuation.

Figure 5.15 shows a comparison of the median subhalo APS between models LOW and HIGH, together with previous results. These include a modeling based on the Via Lactea II subhalo catalog (Lange and Chu, 2014, orange-dashed line) or the Aquarius simulations (Fornasa et al., 2013, blue-dashed line). The green-dashed line corresponds to the semi-analytical modeling, also based on the Aquarius simulations by Ando and Komatsu (2013), using an extended version of Equation 5.22. The latter shows that by accounting for a "beam function-like" suppression factor $|\tilde{u}(\ell)|^2$, the APS attenuation at high ℓ can be reproduced when semi-analytically calculating the APS from the source count distribution. The magenta dot-dashed curve displays the APS from the g15784 simulation by Calore et al. (2014a). Because Calore et al. (2014a) only resolved subhalos with masses $> 10^{8.6}\,\mathrm{M}_\odot$, this spectrum shows a lower overall power. Comparing all models reveals an agreement of different approaches and simulations on the expected APS from Galactic subhalos within one order of magnitude, encompassed by the conservative and optimistic models LOW and HIGH presented in Chapter 4 of this thesis.

---

[27] According to the definition of the Galactic halo smooth and substructure density in Section 4.1, also the smooth components are affected by the subhalo model. However this bias is marginal, and smooth APS components comparable to that shown in Figure 5.14 from the model LOW are obtained for the model HIGH.

[28] The flux $F_{\min}$ in Equation 5.22 corresponds to the flux from the faintest drawn object in each realization. As shown in Appendix C.6, further lowering $F_{\min} \to 0$ adds negligible contribution to the integral.

5.3.4. Simulating all Galactic DM events in a CTA extragalactic survey

The CTA prospects to detect a signal from unresolved sources in the APS are studied for the same extragalactic survey model as introduced in Section 5.1 and adopted in the previous Section 5.2. However, in contrast to the previous section, it is now moved from a simplified proxy of the survey (approximation of the survey by $\sim 2\,\mathrm{h}$ of trials-corrected on-axis observation) to a full simulation of a $T = 500\,\mathrm{h}$ survey dataset. The mock dataset is simulated for an observation pattern as described in Subsection 5.1.1 and consists of isotropic background events and signal events from Galactic DM. The background events are distributed according to the off-axis scaling presented in Figure 3.18, N_{fov} pointing positions, and an exposure of $t_{\mathrm{obs}} = T/N_{\mathrm{fov}}$ for each pointing. Again, a dead time of 5% is applied, resulting into a livetime of $T_{\mathrm{live}} = 475\,\mathrm{h}$ of the survey. Moreover, events are only simulated within an offset of $\vartheta \leq \vartheta_{\mathrm{cut}} = 6^\circ$ from the camera center, a choice that represents the maximum radius for which data events will be reconstructed.

For the Galactic DM signal, events are now distributed according to a large field intensity map of DM annihilation in the survey field shown in Figure 5.2. For this purpose, 500 DM intensity maps are simulated with `CLUMPY` for the models LOW and HIGH on $f_{\mathrm{sky}} = 0.25$, and a reference map is chosen – by means of a χ^2-test – such that its total APS (from the Galactic halo and substructures) is closest to the median APS in the multipole range $100 \leq \ell \leq 1024$.[29] These simulations and calculated APS are the same as used for the MC study already shown in Figure 5.1 for the model HIGH. In Figure 5.16, the Galactic DM power spectrum is shown for the both models LOW and HIGH. In contrast to Figure 5.1, Figure 5.16 now displays the APS from all Galactic DM, including, besides the subhalos, the APS from the smooth Galactic halo. The latter contribution is also shown separately. It can be seen that at multipoles $\ell \gtrsim 100$, for the model HIGH, only the subhalos contribute to the APS, whereas the Galactic halo APS is negligible. This is not the case for the model LOW, where the Galactic halo APS biases the APS up to multipoles $\ell \gtrsim 200$. Because the sky mask window of the CTA extragalactic survey field will omit the analysis of multipoles $\ell \lesssim 100$, the Galactic halo contribution can be neglected for the model HIGH. While in Figure 5.16 (left), the *intensity* APS is presented (for the same benchmark particle physics model from Figure 5.15), Figure 5.16 (right) shows the *fluctuation* APS according to Equation 5.23. The fluctuation APS is constructed by dividing the C_ℓ^I by the square of the mean intensity of all Galactic DM in the survey field. This quantity is now independent of a specific particle physics model. However, the level of the fluctuation APS scales with the intensity level $\langle I \rangle^2$ of the Galactic halo diffuse DM emission, boosted by the unresolved subhalo population. The intensity boost from the low-luminosity subhalos and

---

[29] The result turns out to be quite robust against a particular multipole interval: The map best resembling the median APS in $100 \leq \ell \leq 1024$ is also almost the best description for other multipole ranges.

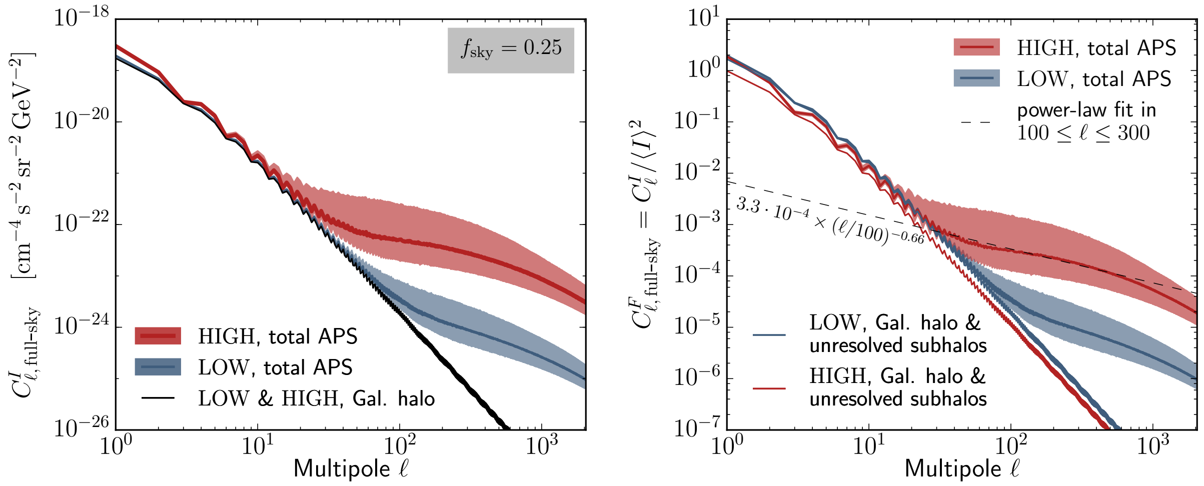

Figure 5.16.: Total APS of Galactic DM for the subhalo models HIGH and LOW, on $f_{\rm sky} = 0.25$. The bands show the median power and its 68% C.I. scatter, and the solid lines the contribution from the Galactic halo alone. *Left panel:* Intensity APS, with the same particle physics as in Figure 5.15. *Right panel:* Fluctuation APS with respect to the total Galactic DM emission of the models. The part-sky spectra have been rescaled to their full-sky equivalent powers (recall Equations 5.39 and 5.40).

sub-substructures is heavily dependent on the DM free-streaming scale and causes a non-linear increase of the diffuse emission. Additionally, the emission from free streaming DM in the Galactic halo is strongly peaked towards the GC, and consequently the diffuse DM intensity is highly anisotropic on large scales. Therefore, statements about the fluctuation APS depend on the DM clustering scales and the sky area under consideration.

In order to search for a subhalo signal in the data, the expected signal APS from subhalos is approximated as a power-law in the multipole range considered in the analysis. The dashed line in Figure 5.16 (right) shows a power-law fit to the APS of the model HIGH in the range $100 \le \ell \le 1024$,

$$\widetilde{C}^F_{\text{HIGH},\,100\le\ell\le1024} \approx 3.3 \times 10^{-4} \times \left(\frac{\ell}{100}\right)^{-0.66} . \tag{5.47}$$

Taking $\widetilde{C}^F_{\ell=100} \approx C_{\rm P}$ as benchmark value (recall Equation 5.21 for the definition of $C_{\rm P}$), the result for the subhalo model HIGH can be rescaled into a sensitivity towards other source populations with approximately constant $C_\ell \approx C_{\rm P}$, or to Galactic DM models with a larger diffuse boost.[30] For Galactic DM, Fornasa et al. (2013) quote $C^F_{\ell=100} \approx 10^{-2}$, whereas Ripken et al. (2014) assume $C^F_{\rm P} = 10^{-3}$. Both fluctuation powers are given relative only to the subhalo intensity.

Figure 5.17 (left) shows a spatial representation of the subhalo model HIGH within the

---

[30] The slope of the subhalo APS slightly changes when sub-subhalos are considered (which are not included in the models LOW and HIGH). The subhalo APS with sub-subhalos (model VAR5) is presented in Appendix C.7.

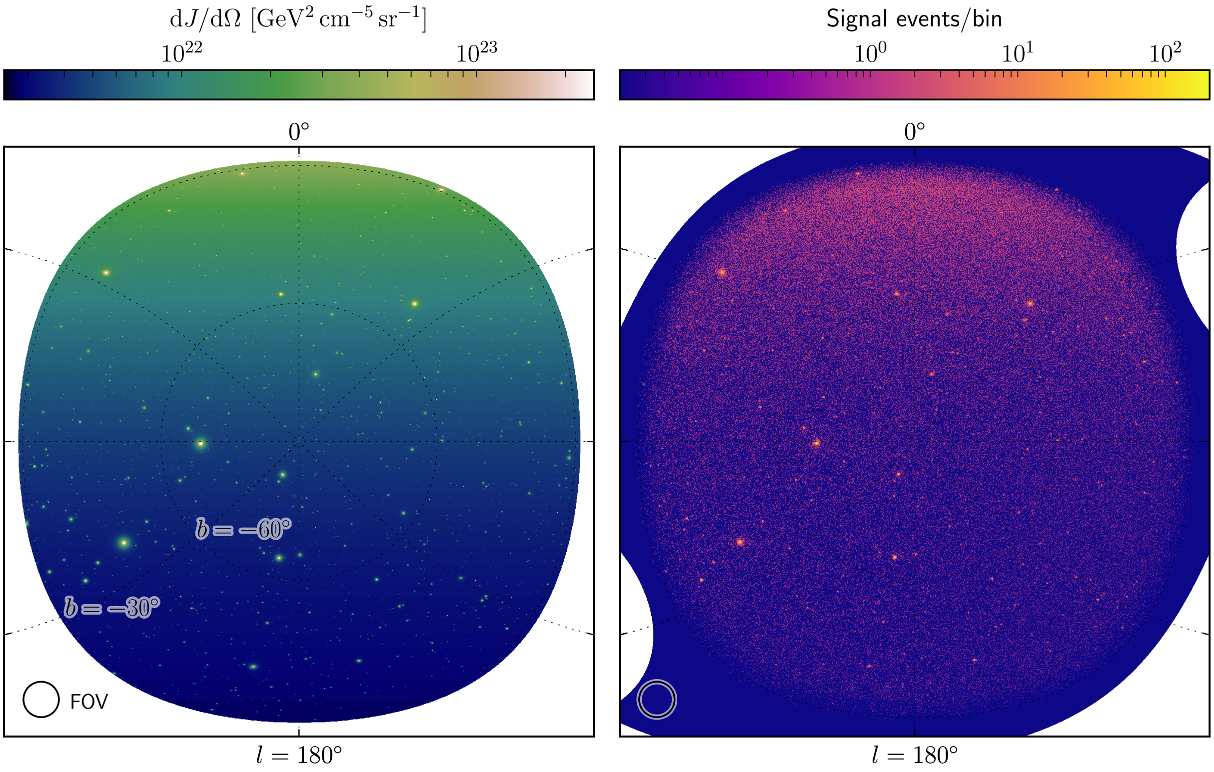

Figure 5.17.: Illustration of the survey simulation. *Left:* J-factor map of Galactic DM (subhalo model HIGH) displayed in Galactic coordinates, with an APS close to the median shown in Figure 5.16. The brightest subhalo in this map is located at $l = 91.1^\circ$, $b = -68.6^\circ$ (latitude counted counter-clockwise) and has a J-factor close to the median brightest subhalos presented in Table 5.1. *Right:* Obtained signal events for $E_\gamma > 30\,\mathrm{GeV}$ from DM annihilation, for a total survey time of $T = 500\,\mathrm{h}$. For illustration purpose, an annihilation spectrum from pure $\chi\chi \to \tau^+\tau^-$ annihilations of $m_\chi = 500\,\mathrm{GeV}$ WIMPs and a cross section of $\langle\sigma v\rangle = 10^{-22}\,\mathrm{cm}^3\,\mathrm{s}^{-1}$ is displayed. Around ~ 100 CPU hours were needed to simulate a total of 4.8×10^6 signal events (13 events/ CPU second). The depicted FOV radius at 500 GeV is 3.5°.

CTA extragalactic survey field.[31] The shown J-factor skymap holds the APS which best represents (out of all simulations) the median power from Figure 5.16. The brightest halo within this map resembles the median brightest halos quoted in Table 5.1: It has a mass of $m = 6.4 \times 10^6\,\mathrm{M}_\odot$, located at a distance of $D = 4.2\,\mathrm{kpc}$ from the observer, and yields the J-factors $\log_{10}(J^\star(\theta_\mathrm{vir},\, 0.1^\circ,\, 0.05^\circ)/\mathrm{GeV}^2\,\mathrm{cm}^{-5}) = 20.2,\, 19.9,\, 19.7$. In Figure 5.17 (left) it can clearly be seen that the diffuse DM emission is not isotropic in this region, but increases by a factor 10 between the part of the region most distant from the GC, compared to the part closest

---

[31] Note that the J-factor map shown in Figure 5.17 is slightly larger than $f_\mathrm{sky} = 0.25$ (by one percent), whereas the CTA survey model from Subsection 5.1.2 (Figure 5.5) effectively covers slightly less than a quarter of the sky ($f_\mathrm{sky} = 23.4\%$), see Subsection 5.1.2.

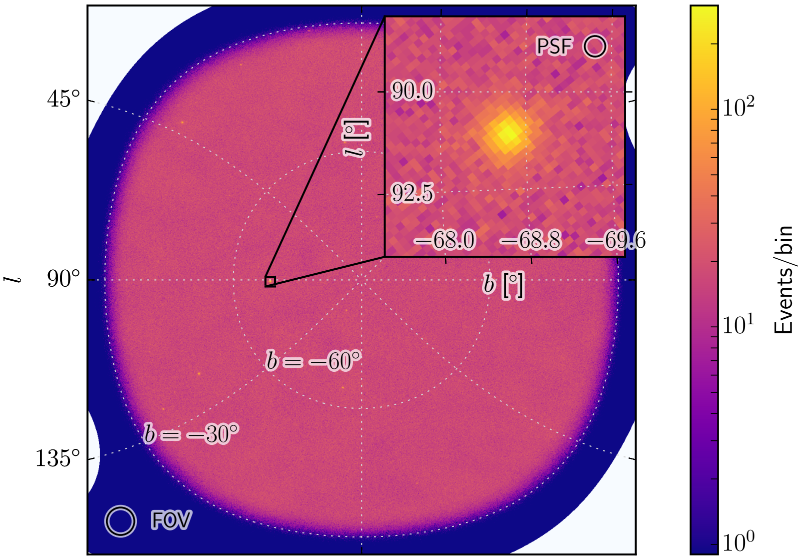

Figure 5.18.: All signal and background events between $30\,\mathrm{GeV} < E < 500\,\mathrm{GeV}$, for a survey with $T = 500\,\mathrm{h}$, $\Delta_{\mathrm{fov}} = 1°$, and the same signal events as shown in Figure 5.17 (right). The map is shown in Galactic coordinates, and contains 2.0×10^8 background events and 4.8×10^6 signal events. The inset shows an area of $2.25° \times 2.25°$ in edge length. The circle illustrating the point spread function (PSF) has a radius of 0.1°, corresponding to the 68% containment radius at $E = 100\,\mathrm{GeV}$. Note that at $E = 30\,\mathrm{GeV}$, the 68% containment radius is as large as 0.2° (see Figure 3.19), such that no spatial extension of the source is visible from this figure with the naked eye. The depicted FOV radius at 500 GeV is 3.5°.

to the GC. Still, the flux from the diffuse emission is $\log_{10}(J_{\mathrm{diffuse\,DM}}(\theta_{0.1°})/\mathrm{GeV}^2\,\mathrm{cm}^{-5}) \leq 17.6$, fainter than the ~ 500 brightest subhalos (compare also to Figure 5.6).

Figure 5.17 (right) shows the simulated signal events from this Galactic J-factor intensity map for the full survey pattern model with $\Delta_{\mathrm{fov}} = 1°$, and the CTA instrument response for Paranal `Prod3 0.5h_avg` cuts. The particle physics model with an annihilation cross section of $\langle \sigma v \rangle = 10^{-22}\,\mathrm{cm}^3\,\mathrm{s}^{-1}$ has been chosen for illustrative purpose, yielding a flux level a hundred times larger than the sensitivity threshold from the analysis in Section 5.2. The simulation of the instrument response relies on the `ctobssim` routine from `ctools`, written in C++ for an optimal performance with parallelization support for OpenMP. Still, the simulation of signal events on a large fraction of the sky is highly expensive, with a speed of ~ 10 events per CPU second (without applying energy dispersion). The simulation of background events is much more efficient (~ 2000 events per CPU second). With this, the simulation of a full survey with background events and signal events above $E = 30\,\mathrm{GeV}$ requires about 130 CPU hours. The simulated events are then binned in energy (eight energy bins between 30 GeV and the WIMP mass) and in sky direction. For the directional binning, events are binned in a HEALPix scheme, orientated in equatorial coordinates, and with $N_{\mathrm{side}} = 2048$, corresponding to a bin size of $\Delta\Omega = 2.50 \times 10^{-7}\,\mathrm{sr} \approx (0.029°)^2$. For displaying purpose, the HEALPix maps are transformed into two-dimensional maps in Cartesian projection, not preserving an equal area $\Delta\Omega$ of each pixel. The event numbers displayed in Figure 5.17 and all subsequent count maps refer to the events in the HEALPix bins. Figure 5.18 shows the signal events from Figure 5.17 (right) together with the residual cosmic-ray background between $30\,\mathrm{GeV} < E < 500\,\mathrm{GeV}$.

Because of the high computational costs, only one signal event map is calculated for the model HIGH, for each combination of 14 WIMP masses between $50\,\mathrm{GeV} < m_\chi < 100\,\mathrm{TeV}$, 20 discrete flux levels (such that different flux levels are not correlated), and the two annihilation channels $\chi\chi \to \tau^+\tau^-$ and $\chi\chi \to b\bar{b}$. The results for the model LOW are then rescaled from the results for the model HIGH. For the background maps, 40 independent realizations are simulated for each of the 8 energy bins, and combined with the signal events.

5.3.5. Likelihood-based recovery of the subhalo angular power spectrum

The APS analysis of γ-ray data serves two purposes: Firstly, to detect a deviation from the APS of background only events and quantify the corresponding C.L., and secondly, to recover the intrinsic source APS. Both can be achieved with a likelihood fit to the power spectrum.

Likelihood function & maximum likelihood ratio: For the analysis of the simulated count maps, the APS of the maps is calculated from the binned HEALPix maps with $N_\mathrm{side} = 2048$. This power spectrum represents the measured intensity APS, $C^I_\mathrm{tot,\,data}(\ell)$, in units of $(\mathrm{Events/bin})^2$. In a given energy interval, the measured APS can be modeled by Equation 5.41,

$$C^I_\mathrm{tot,\,model}(\ell) = (W_\ell^\mathrm{beam})^2\, C^I_\mathrm{sig}(\ell) + C^I_\mathrm{N}\,, \tag{5.48}$$

where the sufficiently fine spatial HEALPix binning guarantees that a suppression from the pixel window function (see Figure 5.19) can be neglected in the multipole range of interest at $\ell \leq 1024$. The beam function W_ℓ^beam of the CTA instrument is calculated from Equation 5.34 for the average point spread function (PSF), $\mathrm{d}P/\mathrm{d}\theta$, in the survey and energy interval under consideration, where the average is taken to be

$$\left\langle \frac{\mathrm{d}P}{\mathrm{d}\theta} \right\rangle(\theta) = \frac{\int_{E_\mathrm{min}}^{E_\mathrm{max}} \int_{\vartheta_\mathrm{cut}} \frac{\mathrm{d}P}{\mathrm{d}\theta}(E,\,\theta,\,\vartheta) \times \frac{\mathrm{d}I}{\mathrm{d}E}(E) \times A_\mathrm{eff}(E,\,\vartheta)\;\; \mathrm{d}\vartheta\,\mathrm{d}E}{\int_{E_\mathrm{min}}^{E_\mathrm{max}} \int_{\vartheta_\mathrm{cut}} \;\frac{\mathrm{d}I}{\mathrm{d}E}(E) \times A_\mathrm{eff}(E,\,\vartheta)\;\; \mathrm{d}\vartheta\,\mathrm{d}E}\,. \tag{5.49}$$

As shown in Figure 3.19, the CTA beam function worsens for large off-axis angles ϑ in the camera field, i.e. it is $\mathrm{d}P/\mathrm{d}\theta = \mathrm{d}P/\mathrm{d}\theta(E,\,\theta,\,\vartheta)$. Adopting the finely spaced survey observation (pattern as illustrated in Figure 5.4), each spot in the sky is observed on average under all offset angles ϑ from the camera center. Then, the effective PSF corresponds to the average over A_eff,

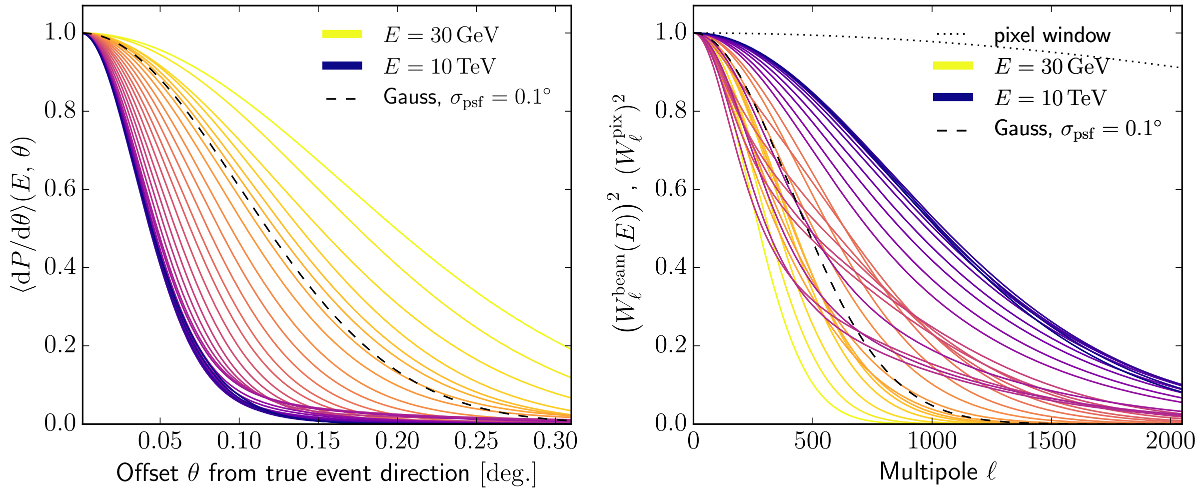

Figure 5.19.: *Left panel:* CTA γ-ray beam functions (PSFs) at different energies, $\langle \mathrm{d}P/\mathrm{d}\theta\rangle(E,\,\theta)$ averaged over $A_{\mathrm{eff}}(E,\,\vartheta)$ from the Paranal `Prod3 0.5h_avg` IRFs. *Right panel:* Corresponding window functions in multipole space. A Gauss curve and its multipole transformation is given for comparison (dashed line). Also, the pixel window function of a finite HEALPix grid with resolution $N_{\mathrm{side}} = 2048$ is shown.

calculated up to $\vartheta_{\mathrm{cut}} = 6°$, in agreement with the cut applied to the event simulation. In a finite energy interval, the effective PSF additionally scales with the energy distribution of signal events from the γ-ray intensity spectrum $\mathrm{d}I/\mathrm{d}E$ in the interval $[E_{\mathrm{min}},\,E_{\mathrm{max}}]$, and the average is also taken over the event rate $\mathrm{d}I/\mathrm{d}E \times A_{\mathrm{eff}}(E,\,\vartheta)$. While the $\mathrm{d}P/\mathrm{d}\theta(E,\,\theta,\,\vartheta)$ are modeled as Gaussian distributions, the resulting $\langle \mathrm{d}P/\mathrm{d}\theta\rangle$ is not Gaussian anymore. The gray curve in Figure 3.19 shows the 68% containment radius of $\langle \mathrm{d}P/\mathrm{d}\theta\rangle$ averaged over $A_{\mathrm{eff}}(E,\,\vartheta)$ from the Paranal `Prod3 0.5h_avg` cuts (and $\mathrm{d}I/\mathrm{d}E \equiv 1$). Figure 5.19 shows the average PSF functions $\langle \mathrm{d}P/\mathrm{d}\theta(E)\rangle$ and differential $W_\ell^{\mathrm{beam}}(E)$ at different energies.

The signal power spectrum, $C^I_{\mathrm{sig}}(\ell)$, is assumed to follow the shape

$$C^I_{\mathrm{sig,\,model}}(\ell;\,C^I_{\mathrm{sig},\,\ell_0},\,s) = C^I_{\mathrm{sig},\,\ell_0} \times \left(\frac{\ell}{\ell_0}\right)^s\,, \tag{5.50}$$

according to the finding from Figure 5.16. In principle, both parameters $C^I_{\mathrm{sig},\,\ell_0}$ and the index s can be left free in the data analysis, measuring any deviation from a flat Poisson-APS ($s = 0$) and indicating the presence of extended or clustered sources. In the following, the sensitivity to detect the subhalos of the model HIGH shall be calculated providing as much information as possible to the likelihood fit, so it is fixed $s \equiv -0.66$. Only one parameter, $C^I_{\mathrm{sig},\,\ell_0}$, is left free in the model (5.50), encoding the intensity level. In case of DM, the intensity scales with the annihilation cross section, $\langle\sigma v\rangle$, such that $C^I_{\mathrm{sig},\,\ell_0}$ can be understood as a function of it, $C^I_{\mathrm{sig},\,\ell_0}(\langle\sigma v\rangle)$. The noise power C^I_{N} is estimated from the number of measured total events, $\widehat{C}^I_{\mathrm{N}} = 4\pi N_{\mathrm{ev}}/N^2_{\mathrm{pix}}$ (recall Equation 5.29). With this, the noise-subtracted and unfolded spectrum is computed,

$$C^I_{\mathrm{sig,\,data}}(\ell) = \left(C^I_{\mathrm{tot,\,data}}(\ell) - \widehat{C}^I_{\mathrm{N}}\right) \times (W^{\mathrm{beam}}_\ell)^{-2}\,, \tag{5.51}$$

and given $C^I_{\mathrm{sig,\,model}}$ and $C^I_{\mathrm{sig,\,data}}$, the binned likelihood function

$$\mathscr{L}(C^I_{\mathrm{sig},\,\ell_0}|\,\vec{C}^I_{\mathrm{sig,\,data}}) = \prod_i^{N_{\mathrm{bins}}} \frac{1}{\sqrt{2\pi\,\langle\sigma^2_{C_{\ell,\,\mathrm{sig}}}\rangle_i}} \exp\left(-\frac{[\langle C^I_{\mathrm{sig,\,data}}\rangle_i - \langle C^I_{\mathrm{sig,\,model}}(C_{\mathrm{sig},\,\ell_0})\rangle_i]^2}{2\,\langle\sigma^2_{C_{\ell,\,\mathrm{sig}}}\rangle_i}\right) \tag{5.52}$$

is constructed. Here, $\vec{C}^I_{\mathrm{sig,\,data}} = C^I_{\mathrm{sig,\,data}}(\ell_1)\ldots C^I_{\mathrm{sig,\,data}}(\ell_N)$ denotes the measured APS at N multipoles between ℓ_1 and ℓ_N, binned in N_{bins} intervals of width $\Delta\ell_i = \ell_{\mathrm{max,\,i}} - \ell_{\mathrm{min,\,i}} + 1$. A binning in multipole space is necessary because neighboring multipoles are correlated. An unbinned Likelihood fit has also been tested, yielding a similar sensitivity (with a $\lesssim 10\%$ worsening). Also, it has been found that an unbinned fit significantly overestimates the reconstructed $\widehat{C}^I_{\mathrm{sig},\,\ell_0}$. This can be understood by the fact that a correlated upward-fluctuation of the $C^I_{\mathrm{sig}}(\ell)$ in the low-ℓ range might suggest a power-law increase for $C^I_{\mathrm{sig,\,model}}$ where none is existent. This effect is less prominent for a binned analysis. A sufficiently coarse binning in $N_{\mathrm{bins}} = 10$ logarithmically spaced multipole bins between ℓ_{min} (specified below) and $\ell_{\mathrm{max}} = 1024$ guarantees that the binned values $\langle C^I_\ell\rangle_i$ fluctuate uncorrelated around the true (signal and/or background) value.

In each bin, the average $\langle C_{\ell,\,\mathrm{sig}}\rangle_i$ is calculated by a weighting through

$$\langle C_{\ell,\,\mathrm{sig}}\rangle_i = \frac{\sum_{\Delta\ell_i} \ell^{-1-0.5\,s}\, C_{\ell,\,\mathrm{sig,\,model}}}{\sum_{\Delta\ell_i} \ell^{-1-0.5\,s}}\,, \tag{5.53}$$

where the sums are taken over the multipoles in the interval $\Delta\ell_i$. The geometric mean is taken as pivot value in each bin,

$$\langle\ell\rangle_i = \sqrt{\ell_{\mathrm{min,\,i}} \times \ell_{\mathrm{max,\,i}}}\,. \tag{5.54}$$

Together with the weighting in Equation 5.53, this allows a correct fit of a power-law source multipole spectrum, i.e. $\langle C_\ell\rangle_i = C(\langle\ell\rangle_i)$ for any C of the shape (5.50). Following Fornasa et al. (2016), the variance in Equation 5.52 is taken from the fitted model, $\langle\sigma^2_{C_{\ell,\,\mathrm{data}}}\rangle_i \approx \langle\sigma^2_{C_{\ell,\,\mathrm{model}}}\rangle_i$. In contrast to the weighting of $\langle C_{\ell,\,\mathrm{sig}}\rangle_i$ according to Equation 5.53, the variance is calculated from Equation 5.44 as the unweighted average in each bin,

$$\langle\sigma^2_{C_{\ell,\,\mathrm{sig}}}\rangle_i = \frac{2}{f_{\mathrm{sky}}\,(\Delta\ell_i)^2} \sum_{\ell\in\Delta\ell_i} \frac{\left(C^I_{\ell,\,\mathrm{sig,\,model}} + \widehat{C}^I_{\mathrm{N}} \times (W^{\mathrm{beam}}_\ell)^{-2}\right)^2}{2\ell+1}\,, \tag{5.55}$$

Note that an additional factor $\Delta\ell_i$ occurs in the denominator because of the binning. The variance $\langle\sigma^2_{C_{\ell,\,\mathrm{sig}}}\rangle_i$ becomes larger when a signal $C^I_{\ell,\,\mathrm{sig,\,model}}$ is present. In the absence of a signal component in the variance, the variance is written as $\langle\sigma^2_{C_{\ell,\,\mathrm{sig}}}(C^I_{\mathrm{sig},\,\ell_0}=0)\rangle_i \equiv \langle\sigma^2_{C_{\ell,\,\mathrm{sig}}}(0)\rangle_i$. Because the variance (5.55) is a function of the signal power to be fitted, the fitting is done iteratively: The likelihood function (5.52) is first maximized for an error $\langle\sigma^2_{C_{\ell,\,\mathrm{sig}}}(0)\rangle_i$, and then the error is adapted according to the fit until convergence is reached. Maximizing the likelihood function, Equation 5.52, under the constraint of the hypothesis of only isotropic background, $C^I_{\mathrm{sig},\,\ell_0}(\langle\sigma v\rangle)=0$, gives a constant,

$$\max \mathscr{L}(C^I_{\mathrm{sig},\,\ell_0}=0\,|\,\vec{C}^I_{\mathrm{sig,\,data}}) = \prod_i^{N_\mathrm{bins}} \frac{1}{\sqrt{2\pi\,\langle\sigma^2_{C_{\ell,\,\mathrm{sig}}}(0)\rangle_i}} \exp\left(-\frac{\langle C^I_{\mathrm{sig,\,data}}\rangle_i^2}{2\,\langle\sigma^2_{C_{\ell,\,\mathrm{sig}}}(0)\rangle_i}\right). \tag{5.56}$$

The test statistic, TS $= -2\log\lambda$, for the presence of a signal in the data reads

$$\begin{aligned}\mathrm{TS} &= -2\,\log\left(\frac{\mathscr{L}(C^I_{\mathrm{sig},\,\ell_0}=0\,|\,\vec{C}_{\mathrm{tot,\,data}})}{\mathscr{L}(\widehat{C}^I_{\mathrm{sig},\,\ell_0}\,|\,\vec{C}_{\mathrm{tot,\,data}})}\right)\\ &= \sum_i^{N_\mathrm{bins}}\left(\frac{[\langle C^I_{\mathrm{sig,\,data}}\rangle_i - \langle C^I_{\mathrm{sig,\,model}}(C_{\mathrm{sig},\,\ell_0})\rangle_i]^2}{\langle\sigma^2_{C_{\ell,\,\mathrm{sig}}}\rangle_i} - \frac{\langle C^I_{\mathrm{sig,\,data}}\rangle_i^2}{\langle\sigma^2_{C_{\ell,\,\mathrm{sig}}}(0)\rangle_i} + \log\frac{\langle\sigma^2_{C_{\ell,\,\mathrm{sig}}}\rangle_i}{\langle\sigma^2_{C_{\ell,\,\mathrm{sig}}}(0)\rangle_i}\right),\end{aligned} \tag{5.57}$$

where $\widehat{C}^I_{\mathrm{sig},\,\ell_0}$ is the maximum likelihood estimator for the signal APS in the data. Lastly, from $\widehat{C}^I_{\mathrm{sig},\,\ell_0}$ the full-sky equivalent APS is obtained by $\widehat{C}^I_{\mathrm{sig},\,\ell_0,\,\text{full-sky}} = \widehat{C}^I_{\mathrm{sig},\,\ell_0}/f_\mathrm{sky}$ (Equation 5.39).

TS distribution and angular power spectrum of the residual cosmic-ray background: The estimator $\widehat{C}^I_\mathrm{N} = 4\pi N_\mathrm{ev}/N^2_\mathrm{pix}$ in Equation 5.57 relies on the assumption that the background events are isotropically distributed on the full sphere. However, as shown in Subsection 5.3.2, a limited sky coverage introduces masking artifacts in the APS. Additionally, it has been shown in Figure 5.5 that the discrete spacing of pointing positions introduces a variation of the exposure. Therefore, the range of multipoles where the assumption of $C^I_\mathrm{N} = \widehat{C}^I_\mathrm{N}$ is valid must be constrained. In Figure 5.20, the APS of residual cosmic-ray background events (for Paranal `Prod3 0.5h_avg` cuts) in the CTA survey field, $T = 500\,\mathrm{h}$, and $\Delta_\mathrm{fov} = 1°$ is presented for different energy intervals. The largest deviation at low multipoles is caused by the sky window of the limited survey field and accounts for almost all artifacts visible in the lower right plot. The lower right figure shows only high-energy events with $E > 5.7\,\mathrm{TeV}$. At these energies, the CTA field of view (FOV) reaches $\vartheta_\mathrm{fov} \approx 4.5°$ (see Table 3.2), resulting in an almost homogeneous exposure. This changes at lower energies, where the FOV radius becomes smaller: A bump rises in the APS at $\ell \approx 80$, corresponding to an angular scale of $180°/\ell \approx 2°$. To exclude the

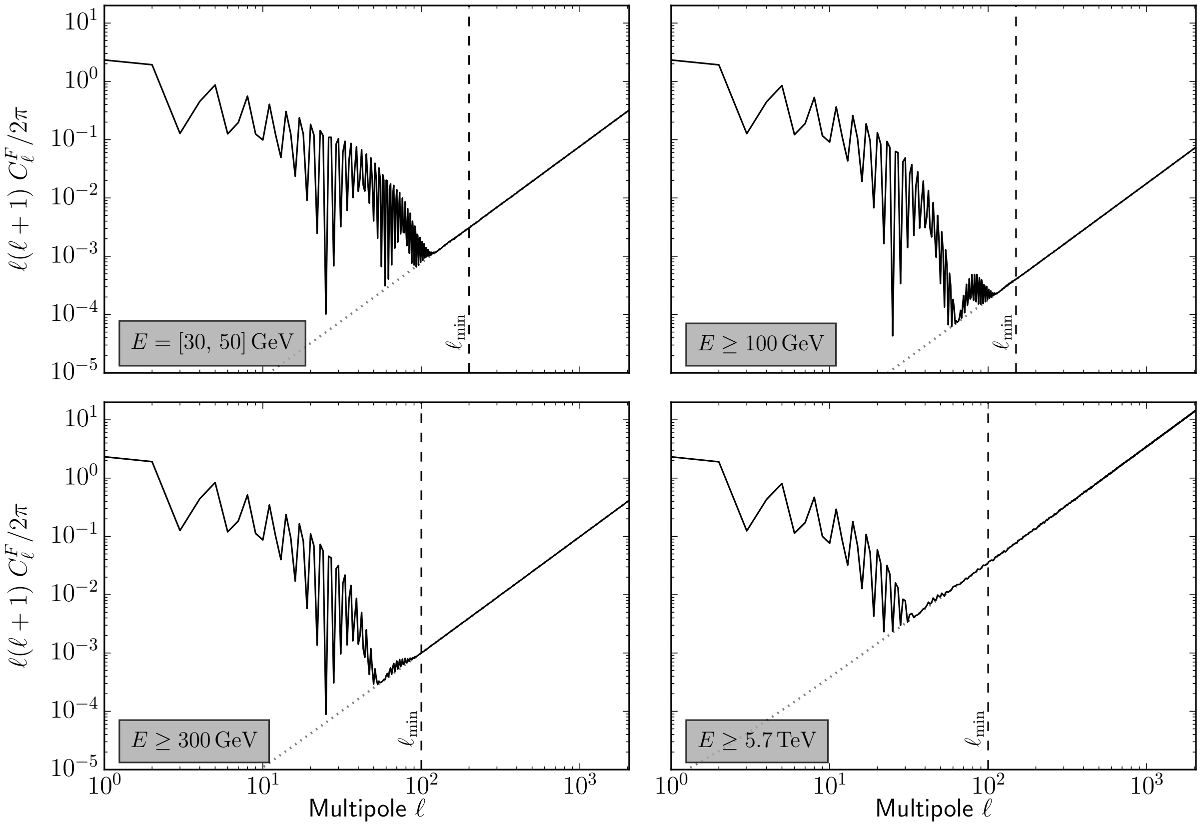

Figure 5.20.: APS of the isotropic background events in the CTA survey field and for an observation spacing of $\Delta_{\mathrm{fov}} = 1°$. The APS is shown for four different energy intervals. The dashed lines denote the lower cut in ℓ-space for each of the four lower energy bounds. The figures show the median $\widetilde{C}_\ell^F$ (black lines), and the 68% C.I. (gray shaded bands) based on 20 simulations each. The gray-dotted lines mark the estimator $\widehat{C}_{\mathrm{N}}^I = 4\pi N_{\mathrm{ev}}/N_{\mathrm{pix}}^2$ computed from the number of events in each energy interval.

contamination of the multipoles at low ℓ, an energy-dependent cut, $\ell_{\mathrm{min}} = \ell_{\mathrm{min}}(E_{\mathrm{min}})$, is applied in ℓ-space, as a function of the lower bound of the analyzed energy bin, E_{min}. The following cuts are chosen: $\ell_{\mathrm{min}}(E_{\mathrm{min}} < 100\,\mathrm{GeV}) = 200$, $\ell_{\mathrm{min}}(100\,\mathrm{GeV} \leq E_{\mathrm{min}} < 200\,\mathrm{GeV}) = 150$, and $\ell_{\mathrm{min}}(E_{\mathrm{min}} \geq 200\,\mathrm{GeV}) = 100$. These cuts are also shown in Figure 5.20 as vertical dashed lines. At high ℓ, the analysis is restricted to $\ell_{\mathrm{max}} \leq 1024$ to avoid uncertainties from the modeling of the beam window function.

Having limited the multipole range, the TS distribution is investigated when applying the likelihood ratio test to background events only. Therefore, 10^3 samples of different sets of background events for the CTA survey are simulated for a $\Delta_{\mathrm{fov}} = 1°$ spacing, and the likelihood ratio test (5.57) is applied. The TS distributions for different energy intervals and cuts ℓ_{min} are

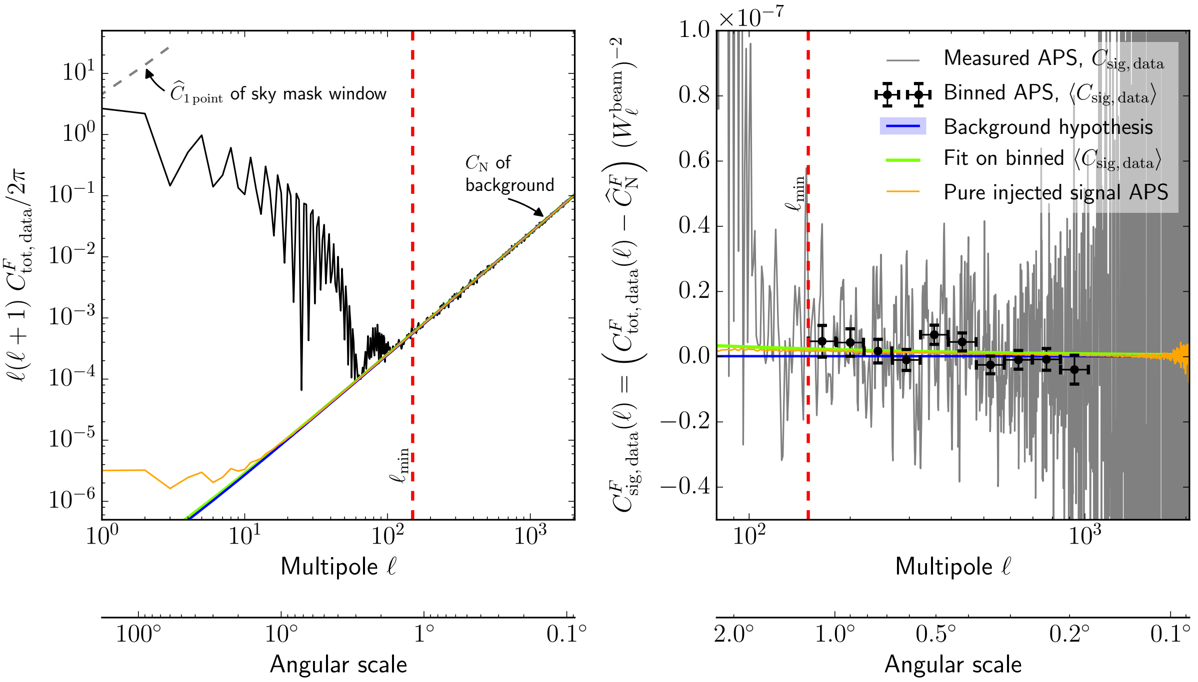

Figure 5.21.: Illustration of the APS likelihood fit at the 95% C.L. sensitivity threshold for $m_\chi = 500\,\mathrm{GeV}$ and $\chi\chi \to \tau^+\tau^-$ annihilation spectrum, and the subhalo model HIGH. The shown spectrum is evaluated in the most sensitive energy interval between [107, 500] GeV, comprising $N_{\mathrm{sig}} = 9.99 \times 10^4$ signal events, and $N_{\mathrm{bck}} = 9.33 \times 10^7$ background events. The spacing is $\Delta_{\mathrm{fov}} = 1°$, and $l_{\min} = 150$. The left plot shows the global spectrum, whereas the right plot shows a closeup of the interval $80 \leq \ell \leq 2048$. In the figure, all fluctuation APS are given with respect to the total events, $C^F = C^I \times N^2_{\mathrm{pix}}/(N_{\mathrm{bck}} + N_{\mathrm{sig}})^2$.

shown in Figure C.8 in Appendix C.8. The distributions are found to be largely independent of the energy threshold and source energy spectrum and fairly reproduce the scaling $p(\mathrm{TS}) \approx 0.5\,\delta(\mathrm{TS}) + 0.5\,\chi^2_{k=1}(\mathrm{TS})$ from Equation 5.12 for one signal degree of freedom.

Illustration of the likelihood fit: In Figure 5.21, the likelihood fit is illustrated at the 95% C.L. sensitivity threshold, for one out of the 40 independent background samples, one out of the 2 × 14 studied WIMP models, and the subhalo model HIGH. The black-solid line shows the ‘measured’ angular power spectrum of the mock signal and background events, after subtracting the noise APS and after unfolding. The blue band indicates the expected error, $\sigma_{C_{\ell,\,\mathrm{sig}}}(C_{\ell,\,\mathrm{sig}} = 0)$ for no signal present in the unbinned APS. For the unbinned error, the variance band is based on the scaling $\sigma_{C_\ell,\,\mathrm{part\text{-}sky}} \approx 1.11\,\sigma_{C_\ell,\,\mathrm{full\text{-}sky}}$ empirically found in Subsection 5.3.2 for $f_{\mathrm{sky}} \approx 0.25$. The black dots shows the binned APS, with the error after binning and maximizing the likelihood, with the green curve showing the corresponding likelihood fit to the binned $\langle C_{\ell,\,\mathrm{sig}}\rangle_i$. The orange line denotes the APS of the injected signal events from DM annihilation only. It can be seen that this fit slightly overestimates the injected C_{sig} from the subhalo sky map, Figure 5.17. Knowing the number of injected DM events,[32] the DM fluctuation APS can be reconstructed from the fitted intensity power spectrum $\widehat{C}^{I}_{\mathrm{sig},\,\ell_0}$. For the example shown in Figure 5.21,

$$\widehat{C}^{F}_{\mathrm{sig},\,\ell=100,\,\mathrm{full\text{-}sky}} = f_{\mathrm{sky}} \times \widehat{C}^{I}_{\mathrm{sig},\,\ell=100\,\mathrm{part\text{-}sky}} \times (N_{\mathrm{pix}}/N_{\mathrm{sig}})^2 \overset{f_{\mathrm{sky}}=0.234}{=} (5.4 \pm 3.5) \times 10^{-4}$$

in agreement with the input spectrum of the subhalo model HIGH in Figure 5.16.

Validation of the fit on the signal APS and PSF: Before presenting the result of the APS analysis in terms of a sensitivity to the DM annihilation cross section, it is investigated whether the maximum likelihood fit correctly recovers the injected signal APS. This may indicate possible errors in the fitting procedure and the modeling of the beam window functions. For a similar analysis, Fornasa et al. (2016) found an underestimation of $\widehat{C}_{\mathrm{sig}}$, using the same likelihood function, and a similar (however opposite) effect is found in this analysis. The gray histogram in Figure 5.22 shows the reconstructed values for $\widehat{C}^{F}_{\mathrm{sig},\,\ell_0}$ for all of the 8 energy bins × 14 WIMP masses × 40 background simulation runs = 4480 likelihood fits for the $\chi\chi \rightarrow \tau^+\tau^-$ WIMP annihilation model at the 95% C.L.. Not all energy bins have a detection in the tested range of flux levels, such that only 3298 fits return a value for $\widehat{C}^{F}_{\mathrm{sig},\,\ell_0}$. In orange, the fit to signal events only from 83 independent[33] maps of simulated events is shown. From Figure 5.22 follows that for DM signal events with and without background, the expected input fluctuation power is well reconstructed by the fits (dashed vertical lines), however with a $\sim 15\%$ upward-bias compared to the solid reference line, $C^{F}_{\mathrm{sig},\,\ell_0} = 3.3 \times 10^{-4}$. One explanation for the remaining slight upward-bias is that upward fluctuations of the ℓ preferably affect the positively constrained fit. Additionally, the estimator $\widehat{C}^{F}_{\mathrm{sig},\,\ell_0}$ is obtained from a power-law fit to an input subhalo power spectrum which does not show a strict power-law behavior. To investigate this further, 100 skymaps with background events and 314 point sources, randomly distributed in the survey field and with equal flux, have been simulated and the expected flat multipole spectrum $\widehat{C}^{F}_{\mathrm{P},\,\mathrm{sig},\,\mathrm{full\text{-}sky}} = f_{\mathrm{sky}}\, 4\pi/314 = 10^{-2}$ has been reconstructed. Like in the case of the subhalo APS, an overestimation of the reconstructed $\widehat{C}^{F}_{\mathrm{P},\,\mathrm{sig},\,\mathrm{full\text{-}sky}}$ by (even slightly larger) $\sim 20\%$ is found, rather independent of the sources' flux level. No clear reason for the overestimation could be finally found, and it is suggested to be aware of this potential issue when applying an APS analysis to CTA data.

---

[32] Recall that it is principally extremely difficult to measure the DGRB *intensity* with Earth-bound instruments and that the number of signal events cannot be inferred from an APS measurement of "real data events" alone.

[33] This is not strictly correct, as event maps of overlapping energy intervals from the same simulations are contained in this set of 'independent' maps.

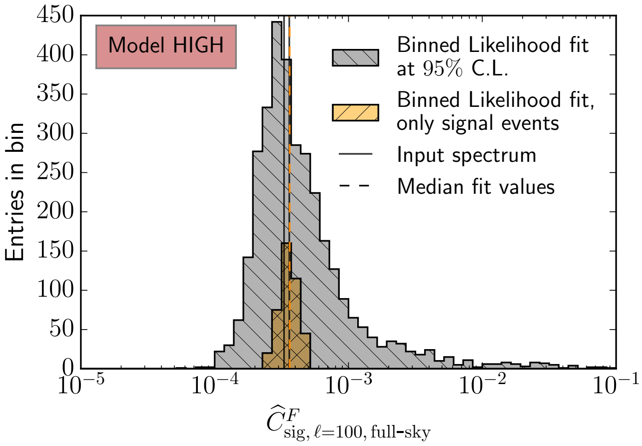

Figure 5.22.: Reconstructed subhalo fluctuation APS $\widehat{C}^F_{\mathrm{sig},\,\ell=100,\,\mathrm{full\text{-}sky}}$, from the simulated Galactic DM distribution (underlying a $\chi\chi \to \tau^+\tau^-$ energy spectrum). The gray histogram relies on 3298 converged fits. The orange histogram shows 83 fits, and is vertically stretched by a factor 5 for display purpose.

5.3.6. Results: Sensitivity to Galactic DM annihilation in the γ-ray APS

APS sensitivity to DM annihilation spectra $\chi\chi \to \tau^+\tau^-$ and $\chi\chi \to b\bar{b}$: Figure 5.23 presents the sensitivity of the CTA extragalactic survey to detect Galactic DM as anisotropies in the APS of the data, based on the presented analysis method. Because the background APS is subject to fluctuations, for each WIMP model the sensitivity is calculated for 40 background samples, and the median sensitivity is given as ensemble average. The sensitivity is quoted in terms of the annihilation cross section, $\langle\sigma v\rangle$, analogous to the results from Section 5.2:

- In the left panel of Figure 5.23, the sensitivity is presented for the two benchmark DM annihilation channels considered throughout this thesis. The solid lines represent the sensitivity to the median APS of Figure 5.16. The shaded bands denote the 68% (95%) statistical uncertainty around this median, originating from the APS variance. These bands have been computed by rescaling the median to the APS uncertainty bands in Figure 5.16, according to:

$$\frac{\langle\sigma v\rangle_1}{\langle\sigma v\rangle_2} = \frac{I_1}{I_2} \approx \sqrt{\frac{C_2^F(\ell = 200)}{C_1^F(\ell = 200)}}\,. \tag{5.58}$$

  Comparing these bands with Figure 5.7, it can be seen that the variance is slightly less for the APS analysis. This can be understood as the fainter halos contributing to the APS somewhat balance the behavior of the population ensemble, which is subject to less scattering than when only considering the brightest object alone.

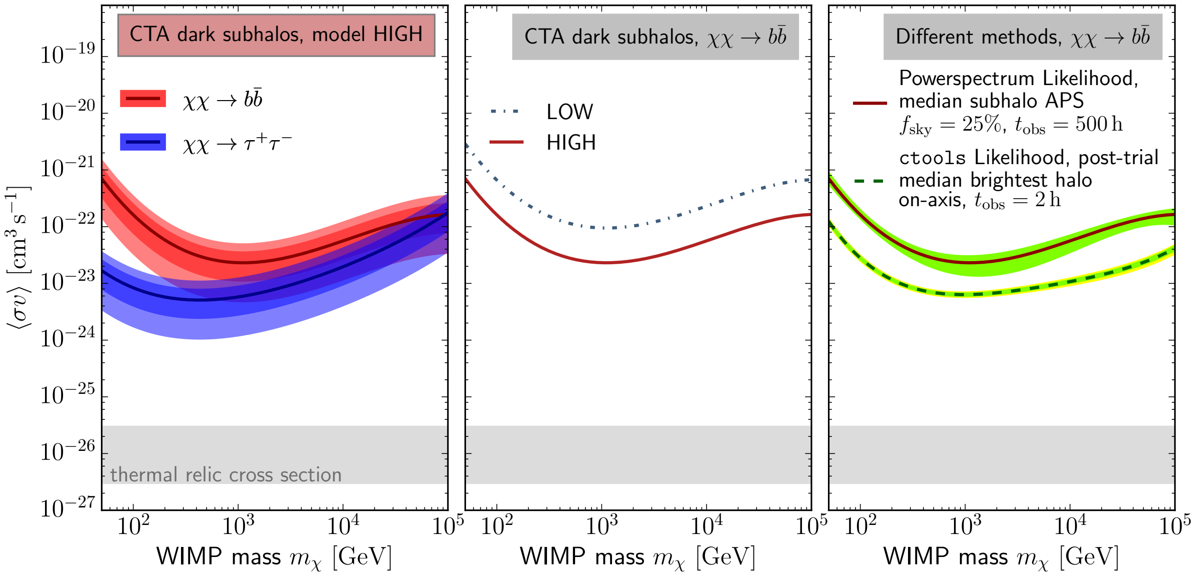

Figure 5.23.: Sensitivity of the CTA extragalactic survey to detect Galactic DM as anisotropies in the APS. The calculation relies on the Paranal `Prod3 0.5h_avg` instrument response, a total survey time of $T = 500\,$h for rastering $f_{\rm sky} = 25\%$ of the sky with $\Delta_{\rm fov} = 1°$. All sensitivities are given at the 95% C.L.. *Left:* median (solid lines) and 68% (95%) C.I. J-factor (model HIGH) uncertainty around the median (colored areas) for annihilation into $b\bar{b}$ and $\tau^+\tau^-$. *Center:* comparison of the subhalo models LOW and HIGH. *Right:* Comparison of the APS analysis to the `ctlike` analysis from Section 5.2. The figure also shows the 68% (green) and 95% (yellow, only for `ctlike`) C.I. bands due to the background fluctuation.

- The central panel shows the impact of the subhalo model uncertainty onto the sensitivity. To save computational costs, the simulation procedure has not been repeated for a J-factor-map of the model LOW. Instead, the sensitivity is rescaled from the median of model HIGH in Figure 5.16 to model LOW by again using the relation (5.58) at $\ell = 200$. As argued before, the APS of the model LOW is more contaminated by the Galactic halo power than the model HIGH, and a rigorous calculation might result in a slightly different result. In any case, a worsening of the sensitivity of around one order of magnitude is obtained, exactly what has been found only when considering the median brightest halos alone for both models in Section 5.2.

- Lastly, the right panel compares the two different methods assessed in this thesis. The result from the APS sensitivity is compared to the `ctlike` sensitivity to the brightest halo for the observation setup which closest matches the APS study: An on-axis observation of the brightest halo over $t_{\rm obs} = 2\,$h, with the same Paranal `Prod3 0.5h_avg` cuts, and corrected for the trials on $f_{\rm sky} \approx 0.25$. This figure shows a factor 5 worse sensitivity of the

> APS calculation compared to the `ctlike` sensitivity – recall that optimistically, a factor $\sim \sqrt{2}$ improvement has been expected at the opening of this section on page 133. This finding is further discussed below. The right panel also displays the 68% (green) and 95% (yellow) C.I. of the sensitivity due to the background fluctuation. Because only 40 background samples have been simulated for the APS analysis, no 95% C.I. is given.

In Figure 5.23 (right), a factor 5 difference of the sensitivities to DM subhalos between the methods investigated in Sections 5.2 and 5.3 is found. Several reasons may contribute to this difference: Firstly, the brightest-halo analysis from Section 5.2 relies on a trials correction to extrapolate from a benchmark template observation to a survey sensitivity. As stated on page 123, a minimal number of trials has been adopted, resulting in a rather optimistic sensitivity. For a factor ~ 100 more trials over the survey field, a somewhat closer match of the methods is obtained. However, to more robustly pinpoint this issue, a blind search for the brightest object has to be rigorously studied: For example, the concept of trials is not existent in a Likelihood analysis with released source coordinates, and the blind search penalty manifests itself in the corresponding test statistic. Secondly, for the brightest halo search, the unbinned Likelihood is calculated on an event-to-event basis, whereas in the anisotropy analysis only coarse energy bins are formed, and only a binned multipole range is considered. This can be understood as discarding more information in the latter case than in the brightest-halo search.

In any case, it is found that the applied APS analysis is not able to significantly improve the detection prospects with CTA towards Galactic DM subhalos. Moreover it is argued in the conclusion that a non-global search for single objects allows the follow-up observation of potential source locations, which is not possible in the search for a global anisotropy. After commenting on some further details on the results of the anisotropy search for DM subhalos, it is shown that an anisotropy analysis of CTA data is nevertheless useful in a broader astrophysical context.

In Table 5.4, the results depicted in Figure 5.23 are studied in more detail for selected WIMP masses and the two annihilation channels, $\chi\chi \rightarrow b\bar{b}$ and $\chi\chi \rightarrow \tau^+\tau^-$. The first two columns show the energy interval $[E_{\mathrm{thresh}}, m_\chi]$, over which the APS analysis gives the most sensitive result. The upper margin of the interval is always fixed to the WIMP mass itself. The following three columns give the number of signal events at the 95% C.L., the number of background events in this energy interval and the background rate. The next three columns finally give the sensitivity at the 95% C.L. in terms of intensity within the considered energy interval, the intensity expressed as a fraction of the DGRB in this interval, and the annihilation cross section as presented in Figure 5.23. The intensity as a fraction of the DGRB, f_{DGRB}, is given relative to the best fit by Abdo et al. (2010), Equation 5.14 (first value), and relative to the model providing the largest DGRB level by Ackermann et al. (2015b), Equation 5.13 (second value). It can be

$\chi\chi \to b\bar{b}$, subhalo model HIGH, `Prod3 0.5h_avg`								
m_χ [GeV]	E_thresh [GeV]	N_sig $\times 10^5$	N_bck $\times 10^7$	$\dot{N}_\text{bck}$ [Hz]	Median 95% C.L. sensitivity			
					DM intensity $[\text{cm}^{-2}\,\text{s}^{-1}\,\text{sr}^{-1}]$	f_DGRB	$\langle\sigma v\rangle$ $[\text{cm}^3\,\text{s}^{-1}]$	$C^F_{f_\text{DGRB}\equiv 1}$
50	30	0.96	2.61	15.3	2.4×10^{-6}	$10^3/10^3$	7.0×10^{-22}	3.5×10^2
100	30	1.98	10.1	58.8	1.2×10^{-6}	450/330	1.6×10^{-22}	3.7×10^1
300	30	2.58	19.3	113.1	1.3×10^{-7}	42/32	3.9×10^{-23}	3.4×10^{-1}
500	30	2.68	20.4	119.5	4.6×10^{-8}	14/11	2.8×10^{-23}	4.1×10^{-2}
1000	30	2.26	21.0	122.7	1.3×10^{-8}	3.8/3.1	2.3×10^{-23}	3.1×10^{-3}
5000	30	1.86	21.3	124.5	1.1×10^{-9}	0.3/0.3	3.7×10^{-23}	2.5×10^{-5}
10^4	800	0.24	0.47	2.7	2.0×10^{-10}	–	5.6×10^{-23}	–
10^5	1500	0.18	0.25	1.5	1.1×10^{-11}	–	1.7×10^{-22}	–

$\chi\chi \to \tau^+\tau^-$, subhalo model HIGH, `Prod3 0.5h_avg`								
m_χ [GeV]	E_thresh [GeV]	N_sig $\times 10^5$	N_bck $\times 10^7$	$\dot{N}_\text{bck}$ [Hz]	Median 95% C.L. sensitivity			
					DM intensity $[\text{cm}^{-2}\,\text{s}^{-1}\,\text{sr}^{-1}]$	f_DGRB	$\langle\sigma v\rangle$ $[\text{cm}^3\,\text{s}^{-1}]$	$C^F_{f_\text{DGRB}\equiv 1}$
50	30	0.91	2.61	15.3	6.3×10^{-8}	37/27	1.8×10^{-23}	2.3×10^{-1}
100	30	1.70	10.1	58.8	6.4×10^{-8}	23/17	8.4×10^{-24}	1.0×10^{-1}
300	66	1.92	14.4	84.0	7.7×10^{-9}	8.0/7.4	5.3×10^{-24}	1.8×10^{-2}
500	107	1.26	9.33	54.5	2.9×10^{-9}	6.0/7.1	5.3×10^{-24}	1.6×10^{-2}
1000	210	0.68	3.20	18.7	8.7×10^{-10}	4.6/10.6	6.2×10^{-24}	3.7×10^{-2}
5000	880	0.22	0.37	2.1	9.4×10^{-11}	–	1.3×10^{-23}	–
10^4	1600	0.17	0.21	1.2	4.2×10^{-11}	–	2.1×10^{-23}	–
10^5	5700	0.09	0.06	0.3	7.4×10^{-12}	–	1.9×10^{-22}	–

Table 5.4.: Sensitivity to the APS for DM annihilation spectra, subhalo model HIGH, and Paranal `Prod3 0.5h_avg` cuts. All events and fluxes are integrated in the energy interval $[E_\text{thresh}, m_\chi]$. The fraction f_DGRB is given relative to the best fit from Abdo et al. (2010) (first value), and the fit model with the highest γ-ray intensity attributed to the DGRB, model B by Ackermann et al. (2015b) (second value). The livetime of the total observation is $T_\text{live} = 475\,\text{h}$, and only events within $\vartheta_\text{cut} = 6°$ are considered.

seen that for a detection of the specific WIMP model, the γ-ray flux from DM considerably overshoots the intensity level of the DGRB in the respective energy interval in all cases but for a $m_\chi \gtrsim 5\,\text{TeV}$ particle annihilating into bottom quarks. No numbers are given for spectra for which most of the emission originates above $E_\gamma \gtrsim 1\,\text{TeV}$, because the numbers would rely on extrapolating beyond the available data from the *Fermi*-LAT. It follows that most models are already excluded by the level of measured DGRB intensity. However, the total Galactic DM intensity level quoted here for the model HIGH is driven by the diffuse emission from the Galactic halo and from unresolved substructures, which are dependent on the model of these emissions. Therefore, the last column in Table 5.4 gives the result in a reversed way: The degree of intrinsic anisotropy, C^F, of Galactic DM is given, for which a DM model would not overshoot

<table>
<tr><th colspan="7">DGRB spectrum (Abdo et al., 2010),
subhalo model HIGH, <code>Prod3 0.5h_avg</code></th></tr>
<tr><th rowspan="2">E_{thresh} [GeV]</th><th rowspan="2">N_{sig}</th><th rowspan="2">N_{bck}</th><th rowspan="2">$\dot{N}_{\mathrm{bck}}$ [Hz]</th><th colspan="3">Median 95% C.L. sensitivity</th></tr>
<tr><th>Intensity $[\mathrm{cm^{-2}\,s^{-1}\,sr^{-1}}]$</th><th>$f_{\mathrm{DGRB}}$</th><th>$C^F_{f_{\mathrm{DGRB}}\equiv 1}$</th></tr>
<tr><td>100</td><td>1.37×10^5</td><td>1.13×10^8</td><td>66.1</td><td>2.2×10^{-9}</td><td>3.6</td><td>$4.2^{+6.6}_{-2.1} \times 10^{-3}$</td></tr>
<tr><td>300</td><td>5.25×10^4</td><td>2.02×10^7</td><td>11.8</td><td>3.9×10^{-10}</td><td>3.0</td><td>$3.0^{+4.1}_{-1.1} \times 10^{-3}$</td></tr>
<tr><td>500</td><td>3.56×10^4</td><td>9.28×10^6</td><td>5.4</td><td>1.8×10^{-10}</td><td>2.8</td><td>$2.6^{+4.1}_{-0.7} \times 10^{-3}$</td></tr>
</table>

<table>
<tr><th colspan="7">DGRB spectrum (Ackermann et al., 2015b, model B),
subhalo model HIGH, <code>Prod3 0.5h_avg</code></th></tr>
<tr><th rowspan="2">E_{thresh} [GeV]</th><th rowspan="2">N_{sig}</th><th rowspan="2">N_{bck}</th><th rowspan="2">$\dot{N}_{\mathrm{bck}}$ [Hz]</th><th colspan="3">Median 95% C.L. sensitivity</th></tr>
<tr><th>Intensity $[\mathrm{cm^{-2}\,s^{-1}\,sr^{-1}}]$</th><th>$f_{\mathrm{DGRB}}$</th><th>$C^F_{f_{\mathrm{DGRB}}\equiv 1}$</th></tr>
<tr><td>100</td><td>1.40×10^5</td><td>1.13×10^8</td><td>66.1</td><td>3.4×10^{-9}</td><td>7.1</td><td>$1.7^{+2.6}_{-0.8} \times 10^{-2}$</td></tr>
<tr><td>300</td><td>–</td><td>–</td><td>–</td><td>$> 4.6 \times 10^{-10}$</td><td>>15</td><td>$> 6 \times 10^{-2}$</td></tr>
<tr><td>500</td><td>–</td><td>–</td><td>–</td><td>$> 6.3 \times 10^{-11}$</td><td>>15</td><td>$> 6 \times 10^{-2}$</td></tr>
</table>

Table 5.5.: Sensitivity to the APS for a generic featureless DGRB spectrum, subhalo model HIGH, and Paranal `Prod3 0.5h_avg` cuts. All events and fluxes are integrated in the energy interval $[E_{\mathrm{thresh}}, m_\chi]$. The livetime of the total observation is $T_{\mathrm{live}} = 475\,\mathrm{h}$, and only events within $\vartheta_{\mathrm{cut}} = 6°$ are considered. The $C^F_{f_{\mathrm{DGRB}}\equiv 1}$ are given with their 68% C.I. around the median sensitivity from background fluctuation.

the DGRB level in the respective energy interval. This fluctuation APS consistent with the DGRB measurement by Ackermann et al. (2015b), $C^F_{f_{\mathrm{DGRB}}\equiv 1}$, is calculated as

$$C^F_{f_{\mathrm{DGRB}}\equiv 1} = C^F_{\mathrm{HIGH},\,\ell=100} \times \left(\frac{I_{\mathrm{DM,\,sens}}}{I_{\mathrm{DGRB}}}\right)^2 = C^F_{\mathrm{HIGH},\,\ell=100} \times f^2_{\mathrm{DGRB}}\,, \tag{5.59}$$

with the DM intensity $I_{\mathrm{DM,\,sens}}$ and f_{DGRB} both as listed in Table 5.4. This reversed approach of interpreting the sensitivity to anisotropies is studied further in the next paragraph.

APS sensitivity to the generic DGRB spectrum: It is another important question to ask whether other source populations could cause detectable fluctuations in the VHE DGRB spectrum. Therefore, the analysis is repeated for a generic DGRB spectrum, with the spectral shape given by Equation 5.13. A calculation for the spectrum from Abdo et al. (2010), given by Equation 5.14, allows a comparison of this analysis with the results from Ripken et al. (2014), who based their calculations on the same spectrum. For the spatial shape and flux levels of sources, the subhalo scenario model HIGH is retained, and it is assumed that the sensitivity to $C^F_{\mathrm{HIGH},\,\ell=100}$ matches the sensitivity to a flat-multipole source class with $C^F_{\mathrm{P}} = \mathrm{const.}$[34] The

---

[34] The analysis has also been performed for 314 randomly distributed point sources in the survey field, already mentioned on page 158 in the context of the fitting validation. In fact, this confirmed that comparable

Source class	fluctuation APS, $C^F_{\ell=100}$	Reference
Millisecond pulsars	3×10^{-2}	Siegal-Gaskins et al. (2011)
Misaligned AGN	$\gtrsim 10^{-3}$	Di Mauro et al. (2014b)
Galactic DM annihilation (HIGH)	3×10^{-4}	This thesis
Unresolved blazars	2×10^{-4}	Ando et al. (2007)
Galactic DM annihilation (LOW)	3×10^{-5}	This thesis
Extragalactic DM annihilation	$\gtrsim 10^{-5}$	Fornasa et al. (2013)
Star-forming galaxies (SFG)	2×10^{-7}	Ando and Pavlidou (2009)

Table 5.6.: Angular power of unresolved members of different source classes, relative to their average intensity, $C^F_\ell = C^I_\ell / \langle I \rangle^2$. Table adapted from Ackermann et al. (2012a), with updated values and references.

results are shown in Table 5.5, for the spectrum from (Abdo et al., 2010, upper panel), and the recent measurement from Ackermann et al. (2015b, lower panel). Three different fixed low-energy thresholds E_{thresh} have been chosen, and the sensitivity is given to the integrated spectrum above E_{thresh}.

From the upper table (blue-shaded row), it can be seen that a fluctuation power of $C^F_{\text{P}} = 2 \times 10^{-3}$ in the DGRB above 300 GeV can be probed with CTA, assuming the pure power-law spectrum from Abdo et al. (2010). Adopting a cut-off of the spectrum above $E_{\text{c}} \approx 200$ GeV, as measured by Ackermann et al. (2015b), the sensitivity worsens by a factor 2 in flux, and a sensitivity to $C^F_{\text{P}} = 1 \times 10^{-3}$ above 100 GeV is obtained (green-shaded row in the lower panel).

Comparing the results from Table 5.5 (blue-shaded row) with the previous CTA study by Ripken et al. (2014), it is found the results from this thesis are found at the rather conservative end of the various CTA configurations explored by Ripken et al. (2014). The detailed technical comparison between this thesis and Ripken et al. (2014) is postponed to Appendix C.9.

Finally, the results from Table 5.5 shall be compared with Table 5.6, which shows a compilation of expected anisotropies from unresolved members of different source classes. Strictly speaking, these values depend on the instrumental flux threshold of resolved sources, and the energy range under consideration. However, an order-of-magnitude assessment of the parameter range reachable with CTA can be read off comparing the different values for C^F. When confronting these values with the intensity contributions estimated in Table 5.3, it follows that the highly anisotropic millisecond pulsars most probably do not account for a bulk of the DGRB anisotropy level and cannot be probed by CTA. However, CTA might constrain the intensity level of misaligned AGN in the VHE regime by an anisotropy analysis. This has been pointed out already by Di Mauro et al. (2014b).

---

sensitivities to $C^F_{f_{\text{DGRB}}\equiv 1}$ as quoted in Table 5.5 are obtained for an underlying flat multipole spectrum.

5.3.7. Discussion (I): Comparison to APS measurements by *Fermi*-LAT

The data recorded by the *Fermi*-LAT has been two times analyzed for anisotropies in the DGRB (Ackermann et al., 2012a; Fornasa et al., 2016). The recent analysis by Fornasa et al. (2016) is based on data from 81 months of observation, reprocessed with the `Pass7` analysis chain. This measurement extends up to γ-ray energies of $\lesssim 500\,\mathrm{GeV}$. Although low significance is obtained at these highest energies, it indicates the behavior of the anisotropic VHE γ-ray sky.

Figure 5.24 displays the auto-correlation Poisson power C_P (constant in ℓ, recall Equation 5.21) over the γ-ray energy, obtained by Fornasa et al. (2016) after masking all sources in the 3FGL. To obtain a dimensionless fluctuation power, their results for the intensity APS are divided by the square of the DGRB intensity in each bin. For describing these intensities, the two model fits considered in this thesis are used. The DGRB anisotropy increases with increasing energy, however, within a large uncertainty. The shaded bands in Figure 5.24 indicate the estimated sensitivity of a CTA extragalactic survey, as calculated in the previous subsection, and listed in Table 5.5. This comparison suggests that although the DGRB anisotropy is observed to increase within the energy range accessible by CTA, it might still be challenging to detect anisotropies in the VHE regime with CTA, unless for unexpectedly anisotropic emitters at the highest energies.

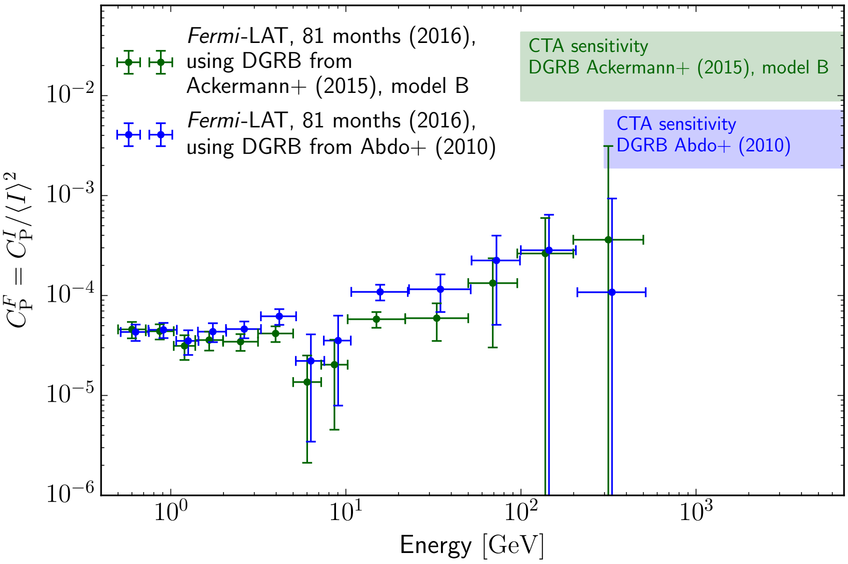

Figure 5.24.: Sensitivity of the CTA extragalactic survey to anisotropies in the DGRB compared to the most recent measurement by the *Fermi*-LAT (Fornasa et al., 2016). The original *Fermi*-LAT results have been divided by the DGRB intensity from Equation 5.13 (green) and the intensity from Equation 5.14 (blue). No additional errors have been considered for the uncertainties of the intensities in each bin. The shaded bands denote the CTA sensitivities quoted in the shaded rows of Table 5.5.

5.3.8. Discussion (II): Instrumental systematics and varying observing conditions

Simulations provide a clean environment, indispensable to calculate an instrument's sensitivity and to interpret measured signals. On the other hand, they constitute an artificial setup which runs the risk of disguising the complexity of "real world data". In the following, several aspects are discussed which can complicate an analysis of the APS from CTA data.

Survey grid spacing: The presented APS results for the CTA extragalactic survey rely on a survey pattern spacing of $\Delta_{\mathrm{fov}} = 1°$. Figure 5.25 shows how the average background APS changes when a coarser pointing of $\Delta_{\mathrm{fov}} = 2°$ or $\Delta_{\mathrm{fov}} = 4°$ is adopted. At the lowest energies, multipoles up to $\ell \lesssim 250$ are contaminated when coarsening the survey tiling to $\Delta_{\mathrm{fov}} \lesssim 2°$ (Figure 5.25, left), whereas at the higher energies, a tiling of $\Delta_{\mathrm{fov}} = 2°$ performs similarly as $\Delta_{\mathrm{fov}} = 1°$. For $\Delta_{\mathrm{fov}} \lesssim 4°$, also the energy regime above 300 GeV is affected by multipole contamination above $\ell \gtrsim 100$. Figure 5.26 displays how this translates into a worsening of the APS sensitivity: For the $\Delta_{\mathrm{fov}} \leq 2°$ case, the cuts $\ell_{\mathrm{min}}(E_{\mathrm{min}} < 100\,\mathrm{GeV}) = 350$, $\ell_{\mathrm{min}}(100\,\mathrm{GeV} \leq E_{\mathrm{min}} < 200\,\mathrm{GeV}) = 300$, and $\ell_{\mathrm{min}}(E_{\mathrm{min}} \geq 200\,\mathrm{GeV}) = 250$ are necessary to truncate exposure artifacts. In the $\ell_{\mathrm{min}} = 250$ regime applicable to high-energy spectra, almost no performance loss is observed compared to the standard cut introduced on page 156. However, restricting the multipole range to $\ell_{\mathrm{min}} \gtrsim 300$, the sensitivity is decreased by up to $\sim 50\%$.

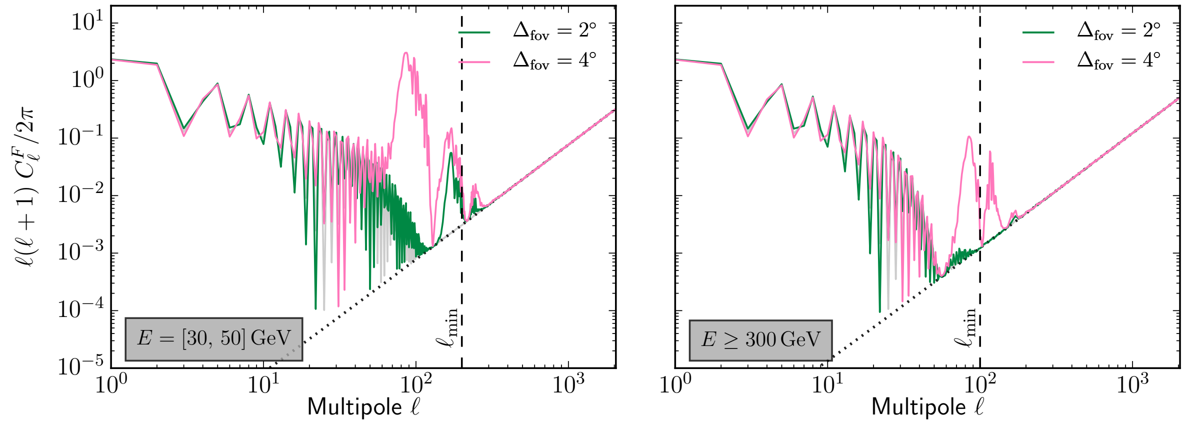

Figure 5.25.: APS of the residual background in the extragalactic survey field on $f_{\mathrm{sky}} = 0.25$ for the different pointing spacings $\Delta_{\mathrm{fov}} = 1°$ (gray shaded lines), $\Delta_{\mathrm{fov}} = 2°$ (green), and $\Delta_{\mathrm{fov}} = 4°$ (violet). The ℓ_{min} values refer to the standard analysis for $\Delta_{\mathrm{fov}} = 1°$.

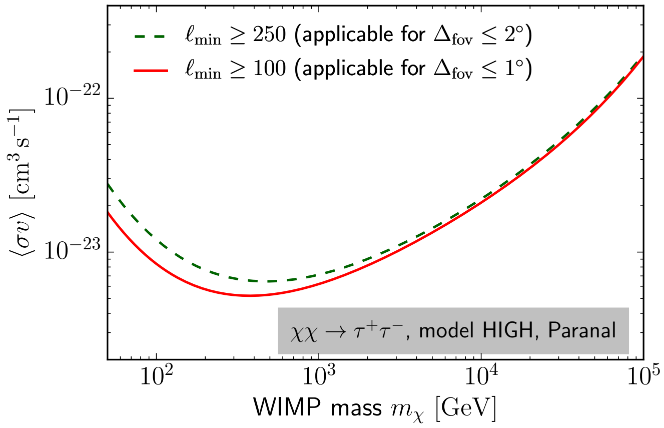

Figure 5.26.: Comparison of the $\ell_{\rm min}$ dependence in the APS likelihood-ratio test. (CTA survey with $t_{\rm obs} = 500\,{\rm h}$, `Prod3 0.5h_avg` IRFs). For the $\Delta_{\rm fov} \leq 2°$ case, $\ell_{\rm min}(E_{\rm min} < 100\,{\rm GeV}) = 350$, $\ell_{\rm min}(100\,{\rm GeV} \leq E_{\rm min} < 200\,{\rm GeV}) = 300$, and $\ell_{\rm min}(E_{\rm min} \geq 200\,{\rm GeV}) = 250$.

Excluding region of known sources and bright stars: The field of the CTA survey will contain already known γ-ray emitters and newly discovered sources in the survey. Those already detected sources have to be excluded in a search for anisotropies. This can be done by fitting a source model to the data and subtracting the signal events. Alternatively, all data from the source region can be excluded. A similar problem arises from the presence of bright stars in the survey field. A bright star in the telescope camera field highly increases the noise current in the Photomultiplier tube (PMT) pixels hit by its light and might eventually damage the PMTs. Therefore, pixels are switched off when the noise overshoots a given threshold current. Consequently, pixels are missing, and shower images in the same area of the camera are less efficiently reconstructed. The effect is most dominant for events hitting the camera from the same direction as the starlight, and a decrease of events towards this sky direction is obtained.[35] Thereby, lower energy events with dimmer shower images are more affected than higher energies.

To avoid that an event loss due to starlight and residua from excluded sources cause a fake signal in the APS, these regions can be masked from the analysis. For this purpose, a Gaussian mask is best suitable, which prevents artifacts in the APS caused by the masking. For investigating the effect of masking, all events in the CTA survey field around the positions of 19 known sources in the TeVCat catalog[36] are masked by a Gaussian window with $\sigma_{\rm mask} = 1°$, corresponding to a total masking of $19 \times 2\pi\,{\rm deg}^2 = 3.6 \times 10^{-2}\,{\rm sr} = 1.2\%$ of the survey field.

---

[35] For the VERITAS instrument, this effect has been found by N. Kelley-Hoskins to cause a $\sim 10\%$ decrease of the event rate within $\lesssim 0.2°$ around the star's position (Internal note to the VERITAS collaboration).

[36] `http://tevcat.uchicago.edu/`

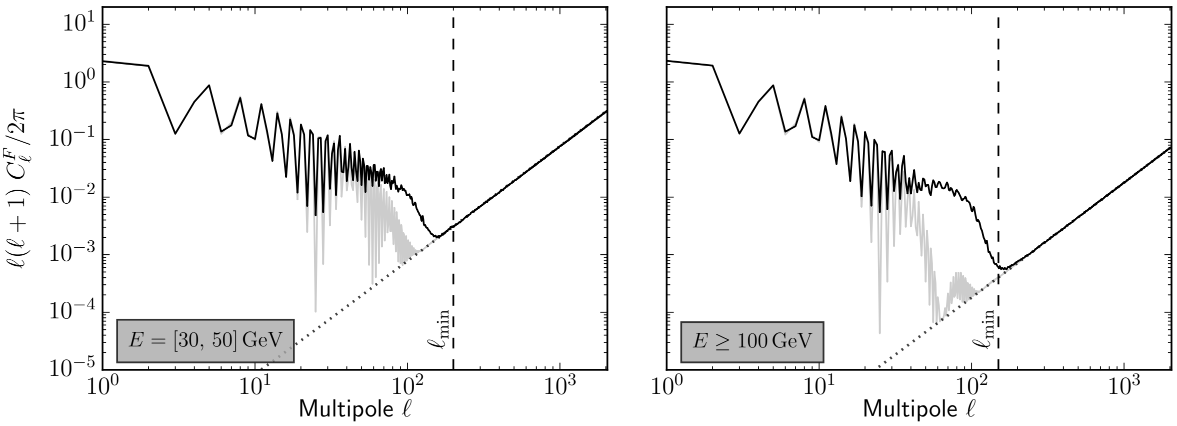

Figure 5.27.: The effect of exclusion regions in the survey region onto the residual background APS. 19 exclusion region with $\sigma_{\rm mask} = 1°$ have been added to the background event maps. The gray curves show the spectra without exclusion regions, the black curves with exclusion regions. A skymap visualizing the excluded regions is shown in Figure 5.29.

This setup is illustrated in Figure 5.29. Subsequently, the APS is computed for 20 realizations of the remaining unmasked background events. Figure 5.27 shows the effect of masking these 19 regions. It can be seen that a mask with $\sigma_{\rm mask} = 1°$ adds a contamination extending to multipoles slightly larger than $\ell = 100$. In consequence, $\ell_{\rm min}$ must be shifted to $\ell_{\rm min} \lesssim 200$. This only marginally reduces the sensitivity, as has been found in the previous paragraph. Applying a larger mask will further suppress the ℓ-contamination at $\ell \gtrsim 100$ at the cost of the loss of data. Alternatively, since the window function of the Gaussian mask can be well determined, an unfolding of the mask with algorithms like MASTER or POLSPICE can be applied. In summary, spatially localizable artifacts in the data can be masked, and applying masks should not pose any severe problems to the analysis method.

Exposure variation: In this thesis, events have been simulated with a time-constant instrument response. However, the survey data will be recorded under different atmospheric conditions and zenith angles, causing varying event rates. For the VERITAS Cygnus survey, an approximate change of $\lesssim 10\%$ over the survey was obtained (Ward, 2010). Given the strict data quality requirements for CTA and the stable atmospheric conditions at the Paranal site, a similar event rate variation is considered as rather conservative assumption for the recording of the extragalactic survey. After simulating a 500 h extragalactic survey with a Gaussian scatter 10% scattering of the background rate, Figure 5.28 shows that such an exposure variation has negligible impact on the analysis of multipoles, $\ell \geq 100$. A visual impression of a 10% acceptance variation is given in Figure 5.30.

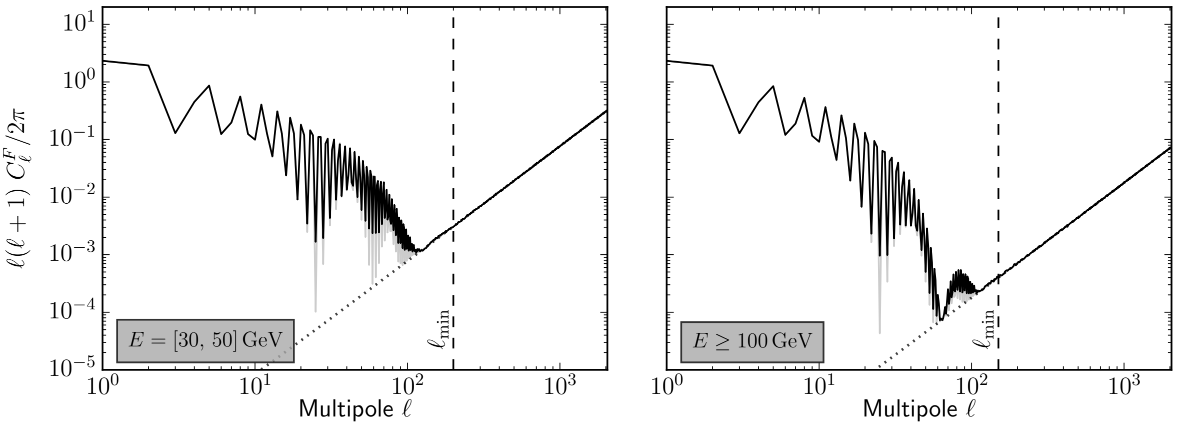

Figure 5.28.: The effect of a 10% variation of the residual background rates from observation to observation onto the APS. The gray curves show the spectra without acceptance variation, the black curves with the applied 10% variation of the acceptance.

Incomplete survey: In contrast to wide-view instruments like the *Fermi*-LAT, the CTA survey data will be collected sequentially, and an analysis over the whole survey field can only be done after the survey is completed. However, an anisotropy analysis can already be performed over a substantial fraction of the whole survey data. Figure 5.30 shows an (arbitrary) example of an incomplete survey based on 288 h of of data (58% of the full survey, $f_{\mathrm{sky}} = 0.13$) and Figure 5.31 the corresponding APS in comparison to the full 500 h ($f_{\mathrm{sky}} = 0.234$) survey. From this follows that as long as a sufficiently large area has been surveyed, masking effects due to the smaller sky area are negligible, and the loss of sensitivity compared to the full survey only manifests in fewer events and a smaller statistical sample of potential objects in the sky.

Background anisotropy of physical origin: Up to this point, the background electrons and misclassified hadron events have been assumed to be perfectly isotropized. Due to the large amount of background events, even a small level of small-scale anisotropy in the background could dominate any γ-ray anisotropy. For $I_\gamma/I_{\mathrm{bck}} \gtrsim 10^{-4}$, a sensitivity to a γ-ray fluctuation of $C_\gamma^F = 10^{-2}$ corresponds to a sensitivity to a fluctuation

$$C_{\mathrm{bck}}^F = \left(\frac{I_\gamma}{I_{\mathrm{bck}}}\right)^2 C_\gamma^F \gtrsim 10^{-8} \times C_\gamma^F \gtrsim 10^{-10} \tag{5.60}$$

of the background. A large-scale cosmic ray anisotropy has in fact been found by the TIBET (Amenomori et al., 2005) and MILAGRO (Abdo et al., 2009) air shower arrays. A preliminary analysis of muon events recorded with the IC86 configuration of the IceCube experiment and first data from HAWC suggest a significant hadronic cosmic-ray anisotropy at the level of $C^F = 10^{-10}$

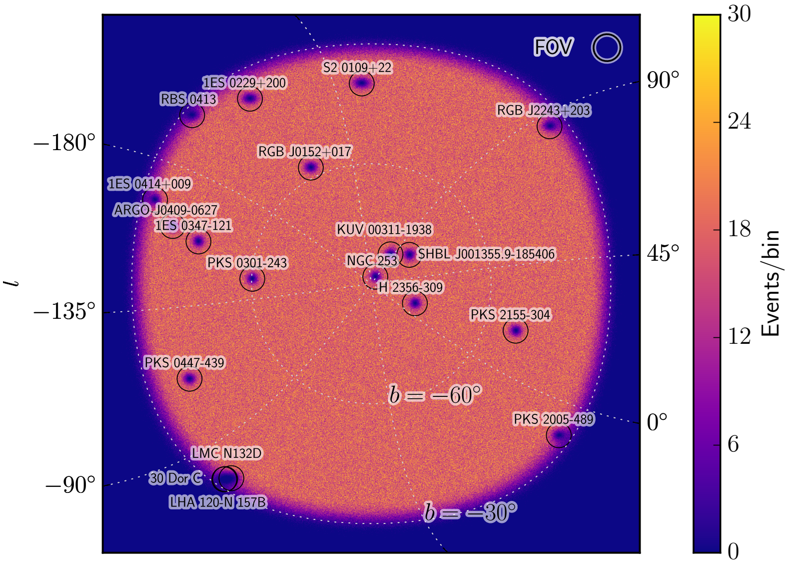

Figure 5.29.: Event map (Galactic coordinates) with the positions of 19 TeVCat sources excluded by a Gaussian mask with $\sigma_{\text{mask}} = 1°$. All events between 30 GeV and 100 TeV are shown.

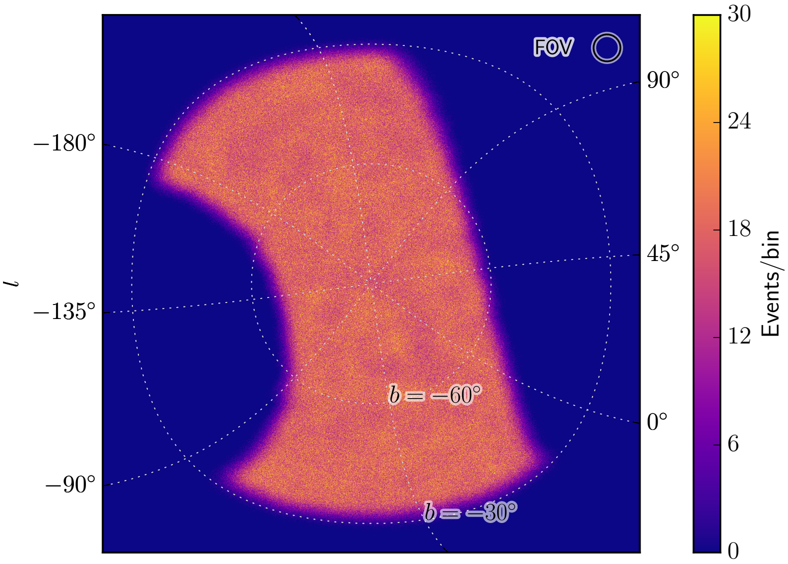

Figure 5.30.: Event map (Galactic coordinates) of an (arbitrarily cut) incomplete survey based on $T = 288\,\text{h}$ of observation, covering $f_{\text{sky}} = 0.13$. This incomplete survey additionally has been simulated with a pointing spacing of $\Delta_{\text{fov}} = 2°$, and an 10% Gaussian acceptance scatter between the observations. All events between 30 GeV and 100 TeV are shown.

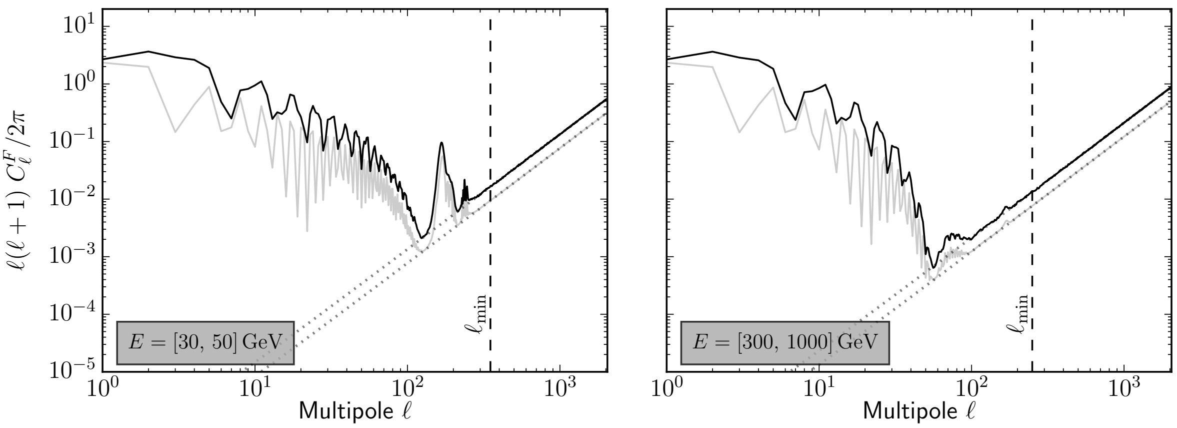

Figure 5.31.: The effect of a limited dataset from an incomplete extragalactic survey with 288 h (58%, $f_{\rm sky} = 0.13$) of data. The gray curves show the spectra from a full 500 h survey on $f_{\rm sky} = 0.13$, the black curves the incomplete mock dataset. This study has been performed with $\Delta_{\rm fov} = 2°$. The main difference between the curves is a constant offset of the noise power, which is a factor 1/0.58 lower for the full survey due to the corresponding larger number of events.

up to $\ell = 40$ (Díaz-Vélez et al., 2015). However, extrapolating the level up to $\ell \gtrsim 100$, and given that less than 1% of all hadrons survive the CTA gamma-hadron separation cuts, remaining potential hadronic cosmic-ray anisotropies are far below CTA's sensitivity to γ-ray anisotropies.

The *Fermi*-LAT instrument has been used to search for anisotropies in the electron flux above 60 GeV, based on more than 1.6×10^6 electron/positron events (Ackermann et al., 2010b). No electron anisotropy above a 3σ significance level has been found at multipole scales $\ell \leq 9$, and an energy-dependent upper limit on the anisotropy was calculated for the dipole term, $C^F_{\ell=1,\,95\%\,\rm C.I.} \lesssim 10^{-2}$. Similar upper limits are obtained from the PAMELA (Adriani et al., 2015) and AMS (Casaus, 2013) experiments. Thus, a contamination of anisotropic electrons at a level of $C^F_{\rm bck} \gtrsim 10^{-10}$ can not be exluded by existing measurements.

Regarding the electrons, however, only primary cosmic electrons, accelerated in point-like sources, are able to contribute to small-scale anisotropies. Because of the synchrotron cooling of high-energy electrons, primary electrons must most plausibly originate from nearby, $d \lesssim 1$ kpc, sources, and only few supernova remnants constitute plausible candidates (Li et al., 2015). Thereby, it is unlikely that a sub-degree ($\ell \gtrsim 100$) anisotropy survives the diffusion of the high-energy electrons emitted by these sources (Hooper et al., 2009; Linden and Profumo, 2013; Di Mauro et al., 2014c). Yet there remains another possibility for generating an electron anisotropy: DM annihilation in nearby subhalos (Borriello et al., 2012a,b). However, also this scenario is considered highly unlikely by Profumo (2015). In summary, a low-level small-scale anisotropy level of the electron flux cannot be excluded, however must be considered as highly unlikely.

6 | Summary and outlook

> *Plus un fait est extraordinaire, plus il a besoin d'être appuyé de fortes preuves. Car ceux qui l'attestent, pouvant ou tromper, ou avoir été trompés, ces deux causes sont d'autant plus probables que la réalité du fait l'est moins en elle-même.*
>
> Pierre Simon Laplace (1812, p. xii)[1]

Results of the thesis: In this thesis, the detectability of Galactic dark matter (DM) density substructure with the future Cherenkov Telescope Array (CTA) has been investigated. Three main results are obtained: Firstly, a semi-analytical modeling has been developed to calculate the γ-ray intensity from annihilation in Galactic DM substructures, and key quantities have been identified which drive the γ-ray intensity observed on Earth. Secondly, the sensitivity of a CTA extragalactic survey to detect γ-rays from Galactic DM substructures has been calculated, using two complementary methods. Thirdly, the model-independent degree of anisotropy in the diffuse γ-ray background (DGRB) above 100 GeV, which can be detected from the ground with the CTA instrument, has been determined.

For the Galactic DM substructure modeling, the `CLUMPY` code has been used to generate hundreds of skymaps for various density models. The semi-analytical models have been calibrated by results from dynamical DM simulations, and variations of the models could be explored within a self-consistent, computationally efficient framework. The average subhalo brightness distributions and properties of the γ-ray-brightest DM clumps have been assessed and their statistical variance has been quantified. The consistency between the subhalo brightness distribution and the angular power spectrum (APS) of the skymaps has been verified by a simple analytical model. By varying several properties of the clumpy DM distribution, which are still disputed in the literature, a confidence margin between an optimistic (HIGH) and conservative

---

[1] The more extraordinary a fact is, the more it needs to be supported by strong evidence. For those who attest to it, could either be deceiving others or deceiving themselves, both of these reasons are all the more probable the more improbable the fact.

(LOW) case has been derived. This margin encompasses most results from various dynamical simulations (with and without feedback from baryonic matter, cold or warm DM) and is in agreement with the DM properties derived from stellar kinematics in dwarf spheroidal galaxies (dSph). In detail, the substructure simulations show that:

- The γ-ray-brightest DM subhalos are objects rather close to the Milky Way (MW) disk in the central region of the Galactic DM halo, at a distance of $\sim 10 - 20\,\mathrm{kpc}$ from Earth. Depending on the survey area and angular resolution of the instrument, slightly different populations are probed. The γ-ray-brightest object has an extended half-emission radius of $\theta_{\mathrm{h}}^{\star} \sim 0.1 - 0.2^{\circ}$ and a mass of $m_{\mathrm{vir}}^{\star} \sim 10^{7}\,\mathrm{M}_{\odot} - 10^{8}\,\mathrm{M}_{\odot}$. These masses are only slightly below the typical DM masses of known dSph galaxies, and so the γ-ray-brightest DM clumps are likely to be dSph galaxies. On the other hand, it is found that lighter objects with $m_{\mathrm{vir}}^{\star} \lesssim 10^{7}\,\mathrm{M}_{\odot}$ are also likely to be found with comparable J-factors. Such objects most probably constitute dark subhalos which can probably only be found in γ-ray surveys.
- Accretion history in a hierarchical structure formation results in highly concentrated substructure densities in the core of the Galactic DM halo. The expected γ-ray brightness due to DM annihilation of the brightest objects at $D_{\mathrm{obs}} \sim 10 - 20\,\mathrm{kpc}$ is found to be very sensitive to these subhalo concentrations. Therefore, more knowledge is needed about the precise DM clustering behavior in the core of today's Milky-Way DM halo.
- Higher subhalo concentrations towards the Galactic center (GC) additionally cause a spatial anisotropy for the most likely direction in the sky in which a γ-ray-bright subhalo is found. For the model HIGH, a factor ~ 4 higher probability to find the brightest object towards the GC is found compared to the opposite direction. Although other effects (e.g., the smooth Galactic DM halo itself) constrain the range of beneficial sky regions for DM observations, a bias of the subhalo distribution should be held in mind for designing promising γ-ray surveys for DM searches.
- A relatively large variance of the expected γ-ray flux from the γ-ray-brightest DM subhalo is obtained. A flux variance spanning almost over a factor 10 is found at the 68% C.I., and even over two orders of magnitude at the 95% C.I.. This scattering is propagated into the calculation of the instrumental sensitivity to DM subhalos.
- In the context of the capabilities of the *Fermi*-LAT, the subhalo modeling has been compared to the previous studies by Bertoni et al. (2015) and Schoonenberg et al. (2016). It is found that the results from this thesis largely agree with those from Schoonenberg et al. (2016), while being slightly more conservative than those from Bertoni et al. (2015).

Based on the modeling of the subhalo flux distribution, the sensitivity of an extragalactic survey with CTA to detect Galactic DM subhalos has been calculated in the second part of the thesis. A survey pointing strategy has been proposed to raster 25% of the extragalactic sky by $\sim 10^4$ single observations over a total time of 500 h, guaranteeing a global homogeneity of the survey exposure better than 1%. The CTA analysis software packages `gammalib` and `ctools` have been used to compute a Likelihood-based sensitivity to detect the γ-ray-brightest subhalo in this survey. Based on the latest calculations of the projected performance of the southern CTA, it has been found that:

- The CTA extragalactic survey is able to probe DM annihilation in the γ-ray-brightest Galactic subhalo at the 95% C.L. for a velocity-averaged annihilation cross section of $\langle \sigma v \rangle \gtrsim 1 \times 10^{-24}\,\mathrm{cm}^3\,\mathrm{s}^{-1}$ for a DM particle mass of $m_\chi \sim 500\,\mathrm{GeV}$ and pure annihilation into τ leptons. For pure annihilation into heavy quarks ($b\bar{b}$), the sensitivity degrades to $\langle \sigma v \rangle \gtrsim 6 \times 10^{-24}\,\mathrm{cm}^3\,\mathrm{s}^{-1}$, with the best sensitivity to a mass of $m_\chi \sim 1\,\mathrm{TeV}$. These values rely on the median brightness of the brightest object in the optimistic subhalo model HIGH. Adopting the conservative model LOW worsens the sensitivity to $\langle \sigma v \rangle$ by one order of magnitude. For all models, the systematic uncertainty of the expected subhalo brightness results in a one order of magnitude uncertainty around the median sensitivity for setting a limit on $\langle \sigma v \rangle$ from a non-detection.
- The survey scan over a quarter of the sky has been characterized by an on-axis observation, corrected for a million independent trials in a blind survey search. This correction reduces the 95% C.L. sensitivity by a factor ~ 5 compared to a pointed on-axis observation towards a known source position. However, this approach of accounting for a "look elsewhere effect" represents a fairly optimistic choice. A rigorous Likelihood calculation with the source coordinates being part of the fit is recommended for future survey analyses of Cherenkov telescope data.
- The sensitivity of this analysis, based on a 500 h dataset of a CTA extragalactic survey, is competitive with a deep-field observation of a single dSph over a similar observation time as presented in the analysis by Lefranc et al. (2016). In contrast, the analysis by Carr et al. (2015) suggests a factor $\gtrsim 10$ better sensitivity for deep dSph observations. However, the expected DM properties of dSph galaxies also suffer from large systematic uncertainties (see, e.g., Bonnivard et al., 2016; Hayashi et al., 2016; Domínguez et al., 2016). In particular, the Segue I dSph, on which the limit by MAGIC and the projection for CTA in Figure 5.7 are based, may show a significantly lower J-factor than previously found in the literature.

The above sensitivities obtained for a survey search for DM subhalos strictly apply only for exclusion limits in case of a non-detection. The sensitivity to *detect* DM subhalos might be actually larger. One may assume that follow-up observations will be done for any sky direction with a $\gtrsim 3\sigma$ fluctuation over the background in the survey data (which is less than the required 5.4σ significance before a trials correction in the applied analysis). In a deep-exposure follow-up observation, subhalos might be found for lower annihilation cross sections than the values presented at the 95% C.L. exclusion limits. However, relatively strong limits on the annihilation cross section have been already set by existing instruments (see Figure 5.7, right).

Subsequently, an alternative method to detect DM subhalos with a CTA large-sky survey has been investigated:

- Following Fornasa et al. (2016), a Likelihood method has been developed to detect subhalos as anisotropies in the angular power spectrum (APS) of the CTA survey data. The method is found to yield a factor ~ 5 worse sensitivity compared to the analysis for the brightest halo only. Several reasons for this discrepancy have been discussed: A more rigorous consideration of trials in a blind survey search is expected to further worsen the sensitivity towards the brightest object. More importantly, it is found that a global anisotropy analysis is not effective for searching entire power-law source count distributions in a dataset. In such a case, most of the angular power is generated by a small number of the brightest objects. Comparing the two pursued analyses shows that less information is lost when focusing only on the single brightest object than when transforming the data into multipole space and excluding artifacts from the transformation.
- Ripken et al. (2014) previously assessed CTA's model-independent ability to detect small-scale anisotropies in the DGRB via a power-spectral analysis. Using a realistic instrumental performance of the final CTA, it is found in this thesis that deep-field observations are highly problematic for an APS analysis due to transformation artifacts. For a shallow large-field survey however, CTA is able to probe anisotropies in the DGRB at energies above $\sim 100\,\mathrm{GeV}$ in the multipole range $100 \lesssim \ell \lesssim 1000$. Depending on the DGRB intensity at TeV scales, a 500 h CTA survey over 25% of the sky is sensitive to relative fluctuations of $C_\mathrm{P}^F \gtrsim 3 \times 10^{-3}$ at the 95% C.L. (for a power-law energy spectrum according to Abdo et al., 2010), or to $C_\mathrm{P}^F \gtrsim 10^{-2}$ for an exponential cut-off of the DGRB intensity at sub-TeV energies (Ackermann et al., 2015b). These sensitivities reach the properties of several candidate VHE source populations. In fact, the range of anisotropies testable with CTA is limited. However, it has been shown that despite a large residual background, probing the DGRB is possible with Earth-bound instruments like CTA.

The results of both analyses (searching for the brightest subhalo and for a subhalo signature in the APS) demonstrate that the large-area extragalactic sky survey, one of the key science projects for CTA, has benefits for many science cases. This thesis has presented two further advantages of the survey data: Competitive limits on the annihilation cross section of weakly interacting massive particles as a candidate for DM can be derived from a search for Galactic DM subhalos, and the DGRB can be probed for anisotropies in the VHE regime. A search for dark subhalos with the extragalactic sky survey is complementary to a dedicated DM program towards dSph galaxies: (i) The survey allocation time is guaranteed independent of a DM context, (ii) the survey data is for the most part not overlapping with dedicated dSph observations (the survey will be mostly taken on the southern sky, whereas the most promising dSph targets are located in the north), and (iii) dark subhalos provide similar detection prospects with complementary systematic uncertainties.

Future perspectives: The case of decaying DM has not been studied in either analyses of this thesis. As all tools have been developed in this thesis, an analogous study for decaying DM would be straightforward to perform, and possibly forms a suitable topic for a Bachelor's or Master's thesis.[2] However, the emission profiles from DM decay in DM clumps are expected to be much broader and to produce an even less intense small-scale power spectrum (see, e.g., Fornasa et al., 2013). This makes it even more difficult to resolve DM subhalos with background-dominated instruments and cancels out the benefit of CTA's good angular resolution. The finding of this thesis that a search for the single brightest object is more promising than an APS analysis also applies for the case of DM decay. If an analogous study of Galactic subhalos is done for decaying DM, it should therefore be focused on the former method.

Complementary to the APS method investigated in this thesis, Lee et al. (2009) and Feyereisen et al. (2015) calculate the 1-point probability distribution function for the photon statistics from Galactic and extragalactic DM structures for the *Fermi*-LAT. This method is also worth investigating in a future study for the data from a CTA extragalactic survey, not only limited to the DM case (for a general application to *Fermi*-LAT data, see also Malyshev and Hogg, 2011; Zechlin et al., 2016b,a).

Overall, the most promising target for indirect DM detection with CTA remains the Galactic center (GC) region. Figure 5.7 has shown that towards the GC, CTA might be able to probe WIMP annihilation cross sections close to the thermal relic cross section of $\langle\sigma v\rangle \lesssim 3 \times 10^{-26}\,\mathrm{cm}^3\,\mathrm{s}^{-1}$. By doing this, CTA will reach a crucial parameter range for testing the plausibility of the DM paradigm. However, much more can be achieved when not relying on a single instrument for the observation of various DM targets. Several experiments are hunting for indirect signatures of DM, each of them suffering from complementary difficulties to separate faint DM signals from the background. On the one hand, CTA will exhibit the best angular resolution ever reached in γ-ray astronomy. On the other hand, still longer exposure times or a larger effective collection area would be needed to probe the canonical DM parameter range

---

[2] See also the report by R. Kieokaew from the summer student program 2015 at DESY Zeuthen.

in subhalos and dSph galaxies with CTA. Imaging atmospheric Cherenkov telescopes can only operate during night while having a relatively small field of view. For long exposure times towards weak and steady γ-ray fluxes, their performance strongly competes with wide-view survey instruments. The *Fermi*-LAT has been in operation since 2008 and will continue its mission until presumably 2018. The HAWC detector in northern Mexico was completed in March 2015, and is continuously surveying two thirds of the entire sky each day in γ-rays above 1 TeV (see Abeysekara et al., 2014, for its indirect DM detection prospects). Novel design concepts for wide-field Cherenkov telescopes have been proposed with the MACHETE (Cortina et al., 2016) or LATTES (Assis et al., 2016) instruments. A combined search between all these instruments by triggering CTA follow-up observations might provide the largest benefit for indirect DM searches in γ-rays for the next decade.

Moreover, to take full advantage of all the (soon-to-be) available γ-ray data, a combination of different analyses and different experiments could help to overcome individual methodological and instrumental shortcomings (Ando, 2016). For example, Fornasa et al. (2013) find a similar APS of extragalactic DM emission compared to the subhalo APS presented in Subsection 5.3.3. However, anisotropies in the DGRB from extragalactic DM sources can be much better unveiled by cross-correlating with complimentary information. Cross-correlation analyses between γ-rays and galaxy catalogs (Ando et al., 2014; Cuoco et al., 2015; Regis et al., 2015; Ando and Ishiwata, 2016), and between γ-rays and the cosmic shear calculated from the measurement of the Cosmic Microwave Background or optical data (Camera et al., 2013, 2015; Shirasaki et al., 2014; Tröster et al., 2017) have been studied. The ongoing optical Dark Energy Survey (Abbott, 2005) and the soon-to-be realized Large Synoptic Survey Telescope (LSST, Ivezic et al., 2008) and Euclid satellite (Laureijs et al., 2011) will therefore provide an unsurpassed mapping of the large-scale structure of the Universe. Although cautious projections have been given for probing microlensing effects from Galactic subhalos (Erickcek and Law, 2011), the Euclid satellite may provide valuable data to find lensing signatures from nearby DM clumps (Beaulieu et al., 2010). For this purpose, also data from GAIA (Prusti et al., 2016) and the soon-to-be launched James-Webb space telescope (Gardner et al., 2006) may be used. Combined analyses between γ-ray and current and future neutrino experiments can be performed (Gammaldi et al., 2015; Murase et al., 2015). Even radio observations can be used for a multi-wavelength search for DM (Fornengo and Regis, 2014; Beck and Colafrancesco, 2016; Calore et al., 2016b).

Apart from combining different instruments, it is also compulsory to independently constrain the DM parameter space or to independently confirm a discovery of particle DM. Many alternative interpretations are possible for unidentified signals, and false claims of a detection may be made at the edge of the instrumental sensitivities. The danger of a rash claim of evidence for particle DM is even higher in the light of the prestigious character of the topic.

For indirect DM searches towards dSph galaxies, the Dark Energy, LSST and Euclid surveys may expose additional DM-rich dSph objects. A better angular and spectroscopic resolution of known dSph with future spectrographs (e.g., with the Prime Focus Spectrograph for the Subaru telescope, Tamura et al., 2016) will help to significantly better determine the expected DM density profiles in known and future dSph objects, resulting in more robust DM constraints from dSph observations.

In summary, numerous next generation experiments for direct, indirect and collider detection of particle DM have either started taking data or will soon be operational. Direct detection experiments may soon reach a sensitivity down to the irreducible background from Solar, atmospheric and diffuse supernova neutrinos. Indirect DM searches via γ-rays and cosmic rays are approaching sensitivities to probe thermal relic annihilation cross sections over a wide range of DM masses. The Large Hadron Collider is now taking data at center-of-mass collision energies of $\sqrt{s} = 13\,\mathrm{TeV}$ ("Run II"), with further upgrades being planned for the next decade, allowing promising combined constraints on DM with indirect and direct DM searches.

A lot of efforts are thus being undertaken to shed light on the nature of DM, and the next decades are likely to bring a decision about the true picture of DM. Whether this will result into a confirmation or rejection of the DM hypothesis, the solution of the DM puzzle will heavily impact our notion of the fundamental laws of nature.

7 | A rugged road to knowledge: The history of dark matter[*]

> *It is [not] possible really to understand the successes of science without understanding how hard it is – how easy it is to be led astray, how difficult it is to know at any time what is the next thing to be done.*
>
> Steven Weinberg (1993, p. 129)

At the beginning of this thesis, the evidence for dark matter was introduced as one of the major unsolved questions of modern physics. The search for dark matter particles concerns a large research community across different fields of physics, producing a dramatically growing number of publications per year. With regard to these current efforts, it appears all the more astounding that the problem of dark matter was neglected for several decades: Already in the 1930s, evidence for dark matter had been correctly noted, but nevertheless the concept of dark matter lived a shadowy existence for more than 30 years. Not before the 1970s, did it advance from a niche problem to a central topic in astrophysics, cosmology and particle physics.

However, from a historical point of view, the erratic history of dark matter turns out to be much less surprising than it appears at first glance: the development of new scientific ideas and the acceptance of significant problems have often followed winding and unexpected paths. No scientific concept develops inevitably and straightforwardly, although it may appear so in retrospect. It is rather the rule than the exception that only in hindsight a new scientific notion is evaluated as fruitful or important – and sometimes only decades later.

The formation of the concept of dark matter reflects exactly such a case of historical contingency. This supplementary essay promotes the history of the dark matter concept as a valuable case study of non-linear progress in science. Firstly, a short review of the development of the dark matter concept is given, complementing what already has been said in Chapter 2. The

---

[*] This supplementary essay has been written for the most part during September – October 2013 at the Max Planck Institute for the History of Science, Berlin.

role of astronomical observations techniques, new concepts in theoretical physics, and changing institutional structures for the emergence of a "dark matter paradigm" are outlined. It is alleged that the acceptance of a dark matter problem was essentially stimulated by the rise of computer technology, which allowed complex numerical simulations to be performed starting in the 1960s. It is then argued that primarily, the delayed emergence of a dark matter problem can be attributed to insufficient research communication between different disciplines. The case of dark matter is compared to the much better known history of the Cosmic Microwave Background (CMB) discovery, and it is demonstrated that both cases share a remarkably similar continuous track of missed opportunities to become aware of an important scientific problem.

The dark matter career – a short historical overview

The modern concept of dark matter can be traced back to works by William Thomson Kelvin around the beginning of the 20th century (Bertone and Hooper, 2016). In a published lecture, Henri Poincaré (1906) outlines Kelvin's ideas to apply kinetic gas theory to assess the mass of the local Milky Way – which was, at that time, the Universe. Poincaré also used the term "dark matter" ("matière obscure" in the French original version of the article), probably for the very first time, for denoting a potential non-visible contribution to the total dynamical "universal" mass. Kelvin's approach was more precisely followed up by the Dutch astronomer Jacobus Kapteyn (1922), who, for the first time, described the "sidereal system" – the Milky Way – as a non-spherical, rotating system of stars. Kapteyn also discussed a contribution of "dark matter" to the dynamical mass. Similar to Kelvin and Poincaré, he concluded that a reasonable extrapolation of the stars' luminosity function towards lower magnitudes provides a mass in agreement with the dynamical estimate. James Jeans (1922) in the same year found a somewhat higher estimate, concluding "two dark [low luminosity] stars to each bright star". Ten years later, Jan Hendrik Oort (1932) used the perpendicular motion of stars in the Solar neighborhood to infer the local mass density. His method already resembled modern measurements of the local baryonic and dark matter densities. He found his result in "unexpectedly good" agreement with the finding by Kapteyn (1922), and, for the first time, expressed his results in terms of a mass density of the Solar neighborhood, $\rho_{\mathrm{tot}}(R_\odot) = 0.092\,\mathrm{M}_\odot/\mathrm{pc}^3$ (corresponding to $3.5\,\mathrm{GeV/cm}^3$). In total, the values for the local Galactic mass density available in the 1930s already came remarkably close to what recent measurements give for the local baryonic mass density (e.g., Flynn et al., 2006). In fact, astronomers from that epoch interpreted their findings by proposing that the total dynamical mass can be explained by an extrapolation of the luminosity function of stars with similar mass-to-light ratio as the Sun, or by postulating some reasonable number of low-luminosity stars, meteors, and gaseous clouds (Bertone and Hooper, 2016).

Almost at the same time, in 1933, the Swiss-born US astronomer Fritz Zwicky studied the kinematics of galaxies in the remote Coma galaxy cluster and found a remarkable discrepancy between visible and dynamically acting matter (Zwicky, 1933, 1937). His reasoning suggested a hundred times bigger mass of the cluster than that estimated by the luminosity of the visible galaxies in the cluster alone (see Subsection 2.1.3 of this thesis). In contrast to the works by Kapteyn, Jeans, and Oort, this seemed to form a very odd result. It was hardly conceivable that low-luminosity stars, gas and planets accounted for such a high ratio of the cluster's mass. Indeed, adopting a much lower value of the Hubble constant, the mass-to-light ratio of the Coma cluster was later corrected to a lower value. Still, Zwicky's conclusion about a large amount of dark matter in the Coma cluster does not have to be revised to this day. This is why Zwicky has later been commonly considered as the "discoverer" of dark matter. It should be noted that, although using the term "dark matter" in German – „Dunkle Materie“ – and having a similar ambition as Kapteyn, Jeans and Oort before, he did not quote these earlier works, although he most probably was aware of them. Subsequently in 1936, Sinclair Smith found evidence for a similar amount of non-visible matter in the Virgo cluster (Smith, 1936), thus generalizing Zwicky's findings.

However, in the following decades, little attention was paid to the discrepancy between luminous and gravitationally acting mass in the galaxy clusters claimed by Zwicky and Smith. The notion of dark matter first experienced a revival when astronomers started to investigate the motion of stars within remote spiral galaxies. Already in 1939 in his PhD thesis, Horace Babcock investigated the rotational velocities of stars in the nearby Andromeda galaxy (M31) and noted an unexpected behavior of the stars rotation in the outer boundaries of the galaxy, which "is hardly to be anticipated from current theories of galactic rotation" (Babcock, 1939). In 1954, Martin Schwarzschild – the son of famous astronomer Karl Schwarzschild – restudied the Andromeda galaxy with better spectroscopic techniques and arrived at similar results (Schwarzschild, 1954).

The development of radio techniques in World War II was a big step forward towards the formation of the field of of radio astronomy in the early 1950s. In 1957, Hendrik van de Hulst and collaborators used the 25-meter telescope at Dwingeloo (Netherlands), the largest worldwide at that time, to observe the Andromeda galaxy in the radio band (van de Hulst et al., 1957). They not only discovered that it harbors hydrogen clouds up to radii far beyond the optically bright stars, but also, by studying the redshift of the HI line (first predicted by van de Hulst in 1944, see Strom, 2013), they determined the clouds' rotational curve. To their surprise, even the extended rotational curve did not decline, but remained flat – suggesting that there must exist much more non-radiating matter in the very outskirts of M31. Despite strengthening and explicitly quoting the earlier works, they did not promote the importance of their results.

The final breakthrough in the awareness of an inconsistency between observation and understanding of galactic dynamics did not come until the late 1970s. US astronomer Vera Rubin and collaborators restudied rotational curves of spiral galaxies only in the optical spectrum, but with a higher precision and for several distinct astronomical sources (Rubin et al., 1978, 1980). In these publications they neither quoted the earlier works nor a term like dark matter; a characteristic pattern for the whole course of dark matter history. Although the results of Rubin et al. were already well-known from investigations of the Andromeda galaxy, and the existing measurements in the radio range should have been no less convincing, it was only at this time that the majority of the astrophysical community became convinced about the oddities in galaxy dynamics.

The previous paragraphs may be considered as the standard story of the history of dark matter. However, as remarked by Sanders (2010), results from computer simulations contemporaneously showed evidence of lacking understanding of galaxy dynamics. Already in the 1960s, Newtonian N-body-simulations were performed and immediately applied to the dynamics of stars within galaxies (von Hoerner, 1960, 1963; Miller and Prendergast, 1968). Despite the fact that very simplified systems were studied in these simulations with low accuracy, the results clearly showed contradictions to the contemporary assumptions on the structure, origin and evolution of galaxies. As a consequence of these simulations, in 1974 Jeremiah Ostriker, James Peebles and Amos Yahil claimed “a halo with a very high mass-to-light ratio surrounding the more visible, largely second-generation part of the Galaxy” (Ostriker et al., 1974).

Lastly, there was a third pillar indicating the existence of dark matter that appeared in parallel in the 1970s. After big-bang cosmology had prevailed in the late 1960s with the discovery of the CMB radiation, a spatial inhomogeneity in the microwave spectrum, which would have explained the structure formation in an evolving universe, was searched for in vain. The missing inhomogeneity suggested that gravitational structure formation must have begun already before the decoupling between radiation and matter in the early Universe. Such a structure formation could have been possible only for non-electromagnetic interacting matter (Subsection 2.1.4 of this thesis). Because this conclusion suggested that exotic elementary particles must account for the largest amount of dark matter, the problem started to gain the attention of the highly active community of particle physics at that time: the modern concept of dark matter was born. In fact, the term “dark matter” was first reused after the early works of the 1930s by elementary particle physicists in the late 1970s, e.g., by White and Rees (1978). Other denominations such as “hidden mass”, e.g., in Milgrom (1983), “missing mass” (Copp, 1982), “hidden matter” (Materne and Tammann, 1976) or similar combinations were still in play until the end of the 1980s. The fact that the term “dark matter” prevailed, may indicate the takeover of the problem by particle physicists and cosmologists at the beginning of the 1980s. In Figure 7.1, it is shown

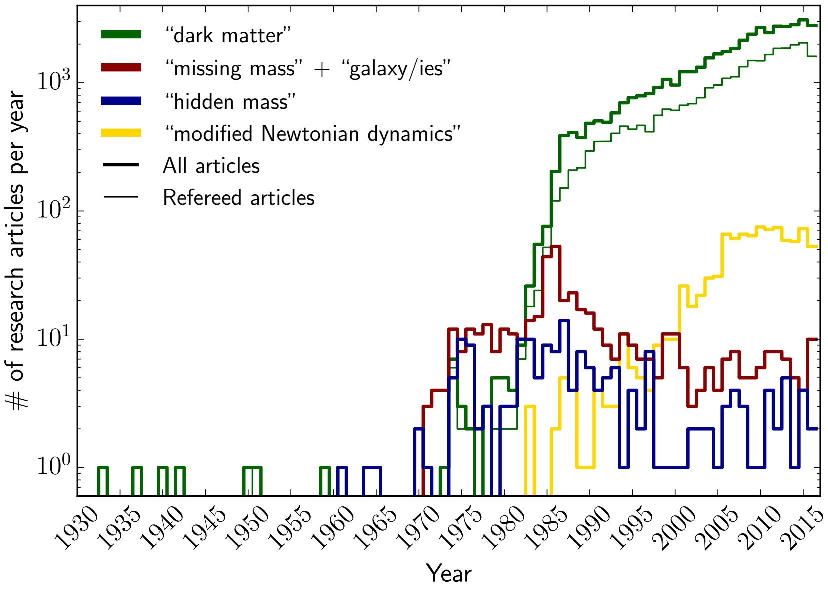

Figure 7.1.: Published research articles relating to dark matter until 2016-09-18, archived in the ADS database. The search query required the three most abundant terms "dark matter" (green), "missing mass" (red), and "hidden mass" (blue) to occur in the title or the abstract. In the case of "missing mass", also the occurrence of "galaxy" or "galaxies" was required, to avoid unrelated results from nuclear and particle physics. Until 2016-09-18, a total number of 44594 preprints and refereed articles containing "dark matter" in the title or abstract is present in the ADS database (the first entry is found for the year 1933, however, it is not the article by Zwicky, 1933). Of these, 3113 (7%) have been published only in 2015, and around 10000 ($\gtrsim$ 20%), in the last three years. For the term "dark matter", refereed articles are displayed separately. The figure also shows that the Modified Newtonian Dynamics (MOND) theory is continuously debated, however with a relatively decreasing significance.

how the different terms have been used since the 1930s in scientific publications, based on the articles contained in the NASA Astrophysics Data System (ADS).[2] These metrics clearly show that around 1980, all terms were equally often used in scientific publications. Since then, the number of publications referring to "dark matter" has dramatically increased, whereas the usage of other denominations again has declined.

Although the dark matter problem was widely accepted by most astronomers and physicists at that time, the 1980s and 1990s were marked by a confusing controversy about the constituents and the nature of dark matter. Numerous suggestions were discussed and rejected: Both neutrinos and so-called MAssive Compact Halo Objects (MACHOs), as well as primordial black holes, were ruled out as main constituents of dark matter. Finally, a consensus was reached that dark

---

[2] Since recently, under `https://ui.adsabs.harvard.edu`, the ADS provides an updated interface to its publication database ("ADS Bumblebee"), which allows complex publication metrics analysis.

matter most probably consists of weakly interacting massive particles, which are not included in the Standard Model of particle physics (Section 2.2). This consensus has been called the "cold dark matter paradigm".[3] In contrast, a failure of classical Gravitation on large scales was also widely discussed throughout this period. The most prominent example of this line of reasoning was the Modified Newtonian Dynamics (MOND) theory by Mordehai Milgrom (1983), later extended into the "Tensor-Vector-Scalar" modification of General Relativity by Jacob Bekenstein (2004).

Finally, the last two decades have consolidated the cold dark matter paradigm, and skeptics about the presence of dark matter have been vastly marginalized. Firstly, through the measurements of the BOOMERanG, Wilkinson Microwave Anisotropy Probe (WMAP), and the Planck experiments, the anisotropies in the CMB spectrum could be measured to a high accuracy, yielding a precise estimate of the Universe's dark matter content (see Subsection 2.1.4). Secondly, a detailed study of objects like the Bullet galaxy cluster (Clowe et al., 2006) fortified the dark matter hypothesis over alternative gravitational theories (see Subsection 2.1.3). Thirdly, since the mid-1990s, computer technology developed to the extent that numerical simulations became possible on cosmological scales. With this, the evolution of the Universe as a whole within a cold dark matter model could be successfully simulated. In fact, these simulations closely matched the observational data of the largest visible structures in the Universe.

In summary, following Trimble (1995), the outlined history of modern dark matter can be roughly divided into four episodes:

- A first episode or "prelude", lasting from around 1900 until 1939: The idea of inferring astronomical mass budgets from dynamical measurements evolved, and was applied to the stars within the Milky Way by William Kelvin, Jacobus Kapteyn, James Jeans and Jan Oort, and to galaxy clusters by Fritz Zwicky and Sinclair Smith. For the latter, Zwicky and Smith found large amounts of non-visible matter in the Coma and Virgo clusters. However, this inference was followed by little contemporary reaction from the astrophysical community.
- An interlude, lasting from around 1945 until 1970: The period of World War II produced new military-driven technologies, and heavily rearranged institutional structures, central topics and locations in worldwide physics. Radio technologies were introduced for astrophysical observations, and computers used for simulations of the dynamics of astrophysical systems. Although further evidence appeared of an insufficient understanding of galactic

---

[3] When talking about paradigms in science, a reference to the original work by Thomas S. Kuhn (1962) should be made. However, the discussion of whether the past history of dark matter can be described with Kuhn's philosophy of science shall be excluded in this essay. For this, the reader is referred to Tremaine (1987); Horvath (2009); Martinez and Trimble (2009), and Trimble (2013).

dynamics, no major attention was paid to the findings in either field, nor were the results from the different communities linked to each other.

- A third episode from about 1970 until about 2000, which marked a "breakthrough of problem awareness": In the 1970s, the problem of non-luminous mass in galaxies and clusters was rediscovered and gained major attention in the astrophysical community. The problem was soon linked to problems in emerging elementary particle physics and physical cosmology, both supporting its acceptance. Non-relativistic (thus called "cold") elementary particles emerged as most probable candidates for constituting the major amount of dark matter in the Universe. However, during this period, it remained controversial whether dark matter really existed or was just an expression for a fundamental lack of understanding of the physics at galactic and intergalactic scales.
- The forth episode lasts from about 2000 until today, and can be denoted as "post-controversial": The matter paradigm of dark matter has prevailed, and a consensus has been established about the elementary particle character of cold dark matter. The discussion about modifications of gravitational theory is widely marginalized and constitutes only a niche research field. However, no particle dark matter has yet been detected, and it still remains unclear which exact kind of elementary particles form dark matter. If, despite the ongoing extensive research efforts, no particle dark matter will be found within the next decades, it is possible that this post-controversial subject will become controversial again.

Delayed dark matter research: A case study for the history of science

The above description of the history of the dark matter problem suggests that for a long time, only a few people attended to problems in galaxy dynamics, without their results being widely discussed. Why did such a long time have to pass until the problem was accepted as fundamental? It has been argued that this can be well understood by the large uncertainties in the underlying datasets. This line of reasoning is promoted by historian of science Tricia Close-Koenig (2001, 2004), who argues that observational techniques before World War II were too poor and measurement uncertainties not well enough understood to give definite convictions about a serious anomaly in galactic dynamics. For example, in his 1954 publication, Martin Schwarzschild stated that the "bewilderingly high value for the mass-luminosity ratio must be considered as very uncertain since the mass and particularly the luminosity of the Coma cluster are still poorly determined." (Schwarzschild, 1954, p. 281). As emphasized by Bertone and Hooper (2016), Zwicky used the value of $H_0 = 558\,\mathrm{km\,s^{-1}\,Mpc^{-1}}$ for the Hubble constant in his seminal papers, for which Hubble and Humason (1931) claimed an accuracy of better than 20%.[4] As we know today, the Hubble constant is more than a factor eight lower than that value, and probably physicists at that time intuitively suspected that the value given by Hubble and Humason (1931) was much more uncertain than stated by the authors.

However, deficient instruments and measurements can only partially explain why scientists neglected the problem of gravitation at large scales for so long. At the latest in the 1950s, there were several unrelated indications for a lack of understanding of the mass constitution of galaxies: The mass-to-light ratios of at least two large galaxy clusters and the rotation curve of M31, measured independently several times with different methods. Virgina Trimble (2013) argues that in the decades after World War II, only a few people followed up galaxy dynamics related research, as other topics were much more in the focus of postwar astrophysics. In particular, she states a “golden age of stellar structure and evolution research” in the 1950s, in a time where nuclear physics processes had been largely understood. Also, the period after World War II marked a phase of extensive military support of relevant scientific research in the United States and the Soviet Union. In astrophysics, topics like thermonuclear reactions in stars, modeling of explosive processes and shock-wave physics touched military relevance. Paul Forman (1987) states a massive influence on the physics research programs conducted in the United States during the Cold War era, especially during the 1950s–1960s, via defense-related funding.

Still, these lines of reasoning do not provide an exhaustive account for the case of a delayed research on dark matter. In addition to the above patterns of explanation, an earlier breakthrough in identifying dark matter problem might have been severely hindered by insufficient research communication within the scientific community. The citation behavior of the dark matter protagonists before the 1980s suggests that dissemination of dark matter knowledge was suppressed both in time and place: There were no strong ties, neither to preceding works, nor between different research groups. The involved researchers barely knew about existing findings related to the problem and possible crosslinks of the problem between neighboring disciplines such as astronomy, numerical astrophysics, particle physics and cosmology. The fact that the dark matter problem was named differently by different communities may be considered a consequence of the isolated research works.

The case insufficient research communication hindering a breakthrough is not an uncommon one. Especially in the history of astrophysics, the back-story of the discovery of the CMB shows remarkable similarities to the history of dark matter.[5] The existence of a CMB radiation as a

---

[4] “It is believed, however, that the uncertainty in the final result is definitely less than 20 per cent and probably not more than 10 per cent.” (Hubble and Humason, 1931, p.76)

[5] The history of the discovery of the CMB radiation is nicely depicted and discussed in the accounts of Weinberg

remnant of an expanding Universe had been predicted at least twice without consequences, by Georges Lemaître (1931) and later, more precisely, by Alpher and Herman (1948). According to Kragh (1996, p. 133), Alpher and Herman's prediction was eventually repeated in at least seven articles in the years after 1948, without bringing anybody to subsequently perform experiments to test these hypotheses. Finally in 1965, J. Peebles and R. Dicke assessed the possibility of a cosmic background radiation, without knowing the earlier works and calculated a blackbody radiation spectrum with the temperature of around 10 Kelvin (Kragh, 2007, p. 202). While they were preparing an experiment to verify their prediction, the radiation had been coincidentally measured by radio astronomers A. Penzias and R. Wilson in the very same year (Penzias and Wilson, 1965). However, Penzias and Wilson became aware of what they measured first when they were informed about the theoretical works by Dicke and Peebles. It is even more striking that the CMB radiation was in fact not only predicted, but also measured before 1965, without realizing its origin. In 1955, "French radio astronomer Émile Le Roux [...] found a temperature [of a measured radiowave signal] of 3 ± 2 Kelvin with a high degree of isotropy" (Denisse et al., 1957; Kragh, 1996, p. 343) and subsequently in 1957, Soviet astrophysicist T. Shmaonov again measured a signal in the microwave domain and reported "that the effective temperature of the radiation was 4 ± 3 Kelvin and that its intensity was independent of the direction of his antenna." (Kragh, 1996, p. 343). Doroshkevich and Novikov (1964) even interpreted a previous measurement by Ohm (1961) in the light of the theory of Alpher et al. (1948) on primordial nucleosynthesis (Kragh, 1996, p. 344). The full list is even longer and is commented on in detail by Kragh (1996).

Analogous to the case of dark matter, the missed opportunities to "discover" the CMB radiation before 1965 was more a problem of communication than a technical obstacle.[6] Of course there are differences between the case of the CMB and dark matter. Firstly, a predicted CMB has been discovered, while the existence of dark matter is still speculative. Secondly, in the dark matter case, it is not the case that a theoretical prediction was not followed by experiments to prove or disprove that theory. Conversely, experimental evidence did not gain the attention of theoreticians who could provide a consistent model for these observations. However, both stories share the property that a new physical concept could have been judged as important considerably faster, if only the results from different communities had been put in context earlier.

The two examples about delayed research communication in the history of astrophysics should thereby be regarded in a broader context. Most disciplines of 20th and 21st century science are divided into highly specialized communities and a diversity of publication journals. Because of

---

(1993, pp. 120ff.), Kragh (1996, pp. 132ff. & pp. 343ff.) and Kragh (2007, pp. 201ff.), giving a collection of further references covering that topic.

[6] For the history of the CMB discovery, this has been already stated by Weinberg (1993, p. 123f.) and Kragh (1996, p. 135).

the number of journals and articles, one may argue that it was – and is – hardly possible to keep track of and contextualize scientific discussions at the margins of one's own research focus. Helge Kragh comments in the context of the CMB discovery that the early predictions of Alpher and Herman (1948) were only published in a nuclear-physics context – although published in *Nature*. He argues that if they were published in an astrophysical journal, they would have possibly gained far more attention (Kragh, 1996, p. 134). Fritz Zwicky's first publication on dark matter in 1933 was published in the Swiss *Helvetica Physica Acta* in German. Also, the Cold War period hindered scientific exchange between physicists from the Western World and the Eastern Bloc. Nowadays, research results are widely freely accessible, especially in physics through the arXiv preprint system, and digitally searchable. However, the tremendous increase of publication output may obscure relevant contributions, especially when there is need for unexpected crosslinks and coincidental encounters.

The histories of dark matter and the CMB show how difficult it may be to make an important discovery, even when all relevant facts and puzzle-pieces are already available. While the history of the CMB has been widely studied, no comprehensive account exists of the history of dark matter, which covers almost a century of research and evidence. Although the solution to the dark matter case is yet to be seen, it provides an extensive case study of how scientific knowledge emerges. It illustrates how, besides empirical and conceptual evidence, social interaction and communication among the scientific community may bolster or thwart a research program.

Appendices

A | Appendix to chapter 2

A.1. Potential of an exponential thin disk

The gravitational potential of the infinitesimally thin exponential disk, Equation 2.1,

$$\Sigma(R) = \frac{M_{\rm disk}}{2\pi\, R_{\rm s}^2}\, e^{R/R_{\rm s}} = \Sigma_0\, e^{R/R_{\rm s}}\,,$$

can be expressed by closed functions in the $Z = 0$ plane (Cuddeford, 1993):

$$\Phi_{\rm disk}(R,\, Z = 0) = -\frac{G\, M_{\rm gal}\, R}{2R_{\rm s}^2}\, [I_0(y)K_1(y) - I_1(y)K_0(y)]\,, \tag{A.1}$$

with $y = R/(2\, R_{\rm s})$ and I_n/K_n the modified Bessel functions of the first/second kind. Solving the Newtonian Lagrange equations yields that $\Phi_{\rm disk}$ allows circular orbits in the $Z = 0$ plane, with the absolute circular velocity v in these orbits at given R,

$$V(R)^2 = R\, \left.\frac{\partial\Phi}{\partial R'}\right|_{R'=R,\, Z=0}\,, \tag{A.2}$$

$$\Rightarrow V_{\rm disk}^2(R,\, Z = 0) = \frac{2\, G\, M_{\rm gal}}{R_{\rm s}^2}\, y^2\, [I_0(y)K_0(y) - I_1(y)K_1(y)]\,. \tag{A.3}$$

A.2. Cosmological quantities and matter power spectrum

A.2.1. Scale factor, Hubble constant, density parameters

The scale factor a is introduced by the Friedmann-Lemaître-Robertson-Walker metric, describing the most general homogeneous and isotropic spacetime in General Relativity,

$$\mathrm{d}s^2 = a^2(t) \left[\frac{\mathrm{d}r^2}{1 - k\, r^2} + r^2\, \mathrm{d}\Omega^2 \right] - \mathrm{d}t^2 \,, \tag{A.4}$$

where $k = 0$, ± 1 and r the radial, and $\mathrm{d}\Omega$ the angular coordinates of the metric. The Hubble parameter then is defined as $H := \dot{a}/a$. The average energy density of a particular species in the Universe can be expressed in units of the critical density,

$$\rho_{\mathrm{crit}}(t) = 3\, H^2(t)/(8\pi G) \,, \tag{A.5}$$

by defining the dimensionless “Omega parameters”, $\Omega_X(t) = \rho_X(t)/\rho_{\mathrm{crit}}(t)$. Here, X denotes the matter species, $X = \mathrm{b}$ (baryonic matter), $X =$ ‘cold’ dark matter (CDM), $X = \mathrm{m}$ (baryonic matter + cold dark matter), $X = \mathrm{r}$ (radiation), $X = \Lambda$ (dark energy). For dark energy, $\rho_\Lambda = \Lambda/(8\pi G)$.

A.2.2. Matter power spectrum

The three-dimensional power spectrum of density fluctuations, $P_\delta(k, z)$, is:

$$P_\delta(k, z) = \frac{8\pi^2}{25} \left(\frac{a_0\, k}{a\, H} \right)^4 \frac{1}{k^3}\, T(k, z)^2\, \mathcal{P}_{\mathcal{R}} \,, \tag{A.6}$$

where $\mathcal{P}_{\mathcal{R}}$ are the primordial density fluctuations from inflation. The transfer function at $z = 0$ is given by

$$T(k, 0) = \begin{cases} 1 & \text{for } k \ll k_{\mathrm{eq}} \\ \left(\frac{k_{\mathrm{eq}}}{k}\right)^2 \ln\left(\frac{k}{k_{\mathrm{eq}}}\right) & \text{for } k \gg k_{\mathrm{eq}}. \end{cases} \tag{A.7}$$

The primordial perturbations, $\mathcal{P}_{\mathcal{R}} \sim A\, k^{n_{\mathrm{s}} - 1}$, have been measured to be scale-invariant with $n_{\mathrm{s}} = 0.968 \pm 0.006$, and $\mathcal{P}_{\mathcal{R}} = A \approx 25 \times 10^{-10}$ (Ade et al., 2016). Then,

$$P_\delta(k, 0) = 6.4 \times 10^5\, T(k, 0)^2 \left(\frac{k}{h\, \mathrm{Mpc}^{-1}} \right) \left(h^{-1} \mathrm{Mpc} \right)^3 \,, \tag{A.8}$$

in agreement with the measurements shown in Figure A.1.

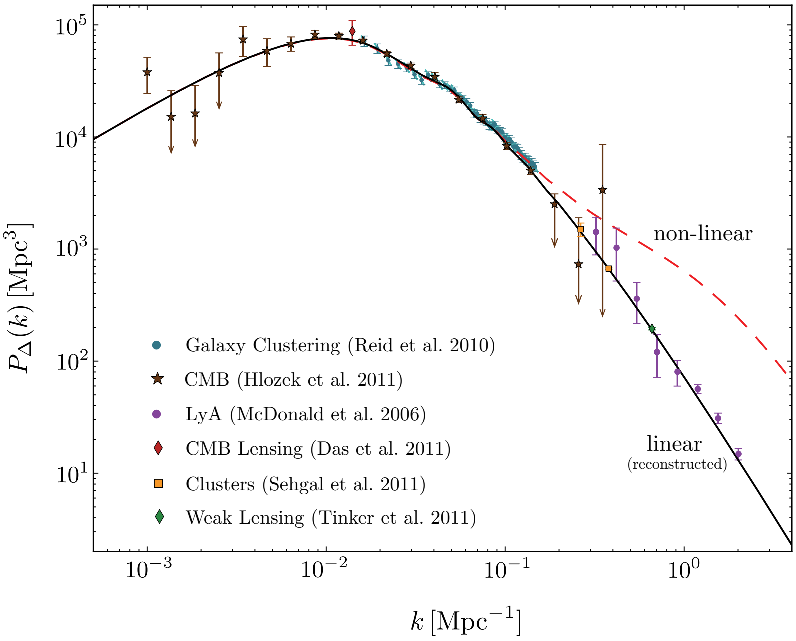

Figure A.1.: Matter power spectrum. Figure taken from Baumann (2013). The spectrum bends around $k_{\mathrm{eq}} = 0.06\,\mathrm{Mpc}^{-1}$, where the corresponding scale $\lambda_{\mathrm{eq}} = 113\,\mathrm{Mpc}$ enters the horizon.

A.2.3. Cosmic length scales

The redshift of horizon entry over-plotted in Figure 2.4 depends on the depicted scale length and is calculated by numerically calculating the proper distance:

$$D_{\mathrm{H}}(t) = a_0\, c_0 \int_{t_0}^{t_1} \frac{1}{a(t')}\,\mathrm{d}t' = c_0 \int_{z_1}^{z_0} \frac{1}{H(z')}\,\mathrm{d}z'\,, \tag{A.9}$$

with $z_0 = \infty$ ($t_0 = 0$), $z_1 = z$. For a flat Universe, $\Omega_{\mathrm{K}} \equiv 0$,

$$H(z) = H_0 \sqrt{\Omega_{\mathrm{m}}^0\,(1+z)^3 + \Omega_{\mathrm{r}}^0\,(1+z)^4 + \Omega_{\Lambda}^0}\,, \tag{A.10}$$

with the cosmological parameters from Ade et al. (2016): $\Omega_{\mathrm{CDM}}^0 = 0.119/h^2$, $\Omega_{\mathrm{b}}^0 = 0.022/h^2$, $\Omega_{\mathrm{r}}^0 = 4.1756/h^2$, $\Omega_{\mathrm{m}}^0 = \Omega_{\mathrm{CDM}}^0 + \Omega_{\mathrm{b}}^0 = 0.141/h^2$, $h = 0.678$. In particular,

$$\Omega_{\mathrm{r}}^0 = \left[1 + \frac{7}{8}\,N_\nu \left(\frac{4}{11}\right)^{4/3}\right] \Omega_\gamma^0 = 1.690\,\Omega_\gamma^0\,, \tag{A.11}$$

with $N_\nu = 3$ neutrino species. The Jeans length for the baryon-photon fluid is calculated by:

$$\lambda_J(z) = 2\pi\sqrt{\frac{2}{3}}\,\frac{c_{\mathrm{s}}(z)}{H_0\,\sqrt{\Omega_{\mathrm{b}}^0\,(1+z)^3 + \Omega_\gamma^0\,(1+z)^4}}\,, \tag{A.12}$$

with the sound speed

$$c_{\mathrm{s}}(z) = \frac{c_0}{\sqrt{3}}\,\frac{1}{\sqrt{1+\frac{3}{4}\frac{\Omega_{\mathrm{b}}^0}{\Omega_{\mathrm{r}}^0}\,(1+z)^{-1}}}\,. \tag{A.13}$$

For four characteristic redshift values, Table A.1 shows the co-moving distance, the corresponding length scale which becomes sub-horizon at that time, and the matter-radiation Jeans length, Equation 2.9,

		$z = 10^5$	$z_{\mathrm{eq}} = 3375$	$z_{\mathrm{dec}} = 1100$	$z = 0$
co-moving horizon	D_{H}	4.6 Mpc	113 Mpc	279 Mpc	14.17 Gpc
	k_{H}	$1.4\,\mathrm{Mpc}^{-1}$	$0.06\,\mathrm{Mpc}^{-1}$	$0.02\,\mathrm{Mpc}^{-1}$	$4.4 \times 10^{-4}\,\mathrm{Mpc}^{-1}$
Jeans length $\Omega_b + \Omega_r$	λ_{J}	18 Mpc	444 Mpc	1.03 Gpc	(3.00 Gpc)
	k_{J}	$0.35\,\mathrm{Mpc}^{-1}$	$0.014\,\mathrm{Mpc}^{-1}$	$0.006\,\mathrm{Mpc}^{-1}$	$(0.002\,\mathrm{Mpc}^{-1})$

Table A.1.: Characteristic cosmic length scales at four characteristic redshift values. The redshift z_{eq} corresponds to the transition from a radiation to a matter dominated universe, and z_{dec} is the time of the CMB photon bath decoupling. For the largest time, the Jeans length of the Universe's coupled baryonic matter and radiation plasma has been larger than the causal horizon, given by D_{H}.

A.3. Analytical derivation of the WIMP freeze-out cross section

In thermal equilibrium, weakly interacting massive particle (WIMP) particle-antiparticle pairs are constantly created from and destroyed by annihilation into some other species X, Y,

$$\chi\overline{\chi} \leftrightarrow XY. \tag{A.14}$$

The number density of the WIMPs in thermal equilibrium, n_{eq}, is dependent on the energy density of the thermal bath, expressed by the photon temperature $T \equiv T_\gamma$. [1] For fermionic WIMPs with a vanishing chemical potential $\mu \approx 0$ (the latter applies for the same amount of particles and anti-particles in the Universe), their thermal equilibrium number density is given

---

[1] Photons are the "thermal reference particles", because they maintain in thermal equilibrium with any other particle until latest. The final thermal decoupling, after which all species in the Universe have been thermally decoupled, occurred at the time of recombination, when electrons and protons formed stable neutral hydrogen.

by (see, e.g., Baumann, 2013):

$$n_{\mathrm{eq}}(T) = \frac{g_\chi}{(2\pi)^3} \int_0^\infty \frac{4\pi p^2 \,\mathrm{d}p}{e^{E/T}+1} = \begin{cases} \dfrac{3\zeta(3)}{4\pi^2} g_\chi T^3 & \text{if } T \gg m_\chi \quad \text{(A.15a)} \\ g_\chi \left(\dfrac{m_\chi T}{2\pi}\right)^{3/2} e^{-\frac{m_\chi}{T}} & \text{if } T \ll m_\chi . \quad \text{(A.15b)} \end{cases}$$

Here, $E^2 = p^2 + m_\chi^2$, and $\zeta(3) = 1.202\ldots$ the Riemann zeta function. In the limit of Equation A.15b, $T \ll m_\chi$, bosons and fermions behave equally, and the average particle energy becomes $\langle E \rangle = m_\chi + \frac{3}{2}T$ according to the Maxwell-Boltzmann distribution. This is the non-relativistic limit, $p \ll m_\chi$. In this limit, at temperatures $T \ll m_\chi$, there is hardly energy left for WIMP creations. The annihilation of the WIMPs dominates over their creation, and the number density is exponentially suppressed with falling temperature. The evolution according to Equation A.15a & Equation A.15b is halted at the time of freeze-out, t_f, when the WIMPs chemically decouple from the thermal equilibrium. In principle, freeze-out may occur at any time, already in the relativistic limit or never. In the following, it is assumed that around t_f the WIMPs already have reached the non-relativistic limit.

The calculation of the time evolution of the number density $n(t)$ of any[2] particle species, departing from thermal equilibrium state into freeze-out, requires the solution of the Boltzmann-equation for an annihilation species,

$$\frac{1}{a^3}\frac{d(na^3)}{dt} = -\langle \sigma v \rangle (n^2 - n_{\mathrm{eq}}^2). \tag{A.16}$$

Here, $a(t)$ denotes the scale factor of an expanding Friedmann-Lemaître universe, and $\langle \sigma v \rangle$ the velocity-averaged annihilation cross section. The right-hand side of Equation A.16 expresses the dilution of the number density in an expanding three-dimensional space. The left hand side contains the collision term, expressing that the system always tries to relax towards equilibrium. The higher $\langle \sigma v \rangle$, the faster it is pushed back towards equilibrium, $n = n_{\mathrm{eq}}$. In Equation A.16, it is already implicitly assumed that there is the same amount of particles χ and antiparticles $\overline{\chi}$, and that the reacting relativistic particles X, Y always remain in thermal equilibrium.

Solving Equation A.16 requires assumptions about $a(t)$, $\langle \sigma v \rangle(t)$ and $T(t)$, and Equation A.15 for $n_{\mathrm{eq}}(T)$. A rigorous solution $n(t)$ can only be obtained numerically, but statements about the relic density $n(t \gg t_f)$ can be given in terms of analytical expressions.

---

[2] Note that Equation A.16 holds for both for matter ($p(\rho) = 0$) and radiation (relativistic particles, $p(\rho) = 1/3$). Although the energy density ρ of radiation dilutes with $\rho \sim a^{-4}$ in an expanding universe, the number density n of radiation still evolves with $n \sim a^{-3}$.

The interaction rate Γ of an individual annihilating particle is given by

$$\Gamma(v, n) = \langle \sigma(v)\, v \rangle \times n, \tag{A.17}$$

where n is the target population for the interacting particle, v the relative velocity between the particle and a particle from the target population, and $\sigma(v)$ the velocity-dependent annihilation cross section. With this and the definition of the Hubble parameter, $H := \dot{a}/a$, one can rewrite Equation A.16 as

$$\frac{1}{H}\frac{\dot{n}}{n} + 3 = -\frac{\Gamma}{H}\left(1 - \frac{n_{\mathrm{eq}}^2}{n^2}\right). \tag{A.18}$$

The freeze-out time, t_f, is formally defined as the moment after which an individual particle undergoes less than one interaction in the whole future of the Universe,

$$\int_{t_f}^{\infty} \Gamma(t)\, \mathrm{d}t = 1. \tag{A.19}$$

For a radiation dominated universe and a temperature dependent $\Gamma(T) \sim T^n$, and $n > 2$,[3] Equation A.19 is equivalent to

$$\Gamma(T_f) = (n-2)\, H(T_f) \approx H(T_f) \tag{A.20}$$

In a radiation dominated universe, the Hubble constant evolves with

$$H(T) = \sqrt{\frac{4\pi^3 G}{45}}\, \sqrt{g_*(T)}\, T^2,$$

where

$$g_*(T) \equiv \sum_{\text{rel. bosons}} g_i \left(\frac{T_i}{T}\right)^4 + \frac{7}{8} \sum_{\text{rel. fermions}} g_i \left(\frac{T_i}{T}\right)^4 \tag{A.21}$$

defines the effective degrees of freedom of the relativistic ("rel.") particles. These degrees of freedom, as a function of temperature, are shown in Figure A.2 for the Standard Model (SM) particle zoo (no relativistic non-SM particles are assumed at any temperature).

To calculate the interaction rate, $\Gamma(T)$, the Boltzmann equation, Equation A.16, is ignored

---

[3] Note that $n = 3$ for velocity independent $\langle \sigma v \rangle$, as $n \sim T^3$ for both radiation and matter. For $\langle \sigma v \rangle \sim T^m$, it is $n = 3 + m$.

[4] For more information of how this number arises, see any standard cosmology textbook, e.g., Baumann (2013).

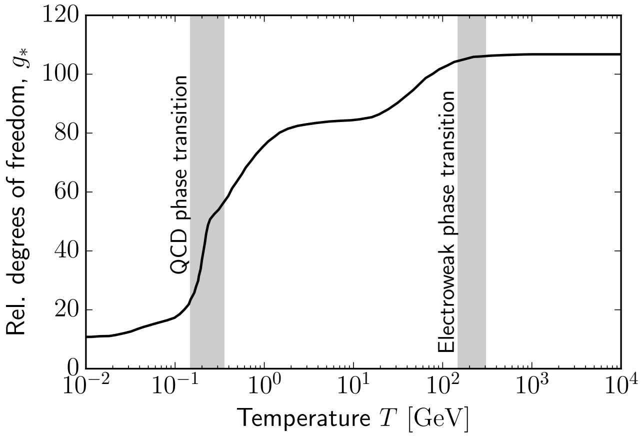

Figure A.2.: Effective degrees of freedom of relativistic SM particles, from Laine and Schröder (2006). For $T \gg 173\,\mathrm{GeV}$ (the top quark mass), this number approaches $g_* = 106.75$.[4] The temperatures of the electroweak and QCD phase transitions are marked as gray-shaded bands.

and it is assumed that until freeze-out, the dark matter (DM) number density follows the non-relativistic equilibrium distribution, Equation A.15a. Then, plugging these expressions into Equation A.20, one obtains ($\langle\sigma v\rangle_f \equiv \langle\sigma v\rangle(T_f)$):

$$\begin{aligned} \langle\sigma v\rangle_f \, g_\chi \left(\frac{m_\chi T_f}{2\pi}\right)^{3/2} e^{-\frac{m_\chi}{T_f}} &= \sqrt{\frac{4\pi^3 G}{45}} \sqrt{g_*(T_f)}\, T_f^2 \\ \sqrt{\frac{m_\chi}{T_f}}\, e^{-\frac{m_\chi}{T_f}} &= \frac{8\pi^3\sqrt{G}}{\sqrt{90}} \frac{\sqrt{g_*(T_f)}}{g_\chi\, m_\chi\, \langle\sigma v\rangle_f}. \end{aligned} \tag{A.22}$$

Here, the velocity-averaged cross section, $\langle\sigma v\rangle$, has been written as a function of the temperature T_f.[5] After freeze-out, the interaction rate has become lower than the expansion rate, such that the interaction process cannot catch up with the expansion to reestablish quasi-stationary equilibrium, i.e. $\Gamma(T) < H(T)$ for $T < T_f$. A sufficient time after freeze-out, $\Gamma \ll H$ holds, and

---

[5] Up to log-corrections, Equation A.22 can be written as:

$$\frac{m_\chi}{T_f} = -\ln\left(\frac{8\pi^3\sqrt{g_*(T_f)}}{\sqrt{90}\,g_\chi}\right) - \ln\left(\sqrt{G}\,m_\chi\right) + \ln\left(m_\chi^2 \times \langle\sigma v\rangle_f\right) + \mathcal{O}\left[\ln\left(\frac{m_\chi}{T_f}\right)\right]$$

Equation A.18 formally becomes

$$\frac{1}{H}\frac{\dot{n}}{n}+3\approx 0 \qquad \text{for} \quad T\ll T_f. \tag{A.23}$$

$$\Leftrightarrow \frac{1}{a^3}\frac{d(na^3)}{dt}\approx 0. \tag{A.24}$$

This is the continuity equation for the number density n in an expanding Friedmann-Lemaître cosmos, and the total number of particles of the frozen-out species is conserved.

If the transition phase $T \lesssim T_f \to T \ll T_f$ is ignored and it is assumed that any interaction is immediately stopped at freeze-out, T_f, then immediately after freeze-out the number density only dilutes with the Hubble-flow. According to Equation A.24 one can write

$$\frac{n(T_0)}{n(T_f)}=\left(\frac{a(T_f)}{a(T_0)}\right)^3. \tag{A.25}$$

Here, the lower temperature T_0 (at a later time $t_0>t_f$) denotes the present-day temperature of the CMB photons. Using the conservation of entropy, $g_{*s}(T)T^3\,a^3=\textit{const.}$, with

$$g_{*s}(T)\equiv\sum_{\text{bosons}} g_i\left(\frac{T_i}{T}\right)^3+\frac{7}{8}\sum_{\text{fermions}} g_i\left(\frac{T_i}{T}\right)^3, \tag{A.26}$$

one can replace the ratio between the scale factor at freeze-out time and today by the corresponding temperatures:

$$\left(\frac{a(T_f)}{a(T_0)}\right)^3=\frac{g_{*s}(T_0)}{g_{*s}(T_f)}\left(\frac{T_0}{T_f}\right)^3.$$

Using this and Equation A.20, Equation A.25 reads:

$$\begin{aligned}
n_\chi(T_0) &= \left(\frac{a(T_f)}{a(T_0)}\right)^3 n_\chi(T_f)\\
&= \frac{g_{*s}(T_0)}{g_{*s}(T_f)}\left(\frac{T_0}{T_f}\right)^3\frac{\Gamma(T_f)}{\langle\sigma v\rangle_f}\approx\frac{g_{*s}(T_0)}{g_{*s}(T_f)}\left(\frac{T_0}{T_f}\right)^3\frac{H(T_f)}{\langle\sigma v\rangle_f}\\
&= \frac{g_{*s}(T_0)}{g_{*s}(T_f)}\left(\frac{T_0}{T_f}\right)^3\sqrt{\frac{4\pi^3G}{45}}\,\frac{\sqrt{g_*(T_f)}}{\langle\sigma v\rangle_f}\,T_f^{\,2}\\
&\approx \sqrt{\frac{4\pi^3G}{45}}\,\frac{T_0^3}{T_f}\,\frac{g_{*s}(T_0)}{\sqrt{g_*(T_f)}}\,\frac{1}{\langle\sigma v\rangle_f}.
\end{aligned}$$

In the last line, $g_*(T_f)\approx g_{*s}(T_f)$ has been assumed. This is justified as at the time of DM freeze-out, there is no known relativistic particle decoupled from the photon bath, and $T_i = T\ \forall$ species i. By multiplying $n_\chi(T_0)$ with the mass m_χ of the particle, and by dividing by today's critical density $\varrho^0_{\text{crit}} = \frac{3}{8\pi G} H(T_0)^2$, one obtains today's dark matter energy fraction of the Universe:

$$\Omega^0_\chi \equiv \frac{\varrho^0_\chi}{\varrho^0_{\text{crit}}} = \frac{m_\chi\, n_\chi(T_0)}{\varrho^0_{\text{crit}}} = \sqrt{\frac{4\pi^3 G}{45}}\,\frac{T_0^3}{\varrho^0_{\text{crit}}}\,\frac{g_{*s}(T_0)}{\sqrt{g_*(T_f)}}\,\frac{m_\chi}{T_f}\,\frac{1}{\langle\sigma v\rangle_f}$$

$$\Leftrightarrow \quad \langle\sigma v\rangle_f = \sqrt{\frac{4\pi^3 G}{45}}\,\frac{T_0^3}{\varrho^0_{\text{crit}}}\,\frac{g_{*s}(T_0)}{\sqrt{g_*(T_f)}}\,\frac{m_\chi}{T_f}\,\frac{1}{\Omega^0_\chi} \tag{A.27}$$

Combining Equation A.22 and Equation A.27 eliminates $\langle\sigma v\rangle_f$ and results in an implicit equation for x_f:

$$g_*^{-1}\,(m_\chi/x_f)\; m_\chi\, x_f^{3/2}\, e^{-x_f} = \sqrt{8\pi^3}\,\frac{\varrho^0_{\text{crit}}}{g_{*s}(T_0)}\,\frac{\Omega^0_\chi}{g_\chi}. \tag{A.28}$$

For a fixed mass m_χ, Equation A.28 can be numerically solved for the unknown x_f, and with the solution, $\langle\sigma v\rangle_f$ can be determined with Equation A.27. The result, $\langle\sigma v\rangle_f$ as a function of m_χ, is finally shown in Figure 2.6.

Figure A.3 illustrates the above calculation compared to a numeric solution of the Boltzmann equations, Equation A.16. Here, the co-moving WIMP number density is shown, which is

$$\frac{a(x)^3\, n_{\text{eq}}(x)}{a(x=1)^3\, n_{\text{eq}}(x=1)} = \begin{cases} x^{3/2}\, e^{1-x}, & 1 \lesssim x \ll x_f \\ x_f^{3/2}\, e^{1-x_f}, & x \gg x_f. \end{cases} \tag{A.29}$$

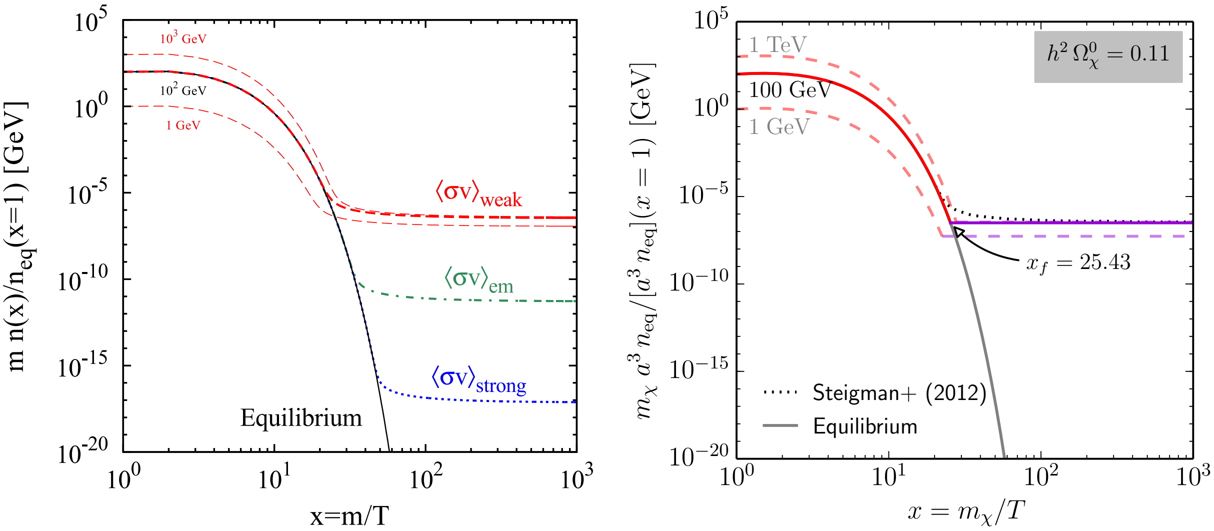

(a) Original figure from Steigman et al. (2012)

(b) Approximate calculation in this thesis

Figure A.3.: Co-moving WIMP number density, as a function of the universal photon temperature T. This comparison between the exact solving of the Boltzmann-equation A.16 by Steigman et al. (2012, *left panel*) and the calculation in this thesis (*right panel*) illustrates the applied approximation: In Fig. (b), the red curves reproduce Equation A.15b. The approximation assumes that the WIMP number density follows this equilibrium until freeze-out at x_f (calculated from Equation A.28). After freeze-out, n is modeled to immediately follow Equation A.25, which is represented by the violet curves, straight lines in the chosen co-moving coordinates. In Fig. (b), the difference between the relic number densities ($T \to 0\,\mathrm{K}$) of the calculation by Steigman et al. (2012, black-dotted line) and the approximate calculation is hardly visible, suggesting also a match of the relic cross section $\langle \sigma v \rangle_f$. Note however, that the vertical axes span over 25 orders of magnitude, such that the 15% difference in $\langle \sigma v \rangle_f$ between the approximate and the precise calculation, as shown in Figure 2.6, is not visible in this plot.

B | Appendix to chapter 4

B.1. Potentials and density profiles of analytical DM halo descriptions

DM halos and subhalos can be described, at first order, by spherical density profiles. For this, generic profiles are used which have been widely applied to different astrophysical contexts.

The most prominent description used for DM halos is the four-parameter Hernquist-Zhao family (Hernquist, 1990; Zhao, 1996), defined by

$$\frac{\mathrm{d}\log\rho}{\mathrm{d}\log r} = -\beta\left[1+\left(\frac{r}{r_\mathrm{s}}\right)^{-\alpha}\right]^{-1} - \gamma\left[1+\left(\frac{r}{r_\mathrm{s}}\right)^{+\alpha}\right]^{-1}\,, \tag{B.1}$$

and $r_\mathrm{s} > 0$, α, β, $\gamma \geq 0$. According to this definition, the mass density ρ is proportional to $r^{-\beta}$ at large radii r ($r \to \infty$) and proportional to $r^{-\gamma}$ at small radii ($r \to 0$). The transition between these two scalings is symmetric around the characteristic scale radius r_s and is smoothed by the parameter α ($\alpha \to 0$: no transition at all, $\alpha \to \infty$: non continuously differentiable slope change at r_s). Equation B.1 encompasses the density profiles by Plummer (1911, $\alpha = 2$, $\beta = 5$, $\gamma = 0$) and Jaffe (1983, $\alpha = 1$, $\beta = 4$, $\gamma = 2$).[1] For the DM case, the most famous member is the Navarro-Frenk-White (NFW) profile with inner logarithmic slope $\gamma = 1$, outer slope $\beta = 3$ and

---

[1] An exhaustive list of commonly known members of Equation B.1 is given by Zhao (1996).

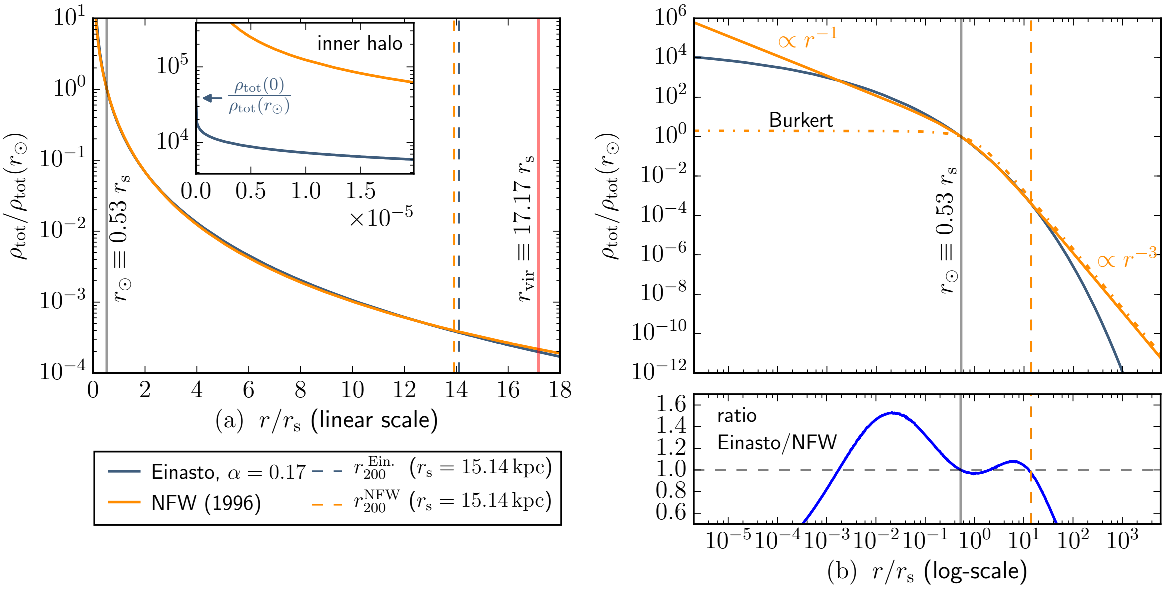

(a) $r/r_{\rm s}$ (linear scale)

(b) $r/r_{\rm s}$ (log-scale)

Figure B.1.: Comparison of different DM density profiles. An Einasto description, Equation B.3, with $\alpha = \alpha_{\rm E} = 0.17$ (pale blue curve) is compared to an NFW profile (Equation B.2, orange curve) and to a Burkert profile (left, Equation B.4, dot-dashed curve).

$\alpha = 1$ proposed by Navarro et al. (1996).[2] For this special case, the potential of Equation B.1 reads:

$$\Phi_{\rm NFW}(r) = -16\pi\, G\, \rho_{\rm s}\, r_{\rm s}^2\, \ln\left(1 + \frac{r}{r_{\rm s}}\right) \frac{r_{\rm s}}{r}\,, \tag{B.2}$$

where $\rho_{\rm s} = \rho(r_{\rm s})$. The analytical expression for the potential of the general form of Equation B.1 can be found in Zhao (1996). Despite its popularity, it is clear that the NFW potential according to Equation B.2 must fail at both very small and large r: Neither is Equation B.2 regular at $r = 0$ $({\rm d}\Phi_{\rm NFW}/{\rm d}r(r = 0) \to \infty)$, nor is the mass of the halo well defined $(r^2\, {\rm d}\Phi_{\rm NFW}/{\rm d}r(r \to \infty) \to \infty)$. Therefore, an alternative description of a spherical DM density profile has been proposed with the Einasto-Sersic profile (Einasto, 1965; Sersic, 1968),

$$\frac{{\rm d}\log\rho}{{\rm d}\log r} = -2\left(\frac{r}{r_{\rm s}}\right)^{\alpha_{\rm E}}\,. \tag{B.3}$$

This profile is characterized by a rolling power-law index, which, provided $r_{\rm s} > 0$, $\alpha_{\rm E} \geq 0$, is -2 at the scale radius $r_{\rm s}$, approaching zero at $r = 0$, and $-\infty$ for $r = \infty$. The parameter $\alpha_{\rm E}$ describes, analogously to α in the Hernquist-Zhao case, the smoothness of the transition of the

---

[2] A Hernquist-Zhao DM profile with steeper inner slope is given by Moore et al. (1999, $\alpha = 1.5$, $\beta = 3$, $\gamma = 1.5$).

rolling power-law index. In the limit $\alpha = \beta \to \infty$, $\gamma = 0$ or $\alpha_\mathrm{E} = \infty$ both the Hernquist-Zhao and the Einasto profiles approach a Heaviside function, $\rho = \rho_\mathrm{s}\,\Theta(r - r_\mathrm{s})$, describing a constant density sphere.

The analytical expression for the potential of the Einasto density defined by Equation B.3 is given by Retana-Montenegro et al. (2012), and a regular potential at $r = 0$ as well as a finite mass are obtained for all $0 < \alpha_\mathrm{E} < \infty$.[3] However, for $\alpha_\mathrm{E} < 1$, it is $\mathrm{d}\rho/\mathrm{d}r(r = 0) \neq 0$, as shown in the inset of Figure B.1 (left). In Figure B.1, an Einasto profile with $\alpha_\mathrm{E} = 0.17$ is compared to a NFW profile with the same scale radius $r_\mathrm{s} = 15.14\,\mathrm{kpc}$ and local DM density of $\rho_\mathrm{DM}(\rho_\odot = 8.0\,\mathrm{kpc}) = 0.4\,\mathrm{GeV\,cm^{-3}}$. From this figure, it can be seen that both descriptions define very similar density profiles, with a power-law index of -2 at $r = r_\mathrm{s}$, diverging from each other only at $r \ll r_\mathrm{s}$ and $r \gg r_\mathrm{s}$. Figure B.1 (left) shows that both descriptions describe a very steep density profile around $r = 0$, and also both profiles show a similar radius r_{200}, within which the mean density is 200 times the critical density. The inset shows that at $r = 0$, the density diverges $\propto 1/r$ for the NFW profile, whereas the Einasto density profile is finite. In Figure B.1 (right), the logarithmic distance scaling clearly reveals the difference between the descriptions. From the lower ratio plot, it follows that the Einasto profile predicts larger densities than a corresponding NFW profile in a regime of radii $r \lesssim r_\mathrm{s}$. This causes the Einasto profile to yield larger J-factors than the corresponding NFW profile for integration angles $\theta_\mathrm{int} \lesssim r_{200}/d$.

A non Hernquist-Zhao variant of the NFW profile has been introduced by Burkert (1995) to describe the empirically determined DM density profiles of dSph galaxies:

$$\frac{\mathrm{d}\log\rho}{\mathrm{d}\log r} = -\left[1 + \left(\frac{r}{r_\mathrm{s}}\right)^{-1}\right]^{-1} - 2\left[1 + \left(\frac{r}{r_\mathrm{s}}\right)^{-2}\right]^{-1}. \tag{B.4}$$

This profile is also shown in Figure B.1 (right). It can be seen that this profile behaves like the NFW description at large radii, whereas it describes a flat, cored halo center. The analytical expression for the potential of the mass density (B.4) can be found in Ferrer and Hunter (2013).

---

[3] The mass $M = 4\pi \int \rho\, r^2\, \mathrm{d}r$ diverges for $\alpha_\mathrm{E} \to 0$.

B.2. Direct comparison of the semi-analytical subhalo modeling to N-body simulation results

A robust quantity to characterize and compare subhalo populations between different simulations is the velocity v_{max}. The velocity v_{max} is the velocity for a circular orbit at radius r_{max} in a spherically symmetric, collisionless potential $\Phi = \Phi(r)$:

$$v_{\mathrm{max}}^2 = r_{\mathrm{max}} \left. \frac{\mathrm{d}\Phi}{\mathrm{d}r} \right|_{r=r_{\mathrm{max}}} , \tag{B.5}$$

where the velocity is maximal:

$$\left. \frac{\mathrm{d}v_{\mathrm{max}}^2(r)}{\mathrm{d}r} \right|_{r=r_{\mathrm{max}}} = 0. \tag{B.6}$$

For N-body simulation results, this quantity can be derived in a model-independent way, without assuming a specific subhalo density profile, by studying the movement of the DM particles bound in the subhalo overdensities. Also, determining v_{max} is not affected by the ambiguity of defining an outer bound of the subhalo potential and its mass.

For the semi-analytical modeling in this thesis, the subhalos are modeled by an Einasto density profile, Equation 4.1 or Equation B.3. With the expressions for Φ and $\mathrm{d}\Phi/\mathrm{d}r = G\, m(r)/r^2$ for the Einasto profile from Retana-Montenegro et al. (2012), Equation B.6 can be written as

$$\exp\left(-s^{\alpha_{\mathrm{E}}}\right) = \frac{\Gamma\left(3/\alpha_{\mathrm{E}}\right)}{\alpha_{\mathrm{E}}\, s^3} \left[1 - \frac{\Gamma\left(3/\alpha_{\mathrm{E}},\, s^{\alpha_{\mathrm{E}}}\right)}{\Gamma\left(3/\alpha_{\mathrm{E}}\right)}\right], \tag{B.7}$$

with $\Gamma\left(a,\, x\right) = \int_x^\infty t^{a-1}\, e^{-t}\, \mathrm{d}t$ the upper incomplete Gamma function, and $\Gamma\left(a\right) = \Gamma\left(a,\, x = 0\right)$. Equation B.7 can be solved numerically for $s = (2/\alpha_{\mathrm{E}})^{1/\alpha_{\mathrm{E}}}\, r_{\mathrm{max}}/r_{\mathrm{s}}$. For $\alpha_{\mathrm{E}} = 0.17$,

$$r_{\mathrm{max}} = 2.204\, r_{\mathrm{s}}. \tag{B.8}$$

Subsequently, v_{max} is calculated to be:[4]

$$v_{\mathrm{max}}^2 = 4\pi\, G\, \frac{\rho_{\mathrm{s}}\, r_{\mathrm{s}}^3}{r_{\mathrm{max}}}\, \frac{\exp(2/\alpha_{\mathrm{E}})}{(2/\alpha_{\mathrm{E}})^{3/\alpha_{\mathrm{E}}}}\, \frac{\Gamma\left(3/\alpha_{\mathrm{E}}\right)}{\alpha_{\mathrm{E}}} \left[1 - \frac{\Gamma\left(3/\alpha_{\mathrm{E}},\, 2/\alpha_{\mathrm{E}}\, (r_{\mathrm{max}}/r_{\mathrm{s}})^{\alpha_{\mathrm{E}}}\right)}{\Gamma\left(3/\alpha_{\mathrm{E}}\right)}\right] \tag{B.9}$$

$$= 11.245\, G\, \rho_{\mathrm{s}}\, r_{\mathrm{s}}^2. \quad \text{for} \quad \alpha_{\mathrm{E}} = 0.17. \tag{B.10}$$

Figure B.2 shows the cumulative distribution of subhalos in the models LOW and HIGH allowing

---

[4] For a NFW profile, it is analogously $r_{\mathrm{max}} = 2.163\, r_{\mathrm{s}}$ and $v_{\mathrm{max}}^2 = 2.717\, G\, \rho_{\mathrm{s}}\, r_{\mathrm{s}}^2$ (see, e.g., Lange and Chu, 2014).

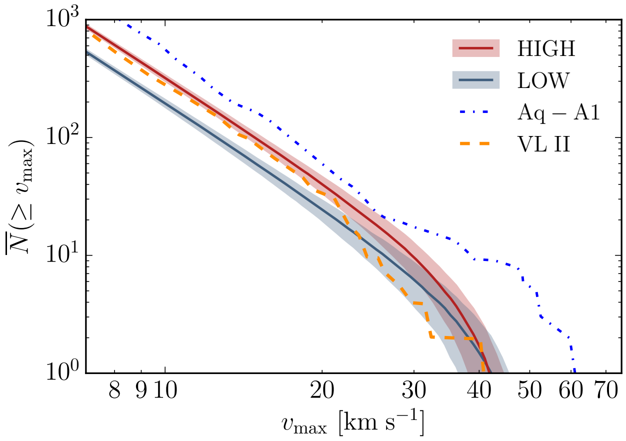

Figure B.2.: Cumulative subhalo number distribution versus $v_{\rm max}$, a measure of the subhalos' inner gravitational potential. The models LOW and HIGH are compared to the Aquarius A1 halo from Springel et al. (2008a, figure 9 bottom) and the Via Lactea II simulation (Diemand et al., 2008, all halos within $R_{1000} = 213\,\rm kpc$). For the models HIGH and LOW of this thesis, all halos with $m_{\rm vir} \geq 10^7\,\rm M_\odot$ within $R_{\rm gal} = 260\,\rm kpc$ are shown. The shaded bands denote the 68% C.I. around the mean. Recall that the model HIGH relies on the P-VLII subhalo concentration prescription, whereas the P-AQ description for the Aquarius simulation (not used in this thesis) predicts even higher concentrations (see Figure 4.2).

circular orbits with $v \geq v_{\rm max}$, averaged over 500 simulations with `CLUMPY`. These distributions are compared to the Aquarius A1 (Springel et al., 2008a) and Via Lactea II (VL II, Diemand et al., 2008) halos. It can be seen that the model HIGH fairly reproduces the properties of the VL II simulation, whereas higher $v_{\rm max}$ values are obtained for the Aq–A1 halo.

B.3. Slices through the J-factor–mass–distance cube of Galactic subhalos computed with `CLUMPY`

Figure B.3 presents the two-dimensional histogram of the distribution in brightness (in terms of the J-factor) and mass for the model LOW, analogous to the model HIGH shown in Figure 4.7 (left). Additionally, the one-dimensional projections along the axes are shown. Due to the (arbitrary) two-dimensional binning, the dotted lines of 0.1 (1) objects per bin do not exhibit a particular physical meaning; however, they indicate additionally to the color scale the topography of the subhalo distribution.

While Figures B.3 and 4.7 have shown the histograms in the J-factor–mass and J-factor–distance planes, Figure B.4 presents the slice through the mass–distance plane. From this figure, the approach for the numerical calculation of Galactic subhalos with the `CLUMPY` code becomes evident. In green, the Aquarius A2 subhalos according to Strigari (2013) are overplotted. Note that the blue-shaded histogram shows the average over 500 simulations.

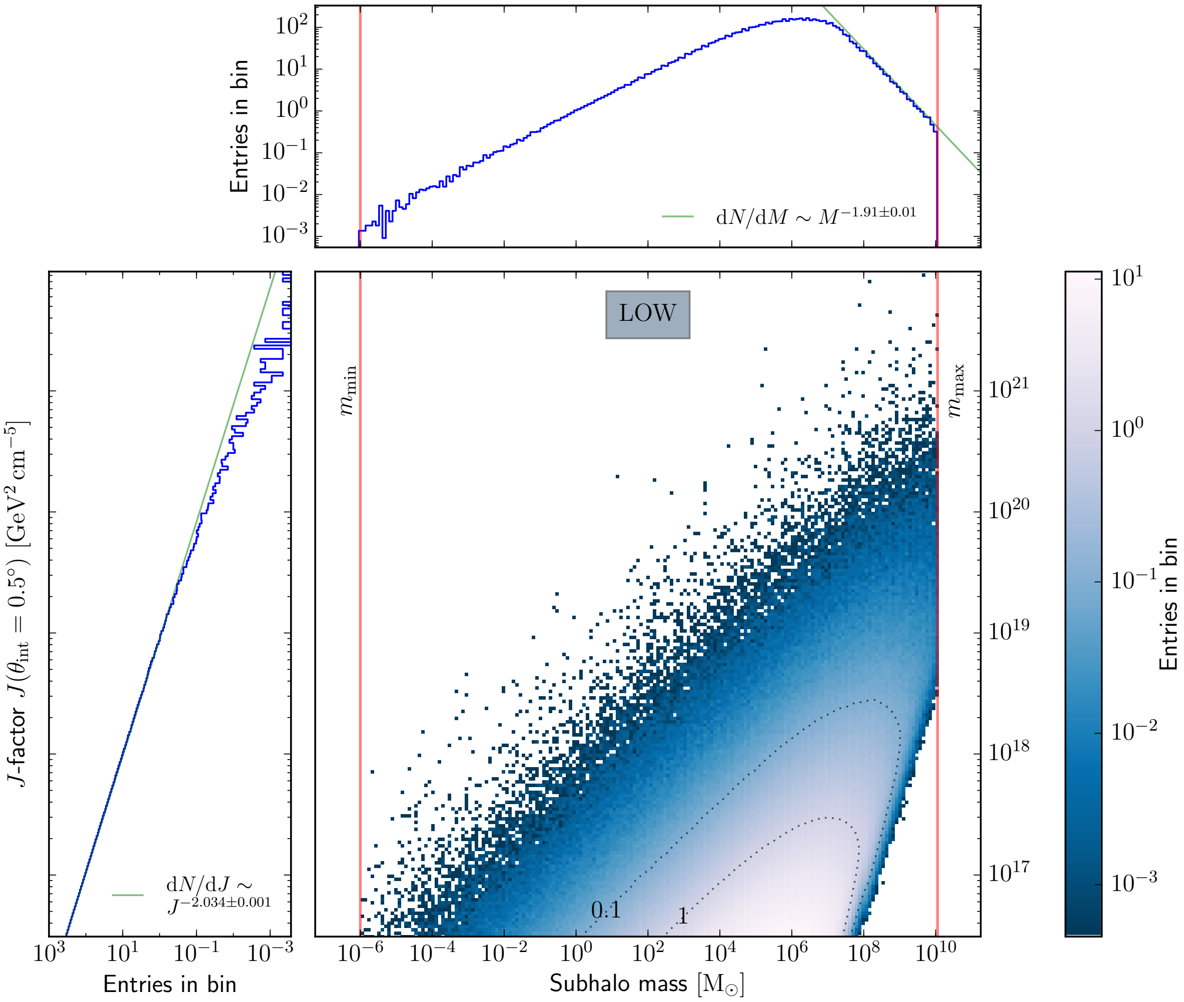

Figure B.3.: Same as Figure 4.7 (left), but for the model LOW instead of HIGH. Moreover, the one-dimensional projections along the J-factor axis (left) and the subhalo mass axis (top) are shown. The projection along the J-factor axis shows that asymptotically, the J-factor distribution is well fitted by a power-law with index 2.03 in this case. The projection along the mass axis shows that for the highest masses, all objects in the Galactic halo are resolved (see Figure B.4), and the input mass spectrum $\mathrm{d}N/\mathrm{d}M \sim M^{-1.9}$ is well reproduced. The dotted lines give surfaces of constant 1 (0.1) subhalo per bin.

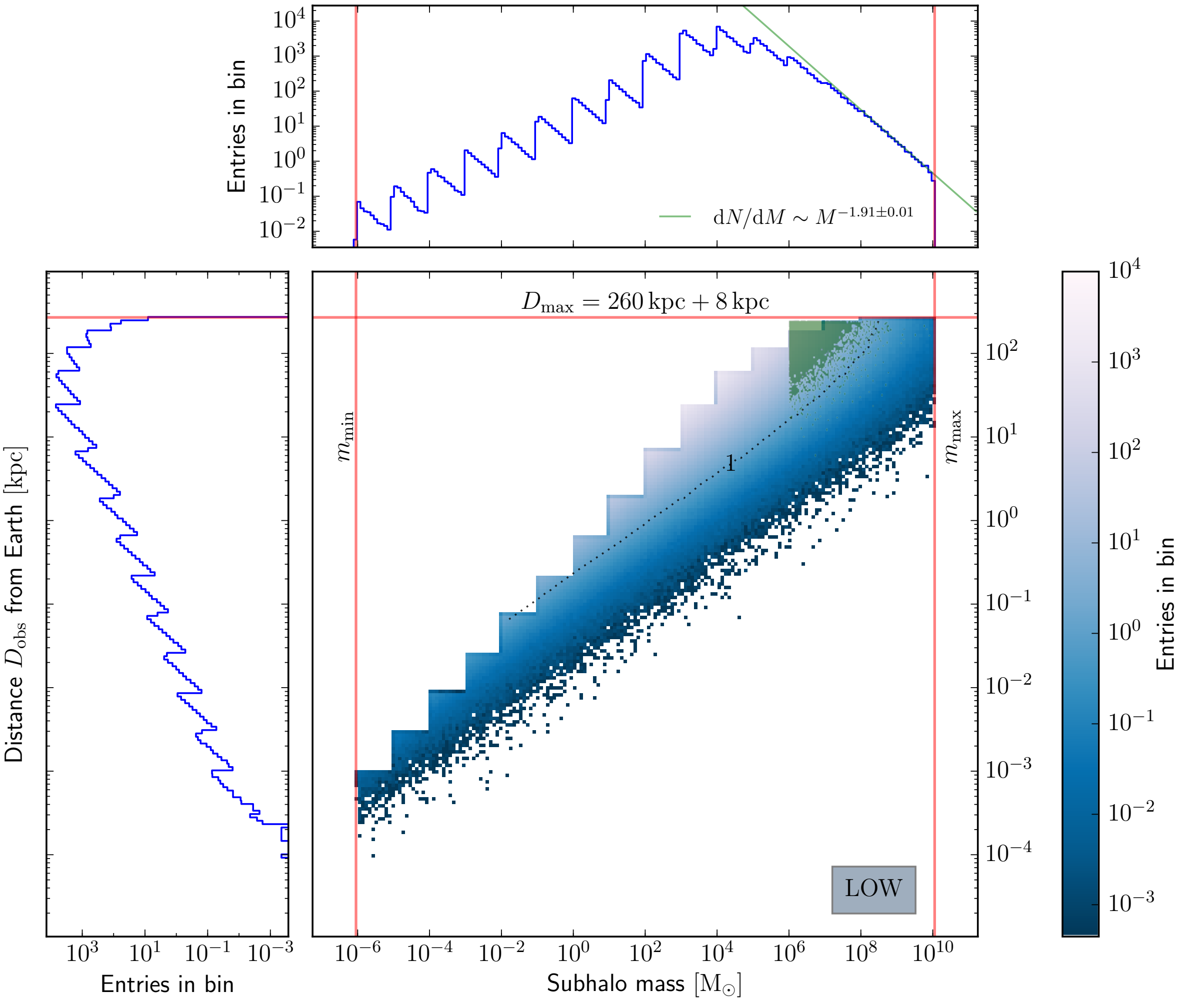

Figure B.4.: Subhalo distribution in the distance–mass plane for the model LOW. This illustrates the economic modeling approach of the `CLUMPY` code: For each subhalo mass decade, resolved subhalos are simulated up to a maximum distance $D_{\mathrm{obs}} = l_{\mathrm{crit}}$ from the observer (see Section 4.2). The heavier the objects, the larger l_{crit} are chosen. For the choices $\theta_{\mathrm{int}} = 0.5°$, $RE_{J_{\mathrm{clumps}}} = 0.35\%$, the resulting thresholds l_{crit} guarantee that all subhalos brighter than $J \approx 5 \times 10^{16}\,\mathrm{GeV^2\,cm^{-5}}$ are simulated, as can be verified in Figure B.3. The green-shaded scatter plot shows the Aquarius–A2 subhalos from Strigari (2013). For comparison, the dotted line indicates the surface of one subhalo per bin for the model LOW.

B.4. Illustration of the sub-subhalo modeling

Figure B.5 displays the calculation of sub-subhalo contributions in `CLUMPY`. In Figure B.5 (a), the subhalo benchmark model LOW on the full sphere is shown, with a zoom into a 15° × 15° region in Figure B.5 (b). Figure B.5 (c) then shows how J-factors and intensities change when a boost from one level of unresolved substructures within subhalos is considered: It can be seen that the emission in the outskirts of individually resolved subhalos is increased, as well as the diffuse background intensity from unresolved subhalos in the Galactic halo. In Figure B.5 (d) the brightest sub-subhalos within the brightest three subhalos in the detailed map are resolved for illustrative purposes; for the derivation of the properties of model VAR5 in the main text, it is not necessary to resolve the sub-subhalos. Also for illustrative purpose, Table B.1 lists the properties of the brightest three resolved subhalos in Figure B.5. From this follows that Figure B.5 shows typically bright dSph-like objects, like e.g., Segue 1. The curves in Figure 4.5 and Figure C.1 are based on halo H1 from Table B.1 and Figure B.5, which fairly matches the properties of the median brightest halo for the model LOW in the Cherenkov Telescope Array (CTA) case from Table C.1.

Halo	$m_{\rm vir}$ [$\mathrm{M}_\odot$]	$D_{\rm obs}$ [kpc]	$r_{\rm s}$ [kpc]	$c_{\rm vir}$	J–factor [GeV^2 cm^{-5}]					
					$\theta = 0.01°$		$\theta = 0.5°$		total	
					LOW	VAR5	LOW	VAR5	LOW	VAR5
H1	4.7×10^8	47	0.56	24.7	1.58×10^{18}	1.58×10^{18}	1.62×10^{19}	1.87×10^{19}	1.80×10^{19}	3.18×10^{19}
H2	9.6×10^8	108	0.91	19.4	5.03×10^{17}	5.03×10^{17}	3.73×10^{18}	5.84×10^{18}	3.97×10^{18}	9.49×10^{18}
H3	6.3×10^7	29	0.31	22.8	5.26×10^{17}	5.26×10^{17}	4.90×10^{18}	6.44×10^{18}	5.38×10^{18}	1.14×10^{19}

Table B.1.: Properties of the subhalos displayed in Figure B.5. Model VAR5 is identical to model LOW, but includes sub-subhalos. As shown in Figure 4.5, differences in the J-factors between model LOW and VAR5 first occur for integration angles $\theta_{\rm int} \gtrsim 0.1°$.

B.5. Reformulating the subhalo population profile by Gao et al. (2004)

Gao et al. (2004) find the subhalos in the GIF2 cosmological simulations well described by the functional form

$$\frac{N(<x)}{N_{200}} = \frac{(1 + a\,c_{200})\,x^\beta}{1 + a\,c_{200}\,x^\alpha}, \qquad x = \frac{R}{R_{200}}, \quad c_{200} = \frac{R_{200}}{R_s}, \quad \beta > \alpha \tag{B.11}$$

$$n(x) := \frac{\mathrm{d}}{\mathrm{d}x}\frac{N(<x)}{N_{200}} = \frac{(1 + a\,c_{200})\,x^{\beta-1}\,(\beta + a\,c_{200}(\beta - \alpha)\,x^\alpha)}{(1 + a\,c_{200}\,x^\alpha)^2}, \tag{B.12}$$

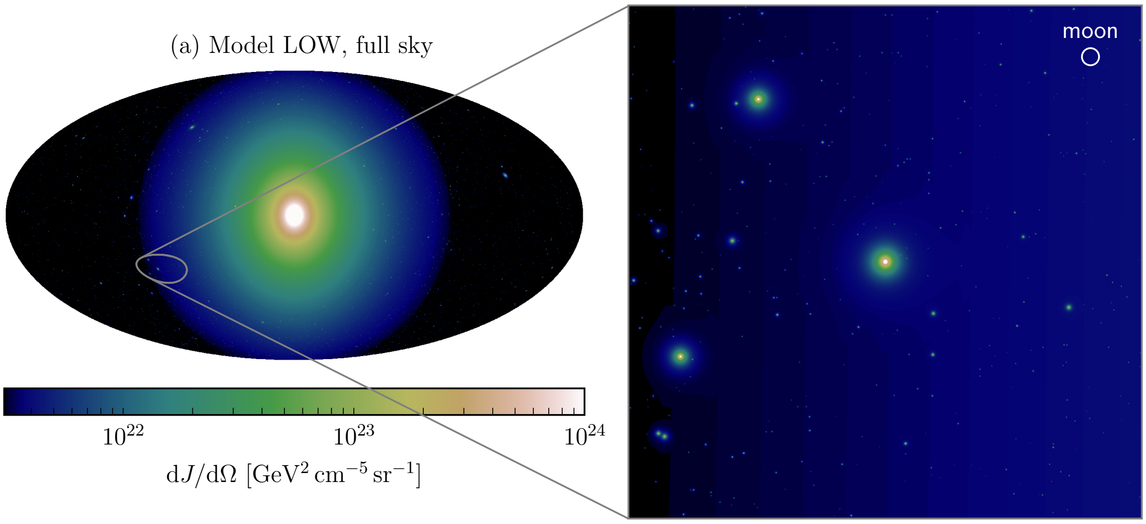

(a) Model LOW, full sky

(b) 15° × 15° detail (no sub-subhalos)

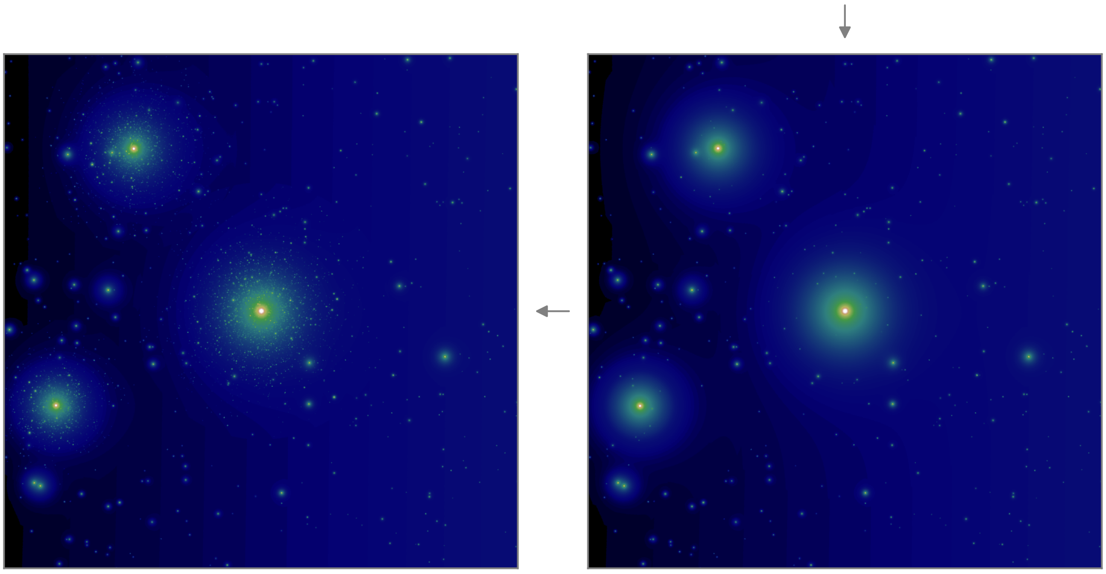

(d) Sub-subhalos, partially resolved

(c) Sub-subhalos, unresolved (model VAR5)

Figure B.5.: Illustration of the intensity boost by sub-subhalos in Galactic subhalos. The brightest three subhalos visible in the detailed maps are H1 (center), H2 (upper left) and H3 (lower left). The detailed properties of these three halos are listed in Table B.1.

with suitable fitted parameters a, α, β, the properties R_s and R_{200} of the host halo, and N_{200} all subhalos within R_{200}. According to the construction of $n(x)$ as derivation of $N(< x)$ and with $x_{\mathrm{tot}} := R_{\mathrm{gal}}/\, R_{200}$ it is

$$\int_0^1 n(x)\,\mathrm{d}x = 1\,, \tag{B.13}$$

$$\int_0^{x_{\mathrm{tot}}} n(x)\,\mathrm{d}x = \frac{(1 + a\,c_{200})\,x_{\mathrm{tot}}^{\beta}}{1 + a\,c_{200}\,x_{\mathrm{tot}}^{\alpha}}\,. \tag{B.14}$$

Furthermore,

$$N_{\mathrm{tot}} = N_{200} \int_0^{x_{\mathrm{tot}}} n(x)\,\mathrm{d}x. \tag{B.15}$$

Knowing N_{tot}, one can use Equation B.15 to substitute N_{200} and obtain the corresponding expression for $N(< \tilde{x})/\, N_{\mathrm{tot}}$ with $\tilde{x} := R/\, R_{\mathrm{gal}}$,

$$\frac{N(< \tilde{x})}{N_{\mathrm{tot}}} = \frac{\int_0^{\tilde{x}} n(x)\,\mathrm{d}x}{\int_0^{x_{\mathrm{tot}}} n(x)\,\mathrm{d}x}\,. \tag{B.16}$$

To obtain a volume density, Equation B.12 is divided by $4\pi\,x^2$,

$$\frac{\mathrm{d}\widetilde{P}}{\mathrm{d}V}(x) := \frac{(1 + a\,c_{200})\,x^{\beta-3}\,(\beta + a\,c_{200}(\beta-\alpha)\,x^{\alpha})}{4\pi\,\left(1 + a\,c_{200}\,x^{\alpha}\right)^2}\,, \tag{B.17}$$

The final probability density is obtained after normalizing $\mathrm{d}\widetilde{P}/\mathrm{d}V$ with respect to R_{gal},

$$\frac{\mathrm{d}P}{\mathrm{d}V}(\tilde{x}) = \frac{\frac{\mathrm{d}\widetilde{P}}{\mathrm{d}V}\left(\frac{R_{\mathrm{gal}}}{R_{200}} \times \tilde{x}\right)}{\int_0^{x_{\mathrm{tot}}} \int_{S^2} \frac{\mathrm{d}\widetilde{P}}{\mathrm{d}V}(x)\,\mathrm{d}V}\,. \tag{B.18}$$

B.6. Power-law source count distributions

As argued throughout this thesis (and, e.g., shown in Figure 4.4), the mean number of halos $\overline{N}(> J)$ with a J-factor larger than J is well described by a power-law distribution over a large range of J-factors,

$$\overline{N}(> J) \equiv \left\langle \int_J^{\infty} \frac{\mathrm{d}N}{\mathrm{d}J'}\,\mathrm{d}J' \right\rangle \approx \left(\frac{J}{J_{\mathrm{lim}}}\right)^{1-\alpha}\,, \tag{B.19}$$

where J_{lim} is defined by $\overline{N}(>J_{\mathrm{lim}}) = 1$, and α is constrained to $\alpha > 1$.[5]

B.7. Mean, median, and variance of the brightest DM halo

For a power-law source count distribution following Equation B.19, the extreme value distribution, which is the expected brightness of the brightest halo, follows a Fréchet distribution (Fréchet, 1928). To derive this probability density for the J-factor of the brightest halo, the probability $P_{\geq 1}$ to obtain at least one object brighter than a given flux J is defined:

$$P_{\geq 1}(J) := \sum_{N=1}^{\infty} p[N(>J) \,|\, \overline{N}(>J)], \tag{B.20}$$

with $p(N \,|\, \overline{N})$ the probability density to obtain exactly N objects brighter than J for an expectation value of $\overline{N}$. Assuming that $p(N \,|\, \overline{N})$ follows a Poisson distribution, the cumulative density function $P_{\geq 1}$ is given by

$$P_{\geq 1}(J) = 1 - \exp[-\overline{N}(>J)]\,. \tag{B.21}$$

For example, Equation B.21 implies that one obtains at least one subhalo brighter than J_{lim} with a chance of $1 - e^{-1} = 63\%$. Plugging in the power-law distribution $\overline{N}(>J)$ according to Equation B.19 into Equation B.21 results in the Fréchet probability density

$$\frac{\mathrm{d}P_{\geq 1}}{\mathrm{d}J}(J) = \frac{\alpha - 1}{J_{\mathrm{lim}}} \exp\left[-\left(\frac{J}{J_{\mathrm{lim}}}\right)^{1-\alpha}\right] \left(\frac{J}{J_{\mathrm{lim}}}\right)^{-\alpha}. \tag{B.22}$$

The expectation value $\overline{J}_{\geq 1}$ and the median $\widetilde{J}_{\geq 1}$ can be given by the following analytical expressions:

$$\overline{J}_{\geq 1} = \int_0^{\infty} J \,\frac{\mathrm{d}P_{\geq 1}}{\mathrm{d}J}\,\mathrm{d}J = \Gamma\left(\frac{1}{1-\alpha} + 1\right) \times J_{\mathrm{lim}}, \tag{B.23}$$

$$\widetilde{J}_{\geq 1} = \ln(2)^{1/(1-\alpha)} \times J_{\mathrm{lim}}. \tag{B.24}$$

Consequently, if the subhalo distribution can be approximated by a power-law distribution according to Equation B.19, then $\overline{J}_{\geq 1}$ and $\widetilde{J}_{\geq 1}$ are suitable analytical descriptions for the mean and median of the brightest halo, i.e. $\overline{J}^{\star} \approx \overline{J}_{\geq 1}$ and $\widetilde{J}^{\star} \approx \widetilde{J}_{\geq 1}$. The probability distribution B.22 is defined for $\alpha > 1$ and is always positively skewed, even with respect to a log-normal distribution. The long tail decreases following a power-law proportional to $J^{-\alpha}$, and thus the

---

[5] The subhalo source count distributions are even better described when including an exponential cut-off at J_{c}, $\overline{N}(>J) = (J/J_{\mathrm{lim}})^{1-\alpha} \exp[-(J - J_{\mathrm{lim}})/J_{\mathrm{c}}]$, according to a Schechter luminosity function (Schechter, 1976).

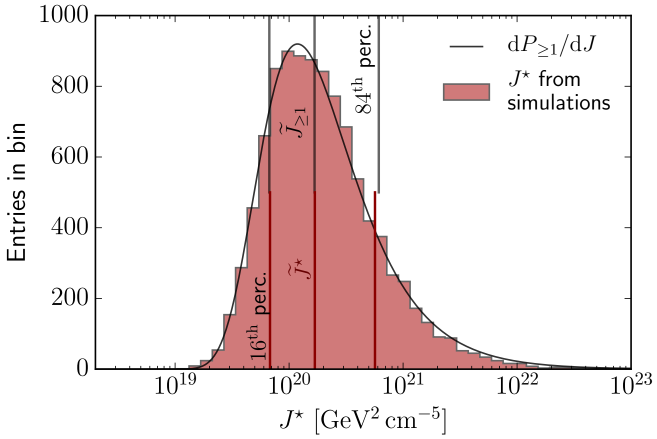

Figure B.6.: Probability distribution of the brightest subhalo $J^\star$ within the CTA survey FOV for model HIGH. For $J^\star$ the brightest halo within $\theta_{\mathrm{int}} = 0.05°$ is selected, but its J-factor then is calculated over its full spatial extent, θ_{vir} (total emission). The histogram (red) is based on 10^4 skymap realizations. The solid curve describes a fit by a Fréchet probability density according to Equation B.22, with $J_{\mathrm{lim}} = 1.2 \times 10^{20}\,\mathrm{GeV}^2\,\mathrm{cm}^{-5}$ (fixed by the 37th percentile from the skymap realizations) and $\alpha = 2.06$ (obtained from a least-square fit to the histogrammed skymap realizations). The vertical lines give the 16th, 50th, and 84th percentiles – from the skymap realizations (bottom half) or from the probability density $\mathrm{d}P_{\geq 1}/\mathrm{d}J$ (top half) – encompassing the 68% CI. Slightly modified figure published in Hütten et al. (2016).

mean is only defined for $\alpha > 2$ ($\overline{J}_{\geq 1} \to \infty$ for $\alpha \leq 2$). The mean is also always larger than the median value.

Figure B.6 shows the distribution of the brightest halo in the model HIGH from the calculation over 10^4 `CLUMPY` runs (red histogram) with a fitted Fréchet density according to Equation B.22 (black line). This confirms that Equation B.22 is an adequate model to describe the scattering of the brightest subhalo, and the long tail of high J-factors predicted by Equation B.22 is reproduced by the direct simulations. The quantiles defining the 68% credible intervals (C.I.) from the simulations are used for displaying the sensitivity variance in Section 5.2. As many astronomical source count distributions are described by power-law scalings, above considerations also apply to other contexts, e.g., the distribution of star cluster luminosities as recently studied by da Silva et al. (2014).

C | Appendix to chapter 5

C.1. Observation strategy for power-law source count distributions

For the argument given in Subsection 5.1.1, isotropically distributed sources on the sky are assumed, which obey a power-law flux source count distribution according to Equation B.19. Then one obtains for the mean number $\overline{N}$ of subhalos with a flux above a given threshold and on a survey area A:

$$\overline{N}(>F,\ A) = \left(\frac{F}{F_{\mathrm{lim,\,fullsky}}}\right)^{1-\alpha} \frac{A}{4\pi\,\mathrm{sr}}\,. \tag{C.1}$$

so that

$$\frac{\overline{N}(>F_1,\ A_1)}{\overline{N}(>F_2,\ A_2)} = \left(\frac{F_1}{F_2}\right)^{1-\alpha} \frac{A_1}{A_2}\,. \tag{C.2}$$

For a fixed total observation time T available to uniformly cover an area of the total size A, an area within A_{FOV} can be observed for $t = T \times (A_{\mathrm{FOV}}/A)$. As the sensitivity to a background dominated flux F goes as $1/\sqrt{t}$, it is $F_1/F_2 = \sqrt{t_2/t_1}$, and $t_1/t_2 = A_2/A_1$, so that

$$\frac{\overline{N}_{\mathrm{detectable}}(A_1, T)}{\overline{N}_{\mathrm{detectable}}(A_2, T)} = \left(\frac{A_1}{A_2}\right)^{\frac{3-\alpha}{2}}, \tag{C.3}$$

with A_1 and A_2 the observed area on the sky and $\overline{N}_{\mathrm{detectable}}$ the mean number of detectable objects. Thus, for a power-law index $\alpha < 3$, the average number of detectable subhalos is $\overline{N}(A_1) > \overline{N}(A_2)$ for $A_1 > A_2$ independent of T, and the probability of detecting an object from the population rises for increasing the survey area. This finding also has been presented in a slightly different way by Dubus et al. (2013).

It is also useful to extract from Equation C.1 the relation

$$\frac{F_{\mathrm{lim,\,A_1}}}{F_{\mathrm{lim,\,A_2}}} = \left(\frac{A_1}{A_2}\right)^{\frac{1}{\alpha-1}}. \tag{C.4}$$

For a power-law distribution, according to Equation B.23 and Equation B.24, this ratio also holds for the mean and median brightest halo,

$$\frac{F_{\mathrm{lim,\,A_1}}}{F_{\mathrm{lim,\,A_2}}} = \frac{\overline{F}^{\star}_{A_1}}{\overline{F}^{\star}_{A_2}} = \frac{\widetilde{F}^{\star}_{A_1}}{\widetilde{F}^{\star}_{A_2}}. \tag{C.5}$$

Thus, for a power-law index $\alpha \approx 2$, the ratio of the mean/median fluxes (or J-factors) of the brightest halo within two survey fields A_1, A_2 is simply proportional to the ratio of the field sizes. This is also confirmed when comparing the DM subhalo source count distributions in Figures 4.4, 5.6 and 5.10.

C.2. Properties of the brightest halo for CTA and *Fermi*-LAT for all models

Table C.1 lists the properties of the brightest DM subhalo in the models LOW and HIGH from the subhalo modeling described in Chapter 4. The numbers give the median and the 68% C.I. around the median, based on 10^4 simulations with `CLUMPY`.

Median properties of brightest subhalo within	CTA scenario: $f_{\rm sky} = 25\%$					
	model LOW			model HIGH		
	$\theta_{\rm int} = 0.05°$	$\theta_{\rm int} = 0.1°$	$\theta_{\rm int} = \theta_{\rm vir}$	$\theta_{\rm int} = 0.05°$	$\theta_{\rm int} = 0.1°$	$\theta_{\rm int} = \theta_{\rm vir}$
$\widetilde{D}^{\star}_{\rm obs}$ [kpc]	32^{+42}_{-23}	30^{+42}_{-22}	27^{+41}_{-20}	7^{+10}_{-5}	8^{+12}_{-6}	10^{+16}_{-8}
$\widetilde{R}^{\star}$ [kpc]	32^{+43}_{-21}	30^{+42}_{-20}	28^{+40}_{-18}	10^{+9}_{-2}	10^{+10}_{-3}	12^{+15}_{-4}
$\log_{10}(\widetilde{m}^{\star}_{\rm vir}/{\rm M}_{\odot})$	$8.7^{+0.9}_{-1.3}$	$8.6^{+0.9}_{-1.3}$	$8.6^{+0.9}_{-1.4}$	$7.4^{+1.4}_{-1.4}$	$7.6^{+1.4}_{-1.5}$	$8.0^{+1.3}_{-1.6}$
$\widetilde{r}^{\star}_{\rm vir}$ [kpc]	14^{+13}_{-9}	14^{+14}_{-9}	14^{+14}_{-9}	$5.4^{+9.5}_{-3.5}$	$5.9^{+11}_{-4.0}$	$8.1^{+14}_{-5.8}$
$\widetilde{r}^{\star}_{\rm s}$ [kpc]	$0.61^{+0.77}_{-0.42}$	$0.59^{+0.81}_{-0.41}$	$0.61^{+0.82}_{-0.45}$	$0.12^{+0.36}_{-0.08}$	$0.14^{+0.43}_{-0.10}$	$0.22^{+0.69}_{-0.17}$
$\widetilde{c}^{\star}_{\rm vir}$	23^{+6}_{-4}	23^{+6}_{-4}	22^{+6}_{-4}	45^{+16}_{-14}	43^{+17}_{-14}	37^{+17}_{-13}
$\widetilde{\theta}^{\star}_{\rm vir}$ [deg]	23^{+15}_{-8}	24^{+16}_{-9}	26^{+15}_{-9}	37^{+16}_{-11}	38^{+15}_{-11}	39^{+15}_{-10}
$\widetilde{\theta}^{\star}_{\rm s}$ [deg]	$1.0^{+1.0}_{-0.4}$	$1.1^{+1.0}_{-0.5}$	$1.2^{+1.0}_{-0.5}$	$1.0^{+1.1}_{-0.5}$	$1.1^{+1.1}_{-0.5}$	$1.3^{+1.1}_{-0.6}$
$\widetilde{\theta}^{\star}_{\rm h}$ [deg]	$0.14^{+0.11}_{-0.06}$	$0.14^{+0.14}_{-0.05}$	$0.16^{+0.12}_{-0.06}$	$0.13^{+0.16}_{-0.05}$	$0.14^{+0.14}_{-0.07}$	$0.18^{+0.14}_{-0.08}$
$\log_{10}\left(\widetilde{J}^{\star}/{\rm GeV}^2\,{\rm cm}^{-5}\right)$	$18.9^{+0.3}_{-0.2}$	$19.1^{+0.3}_{-0.3}$	$19.5^{+0.5}_{-0.3}$	$19.7^{+0.3}_{-0.3}$	$19.9^{+0.4}_{-0.3}$	$20.3^{+0.5}_{-0.4}$

Median properties of brightest subhalo within	*Fermi*-Large Area Telescope (LAT) scenario: $f_{\rm sky} = 82.6\%$					
	model LOW			model HIGH		
	$\theta_{\rm int} = 0.1°$	$\theta_{\rm int} = 0.8°$	$\theta_{\rm int} = \theta_{\rm vir}$	$\theta_{\rm int} = 0.1°$	$\theta_{\rm int} = 0.8°$	$\theta_{\rm int} = \theta_{\rm vir}$
$\widetilde{D}^{\star}_{\rm obs}$ [kpc]	20^{+27}_{-15}	19^{+26}_{-14}	19^{+26}_{-14}	7^{+10}_{-5}	8^{+11}_{-6}	8^{+12}_{-6}
$\widetilde{R}^{\star}$ [kpc]	21^{+26}_{-12}	20^{+25}_{-11}	20^{+25}_{-12}	9^{+9}_{-3}	10^{+10}_{-3}	10^{+11}_{-3}
$\log_{10}(\widetilde{m}^{\star}_{\rm vir}/{\rm M}_{\odot})$	$8.7^{+0.8}_{-1.4}$	$8.7^{+0.9}_{-1.4}$	$8.7^{+0.8}_{-1.4}$	$7.7^{+1.3}_{-1.5}$	$8.1^{+1.2}_{-1.6}$	$8.1^{+1.3}_{-1.5}$
$\widetilde{r}^{\star}_{\rm vir}$ [kpc]	14^{+12}_{-9}	14^{+13}_{-9}	14^{+13}_{-9}	$6.7^{+12}_{-4.6}$	$8.8^{+14}_{-6.1}$	$9.2^{+15}_{-6.3}$
$\widetilde{r}^{\star}_{\rm s}$ [kpc]	$0.63^{+0.75}_{-0.45}$	$0.64^{+0.78}_{-0.46}$	$0.63^{+0.79}_{-0.46}$	$0.13^{+0.42}_{-0.10}$	$0.19^{+0.55}_{-0.15}$	$0.21^{+0.62}_{-0.17}$
$\widetilde{c}^{\star}_{\rm vir}$	23^{+6}_{-4}	22^{+6}_{-4}	22^{+6}_{-4}	50^{+23}_{-16}	44^{+22}_{-15}	43^{+22}_{-15}
$\widetilde{\theta}^{\star}_{\rm vir}$ [deg]	34^{+17}_{-10}	36^{+16}_{-10}	36^{+16}_{-10}	45^{+16}_{-12}	48^{+15}_{-12}	49^{+14}_{-12}
$\widetilde{\theta}^{\star}_{\rm s}$ [deg]	$1.7^{+1.4}_{-0.6}$	$1.9^{+1.5}_{-0.7}$	$1.8^{+1.4}_{-0.7}$	$1.2^{+1.4}_{-0.6}$	$1.5^{+1.6}_{-0.8}$	$1.6^{+1.6}_{-0.8}$
$\widetilde{\theta}^{\star}_{\rm h}$ [deg]	$0.22^{+0.2}_{-0.08}$	$0.25^{+0.2}_{-0.09}$	$0.25^{+0.2}_{-0.09}$	$0.16^{+0.20}_{-0.08}$	$0.20^{+0.20}_{-0.10}$	$0.22^{+0.22}_{-0.11}$
$\log_{10}\left(\widetilde{J}^{\star}/{\rm GeV}^2\,{\rm cm}^{-5}\right)$	$19.4^{+0.3}_{-0.3}$	$19.8^{+0.4}_{-0.3}$	$19.9^{+0.4}_{-0.3}$	$20.3^{+0.4}_{-0.3}$	$20.7^{+0.4}_{-0.3}$	$20.8^{+0.5}_{-0.4}$

Table C.1.: Median properties of the brightest subhalo for the surveys of the *Fermi*-Large Area Telescope (LAT) and CTA, and the subhalo models LOW and HIGH. The uncertainties denote the 68% C.I. around the median. For both instruments, the results for different angular resolutions are given. $D_{\rm obs}$ is the distance from the observer, and R the distance from the Galactic center (GC). $m_{\rm vir}$ is the subhalo mass. $r_{\rm vir}$ and $r_{\rm s}$ denote its virial and scale radius, $c_{\rm vir} = r_{\rm vir}/r_{\rm s}$, and $\theta_{\rm vir,\,s} = \arctan(r_{\rm vir,\,s}/D_{\rm obs})$. $\theta_{\rm h}$ is the radius enclosing half of the total emission, $J(\theta_{\rm h}) = 0.5\,J(\theta_{\rm vir})$. For reliable medians, the values are obtained from a sample of 10^4 simulations.

C.3. Point-like behavior of the brightest subhalo

The average number, $\langle N_s \rangle$, of detected γ-ray signal events obtained in the time interval Δt and originating from a differential flux ϕ, can be written as

$$\langle N_s \rangle = \Delta t \times A_{\mathrm{eff}}(E) \int\limits_{E} \int\limits_{\Delta\Omega} \phi(\Omega,\, E)\, \mathrm{d}\Omega\, \mathrm{d}E\,, \tag{C.6}$$

where the angular resolution of the instrument is neglected, and the effective area, A_{eff}, is assumed to be constant over the considered solid angle $\Delta\Omega$. The number of background events, $\langle N_b \rangle$, from cosmic ray events passing the selection cuts and diffuse γ-rays can be considered as isotropic, and within a small area in field of view (FOV) of the instrument,

$$\langle N_b \rangle \approx \frac{\mathrm{d}\langle N_b \rangle}{\mathrm{d}\Omega}\, \Delta\Omega\,. \tag{C.7}$$

For a Poisson-distributed number N_t of total events, $N_t = N_{\mathrm{s}} + N_{\mathrm{b}}$, one can define the significance S of a detection of N_{s} over N_{b} as (Li and Ma, 1983; Springel et al., 2008b):[1]

$$S = \frac{\langle N_{\mathrm{s}} \rangle}{\sqrt{\langle {N_{\mathrm{t}}}^2 \rangle - \langle N_{\mathrm{t}} \rangle^2}} \overset{\text{Poisson}}{=} \frac{\langle N_{\mathrm{s}} \rangle}{\sqrt{\langle N_{\mathrm{t}} \rangle}}. \tag{C.8}$$

For background dominated measurements, $N_{\mathrm{b}} \gg N_{\mathrm{s}}$, and Equation C.8 becomes

$$S \approx \frac{\langle N_{\mathrm{s}} \rangle}{\sqrt{\langle N_{\mathrm{b}} \rangle}}. \tag{C.9}$$

With $\Delta\Omega \approx \pi\, \theta_{\mathrm{int}}^2$ for a circular symmetric integration area $\Delta\Omega$, one obtains

$$S \propto \frac{\int_{\Delta\Omega} \phi_s(\Omega,\, E)\, d\Omega}{\theta_{\mathrm{int}}} \tag{C.10}$$

For $\phi_s = \phi_{\mathrm{DM}}$ the flux from DM subhalos, $\phi_s = \phi^{\mathrm{PP}} \times J(\Omega)$ (Equation 2.29), and

$$S \propto \frac{\int_{\Delta\Omega} \int_{l.o.s} \rho_{\mathrm{DM}}^2\, \mathrm{d}l\, d\Omega}{\theta_{\mathrm{int}}}\,. \tag{C.11}$$

From Equation C.11, the angle $\theta_{\mathrm{int}}^{\mathrm{opt}}$ can be computed, the optimum integration angle where S maximizes. Figure C.1 shows the significance, $\widetilde{S}$, with the maximum normalized to one, over

---

[1] Precisely, Equation C.8 corresponds to an ON-OFF analysis, where N_{b} OFF events are subtracted from $N_t = N_{\mathrm{s}} + N_{\mathrm{b}}$ ON events, with an OFF region of the same size ($\alpha = 1$) and characteristics as the ON region, containing the signal source (see Li and Ma, 1983, p. 318).

the integration angle θ_{int}, for the brightest subhalos in the model LOW, VAR0, and VAR5 (see Table 4.1). It follows that for an Einasto description of the subhalos (LOW and VAR5), the optimum angular cut is beyond the reach of CTA's angular resolution. The presence of sub-subhalos does not alter this result (VAR5). In case of a NFW description (VAR0), no maximum exists for the significance S. Thus, for an analysis based on Li and Ma (1983), the brightest DM subhalo is best observed at the angular resolution of the instrument. It shall be noted that in the light of this finding, folding the angular resolution of the instrument into Equation C.6 as done by Springel et al. (2008b) would yield an angle $\theta_{\mathrm{int}}^{\mathrm{opt}}$ located almost exactly at the angular resolution.

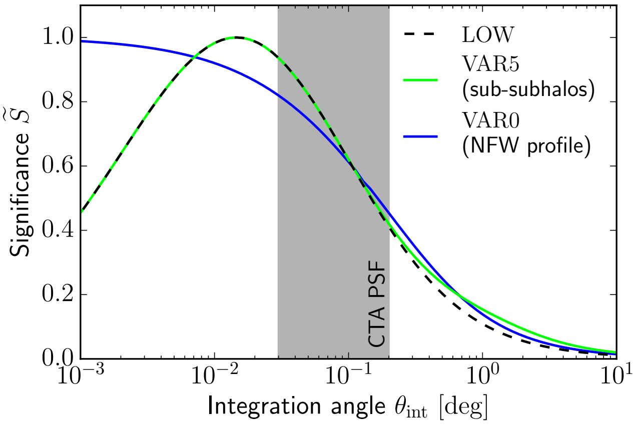

Figure C.1.: Optimum integration angle for a subhalo detection with an ON-OFF analysis according to Li and Ma (1983).

C.4. APS damping by a Gaussian window: a closer look

Event data can be masked by a Gaussian window by either retaining integer values in each bin (by rounding the values in the windowed bins or re-drawing from a Poisson distribution), or by keeping the real values after multiplying with the window. In the latter case of such "smooth" Gaussian windowing, an additional factor 2 is obtained compared to Equation 5.39 for the linear power suppression in the regime $\ell \gg \ell_\mathrm{window}$,

$$\widehat{C}^{I}_{\ell,\,\text{part-sky}} \approx \frac{f_\mathrm{sky}}{2}\, C^{I}_{\ell,\,\text{full-sky}} \;=\; \frac{\sigma^2_\mathrm{window}}{4}\, C^{I}_{\ell,\,\text{full-sky}} \tag{C.12}$$

and accordingly, for the fluctuation angular power spectrum (APS),

$$C^{F}_{\ell,\,\text{part-sky}} \approx \frac{C^{F}_{\ell,\,\text{full-sky}}}{2\, f_\mathrm{sky}} \;=\; \frac{1}{\sigma^2_\mathrm{window}}\, C^{F}_{\ell,\,\text{full-sky}}\,. \tag{C.13}$$

For the toy example of a windowed APS presented in subsection 5.3.2 and Figure 5.13, a corresponding more realistic algorithm for distributing events would be as follows: Firstly, a random position on the sky is drawn. For the resulting position, the distance θ to the window center, and the corresponding Gaussian damping, $d = \exp(-0.5\,(\theta/\sigma_\mathrm{window})^2)$, is evaluated. Then, *for each of the 20 events assigned to a point source*, the value d is compared to a uniform random number $r \in [0,1]$. For $d > r$, *the event assigned to the source is drawn*, and randomly smeared out according to the Gaussian point spread function (PSF).

C.5. Mean, median, and variance of the subhalo APS

A particular realization of point-like sources with fluxes F and an average power-law brightness distribution $\overline{N}(>F)$ scatters around this distribution, and so does the intensity power C^{I}_{P} defined in Equation 5.22. In the following, an estimate of the C^{I}_{P} scatter is derived from the $N(>F)$ scatter. Assuming that only the variation of the brightest object with flux $F^\star$ and the lower flux threshold F_min contribute to the $N(>F)$ variation results in the expression

$$N(F_\mathrm{min},\, F^\star) = \int\limits_{F_\mathrm{min}}^{F_\mathrm{max}=F^\star} \left\langle \frac{\mathrm{d}N}{\mathrm{d}F'} \right\rangle \mathrm{d}F' \approx \left(\frac{F_\mathrm{min}}{F_\mathrm{lim}}\right)^{1-\alpha} - \left(\frac{F^\star}{F_\mathrm{lim}}\right)^{1-\alpha}. \tag{C.14}$$

By using a power-law behavior of the mean differential source count distribution, $\langle \mathrm{d}N/\mathrm{d}F\rangle = (\alpha-1)/F_\mathrm{lim} \times (F/F_\mathrm{lim})^{-\alpha}$, $\alpha > 1$, and replacing F_min by the number N of considered subhalos

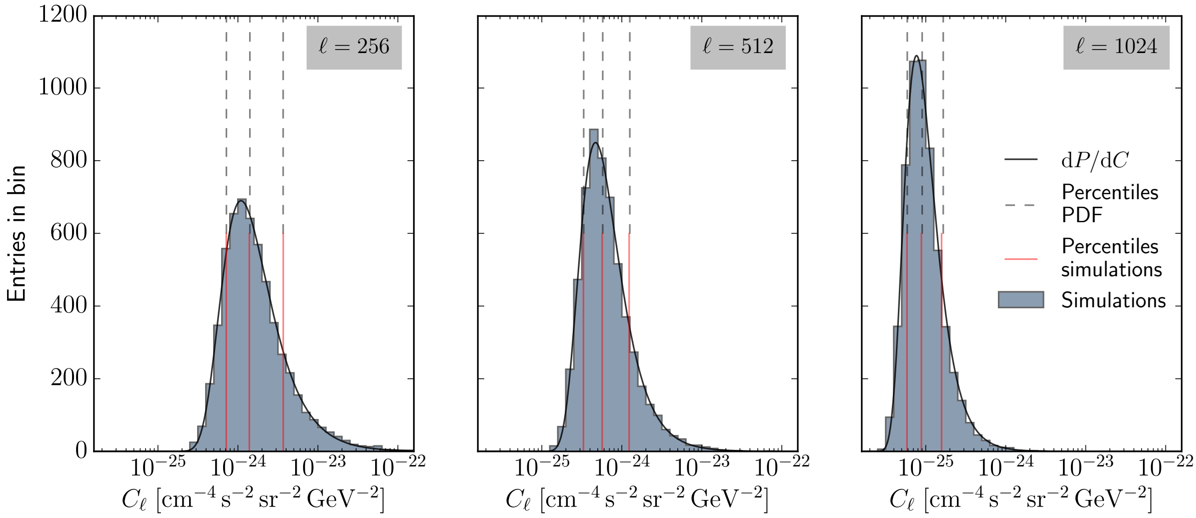

Figure C.2.: Study of the DM subhalo APS variance caused by the flux scattering, for the model LOW and $N_{\mathrm{sample}} = 5000$ simulations, presented at three multipoles ℓ. The spectrum and the underlying particle physics determining the C_ℓ units is the same as shown in Figure 5.14 (however, computed with HEALPix $N_{\mathrm{side}} = 512$ of the J-factor maps). The percentiles give the 68% C.I. around the median (16$^{\mathrm{th}}$, 50$^{\mathrm{th}}$, and 84$^{\mathrm{th}}$ percentile) of the simulations (bottom half) and the fitted Fréchet probability density B.22 (top half).

from Equation C.14, Equation 5.22 can be rewritten as

$$C_{\mathrm{P}}^{I}(F^\star,\, N) \approx \frac{1}{4\pi\beta}\, F_{\mathrm{lim}}^{2}\, \left[\left(\frac{F^\star}{F_{\mathrm{lim}}}\right)^{3-\alpha} - \left\{ \left(\frac{F^\star}{F_{\mathrm{lim}}}\right)^{1-\alpha} + N \right\}^{-\beta} \right], \tag{C.15}$$

with $\beta \equiv (3-\alpha)/(\alpha-1)$ and provided $\alpha < 3$. With this, C_{P}^{I} is now expressed as only a function of the brightest object $F^\star$ and of the total number of objects N. Considering the limit $N \to \infty$, which is equivalent to $F_{\mathrm{min}} \to 0$, Equation C.15 simplifies to

$$C_{\mathrm{P}}^{I}(F^\star,\, N) \quad \overset{N\to\infty}{\approx} \quad \frac{1}{4\pi\beta}\, F_{\mathrm{lim}}^{2}\, \left(\frac{F^\star}{F_{\mathrm{lim}}}\right)^{3-\alpha}. \tag{C.16}$$

C_{P}^{I} from Equation C.15 is highly sensitive to a finite N ($F_{\mathrm{min}} \neq 0$) in the case $\alpha \to 3$, such that the latter approximation is only applicable for α sufficiently smaller than 3, and does not hold for $\alpha \geq 3$. Provided that the approximation Equation C.16 is valid, the median $\widetilde{C}_{\mathrm{P}}^{I}$ is directly related to $\widetilde{F}^\star$

$$\widetilde{C}_{\mathrm{P}}^{I}(F^\star,\, N) \quad \overset{N\to\infty}{\approx} \quad C_{\mathrm{P}}^{I}(\widetilde{F}^\star) \approx \frac{1}{4\pi\beta}\, F_{\mathrm{lim}}^{2}\, \log(2)^{-\beta}. \tag{C.17}$$

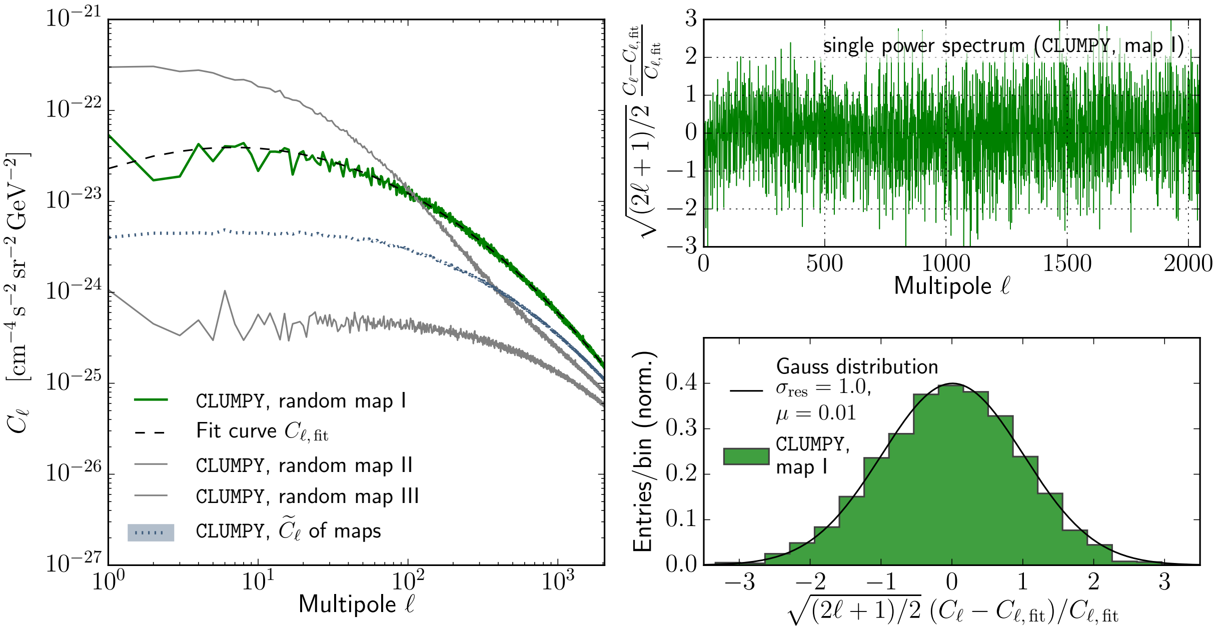

Figure C.3.: Study of the DM subhalo APS variance caused by the spatial subhalo scattering, for the subhalo model LOW on the full sky. On the left, the dotted line within the gray band gives median C_ℓ and the 68% C.I. from 500 realizations, as shown in Figure 5.14. The solid lines display three arbitrary power spectra out of these 500 random realizations of the subhalo distribution in the sky. The spectrum highlighted in green is fitted by a logarithmic polynomial of 3rd degree (dashed line), and the rescaled residuum is shown on the top right. The bottom right figure shows that the scatter is Gaussian.

Assuming the C_{P}^I only to be dependent of $F^\star$ (Equation C.16), the probability density function $\mathrm{d}P/\mathrm{d}C$ ($C \equiv C_{\mathrm{P}}^I$) can be formally written as

$$\frac{\mathrm{d}P}{\mathrm{d}C}(C) = \frac{\mathrm{d}P_{\geq 1}}{\mathrm{d}F}\left(F^\star(C)\right) \times \left|\frac{\mathrm{d}F^\star}{\mathrm{d}C}(C)\right|, \tag{C.18}$$

from which the mean $\overline{C}_{\mathrm{P}}^I$ and standard deviation $\sigma_{C_{\mathrm{P}}}$ can be calculated. An interesting consequence of Equation C.18 is that the probability density of C_{P}^I is proportional to the probability density of $F^\star$, described by a Fréchet distribution (Equation B.22). Figure C.2 reveals that despite the several coarse approximations leading to Equation C.18, the multipole variance of the DM subhalo APS presented in Chapters 4 and 5 (see, e.g., Figure C.3 (left) on the following page) can be surprisingly well described by a fitted Fréchet distribution. Note that these subhalo spectra are not strictly constant in multipole. It follows that like the extreme value distribution of the fluxes, also the angular power spectra arising from power-law source count distributions are found to exhibit a long tail of high-C_ℓ outliers.

The above discussion applies to the variance of the C_ℓ level between different skymap realizations. In case of a constant spectrum, $C_\ell = C_\mathrm{P}$, all multipoles are equally affected by the scattering. In case of the extended subhalos, this is not necessarily the case. Figure C.3 (left) shows how the individual power spectra might differ between different skymap realizations, depending on the angular extension of the brightest subhalos, and depending on how much a single brightest subhalo dominates the spectrum. However, different multipoles are still highly correlated, and the spectra can be well fitted by a polynomial of 3rd degree in logarithmic space, $\ln C_{\ell,\,\mathrm{fit}} = a\,(\ln\ell)^3 + b\,(\ln\ell)^2 + c\,(\ln\ell) + d$. This is done for the green highlighted spectrum in Figure C.3 (left, dashed line). It can be seen that the spectrum additionally scatters around the residuum $C_{\ell,\,\mathrm{fit}}$. This scatter is caused by the randomly distributed objects in angular space, additionally to the previously discussed scatter in flux dimension. This variance is described by Equation 5.43,

$$\sigma_{C_\ell} = C_\ell \sqrt{\frac{2}{2\ell+1}}\,.$$

Figure C.3 (top right) shows the rescaled variance around the residuum $C_{\ell,\,\mathrm{fit}}$, and Figure C.3 (bottom right) illustrates that the variance according to Equation 5.43 is in fact Gaussian and well described by Equation 5.43.

C.6. Convergence of the subhalo APS

The approximate calculations from the previous Appendix C.5 suggest that for a power-law source count distribution with index $\alpha < 3$, the APS converges to a finite value when adding an infinite number of faint sources. By fixing $N \equiv \overline{N}_\mathrm{sub}$ in Equation C.15, C_P^I becomes a function of only $F^\star$, and the median of the function is equivalent to the function of the median, $\widetilde{C}_\mathrm{P}^I(F^\star) \approx C_\mathrm{P}^I(\widetilde{F}^\star)$. With this, the ratio of the median powers

$$\frac{\widetilde{C}_\mathrm{P}^I(F^\star;\,\overline{N})}{\widetilde{C}_\mathrm{P}^I(F^\star;\,N\to\infty)} \approx 1 - \left(1 + \frac{\overline{N}}{\ln(2)}\right)^{-\beta} \tag{C.19}$$

can be constructed. Equation C.19 suggests that the overall power quickly converges for α sufficiently smaller than 3. For $\alpha \approx 2$, the 13 brightest halos account for 95% of the overall power. In particular, for $\alpha \approx 2$, the contribution of the brightest halo alone to the overall power is

$$\frac{\widetilde{C}_\mathrm{P}^I(F^\star)}{\widetilde{C}_\mathrm{P}^I(F^\star;\,N\to\infty)} \approx 1 - \frac{\ln(2)}{\ln(2)+1} \approx 0.59\,. \tag{C.20}$$

Thus in median, the brightest halo alone in a power-law source count distribution with $\alpha \approx 2$ accounts for more than half of the overall APS.

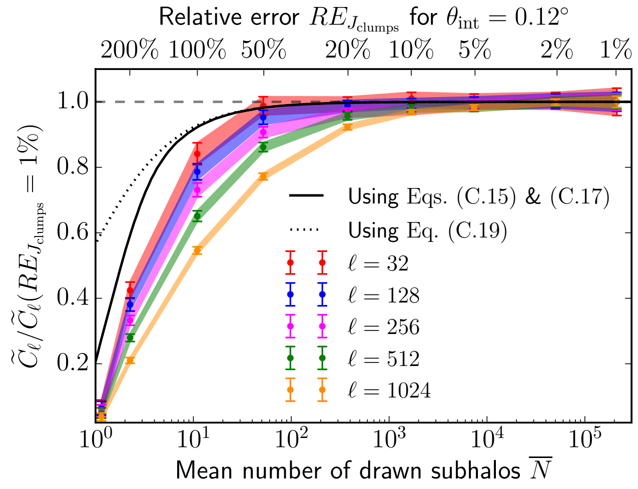

Figure C.4.: Convergence study of the median power $\widetilde{C}_\ell$ (for subhalo J-factor maps, model LOW, computed with `CLUMPY` with a HEALPix resolution of $N_{\mathrm{side}} = 512$ or $\theta_{\mathrm{int}} = 0.12°$) as a function of $RE_{J_{\mathrm{drawn}}}$ (upper x-axis) or, equivalently, the number of drawn clumps $\overline{N}_{\mathrm{sub}}$ (lower x-axis). The different colors show different multipoles ℓ, with error bars from Equation C.21. For comparison, also the two analytical approximations of the convergence are shown, based on Equation C.15 (solid-black line, see text) or the further approximated Equation C.19 (dotted line). Figure published in Hütten et al. (2016).

For the case of extended subhalos and for a rigorous, less simplifying treatment as developed in Appendix C.5, a Monte-Carlo (MC) study by drawing Galactic DM subhalos (according to the model LOW of this thesis) with the `CLUMPY` code is performed. Figure C.4 shows the ratio $\widetilde{C}_\ell/\widetilde{C}_\ell(N \to \infty)$ obtained from the MC samples at different multipoles ℓ. The medians are calculated over $N_{\mathrm{sample}} = 5000$ simulations. The large sample size $N_{\mathrm{sample}} = 5000$ is necessary in order to reach at least a 5% relative accuracy of the ratio of the medians at the lowest multipoles, as given by the sample error of the median (indicated by the shaded bands in Figure C.4)

$$\Delta\widetilde{C} = \frac{1}{2\,\frac{\mathrm{d}P}{\mathrm{d}C}(\widetilde{C})\,\sqrt{N_{\mathrm{sample}}}}\,. \tag{C.21}$$

From Figure C.4 follows that for a rigorous consideration of the extended subhalos, the APS converges differently at different multipoles, but reaches 95% of the overall power $\widetilde{C}_\ell(N_{\mathrm{sub}} \to \infty)$ at all multipoles $\ell \leq 1024$ for $N \gtrsim 10^4$ resolved subhalos. This requirement is demanded for all power spectra presented in this thesis, and an corresponding amount of subhalos is computed. The black dotted line indicates the expected convergence calculated from the ℓ-independent power-law approximation Equation C.19 with $\alpha = 2.03$ (obtained for the subhalo model LOW). Equation C.19 relies on a fixed $\overline{N}$, which is not the case for the MC simulations, where N

clumps are drawn according a Poisson distribution. The additional degree of freedom of a sample to sample variation of N clumps shifts down the median power for a low average $\overline{N}$. The solid-black line in Figure C.4 shows a more accurate numerical calculation, where the median from Equation C.15 is divided by Equation C.17, yielding an even better agreement with the convergence of the subhalo simulations.

C.7. Subhalo APS with sub-substructures

Figure C.5 compares the APS of the subhalos on the full sky between the models LOW and VAR5 (including sub-subhalos). While the curve for the model LOW is identical to the one shown in Figure 5.14, the green band shows how the APS changes when unresolved sub-subhalos are considered (the consideration of sub-subhalos as defined in Subsection 4.1.3 is the only difference between the two models). It can be seen that the overall power is increased for the model VAR5 caused by the increased emission due to the sub-subhalo boost. Additionally, the larger spatial extension of the subhalos' γ-ray emission due to the sub-subhalo contribution in their outskirts causes a more dominant bending of the APS curve at multipoles $\ell \gtrsim 100$. Thus, in the case of the presence of sub-subhalos, the subhalo APS is even less Poisson-like (i.e., constant in ℓ) than without sub-subhalos. Note that the power spectra converge at high ℓ, which reflects the finding that sub-subhalos do not contribute to the emission from the inner cusps (see Figure 4.5).

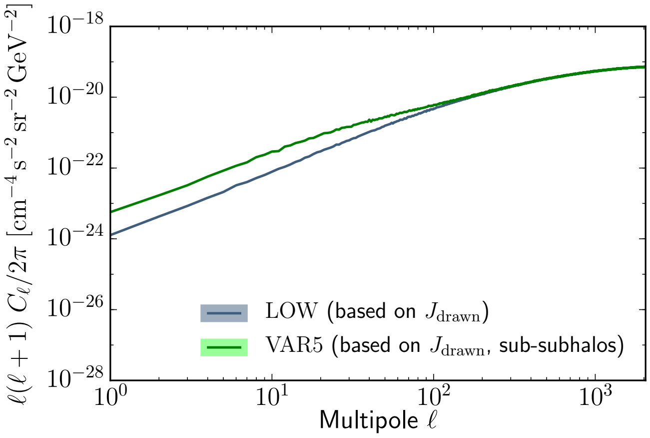

Figure C.5.: γ-ray intensity APS from Galactic DM on the full sky for the subhalo models LOW (pale blue) and VAR5 (green, one level of unresolved sub-subhalos in the subhalos), based on the resolved subhalos, $J_{\rm drawn}$. The bands show the median power and its 68% C.I. scatter from 500 simulations. The same particle physics as in Figure 5.15 has bee chosen, namely, a thermal relic cross-section, $m_\chi = 200\,\mathrm{GeV}$, and $\chi\chi \to b\bar{b}$, and showing the differential intensity APS at 4 GeV.

C.8. APS background and test statistic distributions of the likelihood ratio tests

Figure C.7 presents the test statistic (TS) distribution of the `ctools` analysis in Section 5.2 and Figure C.8 the test statistic of the maximum Likelihood ratio test, Equation 5.52, applied to 10^3 background realizations for different thresholds in energy and ℓ-space. The solid-black fit curve in Figure C.8 (bottom right) shows that for suitable thresholds in energy and ℓ-dimension, the TS distribution follows the form of Equation 5.12, $p(\mathrm{TS}) = \frac{1}{2}\,\delta(\mathrm{TS}) + \frac{1}{2}\,\chi^2_{k=1}(\mathrm{TS})$.

?? shows the variance of isotropic shot noise on $f_{\mathrm{sky}} = 0.25$ for the APS analysis in Section 5.3, as determined from the same 10^3 background simulations underlying Figure C.8.

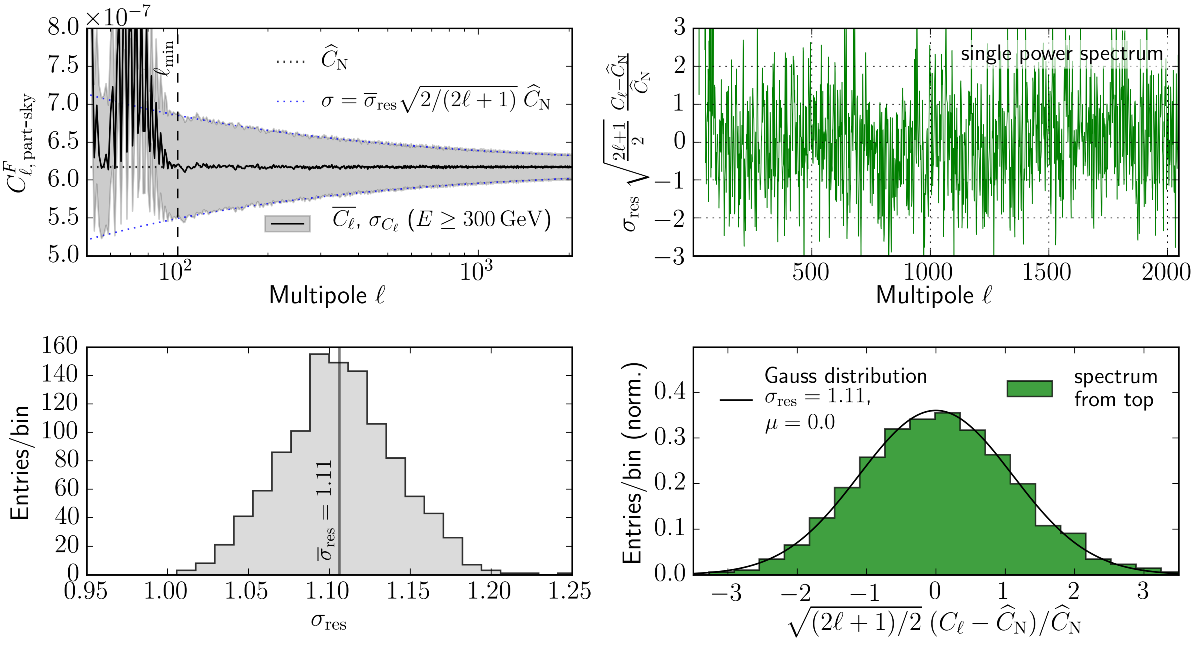

Figure C.6.: Study of the APS variance of isotropic shot noise on a limited sky patch $\Delta\Omega = \pi$ ($f_{\mathrm{sky}} = 0.25$). In gray, the result from 1000 MC samples is shown, in green the example of a single spectrum. From the left figures follows that on average, the Gaussian standard deviation of the multipoles is throughout a factor 1.11 larger than as expected on the full sky. The right figures show that the scatter is Gaussian.

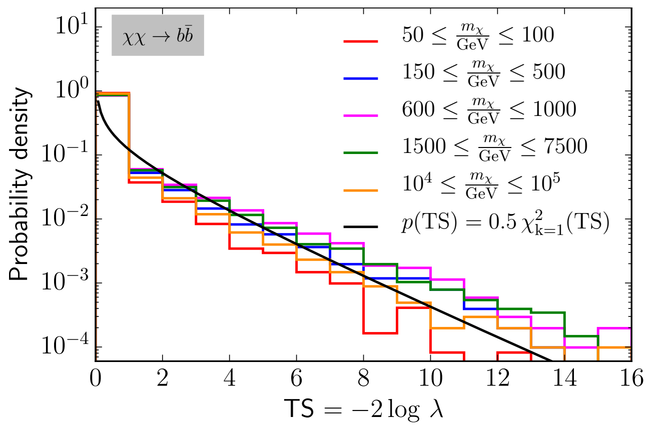

Figure C.7.: Distribution of the TS values for the `ctlike` likelihood ratio test from Section 5.2, over background events, assuming a $\chi\chi \to b\bar{b}$ signal spectrum. The statistic relies on 10^5 simulations, distributed over 24 spectra, and merged into five groups. The black line shows the expected TS distribution.

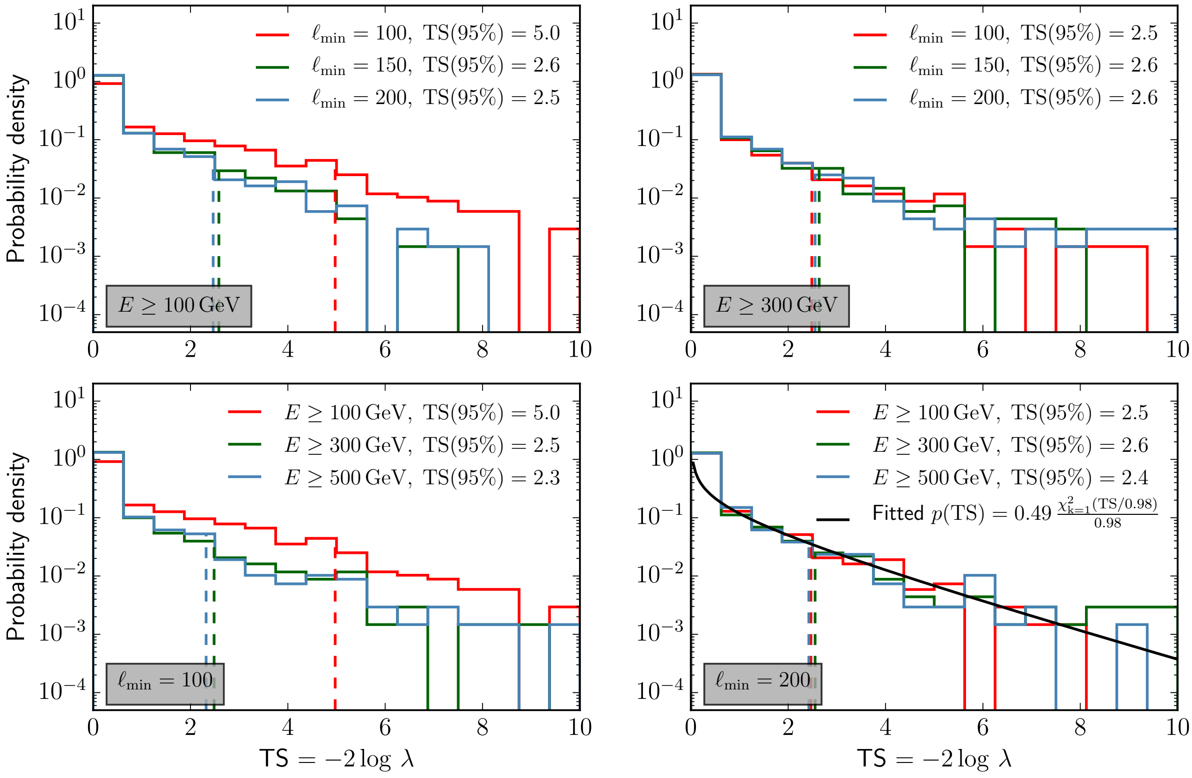

Figure C.8.: Test statistic distribution of the APS likelihood ratio test from Section 5.3. The distributions rely on 1000 MC simulations of background events in the CTA survey field with $\Delta_{\mathrm{fov}} = 1°$.

C.9. Comparison to the previous APS sensitivity study for CTA by Ripken et al. (2014)

The sensitivity of Cherenkov telescopes to spatial anisotropies in their data has been previously studied by Ripken et al. (2014). They found that “a relative contribution of $\sim 10\%$ from dark matter annihilation to the extragalactic diffuse γ-ray background can be detected with planned configurations of CTA”. More precisely, they explored different models of a simplistic instrumental performance model for CTA and different observation setups (in observation time and single vs. multiple pointings). For their most optimistic performance assumptions and 1000 h of observation onto a single sky patch, they found a sensitivity to an intrinsic diffuse γ-ray background (DGRB) fluctuation of $C_{\mathrm{P}}^{F} = 1.8 \times 10^{-5}$. By postulating an astrophysical fluctuation power of $C_{\mathrm{P,\,astro}}^{F} \equiv 10^{-5}$ and a DM fluctuation power of $C_{\mathrm{P,\,DM}}^{F} \equiv 10^{-3}$ contributing to the DGRB, they calculated the detectable DM fraction, f_{DM}, in the DGRB via the relation (see Equation 5.24)

$$C_{\mathrm{DGRB}}^{F} = 1.8 \times 10^{-5} = (1 - f_{\mathrm{DM}})^2 \times C_{\mathrm{P,\,astro}}^{F} + f_{\mathrm{DM}}^2 \times C_{\mathrm{P,\,DM}}^{F} \,.$$

Here, C_{DGRB}^{F} denotes the degree of anisotropy of the DGRB. If one accounts for all anisotropy in the DGRB to DM (or any other specific source population), then the results from Ripken et al. (2014) can be read as $C_{f_{\mathrm{DGRB}} \equiv 1}^{F} = C_{\mathrm{DGRB}}^{F}$, giving sensitivities not to different fractions of DM to the DGRB (with fixed $C_{\mathrm{P,\,DM}}^{F}$), but to different levels of anisotropy, $C_{f_{\mathrm{DGRB}} \equiv 1}^{F}$, from DM (or any other source population) in the DGRB.

The upper panel of Table C.2 lists their results for three adopted CTA model and observational configurations. Because Ripken et al. (2014) calculated with an extrapolated DGRB spectrum according to Abdo et al. (2010, Equation 5.14), these values have to be compared with the upper panel of Table 5.5. The sensitivities quoted in Table C.2 (upper panel) rely on 1000 h of observation, distributed over 10 single pointings, whereas the setup of this thesis (Table 5.5) assumes 500 h of observation distributed over 11,648 pointings. Still, the blue-shaded rows in Table 5.5 and Table C.2 correspond to the setups which can be best compared with each other: The obtained sensitivities refer to the same energy interval, the same underlying source spectrum, and a comparable number of signal and background events. For comparing the results of the blue-shaded rows, the intensity with intrinsic anisotropy $C_{\mathrm{P}}^{F} = 7.2 \times 10^{-4}$ is calculated, to which the analysis of this thesis is sensitive to. The analysis from Ripken et al. (2014) detects such an anisotropy in an intensity of the level of the DGRB, I_{DGRB}, whereas this analysis would be sensitive to

$$\frac{I(C_{\mathrm{P}}^{F} = 7.2 \times 10^{-4})}{I_{\mathrm{DGRB}}} = \sqrt{\frac{3.0 \times 10^{-3}}{7.2 \times 10^{-4}}} = 2.0\,, \tag{C.22}$$

DGRB spectrum (Abdo et al., 2010), Analysis from Ripken et al. (2014)					
setup	E_{thresh} [GeV]	N_{sig}	N_{bck}	$\dot{N}_{\text{bck}}$ [Hz]	95% C.L. sensitivity $C^F_{f_{\text{DGRB}}\equiv 1}$
10×100h	100	6.69×10^4	3.60×10^7	$\equiv 10$	3.0×10^{-4}
10×100h	300	4.26×10^4	3.60×10^7	$\equiv 10$	7.2×10^{-4}
10×100h	300	4.26×10^4	3.60×10^6	$\equiv 1$	9.5×10^{-5}

DGRB spectrum (Abdo et al., 2010), survey setup, subhalo model HIGH, instrument response from Ripken et al. (2014)						
T_{live} [h]	E_{thresh} [GeV]	N_{sig}	N_{bck}	$\dot{N}_{\text{bck}}$ [Hz]	Med. 95% C.L. sensitivity f_{DGRB}	 $C^F_{f_{\text{DGRB}}\equiv 1}$
475	300	5.18×10^4	1.71×10^7	10.0	2.8	2.6×10^{-3}
950	300	7.66×10^4	3.43×10^7	10.0	2.0	1.3×10^{-3}

Table C.2.: *Upper panel:* Results of the analysis by Ripken et al. (2014, their Table 2), for their choice of $\sigma_{\text{fov}} = 4°$, and the observation setup $10 \times 100\,\text{h}$. Here, the background rate and time were fixed, and the minimum fluctuation APS, C^F_{sens} of the full DGRB was searched, to which the analysis was sensitive. *Lower panel:* Using the instrumental model from Ripken et al. (2014), but applied to the observational CTA extragalactic survey setup adopted in this thesis, at two different observation times.

a factor 2 larger intensity. Thus, this thesis suggests a slightly worse sensitivity of CTA to anisotropies in the DGRB than has been projected by Ripken et al. (2014) for a comparable observational setup. The results are remarkably close given the different assumptions about the underlying CTA instrumental performances, the observational setup, and the applied analysis method. In the following, a closer look is taken on the origins of the factor two difference.

Comparison of the different instrumental models: For the CTA instrumental model, Ripken et al. (2014) assumed

- an on-axis effective collection area of $A_{\text{eff}}(\vartheta = 0°) = 10^5\,\text{m}^2$ at energies $E < 300\,\text{GeV}$, and an effective area of $A_{\text{eff}}(\vartheta = 0°) = 3 \times 10^5\,\text{m}^2$ at energies $E \geq 300\,\text{GeV}$,
- the off-axis effective area to decrease according to a Gaussian, $A_{\text{eff}}(\vartheta) = A_{\text{eff}}(\vartheta = 0°) \times \exp(-0.5\,\vartheta/\sigma_{\text{fov}})$, with $\sigma_{\text{fov}} = 4°, 5°$. Here, their results for $\sigma_{\text{fov}} = 4°$ are used for comparison, as they match closest to the `Prod3` performance,
- a background rate of $1\,\text{Hz}$ or $10\,\text{Hz}$ in the whole camera FOV,
- and a Gaussian PSF with constant width, $\sigma_{\text{psf}} = 0.05°$, or equivalently, $\theta_{68\%} = 0.076°$.

When having presented the CTA instrumental response in Chapter 3, the effective area model from Ripken et al. (2014) has been overplotted in Figure 3.16, and its properties have been compared in detail with the `Prod3` values in Table 3.2. Above 300 GeV, when folded with the DGRB spectrum (5.14) from Abdo et al. (2010), the instrument response function (IRF) model from Ripken et al. (2014) yields a similar signal rate, $\dot{N}_{\mathrm{sig}}(\geq 300\,\mathrm{GeV}) = 1.18 \times 10^{-2}\,\mathrm{Hz}$ (no ϑ_{cut} cut), compared to $\dot{N}_{\mathrm{sig}}(\geq 300\,\mathrm{GeV}) = 1.15 \times 10^{-2}\,\mathrm{Hz}$ (with $\vartheta_{\mathrm{cut}} = 6°$) for the Paranal `Prod3 0.5h_avg` cuts.[2] The same applies for the background rates for the model with $\dot{N}_{\mathrm{bck}}(\geq 300\,\mathrm{GeV}) \equiv 10\,\mathrm{Hz}$ (Ripken et al., 2014, no ϑ_{cut} cut), compared to $\dot{N}_{\mathrm{bck}}(\geq 300\,\mathrm{GeV}) = 11.2\,\mathrm{Hz}$ (Paranal `Prod3 0.5h_avg`, $\vartheta_{\mathrm{cut}} = 6°$). The lower panel of Table C.2 lists the result for repeating the survey analysis setup (500 hrs extragalactic survey on $f_{\mathrm{sky}} = 0.234$) with the IRF model from Ripken et al. (2014, $\sigma_{\mathrm{fov}} = 4°$) and the extrapolated DGRB spectrum from Abdo et al. (2010). In fact, a comparable sensitivity above 300 GeV is reached compared to the values quoted in Table 5.5.

Comparison of the different adopted observing times: The analysis of this thesis is repeated for a survey setup with 1000 hrs exposure on an extragalactic survey on $f_{\mathrm{sky}} = 0.234$, with the IRF model from (Ripken et al., 2014, $\sigma_{\mathrm{fov}} = 4°$) and the extrapolated DGRB spectrum from Abdo et al. (2010). The lower panel Table C.2 shows that the double amount in exposure time results in a factor $2.8/2.0 \sim \sqrt{2}$ improved sensitivity. The missing factor of $\sqrt{2}$ for the factor 2 difference found in Equation C.22 then is caused by the different observation setups (large-area survey vs. ten deep fields).

Comparison of the different analysis methods: From the previous comparisons results that the different observation setup and the different analysis method applied in this thesis results in a combined worsening of the sensitivity by a factor $\sim \sqrt{2}$ compared to Ripken et al. (2014). Whereas this thesis adopts a likelihood-ratio approach as presented in Subsection 5.3.5, Ripken et al. (2014) make use of an unbinned χ^2-test. For multipoles $\ell \gg \ell_{\mathrm{window}}$ and (background dominated) pure shot-noise APS, $\langle C_\ell \rangle = \widehat{C}_{\mathrm{N}}$, the C_ℓ are normal distributed around $\widehat{C}_{\mathrm{N}}$, and the square deviation,

$$\chi^2 = \sum_{\ell_{\mathrm{min}}}^{\ell_{\mathrm{max}}} \left(\frac{C_\ell - \widehat{C}_{\mathrm{N}}}{\sigma_{C_{\mathrm{N}}}} \right)^2 , \tag{C.23}$$

follows a χ^2-distribution with $\ell_{\mathrm{max}} - \ell_{\mathrm{min}} + 1$ degrees of freedom.[3] The variance σ_{C_ℓ} is estimated according to the results from Subsection 5.3.2 accounting for the correlation of neighboring multipoles,

$$\widehat{\sigma}_{C_{\mathrm{N}}}(f_{\mathrm{sky}} \approx 0.25) = 1.11 \sqrt{\frac{2}{2\ell + 1}}\, C_{\mathrm{N}} \,. \tag{C.24}$$

---

[2] Note that when comparing this rate to the events quoted in Table 5.5 that $N_{\mathrm{sig}}(\geq 300\,\mathrm{GeV})$ from Table 5.5 corresponds to 2.8 times the DGRB intensity.

[3] Note that all ℓ account for the degrees of freedom, as $\widehat{C}_{\mathrm{N}}$ is not estimated from the measured C_ℓ (e.g., as mean), but according to Equation 5.29 from the recorded number of events.

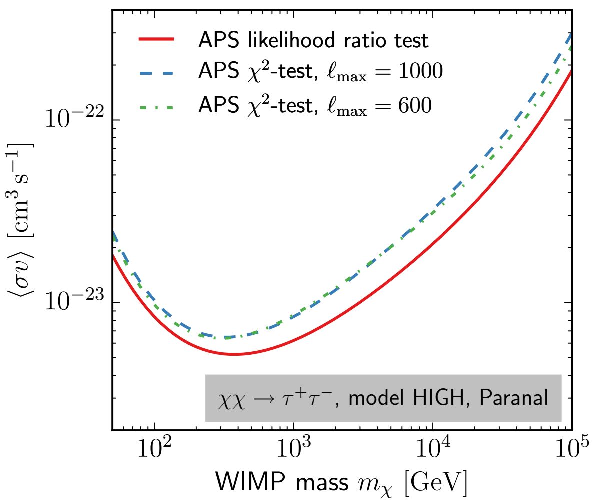

Figure C.9.: Comparison between the likelihood-ratio and χ^2-test to detect anisotropies in the CTA survey γ-ray count maps at the 95% C.L. The comparison is shown for the subhalo model HIGH, and a $\chi\chi \to \tau^+\tau^-$ annihilation spectrum ($f_{\mathrm{sky}} = 0.234$, $\Delta_{\mathrm{fov}} = 1°$, $T = 500\,\mathrm{h}$, `Prod3 0.5h_avg` IRF).

The value of $\ell_{\min}$ as a function of the lower bound of the energy bin is chosen as for the likelihood ratio test. As upper limit of the tested ℓ-range, Ripken et al. (2014) selected $\ell_{\max} \equiv 10^3$. For the confidence level $p = 0.95$ and the values $\ell_{\min} = 100,\, 150,\, 200$, one accordingly obtains a rejection of the background-only hypothesis for $\chi^2 > \chi^2(p = 0.95)_{k=901,\,851,\,801} = 971.9,\, 920.0,\, 868.0$. The stability of the test with respect to the assumption of $\ell_{\max}$ has been checked by considering also $\ell_{\max} \equiv 600$, and correspondingly $\chi^2 > \chi^2(p = 0.95)_{k=501,\,451,\,401} = 554.2,\, 501.5,\, 448.7$. The sensitivity is computed analogously to the likelihood ratio test: For 40 independent MC samples of signal and background events, the lowest flux level is searched where the test can reject the background hypothesis at the 95% confidence level (C.L.), and the sensitivity is set to the median flux threshold. The procedure is repeated for different energy thresholds, $E_{\min}$, and the energy interval providing the best sensitivity is chosen. Figure C.9 shows the result of the sensitivity comparison between the unbinned χ^2-test and the binned likelihood ratio test (Equation 5.57) in terms of the sensitivity to a $\chi\chi \to \tau^+\tau^-$ spectrum. It can be seen that the likelihood test is around $\sim 25\% - 40\%$ more sensitive than the χ^2-test. Also, it is visible that the performance of the χ^2-test depends on the choice of $\ell_{\max}$, with a difference between the χ^2-tests of about $\lesssim 10\%$ at the highest DM masses.

Summary: From the comparison with Ripken et al. (2014), it follows that their instrumental model $\sigma_{\mathrm{fov}} = 4°$, $\dot{N}_{\mathrm{bck}} = 10\,\mathrm{Hz}$ from above 300 GeV well matches the Paranal `Prod3 0.5h_avg` performance, whereas they obtained a factor $\sim \sqrt{2}$ better CTA sensitivity to fluctuations in the DGRB for their observation and analysis setup. While the sensitivity of a likelihood ratio test is slightly better than the χ-test adopted by Ripken et al. (2014), the shallow exposure survey setup reduces the sensitivity compared to ten deep-fields as considered by Ripken et al. (2014). However, the latter statement does not include the finding from Subsection 5.1.1 that the median expected signal APS from power-law source count distribution lowers in smaller fields. Also, the following section shows that a realistic non-Gaussian off-axis instrumental performance complicates the usage of single deep-field observations.

C.10. Survey vs. deep-field observations for an APS analysis

The study from Ripken et al. (2014) suggests that deep-field observations with CTA yield somewhat more sensitive results towards anisotropies than a wide-field shallow survey. However, this only applies for suitable field of view (FOV) shapes of small FOV instruments. Ripken et al. (2014) calculated with an energy-independent constant Gaussian FOV. A Gaussian window with σ_{fov} in angular space translates into a smooth Gaussian window in multipole space, where $\ell_{\mathrm{window}} \approx 180°/\sigma_{\mathrm{fov}}$ (see Subsection 5.3.2). At $\ell > \ell_{\mathrm{window}}$, the window function in multipole space is exponentially suppressed, such that no severe multipole contamination is obtained at larger multipoles.

However, this simple picture changes for non-Gaussian windows in angular space. As presented in Chapter 3, the CTA acceptance is not Gaussian, and differs at different energies. Additionally, the event reconstruction is limited to some angle ϑ_{cut} offset from the camera center, beyond which no events are reconstructed.[4] The sharper the effective window edge in angular space, the more oscillations globally contaminate the modes in multipole space. This effect is usually termed as spectral leakage in Euclidean Fourier methods. Figure C.10 shows the residual background APS from a single observation in the sky over 300 h for the Paranal `50h_avg` cuts. The left panel shows the spectrum for a single pointing "on source" in the sky, whereas the right panel shows the spectrum when distributing the 300 h observation time into four wobbled observations with 1.5° offset from a central pointing position. The two different pointing modes are visualized in Figure C.13. The spectral leakage contaminates multipoles up to $\ell_{\mathrm{min}} \gtrsim 1000$ for a deep single observation (left panel), and only slightly lowers for a wobbled observation (right panel, $\ell_{\mathrm{min}} \gtrsim 700$). Therefore, the direct "un-unwindowed" analysis as applied in this thesis and by Ripken et al. (2014) is not anymore appropriate. Ripken et al. (2014) also consider a joint analysis of ten different pointings over a total observation time of 1000 h. However, this does not change the picture, as shown Figure C.11. Here, 1000 h have been distributed in wobble

---

[4] To obtain a smooth Gaussian window in multipole space as shown in Ripken et al. (2014), events up to $\vartheta_{\mathrm{cut}} \gtrsim 3\,\sigma_{\mathrm{fov}} = 12°$ have to be considered.

observation mode over eight pointings in the sky (for the example of eight dSph candidates discovered in the Dark Energy Survey by Bechtol et al. (2015), visualized in Figure C.14). Still, $\ell_{\min} \gtrsim 400$ must be chosen for this setup. Likewise, combining the survey data with deep-field observations does not attenuate the multipole oscillations. For uncorrelated data sets, the joint APS of added data sets is roughly the sum of the individual spectra, and the oscillations are preserved. This is confirmed by calculating the APS of a 500 h survey (as shown in Figure 5.20) together with the deep-field setup from this paragraph. These spectra are shown in Figure C.12.

In principle, for given mask shapes, the spectral leakage can be eliminated by an unwindowing algorithm. However, even provided a perfect knowledge of the masking window in a given energy interval (as it is the case for the simulations performed in this thesis), the unmasked spectrum can only be reconstructed at the price of coarse binning and noise amplification. For artifacts being orders of magnitude larger than the physical signal in C_ℓ space, any information about the signal is likely to be buried in numeric noise and the systematic uncertainty about the mask. This also has been noted by Ackermann et al. (2012a). A rigorous investigation of unmasking small field-of-view γ-ray data is yet to be done. However, given the advantage of a large survey to increase the statistical sample of sources, it is unlikely that much can be gained by an APS analysis of deep-field observations.

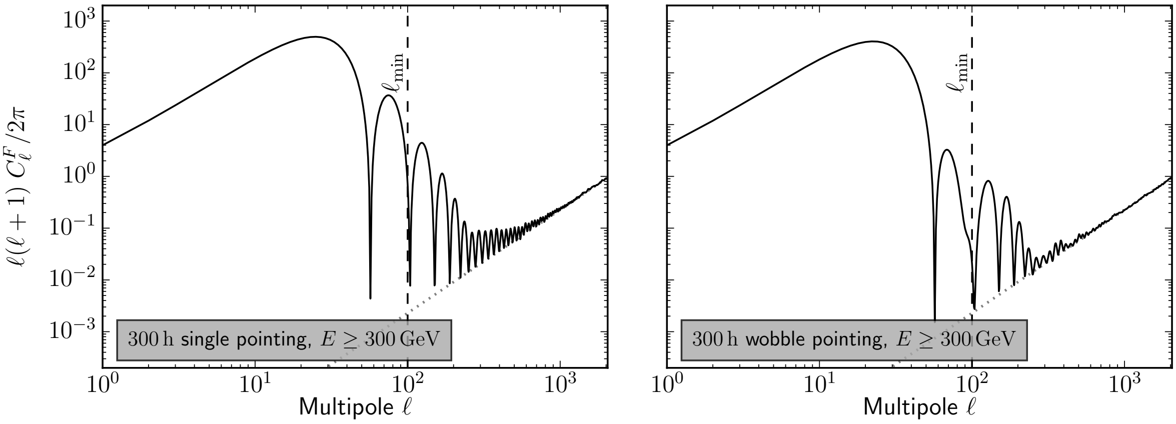

Figure C.10.: Background APS from 300 h of simulated observation (with `Paranal 50h_avg` cuts) towards a single position in the sky. *Left panel:* Single observation towards the pointing. *Right panel:* Total observation time distributed over four observations, pointed 1.5° offset from a central position ("wobble observation mode"). Events are simulated up to $\theta_{\text{cut}} = 6°$ offset from the camera center. These spectra correspond to the maps shown in Figure C.13.

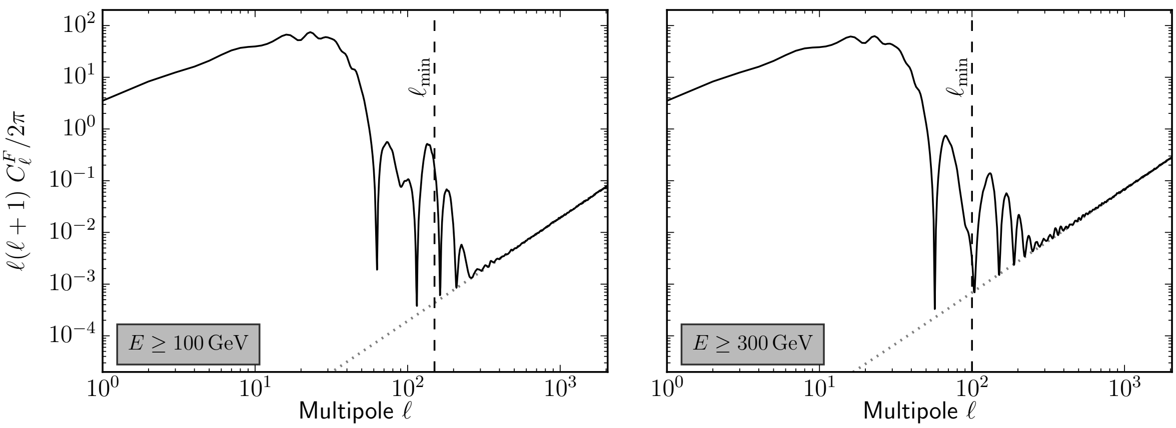

Figure C.11.: Background APS from 1000 h of simulated observation (with `Paranal 50h_avg` cuts) in wobble mode towards the eight dSph candidates discovered by Bechtol et al. (2015). The map shows a total number of 2.01×10^{8} background events $> 30\,\mathrm{GeV}$.

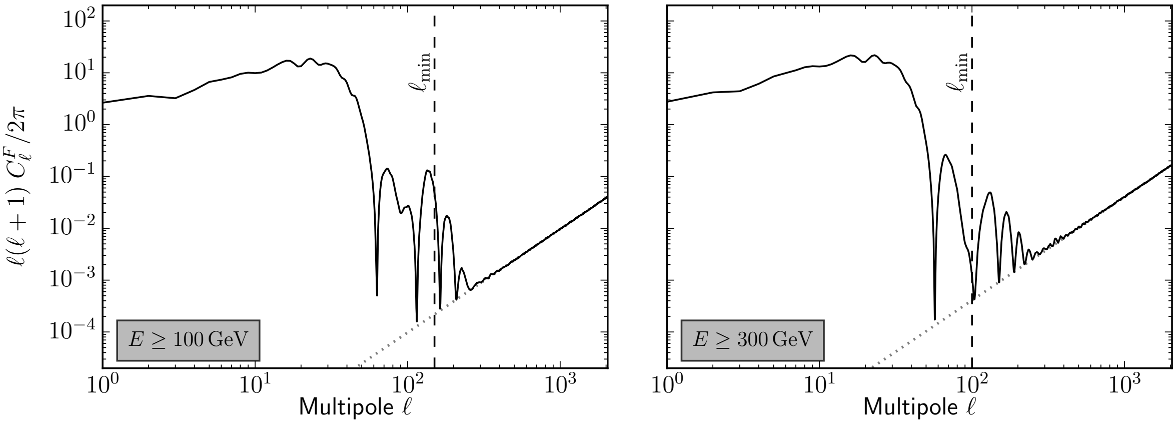

Figure C.12.: Background APS from 1000 h of simulated observation (with `Paranal avg_50h` cuts) towards eight individual pointings, together with the background events from a 500 h extragalactic survey with `Paranal 0.5h_avg` cuts. Due to the different cuts, both observation sets provide a similar number of events, 2.01×10^{8} events $> 30\,\mathrm{GeV}$ from the individual pointings, and 2.14×10^{8} events from the survey.

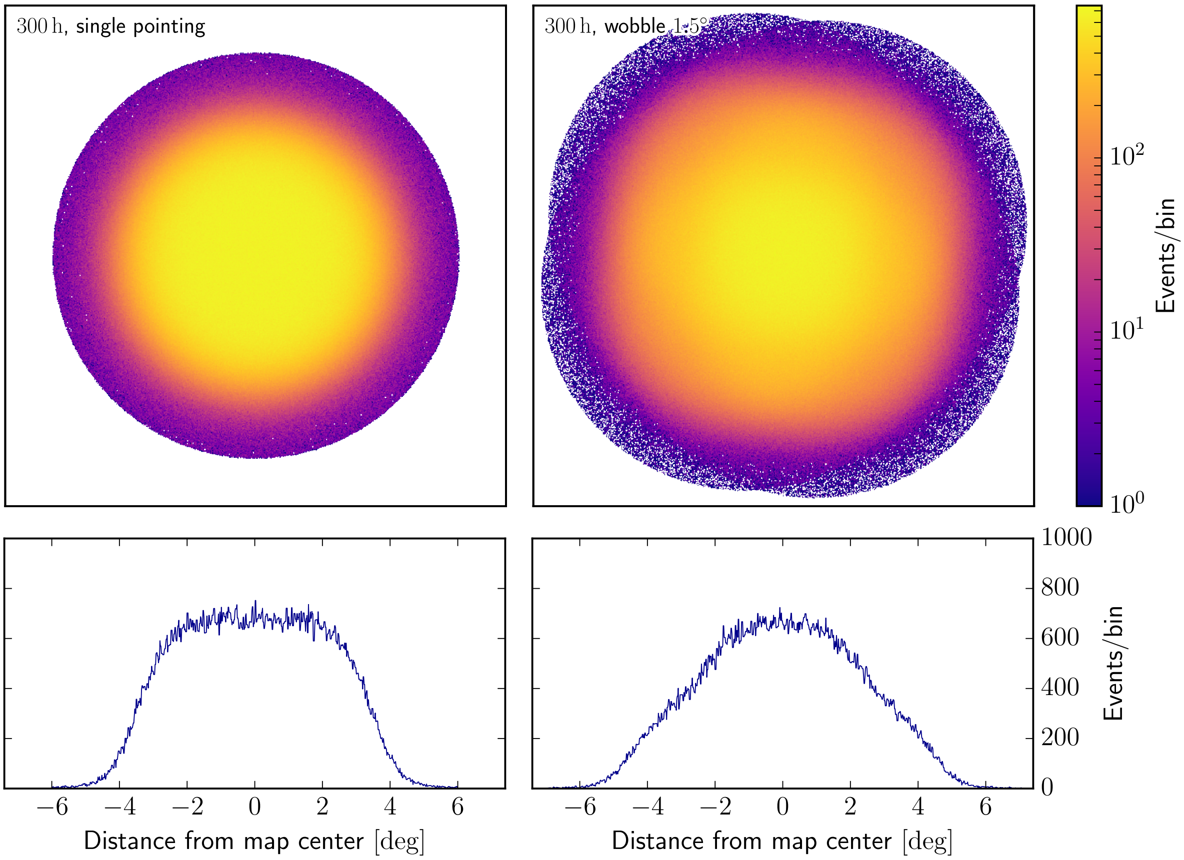

Figure C.13.: Event map of simulated total 300 h of observation (with `Paranal avg_50h` cuts) towards a single position in the sky. *Left panel:* Single observation towards the pointing. *Right panel:* Total observation time distributed over four observations, pointed 1.5° offset from a central position ("wobble observation mode"). Events are simulated up to $\theta_{\text{cut}} = 6°$ offset from the camera center. The maps contain a total number of 3.14×10^7 background events $> 100\,\text{GeV}$.

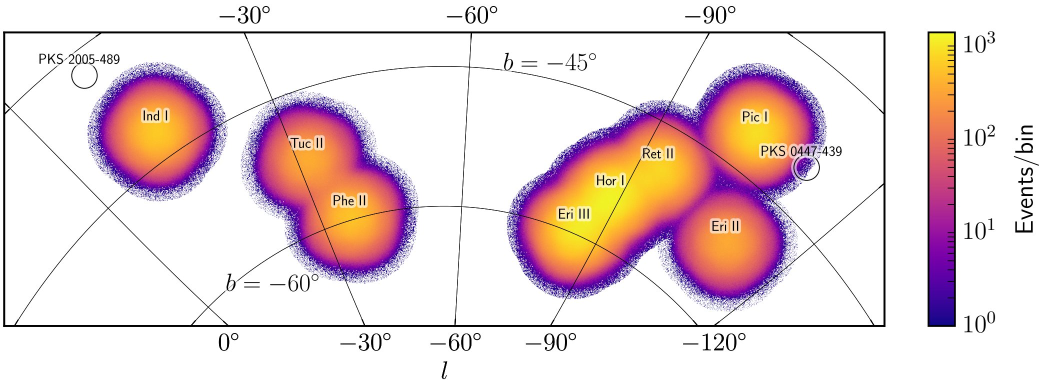

Figure C.14.: Event map (Galactic coordinates) of simulated total 1000 h of observation in wobble-mode (with `Paranal avg_50h` cuts) towards the dSph candidates found by Bechtol et al. (2015). The map shows a total number of 2.01×10^8 background events $> 30\,\text{GeV}$.

List of Acronyms

2dF	Two-degree-Field Galaxy Redshift Survey, 26
3FGL	*Fermi*-Large Area Telescope (LAT) 4-year Point Source Catalog, 130, 165
AGN	Active Galactic Nucleus, 26, 136, 164
AMS	Alpha Magnetic Spectrometer, 46, 134, 171
APS	Angular power spectrum, 28, 97, 109, 111, 112, 127, 133, 136–149, 152–155, 157–161, 163–169, 173, 176–178, 220–226, 228, 230–233
a.s.l.	above sea level, 56, 65, 80
BDT	Boosted decision tree, 68
CDM	Cold dark matter, 26, 31, 194
C.I.	Credible interval, 117, 119, 125, 127, 130, 146, 148, 155, 159, 160, 163, 171, 174, 207, 214, 216, 221, 222, 225
C.L.	Confidence level, 111, 117, 120, 123, 125, 127, 129, 133, 152, 157–159, 161, 163, 175, 176, 228, 230, 231
CMB	Cosmic Microwave Background, 23, 25, 26, 28, 31, 40, 84, 181, 184, 186, 188–190, 196, 200
COBE	Cosmic Background Explorer, 25
CTA	Cherenkov Telescope Array, 5, 7, 12–14, 44, 49, 56, 65–72, 74, 76–78, 80, 83, 97, 102, 103, 106, 109, 110, 112, 113, 115, 117, 119–125, 127, 129, 130, 132, 133, 137, 145, 148, 149, 151–153, 155, 156, 158, 159, 161, 164–169, 173–177, 210, 218, 226, 228, 229, 231, 232, 237, 238
DGRB	Diffuse γ-ray background, 13, 14, 74, 76, 109, 111, 133–137, 157, 161, 163–165, 173, 176, 178, 228–231

DM	Dark matter, 5, 7, 11–14, 17–36, 38, 40, 42–49, 78, 81, 83–87, 89, 91, 94, 97–99, 103–105, 109–113, 117, 120, 122–125, 127, 129, 130, 132–134, 136, 137, 139, 145, 146, 148, 149, 153, 157–159, 161, 163, 164, 171, 173–179, 198, 200, 203–206, 216, 218, 221–223, 225, 228, 230
dSph	dwarf spheroidal galaxy, 21, 23, 44, 45, 83, 91, 97, 104–106, 113, 119, 120, 125, 127, 130, 173–178, 205, 210, 232, 233
EAS	Extended air shower, 56
EGRET	Energetic Gamma Ray Experiment Telescope, 44
FOV	Field of view, 56, 61, 65–67, 70, 72, 74, 76, 77, 80, 81, 113, 115, 144, 149, 151, 155, 218, 229, 232
GC	Galactic center, 44, 45, 95, 110, 113, 117, 119, 146, 148, 149, 174, 177, 216
H.E.S.S.	High Energy Stereoscopic System, 45, 56, 57, 70, 125, 127, 129, 134
IACT	Imaging Atmospheric Cherenkov Telescope, 52, 56, 57, 59–62, 64–66, 68–70, 113, 143
IRF	Instrument response functions, 68, 70, 72, 78, 124, 125, 127, 153, 166, 229–231
LAT	Large Area Telescope on board the *Fermi* satellite, 12, 13, 45, 46, 49, 72, 76, 78, 80, 81, 102, 103, 106, 113, 117, 119, 125, 127, 130, 132–137, 161, 164, 165, 169, 171, 174, 177, 216, 237
ΛCDM	Λ-cold dark matter (universe), 28, 84, 89, 94, 103
LST	Cherenkov Telescope Array (CTA) large size telescope, 65, 66, 70, 77, 129
MACHOs	Massive compact halo objects, 24, 185
MAGIC	Major Atmospheric Gamma Imaging Cherenkov Telescopes, 45, 56, 57, 65, 70, 125, 175
MC	Monte-Carlo (random simulation), 58, 64, 71, 72, 74, 76, 111, 120, 124, 144, 148, 223, 224, 226, 230
MOND	Modified Newtonian Dynamics, 18, 23, 185
MSSM	Minimal Supersymmetric Standard Model, 34–36, 38, 43

MST	Cherenkov Telescope Array (CTA) medium size telescope, 65–67, 70
mSUGRA	minimal supergravity, 36, 38
MW	Milky Way, 18–21, 23, 24, 44, 83–86, 91, 95, 104–106, 120, 127, 134, 174
NFW	Navarro-Frenk-White (density profile), 18, 85, 87, 90, 91, 95, 100, 203–205, 218
PAMELA	Payload for Antimatter Matter Exploration and Light-nuclei Astrophysics, 46, 134, 171
pMSSM	phenomenological Minimal Supersymmetric Standard Model, 38, 48
PMT	Photomultiplier tube, 59, 61, 64, 65, 67, 68, 70, 77, 166
PSF	Point spread function, 65, 66, 77, 78, 151–153, 220, 229
SDSS	Sloan Digital Sky Survey, 26
SFG	Star-forming galaxy, 136, 164
SM	Standard Model of Particle Physics, 33–36, 38, 40, 42, 43, 46, 47, 198
SST	Cherenkov Telescope Array (CTA) small size telescope, 65, 67, 70, 127
SUSY	Supersymmetric Standard Model of Particle Physics, 34, 43, 47
TS	Test statistic, 78, 115, 124, 155, 156, 226
VERITAS	Very Energetic Radiation Imaging Telescope Array System, 45, 56, 57, 59, 61, 62, 70, 125, 134, 166, 168
VHE	Very-high-energy, 13, 37, 49, 53, 62, 65, 66, 80, 109, 113, 132, 133, 135, 137, 163–165, 176
VL II	Via Lactea II simulations (Diemand et al., 2008), 84, 90, 92, 94, 95, 103, 117, 130, 206
WIMP	Weakly Interacting Massive Particle, 11–13, 17, 30–34, 36–38, 40, 43, 45–48, 122, 125, 149, 151, 152, 157–159, 161, 177, 196, 197, 201
WMAP	Wilkinson Microwave Anisotropy Probe, 28, 85, 186

List of Figures

List of Tables

Bibliography

The page numbers following the bibliographical references point to the pages in this dissertation on which the reference is used. In the PDF version of this document, cross links to these pages, the journal online versions of articles, and their arXiv preprint versions are provided if available.

Aalseth, C. E., Barbeau, P. S., Colaresi, J., et al. (2014). Search for An Annual Modulation in Three Years of CoGeNT Dark Matter Detector Data. `arXiv:1401.3295`. Cited on p. 47.

Aartsen, M. G., Abbasi, R., Abdou, Y., et al. (2013a). Search for Dark Matter Annihilations in the Sun with the 79-String IceCube Detector. *Physical Review Letters*, 110(13):131302, `arXiv:1212.4097`. Cited on p. 46.

Aartsen, M. G., Abbasi, R., Abdou, Y., et al. (2013b). IceCube search for dark matter annihilation in nearby galaxies and galaxy clusters. *Physical Review D*, 88(12):122001, `arXiv:1307.3473`. Cited on p. 46.

Aartsen, M. G., Abraham, K., Ackermann, M., et al. (2016a). Improved limits on dark matter annihilation in the Sun with the 79-string IceCube detector and implications for supersymmetry. *Journal of Cosmology and Astroparticle Physics*, 2016(04):022, `arXiv:1601.00653`. Cited on p. 46.

Aartsen, M. G., Abraham, K., Ackermann, M., et al. (2016b). All-flavour search for neutrinos from dark matter annihilations in the Milky Way with IceCube/DeepCore. *The European Physical Journal C*, 76(10):531, `arXiv:1606.00209`. Cited on p. 46.

Abazajian, K. N. (2011). The consistency of Fermi-LAT observations of the galactic center with a millisecond pulsar population in the central stellar cluster. *Journal of Cosmology and Astroparticle Physics*, 2011(03):010, `arXiv:1011.4275`. Cited on p. 45.

Abazajian, K. N., Fuller, G. M., and Patel, M. (2001). Sterile neutrino hot, warm, and cold dark matter. *Physical Review D*, 64(2):023501, `arXiv:astro-ph/0101524`. Cited on p. 30.

Abbott, T. M. C. (2005). The Dark Energy Survey. `arXiv:astro-ph/0510346`. Cited on pp. 105 and 178.

Abdallah, H., Abramowski, A., Aharonian, F. A., et al. (2016a). H.E.S.S. Limits on Linelike Dark Matter Signatures in the 100 GeV to 2 TeV Energy Range Close to the Galactic Center. *Physical Review Letters*, 117(15):151302, `arXiv:1609.08091`. Cited on p. 45.

Abdallah, H., Abramowski, A., Aharonian, F. A., et al. (2016b). Search for Dark Matter Annihilations towards the Inner Galactic Halo from 10 Years of Observations with H.E.S.S. *Physical Review Letters*, 117(11):111301, `arXiv:1607.08142`. Cited on p. 45.

Abdo, A. A., Ackermann, M., Ajello, M., et al. (2010). Spectrum of the Isotropic Diffuse Gamma-Ray Emission Derived from First-Year Fermi Large Area Telescope Data. *Physical Review Letters*, 104(10):101101, `arXiv:1002.3603`. Cited on pp. 134, 135, 137, 161, 162, 163, 164, 176, 228, 229, and 230.

Abdo, A. A., Allen, B. T., Aune, T., et al. (2011). Observation and Spectral Measurements of the Crab Nebula with Milagro. *The Astrophysical Journal*, 750(1):63, `arXiv:1110.0409`. Cited on p. 67.

Abdo, A. A., Allen, B. T., Aune, T., et al. (2009). The Large Scale Cosmic-Ray Anisotropy as Observed with Milagro. *The Astrophysical Journal*, 698(2):2121–2130, `arXiv:0806.2293`. Cited on p. 169.

Abeysekara, A. U., Alfaro, R., Alvarez, C., et al. (2014). Sensitivity of HAWC to high-mass dark matter annihilations. *Physical Review D*, 90(12):122002, `arXiv:1405.1730`. Cited on p. 178.

Abramowski, A., Aharonian, F. A., Ait Benkhali, F., et al. (2014). Search for dark matter annihilation signatures in H.E.S.S. observations of dwarf spheroidal galaxies. *Physical Review D*, 90(11):112012, `arXiv:1410.2589`. Cited on p. 45.

Accardo, L., Aguilar, M., Aisa, D., et al. (2014). High Statistics Measurement of the Positron Fraction in Primary Cosmic Rays of 0.5–500 GeV with the Alpha Magnetic Spectrometer on the International Space Station. *Physical Review Letters*, 113(12):121101. Cited on p. 46.

Acharya, B., Actis, M., Aghajani, T., et al. (2013). Introducing the CTA concept. *Astroparticle Physics*, 43:3–18. Cited on pp. 12, 65, 66, and 71.

Ackermann, M., Ajello, M., Albert, A., et al. (2015a). Updated search for spectral lines from Galactic dark matter interactions with pass 8 data from the Fermi Large Area Telescope. *Physical Review D*, 91(12):122002, `arXiv:1506.00013`. Cited on p. 45.

Ackermann, M., Ajello, M., Albert, A., et al. (2015b). The spectrum of isotropic diffuse gamma-ray emission between 100 MeV and 820 GeV. *The Astrophysical Journal*, 799(1):86, `arXiv:1410.3696`. Cited on pp. 75, 76, 134, 135, 136, 137, 161, 162, 163, 164, and 176.

Ackermann, M., Ajello, M., Albert, A., et al. (2015c). Search for extended gamma-ray emission from the Virgo galaxy cluster with Fermi-LAT. *The Astrophysical Journal*, 812(2):159, `arXiv:1510.00004`. Cited on p. 45.

Ackermann, M., Ajello, M., Albert, A., et al. (2012a). Anisotropies in the diffuse gamma-ray background measured by the Fermi LAT. *Physical Review D*, 85(8):083007, `arXiv:1202.2856`. Cited on pp. 13, 45, 133, 137, 142, 164, 165, and 233.

Ackermann, M., Ajello, M., Albert, A., et al. (2015d). Limits on Dark Matter Annihilation Signals from the Fermi LAT 4-year Measurement of the Isotropic Gamma-Ray Background. *Journal of Cosmology and Astroparticle Physics*, 2015(09):008, `arXiv:1501.05464`. Cited on pp. 45 and 137.

Ackermann, M., Ajello, M., Allafort, A., et al. (2012b). Measurement of Separate Cosmic-Ray Electron and Positron Spectra with the Fermi Large Area Telescope. *Physical Review Letters*, 108(1):011103, `arXiv:1109.0521`. Cited on p. 46.

Ackermann, M., Ajello, M., Allafort, A., et al. (2010a). Constraints on dark matter annihilation in clusters of galaxies with the Fermi Large Area Telescope. *Journal of Cosmology and Astroparticle Physics*, 2010(05):025, `arXiv:1002.2239`. Cited on p. 45.

Ackermann, M., Ajello, M., Atwood, W. B., et al. (2010b). Searches for cosmic-ray electron anisotropies with the Fermi Large Area Telescope. *Physical Review D*, 82(9):092003, `arXiv:1008.5119`. Cited on p. 171.

Ackermann, M., Ajello, M., Atwood, W. B., et al. (2016). 2FHL: The Second Catalog of Hard Fermi-LAT Sources. *The Astrophysical Journal Supplement Series*, 222(1):5, `arXiv:1508.04449`. Cited on p. 13.

Ackermann, M., Albert, A., Anderson, B., et al. (2015e). Searching for Dark Matter Annihilation from Milky Way Dwarf Spheroidal Galaxies with Six Years of Fermi Large Area Telescope Data. *Physical Review Letters*, 115(23):231301, `arXiv:1503.02641`. Cited on pp. 45, 105, 126, and 132.

Ackermann, M., Albert, A., Baldini, L., et al. (2012c). Search for Dark Matter Satellites using the Fermi-LAT. *The Astrophysical Journal*, 747(2):121, `arXiv:1201.2691`. Cited on p. 45.

Actis, M., Agnetta, G., Aharonian, F. A., et al. (2011). Design concepts for the Cherenkov Telescope Array CTA: an advanced facility for ground-based high-energy gamma-ray astronomy. *Experimental Astronomy*, 32(3):193–316, `arXiv:1008.3703`. Cited on pp. 65, 68, and 71.

Ade, P. A. R., Aghanim, N., Arnaud, M., et al. (2016). Planck 2015 results. *Astronomy & Astrophysics*, 594:A13, `arXiv:1502.01589`. Cited on pp. 25, 29, 31, 85, 89, 194, and 195.

Adriani, O., Barbarino, G. C., Bazilevskaya, G. A., et al. (2011). PAMELA Measurements of Cosmic-Ray Proton and Helium Spectra. *Science*, 332(6025):69–72, `arXiv:1103.4055`. Cited on p. 134.

Adriani, O., Barbarino, G. C., Bazilevskaya, G. A., et al. (2009). An anomalous positron abundance in cosmic rays with energies 1.5–100 GeV. *Nature*, 458(7238):607–609, `arXiv:0810.4995`. Cited on p. 46.

Adriani, O., Barbarino, G. C., Bazilevskaya, G. A., et al. (2015). Search for anisotropies in cosmic-ray positrons detected by the PAMELA experiment. *The Astrophysical Journal*, 811(1):21, `arXiv:1509.06249`. Cited on p. 171.

Aghanim, N., Arnaud, M., Ashdown, M., et al. (2016). Planck 2015 results. XI. CMB power spec- tra, likelihoods, and robustness of parameters. *Astronomy & Astrophysics*, 594:A11, `arXiv:1507.02704`. Cited on p. 29.

Agnese, R., Ahmed, Z., Anderson, A. J., et al. (2013). Silicon Detector Dark Matter Results from the Final Exposure of CDMS II. *Physical Review Letters*, 111(25):251301, `arXiv:1304.4279`. Cited on p. 47.

Aguilar, M., Aisa, D., Alpat, B., et al. (2015a). Precision Measurement of the Proton Flux in Primary Cosmic Rays from Rigidity 1 GV to 1.8 TV with the Alpha Magnetic Spectrometer on the International Space Station. *Physical Review Letters*, 114(17):171103. Cited on p. 134.

Aguilar, M., Aisa, D., Alpat, B., et al. (2015b). Precision Measurement of the Helium Flux in Primary Cosmic Rays of Rigidities 1.9 GV to 3 TV with the Alpha Magnetic Spectrometer on the International Space Station. *Physical Review Letters*, 115(21):211101. Cited on p. 134.

Aguilar, M., Aisa, D., Alvino, A., et al. (2014). Electron and Positron Fluxes in Primary Cosmic Rays Measured with the Alpha Magnetic Spectrometer on the International Space Station. *Physical Review Letters*, 113(12):121102. Cited on pp. 134 and 136.

Aharonian, F. A., Akhperjanian, A. G., Barres de Almeida, U., et al. (2008a). Energy Spectrum of Cosmic-Ray Electrons at TeV Energies. *Physical Review Letters*, 101(26):261104, `arXiv:0811.3894`. Cited on pp. 134 and 136.

Aharonian, F. A., Akhperjanian, A. G., Bazer-Bachi, A. R., et al. (2006). Observations of the Crab nebula with H.E.S.S. *Astronomy & Astrophysics*, 457(3):899–915, `arXiv:astro-ph/0607333`. Cited on p. 69.

Aharonian, F. A., Buckley, J., Kifune, T., et al. (2008b). High energy astrophysics with ground-based gamma ray detectors. *Reports on Progress in Physics*, 71(9):096901. Cited on pp. 52, 55, and 59.

Ahrens, J., Bahcall, J., Bai, X., et al. (2004). Status of the IceCube Neutrino Observatory. *New Astronomy Reviews*, 48(5-6):519–525. Cited on p. 46.

Ajello, M., Gasparrini, D., Sánchez-Conde, M. Á., et al. (2015). The Origin of the Extragalactic Gamma-Ray Background and Implications for Dark-Matter Annihilation. *The Astrophysical Journal*, 800(2):L27, `arXiv:1501.05301`. Cited on p. 136.

Akerib, D., Alvaro-Dean, J., Armel, M., et al. (2004). Installation and commissioning of the CDMSII experiment at Soudan. *Nuclear Instruments and Methods in Physics Research A*, 520(1-3):116–119. Cited on p. 48.

Albert, A., Anderson, B., Bechtol, K., et al. (2017). Searching for Dark Matter Annihilation in Recently Discovered Milky Way Satellites with Fermi-LAT. *The Astrophysical Journal*, 834(2):110, `arXiv:1611.03184`. Cited on p. 45.

Aleksić, J., Ansoldi, S., Antonelli, L., et al. (2014). Optimized dark matter searches in deep observations of Segue 1 with MAGIC. *Journal of Cosmology and Astroparticle Physics*, 2014(02):008, `arXiv:1312.1535`. Cited on pp. 46 and 126.

Allanach, B. (2002). SOFTSUSY: A program for calculating supersymmetric spectra. *Computer Physics Communications*, 143(3):305–331, `arXiv:hep-ph/0104145`. Cited on p. 38.

Alpher, R. A., Bethe, H., and Gamow, G. (1948). The Origin of Chemical Elements. *Physical Review*, 73(7):803–804. Cited on p. 189.

Alpher, R. A. and Herman, R. (1948). Evolution of the Universe. *Nature*, 162(4124):774–775. Cited on pp. 189 and 190.

Ambrosi, G., Awane, Y., Baba, H., et al. (2013). The Cherenkov Telescope Array Large Size Telescope. *Proceedings of the 33rd International Cosmic Ray Conference*, `arXiv:1307.4565`. Cited on p. 66.

Amenomori, M., Ayabe, S., Cui, S. W., et al. (2005). Large-Scale Sidereal Anisotropy of Galactic Cosmic-Ray Intensity Observed by the Tibet Air Shower Array. *The Astrophysical Journal*, 626(1):L29–L32, `arXiv:astro-ph/0505114`. Cited on p. 169.

Anderhalden, D. and Diemand, J. (2013). Density profiles of CDM microhalos and their implications for annihilation boost factors. *Journal of Cosmology and Astroparticle Physics*, 2013(04):009, `arXiv:1302.0003`. Cited on p. 91.

Ando, S. (2009). Gamma-ray background anisotropy from Galactic dark matter substructure. *Physical Review D*, 80(2):023520, `arXiv:0903.4685`. Cited on pp. 139 and 147.

Ando, S. (2016). Dark matter indirect searches: Multi-wavelength and anisotropies. *Journal of Physics: Conference Series*, 718:022002. Cited on p. 178.

Ando, S., Benoit-Lévy, A., and Komatsu, E. (2014). Mapping dark matter in the gamma-ray sky with galaxy catalogs. *Physical Review D*, 90(2):023514, `arXiv:1312.4403`. Cited on p. 178.

Ando, S. and Ishiwata, K. (2015). Constraints on decaying dark matter from the extragalactic gamma-ray background. *Journal of Cosmology and Astroparticle Physics*, 2015(05):024, `arXiv:1502.02007`. Cited on p. 46.

Ando, S. and Ishiwata, K. (2016). Constraining particle dark matter using local galaxy distribution. *Journal of Cosmology and Astroparticle Physics*, 2016(06):045, `arXiv:1604.02263`. Cited on p. 178.

Ando, S. and Komatsu, E. (2013). Constraints on the annihilation cross section of dark matter particles from anisotropies in the diffuse gamma-ray background measured with Fermi-LAT. *Physical Review D*, 87(12):123539, `arXiv:1301.5901`. Cited on pp. 13, 45, 137, and 147.

Ando, S., Komatsu, E., Narumoto, T., et al. (2007). Dark matter annihilation or unresolved astrophysical sources? Anisotropy probe of the origin of the cosmic gamma-ray background. *Physical Review D*, 75(6):063519, `arXiv:0612467`. Cited on p. 164.

Ando, S. and Pavlidou, V. (2009). Imprint of galaxy clustering in the cosmic gamma-ray background. *Monthly Notices of the Royal Astronomical Society*, 400(4):2122–2127, `arXiv:0908.3890`. Cited on p. 164.

Angloher, G., Bauer, M., Bavykina, I., et al. (2012). Results from 730 kg days of the CRESST-II Dark Matter search. *The European Physical Journal C*, 72(4):1971, `arXiv:1109.0702`. Cited on p. 47.

Angulo, R. E., Lacey, C. G., Baugh, C. M., et al. (2009). The fate of substructures in cold dark matter haloes. *Monthly Notices of the Royal Astronomical Society*, 399(2):983–995, `arXiv:0810.2177`. Cited on p. 87.

Arkani-Hamed, N., Finkbeiner, D. P., Slatyer, T. R., et al. (2009). A theory of dark matter. *Physical Review D*, 79(1):015014, `arXiv:0810.0713`. Cited on p. 34.

Assis, P., de Almeida, U. B., Blanco, A., et al. (2016). Design and expected performance of a novel hybrid detector for very-high-energy gamma astrophysics. `arXiv:1607.03051`. Cited on p. 178.

Atwood, W. B. (2009). The Large Area Telescope on the Fermi Gamma-ray Space Telescope Mission. *The Astrophysical Journal*, 697(2):1071–1102, `arXiv:0902.1089`. Cited on pp. 12, 80, and 132.

Atwood, W. B., Albert, A., Baldini, L., et al. (2013). Pass 8: Toward the Full Realization of the Fermi-LAT Scientific Potential. *Proceedings of the 2012 Fermi Symposium*, `arXiv:1303.3514`. Cited on pp. 131 and 132.

Auger, M. W., Treu, T., Gavazzi, R., et al. (2010). Dark Matter Contraction and the Stellar Content of Massive Early-type Galaxies: Disfavoring "Light" Initial Mass Functions. *The Astrophysical Journal*, 721(2):L163–L167, `arXiv:1007.2409`. Cited on p. 23.

Babcock, H. W. (1939). The rotation of the Andromeda Nebula. *Lick Observatory Bulletins*, 19:41–51. Cited on pp. 20 and 183.

Baehr, J. (2012). Status of the CTA medium size telescope prototype. *AIP Conference Proceedings*, 1505:753–757, `arXiv:1212.3110`. Cited on p. 67.

Bahcall, N. A. and Fan, X. (1998). The Most Massive Distant Clusters: Determining Ω and σ_8. *The Astrophysical Journal*, 504(1):1–6, `arXiv:astro-ph/9803277`. Cited on p. 23.

Baldini, L. (2014). Space-Based Cosmic-Ray and Gamma-Ray Detectors: a Review. `arXiv:1407.7631`. Cited on pp. 72 and 78.

Bartels, R. and Ando, S. (2015). Boosting the annihilation boost: Tidal effects on dark matter subhalos and consistent luminosity modeling. *Physical Review D*, 92(12):123508, `arXiv:1507.08656`. Cited on p. 88.

Bartels, R., Krishnamurthy, S., and Weniger, C. (2016). Strong Support for the Millisecond Pulsar Origin of the Galactic Center GeV Excess. *Physical Review Letters*, 116(5):051102, `arXiv:1506.05104`. Cited on p. 45.

Bauer, D., Buckley, J., Cahill-Rowley, M., et al. (2015). Dark matter in the coming decade: Complementary paths to discovery and beyond. *Physics of the Dark Universe*, 7-8:16–23, `arXiv:1305.1605`. Cited on p. 48.

Baumann, D. (2013). Cosmology. *Lecture Notes*. Cited on pp. 27, 195, 197, and 198.

Beaulieu, J. P., Bennett, D. P., Batista, V., et al. (2010). EUCLID: Dark Universe Probe and Microlensing planet Hunter. *Pathways Towards Habitable Planets*, 430:266, `arXiv:1001.3349`. Cited on p. 178.

Bechtol, K., Drlica-Wagner, A., Balbinot, E., et al. (2015). Eight New Milky Way Companions Discovered in First-Year Dark Energy Survey Data. *The Astrophysical Journal*, 807(1):50, `arXiv:1503.02584`. Cited on pp. 233, 234, and 235.

Beck, G. and Colafrancesco, S. (2016). A Multi-frequency analysis of dark matter annihilation interpretations of recent anti-particle and γ-ray excesses in cosmic structures. *Journal of Cosmology and Astroparticle Physics*, 2016(05):013, `arXiv:1508.01386`. Cited on p. 178.

Begeman, K. G., Broeils, A. H., and Sanders, R. H. (1991). Extended rotation curves of spiral galaxies: dark haloes and modified dynamics. *Monthly Notices of the Royal Astronomical Society*, 249(3):523–537. Cited on p. 20.

Behera, B., Baehr, J., Grünewald, S., et al. (2012). Optical design and calibration of a medium size telescope prototype for the CTA. *Proceedings of SPIE*, page 844417. Cited on p. 67.

Bekenstein, J. D. (2004). Relativistic gravitation theory for the modified Newtonian dynamics paradigm. *Physical Review D*, 70(8):083509, `arXiv:astro-ph/0403694`. Cited on p. 186.

Bélanger, G., Boudjema, F., Pukhov, A., et al. (2015). micrOMEGAs4.1: Two dark matter candidates. *Computer Physics Communications*, 192:322–329, `arXiv:1407.6129`. Cited on p. 38.

Belikov, A. V., Buckley, M. R., and Hooper, D. (2012). Searching for dark matter subhalos in the Fermi-LAT second source catalog. *Physical Review D*, 86(4):043504, `arXiv:1111.2613`. Cited on p. 132.

Bellm, J., Gieseke, S., Grellscheid, D., et al. (2016). Herwig 7.0/Herwig++ 3.0 release note. *The European Physical Journal C*, 76(4):196, `arXiv:1512.01178`. Cited on p. 40.

Berezinsky, V., Dokuchaev, V., and Eroshenko, Y. (2003). Small-scale clumps in the galactic halo and dark matter annihilation. *Physical Review D*, 68(10):103003, `arXiv:astro-ph/0301551`. Cited on pp. 28 and 84.

Bergström, L. (2009). Dark matter candidates. *New Journal of Physics*, 11(10):105006, `arXiv:0903.4849`. Cited on p. 11.

Bergström, L. and Ullio, P. (1997). Full one-loop calculation of neutralino annihilation into two photons. *Nuclear Physics B*, 504(1-2):27–44, `arXiv:hep-ph/9706232`. Cited on pp. 38 and 39.

Bergström, L., Ullio, P., and Buckley, J. H. (1998). Observability of γ-rays from dark matter neutralino annihilations in the Milky Way halo. *Astroparticle Physics*, 9(2):137–162, `arXiv:astro-ph/9712318`. Cited on p. 84.

Berlin, A. and Hooper, D. (2014). Stringent constraints on the dark matter annihilation cross section from subhalo searches with the Fermi Gamma-Ray Space Telescope. *Physical Review D*, 89(1):016014, `arXiv:1309.0525`. Cited on p. 130.

Bernabei, R. and Belli, P. (2010). Annual modulation signature with large mass highly radiopure NaI(Tl). In Bertone, G., editor, *Particle Dark Matter. Observations, Models and Searches*, chapter 18, pages 370–382. Cambridge University Press, New York. Cited on p. 47.

Bernabei, R., Belli, P., Cappella, F., et al. (2013). Final model independent result of DAMA/LIBRA–phase1. *The European Physical Journal C*, 73(12):2648, `arXiv:1308.5109`. Cited on p. 47.

Bernabei, R., Belli, P., Cappella, F., et al. (2014). No role for neutrons, muons and solar neutrinos in the DAMA annual modulation results. *The European Physical Journal C*, 74(12):3196, `arXiv:1409.3516`. Cited on p. 47.

Bernlöhr, K. (2000). Impact of atmospheric parameters on the atmospheric Cherenkov technique. *Astroparticle Physics*, 12(4):255–268, `arXiv:astro-ph/9908093`. Cited on pp. 58 and 66.

Bernlöhr, K. (2008). Simulation of imaging atmospheric Cherenkov telescopes with CORSIKA and sim_telarray. *Astroparticle Physics*, 30(3):149–158, `arXiv:0808.2253`. Cited on p. 68.

Bernlöhr, K., Barnacka, A., Becherini, Y., et al. (2013). Monte Carlo design studies for the Cherenkov Telescope Array. *Astroparticle Physics*, 43:171–188, `arXiv:1210.3503`. Cited on pp. 68 and 69.

Bertin, G., Bertola, F., Buson, L. M., et al. (1994). A search for dark matter in elliptical galaxies: Radially extended spectroscopic observations for six objects. *Astronomy & Astrophysics*, 292:381–391. Cited on p. 21.

Bertone, G. (2010a). *Particle Dark Matter. Observations, Models and Searches.* Cambridge University Press, New York. Cited on p. 30.

Bertone, G. (2010b). The moment of truth for WIMP dark matter. *Nature*, 468(7322):389–393, `arXiv:1011.3532`. Cited on p. 30.

Bertone, G., Calore, F., Caron, S., et al. (2016). Global analysis of the pMSSM in light of the Fermi GeV excess: prospects for the LHC Run-II and astroparticle experiments. *Journal of Cosmology and Astroparticle Physics*, 2016(04):037–037, `arXiv:1507.07008`. Cited on p. 48.

Bertone, G. and Hooper, D. (2016). A History of Dark Matter. `arXiv:1605.04909`. Cited on pp. 182 and 187.

Bertone, G., Hooper, D., and Silk, J. (2005). Particle dark matter: evidence, candidates and constraints. *Physics Reports*, 405(5-6):279–390, `arXiv:hep-ph/0404175`. Cited on pp. 32, 34, 35, 36, 37, 47, and 48.

Bertoni, B., Hooper, D., and Linden, T. (2015). Examining The Fermi-LAT Third Source Catalog in search of dark matter subhalos. *Journal of Cosmology and Astroparticle Physics*, 2015(12):035, `arXiv:1504.02087`. Cited on pp. 12, 130, 131, and 174.

Besla, G. (2015). The Orbits and Total Mass of the Magellanic Clouds. `arXiv:1511.03346`. Cited on p. 87.

Biller, S. (1996). Hypothesis ranking and the context of probabilities in an open-ended search. *Astroparticle Physics*, 4(3):285–291. Cited on p. 123.

Binney, J. J., Davies, R. L., and Illingworth, G. D. (1990). Velocity mapping and models of the elliptical galaxies NGC 720, NGC 1052, and NGC 4697. *The Astrophysical Journal*, 361:78. Cited on p. 21.

Binney, J. J. and Tremaine, S. (2008). *Galactic Dynamics.* Princeton University Press, Princeton, 2nd edition. Cited on pp. 21, 22, 28, and 88.

Blum, K. (2011). DAMA vs. the annually modulated muon background. `arXiv:1110.0857`. Cited on p. 47.

Bond, J. R., Cole, S., Efstathiou, G., et al. (1991). Excursion set mass functions for hierarchical Gaussian fluctuations. *The Astrophysical Journal*, 379:440. Cited on p. 28.

Bonnivard, V., Combet, C., Daniel, M., et al. (2015a). Dark matter annihilation and decay in dwarf spheroidal galaxies: the classical and ultrafaint dSphs. *Monthly Notices of the Royal Astronomical Society*, 453(1):849–867, `arXiv:1504.02048`. Cited on pp. 21, 44, and 105.

Bonnivard, V., Combet, C., Maurin, D., et al. (2014). Spherical Jeans analysis for dark matter indirect detection in dwarf spheroidal galaxies - impact of physical parameters and triaxiality. *Monthly Notices of the Royal Astronomical Society*, 446(3):3002–3021, `arXiv:1407.7822`. Cited on p. 21.

Bonnivard, V., Hütten, M., Nezri, E., et al. (2015b). CLUMPY: Jeans analysis, γ-ray and neutrino fluxes from dark matter (sub-)structures. *Computer Physics Communications*, 200:336–349, `arXiv:1506.07628`. Cited on pp. 14, 91, 94, 97, 98, 100, and 146.

Bonnivard, V., Maurin, D., and Walker, M. G. (2016). Contamination of stellar-kinematic samples and uncertainty about dark matter annihilation profiles in ultrafaint dwarf galaxies: the example of Segue I. *Monthly Notices of the Royal Astronomical Society*, 462(1):223–234, `arXiv:1506.08209`. Cited on pp. 127 and 175.

Boodin, J. E. (1943). The Vision of Parmenides. *The Philosophical Review*, 52(6):578. Cited on p. 83.

Borriello, E., Maccione, L., and Cuoco, A. (2012a). Dark matter electron anisotropy: A universal upper limit. *Astroparticle Physics*, 35(8):537–546, `arXiv:1012.0041`. Cited on p. 171.

Borriello, E., Maccione, L., and Cuoco, A. (2012b). Electron anisotropy: A tool to discriminate dark matter in cosmic rays. *Journal of Physics: Conference Series*, 375(1):012031. Cited on p. 171.

Bosma, A. (1978). *The distribution and kinematics of neutral hydrogen in spiral galaxies of various morphological types*. PhD thesis, Groningen University. Cited on p. 20.

Bovy, J. and Rix, H.-W. (2013). A direct dynamical measurement of the Milky Way's disk surface density profile, disk scale length, and dark matter profile at 4 kpc $<$ R $<$ 9 kpc. *The Astrophysical Journal*, 779(2):115, `arXiv:1309.0809`. Cited on pp. 18 and 19.

Boylan-Kolchin, M., Bullock, J. S., and Kaplinghat, M. (2011). Too big to fail? The puzzling darkness of massive Milky Way subhaloes. *Monthly Notices of the Royal Astronomical Society: Letters*, 415(1):L40–L44, `arXiv:1103.0007`. Cited on p. 94.

Boylan-Kolchin, M., Ma, C.-P., and Quataert, E. (2008). Dynamical friction and galaxy merging time-scales. *Monthly Notices of the Royal Astronomical Society*, 383(1):93–101, `arXiv:0707.2960`. Cited on p. 87.

Bradač, M., Allen, S. W., Treu, T., et al. (2008). Revealing the Properties of Dark Matter in the Merging Cluster MACS J0025.4−1222. *The Astrophysical Journal*, 687(2):959–967, `arXiv:0806.2320`. Cited on p. 23.

Bringmann, T., Bergström, L., and Edsjö, J. (2008). New gamma-ray contributions to supersymmetric dark matter annihilation. *Journal of High Energy Physics*, 2008(01):049–049, `arXiv:0710.3169`. Cited on p. 37.

Bringmann, T. and Calore, F. (2014). Significant Enhancement of Neutralino Dark Matter Annihilation from Electroweak Bremsstrahlung. *Physical Review Letters*, 112(7):071301, `arXiv:1308.1089`. Cited on p. 37.

Bringmann, T., Calore, F., Di Mauro, M., et al. (2014). Constraining dark matter annihilation with the isotropic γ-ray background: Updated limits and future potential. *Physical Review D*, 89(2):023012, `arXiv:1303.3284`. Cited on p. 13.

Bringmann, T., Huang, X., Ibarra, A., et al. (2012). Fermi LAT search for internal bremsstrahlung signatures from dark matter annihilation. *Journal of Cosmology and Astroparticle Physics*, 2012(07):054, `arXiv:1203.1312`. Cited on pp. 37, 38, and 41.

Brooks, A. M., Kuhlen, M., Zolotov, A., et al. (2013). A Baryonic Solution to the Missing Satellites Problem. *The Astrophysical Journal*, 765(1):22, `arXiv:1209.5394`. Cited on p. 94.

Brun, P., Moulin, E., and Diemand, J. (2011). Searches for dark matter subhaloes with wide-field Cherenkov telescope surveys. *Physical Review D*, 83(1):015003, `arXiv:1012.4766`. Cited on pp. 117, 118, 129, and 130.

Bryan, G. L. and Norman, M. L. (1998). Statistical Properties of X-ray Clusters: Analytic and Numerical Comparisons. *The Astrophysical Journal*, 495(1):80–99, `arXiv:astro-ph/9710107`. Cited on p. 89.

Buchmüller, W., Covi, L., Hamaguchi, K., et al. (2007). Gravitino dark matter in R-parity breaking vacua. *Journal of High Energy Physics*, 2007(03):037–037, `arXiv:hep-ph/0702184`. Cited on p. 44.

Buckley, M. R., Hooper, D., and Kumar, J. (2013). Phenomenology of Dirac neutralino dark matter. *Physical Review D*, 88(6):063532, `arXiv:1307.3561`. Cited on p. 35.

Bullock, J. (2013). Notes on the missing satellites problem. In Martínez-Delgado, D., Mediavilla, E., editors. *Local Group Cosmology*, pages 95–122, `arXiv:1009.4505`. Cited on p. 94.

Bullock, J., Kaplinghat, M., and Strigari, L. (2010). Milky Way satellites. In Bertone, G., editor, *Particle Dark Matter. Observations, Models and Searches*, chapter 3, pages 38–55. Cambridge University Press, New York. Cited on p. 105.

Bullock, J. S., Kolatt, T. S., Sigad, Y., et al. (2001). Profiles of dark haloes: evolution, scatter and environment. *Monthly Notices of the Royal Astronomical Society*, 321(3):559–575, `arXiv:astro-ph/9908159`. Cited on pp. 88, 93, and 94.

Buote, D. A. and Humphrey, P. J. (2012). Dark Matter in Elliptical Galaxies. In Kim, D.-W. and Pellegrini, S., editors, *Hot Interstellar Matter in Elliptical Galaxies*, pages 235–277. Springer, Heidelberg. Cited on p. 21.

Burkert, A. (1995). The Structure of Dark Matter Halos in Dwarf Galaxies. *The Astrophysical Journal*, 447(1):10, `arXiv:astro-ph/9504041`. Cited on pp. 91 and 205.

Byrum, K., Humensky, T. B., Benbow, W., et al. (2015). A Medium Sized Schwarzschild-Couder Cherenkov Telescope Mechanical Design Proposed for the Cherenkov Telescope Array. *Proceedings of the 34th International Cosmic Ray Conference*, `arXiv:1509.03074`. Cited on p. 65.

Cahill-Rowley, M., Cotta, R., Drlica-Wagner, A., et al. (2015). Complementarity of dark matter searches in the phenomenological MSSM. *Physical Review D*, 91(5):055011, `arXiv:1405.6716`. Cited on p. 48.

Calcáneo-Roldán, C. and Moore, B. (2000). Surface brightness of dark matter: Unique signatures of neutralino annihilation in the galactic halo. *Physical Review D*, 62(12):123005, `arXiv:astro-ph/0010056`. Cited on p. 84.

Calore, F., Bozorgnia, N., Lovell, M., et al. (2016a). The Fermi GeV excess: challenges for the dark matter interpretation. *Journal of Physics: Conference Series*, 718:042010. Cited on p. 45.

Calore, F., Cholis, I., and Weniger, C. (2015). Background model systematics for the Fermi GeV excess. *Journal of Cosmology and Astroparticle Physics*, 2015(03):038, `arXiv:1409.0042`. Cited on p. 45.

Calore, F., De Romeri, V., Di Mauro, M., et al. (2014a). γ-ray anisotropies from dark matter in the Milky Way: the role of the radial distribution. *Monthly Notices of the Royal Astronomical Society*, 442(2):1151–1156, `arXiv:1402.0512`. Cited on p. 147.

Calore, F., Di Mauro, M., and Donato, F. (2014b). Diffuse gamma-ray emission from galactic pulsars. *The Astrophysical Journal*, 796(1):14, `arXiv:1406.2706`. Cited on p. 136.

Calore, F., Di Mauro, M., Donato, F., et al. (2016b). Radio detection prospects for a bulge population of millisecond pulsars as suggested by Fermi LAT observations of the inner Galaxy. *The Astrophysical Journal*, 827(2):143, `arXiv:1512.06825`. Cited on p. 178.

Camera, S., Fornasa, M., Fornengo, N., et al. (2013). A novel approach in the WIMP quest: Cross-Correlation of Gamma-Ray Anisotropies and Cosmic Shear. *The Astrophysical Journal*, 771(1):L5, `arXiv:1212.5018`. Cited on p. 178.

Camera, S., Fornasa, M., Fornengo, N., et al. (2015). Tomographic-spectral approach for dark matter detection in the cross-correlation between cosmic shear and diffuse γ-ray emission. *Journal of Cosmology and Astroparticle Physics*, 2015(06):029, `arXiv:1411.4651`. Cited on p. 178.

Campbell, S. S. (2015). Angular power spectra with finite counts. *Monthly Notices of the Royal Astronomical Society*, 448(3):2854–2878, `arXiv:1411.4031`. Cited on p. 144.

Carlberg, R. G., Yee, H. K. C., Morris, S. L., et al. (1999). The $\Omega_\mathrm{M} - \Omega_\Lambda$ Dependence of the Apparent Cluster Ω. *The Astrophysical Journal*, 516(2):552–558. Cited on p. 23.

Carr, J., Balazs, C., Bringmann, T., et al. (2015). Prospects for Indirect Dark Matter Searches with the Cherenkov Telescope Array (CTA). *Proceedings of the 34th International Cosmic Ray Conference*, `arXiv:1508.06128`. Cited on pp. 125, 126, and 175.

Casaus, J. (2013). Determination of the positron anisotropy with AMS. *Proceedings of the 33rd International Cosmic Ray Conference*. Cited on p. 171.

Cembranos, J. A. R., de la Cruz-Dombriz, A., Dobado, A., et al. (2011). Photon spectra from WIMP annihilation. *Physical Review D*, 83(8):083507, `arXiv:1009.4936`. Cited on p. 41.

Chandrasekhar, S. (1943a). Dynamical Friction. I. General Considerations: the Coefficient of Dynamical Friction. *The Astrophysical Journal*, 97:255. Cited on p. 88.

Chandrasekhar, S. (1943b). Dynamical Friction. II. The Rate of Escape of Stars from Clusters and the Evidence for the Operation of Dynamical Friction. *The Astrophysical Journal*, 97:263. Cited on p. 88.

Chandrasekhar, S. (1943c). Dynamical Friction. III. a More Exact Theory of the Rate of Escape of Stars from Clusters. *The Astrophysical Journal*, 98:54. Cited on p. 88.

Charbonnier, A., Combet, C., Daniel, M., et al. (2011). Dark matter profiles and annihilation in dwarf spheroidal galaxies: prospectives for present and future γ-ray observatories – I. The classical dwarf spheroidal galaxies. *Monthly Notices of the Royal Astronomical Society*, 418(3):1526–1556, `arXiv:1104.0412`. Cited on pp. 21 and 105.

Charbonnier, A., Combet, C., and Maurin, D. (2012). CLUMPY: A code for γ-ray signals from dark matter structures. *Computer Physics Communications*, 183(3):656–668, `arXiv:1201.4728`. Cited on pp. 86, 97, 98, and 99.

Charles, E., Sánchez-Conde, M. Á., Anderson, B., et al. (2016). Sensitivity projections for dark matter searches with the Fermi large area telescope. *Physics Reports*, 636(May):1–46, `arXiv:1605.02016`. Cited on p. 45.

Cherenkov, P. A. (1934). Visible Emission of Clean Liquids by Action of γ-radiation. *Doklady Akademii Nauk SSSR*, 2:451. Cited on p. 58.

Ciotti, L. and Pellegrini, S. (2004). On the use of X-rays to determine dynamical properties of elliptical galaxies. *Monthly Notices of the Royal Astronomical Society*, 350(2):609–614, `arXiv:astro-ph/0401588`. Cited on p. 21.

Cirelli, M., Corcella, G., Hektor, A., et al. (2011). PPPC 4 DM ID: a poor particle physicist cookbook for dark matter indirect detection. *Journal of Cosmology and Astroparticle Physics*, 2011(03):051, `arXiv:1012.4515`. Cited on pp. 40, 41, 97, 123, and 130.

Cirelli, M. and Giesen, G. (2013). Antiprotons from Dark Matter: Current constraints and future sensitivities. *Journal of Cosmology and Astroparticle Physics*, 2013(04):015–015, `arXiv:1301.7079`. Cited on p. 46.

Close-Koenig, T. L. (2001). *Lunatic on a mountain: Fritz Zwicky and the early history of dark matter*. Master's thesis, Saint Mary's University, Halifax. Cited on p. 187.

Close-Koenig, T. L. (2004). *Dark Matters: The Pre-controversial Years of a Contemporary Controversy*. Master's thesis, University of Oslo. Cited on p. 187.

Clowe, D., Bradač, M., Gonzalez, A. H., et al. (2006). A Direct Empirical Proof of the Existence of Dark Matter. *The Astrophysical Journal*, 648(2):L109–L113, `arXiv:astro-ph/0608407`. Cited on pp. 23, 24, and 186.

Clowe, D., Gonzalez, A. H., and Markevitch, M. (2004). Weak-Lensing Mass Reconstruction of the Interacting Cluster 1E 0657−558: Direct Evidence for the Existence of Dark Matter. *The Astrophysical Journal*, 604(2):596–603, `arXiv:astro-ph/0312273`. Cited on p. 23.

Coe, D. (2010). Dark Matter Halo Mass Profiles. `arXiv:1005.0411`. Cited on p. 92.

Combet, C., Maurin, D., Nezri, E., et al. (2012). Decaying dark matter: Stacking analysis of galaxy clusters to improve on current limits. *Physical Review D*, 85(6):063517, `arXiv:1203.1164`. Cited on p. 45.

Conrad, J. (2015). Statistical issues in astrophysical searches for particle dark matter. *Astroparticle Physics*, 62:165–177, `arXiv:1407.6617`. Cited on p. 124.

Conrad, J., Cohen-Tanugi, J., and Strigari, L. E. (2015). WIMP searches with gamma rays in the Fermi era: Challenges, methods and results. *Journal of Experimental and Theoretical Physics*, 121(6):1104–1135, `arXiv:1503.06348`. Cited on pp. 12 and 45.

Copp, C. (1982). Relativistic cosmology I: Paradigm commitment and rationality. *Astronomy Quarterly*, 4(15):103–116. Cited on p. 184.

Cortina, J., López-Coto, R., and Moralejo, A. (2016). MACHETE: A transit imaging atmospheric Cherenkov telescope to survey half of the very high energy γ-ray sky. *Astroparticle Physics*, 72:46–54, `arXiv:1507.02532`. Cited on p. 178.

Courteau, S., Cappellari, M., de Jong, R. S., et al. (2014). Galaxy masses. *Reviews of Modern Physics*, 86(1):47–119, `arXiv:1309.3276`. Cited on p. 20.

Cowan, G., Cranmer, K., Gross, E., et al. (2011). Asymptotic formulae for likelihood-based tests of new physics. *The European Physical Journal C*, 71(2):1–19, `arXiv:1007.1727`. Cited on p. 124.

Cuddeford, P. (1993). On the potentials of galactic discs. *Monthly Notices of the Royal Astronomical Society*, 262(4):1076–1086. Cited on p. 193.

Cuoco, A., Xia, J.-Q., Regis, M., et al. (2015). Dark matter searches in the gamma-ray extragalactic background via cross-correlations with galaxy catalogues. *The Astrophysical Journal Supplement Series*, 221(2):29, `arXiv:1506.01030`. Cited on p. 178.

Cushman, P., Galbiati, C., McKinsey, D. N., et al. (2013). Snowmass CF1 Summary: WIMP Dark Matter Direct Detection. page 47, `arXiv:1310.8327`. Cited on p. 47.

Cyr-Racine, F.-Y., Moustakas, L. A., Keeton, C. R., et al. (2016). Dark census: Statistically detecting the satellite populations of distant galaxies. *Physical Review D*, 94(4):043505, `arXiv:1506.01724`. Cited on p. 24.

da Silva, R. L., Krumholz, M. R., Fumagalli, M., et al. (2014). An analytic method to compute star cluster luminosity statistics. *Monthly Notices of the Royal Astronomical Society*, 438(3):2355–2370. Cited on p. 214.

D'Amico, G., Kamionkowski, M., and Sigurdson, K. (2011). Dark Matter Astrophysics. In Matarrese, S., Colpi, M., Gorini, V., et al., editors. *Dark Matter and Dark Energy*, pages 241–272, `arXiv:0907.1912`. Cited on pp. 23 and 48.

Davies, J. M. and Cotton, E. S. (1957). Design of the quartermaster solar furnace. *Solar Energy*, 1(2-3):16–22. Cited on p. 67.

Daylan, T., Finkbeiner, D. P., Hooper, D., et al. (2016). The characterization of the gamma-ray signal from the central Milky Way: A case for annihilating dark matter. *Physics of the Dark Universe*, 12:1–23, `arXiv:1402.6703`. Cited on p. 45.

Dehnen, W. and Binney, J. J. (1998). Mass models of the Milky Way. *Monthly Notices of the Royal Astronomical Society*, 294(3):429–438, `arXiv:astro-ph/9612059`. Cited on p. 20.

Del Popolo, A., Lima, J., Fabris, J. C., et al. (2014). A unified solution to the small scale problems of the ΛCDM model. *Journal of Cosmology and Astroparticle Physics*, 2014(04):021, `arXiv:1404.3674`. Cited on p. 94.

Denisse, J.-F., Lequeux, J., and Le Roux, E. (1957). Nouvelles observations du rayonnement du ciel sur la longueur d'onde 33 cm. *Comptes Rendus de l'Académie des Sciences*, 244:3030–3033. Cited on p. 189.

Dermer, C. D. (2007). The Extragalactic γ-ray Background. *AIP Conference Proceedings*, 921:122–126, `arXiv:0704.2888`. Cited on pp. 13 and 134.

Di Mauro, M. (2016a). Isotropic diffuse and extragalactic γ-ray background: emission from extragalactic sources vs dark matter annihilating particles. *Journal of Physics: Conference Series*, 718:042019, `arXiv:1601.04322`. Cited on p. 137.

Di Mauro, M. (2016b). The origin of the Fermi-LAT γ-ray background. `arXiv:1601.04323`. Cited on p. 136.

Di Mauro, M., Calore, F., Donato, F., et al. (2014a). Diffuse γ-ray emission from misaligned active galactic nuclei. *The Astrophysical Journal*, 780(2):161, `arXiv:1304.0908`. Cited on p. 136.

Di Mauro, M., Cuoco, A., Donato, F., et al. (2014b). Fermi-LAT γ-ray anisotropy and intensity explained by unresolved radio-loud active galactic nuclei. *Journal of Cosmology and Astroparticle Physics*, 2014(11):021, `arXiv:1407.3275`. Cited on p. 164.

Di Mauro, M. and Donato, F. (2015). Composition of the Fermi-LAT isotropic gamma-ray background intensity: Emission from extragalactic point sources and dark matter annihilations. *Physical Review D*, 91(12):123001, `arXiv:1501.05316`. Cited on p. 137.

Di Mauro, M., Donato, F., Fornengo, N., et al. (2014c). Interpretation of AMS-02 electrons and positrons data. *Journal of Cosmology and Astroparticle Physics*, 2014(04):006, `arXiv:1402.0321`. Cited on p. 171.

Díaz-Vélez, J. C., Fiorino, D. W., Desiati, P., et al. (2015). Full-Sky Analysis of Cosmic-Ray Anisotropy with IceCube and HAWC. *Proceedings of the 34th International Cosmic Ray Conference*, `arXiv:1510.04134`. Cited on p. 171.

Diemand, J., Kuhlen, M., and Madau, P. (2007). Formation and Evolution of Galaxy Dark Matter Halos and Their Substructure. *The Astrophysical Journal*, 667(2):859–877, `arXiv:astro-ph/0703337`. Cited on pp. 83 and 88.

Diemand, J., Kuhlen, M., Madau, P., et al. (2008). Clumps and streams in the local dark matter distribution. *Nature*, 454(7205):735–738, `arXiv:0805.1244`. Cited on pp. 12, 83, 84, 90, 95, 130, 207, and 239.

Diemer, B. and Kravtsov, A. V. (2015). A universal model for halo concentrations. *The Astrophysical Journal*, 799(1):108, `arXiv:1407.4730`. Cited on p. 87.

Djouadi, A., Rosier-Lees, S., Bezouh, M., et al. (1999). The Minimal Supersymmetric Standard Model: Group Summary Report. `arXiv:hep-ph/9901246`. Cited on pp. 38 and 39.

Dodelson, S. (2003). *Modern cosmology*. Academic Press, Amsterdam. Cited on p. 28.

Dodelson, S. and Widrow, L. M. (1994). Sterile neutrinos as dark matter. *Physical Review Letters*, 72(1):17–20, `arXiv:hep-ph/9303287`. Cited on p. 30.

Domínguez, A., Finke, J. D., Prada, F., et al. (2013). Detection of the cosmic γ-ray horizon from multiwavelength observations of blazars. *The Astrophysical Journal*, 770(1):77, `arXiv:1305.2162`. Cited on p. 135.

Domínguez, R., Fellhauer, M., Blaña, M., et al. (2016). Could Segue 1 be a destroyed star cluster? – A dynamical perspective. *Monthly Notices of the Royal Astronomical Society*, 461(4):3630–3638, `arXiv:1606.08778`. Cited on pp. 127 and 175.

Donato, F., Fornengo, N., Maurin, D., et al. (2004). Antiprotons in cosmic rays from neutralino annihilation. *Physical Review D*, 69(6):063501, `arXiv:astro-ph/0306207`. Cited on p. 46.

Doro, M. (2011). CTA – A project for a new generation of Cherenkov telescopes. *Nuclear Instruments and Methods in Physics Research Section A: Accelerators, Spectrometers, Detectors and Associated Equipment*, 630(1):285–290, `arXiv:0908.1410`. Cited on p. 65.

Doroshkevich, A. and Novikov, I. (1964). Mean Density of Radiation in the Metagalaxy and Certain Problems in Relativistic Cosmology. *Soviet Physics Doklady*, 9:111. Cited on p. 189.

Drlica-Wagner, A., Albert, A., Bechtol, K., et al. (2015). Search for Gamma-Ray Emission from DES Dwarf Spheroidal Galaxy Candidates with Fermi-LAT Data. *The Astrophysical Journal*, 809(1):L4, `arXiv:1503.02632`. Cited on p. 45.

Dubus, G., Contreras, J., Funk, S., et al. (2013). Surveys with the Cherenkov Telescope Array. *Astroparticle Physics*, 43:317–330, `arXiv:1208.5686`. Cited on pp. 110, 113, 114, 115, 116, and 216.

Dye, S., Evans, N. W., Belokurov, V., et al. (2008). Models of the Cosmic Horseshoe gravitational lens J10044112. *Monthly Notices of the Royal Astronomical Society*, 388(1):384–392, `arXiv:0804.4002`. Cited on p. 23.

Edsjö, J. (1997). Aspects of Neutrino Detection of Neutralino Dark Matter. *PhD thesis, Uppsala University*, `arXiv:hep-ph/9704384`. Cited on p. 35.

Edsjö, J. and Gondolo, P. (1997). Neutralino relic density including coannihilations. *Physical Review D*, 56(4):1879–1894, `arXiv:hep-ph/9704361`. Cited on p. 33.

Efstathiou, G. and Bond, J. R. (1986). Microwave Background Fluctuations and Dark Matter. *Philosophical Transactions of the Royal Society A: Mathematical, Physical and Engineering Sciences*, 320(1556):585–594. Cited on p. 26.

Einasto, J. (1965). On the Construction of a Composite Model for the Galaxy and on the Determination of the System of Galactic Parameters. *Trudy Astrofizicheskogo Instituta Alma-Ata*, 5:87–100. Cited on pp. 85 and 204.

Einasto, J. (2009). Dark Matter. `arXiv:0901.0632`. Cited on p. 11.

Ellis, J. and Olive, K. A. (2010). Supersymmetric Dark Matter Candidates. In Bertone, G., editor. *Particle Dark Matter. Observations, Models and Searches*, pages 142–163, `arXiv:1001.3651`. Cited on p. 37.

Engel, R., Heck, D., and Pierog, T. (2011). Extensive Air Showers and Hadronic Interactions at High Energy. *Annual Review of Nuclear and Particle Science*, 61(1):467–489. Cited on p. 63.

Erickcek, A. L. and Law, N. M. (2011). Astrometric Microlensing by Local Dark Matter Subhalos. *The Astrophysical Journal*, 729(1):49, `arXiv:1007.4228`. Cited on pp. 24 and 178.

Essig, R., Manalaysay, A., Mardon, J., et al. (2012). First Direct Detection Limits on Sub-GeV Dark Matter from XENON10. *Physical Review Letters*, 109(2):021301, `arXiv:1206.2644`. Cited on p. 46.

Falk, T., Olive, K. A., and Srednicki, M. (1994). Heavy sneutrinos as dark matter. *Physics Letters B*, 339(3):248–251, `arXiv:hep-ph/9409270`. Cited on p. 34.

Famaey, B. (2015). Dark Matter in the Milky Way. `arXiv:1501.01788v1`. Cited on p. 85.

Fedorova, E., Sliusar, V. M., Zhdanov, V. I., et al. (2016). Gravitational microlensing as a probe for dark matter clumps. *Monthly Notices of the Royal Astronomical Society*, 457(4):4147–4159, `arXiv:1601.07428`. Cited on p. 24.

Fegan, D. (1996). The art and power of Čerenkov imaging. *Space Science Reviews*, 75(1-2):137–151. Cited on pp. 61 and 69.

Feng, J. L., Kaplinghat, M., and Yu, H.-B. (2010). Sommerfeld enhancements for thermal relic dark matter. *Physical Review D*, 82(8):083525, `arXiv:1005.4678`. Cited on p. 34.

Ferrer, F. and Hunter, D. R. (2013). The impact of the phase-space density on the indirect detection of dark matter. *Journal of Cosmology and Astroparticle Physics*, 2013(09):005, `arXiv:1306.6586`. Cited on p. 205.

Feyereisen, M. R., Ando, S., and Lee, S. K. (2015). Modelling the flux distribution function of the extragalactic gamma-ray background from dark matter annihilation. *Journal of Cosmology and Astroparticle Physics*, 2015(09):027, `arXiv:1506.05118`. Cited on p. 177.

Flynn, C., Holmberg, J., Portinari, L., et al. (2006). On the mass-to-light ratio of the local Galactic disc and the optical luminosity of the Galaxy. *Monthly Notices of the Royal Astronomical Society*, 372(3):1149–1160, `arXiv:astro-ph/0608193`. Cited on p. 182.

Forman, P. (1987). Behind Quantum Electronics: National Security as Basis for Physical Research in the United States, 1940-1960. *Historical Studies in the Physical and Biological Sciences*, 18(1):149–229. Cited on p. 188.

Fornasa, M., Cuoco, A., Zavala, J., et al. (2016). Angular power spectrum of the diffuse gamma-ray emission as measured by the Fermi Large Area Telescope and constraints on its dark matter interpretation. *Physical Review D*, 94(12):123005, `arXiv:1608.07289`. Cited on pp. 13, 45, 133, 137, 154, 158, 165, and 176.

Fornasa, M. and Sánchez-Conde, M. Á. (2015). The nature of the Diffuse Gamma-Ray Background. *Physics Reports*, 598:1–58, `arXiv:1502.02866`. Cited on pp. 136 and 137.

Fornasa, M., Zavala, J., Sánchez-Conde, M. Á., et al. (2013). Characterization of dark-matter-induced anisotropies in the diffuse gamma-ray background. *Monthly Notices of the Royal Astronomical Society*, 429(2):1529–1553, `arXiv:1207.0502`. Cited on pp. 13, 40, 85, 147, 149, 164, 177, and 178.

Fornengo, N. and Regis, M. (2014). Particle dark matter searches in the anisotropic sky. *Frontiers in Physics*, 2(February):16, `arXiv:1312.4835`. Cited on p. 178.

Fortin, J.-F. and Tait, T. M. P. (2012). Collider constraints on dipole-interacting dark matter. *Physical Review D*, 85(6):063506, `arXiv:1103.3289`. Cited on p. 35.

Fox, P. J., Harnik, R., Kopp, J., et al. (2012). Missing energy signatures of dark matter at the LHC. *Physical Review D*, 85(5):056011, `arXiv:1109.4398`. Cited on p. 48.

Franceschini, A., Rodighiero, G., and Vaccari, M. (2008). Extragalactic optical-infrared background radiation, its time evolution and the cosmic photon-photon opacity. *Astronomy & Astrophysics*, 487(3):837–852, `arXiv:0805.1841`. Cited on p. 135.

Fréchet, M. (1928). Sur la loi de probabilité de l'écart maximum. *Annales de la Société Polonaise de Mathématique*, 6. Cited on p. 213.

Freeman, K. C. (1970). On the Disks of Spiral and so Galaxies. *The Astrophysical Journal*, 160(June):811. Cited on p. 18.

Funk, S. (2015). Ground- and Space-Based Gamma-Ray Astronomy. *Annual Review of Nuclear and Particle Science*, 65(1):245–277, `arXiv:1508.05190`. Cited on p. 12.

Funk, S. and Hinton, J. (2013). Comparison of Fermi-LAT and CTA in the region between 10–100GeV. *Astroparticle Physics*, 43:348–355, `arXiv:1205.0832`. Cited on p. 79.

Gammaldi, V., Cembranos, J., de la Cruz-Dombriz, A., et al. (2015). Gamma-ray and Neutrino Fluxes from Heavy Dark Matter in the Galactic Center. *Physics Procedia*, 61:694–703, `arXiv:1404.2067`. Cited on p. 178.

Gan, J., Kang, X., Van Den Bosch, F. C., et al. (2010). An improved model for the dynamical evolution of dark matter subhaloes. *Monthly Notices of the Royal Astronomical Society*, 408(4):2201–2212, `arXiv:1007.0023`. Cited on pp. 87 and 88.

Gao, L., Navarro, J. F., Frenk, C. S., et al. (2012). The Phoenix Project: the dark side of rich Galaxy clusters. *Monthly Notices of the Royal Astronomical Society*, 425(3):2169–2186, `arXiv:1201.1940`. Cited on pp. 84, 87, and 95.

Gao, L., White, S. D. M., Jenkins, A., et al. (2004). The subhalo populations of ΛCDM dark haloes. *Monthly Notices of the Royal Astronomical Society*, 355(3):819–834, `arXiv:astro-ph/0404589`. Cited on pp. 87, 95, and 210.

Garbari, S., Liu, C., Read, J. I., et al. (2012). A new determination of the local dark matter density from the kinematics of K dwarfs. *Monthly Notices of the Royal Astronomical Society*, 425(2):1445–1458, `arXiv:1206.0015`. Cited on p. 85.

Gardner, J. P., Mather, J. C., Clampin, M., et al. (2006). The James Webb Space Telescope. *Space Science Reviews*, 123(4):485–606, `arXiv:astro-ph/0606175`. Cited on p. 178.

Gentile, G., Salucci, P., Klein, U., et al. (2004). The cored distribution of dark matter in spiral galaxies. *Monthly Notices of the Royal Astronomical Society*, 351(3):903–922, `arXiv:0403154`. Cited on p. 86.

Geringer-Sameth, A., Koushiappas, S. M., and Walker, M. (2015). Dwarf galaxy annihilation and decay emission profiles for dark matter experiments. *The Astrophysical Journal*, 801(2):74, `arXiv:1408.0002`. Cited on pp. 21 and 44.

Giacchino, F., Lopez-Honorez, L., and Tytgat, M. H. (2014). Bremsstrahlung and gamma ray lines in 3 scenarios of dark matter annihilation. *Journal of Cosmology and Astroparticle Physics*, 2014(08):046, `arXiv:1405.6921`. Cited on p. 38.

Giesen, G. (2015). AMS-02 antiprotons, at last! Secondary astrophysical component and immediate implications for Dark Matter. *Journal of Cosmology and Astroparticle Physics*, 2015(09):12, `arXiv:1504.04276`. Cited on p. 46.

Giocoli, C., Tormen, G., Sheth, R. K., et al. (2010). The substructure hierarchy in dark matter haloes. *Monthly Notices of the Royal Astronomical Society*, 404(1):502–517, `arXiv:0911.0436`. Cited on pp. 87 and 92.

Giuliani, A. (2011). Dark Matter Direct and Indirect Detection. In Matarrese, S., Colpi, M., Gorini, V., et al., editors. *Dark Matter and Dark Energy*, pages 295–328. Cited on p. 36.

Gómez-Vargas, G., Cuoco, A., Linden, T., et al. (2014). Dark matter implications of Fermi-LAT measurement of anisotropies in the diffuse gamma-ray background. *Nuclear Instruments and Methods in Physics Research Section A: Accelerators, Spectrometers, Detectors and Associated Equipment*, 742:149–153, `arXiv:1303.2154`. Cited on pp. 45 and 137.

Gondolo, P., Edsjö, J., Ullio, P., et al. (2004). DarkSUSY: computing supersymmetric dark matter properties numerically. *Journal of Cosmology and Astroparticle Physics*, 2004(07):008, `arXiv:astro-ph/0406204`. Cited on p. 38.

Goodman, J., Ibe, M., Rajaraman, A., et al. (2010). Constraints on dark matter from colliders. *Physical Review D*, 82(11):116010, `arXiv:1008.1783`. Cited on p. 48.

Górski, K. M., Hivon, E., Banday, A. J., et al. (2005). HEALPix: A Framework for High-Resolution Discretization and Fast Analysis of Data Distributed on the Sphere. *The Astrophysical Journal*, 622(2):759–771, `arXiv:astro-ph/0409513`. Cited on pp. 97, 114, and 139.

Graham, D. (2010). *The Texts of Early Greek Philosophy: The Complete Fragments and Selected Testimonies of the Major Presocratics*, volume 1. Cambridge University Press, Cambridge. Cited on p. 83.

Green, A. M., Hofmann, S., and Schwarz, D. J. (2004). The power spectrum of SUSY-CDM on subgalactic scales. *Monthly Notices of the Royal Astronomical Society*, 353(3):L23–L27, `arXiv:astro-ph/0309621`. Cited on pp. 28 and 87.

Grieder, P. K. (2010). *Extensive Air Showers*. Springer, Heidelberg. Cited on pp. 50, 52, 53, 58, 61, and 64.

Griest, K. and Kamionkowski, M. (1990). Unitarity limits on the mass and radius of dark-matter particles. *Physical Review Letters*, 64(6):615–618. Cited on p. 32.

Griest, K. and Seckel, D. (1991). Three exceptions in the calculation of relic abundances. *Physical Review D*, 43(10):3191–3203. Cited on p. 33.

Grillo, C. (2012). On the average density profile of dark-matter halos in the inner regions of massive early-type galaxies. *The Astrophysical Journal*, 747(1):L15, `arXiv:1202.3791`. Cited on p. 23.

Gross, E. and Vitells, O. (2010). Trial factors for the look elsewhere effect in high energy physics. *The European Physical Journal C*, 70(1-2):525–530, `arXiv:1005.1891`. Cited on p. 123.

Guenette, R. (2010). *VERITAS observations of galactic compact objects*. PhD thesis, McGill University. Cited on p. 51.

Gupta, A., Mathur, S., Krongold, Y., et al. (2012). A huge reservoir of ionized gas around the Milky Way: Accounting for the Missing Mass? *The Astrophysical Journal*, 756(1):L8, `arXiv:1205.5037`. Cited on p. 20.

Han, J., Cole, S., Frenk, C. S., et al. (2016). A unified model for the spatial and mass distribution of subhaloes. *Monthly Notices of the Royal Astronomical Society*, 457(2):1208–1223, `arXiv:1509.02175`. Cited on pp. 87 and 95.

Hansen, M. J. (2011). Parmenides B6.1–2 without a Modal Fallacy. *Aporia*, 21(1). Cited on p. 83.

Hayashi, K., Ichikawa, K., Matsumoto, S., et al. (2016). Dark matter annihilation and decay from non-spherical dark halos in galactic dwarf satellites. *Monthly Notices of the Royal Astronomical Society*, 461(3):2914–2928, `arXiv:1603.08046`. Cited on pp. 106 and 175.

Heck, D., Knapp, J., Capdevielle, J., et al. (1998). *CORSIKA: a Monte Carlo code to simulate extensive air showers*. TIB Hannover, Hannover. Cited on p. 68.

Hegel, G. W. F. (1820). *Grundlinien der Philosophie des Rechts. Naturrecht und Staatswissenschaft im Grundrisse*. Nicolai, Berlin. Cited on p. 83.

Hernquist, L. (1990). An analytical model for spherical galaxies and bulges. *The Astrophysical Journal*, 356(9):359. Cited on p. 203.

Hessman, F. V. (2015). The difficulty of measuring the local dark matter density. *Astronomy & Astrophysics*, 579:A123, `arXiv:1506.00384`. Cited on p. 85.

Hezaveh, Y. D., Dalal, N., Marrone, D. P., et al. (2016). Detection of lensing substructure using ALMA observations of the dusty galaxy SDP.81. *The Astrophysical Journal*, 823(1):37, `arXiv:1601.01388`. Cited on p. 24.

High, F. W., Hoekstra, H., Leethochawalit, N., et al. (2012). Weak-Lensing Mass Measurements of Five Galaxy Clusters in the South Pole Telescope Survey Using Magellan/Megacam. *The Astrophysical Journal*, 758(1):68, `arXiv:1205.3103`. Cited on p. 24.

Hillas, A. M. (1985). Cerenkov light images of EAS produced by primary gamma. *Proceedings of the 19th International Cosmic Ray Conference*, (3):445–448. Cited on p. 69.

Hillas, A. M. (1996). Differences between gamma-ray and hadronic showers. *Space Science Reviews*, 75(1-2):17–30. Cited on p. 60.

Hillas, A. M. (2013). Evolution of ground-based gamma-ray astronomy from the early days to the Cherenkov Telescope Arrays. *Astroparticle Physics*, 43:19–43. Cited on p. 56.

Hinton, J. (2009). Ground-based gamma-ray astronomy with Cherenkov telescopes. *New Journal of Physics*, 11(5):055005, `arXiv:0803.1609`. Cited on p. 71.

Hisano, J., Matsumoto, S., Nojiri, M. M., et al. (2005). Nonperturbative effect on dark matter annihilation and gamma ray signature from the galactic center. *Physical Review D*, 71(6):063528, `arXiv:hep-ph/0412403`. Cited on p. 34.

Hivon, E., Górski, K. M., Netterfield, C. B., et al. (2002). MASTER of the Cosmic Microwave Background Anisotropy Power Spectrum: A Fast Method for Statistical Analysis of Large and Complex Cosmic Microwave Background Data Sets. *The Astrophysical Journal*, 567(1):2–17, `arXiv:astro-ph/0105302`. Cited on p. 142.

Ho, C. M. and Scherrer, R. J. (2013). Anapole dark matter. *Physics Letters B*, 722(4-5):341–346, `arXiv:1211.0503`. Cited on p. 36.

Hofmann, S., Schwarz, D. J., and Stöcker, H. (2001). Damping scales of neutralino cold dark matter. *Physical Review D*, 64(8):083507, `arXiv:astro-ph/0104173`. Cited on p. 28.

Holder, J., Atkins, R., Badran, H., et al. (2006). The first VERITAS telescope. *Astroparticle Physics*, 25(6):391–401, `arXiv:astro-ph/0604119`. Cited on p. 62.

Hooper, D., Blasi, P., and Serpico, P. D. (2009). Pulsars as the sources of high energy cosmic ray positrons. *Journal of Cosmology and Astroparticle Physics*, 2009(01):025, `arXiv:0810.1527`. Cited on p. 171.

Hooper, D. and Linden, T. (2011). Origin of the gamma rays from the Galactic Center. *Physical Review D*, 84(12):123005, `arXiv:1110.0006`. Cited on p. 45.

Horvath, J. E. (2009). Dark matter, dark energy and modern cosmology: the case for a Kuhnian paradigm shift. *Cosmos and History*, 5(2):287–303, `arXiv:0809.2839`. Cited on p. 186.

Hubble, E. and Humason, M. L. (1931). The Velocity-Distance Relation among Extra-Galactic Nebulae. *The Astrophysical Journal*, 74(427):43. Cited on p. 188.

Hütten, M., Combet, C., Maier, G., et al. (2016). Dark matter substructure modelling and sensitivity of the Cherenkov Telescope Array to Galactic dark halos. *Journal of Cosmology and Astroparticle Physics*, 2016(09):047, `arXiv:1606.04898`. Cited on pp. 14, 71, 73, 75, 91, 93, 96, 101, 103, 104, 105, 106, 110, 114, 118, 119, 120, 125, 126, 131, 146, 214, and 224.

Huxley, T. (1893). *Collected Essays*, volume 8. D. Appleton and company, New York. Cited on p. 30.

Ibarra, A., Lamperstorfer, A. S., and Silk, J. (2014). Dark matter annihilations and decays after the AMS-02 positron measurements. *Physical Review D*, 89(6):063539, `arXiv:1309.2570`. Cited on p. 46.

Iocco, F., Pato, M., and Bertone, G. (2015). Evidence for dark matter in the inner Milky Way. *Nature Physics*, 11(3):245–248, `arXiv:1502.03821`. Cited on pp. 18 and 19.

Ishiyama, T. (2014). Hierarchical Formation of Dark Matter Halos and the Free Streaming Scale. *The Astrophysical Journal*, 788(1):27, `arXiv:1404.1650`. Cited on p. 91.

Ishiyama, T., Makino, J., and Ebisuzaki, T. (2010). Gamma-ray Signal from Earth-mass Dark Matter Microhalos. *The Astrophysical Journal*, 723(2):L195–L200, `arXiv:1006.3392`. Cited on p. 91.

Ivezic, Z., Tyson, J. a., Abel, B., et al. (2008). LSST: from Science Drivers to Reference Design and Anticipated Data Products. `arXiv:0805.2366`. Cited on p. 178.

Jackson, J. (1998). *Classical Electrodynamics*. John Wiley & Sons, New York, 3rd edition. Cited on pp. 58 and 59.

Jacob, M. and Wick, G. (1959). On the general theory of collisions for particles with spin. *Annals of Physics*, 7(4):404–428. Cited on p. 32.

Jaffe, W. (1983). A simple model for the distribution of light in spherical galaxies. *Monthly Notices of the Royal Astronomical Society*, 202(4):995–999. Cited on p. 203.

Jeans, J. H. (1922). The Motions of Stars in a Kapteyn-Universe. *Monthly Notices of the Royal Astronomical Society*, 82(3):122–132. Cited on p. 182.

Jin, H.-B., Wu, Y.-L., and Zhou, Y.-F. (2015). Upper limits on dark matter annihilation cross sections from the first AMS-02 antiproton data. *Physical Review D*, 92(5):055027, `arXiv:1504.04604`. Cited on p. 46.

Jungman, G. and Kamionkowski, M. (1995). γ-rays from neutralino annihilation. *Physical Review D*, 51(6):3121–3124, `arXiv:hep-ph/9501365`. Cited on pp. 36 and 38.

Jungman, G., Kamionkowski, M., and Griest, K. (1996). Supersymmetric dark matter. *Physics Reports*, 267(5-6):195–373, `arXiv:hep-ph/9506380`. Cited on pp. 33, 35, and 36.

Kahn, F. D. and Waltjer, L. (1959). Intergalactic Matter and the Galaxy. *The Astrophysical Journal*, 130(4):705. Cited on p. 23.

Kalberla, P. M. and Kerp, J. (2009). The HI Distribution of the Milky Way. *Annual Review of Astronomy and Astrophysics*, 47(1):27–61. Cited on p. 19.

Kamionkowski, M. and Turner, M. S. (1991). Distinctive positron feature from particle dark-matter annihilations in the galatic halo. *Physical Review D*, 43(6):1774–1780. Cited on p. 46.

Kampert, K.-H. and Watson, A. A. (2012). Extensive air showers and ultra high-energy cosmic rays: a historical review. *The European Physical Journal H*, 37(3):359–412, `arXiv:1207.4827`. Cited on p. 56.

Kapteyn, J. C. (1922). First Attempt at a Theory of the Arrangement and Motion of the Sidereal System. *The Astrophysical Journal*, 55:302. Cited on p. 182.

Khaire, V. and Srianand, R. (2015). Star formation history, dust correction, and the extragalactic background light. *The Astrophysical Journal*, 805(1):33. Cited on p. 135.

Knödlseder, J., Mayer, M., Deil, C., et al. (2016). GammaLib and ctools. *Astronomy & Astrophysics*, 593:A1, `arXiv:1606.00393`. Cited on pp. 77, 115, and 121.

Knox, L. (1995). Determination of inflationary observables by cosmic microwave background anisotropy experiments. *Physical Review D*, 52(8):4307–4318. Cited on pp. 141, 142, 144, and 145.

Kolb, E. W. and Slansky, R. (1984). Dimensional reduction in the early universe: Where have the massive particles gone? *Physics Letters B*, 135(5-6):378–382. Cited on p. 30.

Komatsu, E., Wandelt, B. D., Spergel, D. N., et al. (2002). Measurement of the Cosmic Microwave Background Bispectrum on the COBE DMR Sky Maps. *The Astrophysical Journal*, 566(1):19–29, `arXiv:astro-ph/0107605`. Cited on p. 142.

Koopmans, L. V. E., Bolton, A., Treu, T., et al. (2009). The Structure & Dynamics of Massive Early-type Galaxies: On Homology, Isothermality and Isotropy inside one Effective Radius. *The Astrophysical Journal*, 703(1):L51–L54, `arXiv:0906.1349`. Cited on p. 23.

Kragh, H. (1996). *Cosmology and Controversy*. Princeton University Press, Princeton. Cited on pp. 189 and 190.

Kragh, H. (2007). *Conception of Cosmos. From myths to the accelerating universe: A history of cosmology*. Oxford University Press, Oxford. Cited on p. 189.

Kraushaar, W. L., Clark, G. W., Garmire, G. P., et al. (1972). High-Energy Cosmic Gamma-Ray Observations from the OSO-3 Satellite. *The Astrophysical Journal*, 177:341. Cited on p. 135.

Kuhlen, M., Diemand, J., and Madau, P. (2007). The Shapes, Orientation, and Alignment of Galactic Dark Matter Subhalos. *The Astrophysical Journal*, 671(2):1135–1146, `arXiv:0705.2037`. Cited on p. 95.

Kuhlen, M., Diemand, J., and Madau, P. (2008). The Dark Matter Annihilation Signal from Galactic Substructure: Predictions for GLAST. *The Astrophysical Journal*, 686(1):262–278, `arXiv:0805.4416`. Cited on p. 130.

Kuhlen, M., Madau, P., and Silk, J. (2009). Exploring Dark Matter with Milky Way Substructure. *Science*, 325(5943):970–973, `arXiv:0907.0005`. Cited on p. 130.

Kuhlen, M., Vogelsberger, M., and Angulo, R. (2012). Numerical simulations of the dark universe: State of the art and the next decade. *Physics of the Dark Universe*, 1(1-2):50–93, `arXiv:1209.5745`. Cited on p. 84.

Kuhn, T. S. (1962). *The Structure of Scientific Revolutions*. University of Chicago Press, Chicago. Cited on p. 186.

Laine, M. and Schröder, Y. (2006). Quark mass thresholds in QCD thermodynamics. *Physical Review D*, 73(8):085009, `arXiv:hep-ph/0603048`. Cited on pp. 31 and 199.

Lake, G. (1990). High dark matter densities and the formation of extreme dwarf galaxies. *The Astrophysical Journal*, 356:L43. Cited on pp. 12 and 44.

Lange, J. U. and Chu, M.-C. (2014). Can galactic dark matter substructure contribute to the cosmic gamma-ray anisotropy? *Monthly Notices of the Royal Astronomical Society*, 447(1):939–947, `arXiv:1412.5749`. Cited on pp. 45, 147, and 206.

Laplace, P. S. (1812). *Théorie analytique des probabilités.* V. Courcier Imprimeur – Libraire pour les Mathématiques, Paris, 2nd edition. Cited on p. 173.

Laureijs, R., Amiaux, J., Arduini, S., et al. (2011). Euclid Definition Study Report. `arXiv:1110.3193`. Cited on p. 178.

Lee, S. (2010). Spherical collapse model with and without curvature. *Physics Letters B*, 685(2-3):110–114, `arXiv:0909.0826`. Cited on p. 89.

Lee, S. K., Ando, S., and Kamionkowski, M. (2009). The gamma-ray-flux PDF from galactic halo substructure. *Journal of Cosmology and Astroparticle Physics*, 2009(07):007, `arXiv:0810.1284`. Cited on p. 177.

Lefranc, V., Mamon, G. A., and Panci, P. (2016). Prospects for annihilating Dark Matter towards Milky Way's dwarf galaxies by the Cherenkov Telescope Array. *Journal of Cosmology and Astroparticle Physics*, 2016(09):021, `arXiv:1605.02793`. Cited on p. 175.

Lefranc, V. and Moulin, E. (2015). Dark matter search in the inner Galactic halo with H.E.S.S. I and H.E.S.S. II. *Proceedings of the 34th International Cosmic Ray Conference*, `arXiv:1509.04123`. Cited on p. 126.

Lemaître, A. G. (1931). A Homogeneous Universe of Constant Mass and Increasing Radius accounting for the Radial Velocity of Extra-galactic Nebulae. *Monthly Notices of the Royal Astronomical Society*, 91(5):483–490. Cited on p. 189.

Li, T.-P. and Ma, Y.-Q. (1983). Analysis methods for results in gamma-ray astronomy. *The Astrophysical Journal*, 272:317. Cited on pp. 69, 121, 125, 127, 218, 219, and 244.

Li, X., Shen, Z.-Q., Lu, B.-Q., et al. (2015). 'Excess' of primary cosmic ray electrons. *Physics Letters B*, 749:267–271, `arXiv:1412.1550`. Cited on p. 171.

Linden, T. and Profumo, S. (2013). Probing the Pulsar Origin of the Anomalous Positron Fraction with AMS-02 and Atmospheric Cherenkov Telescopes. *The Astrophysical Journal*, 772(1):18, `arXiv:1304.1791`. Cited on p. 171.

Lokas, E. L. and Mamon, G. A. (2003). Dark matter distribution in the Coma cluster from galaxy kinematics: breaking the mass-anisotropy degeneracy. *Monthly Notices of the Royal Astronomical Society*, 343(2):401–412, `arXiv:astro-ph/0302461`. Cited on p. 22.

Lovell, M. R., Eke, V., Frenk, C. S., et al. (2012). The haloes of bright satellite galaxies in a warm dark matter universe. *Monthly Notices of the Royal Astronomical Society*, 420(3):2318–2324, `arXiv:1104.2929`. Cited on p. 94.

Mabry, R. (1999). Proof without Words: $1/4 + 1/16 + 1/64 + ... = 1/3$. *Mathematics Magazine*, 72(1):63. Cited on p. 49.

Madau, P., Diemand, J., and Kuhlen, M. (2008). Dark Matter Subhalos and the Dwarf Satellites of the Milky Way. *The Astrophysical Journal*, 679(2):1260–1271, `arXiv:0802.2265`. Cited on pp. 94, 95, and 96.

Maier, G. and Knapp, J. (2007). Cosmic-ray events as background in imaging atmospheric Cherenkov telescopes. *Astroparticle Physics*, 28(1):72–81, `arXiv:0704.3567`. Cited on p. 63.

Malkin, Z. M. (2013). Analysis of determinations of the distance between the sun and the galactic center. *Astronomy Reports*, 57(2):128–133, `arXiv:1301.7011`. Cited on p. 86.

Malyshev, D. and Hogg, D. W. (2011). Statistics of gamma-ray point sources below the Fermi detection limit. *The Astrophysical Journal*, 738(2):181, `arXiv:1104.0010`. Cited on p. 177.

Mandelbaum, R. (2014). Galaxy Halo Masses from Weak Gravitational Lensing. *Proceedings of the International Astronomical Union*, 10(S311):86–95, `arXiv:1408.1591`. Cited on p. 24.

Mandelbaum, R., Seljak, U., and Hirata, C. M. (2008). A halo mass–concentration relation from weak lensing. *Journal of Cosmology and Astroparticle Physics*, 2008(08):006, `arXiv:0805.2552`. Cited on p. 23.

Martin, S. P. (2010). A Supersymmetry Primer. *Advanced Series on Directions in High Energy Physics*, 21:1–153, `arXiv:hep-ph/9709356`. Cited on pp. 11, 34, and 35.

Martinez, V. J. and Trimble, V. (2009). Cosmologists in the dark. *Proceedings of the conference "Cosmology across Cultures"*, `arXiv:0904.1126`. Cited on p. 186.

Massó, E., Mohanty, S., and Rao, S. (2009). Dipolar dark matter. *Physical Review D*, 80(3):036009, `arXiv:0906.1979`. Cited on p. 35.

Materne, J. and Tammann, G. A. (1976). On the stability of groups of galaxies and the question of hidden matter. *Stars and galaxies from observational points of view*, (1):455–462. Cited on p. 184.

Mather, J. C., Cheng, E. S., Eplee, R. E., J., et al. (1990). A preliminary measurement of the cosmic microwave background spectrum by the Cosmic Background Explorer (COBE) satellite. *The Astrophysical Journal*, 354(4):L37. Cited on p. 25.

Mathews, W. G. and Brighenti, F. (2003). Stellar Orbits and the Interstellar Gas Temperature in Elliptical Galaxies. *The Astrophysical Journal*, 599(2):992–996, `arXiv:astro-ph/0309367`. Cited on p. 21.

Maxwell, A. J., Wadsley, J., and Couchman, H. M. P. (2015). The Energetics of Cusp Destruction. *The Astrophysical Journal*, 806(2):229, `arXiv:1505.00825`. Cited on p. 94.

Mayer-Hasselwander, H., Bertsch, D., Dingus, B., et al. (1998). High-energy gamma-ray emission from the Galactic Center. *Astronomy & Astrophysics*, 335:161–172. Cited on p. 44.

McMillan, P. J. (2017). The mass distribution and gravitational potential of the Milky Way. *Monthly Notices of the Royal Astronomical Society*, 465(1):76–94, `arXiv:1608.00971`. Cited on p. 20.

Meagher, K. (2015). Six years of VERITAS observations of the Crab. *Proceedings of the 34th International Cosmic Ray Conference*, `arXiv:1508.06442`. Cited on p. 79.

Meegan, C., Lichti, G., Bhat, P. N., et al. (2009). The Fermi Gamma-Ray Burst Monitor. *The Astrophysical Journal*, 702(1):791–804, `arXiv:0908.0450`. Cited on p. 81.

Mellier, Y. (2010). Gravitational lensing and dark matter. In Bertone, G., editor, *Particle Dark Matter. Observations, Models and Searches*, chapter 4, pages 56–82. Cambridge University Press, New York. Cited on p. 23.

Méndez, R. H., Riffeser, A., Kudritzki, R., et al. (2001). Detection, Photometry, and Slitless Radial Velocities of 535 Planetary Nebulae in the Flattened Elliptical Galaxy NGC 4697. *The Astrophysical Journal*, 563(1):135–150, `arXiv:astro-ph/0109075`. Cited on p. 21.

Metcalf, R. B. and Madau, P. (2001). Compound Gravitational Lensing as a Probe of Dark Matter Substructure within Galaxy Halos. *The Astrophysical Journal*, 563(1):9–20, `arXiv:astro-ph/0108224`. Cited on p. 24.

Milgrom, M. (1983). A modification of the Newtonian dynamics as a possible alternative to the hidden mass hypothesis. *The Astrophysical Journal*, 270:365. Cited on pp. 18, 184, and 186.

Miller, R. H. and Prendergast, K. H. (1968). Stellar Dynamics in a Discrete Phase Space. *The Astrophysical Journal*, 151(February):699. Cited on p. 184.

Mirabal, N., Charles, E., Ferrara, E. C., et al. (2016). 3FGL Demographics Outside the Galactic Plane using Supervised Machine Learning: Pulsar and Dark Matter Subhalo Interpretations. *The Astrophysical Journal*, 825(1):69, `arXiv:1605.00711`. Cited on p. 132.

Mirabal, N., Frías-Martinez, V., Hassan, T., et al. (2012). Fermi's sibyl: mining the gamma-ray sky for dark matter subhaloes. *Monthly Notices of the Royal Astronomical Society: Letters*, 424(1):L64–L68, `arXiv:1205.4825`. Cited on p. 132.

Mo, H., van den Bosch, F., and White, S. (2010). *Galaxy Formation and Evolution*. Cambridge University Press, Cambridge. Cited on p. 28.

Mocchiutti, E., Ambriola, M., Bartalucci, S., et al. (2003). Composition of cosmic ray particles in the atmosphere as measured by the CAPRICE98 balloon borne apparatus. *Proceedings of the 28th International Cosmic Ray Conference*, pages 1627–1630. Cited on p. 55.

Molière, G. (1942). Die räumliche und Winkelverteilung der Teilchen in den Luftschauern der Höhenstrahlung. *Die Naturwissenschaften*, 30(5-6):87–89. Cited on p. 52.

Moliné, Á., Sánchez-Conde, M. Á., Palomares-Ruiz, S., et al. (2017). Characterization of subhalo structural properties and implications for dark matter annihilation signals. *Monthly Notices of the Royal Astronomical Society*, 466(4):4974–4990, `arXiv:1603.04057`. Cited on pp. 93, 96, and 103.

Mollitor, P., Nezri, E., and Teyssier, R. (2014). Baryonic and dark matter distribution in cosmological simulations of spiral galaxies. *Monthly Notices of the Royal Astronomical Society*, 447(2):1353–1369, `arXiv:1405.4318`. Cited on pp. 85, 88, and 94.

Moore, B., Quinn, T., Governato, F., et al. (1999). Cold collapse and the core catastrophe. *Monthly Notices of the Royal Astronomical Society*, 310(4):1147–1152, `arXiv:astro-ph/9903164`. Cited on p. 204.

Moustakas, L. A. and Metcalf, R. B. (2003). Detecting dark matter substructure spectroscopically in strong gravitational lenses. *Monthly Notices of the Royal Astronomical Society*, 339(3):607–615, `arXiv:astro-ph/0206176`. Cited on p. 24.

Murase, K., Laha, R., Ando, S., et al. (2015). Testing the Dark Matter Scenario for PeV Neutrinos Observed in IceCube. *Physical Review Letters*, 115(7):071301, `arXiv:1503.04663`. Cited on p. 178.

Navarro, J. F., Frenk, C. S., and White, S. D. M. (1996). The Structure of Cold Dark Matter Halos. *The Astrophysical Journal*, 462:563, `arXiv:astro-ph/9508025`. Cited on pp. 18, 85, 88, 90, 92, and 204.

Navarro, J. F., Ludlow, A., Springel, V., et al. (2010). The diversity and similarity of simulated cold dark matter haloes. *Monthly Notices of the Royal Astronomical Society*, 402(1):21–34, `arXiv:0810.1522`. Cited on p. 85.

Nesti, F. and Salucci, P. (2012). The Local Dark Matter Density. `arXiv:1212.3670`. Cited on p. 85.

Nesti, F. and Salucci, P. (2013). The Dark Matter halo of the Milky Way, AD 2013. *Journal of Cosmology and Astroparticle Physics*, 2013(07):016, `arXiv:1304.5127`. Cited on pp. 20 and 86.

Nezri, E., White, R., Combet, C., et al. (2012). γ-rays from annihilating dark matter in galaxy clusters: stacking versus single source analysis. *Monthly Notices of the Royal Astronomical Society*, 425(1):477–489, `arXiv:1203.1165`. Cited on p. 45.

Oberst, J. L. (2009). *Heidegger on Language and Death: The Intrinsic Connection in Human Existence*. Bloomsbury Publishing, London. Cited on p. 83.

Ohm, E. A. (1961). Receiving System. *Bell System Technical Journal*, 40(4):1065–1094. Cited on p. 189.

Okabe, N. and Smith, G. P. (2016). LoCuSS: weak-lensing mass calibration of galaxy clusters. *Monthly Notices of the Royal Astronomical Society*, 461(4):3794–3821, `arXiv:1507.04493`. Cited on p. 24.

Olive, K. (2014). Review of Particle Physics. *Chinese Physics C*, 38(9):090001. Cited on pp. 54 and 55.

Oort, J. H. (1932). The force exerted by the stellar system in the direction perpendicular to the galactic plane and some related problems. *Bulletin of the Astronomical Institutes of the Netherlands*, 6(238):249–287. Cited on p. 182.

Ostriker, J. P., Peebles, P. J. E., and Yahil, A. (1974). The size and mass of galaxies, and the mass of the universe. *The Astrophysical Journal*, 193:L1. Cited on p. 184.

Owen, G. E. L. (1960). Eleatic Questions. *The Classical Quarterly*, 10(1-2):84. Cited on p. 83.

Padmanabhan, T. (1993). *Structure Formation in the Universe*. Cambridge University Press, Cambridge. Cited on pp. 26 and 27.

Page, L., Barnes, C., Hinshaw, G., et al. (2003). First-Year Wilkinson Microwave Anisotropy Probe (WMAP) Observations: Beam Profiles and Window Functions. *The Astrophysical Journal Supplement Series*, 148(1):39–50, `arXiv:astro-ph/0302214`. Cited on p. 142.

Pareschi, G., Agnetta, G., Antonelli, L. A., et al. (2013). The dual-mirror Small Size Telescope for the Cherenkov Telescope Array. *Proceedings of the 33rd International Cosmic Ray Conference*, `arXiv:1307.4962`. Cited on pp. 65 and 67.

Peebles, P. J. E. (1980). *Large-Scale Structure of the Universe*. Princeton University Press, Princeton. Cited on pp. 26, 89, and 142.

Penzias, A. A. and Wilson, R. W. (1965). A Measurement of Excess Antenna Temperature at 4080 Mc/s. *The Astrophysical Journal*, 142(1):419. Cited on pp. 25 and 189.

Perkins, D. (2003). *Particle Astrophysics*. Oxford Master Series in Physics, Oxford, 1st edition. Cited on p. 54.

Pieri, L., Bertone, G., and Branchini, E. (2008). Dark matter annihilation in substructures revised. *Monthly Notices of the Royal Astronomical Society*, 384(4):1627–1637, `arXiv:0706.2101`. Cited on p. 130.

Pieri, L., Lavalle, J., Bertone, G., et al. (2011). Implications of high-resolution simulations on indirect dark matter searches. *Physical Review D*, 83(2):023518, `arXiv:0908.0195`. Cited on pp. 92, 93, 96, and 130.

Plummer, H. C. (1911). On the Problem of Distribution in Globular Star Clusters. *Monthly Notices of the Royal Astronomical Society*, 71(5):460–470. Cited on p. 203.

Poincaré, H. (1906). The Milky Way and the Theory of Gases. *Popular Astronomy*, 14:475–488. Cited on p. 182.

Poutanen, T., Maino, D., Kurki-Suonio, H., et al. (2004). Cosmic microwave background power spectrum estimation with the destriping technique. *Monthly Notices of the Royal Astronomical Society*, 353(1):43–58, `arXiv:astro-ph/0404134`. Cited on p. 142.

Prada, F., Klypin, A. A., Cuesta, A. J., et al. (2012). Halo concentrations in the standard Λ cold dark matter cosmology. *Monthly Notices of the Royal Astronomical Society*, 423(4):3018–3030, `arXiv:1104.5130`. Cited on pp. 92 and 94.

Press, W. H. and Schechter, P. (1974). Formation of Galaxies and Clusters of Galaxies by Self-Similar Gravitational Condensation. *The Astrophysical Journal*, 187:425. Cited on pp. 28 and 87.

Profumo, S. (2015). An observable electron-positron anisotropy cannot be generated by dark matter. *Journal of Cosmology and Astroparticle Physics*, 2015(02):043, `arXiv:1405.4884`. Cited on p. 171.

Profumo, S. and Jeltema, T. E. (2009). Extragalactic Inverse Compton Light from Dark Matter annihilation and the Pamela positron excess. *Journal of Cosmology and Astroparticle Physics*, 2009(07):020, `arXiv:0906.0001`. Cited on p. 40.

Profumo, S., Sigurdson, K., and Kamionkowski, M. (2006). What Mass Are the Smallest Protohalos? *Physical Review Letters*, 97(3):031301, `arXiv:astro-ph/0603373`. Cited on p. 28.

Prusti, T., de Bruijne, J. H. J., Brown, A. G. A., et al. (2016). The Gaia mission. *Astronomy & Astrophysics*, 595:A1, `arXiv:1609.04153`. Cited on p. 178.

Read, J. I. (2014). The local dark matter density. *Journal of Physics G: Nuclear and Particle Physics*, 41(6):063101, `arXiv:1404.1938`. Cited on p. 85.

Regis, M., Xia, J.-Q., Cuoco, A., et al. (2015). Particle Dark Matter Searches Outside the Local Group. *Physical Review Letters*, 114(24):241301, `arXiv:1503.05922`. Cited on p. 178.

Reinecke, M. and Seljebotn, D. S. (2013). Libsharp – spherical harmonic transforms revisited. *Astronomy & Astrophysics*, 554:A112, `arXiv:1303.4945`. Cited on p. 139.

Retana-Montenegro, E., Van Hese, E., Gentile, G., et al. (2012). Analytical properties of Einasto dark matter haloes. *Astronomy & Astrophysics*, 540:A70, `arXiv:1202.5242`. Cited on pp. 205 and 206.

Rico, J., Wood, M., Drlica-Wagner, A., et al. (2016). Limits to dark matter annihilation cross-section from a combined analysis of MAGIC and Fermi-LAT observations of dwarf satellite galaxies. *Journal of Cosmology and Astroparticle Physics*, 2016(02):039, `arXiv:1508.05827`. Cited on p. 46.

Ripken, J., Cuoco, A., Zechlin, H.-S., et al. (2014). The sensitivity of Cherenkov telescopes to dark matter and astrophysical anisotropies in the diffuse gamma-ray background. *Journal of Cosmology and Astroparticle Physics*, 2014(01):049, `arXiv:1211.6922`. Cited on pp. 13, 73, 74, 111, 133, 143, 149, 163, 164, 176, 228, 229, 230, 231, 232, and 245.

Rix, H.-W. and Bovy, J. (2013). The Milky Way's stellar disk. *The Astronomy and Astrophysics Review*, 21(1):61, `arXiv:1301.3168`. Cited on p. 20.

Romanowsky, A. J., Strader, J., Spitler, L. R., et al. (2009). Mapping the Dark Side with DEIMOS: Globular Clusters, X-ray Gas, and Dark Matter in the NGC 1407 Group. *The Astronomical Journal*, 137(6):4956–4987, `arXiv:0809.2088`. Cited on p. 21.

Rosenberg, L. J. and van Bibber, K. A. (2000). Searches for invisible axions. *Physics Reports*, 325(1):1–39. Cited on p. 30.

Rossi, B. and Greisen, K. (1941). Cosmic-Ray Theory. *Reviews of Modern Physics*, 13(4):240–309. Cited on p. 52.

Roszkowski, L., Sessolo, E. M., and Williams, A. J. (2015). Prospects for dark matter searches in the pMSSM. *Journal of High Energy Physics*, 2015(2):14, `arXiv:1411.5214`. Cited on p. 39.

Rousselle, J., Connaughton, V., Errando, M., et al. (2013). Schwarzschild-Couder telescope for the Cherenkov Telescope Array: development of the optical system. *Proceedings of SPIE*, page 886104, `arXiv:1307.4072`. Cited on p. 67.

Rubin, V. C., Thonnard, N., and Ford, W. K. J. (1980). Rotational properties of 21 SC galaxies with a large range of luminosities and radii, from NGC 4605 (R = 4kpc) to UGC 2885 (R = 122 kpc). *The Astrophysical Journal*, 238:471–487. Cited on pp. 20 and 184.

Rubin, V. C., Thonnard, N., and Ford, W. K., J. (1978). Extended rotation curves of high-luminosity spiral galaxies. IV - Systematic dynamical properties, SA through SC. *The Astrophysical Journal*, 225(3):L107–L111. Cited on pp. 20 and 184.

Sahakian, V., Aharonian, F., and Akhperjanian, A. (2006). Cherenkov light in electron-induced air showers. *Astroparticle Physics*, 25(4):233–241. Cited on p. 53.

Sánchez-Conde, M. Á. and Prada, F. (2014). The flattening of the concentration-mass relation towards low halo masses and its implications for the annihilation signal boost. *Monthly Notices of the Royal Astronomical Society*, 442(3):2271–2277, `arXiv:1312.1729`. Cited on pp. 92, 93, and 96.

Sanders, R. H. (2010). *The Dark Matter Problem: A Historical Perspective*. Cambridge University Press, Cambridge. Cited on p. 184.

Sanders, R. H. (2014). A dearth of dark matter in strong gravitational lenses. *Monthly Notices of the Royal Astronomical Society*, 439(2):1781–1786, `arXiv:1310.6148`. Cited on pp. 23 and 47.

Sawala, T., Frenk, C. S., Fattahi, A., et al. (2016). The APOSTLE simulations: solutions to the Local Group's cosmic puzzles. *Monthly Notices of the Royal Astronomical Society*, 457(2):1931–1943, `arXiv:1511.01098`. Cited on pp. 85, 94, and 95.

Schechter, P. (1976). An analytic expression for the luminosity function for galaxies. *The Astrophysical Journal*, 203:297. Cited on p. 213.

Schneider, A., Smith, R. E., and Reed, D. (2013). Halo mass function and the free streaming scale. *Monthly Notices of the Royal Astronomical Society*, 433(2):1573–1587, `arXiv:1303.0839`. Cited on p. 27.

Schoonenberg, D., Gaskins, J., Bertone, G., et al. (2016). Dark matter subhalos and unidentified sources in the Fermi 3FGL source catalog. *Journal of Cosmology and Astroparticle Physics*, 2016(05):028, `arXiv:1601.06781`. Cited on pp. 12, 130, 131, 132, and 174.

Schwarzschild, M. (1954). Mass distribution and mass-luminosity ratio in galaxies. *The Astronomical Journal*, 59(1220):273. Cited on pp. 183 and 187.

Sersic, J. (1968). *Atlas de galaxias australes*. Cited on pp. 85 and 204.

Sheth, R. K. and Lemson, G. (1999). The forest of merger history trees associated with the formation of dark matter haloes. *Monthly Notices of the Royal Astronomical Society*, 305(4):946–956, `arXiv:astro-ph/9805322`. Cited on p. 28.

Sheth, R. K., Mo, H. J., and Tormen, G. (2001). Ellipsoidal collapse and an improved model for the number and spatial distribution of dark matter haloes. *Monthly Notices of the Royal Astronomical Society*, 323(1):1–12, `arXiv:astro-ph/9907024`. Cited on p. 28.

Shirasaki, M., Horiuchi, S., and Yoshida, N. (2014). Cross correlation of cosmic shear and extragalactic gamma-ray background: Constraints on the dark matter annihilation cross section. *Physical Review D*, 90(6):063502, `arXiv:1404.5503`. Cited on p. 178.

Siegal-Gaskins, J. M. (2008). Revealing dark matter substructure with anisotropies in the diffuse gamma-ray background. *Journal of Cosmology and Astroparticle Physics*, 2008(10):040, `arXiv:0807.1328`. Cited on p. 95.

Siegal-Gaskins, J. M., Reesman, R., Pavlidou, V., et al. (2011). Anisotropies in the gamma-ray sky from millisecond pulsars. *Monthly Notices of the Royal Astronomical Society*, 415(2):1074–1082, `arXiv:1011.5501`. Cited on p. 164.

Silk, J. (1989). Cold dark matter annihilations: A source of gamma rays and antiprotons. *Nuclear Physics B - Proceedings Supplements*, 10(2):108–113. Cited on p. 46.

Silk, J. and Bloemen, H. (1987). A gamma-ray constraint on the nature of dark matter. *The Astrophysical Journal*, 313:L47. Cited on p. 44.

Silk, J. and Stebbins, A. (1993). Clumpy cold dark matter. *The Astrophysical Journal*, 411(1):439. Cited on p. 12.

Simon, J. D. and Geha, M. (2007). The Kinematics of the Ultra-faint Milky Way Satellites: Solving the Missing Satellite Problem. *The Astrophysical Journal*, 670(1):313–331, `arXiv:0706.0516`. Cited on p. 21.

Simon, J. D., Geha, M., Minor, Q. E., et al. (2011). A Complete Spectroscopic Survey of the Milky Way Satellite Segue 1: The Darkest Galaxy. *The Astrophysical Journal*, 733(1):46, `arXiv:1007.4198`. Cited on p. 21.

Sjöstrand, T., Ask, S., Christiansen, J. R., et al. (2015). An introduction to PYTHIA 8.2. *Computer Physics Communications*, 191(1):159–177, `arXiv:1410.3012`. Cited on p. 40.

Smith, S. (1936). The Mass of the Virgo Cluster. *The Astrophysical Journal*, 83(532):23. Cited on p. 183.

Smoot, G. F., Bennett, C. L., Kogut, A., et al. (1992). Structure in the COBE differential microwave radiometer first-year maps. *The Astrophysical Journal*, 396:L1. Cited on p. 26.

Springel, V., Frenk, C. S., and White, S. D. M. (2006). The large-scale structure of the Universe. *Nature*, 440(7088):1137–1144, `arXiv:astro-ph/0604561`. Cited on p. 26.

Springel, V., Wang, J., Vogelsberger, M., et al. (2008a). The Aquarius Project: the subhaloes of galactic haloes. *Monthly Notices of the Royal Astronomical Society*, 391(4):1685–1711, `arXiv:0809.0898`. Cited on pp. 12, 83, 84, 87, 88, 90, 93, 94, 95, 96, 103, and 207.

Springel, V., White, S. D. M., Frenk, C. S., et al. (2008b). Prospects for detecting supersymmetric dark matter in the Galactic halo. *Nature*, 456(7218):73–76, `arXiv:0809.0894`. Cited on pp. 102, 130, 218, and 219.

Springel, V., White, S. D. M., Jenkins, A., et al. (2005). Simulations of the formation, evolution and clustering of galaxies and quasars. *Nature*, 435(7042):629–636, `arXiv:astro-ph/0504097`. Cited on p. 83.

Staszak, D. (2015). A Cosmic-ray Electron Spectrum with VERITAS. *Proceedings of the 34th International Cosmic Ray Conference*, `arXiv:1508.06597`. Cited on pp. 126, 134, and 136.

Stecker, F. (1988). Gamma ray constraints on dark matter reconsidered. *Physics Letters B*, 201(4):529–532. Cited on p. 44.

Steigman, G., Dasgupta, B., and Beacom, J. F. (2012). Precise relic WIMP abundance and its impact on searches for dark matter annihilation. *Physical Review D*, 86(2):023506, `arXiv:1204.3622`. Cited on pp. 32 and 202.

Stoehr, F., White, S. D. M., Springel, V., et al. (2003). Dark matter annihilation in the halo of the Milky Way. *Monthly Notices of the Royal Astronomical Society*, 345(4):1313–1322, `arXiv:astro-ph/0307026`. Cited on p. 130.

Strigari, L. E. (2013). Galactic searches for dark matter. *Physics Reports*, 531(1):1–88, `arXiv:1211.7090`. Cited on pp. 207 and 209.

Strom, R. G. (2013). How was atomic HI ($\lambda = 21$ cm line) in space discovered? *International Journal of Modern Physics: Conference Series*, 23:472–477. Cited on p. 183.

Sunyaev, R. and Zeldovich, Y. B. (1970). Small-Scale Fluctuations in the CMB. *Astrophysics and Space Science*, 6(3):358–376. Cited on p. 23.

Swain, G. and Dence, T. (1998). Archimedes' Quadrature of the Parabola Revisited. *Mathematics Magazine*, 71(2):123. Cited on p. 51.

Szapudi, I., Prunet, S., Pogosyan, D., et al. (2001). Fast Cosmic Microwave Background Analyses via Correlation Functions. *The Astrophysical Journal*, 548(2):L115–L118. Cited on p. 142.

Tamborra, I., Ando, S., and Murase, K. (2014). Star-forming galaxies as the origin of diffuse high-energy backgrounds: gamma-ray and neutrino connections, and implications for starburst history. *Journal of Cosmology and Astroparticle Physics*, 2014(09):043, `arXiv:1404.1189`. Cited on p. 136.

Tamm, I. and Frank, I. (1937). Coherent Radiation of Fast Electrons in a Medium. *Doklady Akad. Nauk SSSR*, 14:107. Cited on p. 59.

Tamura, N., Takato, N., Shimono, A., et al. (2016). Prime Focus Spectrograph (PFS) for the Subaru telescope: overview, recent progress, and future perspectives. *Proceedings of SPIE*, page 99081M, `arXiv:1608.01075`. Cited on p. 179.

Tasitsiomi, A. and Olinto, A. V. (2002). Detectability of neutralino clumps via atmospheric Cherenkov telescopes. *Physical Review D*, 66(8):083006, `arXiv:astro-ph/0206040`. Cited on p. 84.

Taylor, J. E. and Babul, A. (2005). The evolution of substructure in galaxy, group and cluster haloes – III. Comparison with simulations. *Monthly Notices of the Royal Astronomical Society*, 364(2):535–551, `arXiv:astro-ph/0410049`. Cited on p. 88.

Tinker, J., Kravtsov, A. V., Klypin, A., et al. (2008). Toward a Halo Mass Function for Precision Cosmology: The Limits of Universality. *The Astrophysical Journal*, 688(2):709–728, `arXiv:0803.2706`. Cited on p. 28.

Tisserand, P., Le Guillou, L., Afonso, C., et al. (2007). Limits on the MACHO content of the Galactic Halo from the EROS-2 Survey of the Magellanic Clouds. *Astronomy and Astrophysics*, 469(2):387–404, `arXiv:astro-ph/0607207`. Cited on p. 24.

Tolkien, J. R. R. (1937). *The Hobbit or There and Back Again*. George Allen & Unwin, London. Cited on p. 17.

Tremaine, S. (1987). A Historical Perspective on Dark Matter. *Proceedings of the 117th Symposium of the International Astronomical Union, 1985*, pages 547–549. Cited on p. 186.

Treu, T. (2010). Strong Lensing by Galaxies. *Annual Review of Astronomy and Astrophysics*, 48(1):87–125, `arXiv:1003.5567`. Cited on p. 21.

Treu, T., Koopmans, L. V. E., Sand, D. J., et al. (2003). The dark matter halos of spheroidal galaxies and clusters of galaxies. `arXiv:astro-ph/0311052`. Cited on p. 23.

Trimble, V. (1995). Looking backward, darkly. In *AIP Conference Proceedings*, volume 336, pages 57–70. Cited on p. 186.

Trimble, V. (2013). History of Dark Matter in Galaxies. In Oswalt, T. D. and Gilmore, G., editors, *Planets, Stars and Stellar Systems*, volume 5, chapter 21, pages 1091–1118. Springer Netherlands, Dordrecht. Cited on pp. 186 and 188.

Tröster, T., Camera, S., Fornasa, M., et al. (2017). Cross-correlation of weak lensing and gamma rays: implications for the nature of dark matter. *Monthly Notices of the Royal Astronomical Society*, 467(3):2706–2722, `arXiv:1611.03554`. Cited on p. 178.

Undagoitia, T. M. and Rauch, L. (2016). Dark matter direct-detection experiments. *Journal of Physics G: Nuclear and Particle Physics*, 43(1):013001. Cited on p. 46.

Uson, J. M. and Wilkinson, D. T. (1982). Search for Small-Scale Anisotropy in the Cosmic Microwave Background. *Physical Review Letters*, 49(19):1463–1465. Cited on p. 26.

van de Hulst, H. C., Raimond, E., and van Woerden, H. (1957). Rotation and density distribution of the Andromeda nebula derived from observations of the 21-cm line. *Bulletin of the Astronomical Institutes of the Netherlands*, 14(480):1–16. Cited on p. 183.

van der Marel, R. P., Fardal, M., Besla, G., et al. (2012). The M31 Velocity Vector. II. Radial Orbit Towards the Milky Way and Implied Local Group Mass. *The Astrophysical Journal*, 753(1):8, `arXiv:1205.6864`. Cited on p. 23.

Vassiliev, V., Fegan, S., and Brousseau, P. (2007). Wide field aplanatic two-mirror telescopes for ground-based γ-ray astronomy. *Astroparticle Physics*, 28(1):10–27, `arXiv:astro-ph/0612718`. Cited on pp. 67 and 68.

Vercellone, S. (2014). The next generation Cherenkov Telescope Array observatory: CTA. *Nuclear Instruments and Methods in Physics Research Section A: Accelerators, Spectrometers, Detectors and Associated Equipment*, 766:73–77. Cited on pp. 66, 67, and 71.

Viel, M., Becker, G. D., Bolton, J. S., et al. (2013). Warm dark matter as a solution to the small scale crisis: New constraints from high redshift Lyman-α forest data. *Physical Review D*, 88(4):043502, `arXiv:1306.2314`. Cited on p. 27.

Vincent, S. (2015). A Monte Carlo template-based analysis for very high definition imaging atmospheric Cherenkov telescopes as applied to the VERITAS telescope array. *Proceedings of the 34th International Cosmic Ray Conference*, `arXiv:1509.01980`. Cited on p. 69.

Vogl, S. (2014). *Majorana Dark Matter: The Power of Direct, Indirect and Collider Searches*. PhD thesis, TU München. Cited on p. 33.

Völk, H. J. and Bernlöhr, K. (2009). Imaging very high energy gamma-ray telescopes. *Experimental Astronomy*, 25(1-3):173–191, `arXiv:0812.4198`. Cited on pp. 61 and 62.

von Hoerner, S. (1960). Die numerische Integration des n-Körper-Problemes für Sternhaufen, I. *Zeitschrift für Astrophysik*, 50:184–214. Cited on p. 184.

von Hoerner, S. (1963). Die numerische Integration des n-Körper-Problems für Sternhaufen, II. *Zeitschrift für Astrophysik*, 57:47–82. Cited on p. 184.

von Leutsch, E. and Schneidewin, F. W. (1839). *Corpus paroemiographorum Graecorum*, volume 1. G. Olm, Hildesheim. Cited on p. 11.

Wald, A. (1943). Tests of Statistical Hypotheses Concerning Several Parameters When the Number of Observations is Large. *Transactions of the American Mathematical Society*, 54(3):426. Cited on p. 124.

Walker, M. G., Mateo, M., Olszewski, E. W., et al. (2009). A Universal Mass Profile for Dwarf Spheroidal Galaxies? *The Astrophysical Journal*, 704(2):1274–1287, `arXiv:0906.0341`. Cited on p. 21.

Wandelt, B. D., Hivon, E., and Górski, K. M. (2001). Cosmic microwave background anisotropy power spectrum statistics for high precision cosmology. *Physical Review D*, 64(8):083003, `arXiv:astro-ph/0008111`. Cited on p. 142.

Ward, J. E. (2010). *The VERITAS survey of the cygnus region of the galactic plane*. PhD thesis, University College Dublin. Cited on p. 168.

Wechsler, R. H., Bullock, J. S., Primack, J. R., et al. (2002). Concentrations of Dark Halos from Their Assembly Histories. *The Astrophysical Journal*, 568(1):52–70, `arXiv:astro-ph/0108151`. Cited on p. 94.

Weekes, T. C. (2007). Revealing the Dark TeV Sky: The Atmospheric Cherenkov Imaging Technique for Very High Energy Gamma-ray Astronomy. *Energy Budget in the High Energy Universe*, pages 282–302, `arXiv:astro-ph/0606130`. Cited on p. 56.

Weekes, T. C., Cawley, M. F., Fegan, D. J., et al. (1989). Observation of TeV gamma rays from the Crab nebula using the atmospheric Cerenkov imaging technique. *The Astrophysical Journal*, 342:379. Cited on p. 56.

Weinberg, S. (1993). *The first three minutes: a modern view of the origin of the universe*. Flamingo/HarperCollins Publishers, New York. Cited on pp. 181, 188, and 189.

Wetzel, A. R., Hopkins, P. F., Kim, J.-h., et al. (2016). Reconciling dwarf galaxies with ΛCDM cosmology: Simulating a realistic population of satellites around a Milky Way-mass galaxy. *The Astrophysical Journal*, 827(2):L23, `arXiv:1602.05957`. Cited on p. 85.

White, M. (2001). The mass of a halo. *Astronomy and Astrophysics*, 367(1):27–32, `arXiv:astro-ph/0011495`. Cited on p. 92.

White, S. D. M., Frenk, C. S., and Davis, M. (1983). Clustering in a neutrino-dominated universe. *The Astrophysical Journal*, 274(2):L1. Cited on p. 28.

White, S. D. M. and Rees, M. J. (1978). Core condensation in heavy halos: a two-stage theory for galaxy formation and clustering. *Monthly Notices of the Royal Astronomical Society*, 183(3):341–358. Cited on p. 184.

Wilks, S. S. (1938). The Large-Sample Distribution of the Likelihood Ratio for Testing Composite Hypotheses. *The Annals of Mathematical Statistics*, 9(1):60–62. Cited on p. 124.

Wittgenstein, L. (1922). *Tractatus Logico-Philosophicus. Logisch-philosophische Abhandlung.* Routledge & Kegan Paul Ltd., London. Cited on p. 83.

Zackrisson, E. and Riehm, T. (2010). Gravitational Lensing as a Probe of Cold Dark Matter Subhalos. *Advances in Astronomy*, 2010:1–14, `arXiv:0905.4075`. Cited on p. 24.

Zavala, J., Vogelsberger, M., Slatyer, T. R., et al. (2011). Cosmic X-ray and gamma-ray background from dark matter annihilation. *Physical Review D*, 83(12):123513, `arXiv:1103.0776`. Cited on p. 40.

Zechlin, H.-S., Cuoco, A., Donato, F., et al. (2016a). Statistical Measurement of the Gamma-ray Source-count Distribution as a Function of Energy. *The Astrophysical Journal*, 826(2):L31, `arXiv:1605.04256`. Cited on p. 177.

Zechlin, H.-S., Cuoco, A., Donato, F., et al. (2016b). Unveiling the Gamma-ray Source Count Distribution Below the Fermi Detection Limit with Photon Statistics. *The Astrophysical Journal Supplement Series*, 225(2):18, `arXiv:1512.07190`. Cited on p. 177.

Zechlin, H.-S., Fernandes, M. V., Elsässer, D., et al. (2012). Dark matter subhaloes as gamma-ray sources and candidates in the first Fermi-LAT catalogue. *Astronomy & Astrophysics*, 538:A93, `arXiv:1111.3514`. Cited on p. 130.

Zechlin, H.-S. and Horns, D. (2012). Unidentified sources in the Fermi-LAT second source catalog: the case for DM subhalos. *Journal of Cosmology and Astroparticle Physics*, 2012(11):050, `arXiv:1210.3852`. Cited on pp. 12, 130, and 132.

Zhao, H. (1996). Analytical models for galactic nuclei. *Monthly Notices of the Royal Astronomical Society*, 278(2):488–496, `arXiv:astro-ph/9509122`. Cited on pp. 203 and 204.

Zhao, H. (2004). Dynamical friction for dark halo satellites: effects of tidal mass loss and growing host potential. *Monthly Notices of the Royal Astronomical Society*, 351(3):891–902, `arXiv:astro-ph/0403564`. Cited on p. 88.

Zitzer, B. (2015). Search for Dark Matter from Dwarf Galaxies using VERITAS. *Proceedings of the 34th International Cosmic Ray Conference*, `arXiv:1509.01105`. Cited on p. 45.

Zwicky, F. (1933). Die Rotverschiebung von extragalaktischen Nebeln. *Helvetica Physica Acta*, 6:110–127. Cited on pp. 22, 183, and 185.

Zwicky, F. (1937). On the Masses of Nebulae and of Clusters of Nebulae. *The Astrophysical Journal*, 86(3):217. Cited on pp. 22 and 183.

ERKLÄRUNG

Ich erkläre, dass ich die vorliegende Dissertation selbständig und nur unter Verwendung der von mir gemäß § 7 Abs. 3 der Promotionsordnung der Mathematisch-Naturwissenschaftlichen Fakultät, veröffentlicht im Amtlichen Mitteilungsblatt der Humboldt-Universität zu Berlin Nr. 126/2014 am 18.11.2014, angegebenen Hilfsmittel angefertigt habe.

Berlin, den 4.5.2017 ....

Moritz Hütten

Curriculum vitae and publication list

The curriculum vitae and the publication list are not included in the online version of this document.